Springer Series on Polymer and Composite Materials

Vijay Kumar
Babulal Chaudhary
Vishal Sharma
Kartikey Verma *Editors*

Radiation Effects in Polymeric Materials

Springer

Springer Series on Polymer and Composite Materials

Series editor

Susheel Kalia, Army Cadet College Wing, Indian Military Academy, Dehradun, India

More information about this series at http://www.springer.com/series/13173

Vijay Kumar · Babulal Chaudhary ·
Vishal Sharma · Kartikey Verma
Editors

Radiation Effects in Polymeric Materials

Springer

Editors
Vijay Kumar
Department of Physics
National Institute of Technology (NIT)
Srinagar, Jammu and Kashmir, India

Babulal Chaudhary
Indo-US Science and Technology Forum
(IUSSTF)
New Delhi, Delhi, India

Vishal Sharma
Institute for Forensic Science and
Criminology
Panjab University
Chandigarh, India

Kartikey Verma
Department of Chemical Engineering
Indian Institute of Technology
Kanpur, Uttar Pradesh, India

ISSN 2364-1878 ISSN 2364-1886 (electronic)
Springer Series on Polymer and Composite Materials
ISBN 978-3-030-05769-5 ISBN 978-3-030-05770-1 (eBook)
https://doi.org/10.1007/978-3-030-05770-1

Library of Congress Control Number: 2018965431

This Springer imprint is published by the registered company Springer Nature Switzerland AG
The registered company address is: Gewerbestrasse 11, 6330 Cham, Switzerland

Contents

About the Editors

Dr. Vijay Kumar is presently working as an assistant professor, Department of Physics, National Institute of Technology, Srinagar (India). He was a postdoc fellow in Professor Swart's group at the University of the Free State, South Africa, from April 2013 to December 2015. He received his Ph.D. (Physics/Material Science) from Sant Longowal Institute of Engineering and Technology, Longowal (Deemed University). During the last 8 years of his research career, he has published more than 75 research papers in many of the reputed international journals, which attracted more than 2100 citations. He has already edited two books for Springer and Wiley, respectively. He is a reviewer for about 40 international and national professional journals in his field (or in related fields) and active as an editorial board member. He is a leading guest editor of Virtual Special Issue of VACUUM and Materials Today: Proceedings (both Elsevier). He has received the "Teacher with Best Research Contribution Award" (Chandigarh University) and the Young Scientist Award under the fast-track scheme of Department of Science and Technology (Ministry of Science and Technology, Government of India), New Delhi, member of Scientific Advisory Committee for Initiative for Research and Innovation in Science (IRIS). His current research involves the synthesis and spectroscopic investigations of rare earth/transitional metal ions doped nanomaterials, nanocomposites, and hybrid materials to make color-tunable emission in solid-state lighting and white-light LEDs. He is also working on the synthesis and characterization of a biomaterial with electro-conductive properties that could be used in biomedical applications with better biocompatibility.

Dr. Babulal Chaudhary has been working as Scientific Program Officer in Indo-US Science and Technology Forum, New Delhi. He received his B.Sc. in Physics, Chemistry, and Maths; M.Sc. in Electronics from University of Lucknow, Lucknow, Uttar Pradesh, India; and M.Tech. in Electronics and Communication from Uttar Pradesh Technical University, Lucknow. He has obtained his Ph.D. in Physics, from University of Lucknow, Lucknow, Uttar Pradesh, India. His research interests include synthesis, and characterization of thin films, nanocomposites,

carbon-based materials like CNT, graphene oxide (GO), and rGO for energy harvesting and storage. He has published more than 20 research papers in several international journals, along with more than 12 publications in proceedings of international/national conferences.

Dr. Vishal Sharma is presently working as an assistant professor, Institute of Forensic Science and Criminology, Panjab University, Chandigarh (India). He has obtained his Ph.D. degree in Physics discipline from Kurukshetra University, Kurukshetra, India, and Inter University Accelerator Centre (IUAC-an autonomous center of UGC, GOI), New Delhi (India) in 2007. He has performed a series of experiments on Swift Heavy Ions at IUAC. He is the recipient of DAE Young Scientist Research Award in the year 2011. His current research interest is in the study of energy loss and energy loss straggling of heavy Ions in polymers, polymer nanocomposites for different applications, development of inorganic nanoparticles/nanophosphor in latent fingermark and lip mark detection for forensic applications, Chemometrics in forensic science and development of various methods for the analysis of trace exhibits in forensic science. He is the author of over 50 scientific papers and four chapters with maximum impact factor up to 8.5. He has delivered keynote, invited talk, session chair and presented his work in various national and international conferences.

Dr. Kartikey Verma has been working as Young Scientist Fellow (DST Young Scientist Fellow) in Department of Chemical Engineering at Indian Institute of Technology, Kanpur, India. He received his B.Sc. in Physics, Chemistry, and Maths; M.Sc. in Electronics; and Ph.D. in Physics, from University of Lucknow, Lucknow, Uttar Pradesh, India. His research interests include processing, and characterization of thin films, polymer matrix composites, nanocomposites, bio-based polymers, and graphene-based materials for energy harvesting and storage. He has published more than 15 research papers in several international journals, along with more than 20 publications in proceedings of international/national conferences.

Effects of Radiation on the Environment

Gurpreet Kaur and Jandeep Singh

Abstract The origin and existence of life on Earth owe to the presence of radiations that triggered photochemical transformations for sustainable life forms. The classification of radiations into ionizing and non-ionizing radiations, on the basis of interaction with matter, distinguishes their role in the evolution of the environment and its components. With advancement in scientific knowledge, there has been vast development in technological processes that utilize radiations for human benefits. But sometimes radiations pose to be potential risk for environment especially when used as weapon for mass destruction and during human negligence leading to catastrophic disasters.

Keywords Radioactivity · Non-ionizing radiations · Ionizing radiations · Health effects

Abbreviations

EM	Electromagnetic
Js	Joule seconds
UV	Ultraviolet
nm	Nanometer
NIR	Non-ionizing radiation
IR	Infrared
RF	Radio frequency
ELF	Extremely low frequency
Hz	Hertz
μw	Microwave

G. Kaur
Department of Chemistry, Gujranwala Guru Nanak Khalsa College, Civil Lines, Ludhiana 141001, Punjab, India

J. Singh (✉)
Department of Chemistry, Lovely Professional University, Phagwara 144411, Punjab, India
e-mail: singhjandeep@gmail.com

V. Kumar et al. (eds.), *Radiation Effects in Polymeric Materials*, Springer Series on Polymer and Composite Materials, https://doi.org/10.1007/978-3-030-05770-1_1

vis	Visible
EMFs	Electromagnetic fields
GPS	Global positioning systems
NRPB	National Radiological Protection Board
ICNIRP	International Commission on Non-Ionizing Radiation Protection
UNSCEAR	United Nations Scientific Committee on the Effects of Atomic Radiation
CNSC	Canadian Nuclear Safety Commission
SI	System International
HCFCs	Hydrochlorofluorocarbons
CT	Computed tomography
DNA	Deoxyribonucleic acid
RNA	Ribonucleic acid
GCR	Galactic cosmic radiation
RF-EMFs	Radiofrequency electromagnetic fields
NPPs	Nuclear power plants
HFCs	Hydrochlorofluorocarbons
CFCs	Chlorofluorocarbons
VOCs	Volatile organic compounds
NO	Nitrous oxide
CAT	Computed axial tomography
INES	International Nuclear Event Scale

1 Introduction

Nature operates nano-devices that generate and sustain all possible life on Earth, using a clean, free, abundant, and readily available power source, i.e., sunlight. The organisms on Earth have evolved to sense and respond to solar radiation in several ways extending from photosynthesis to circadian rhythms and vision [1–4]. EM fields are omnipresent in today's world since they are interconnected with electronic surveillance systems, electricity, and numerous wireless communications. The EM spectrum is composed of an extensive variety of EM fields, including radio waves, static fields, visible light, UV radiation, and X-rays. The essential characteristics of EM fields are the wavelength and frequency. The lower part of the EM spectrum (low-energy region) is generally referred with respect to the frequency, while the upper end (high-energy portion) is usually represented in the terms of wavelength (Fig. 1). The energy ($\boldsymbol{E}$) of radiation is directly proportional to its frequency (υ) and is described by Planck's law as:

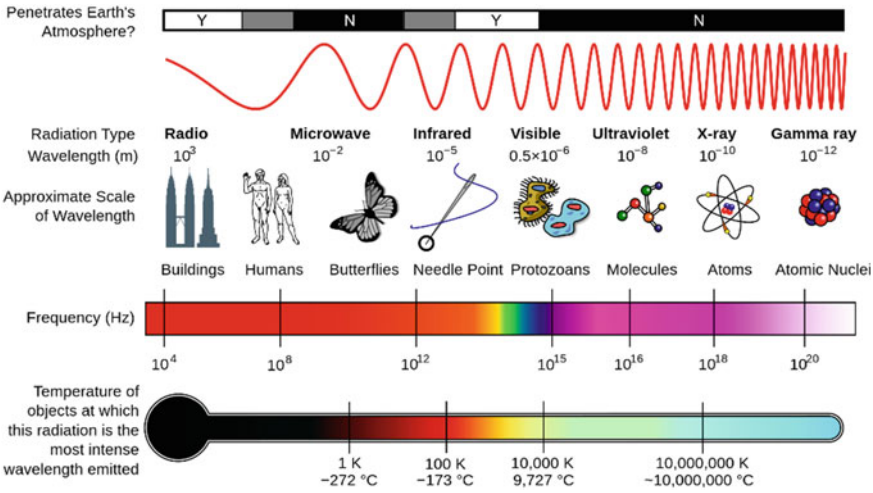

Fig. 1 Correlation between wavelength, frequency, and their corresponding measure

$$\boldsymbol{E} = \boldsymbol{h}\boldsymbol{v} \left(h \text{ is Planck's constant with value } 6.626176 \times 10^{-34} \text{ Js}\right)$$

The EM spectrum is broadly classified, on the basis of interaction with matter, into high-energy ionizing and weak NIR. The ionizing radiations are characterized by their capability to disrupt chemical bonds into its constituent ions. In contrast, the radiation is classified to be non-ionizing, when the energy is feeble to break chemical bonds. The borderline case of ionizing and NIR lies roughly at the higher end of the UV band, i.e., a region of 100–200 nm [5].

2 Discovery of Radioactivity

The discovery of radioactivity seems to have been initiated with the origin of the concept of X-rays by Becquerel that emanated from the portion of bright glowing Crookes tube due to fluorescence or phosphorescence. Marie and Pierre Curie too investigated this property of certain materials and named this phenomenon as radioactivity (Fig. 2). Marie Curie performed many researches on the nature of radioactivity and recognized that the activity of any given material is unaffected by any physical or chemical process like chemical or heat and that the activity of any radioactive salt is directly proportional to the quantity of material [6].

> We must not forget that when radium was discovered no one knew that it would prove useful in hospitals. The work was one of pure science. And this is a proof that scientific

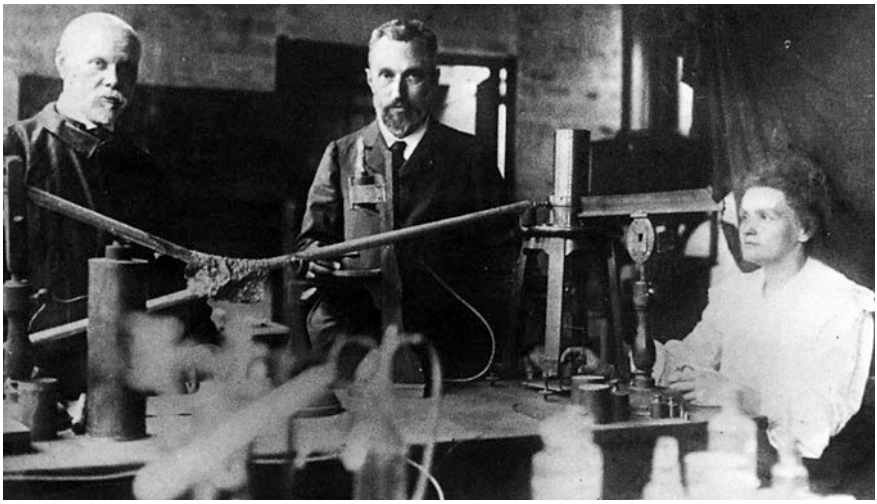

Fig. 2 Marie Curie and Pierre Curie along with Henri Becquerel

> work must not be considered from the point of view of the direct usefulness of it. It must be done for itself, for the beauty of science, and then there is always the chance that a scientific discovery may become like the radium, a benefit for mankind.
>
> —Marie Curie

3 Types and Sources of Radiation

All life has evolved in an environment filled with radiation. The literal meaning of radiation is the type of energy given off from the source of its origin. Thus, radiation can be redefined as the form of energy propagating as particle waves. Some of the high-frequency radiations are gamma, X, and UV rays; while lower energy spectrum includes micro- and radio waves. The high-energy radiations include cosmic, gamma, and X-rays are imperceptible and invisible to human are classified as 'ionizing radiations,' while all low-energy radiations consisting of UV, visible, IR, μw, and radio waves are categorized as 'NIR' and are considered as safe by many scientists at common exposure levels. NIR is further sub-categorized as: (1) ELF energy waves that are produced and emitted by power stations, power lines, and some electrical equipment; and (2) radio and μw frequencies given off by wireless communication technologies, cordless and cellular phones, and some electrical materials [7]. Radiations exist in forms, i.e., (a) non-ionizing and (b) ionizing (Fig. 3). This categorization is based on the energy of radiation for the ability to ionize matter.

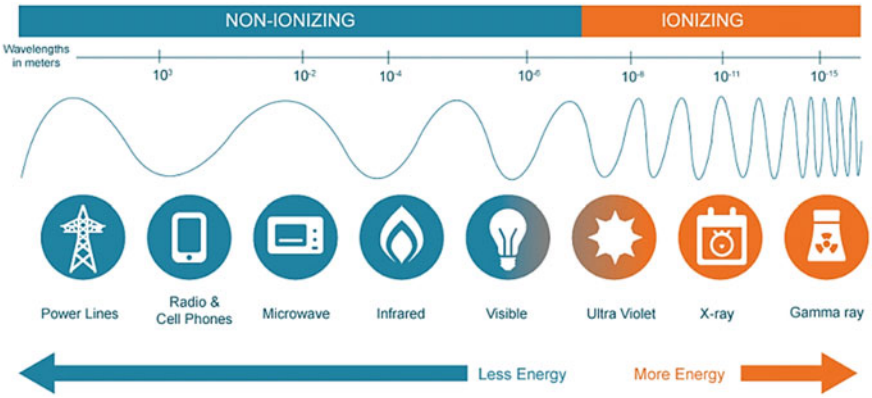

Fig. 3 Distinction between ionizing and non-ionizing radiations on the basis of wavelength

3.1 Non-ionizing Radiations

The sources of origin for NIR can be:

(a) Natural source (from sunlight and lightning discharges).
(b) Man-made source (from wireless communications, medical treatments, industrial applications, and research development).

The band of NIR is essentially further categorized as optical and EM field radiations (Fig. 4). On the basis of energy, the optical radiations have been further sub-categorized into UV, visible, and IR regions; EM fields have been collectively subgrouped into RF region that has μw, very high-frequency and low-frequency radio waves [8, 9].

On the basis of frequency, NIR part of the EM spectrum can be divided into five energy regions [1–5]:

1. Static electric and magnetic fields: 0 Hz.
2. ELF fields: 0–300 Hz.
3. RF and μw radiations: 3×10^{3}–300×10^{6} Hz.

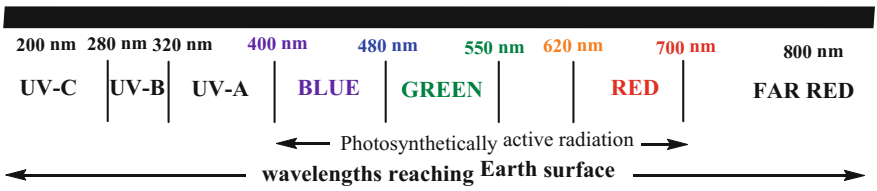

Fig. 4 Optical radiations as a part of NIR

4. Optical radiations: infrared (IR): above 3×10^9–300×10^9 Hz and visible 300×10^9–1.5×10^{12} Hz.
5. UV radiations: 1.5×10^{12}–30×10^{12} Hz.

NIR region comprises the long-range wavelength (>100 nm) having low photonic energy (<12.4 eV) of the EM spectrum, with frequency ranging from 1 to 3×10^{15} Hz. Most forms of NIR are non-perceivable by any of the human senses, unless the intensity is high enough to be felt as heat. Most of the health effects of NIR are dependent upon the penetration power into human body and are frequency-dependent. The optical radiations are the portion of NIR and are formulated under UV–Vis radiations, while those with subsequently lower energies form the part of IR region. The origin of NIR is as follows:

(a) The natural source of UV–visible radiation is the sun.
(b) The man-made sources include oxy-gas welding, arc welding, sunlamps, sterilization (germicidal) lamps lasers (UV), low- and high-pressure gas discharge lamps. Many medical applications utilize UV rays for surgical and neonatal phototherapy, as lasers in physiotherapy heat lamps.
(c) The sources of IR radiation are superheating processes that include synthesis of glass, steelmaking, welding, and lasers (IR) [10–12].

3.1.1 EM Field Radiations

They can be subgrouped into RF region that has μw, very high-frequency and low-frequency radio waves. Most of the electronic gadgets utilize non-ionizing radiations as in GPS, television stations, cellular telephones, radio stations, cordless phones, garage door openers, and in many more devices. In some other forms, ELF and EMF radiations form a part of Earth's magnetic field, along with the magnetic field exposure from nearness to electricity transmission lines, electrical machinery, home appliances, and electric wiring. Moreover, most of the ELF waves do not pose any health risk [13]. Some of the hazardous risks emerging from overexposure of NIR are summarized in Table 1.

The biological effects of NIR exposures significantly depend upon some dominant factors like instance energy, intensity and influx of the incident radiations, characteristics of emission source, distance of source from subject, extent of exposure, prevailing environmental conditions, biological characteristics, and spatial orientation of the radiation-affected tissues (molecular composition, skin coloration). The prolonged exposure of human body to UV rays (from sunlight) can cause acute or chronic health effect on the immune system, eyes and skin, the most common being tanning and sunburn.

The qualitative effect of ELF radiations is insufficient, and most of the data relates IR, visible, and UV radiations to physiological response in animal and plant tissues. The biological effects which are the consequence of tissue heating by RF radiation are referred to as 'thermal' effects. In majority of the cases, biological

Table 1 Effect of continuous exposure to different radiations

Radiation	Wavelength	Biological Effects
	100 nm	Skin – Erythema
UVC		Eye – Photokeratitis
	280 nm	Skin – Erythema
UVB		***Skin cancer***[a]
	315 nm	Eye – Photochemical cataract
UVA		Photosensitive skin reactions
Visible	400 –	Skin – Erythema
	780 nm	***Skin photo–ageing, Skin cancer***[a]
		Eye – Photochemical & thermal retinal injury
IRA		Eye – Thermal retinal injury
IRB		Eye – Thermal retinal injury, thermal cataract
IRC	14 μm	***Skin burn***[a]
		Eye – Corneal burn, cataract
	3 μm	***Skin burn***[a]
	1 mm	Eye Corneal burn, cataract
		Heating of body surface
	1 – 10 cm	Heating of body surface
μw		Heating with penetration depth of 10 mm
	1–10 km	Raised body temperature
Static	100 Mm	Cumulation of charge on body surface Disturbance of nerve & muscle responses Magnetic field vertigo/ nausea
		Electric field charge on body surface

[a]Indicates long-term effect on continuous exposure to the radiations for prolonged time

Adapted from Ref. [13]; open-source content for public information

systems have preventive methods to normalize their body temperature, but in case of intense exposures, the organism can collapse. Today, research is extensively based on low RF radiation levels of exposure from mobile phones and their base stations thereby producing *nonthermal effect*s.

The long-term UV exposure promotes cell degeneration, damage to fibrous tissue and blood vessels that eventually leads to premature skin aging and inflammatory reactions to the eye, such as photokeratitis (as in Table 1). Some of the recent studies prove that with the rise in environmental UV radiation levels, there is alarming risk of contagious diseases. Thus, there is an urgent requirement for creating awareness related to the health hazards due to UV rays and to promote such lifestyle deviations that may inverse the trend in skin cancers [14–16].

3.1.2 RF and μw Radiations

The long wavelength RF radiations transmitted from the towers of mobile base stations have received considerable attention. Most common public locations for exposure are ground-level-facing antennas and the buildings beneath those antennas. NRPB has measured exposure levels at most common public locations around the base stations, and the average exposure levels were found to be 0.00002% of the ICNIRP public exposure guidelines, and maximum levels of exposure were found to be within 0.02% of the permissible limits. The typical power density of radiation exposure was less than 0.0001 $mWcm^{-2}$ (i.e., less than 0.01% of the ICNIRP public exposure guidelines). Moreover, indoor power flux intensity was substantially lower than outdoor power flux density.

The key radiation exposure arising at work, home, or school is measured using electric fields that depends upon the voltage and distance from the source. Any exposure to magnetic fields is a result of some fluctuations in electric power lines and the use of electrical appliances. The electric fields from the power lines are present everywhere and thus expose the whole body, whereas the appliance sources fluctuate and temporarily expose parts of the body [5, 17–20].

3.2 Ionizing Radiation

The radiation in the form of particles (alpha, beta, and neutron particles) or EM waves (X and γ-rays) with distinct energy is capable of ionizing the materials. These radiations have a symbolic representation as shown in Fig. 5. Owing to the difference in energy, these particles and radiations have variable penetrating power, which significantly affects the living tissues (Fig. 6). The more energetic radiations are capable of striking electrons out the orbits from the nucleus. The source of ionizing radiation can be both natural as well as artificial radioactive product and materials. The effect of ionizing radiations along with its destructive power can be understood in details.

Fig. 5 Signatory for potentially disastrous radiations

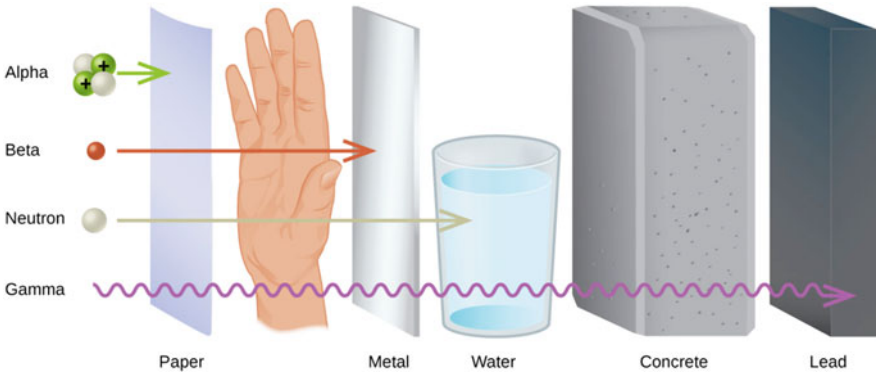

Fig. 6 Penetration power of different types of ionizing radiations

3.2.1 Alpha Radiation (α)

Alpha particles consist of two protons and two neutrons carrying double positive charge (Fig. 7). Owing to the high mass/charge ratio, they have partial ability to penetrate matter. The increase in charge signifies the extended interaction with the surrounding atoms which reduces the energy and hence penetrating power of the particle. Thus, α-particle rays can be blocked even by a thin paper or even the upper layer of human skin and do not tend to have any significant radiation hazard. But in

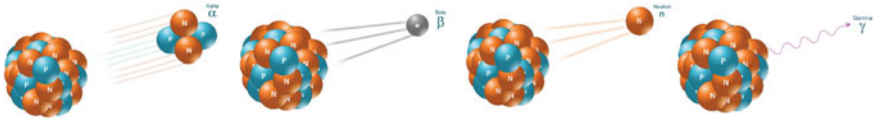

Fig. 7 Formation of alpha particle, beta particle, neutron, and high-energy gamma rays from nucleus

case α-particles from emitted nuclear materials are absorbed inside human body (by inhalation or ingestion), the energy emitted by them is completely absorbed into the bodily tissues, so they are just an internal hazard [5, 6, 11, 21].

3.2.2 Beta Radiation (β)

Beta radiations comprise negatively charged electron-like particles ejected from the nucleus of an atom (Fig. 7). Since β-particles carry less charge (in comparison to alpha particles) and much less mass, they have more charge/mass ratio that provides them higher penetrating power in comparison with α-particles. These particles can easily pass through one/two centimeter(s) of any living tissue but still can be blocked by 1-mm-thick shielding of glass, metal, or plastic. β-particle rays have sufficient energy to penetrate soft outer walls of plants and animals especially humans, and they deposit energy at inner layer of skin that can initiate a disease. In spite of this, β-particles have restricted ability to infiltrate into the deeper tissues and organs of the body. β-particle discharging nuclear materials are hazardous, if present inside the body. For example, if a nuclear emitter like tritium is inhaled, it can cause some internal radiation damage [5, 6, 11, 21].

3.2.3 Neutron Radiation (N)

The spontaneous fission of an unstable nuclide is the natural source of neutrons (*n*) (Fig. 7). One of the highly common neutron sources is the nuclear reactor, where radioactive isotope of uranium or plutonium is split into stable nuclide that is associated with neutron emission. The neutrons, produced by the emission from an unstable nucleus or due to atomic fission or nuclear fusion or has natural occurrence as a constituent of cosmic radiations, have a very high penetrating power. The neutrons have tendency to initiate chain reactions where an emission from a fission bombards the adjacent atomic nucleus and initiates another fission event. The reaction can go on indefinitely until complete consumption of nuclear material. The bombarding of nucleus with photon radiation or alpha particles can too lead to neutron emission. Neutron radiations have the power to infiltrate human tissues and organs, in case of external radiation source. Neutron radiation can be blocked by absorption of hydrogen atoms-rich organic/polymer materials, such as paraffin wax

and plastics, due to alike atomic weights of neutrons and hydrogen atoms and rapid collisions between them [5, 6, 11, 21].

3.2.4 High-Energy Photon Radiation (Gamma [γ] and X-Rays)

The high-energy EM photonic radiation comprises two types of radiations: (a) γ- and (b) X-rays (Fig. 7). The de-excitation of electrons from inner nuclear shells emits γ photonic radiations, while X-rays originate outside the atomic nucleus, and is much lower in energy in comparison with γ-rays. The penetration power of these photonic radiations is very deep, and the reduction in intensity is feasible only by the use of thick dense materials, such as steel or lead. Since X- and γ-rays are high-frequency radiations, they can travel to longer distances un-deflected and easily penetrate all type of tissues and organs, even when in case of external radiation source. These kinds of radiations have devastating effect on the environment, i.e., flora, fauna, and animals. The decay of cobalt-60 (^{60}Co) to nickel-60 (^{60}Ni) is associated with γ photonic ray emission [5, 6, 11, 21].

4 Natural Sources of Ionizing Radiation

Radiations being omnipresent and invisible have created the evolutionary trend in life adapting to the environment in substantial way toward ionizing radiations, creating transformations in human bodies too. The natural occurrence of radioisotopes is a consequence of cosmic rays' interaction with atmospheric molecules. For example, radioisotope of hydrogen, i.e., tritium, is created as a result of cosmic rays' interaction with atmospheric hydrogen gas molecules. But most of the other radioisotopes of thorium and uranium were formed with the origin of Earth from sun and still exist in our environment. The UNSCEAR identifies four major sources of public exposure to natural radiation:

4.1 Radon

Radon is another abundant naturally occurring radioactive gas released from radioactive Earth elements, like uranium present in variable quantities in soils, water, and rocks. Radon is present everywhere and accounts for the largest proportion of our annual average radiation dose, i.e., approximately 56%. The unavoidable and longer exposure to radon gas intensifies the risk of lung cancer [21–24].

4.2 Cosmic Radiation

Cosmic rays are irradiated by ultra-high-energy solar flare radiations and have very high energy that penetrates our atmosphere consistently. The only sources of cosmic rays are galaxies and the sun and, thus, are also known as GCR. Most GCR originates from sources external to our solar system that consists of 98% baryons and 2% electrons. Baryons are the particles that consist of protons (87% of the baryons) and to some extent of helium ions (11%) and heavier ions like carbon and iron, possessing energies in the range of 10^8–10^{20} eV. The cosmic ray interactions also result in cosmogenic radionuclides (e.g., ^{3}H and ^{14}C), which are naturally radioactive. As a result of these interactions, alpha particles, electrons, muons, neutrons, pions (charged and neutral), positrons, protons, and gamma radiations are formed in the air. Several secondary particles are produced by the breakup of cosmic ions and atoms of interstellar and atmospheric gas. The radiation doses from these cosmic rays are greater at higher altitudes, and those traveling regularly by airplane regularly receive an additional dose (discussed in Sect. 7.11) [25, 26].

4.3 Natural Radioactivity in Food

Owing to the existence of radioactive material in soil and oceans, their absorption to our body is in insignificant quantity from soil and water. The incorporation of radioactive material into food is accumulated by plant, which at later stages is passed on to the animals (Fig. 8). The prime contribution to this radiation dose in plants is in the elemental form of potassium-40 (^{40}K) which is an essential element in most of the fruits and vegetables. But due to the limited uptake of potassium in our body, the effects are not amplified.

Ionizing radiations directly influence the basic structures in tissues like DNA, proteins, RNA, and carbohydrates. The photochemical degradation of such molecules produces free radicals, which in turn leads to chain reaction in an organism. The cytochemical effect of overexposure to radiations may be classified as

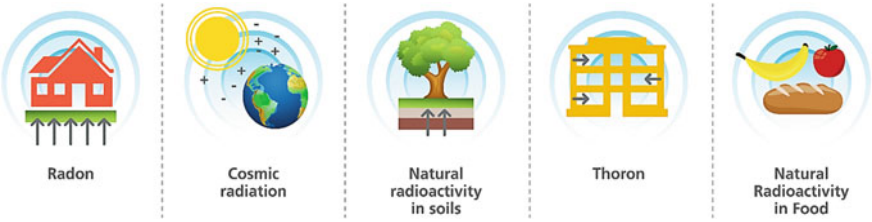

Fig. 8 Natural sources of radioactivity. Adapted from Ref. [33]; open-source content for public information

Table 2 Average public exposures by radiation

Source	Radiation intensity (mSv)
Natural sources	
Food	0.29
Cosmic	0.39
Soil	0.48
Radon	1.3
Artificial sources	
Nuclear power plants	0.0002
Chernobyl accident	0.002
Weapons	0.005
Medicine	0.03
Radiology	0.65

deterministic or random leading to cellular damage or in acute case death which is determined by the threshold radiation dose [27, 28]. The amount of radiations received from natural sources are listed in Table 2.

5 Artificial (Man-Made) Sources of Ionizing Radiation

Humans are consistently susceptible to synthetically modified radiation sources which are the result of medical treatment machines and radioactive material-related research and power generation. Most of the radioisotopes are the by-products formed from operative nuclear reactors and radioisotope cyclotrons. The extensive use of radioisotopes in industrial manufacturing, nuclear medicine, and the agriculture makes up most of the synthetic application. The common sources of radiation are as follows.

5.1 Medicine

The highest exploited medical application is X-ray machines to diagnose diseases. The radioactive nuclear isotopes assist in the diagnosis of certain diseases; for, e.g., thyroid-related diagnosis requires the use of iodine-131 (^{131}I) labeled isotope, and diagnostic imaging procedures use technetium-99 (^{99}Tc) as radioactive tracer. The CNSC regulates all these applications related to the use of nuclear products in medicine and its application for biomedical equipment production. Along with it, CNSC also certifies all those reactors and particle accelerators that synthesize such isotopes required for various industrial and medical applications. In industries, the radiation finds its use in nuclear gauges used during laying of roads and in the density gauges that channelize and regulate material flow through pipes.

Radiations

Ionizing	Non-Ionizing
Gamma rays	**Electromagnetic and Radiowaves**
Nuclear Medicine	Magnetic Resonance Imaging
Positron Emission Tomography	
Radiation Therapy	
Single Emission Photon CT	
X - rays	**Ultrasound**
Computer Radiography	Ultrasonography
CT	Echocardiography
Digital Substraction Angiography	Anesthesiology
Fluoroscopy	Angiology
Mammography	Urology
Radiation Therapy	
Duel Energy X-ray Absorptiometry	
Radiography	
Protons	
Proton therapy	

Scheme 1 Medical applications of non-ionizing and ionizing radiations

Sometimes, radioactive nuclides find application in smoke sensors and in dark glowing exit signboards. Some other applications of radiation are listed in Scheme 1 [29–31].

5.2 Nuclear Fuel Cycle

NPPs require radioactive materials like uranium and plutonium to kick up a chain reaction that generates energy to produce steam, which in turn drives turbines for electricity production. NPPs release small and quantified amount of radioactive material to the surrounding environment in a controlled manner. But in most of the cases, the radioactive waste release is regulated to confirm the public dose to be within regulatory limits.

5.3 Atmospheric Testing

The testing of atomic weapons since the World War II till today has released immense concentrations of atmospheric particulate radioactive content, called fallout, into Earth environment, most of which have sedimented on the ground, but

still some percentage it have been incorporated into our biodiversity. Most of the radioactive fallout was decomposed due to short half-lives, but some of the content still continues to decay, and people receive dosages from the radioactive fallout every year but to a much lesser extent [32, 33].

5.4 *Chernobyl Accident*

The night of April 26, 1986, at Chernobyl Nuclear Power Plant, Ukraine, witnessed an explosion that released substantial amount of radioactive content into the atmosphere. The accident uncontrollably released by-products from the decomposition of radioactive uranium-235 (^{235}U) for ten consecutive days. The principal content in radioactivity that disrupted population was the short-lived iodine-131 (^{131}I) and long-lived cesium-137 (^{137}Cs). As per emission amounts, the estimation is that all the xenon gas, about 50% of the iodine and cesium, in Chernobyl from the core of the fourth reactor (almost 192 ton) was released into the environment. The radioactivity spread throughout the atmosphere is still present in our environment [34, 35].

5.5 *Radiation in the Workplace*

People working with instruments using radioactive materials have numerous advantages, especially in education/research, medicine, and industry (Fig. 9). But these people receive radiation doses, which are below the threshold level as shown in Table 3 [33–35].

Fig. 9 Unavoidable radiation exposures. Adapted from Ref. [33]; open-source content for public information

Table 3 Health effect of radiation dosage

Dose (mSv)	Health effect/radiation equivalence
5000 ≥	Immediate death within minutes (found at fourth reactor core of Chernobyl)
5000–2500	Radiation poisoning, nausea, and vomiting
2500–1000	Initiation of cancer to death within few days
1000–500	Risk of cancer is very high; radiation from Fukushima Reactor 2
500–400	Decrease in blood count that returns to normal in few days
400–250	Radiation levels in Fukushima
250–100	Upper limit for radiation emergency workers
100–50	Radiation dose is equivalent to computed axial tomography (CAT)
50–30	Upper limit for radiation workers in disaster management; smoking two cigarette packs in a day
30–10	Average annual radiation exposure for workers of nuclear energy plants
10–7	Average radiation experienced by human in Brazil
7–5	CT scan of chest
5–2	Annual radiation exposure of normal human from atmosphere and soil
2–1	Radiation dose from medical care
1–0.4	Gastrointestinal X-ray scan
0.4–0.1	Radiation gained during one complete trip from New York to Tokyo
0.1–0.05	Chest X-ray scan
0.1–0.01	Standard radiation dose at clearance level; eating a banana

6 Radiation Units

Roentgen: It defines the measurement of energy produced by gamma or X-ray in a cubic centimeter of air. It is abbreviated with the capital 'R'. One milliroentgen, abbreviated 'mR', is one-thousandth of a roentgen. One microroentgen, abbreviated 'μR', is one-millionth of a roentgen.

Radiation Absorbed Dose: It represents the measuring unit for expressing the absorption of all types of ionizing radiations (alpha, beta, gamma, neutrons, etc.) into any medium. It is abbreviated as RAD. One RAD has an equivalence of absorbing 100 ergs of energy per gram of tissue.

Roentgen Equivalent Man: It is the measurement of dose of any type of radiation that has potential biological effect on tissues. It is abbreviated as REM. Since different radiations have variable biological effects, the dosage is represented by 'quality factor' (Q). For example, a person receiving a dosage of gamma radiation will suffer much less damage than a person receiving the same dosage from thermal neutrons, by a factor of three. So thermal neutrons will cause three times more damage than gamma rays. Therefore, thermal neutron radiation has a quality factor of three. The Q factor for a few radiation types is shown in Table 4.

Table 4 Quality factor of various radiations

Radiation type	Quality factor (Q)
β, γ, and X-rays	1
Thermal neutrons	3
Fast n, α, and protons	10
Heavy and recoil nuclei	20

The only dissimilarity among REM and RAD is that the REM measures biological effect of absorbed radiation whereas RAD measures the amount of radiation absorbed by tissue. For general purposes, most physicists agree that the roentgen, RAD, and REM may be considered equivalent.

6.1 SI Units

The measurement of ionizing radiation can be carried out in four different ways and expressed in eight different units. The amount of radiation energy absorbed per kilogram of tissue is called the absorbed dose and is expressed in units called grays (Gy) named after the English physicist and pioneer in radiation biology, Harold Gray. The comparison between absorbed doses of various radiations should be subjected to their potential to cause certain types of biological damage. This weighted dose is called the equivalent dose, which is evaluated in units called sieverts (Sv), named after the Swedish scientist Rolf Sievert. The SI units for radiation measurements are 'grays' and 'sieverts' for absorbed dose and equivalent dose, respectively.

The activity of the source can be determined in the units of disintegrations per second/Curies/Becquerels: the radiation to which an object is exposed in roentgens; the radiation absorbed by the object in units of RAD or Gy; or the radiation dose in units of REM or Sv. The Curie (Ci), originally defined as the activity of one gram of ^{226}Ra, is now defined as 3.7×10^{10} disintegrations per second. The Becquerel (Bq), which is 1 disintegration/s, is the SI unit for activity, and 1 Curie is therefore 3.700×10^{10} Bq. The roentgen (R) is the quantity of X or γ radiation needed to produce 1 esu of charge per cm^3 of dry air at STP. The units of roentgen are however limited to the use with X- or γ radiation with an energy less than 3 MeV. The literal meaning of word radiation only refers to ionizing radiation. Roentgen was bestowed with Nobel Prize in Physics in 1901 for his recognition of the extraordinary discovery. This radiating energy is capable of damaging living tissue, and the amount of energy deposited in living tissue is expressed in terms of a quantity called dose.

The conversion from one system to another is simple and is given Table 5.

Threshold Radiation Value: The occupational worker can be exposed to a maximum limit of 5000 mREM/yr, whereas for rest of population, the exposure limit is set at 500 mREM/yr above background radiation. The long-term exposure

Table 5 Interconversion between various radiation units

1 mSv = 100 mREM
1 mSv = 100 mRAD
1 mGy = 100 mRAD
1 mGy = 100 mREM
1 mGy = 1 mSv
1 mSv = 114 mR
1 mRAD = 1 mREM
1 mREM = 1.14 mR
1 mRAD = 1.14 mR

for background radiations is set at 1 mSv per year above the background radiation level.

The calculations for this value give us information about radiation uptake in a year.

1 mSv to an hourly radiation exposure rate.
There are 365 days/yr × 24 h/day = 8760 h.
1 mSv/8760 h = 0.000114 mSv/h = 0.114 μSv/h.
This in fact is extremely low level of radiation exposure.

But, typical background radiation averages 3.0–3.5 mSv/yr [6, 13, 36].

7 Effects of Radiation to Environment

The deprivation in air quality is among one of the key environmental threats in front of modern society. The human activities have resulted in the emission of different toxic chemicals to our atmosphere, which further create lethal compounds on exposure to appropriate UV rays. UV radiation generates ground-level ozone (O_3) and some particulate matter (PM, frequently called aerosol) that include nitrate, sulfate, and organic aerosols causing adverse effect on human health and the environment. UV promotes the formation of hydroxyl radicals that act as cleaning agents for troposphere. The radicals restrict the lifetime of many gases like methane, HFCs, CFCs, sulfur, and nitrogen oxides that are important to tropo- and stratosphere and control the climate change. The ozone layer concentrations in urban area are determined by some key factors; i.e., the quantity of ozone in the air of urban environment is essential along with the reactions that involve the chemicals, like VOCs and NO, and produce ozone via UV-driven photochemistry. The origin of these chemicals is from both biogenic and anthropogenic sources. Some processes like dry deposition (loss at the surface) help in removal of ozone from the stratosphere. The ozone concentration can be altered by modifying troposphere or stratosphere exchange along with the modification in worldwide atmospheric composition, especially the greenhouse gases. The atmospheric cloudiness is

widely affected by human activity, and the evidence is that uncontrolled air pollution has exaggerated effect of solar radiation at many locations worldwide. These climate changes have adverse effect on human health and have led to allergic respiratory diseases including bronchial asthma having direct impact from excessive by-products formed by the interaction of air pollution with UV radiations. The presence of allergenic pollens in the atmosphere sometimes prolongs due to climate change and thus can increase the frequency and severity of such diseases [37–41].

The exposure to radiation has been continuously declining due to consistent physical decay of the radionuclides and their deeper vertical penetration into the soil. The radiological sciences have made enormous strides for the development of an accurate assessment of radiation hazards for humans. The past six decades have made fruitful modifications for radiation protection of humans with respect to dose, relative biological effectiveness on radiation quality, nuclide-specific distributions within the body, and the lifetime body burden of the contaminant. The 7% of radiations emitted from the sun lie in the UV range (200–400 nm). Upon traveling through stratosphere, the composition of the UV radiation gets modified and the total flux transmitted is significantly condensed. The short UV-C rays (200–280 nm) are totally absorbed by the atmospheric gases, while UV-B rays (280–320 nm) get absorbed by ozone cover, thus limiting the transmission to the Earth's surface, and UV-A radiation (320–400 nm) completely passes through ozone. The un-absorbed UV-B rays that reach Earth's surface cause serious implications for all living organisms [17, 42, 43].

The exposure to UV(B/C) radiation has both benefits and risks for human health. The best defined direct benefit is the synthesis of vitamin D from cholesterol. Some of the indirect benefits include change in food quality and disinfection of surface drinking water. The depletion of ozone shell has led to an enormous increase in input of solar UV-B radiation penetrating Earth's surface, causing major penalties for human health. The optimal exposure is variable as per individual and region thus having both direct and indirect effects on health. The adverse effects include cataracts, skin cancers, and recurrence of some viral infections. The long duration exposures to UV radiation suppress immune response and may be beneficial for certain disorders such as for autoimmune disease (e.g., multiple sclerosis) and allergy, but is harmful owing to initiation of skin cancer. A specific example is the increase in conjunctival melanomas for population closer location to the equator. The presence of UV-induced mutations in form of tumors strongly supports UV-B radiations to be the culprit [16, 44].

The adverse health effects of ionizing radiations were revealed after the discovery of X-rays, in 1895. Higher exposure to ionizing radiation leads to increase in risk of cancer throughout the lifespan. The exposure to high-energy ionizing radiations, even at mild dosages, damages genetic material in cells that eventually results in either radiation-induced cancer at later stage of life or inheritable disease in the descendants of the exposed individuals. This effect is known as stochastic effects. The most sensitive organ to these effects is testicles that cause heritable abnormalities which get induced in the germ cells or gametes [45, 46].

7.1 Impact of UV Radiations on Atmosphere

All these processes are easily altered by the change in the amount and intensity of UV radiation, caused by the variation in elevation of the sun levels and diminution by air pollutants and clouds. Thus, the reduction in ozone concentration has led to increase in UV-B radiation intensity in troposphere, with increase in the rate of the photolytic processes. An indirect consequence of this environmental composition change is the rise in average temperature and increase in rate of several reactions. It has led to high concentration of ozone in polluted regions, increasing mortality rate.

The solar UV-B and UV-A radiations drive many chemical transformations occurring in the atmosphere. This wavelength region results in photodissociation of few atmospheric gases like nitrogen dioxide (NO_2), ozone (O_3) (Eq. 1), and formaldehyde (HCHO). This directly links stratospheric ozone depletion, air quality, and climate change.

$$O_3 \overset{h\nu\ (32\ \text{nm})}{\longrightarrow} O_2 + O(^1D) \tag{1}$$

The hydroxyl radical cleans stratosphere by converting air pollutants into water-soluble forms and is easily detached from the atmosphere via precipitation. ȮH radicals further react with sulfur and nitrogen oxides producing sulfuric and nitric acids, respectively, and on reacting with hydrocarbons and other VOCs, it produces alcohols, aldehydes, ketones, etc. (as shown in Fig. 10). Along with UV radiation, other factors that affect the concentration of ȮH, O_3, and aerosols are various nitrogen oxides $(NO)_x$, VOCs, water vapor, temperature, and meteorological transport, some of which are also influenced by changes in climate.

UV rays strongly influence the destruction of ozone layer in troposphere, through the series of photochemical reactions. Ionizing radiations can easily eject electrons from any atom, thus creating charged atom. The drastic climate changes in atmosphere may vary stratosphere or troposphere ozone flux and can lead to long-term chemical changes in stratosphere and troposphere. UV radiation strategically controls the formation of photochemical smog that initiates the formation of ȮH radicals, which in turn controls the climate change and the concentration of

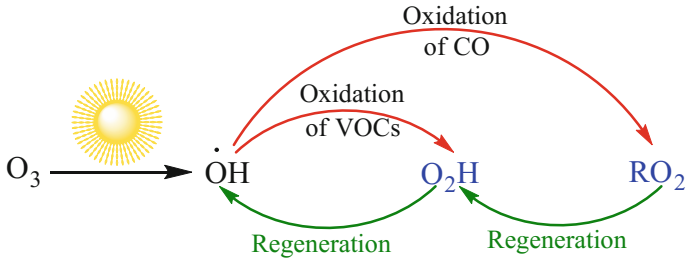

Fig. 10 Proposed changes in chemistry of ȮH radical in atmosphere. The arrows represent reactions in atmosphere

ozone inhalation gases, such as methane and HCFCs in the atmosphere. The damage to biomolecules generally occurs via direct photochemical deterioration or by the synthesis of oxygen-free radical species like hydrogen peroxide and superoxide, which enhances the oxidative impairment within the cell. The overall stress is revealed in relation to improved energy requirement for protection and repair. The fluctuations in the composition of lipid content affect the cellular nutritious quality for advanced trophic levels. The growth rate impairment is due to the photochemical damage and increase in energy requirements under severe light exposures. Moreover, the UV radiations also result in the bleaching of pigmented cells, at high UV fluxes [41, 47–51].

Stratospheric ozone layer depletion is the most dangerous phenomena arising as a consequence of anthropogenic interaction with the global environment. The depletion of the ozone layer is promoted by chlorofluorocarbons and other chlorinated and brominated substances that are directly or indirectly emitted into the atmosphere. In the troposphere, ozone gas reaches the stratosphere, where UV radiations break fragments into separate chlorine and bromine molecules, with the subsequent release of halogen atoms. These halogen atoms/radicals initiate the catalytic cycles that progressively destroy stratospheric ozone layer; one chlorine atom has the potential to destroy as many as 100,000 ozone molecules before finally being removed from the stratosphere.

The effects of UV rays on biotic (microbial) and abiotic (photodegradation) developments are interdependent, and certain evidence proves that the photodegradation can alter (wholly or partially) compounds in such a way that it can improve or inhibit consequent microbial decay of litter, known as photopriming. Thus, the direct photodegradation creates negligible effect on the loss of litter mass, but the subsequent biological turnover can be interrelated with the extent of previous exposure to radiation. These UV radiation-mediated modifications in plant tissue chemistry involve stimulation for the synthesis of phenolic substituents that protects plants against excess UV rays, though the amount of various chemical constituents like C, N, P, K, and lignin can too vary [52].

7.2 Implications of Radiation on Human Health

The intense research has been carried out to study the effect of radiation on human health and its role in the destruction of benign tumor cells with radiation, and this treatment is popularly known as radiotherapy. The extent of radiation dose required in radiotherapy treatments depends upon the category and phase of cancer under treatment. Some of the other effects of radiations on various parts of human body are given in Table 6.

Table 6 Effect on body parts in case of radiation overexposure

Organ	Effect
Brain	Fatigue, nausea
Hair	Loss of hair follicles and baldness
Intestine lining	Diarrhea and malnutrition
Bone marrow and white blood cells	Immune system failure
Uterus	Destruction of eggs
Body	DNA cleavage

7.3 Delayed Health Effects

The prominent health effects occur after prolonged exposure to the radiations. The maximum deferred health effects are stochastic effects where the probability of occurrence depends upon the amount and the type of radiation dose received. In most of the cases, such health effects are supposed to be due to the changes in the cellular genetic material upon subsequent to radiation exposure. The radiations effect is observed especially in the form of leukemia, bone, and thyroid cancer that starts to appear within few years after exposure. The radiation damages reproductive cells, especially the sperms or ovum, that can permanently cause heritable mutant offspring defects.

7.4 Effects on Fetus/Children

A fetus or embryo can be exposed to radiations through the mother via nutrition, i.e., internal exposure or directly through external exposure. For most radiation exposure events, fetus is safe inside the uterus, since the radiation dose is significantly lower than that received by the mother. But, the embryo and fetus are predominantly delicate to radiation effect; the health effect of exposure can be severe or extreme, even at the radiation doses that are much lower than those that immediately affect the mother. Some of the deformities are impaired brain function, growth retardation, and cancer. In case, the embryos and/or fetuses get severely affected, survival is impossible!

The health effects in human beings depend on certain physical factors, i.e., anatomical and physiological differences among children and adults. Owing to the smaller size of kids, the organs are close together and thus the concentration of radionuclides is intense in specific organ than it would have been for adults. The epidemiological studies reveal that the people below the age of 20 years are about twice more susceptible as adults to be infected by leukemia following the same levels of radiation exposure [52].

The high-energy radiation (X-rays or γ-rays) has severe effect on fetus growing in the mother's womb. The exposure to X-rays during the first month of onset of

pregnancy results in miscarriage and abortion. The exposure of fetus to X-rays at later stages of pregnancy causes severe abnormalities in developing baby; i.e., any radiation above 200 R creates deformities in newborn. In most of the cases, the reported abnormalities are microcephaly, oxycephaly, microphthalmia, and optic atrophy, along with the retarded growth and hormonal imbalance. In such cases, the risk for development of cancer at some stage of life is quite high.

The risks of prenatal exposure to ionizing radiation vary and are based on the stage of development. An embryo is most vulnerable to the effects of radiation during organogenesis, i.e., the duration from two to seven weeks after conception and in the early fetal period, i.e., two to four months after conception. The effects of exposure can be mutagenic, carcinogenic, and/or teratogenic and are directly associated with the level of radiation exposure. The estimation of risk for teratogenic, i.e., non-cancerous fetal development, and the carcinogenic effect was considered from the survivors of atomic bomb and nuclear fallout during initial diagnosis in pregnant women, and other animal studies [53–58]. The effect of radiation on fetus from the time of conception is elaborated in Table 7.

Table 7 A fact sheet for clinics (open-source content for public information)

	Fetal development stage				
			Fetogenesis		
Radiation dose	2 weeks postconception	3–7 weeks postconception	8–15 weeks postconception	16–25 weeks postconception	26–38 weeks postconception
Below 50 mSv	Undetected non-cancerous health effects			Non-cancerous health effects are unlikely	
50–500 mSv	Failure to implant the egg increases slightly, and the surviving embryos will not have any cancerous effects	Chances of major malformations increases; embryo growth may be restricted	Restriction in growth along with decrease in IQ level which may be accompanied by mental retardation		
Above 500 mSv	High probability of egg implant and the surviving embryos will not have any cancerous effects	Chances of miscarriage and high chances of major neurological deformities	Restriction in growth along with decrease in IQ level which may be accompanied by severe mental retardation. Chances of malformation increase by 20%	Chances of miscarriage; restriction in growth along with decrease in IQ level which may be accompanied by severe mental retardation	Incidence of miscarriage and neonatal death likely

Reprinted with permission from Elsevier from Centres for Disease Control and Prevention, Radiation and pregnancy, Atlanta, USA

7.5 Effects on Genetic Materials

Many studies have been carried out on cultivated plants after exposing them to various degrees of ionizing radiations. The effects of high levels of radiation on plants include damage to DNA molecules that include DNA sequence 'inversion' (TCAG converted to GACT) and in few cases sequence deletion or chromosomal aberrations, i.e., changes observable in growth reduction due to chromosome structure deformation and is defined by the reduction in the rate of plant growth along with diminished power of seed germination. DNA is highly sensitive toward UV-B irradiation thus causing phototransformations and increased production of cyclobutane pyrimidine dimers and pyrimidine pyrimidinone (6:4) dimers. Since DNA and RNA polymerases are incompetent to read complete photoproducts, their exclusion is important for DNA replication and transcription. To circumvent the cytotoxic effects of UV-persuaded DNA damage, most organisms have established some multifaceted repair mechanisms including removal, recombination, repair, and photoreactivation of damaged ribonucleotides (Fig. 11) [59–61].

7.6 Effect on Plants

The elevation in UV-B radiation intensity promotes pleiotropic effects on plant growth, morphology, and physiology, but plants respond variably to low and high UV-B radiation, due to stimulation of protective and repair mechanisms that deal with any change in stress. Plants grown at higher geographical altitudes are more UV-B-tolerant in comparison with the those sown at lower altitudes having less UV-B radiation exposure levels. Photomorphogenesis in seedlings is primarily regulated by red-/far-red-absorbing phytochromes (phy A-E) and by blue/UV-A-absorbing cryptochromes. Interestingly, the lower dose of UV-B can too develop photomorphogenesis in etiolated sprouts, since they get initiated by wavelengths in the range of 250–280 nm. Thus, UV-B rays have potential to stimulate a broad biosynthetic pathway that leads to disruption in normal morphogenesis.

The most common defensive mechanism against potentially harmful radiations is the automatic biosynthesis of high amounts of UV-absorbing phytochemicals that are essentially secondary phenolic metabolites like substituted flavonoids and

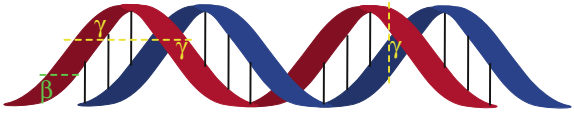

α particles (no effect)
β particles (breakage of single strand)
γ rays (breakage of double strand)

Fig. 11 Extent of damage caused by different types of radiations on DNA

hydroxycinnamate esters. These secreted chemicals get accumulated in epidermal cell vacuoles as a response to UV-B rays which diminish the infiltration of the UV-B rays into deeper cell layers causing minimal effect on the absorption of visible light region. Thus, the use of sunscreens by human beings to minimize UV infiltration is mimicking of common plant protection response behavior. Most of these sunscreens contain high levels of phenolic compounds secreted by plants.

Terrestrial ecosystem is the largest storehouse of active organic carbon-rich biosphere that includes biomes of variable climate regimes having various organisms accommodated to these conditions. The important ecosystem facilities are food and fiber, along with the protection of watersheds and regulation of water quality in the lithosphere. The response is characterized by insignificant reduction in leaf area and growth rate, since increase in UV-B radiation intensity leads to the biochemical and physiological changes. The plant exposed to UV-B radiations modifies frequently and has huge effects on the interactions between plants and consumer organisms where the expression of several genes are involved in natural senescence phenomena [48, 51, 58, 59, 61].

7.7 *Effect on Animals*

Most of the vertebrate animals and insects are well protected from UV radiations by their external body coverings like fur, feathers, and pigmentation. But, some of the other species, like amphibians, are much less protected than other vertebrates. On southern hemisphere region with extreme cold conditions, the reduction in intensity of solar UV-B radiation has led to the modification in soil microbes that has further transformed the quality and/or quantity of root exudates. The importance of root exudations lies in the fact that they offer adequate amount of the energy and carbon for microbes present in soil. Solar UV-B radiations prevent the plant growth, though to smaller extent, i.e., less than 20%, and are enhanced in herbaceous species in comparison with woody perennial species. These radiations provoke diverse acclimation responses, including increased DNA repair capacity, activity of antioxidant enzymes, and accumulation of phenolic compounds [51].

In case of mammals, the ionizing radiations produce detrimental effects on health. Some of the animals investigated are donkeys, pigs, bulls, cows, sheep, monkeys, dogs, rabbits, and goats. The widely studied radiations are the external γ-rays, a few in vitro studies (administered to the animals via ingestion) using β emitters (<10 keV and >10 keV) and neutrons of various energies. The effects on reproductive system were extensively analyzed that is followed by mutation induction, mortality, and morbidity. An extensive range of doses and dose rates has been used in studies with non-human mammals. The procedure considered for reproductive capacity demonstrated impaired fertility that includes reduction in fertility span, induction of sterility, declination in female and male reproductive cells count, or fertility-related parameters like litter number, litter size, embryos with malformations, sex ratio, preimplantation, or postimplantation death. The

prolonged exposure to UV radiations results in impairment of immune response in mammalian systems, including humans. This effect is caused by a variety of histological and biochemical mechanisms that occur due to the induction of interleukins by keratinocytes, reduction in numbers of Langerhans cells in the skin, change in their response to antigens, and possible DNA damage (Fig. 12) [47].

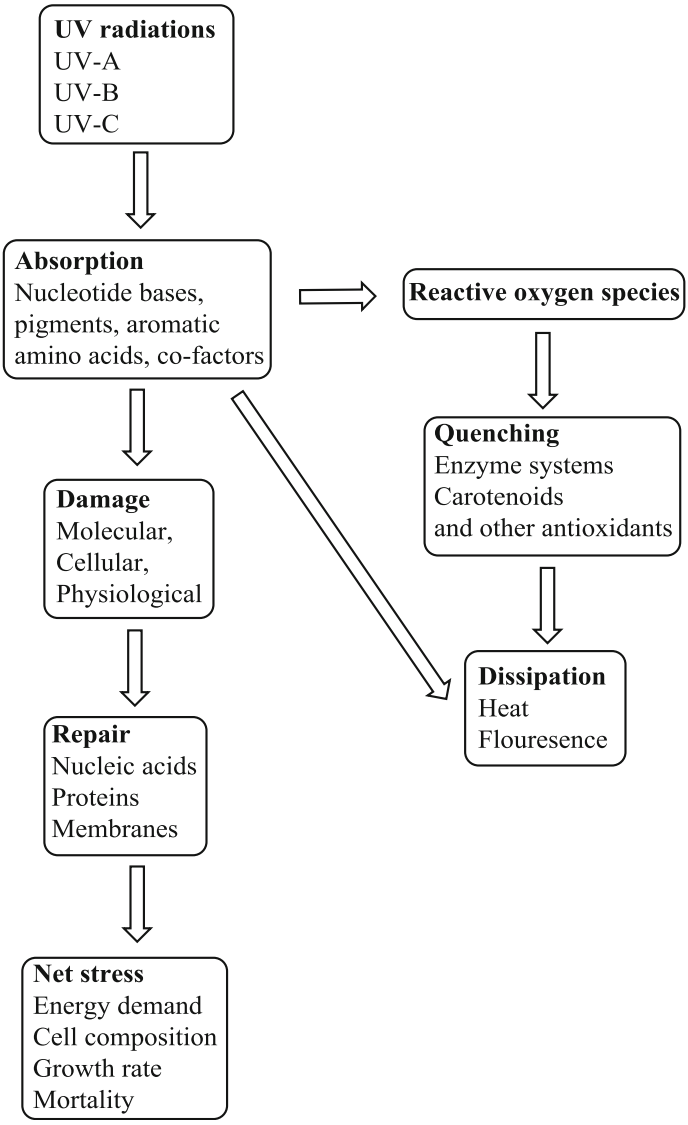

Fig. 12 Pathways from UV radiation exposure to cellular stress

7.8 UV Damage to Aquatic Organisms

Solar UV-B radiation has potentially wide range of detrimental effects in aquatic species and is usually revealed as reduced productivity on freshwater and marine organisms, including bacterioplankton and phytoplankton. Most of the UV radiations, till wavelength of 320 nm, get strongly absorbed by ozone and to some extent by oxygen. The short-term and cumulative times at which the aquatic organisms are exposed to UV radiations are determined by the duration of time and periodicity that aquatic organisms spend in and out of the UV photic zone (Fig. 13). This represents the equilibrium between organism damage and organism repair.

UV radiations have high impact on cellular constituents like biomolecules and their physiological responses to environment that include mitigating strategies and repair mechanisms. The duration and altitude of solar UV rays have also modified the morphology of filamentous cyanobacteria (Arthrospira) which has been popularly known to have natural resistance against any type of solar radiation [47, 62, 63].

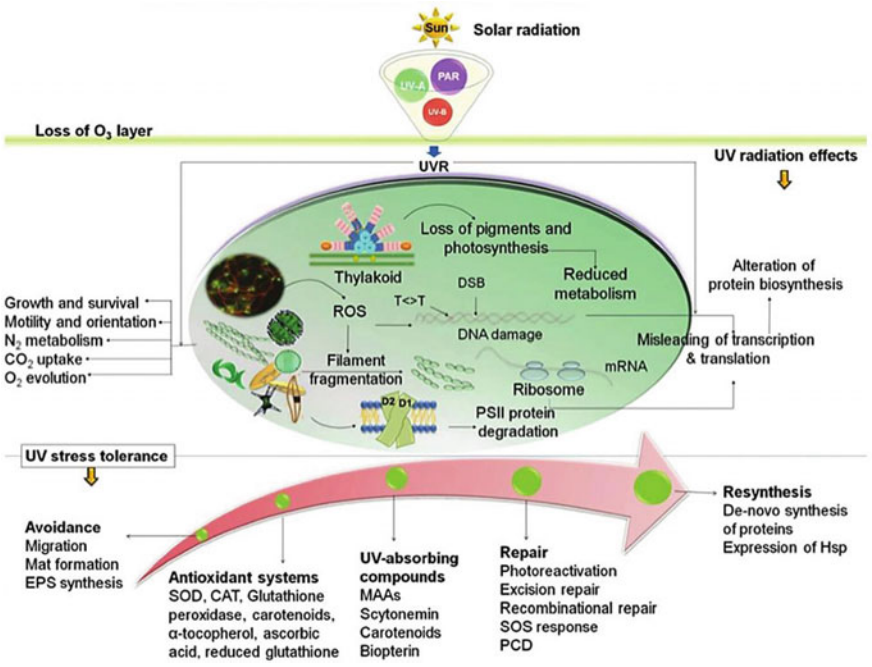

Fig. 13 Effects of solar UV radiation on biomolecules, cellular components, and physiological responses as well as mitigating strategies and repair mechanisms. Reprinted from [63], ©2015 with permission from The Royal Society of Chemistry

7.9 RF-EMFs' Exposures in Kindergarten Children

Human population is always and continuously exposed to artificial sources of RF-EMFs. The RF-EMF radiations are classified on the basis of sources of radiation with respect to human body, i.e., near-field sources (cell phones, iPad, laptops, and tablets) and far-field sources (Wi-Fi routers, mobile phone base stations, radio/television, broadcasting towers, and so on). The exposure to RF-EMFs has resulted in antagonistic health effects as well as biological effects in human beings, especially the children. The exposure of radiations from mobile phone base stations is among the biggest source of environmental and far-field individual exposures. Wi-Fi cellular radiations contribute insignificantly to the overall personal and environmental RF-EMF exposures in comparison with other RF-EMF sources like mobile phone stations. The study is really important since it describes the 16 radio frequency bands detected at the mobile phone base stations. Among all those bands, GSM 900 MHz frequency band contributes maximum to the total environmental and personal RF-EMF exposures in kindergartens in Melbourne. Though the studies have shown no major effect on children, still the investigations are ongoing to know any type of effect on the kids [64–69].

7.10 Solar UV Exposure in Construction Workers

Short-term UV dosimetric measurements in labors working under direct sunlight during cloudless periods displayed high radiation exposures. The daily effective exposure was exceeded, in most cases, and international recommendation for solar occupational exposure of unprotected skin by several orders of magnitude. As per the Lucas report findings, the severe consequence of overexposure to UV radiations is malignant melanoma, which can be treated, if detected at initial stages. UV radiations are the only major global cause of melanoma and other skin cancers. Melanoma and skin cancer are rising problems at locations having high perceptions of UV rays, especially in Spain and the rest of Europe, since its incidence has amplified significantly in the past 20 years [70–72].

7.11 Effect of Cosmic Radiation on Airline Flyers

The growing mobility of our society is associated with continuous increase of air travel. This has led to an enormous increase in the number of persons being exposed to cosmic radiation, essentially the pilots and cabin crews. Moreover, the number of frequent travelers and astronauts is too exposed to cosmic radiation

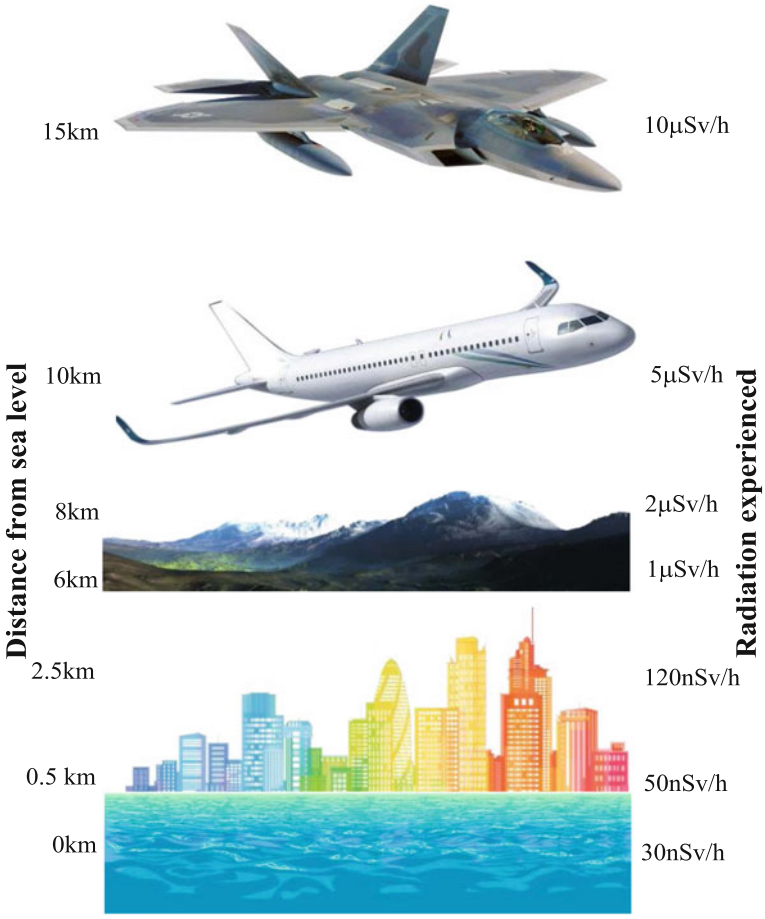

Fig. 14 Level of radiation experienced at various altitudes

during their travel and mission, simultaneously. In addition to occupational and non-occupational radiation exposures, cosmic radiation also impacts microelectronic components onboard of aircraft, spacecraft, and space stations. Our atmosphere acts as natural shield for prevention of most of the high-energy radiations coming from our galaxy. But the jets fly at an altitude of 8–16 km above the sea level where the atmospheric shield has lesser effect (Fig. 14). Moreover, the impact of cosmic radiations is enhanced at poles in comparison with equator. The study indicates that the effective dose rate of cosmic radiations at an altitude of 8 km is six times higher at poles as compared to equator, while at 16 km the dose rate is nine times than that at equator [73–75].

8 Radiation Disasters in History

8.1 Chernobyl Nuclear Disaster

The most severe radiation accident in human civilization occurred at the Chernobyl Nuclear Power Plant on April 26, 1986. The accident was caused due to human negligence and resulted in the largest uncontrolled radioactive release into the environment ever recorded for any civilian operation for about ten days. The earliest signs of contamination included an abrupt change in the short-lived radionuclide iodine-131 (^{131}I) generally found in fresh milk with a half-life of eight days; subsequent deficiency of rapid counteractions led to high doses to the thyroid gland, especially in kids. The severe radiobiological effects were recognized in the Chernobyl, and after 30 years, the radiation levels have plunged to 1% of the original levels due to continuous decay in radionuclide and the penetration of some radionuclides into the soil. Till today, many cytogenetic anomalies due to continuous radiation are still being reported from plants and animals within the 30-km exclusion zone [76–80].

8.2 Fukushima Nuclear Disaster

Another massive nuclear accident befell on March 11, 2011, at the coastal city of Japan that was triggered by and earthquake with magnitude of 9.0 on Richter scale. Since the epicenter was 180 km away from the reactor site, it was previously assumed to be of category 5 nuclear accident by the INES, but later on measuring the activity and severity of disaster, it was labeled as level 7, the highest after Chernobyl disaster [72, 81, 82]. The assessment of any nuclear disaster into any category is labeled in Table 8.

Table 8 Classification of nuclear accidents on the scale

Level	Category name	Reported accidents	Cause
7	Disastrous	Chernobyl (1986)	Man-made
		Fukushima (2011)	Natural
6	Major	NA	NA
5	Serious	Three Mile Island (1979)	Man-made
4	Large	Windscale (1957)	Man-made
3	Accident	NA	NA
2	Incident	Medical negligence	Man-made
1	Anomaly	Research work	Man-made

NA Not available

Table 9 Worldwide estimate of serious radiation accident

Type of accident	1945–1965	1966–1986	1987–2007
Accident at nuclear facilities	19	12	4
Industrial accidents	2	50	28
Orphan source accidents	3	15	16
Accidents in academia and research	2	16	4
Accidents in medicine	NA	18	14

8.3 Three Mile Island Nuclear Disaster

The second nuclear disaster was a result of multiple human negligence at unit 2 of nuclear reactor situated on Three Mile Island, Dauphin County, Pennsylvania, USA. The incident occurred on March 28, 1979, when the reactor unit was running to 97%; its capacity was not cooled thermally due to technical and manual snag in supply of water, which eventually resulted in meltdown of core of the reactor. The radioactive materials were dispersed into the environment, and the disaster was categorized under level 5 [83].

8.4 Windscale Nuclear Disaster

The first-ever nuclear disaster was witnessed by Great Britain on October 10, 1957, when Unit 1 of two-pile Windscale facility caught fire owing to massive overheating of reactor beyond 673 K of temperature. The fire continued for three consecutive days thereby releasing huge amounts of radioactive contaminants into environment that spread across the UK and Europe. This accident falls under level 4 category that led to significant increase in a number of thyroid cancer patients [84]. During all these radiation disasters, there was enormous release of radioactive isotopes like ^{131}I, ^{137}Cs, ^{133}Xe, and ^{90}Sr that contaminated Earth's atmosphere.

The number of radiation disasters occurred in history is listed in Table 9.

9 Summary

Life is impossible without radiations, and the origin of Earth and nature is gift of radiations. The evolution of life since billions of years was possible owing to ionizing radiations. The continuous exposure of animals and plants to both natural and man-made radiations from sources from time to time has induced prominent effects to either cope up with these radiations or to mutate. There have been enormous efforts to investigate health effects of radiations, and the results indicate a striking balance between societal benefits and the risks of radiation toward the

health and the environment. The role of society is to develop more comprehensive knowledge of the environment, i.e., from global scale down to the chemical reactions that take place in air, water, and soil and within living organisms. Some of the novel and more powerful detection methods for analyzing radiations will be required. Moreover, it will be essential to develop a systematic approach to this complex networking of chemical, physical, and biological processes that can be monitored and evaluated.

10 Conclusion

The need of time is the monitoring of environmental radiation via some programs that must be carried out using nuclear facilities to safeguard people, animals and vegetation and climate from the ill effects of radiations. There must be certain government and industry radiation control programs routinely to countercheck the levels of radioactivity in the air, drinking water, surface water, soil, and food. This further requires the implementation of science and engineering to resolve and abort such problems and increase the level of understanding for the relevant issues. The expansion of knowledge will help in full protection, restoration, and preservation of our environment.

References

1. Croce R, Van Amerongen H (2014) Nat Chem Biol 10:492
2. Chikkaraddy R, de Nijs B, Benz F, Barrow SJ, Scherman OA, Rosta E, Demetriadou A, Fox P, Hess O, Baumberg JJ (2016) Nature 535:127
3. Balzani V, Bergamini G, Ceroni P (2015) Angew Chemie—Int Ed 54:11320
4. Kay ER, Leigh DA (2006) Nature 440:286
5. Ahlbom A, Feychting M (2003) Electromag Radiat, 157
6. Martin JE (2013) Physics for radiation protection, 3rd edn. Wiley, USA
7. Canadian Nuclear Safety Commission (2012) Introduction to radiation
8. Eisenbud M (1995) Radioactivity from natural, industrial, and other sources. J Radioanal Nucl Chem 197:15
9. Brenner DJ, Hall EJ (2007) N Engl J Med 357:2277
10. Ahlbom A, Feychting M (2003) Electromag radiat Br Med Bull 68:157
11. Bodner GM, Rhea TA (1978) Natural sources of ionizing radiation, 7
12. Parker RC (1977) Radiat Environ 54:7102
13. Ng KH (2003) Proc Int Conf Non-Ionizing Radiat UNITEN, 1
14. Gajšek P, Ravazzani P, Wiart J, Grellier J, Samaras T, Thuroczy G (2013) J Expo Sci Environ Epidemiol, 1
15. Nations U, Programme E (2016) Photochem Photobiol Sci 15:141
16. United Nations Environment Programme, Environmental Effects Assessment Panel (2017) Environmental effects of ozone depletion and its interactions with climate change: progress report, 2016. Photochem Photobiol Sci 16:107

17. Hinton TG, Bedford JS, Congdon JC, Whicker FW, McMahon D, Litvinetz O, Leonovich E, Karmaus W (2004) Radiat Res 162:332
18. Eliyahu I, Hareuveny R, Riven M, Kandel S, Kheifets L (2017) Environ Res 158:295
19. Pasquino N (2017) Measurement 109:373
20. Urbinello D, Joseph W, Huss A, Verloock L, Beekhuizen J, Vermeulen R, Martens L, Röösli M (2014) Environ Int 68:49
21. UNSCEAR (2008) Sources and effects of ionizing radiation. United Nation
22. Huxtable D, Read D, Shaw G (2017) J Environ Radioact 167:36
23. Ciobanu MC, Catalina T, Dogaru G (2016) Energy Procedia 85:118
24. Hanson DJ (2011) Chem Eng News 89(34):36
25. Hutchison SG, Hutchison FI (1997) J Chem Educ 74:501
26. Allen WF (1966) J Chem Edu 43(11):592
27. Chiu HS, Huang PJ, Wuu JL, Wang JJ (2013) Appl Radiat Isot 81:356
28. Merz S, Steinhauser G, Hamada N (2013) Environ Sci Technol 47:1248
29. Reed AB (2011) J Vasc Surg 53:3S
30. Zovinka EP, Sunseri DR (2002) J Chem Educ 79:1331
31. Yanagisawa K (2015) Energy Procedia 71:360
32. USNRC Technical Training Center Natural and Radiation Man–Made Radiation Sources. React Concepts Man, 1–12
33. Radiological Protection Institute of Ireland (2013) Sources of ionising radiation. Fact Sheet, 3
34. Kortov V, Ustyantsev Y (2013) Radiat Meas 55:12
35. Cardis E, Hatch M (2011) Clin Oncol 23:251
36. Mlekodaj RL (2008) Basic units and concepts in radiation exposures, 23
37. Morgenstern O, Zeng G, Abraham NL, Telford PJ, Braesicke P, Pyle JA, Hardiman SC, O'Connor FM, Johnson CE (2013) J Geophys Res [Atmos] 118:1028
38. Gan CM, Pleim J, Mathur R, Hogrefe C, Long CN, Xing J, Roselle S, Wei C (2014) Atmos Chem Phys 14:1701
39. Abrutzky R, Dawidowski L, Matus P, Lankao PR (2012) J Environ Prot (Irvine, Calif) 3:262
40. Amato GD, Cecchi L, Amato MD, Liccardi G (2010) J Investig Allergol Clin Immunol 20:95
41. Madronich S, Shao M, Wilson SR, Solomon KR, Longstreth JD, Tang X (2011) Photochem Photobiol Sci 10:280
42. Lindgren A, Stepanova E, Vdovenko V, McMahonet D, Litvinetz O, Leonovich E, Karmaus W (2015) J Expo Sci Environ Epidemiol 25:334
43. Real A, Sundell-Bergman S, Knowles JF, Woodhead DS, Zinger I (2004) J Radiol Prot 24: A123
44. Norval M, Lucas RM, Cullen AP, de Gruijl FR, Longstreth J, Takizawa Y, van der Leun JC (2011) Preface Photochem Photobiol Sci 10:199
45. Kamiya K, Ozasa K, Akiba S, Niwa O, Kodama K, Takamura N, Zaharieva EK, Kimura Y, Wakeford R (2015) Lancet 386:469
46. Okano T, Ishiniwa H, Onuma M, Shindo J, Yokohata Y, Tamaoki M (2016) Sci Rep 6:23601
47. de More S, Demers S, Vernet M (2001) Trans Am Geophys Union 82(41):477
48. Mishchenko M, Travis L, Lacis A (2015) Second Edi. Encycl Atmos Sci. 5:27
49. Sharma S, Sharma P, Khare M (2017) Atmos Environ 159:34
50. Ballaré CL, Caldwell MM, Flint SD, Robinson SA, Bornman JF (2011) Photochem Photobiol Sci 10:226
51. Caldwell MM, Bornman JF, Ballar CL, Flint SD, Kulandaivelu G (2007) Photochem Photobiol Sci 6:252
52. Bornman JF, Barnes PW, Robinson SA, Ballaré CL, Flint SD, Caldwell MM (2015) Photochem Photobiol Sci 14:88
53. Shaw P, Duncan A, Vouyouka A, Ozsvath K (2011) J Vasc Surg 53:28S
54. Prescher LM, Butler WJ, Vachon TA, Henry MC, Latendresse T, Ignacio RC Jr (2015) J Pediatr Surg Case Reports 3:554
55. Megaw L, Clemens T, Dibben C, Weller R, Stock S (2017) Environ Res 155:335
56. Stabin MG (2017) Phys Medica. https://doi.org/10.1016/j.ejmp.2017.04.001

57. Nonn RA, Gross NJ (1996) Curr Opin Pulm Med 2:390
58. Williams PM, Fletcher S (2010) Am Fam Physician 82:488
59. Frohnmeyer H, Staiger D (2003) Plant Physiol 133:1420
60. Hinton TG, Alexakhin R, Balonov M, Gentner N, Hendry J, Prister B, Strand P, Woodhead D (2007) Health Phys 93:427
61. Geard CR (1982) In: Pizzarello DJ, Colombetti LG (eds). Radiat Biol, 83–109
62. Häder DP, Helbling EW, Williamson CE, Worrest RC (2011) Photochem Photobiol Sci 10:242
63. Häder DP, Williamson CE, Wängberg SA, Rautio M, Rose KC, Gao K, Helbling W, Sinha RP, Worrest R (2015) Photochem Photobiol Sci 14:108
64. Bhatt CR, Redmayne M, Billah B, Abramson MJ, Benke G (2016) Nat Publ Gr, 1
65. Beekhuizen J, Kromhout H, Bürgi A, Huss A, Vermeulen R (2015) J Expo Sci Environ Epidemiol 251:53
66. Cansiz M, Abbasov T, Kurt MB, Celik AR (2016) J Expo Sci Environ Epidemiol, 1
67. Termorshuizen F, Wijga A, Garssen J, Outer PND, Slaper H, Loveren HV (2002) J Expo Anal Environ Epidemiol 12:204
68. Genuis SJ (2008) Public Health 122:113
69. Jovanovic D, Bragard G, Picard D, Chauvin S (2015) J Expo Sci Environ Epidemiol 25:80
70. Serrano M-A, Cañada J, Moreno JC (2013) J Expo Sci Environ Epidemiol 23:525
71. Molina MJ, Seinfeld JH (2011) The environment challenges for the chemical sciences in the 21st century science and technology. The National Academies Press, Washington DC, USA
72. Labib A (2014) Learn from Fail, 123
73. Paschoa AS, Steinhäusler F (2010) Radioact Environ 17:87
74. Barish RJ (2004) J Am Coll Radiol 1:784
75. Friedberg W, Copeland K, Duke FE, Darden EB (2005) Adv Sp Res 36:1653
76. Shaw D, Elger B (2013) Lancet Oncol 14:1042
77. Adelman DS, Theiss MA, Goudounis J (2014) J Radiol Nurs 33:100
78. Pearce F (2017) New Sci 234:42
79. Nations U, Programme Effects and Sources
80. Fushiki S (2013) Brain Dev 35:220
81. Kim Y, Kim M, Kim W (2013) Energy Policy 61:822–828
82. Labib A, Harris MJ (2015) Eng Fail Anal 47:117
83. Perrow C (1981) Society 18:17
84. Wakeford R (2007) J Radiol Prot 27:211

Radiation Physics and Chemistry of Polymeric Materials

Paramjit Singh and Rajesh Kumar

Abstract The material properties can be modified/tailored by either of the techniques available such as top-down method, bottom-up method, composite ratio variation, doping of a suitable dopant, ion beam-related methods and many others. The modifications by ion beam and radiation treatment are quite effective techniques to calibrate the physical, chemical, surface and structural properties of the materials. Polymeric materials are highly radiation sensitive and their properties can be modified by exposing the material to different ions and radiation such as gamma rays, electron and proton beams as well as swift heavy ions. The focus of the present discussion is pointed towards the radiation (mainly swift heavy ions and gamma rays) induced modification of polymeric materials and their physical and chemical aspects. The fundamental concepts of energy transfer of swift heavy ions and the post-irradiation effects such as cross-linking and chain scissoring of polymeric materials have been discussed in this chapter. The polymeric chain scissoring and cross-linking are related to the structural, chemical, surface, electrical and free volume properties of the polymers. The concept of free volume is further related to gas diffusion and separation properties of some of the polymers. The discussion is limited up to the radiation-sensitive polymers such as polymethyl methacrylate, polyethylene terephthalate and polyallyl diglycol carbonate polymers in the present chapter. The applications related to ion beam technology have been discussed in the last section of this chapter.

P. Singh (✉)
Gujranwala Guru Nanak Khalsa College, Civil Lines, Ludhiana 141001, Punjab, India
e-mail: psd1985@gmail.com

R. Kumar
University School of Basic and Applied Sciences, Guru Gobind Singh Indraprastha University, Dwarka, New Delhi 110078, India
e-mail: rajeshpositron@gmail.com

R. Kumar
Mechanical, Aerospace and Nuclear Engineering, Rensselaer Polytechnic Institute (RPI), 110, 8th Street, Troy, NY 12180, USA

V. Kumar et al. (eds.), *Radiation Effects in Polymeric Materials*, Springer Series on Polymer and Composite Materials, https://doi.org/10.1007/978-3-030-05770-1_2

Keywords Swift heavy ions · Polymers · Free volume · Positron annihilation lifetime spectroscopy · Cross-linking · Chain scissoring

Abbreviations

CS	Crystallite size
E_g	Band gap energy
FFV	Fractional free volume
FV	Free volume
I_3	Intensity of o-Ps
LET	Linear energy transfer
o-Ps	Ortho-positronium
PADC	Polyally diglycol carbonate
PALS	Positron annihilation lifetime spectroscopy
PET	Polyethylene terephthalate
PITMs	Polymer ion track membranes
PMMA	Polymethyl methacrylate
p-Ps	Para-positronium
R	Hole radius
RGA	Residual gas analyses
S_e	Electronic energy loss
SHI	Swift heavy ions
S_n	Nuclear energy loss
SRIM	Strength and range of ions in matter
SSNTDs	Solid-state nuclear track detectors
TRIM	Transport of ions in matter
XRD	X-ray diffraction
Z	Atomic number
τ_3	Lifetime of o-Ps

1 Introduction

Radiation is simply an energy emitted from a suitable source such as heat and light. The amount of energy or intensity of the radiation decides its category that whether it is ionizing or non-ionizing. The ionization potential of atoms ranges from a few electron volts for alkali elements to 24.5 eV for helium (noble gas) [1]. The non-ionizing radiation can move the atoms in a molecule or make them vibrate (called excitation), but unable to remove any electron from those atoms, for example, sound waves, visible light and microwaves. The ionizing radiations, on the other hand, have enough energy to ionize atoms, e.g. X-rays, beta rays, alpha rays, swift heavy ions (SHI) and gamma radiation. Coulomb per kilogram (C/kg) is

the SI unit of ionizing radiation exposure. Gamma rays are electromagnetic radiation of high-frequency and high-energy photons. Gamma rays are denoted by Greek letter 'γ'. An unstable nucleus decays gamma rays to get stability. These rays were discovered in 1900 by a French chemist and physicist Paul Villiard and so named as gamma by Ernest Rutherford in 1903. The SI units of gamma rays are grey (Gy) which is measured in J/kg. 1 Gy is the amount of radiation required to deposit 1 J of energy in 1 kg of matter. Various types of radiation including heavy ions (in MeV range), light ions (in keV range), highly focused microscopic beams and high-intensity pulses, soft and coherent X-rays, gamma rays, electron, proton and neutron beams are used for irradiating the materials depending upon the type of modification one needs for required applications. Accelerated ions and electron beam have an advantage over radioactive radiation that the problem of disposing of the radiation source (or shielding from the environment, when not in use) is eliminated.

Polymers are already familiar in the industries as well as research fields. There are hundreds of polymeric materials existing in the market for various applications. The scientific community is continuously modifying and mixing polymers to blends, clays or composites to modify their properties. The field of polymer study and research is broad and the available information is diverse which is too wide to be explained here. The polymeric properties can be tailored or modified by irradiating the polymer with suitable ionizing radiation. The radiation physics and chemistry of polymeric materials are widely applicable in modifying the structural, chemical, mechanical, optical, thermal, magnetic, surface, electrical and many other properties of the polymeric materials.

2 Polymer Ion Interactions

The energy transferred $\left(\frac{\mathrm{d}E}{\mathrm{d}x}\right)$ by impinging ion is divided into three main components:

$$\frac{\mathrm{d}E}{\mathrm{d}x} = \left(\frac{\mathrm{d}E}{\mathrm{d}x}\right)_{\text{nuclear}} + \left(\frac{\mathrm{d}E}{\mathrm{d}x}\right)_{\text{electronic}} + \left(\frac{\mathrm{d}E}{\mathrm{d}x}\right)_{\text{radiation}}$$

The first one is nuclear energy loss, and the second one is electronic energy loss. The third component of energy loss is in the form of bremsstrahlung and Cerenkov, which is negligibly small in case of SHI. The most of energy loss is shared by nuclear (elastic collision) and electronic (inelastic collision) components.

2.1 Elastic and Inelastic Collisions

(i) The nuclear energy loss (S_n) is caused by scattering of the projectile by the screened nuclear potential of the target atoms (Rutherford scattering) [2]. The atoms are displaced from their sites creating vacancies and interstitials. The nuclear energy loss leads to two main effects mainly: displacement of atoms and/or creation of phonons. The maximum S_n occurs near the end of ion track because ion speed becomes comparable to the Bohr velocity (orbital electron velocity) [3].

(ii) The inelastic collision of SHI with the atomic electrons of the matter is known as electronic energy loss (S_e). In this collision, SHI leaves a trail of changed material along its path through the medium, which is called latent ion track. These tracks can have different shapes such as conical, cylindrical and funnel like and their size varies from micrometer to nanometre range. The mechanism responsible for ion track creation can be explained by two popularly known models: Coulomb explosion model and thermal spike model.

2.1.1 Coulomb Explosion Model

When SHI passes through the atoms or molecule of the target, it produces the long cylindrical zone of positively charged ions. This cylinder containing positively charged ions explodes rapidly due to Coulomb repulsion of these positively charged ions. Due to this cylindrical shock wave, ion tracks are formed along the trajectory of the ion [4, 5].

2.1.2 Thermal Spike Model

The inelastic collision of SHI with target molecules ejects electrons from the molecular atoms. These ejected electrons have sufficient kinetic energy to induce electronic excitation by transmitting energy to the lattice through electron–phonon interactions. Due to this, the local lattice temperature of the material is increased above the melting point followed by rapid quenching of the molten matter resulting in the track formation [6–8].

The tracks can be tailored by projectile energy transfer and polymer type to some extent, and their size and shape can be tailored by controlled chemical etching as a function of etching time. The schematic of track formation and etching is shown in Fig. 1 [9]. There are numerous applications based on the size of these tracks which can be controlled by optimizing the etching time and conditions. Some of the polymers have been reported for gas separation applications after controlling the size of these tracks. The details are discussed in this chapter.

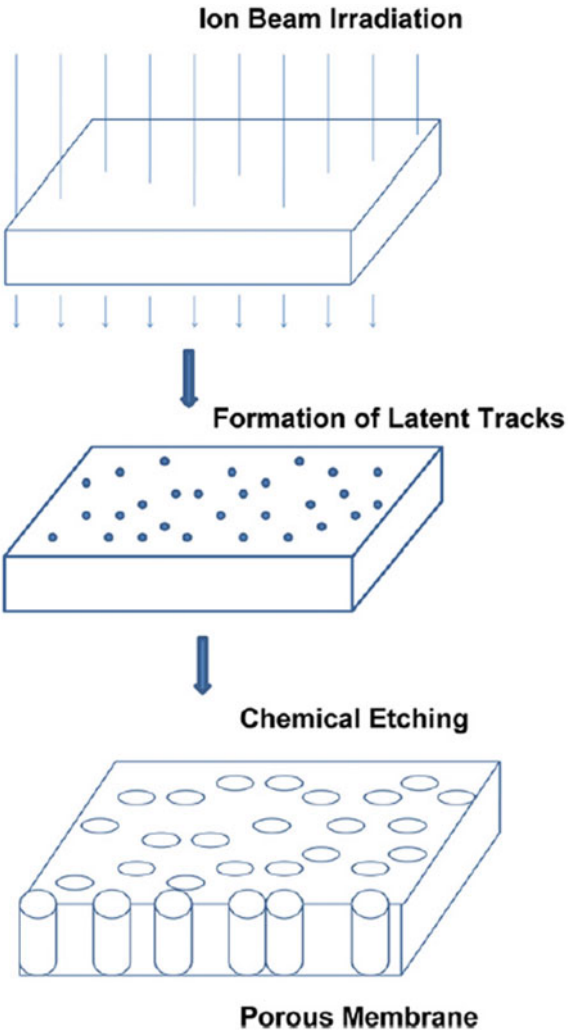

Fig. 1 Schematic for preparation of etched tracks in polymer membrane. Reproduced with permission from [9]

2.2 *Stopping and Range of Ions in Polymers*

The amount of damage produced by irradiation in solid target, particularly electronic energy loss (S_e), nuclear energy loss (S_n) and projected range can be estimated by using Monte Carlo simulation techniques such as stopping and range of ions in matter (SRIM) and transport of ions in matter (TRIM). This code is based on the binary collision approximation (BCA) approach and uses statistical algorithms to calculate how the moving ion loses its energy in the target. The distribution and ionization energy lost by the ion into the target, backscattered and transmitted ions and energy transferred to recoil atoms can be calculated using TRIM. In addition to

it, the detailed calculation with full damage cascades monolayer collision, surface sputtering calculations, neutron/electron/photon cascades and various ion energy/angle/positions and multi-layer biological targets can be estimated using TRIM [10]. There are other computational atomistic methods used for modelling irradiation effects in solids such as molecular dynamics with empirical potentials, density functional theory (DFT) based methods, tight-binding methods, time-dependent DFT simulations, phenomenological descriptions of electronic excitation and kinetic Monte Carlo approach. The discussion of these methods is beyond the scope of this chapter and can be read elsewhere [2].

The nuclear energy loss dominates in the range of 10^{-3}–10^{-2} MeV of ion energy ($\sim$1 keV/amu), while electronic energy loss is prominent at higher energies in the MeV to GeV range ($\sim$1 MeV/amu or more). The different ions can have different energy loss ranges depending upon their atomic number (Z), velocity as well as mass and atomic number of the target material. The S_e and S_n values increase with the increase of atomic number (Z) of impinging ion. Heavy Z value ions have the maximum S_e value up to 10,000 MeV energy, which is not practically possible for normal accelerators to produce such a huge amount of energy. The Fig. 2 explains a typical example of the variation of dE/dx of different energetic ions in polymethyl methacrylate (PMMA) polymer (calculated using SRIM code, density of PMMA 1.19 g/cm^3) over a wide range of energy (1 eV to 100 GeV). The peak values shift towards higher MeV range as the Z value of impinging ion is increased. The stopping power of any compound in SRIM is estimated by linear combination of stopping powers of its individual elements using Braggs rule [11]. The accuracy of Braggs rule (and hence SRIM) depends on the detailed orbital and excitation structure of the matter and the bonding changes may alter the strength of ion's interaction with the target medium. Still, the deviation is less than 20% [10]. Hence, a good estimate about variation of S_e and S_n values can be taken from these energy loss plots for a given ion. It is clear from Fig. 2a–c that S_n value is negligibly small in case of SHI irradiations, so it has a little effect upon the modifications of the ion irradiations. The peak value of S_e ranges between 10 and 100 MeV energy for most of the ions. The accurate sample thickness of the target polymer and energy range of the ion to be irradiated can be estimated by using SRIM projected range and S_e calculations, respectively, at the time of framing the experiment. The Fig. 2 is a typical example of PMMA polymer; the similar effects can also be estimated for other polymers.

2.3 *Irradiation Effects on Polymers*

The nuclear and electronic energy losses, i.e. S_n and S_e values in the target polymer, lead to certain modifications such as cross-linking (gelling) and scissoring (degradation) of polymeric chains which affect the physical, chemical, electrical, surface and many other properties of the material. Table 1 describes the list of polymers which mostly cross-link or degrade after ion irradiations [12]. Qualitatively, the polymeric chains get cross-linked and scissored simultaneously

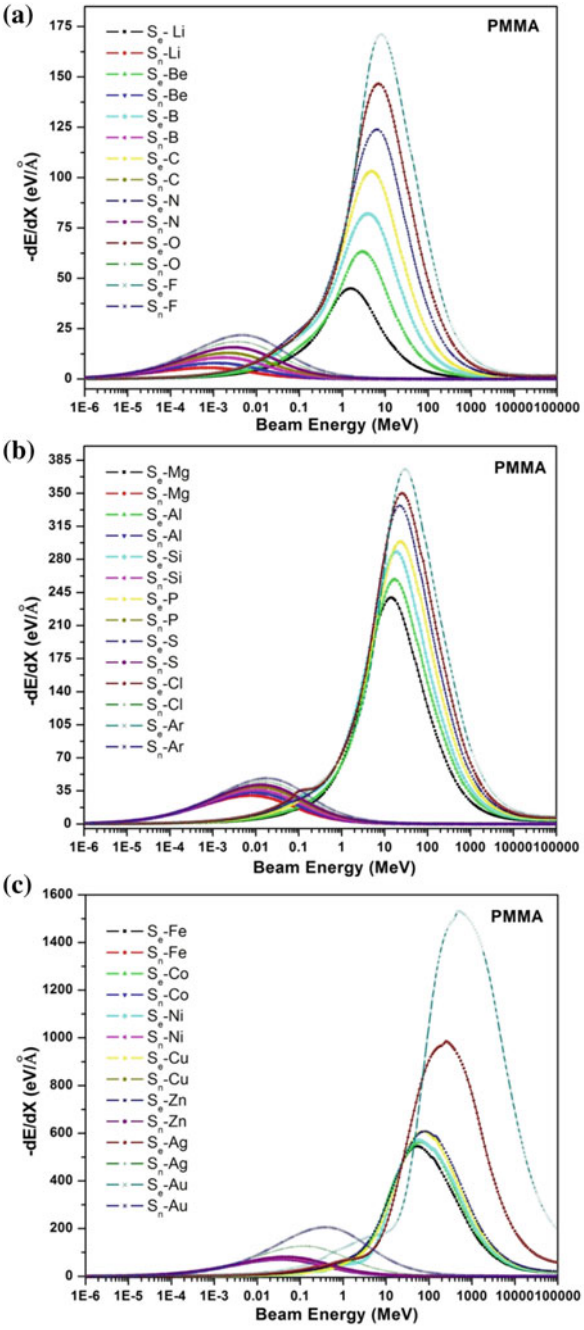

Fig. 2 SRIM calculated plot of energy versus nuclear energy loss $(-dE/dx)_n$ and electronic energy loss $(-dE/dx)_e$ for irradiation of different ions upon PMMA polymer

Table 1 Radiation characteristics of generic polymers

Mainly cross-linking	Mainly scission
Polyethylene	Polyisobutylene
Polyacrylates	Polymethacrylates
Polyvinyl chloride	Polymethylstyrene
Polysiloxanes	Polymethacrylamides
Polyamides	Polyvinylidene chloride
Polystyrene	Polytetrafluoroethylene
Polyacrylamides	Polypropylene ether
Ethylene vinylacetate	Cellulose

Reproduced with permission from [12]

during irradiation of polymers, but the dominance of one factor over the other for a given polymer depends upon number of factors such as polymer structure, type and energy of ion, sample thickness and ion fluence (number of ions per unit volume) [13, 14]. The structural and composition changes in the polymers have been reported in the last decade by many groups; some reports are discussed below.

Inelastic collisions produce the excitation and ionization of the orbital electrons of the atoms of the target material and as a result of it, liberation of gasses species such as hydrogen, carbon dioxide, carbon monoxide, helium, less abundant heavier molecular species and their reaction products occur [15–17]. The gas liberation can be estimated from residual gas analyses (RGA) at the time of irradiation. Wang studied the liberation of hydrogen gas and cross-linking of 50 keV nitrogen ion-implanted polystyrene-co-acrylonitrile polymer films of thickness in the range of 500–2500 Å [18]. He reported the dissociation of hydrogen atoms from the C–H bonds near the surface region (0–900 Å), thereby producing carbon-based free radicals due to electronic ionization/excitation. The liberated hydrogen gas diffused out of the sample, and carbon-based free radicals cross-linked each other as the matrix cooled down and eventually formed a large three-dimensional (3D) carbon network near the surface. Similar results of hydrogen gas liberation were reported by Hnatowicz et al. in their 3 MeV Si^{2+}, 3.25 MeV Cu^{2+} and 4.8 MeV Ag^{2+} ion-irradiated polyether-ether-ketone polymer samples [19]. They reported that gaseous release increased with increase of ion fluence from 10^{12} to 10^{13} ions/cm^2. Similar results were reported by their group in earlier reports upon polyimide polymer by keV ions irradiations [20]. Similarly, the RGA analyses of low-energy (keV) proton and nitrogen ion-irradiated ethylene tetrafluoroethylene polymer showed the liberation of H_2 and HF gasses in another report [21].

3 Concept of Free Volume

The cross-linking and chain scissoring of polymeric chains actually modify the polymeric free volume, which is further related to some other properties such as transport properties, glass transition temperature, ion conductivity, degree of polymerization and permeability of gasses which are related to the free volume [22–28]. There are static and pre-existing holes in the amorphous phase of polymers, which occur due to irregular packing of molecular chains. Another category is dynamic and transient holes, which occur due to molecular relaxation of polymeric chains. The density of amorphous polymer decreases by 10% due to the presence of these types of holes as compared to the density of the crystalline state of the same material [29]. Thermal, mechanical and relaxation properties of polymers are affected by the relative percentage of these holes [29]. The volume occupied by these holes is called free volume, and it can be modified by ion beam treatment [30]. Depending upon the polymer chains packing; free volume is further categorized into following types [31].

Hole free volume: There is a free space among the perfectly aligned polymeric chains of a particular polymer; this free space is called hole free volume.

Configurational free volume: The insufficient chain packing causes creation of an additional free space which is called configurational free volume.

Fluctuation (dynamic) free volume: The movement of polymeric side chains creates transient gaps, which create an extra free volume called fluctuation free volume.

Although it is difficult to determine the concentration or type of the defect generated, the overall change in free volume can be calculated using either of the techniques available such as positron annihilation lifetime spectroscopy (PALS), Doppler broadening spectroscopy (DBS) or angular correlation of annihilation radiation (ACAR). Presently, we will discuss PALS technique.

3.1 Positron Annihilation Lifetime Spectroscopy

Positron annihilation lifetime spectroscopy (PALS) is a non-destructive and reliable technique used to find free volume of the polymers. This technique is used to find lifetime of a positron and its bound state with an electron called positronium. The spin state of electron and positron with respect to each other further divides the positronium into two categories: ortho-positronium (o-Ps, parallel spin, $^3S_1$ spin state) and para-positronium (p-Ps, antiparallel spin, $^1S_0$ spin state) [32]. The electron density is small in an open volume defect (such as vacancy or its agglomerates) of any material (semiconductor or amorphous), so the lifetime of positron increases with respect to defect-free region after it is trapped in such defects. The spectrum of positron annihilation counts obtained from PALS experiment looks like Fig. 3 [33]. After the data analyses obtained from the PALS experiment, three lifetimes (τ_1 for

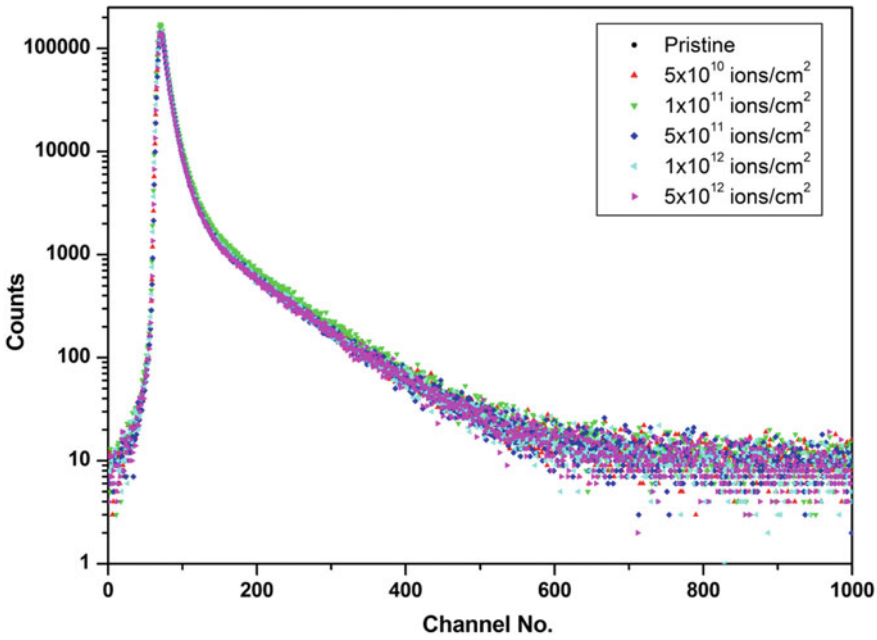

Fig. 3 PALS spectra of pristine and C^{5+} ion-irradiated PMMA polymer at various fluences. Reproduced with permission from [33]

p-Ps annihilation, τ_2 for free positron annihilation and τ_3 for o-Ps annihilation) and corresponding intensities (I_1, I_2 and I_3) are obtained. Annihilation of o-Ps and hence its lifetime (τ_3) are directly correlated to polymeric free volume. The intensity (I_3) of o-Ps is directly related to defect concentration. It represents the o-Ps formation probability. Hence, the PALS technique gives useful information about kind and concentration of the defect. The graphical representation of free volume modification by ion beam technology is shown in Fig. 4 [3, 34].

The Tao-Eldrup model is used to find the value of hole radius (R) [35, 36] by using Eq. (1),

$$\tau_3 = \tau_0 \cdot \left[1 - \frac{R}{R+\Delta R} + \frac{1}{2\pi} \cdot \sin\left(\frac{2\pi R}{R+\Delta R}\right)\right]^{-1} \quad (1)$$

The value of τ_o is 0.5 ns and ΔR = 0.166 nm. These values were obtained by fitting Eq. (1) in holes of known mean radii in porous materials [37]. ΔR is the thickness of the homogenous electron layer in which the positron annihilates.

The free volume (FV) in polymers can be calculated using the formula given by Eq. 2.

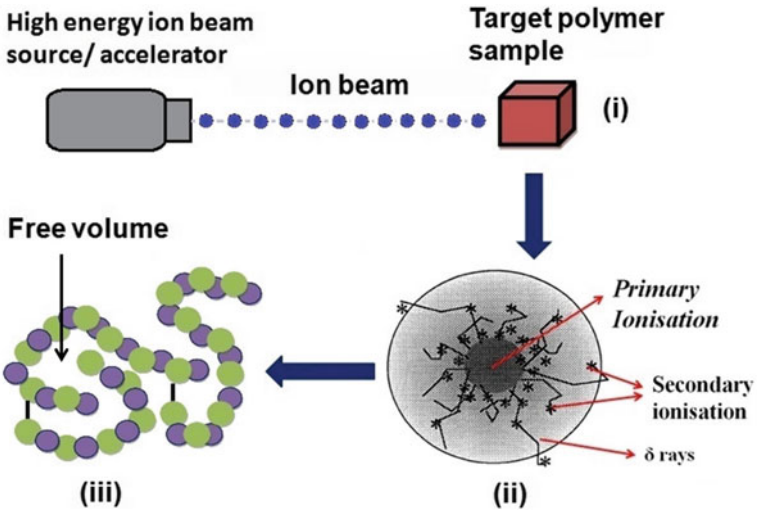

Fig. 4 Graphical representation of free volume modification of polymeric chains by ion irradiation. Reproduced with permission from [3, 34]

$$\mathrm{FV} = \frac{4}{3}\pi R^3 \tag{2}$$

Here, R is hole radius calculated using Eq. (1) considering the cavities to be nearly spherical.

Another term which is called the fractional free volume (FFV) is calculated using the formula given by Eq. 3.

$$\mathrm{FFV} = C \cdot \mathrm{FV} \cdot I_3 = C\left(\frac{4}{3}\pi R^3\right) I_3 \tag{3}$$

Here, C is a structural constant, and its value is ~ 0.0018 [38]. All these discussed parameters (R, FV and FFV) will be used in the next sections.

4 Polymethyl Methacrylate

The polymethyl methacrylate (PMMA) polymer is a thermoplastic polymer with chemical formula $[C_5H_8O_2]_n$. It is a transparent and colourless polymer having a melting point of 160 °C and approximate density of 1.19 g/cm^3. The glass transition temperature of PMMA varies in the range of 100–105 °C. PMMA polymer is used by medical accessories manufacturing industries for producing various products such as acetabular cups, patellar prostheses, cements for fixing hip and joint prostheses and filler in dentistry or vertebroplasty [34, 39, 40].

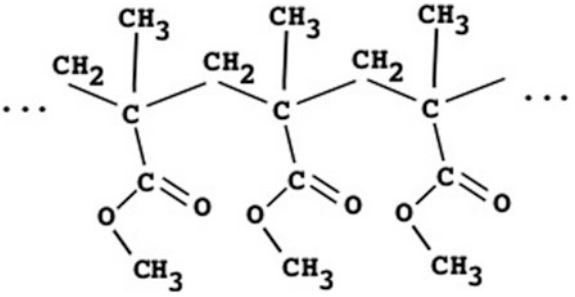

Fig. 5 Structure of PMMA [Reproduced with permission from [34]]

PMMA is a radiation-sensitive polymer. It is considered to be degrading (chain scissoring) type polymer after irradiation because the increase of its solubility and high emission rate after ion irradiation is related to chain scissoring [41]. One of the prominent reasons of this chain-scissoring property is the presence of side chains around quaternary carbon atom in the structure of PMMA (Fig. 5) which restrict the chain mobility and hinder cross-linking [34]. Nathawat et al. reported chain scissoring after electron beam (10 keV energy) irradiation upon PMMA films of 20 μm thickness [42]. But prolonged irradiations give contrary results; i.e., it can show both cross-linking and chain scissoring after ion irradiation [41]. There are other reports which claim PMMA to be cross-linked after ion irradiation [13, 43–45]. The emission of volatile gasses plays a vital role in the modification of ion-irradiated PMMA. In a report, Hossain et al. performed on- line RGA of PMMA while irradiating with 4.5 MeV/u Au ions as shown in Fig. 6 [46]. Their RGA analyses showed that the main volatile fragments of irradiated PMMA polymer were H_2, CH_3, CH_4, CO and CO_2, the latter presumably produced from the unstable CH_3OCO radical originating from the side chain scission. This mechanism is shown in Fig. 7 [46]. This was initiated by homolytic bond breaking by the highly energetic δ-electrons [46].

So, the above discussion implies that both the effects of cross-linking and degradation occur after ion irradiation, but the overall modifications depend upon

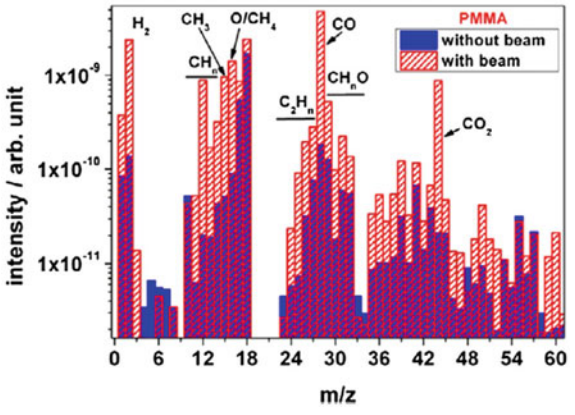

Fig. 6 Outgassing spectra of PMMA polymer irradiated with 4.5 MeV/u Au ions. Reproduced with permission from [46]

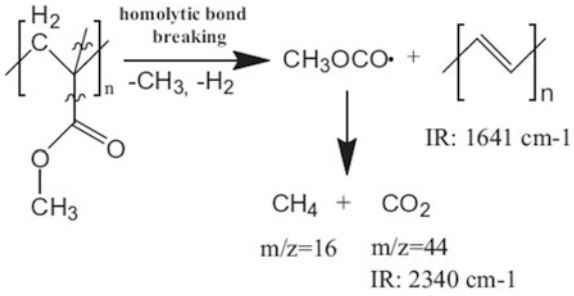

Fig. 7 A possible mechanism of volatile products formation of PMMA foil. Reproduced with permission from [46]

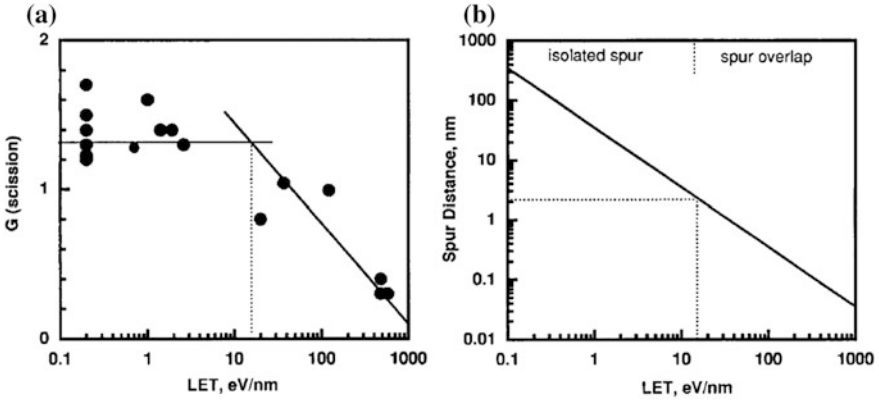

Fig. 8 **a** Scission yield *G* (s) and **b** spur distance as a function of LET for PMMA irradiated by various radiation sources. Reproduced with permission from [13]

ion fluence, ion energy and its *Z* value. The linear energy transfer (LET) plays a vital role in degradation and/or cross-linking of polymeric chains. The high LET ion irradiation of PMMA can modify surface mechanical properties which can be used in the industry where highly cross-linked surfaces are necessary [13].

Lee et al. investigated the degree of scissoring and cross-linking in details for 2 MeV He^+ and Ar^+ ions, 4.5 MeV e-beam and 1.1/1.3 MeV Co^{60} gamma radiation-irradiated PMMA samples (for low and high LET ions) [13]. They carried out gel permeation chromatography (GPC) analyses and measured hardness changes to analyse the degree of cross-linking. The number density of spurs (a discrete loss of energy by SHIs) and their separation are the deciding factors for the degree of cross-linking and degradation for a given LET of irradiated ions [47–49]. In their experiment, the spur distance and scission yield decreased with the increase of LET as shown in Fig. 8 [13]. It shows that low LET implies widely separated spurs which means a significant fraction of deposited energy remains within chains,

leading frequently to chain scissoring, and thus degrades the material. The number of spurs per unit track length increases with the increase of LET which forms a continuous column of overlapping radicals and hence cross-links the polymeric chains. It concludes that low LET affects single molecular chain due to which the chain scission occurs, but on the other hand, high LET produces a high concentration of free radicals, as a result of which the tracks get overlapped and cross-link the molecular chains [13].

Our group reported effects of 50 MeV Li^{3+} and 70 MeV C^{5+} ions and gamma radiation exposure upon free volume of the PMMA polymer using PALS analyses at various fluences and doses, respectively [33, 34]. After data analyses, variations of R and I_3 as a function of ion fluence and gamma dose are shown in Fig. 9. The value of R and FV for lithium ion-irradiated polymers was observed to be decreased at fluences of 1.0×10^{11} and 5.0×10^{11} ions/cm^2 from pristine value, followed by a small increment in their values up to maximum increment at a fluence of 5.0×10^{12} ions/cm^2. The value of R remained almost unchanged for the case of gamma exposure as shown in Fig. 9. The carbon ions exposure gave similar results as those of lithium ions irradiations as shown in Table 2 [33]. The irradiation causes cross-linking, and the polymer chains come closer due to the free radical formation,

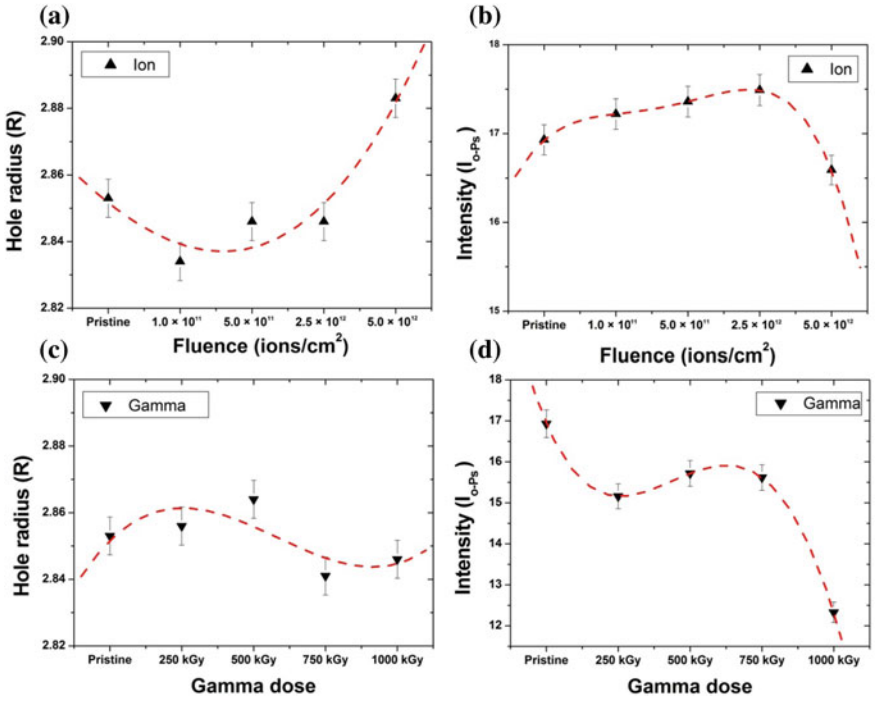

Fig. 9 Variation of **a** hole radius and **b** o-Ps intensity versus ion fluence of the Li^{3+} ions irradiated PMMA samples. Variation of **c** hole radius (R) and **d** o-Ps intensity versus gamma dose of the gamma radiation exposed PMMA sample. Reproduced with permission from [34]

Table 2 Calculated values of radius of free volume hole (R), free volume (FV) and fractional volume (FFV) in pristine and irradiated PMMA samples

Fluence (ions/cm^2)	R (Å)	FV (Å^3)	FFV
Pristine	3.04	117.78	6.67
5×10^{10}	3.00	113.84	5.92
1×10^{11}	2.99	112.16	5.88
5×10^{11}	2.97	110.63	5.90
1×10^{12}	2.99	112.52	5.75
5×10^{12}	2.99	112.62	5.82

Typical errors in the quantities are 0.01Å, 1.15 Å^3 and 0.21, respectively
Reproduced with permission from [33]

which results in the decrease of hole radius and hence the free volume [50]. So the polymeric chains cross-linked at a fluence of 1.0×10^{11} ions/cm^2. In addition to it, the increased surface roughness is related to cross-linking of polymeric chains that leads to change in free volume fraction in modified surface layers [51, 52]. The value of I_3 remained almost constant and decreased at a fluence of 5×10^{12} ions/cm^2, and gamma exposure showed irregular variations of I_3. The value of I_3 depends upon several parameters like the chemical composition of material under study, the type and energy of incident ion/radiation and mechanical history of the sample and its polarity [53]. The probability of formation of o-Ps decreased at a fluence of 5×10^{12} ions/cm^2. In addition to it, there is a certain probability that o-Ps could have reacted chemically with molecules either by chemical inhibition due to which τ_3 decreased or by chemical quenching which is responsible for decrease in value of I_3 [54]. The free volume increased due to increase in value of R at higher fluences. There are two factors which may be responsible for the growth of hole radius. The rise in temperature factor is considerable at a fluence of 5.0×10^{12} ions/cm^2, which may increase R and FV [55]. There is another explanation reported, according to which the carbon clusters act as positron scattering centres and decrease the positron mobility due to which the positron formation probability increases, thereby increasing the value of FV [53]

In addition to the free volume, the radiation treatment modifies the structural as well as optical properties of the polymers. The X-ray diffraction (XRD) studies reveal the modification of crystallite size (calculated using Scherrer formula, see Appendix). The ion irradiation increased the crystallite size (C.S.) by $\sim$11% (8.7–9.7 Å), while gamma exposure decreased C.S. by $\sim$10%. The amorphous nature increased after SHI and gamma irradiations. UV–visible studies revealed the shift of optical absorption edge towards longer wavelength leading to decrease in band gap energy (E_g) of the sample gradually with increase of gamma dose and ion fluences. The value of E_g (calculated using Tauc's relation, see Appendix) decreased by 12% (from 5.04 to 4.43 eV) in case of lithium and gamma exposure for direct transition and 24% (from 4.23 to 3.21 eV) in case of carbon ion irradiation for indirect transitions. These variations are shown in Fig. 10 [34].

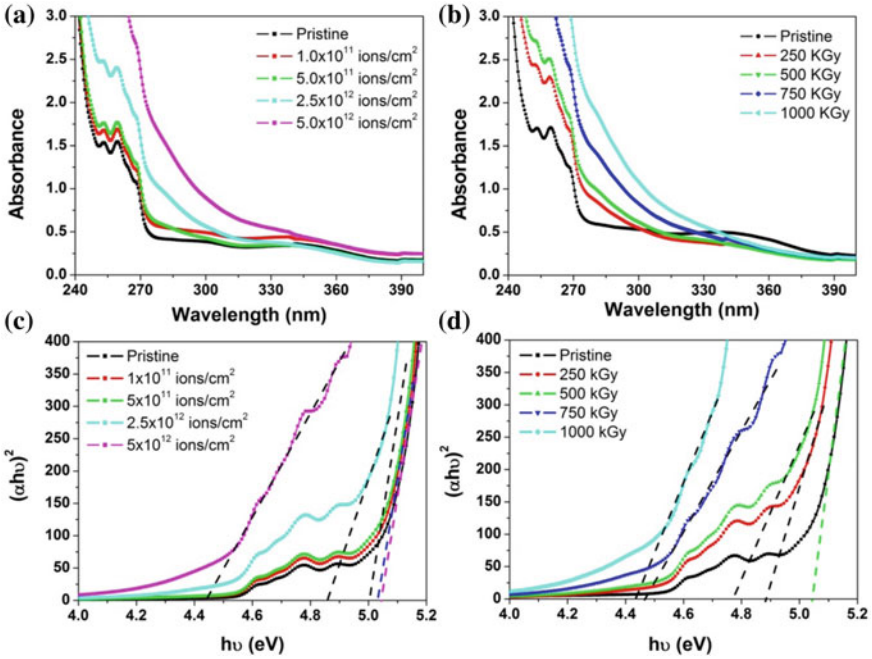

Fig. 10 UV–visible spectra of pristine and **a** Li^{3+} ions irradiated and **b** gamma radiation-exposed PMMA polymer. The dependence of $(\alpha hv)^{1/2}$ on photon energy (hv) for pristine and **c** Li^{3+} ions irradiated and **d** gamma radiation-exposed PMMA polymer. Reproduced with permission from [34]

The irradiation conditions can be optimized to obtain cross-linking of PMMA polymeric chains. Unai et al. reported two-step irradiation method (low flux followed by high flux) to achieve short exposure time to induce cross-linking of PMMA polymeric chains while maintaining the exposed regions free of blisters [56]. The thin-film transistors can be produced by using cross-linked PMMA gate dielectrics, which have high carrier mobility and can be operated at low voltages [57]. Hong et al. fabricated waveguides in PMMA by proton implantation in order to increase the mode number and refractive index [58].

The surface hardness and conductivity can be tailored/increased by doping the polymer with suitable metallic nanoparticles followed by ion irradiation. Singh et al. reported the increase in ac conductivity of copper-doped PMMA after the radiation treatment of 140 MeV silver ions as shown in Fig. 11 [59]. The Fig. 11 clarifies that ac conductivity increased with increase of frequency, filler concentration as well as ion fluence [59]. This concludes that ion irradiation promotes metal to polymer bonding by depleting the hydrogen from the carbon network of the polymer due to the emission of gaseous species [60, 61].

The doping of metal nanoparticles or grafting of the polymers with other suitable nano-sized materials modifies the material properties significantly in terms of small

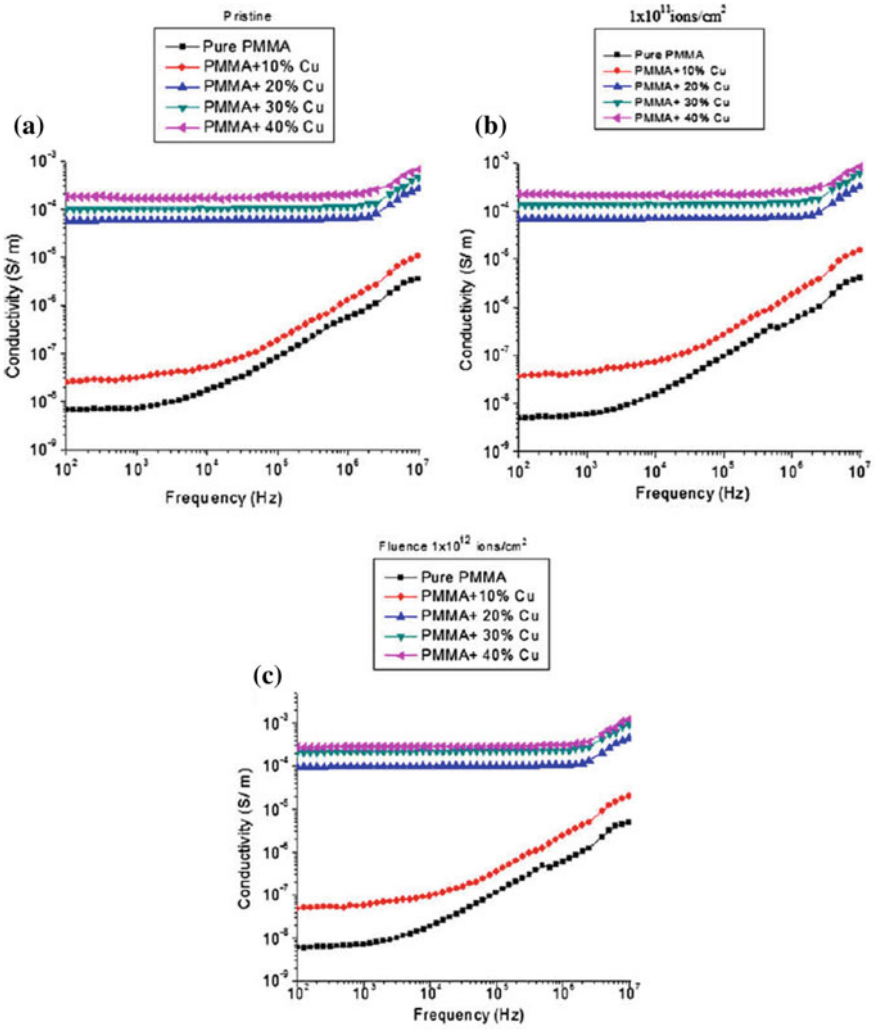

Fig. 11 Frequency dependence of the conductivity of PMMA/Cu composites at different concentrations of Cu filler (10–40%) for **a** pristine samples, **b** irradiated with silver ions at a fluence of 1×10^{11} ions/cm^2 and **c** irradiated at a fluence of 1×10^{12} ions/cm^2. Reproduced with permission from [59]

size, surface and quantum size effects as well as macroscopic quantum tunnel effect [62–64, 66]. The silane coupling agents (having ability to form a bond between organic and inorganic materials) can be used to cover the surfaces of polymer composites doped with magnetic particles; these composites are used for wave absorbers for the quasi-microwave band which are thinner (2 mm) than conventional spinel-type ferrite absorbers (6–7 mm) [65]. This property of least thickness

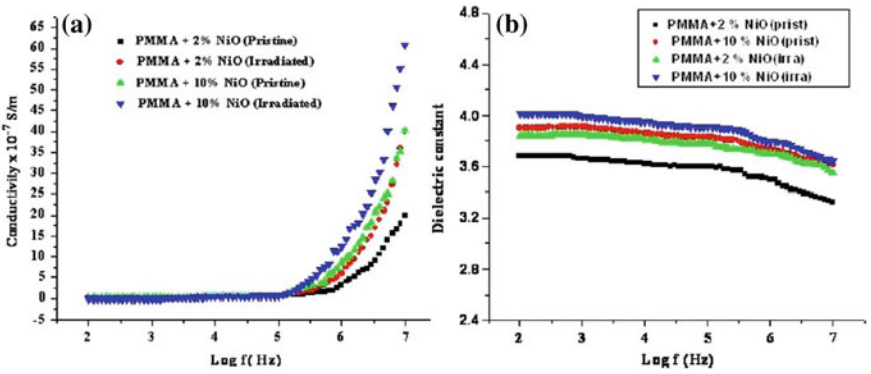

Fig. 12 Variation of **a** ac conductivity and **b** dielectric constant as a function of log frequency for pristine and irradiated samples [Reproduced with permission from [66]

(or more thinness) results from permeability and permittivity values that are higher than those of conventional systems [65]. Gavade et al. reported the effects of lithium ion irradiation on dielectric properties of NiO nanoparticles dispersed in PMMA polymer matrix [66]. The conductivity and dielectric constant were measured as a function of frequency (1–10 MHz range) for 2 and 10% NiO doping for pristine and irradiated samples, respectively. The plots are shown in Fig. 12 [66]. The conductivity and dielectric constant increased with increase of doping concentration. The potential barrier depleted due to increase of conduction between filler particle aggregates in the doped composite, as a result of which conductivity and dielectric constant increased; both of these properties further increased with ion irradiation. The gaseous emission during irradiation converts polymeric structure into hydrogen-depleted carbon network, which promotes metal to polymer bonding and hence makes the composite more conductive [66].

5 Polyethylene Terephthalate

Polyethylene terephthalate (PET) is a semi-crystalline thermoplastic polyester derived from polyethylene terephthalate. Its chemical formula is $[C_{10}H_8O_4]_n$. Its melting point is 260 °C, and the density is approximately 1.31 g/cm^3. The glass transition temperature of PET varies between 67 ºC and 81 °C. PET polymer has commercial applications in the fabrication of various electrical instruments, packaging, X-ray sheets, plastic bottles and blood vessel disease treatments (atherosclerosis) [67, 68].

PET membranes have great utilization for gas separation applications. The permeability (rate of flow of gas) and selectivity (ability of a membrane to accomplish a given separation) are important parameters of a membrane to be used as a gas separating membrane commercially. The other commercially available

polymer membranes are polysulfone, polyimides, tetrabromopolycarbonate, cellulose acetate, poly(phenylene oxide), polyimide, silicon rubber, silicon rubber, poly (trimethylsilyl propyne) and many more [69]. PET membranes have an advantage of high gas permeability and permeation selectivity among the other commercially available gas separating membranes such as metal and ceramic membranes. The permeability coefficient (P) is related to diffusion coefficient (D) and solubility coefficient (S) by the relation $P = DS$. The value of P varies in the range of 10^{-4} to 10^{4} Barrer in case of polymer membranes [69]. Generally, the permeability of the membrane increases at the cost of permeation selectivity, but ion beam irradiation technology for the production of tracks has overcome this limitation. The pore size and porosity are two parameters in case of track-etched polymeric membranes that make them distinct advantageous over conventional membranes. Both of these parameters are independent of each other and can be varied in an easily controlled manner over several orders of magnitude [9]. Pore size is a function of etching time, while porosity is a function of irradiation process [70]. The polymeric membrane is subjected to chemical etching process after the tracks are formed by ion irradiation. The etching time and irradiation fluence can be calibrated in order to get membranes of desired pore size and porosity. The membranes with pore sizes from about 10 nm to several micrometres are commercially available [71]. The conditions of chemical etching affect the pore shape [72]. The pore size of PET can be controlled by the track formation by ion irradiation followed by chemical etching. The mechanical stability and permeability can be increased simultaneously by performing gelation in the pores of track-etched PET membranes [71, 73]. Further improvements can be achieved through functionalization of membranes via different routes as explained in details by Ulbricht et al. [71]. One such example is shown in Fig. 13 [74]. This figure shows the SEM image of track-etched PET membranes functionalized via 'grafting from' with an amino-functional polyacrylate [74].

The pore size of the membranes can be controlled by changing the etching time for suitable applications. Awasthi et al. increased the permeability of different gasses by controlling the pore size of 25-μm-thick PET membranes after irradiating with 100 MeV Cl^{9+} ions as a function of etching time [9]. They reported outer diameter of the pores to be 2 μm as shown in Fig. 14 and pore size of 70–120 nm for different etching times [9]. The etching time affected the permeability of the gasses. The permeability of different gasses increased with increase of etching time as shown in Fig. 15 [9].

The free volume and distribution of the effective micropore size of the free volume elements are interconnected [75, 76]. The gas diffusion properties are related to amount and distribution of free volume [31]. The gas permeability and free volume are directly related to each other [30]. So, it is important to study free volume so that permeation can be estimated. Our group reported the modifications in the free volume of PET polymer by controlled irradiation of carbon, lithium and gamma radiation. The value of R and FV increased after lithium ion irradiation as shown in Fig. 16 [77]. The variations of R and FFV as a function of carbon ion fluence and gamma dose have been plotted in Fig. 17a–d [78]. The values of R, FV and FFV were almost unchanged after gamma exposure. The gamma exposure is

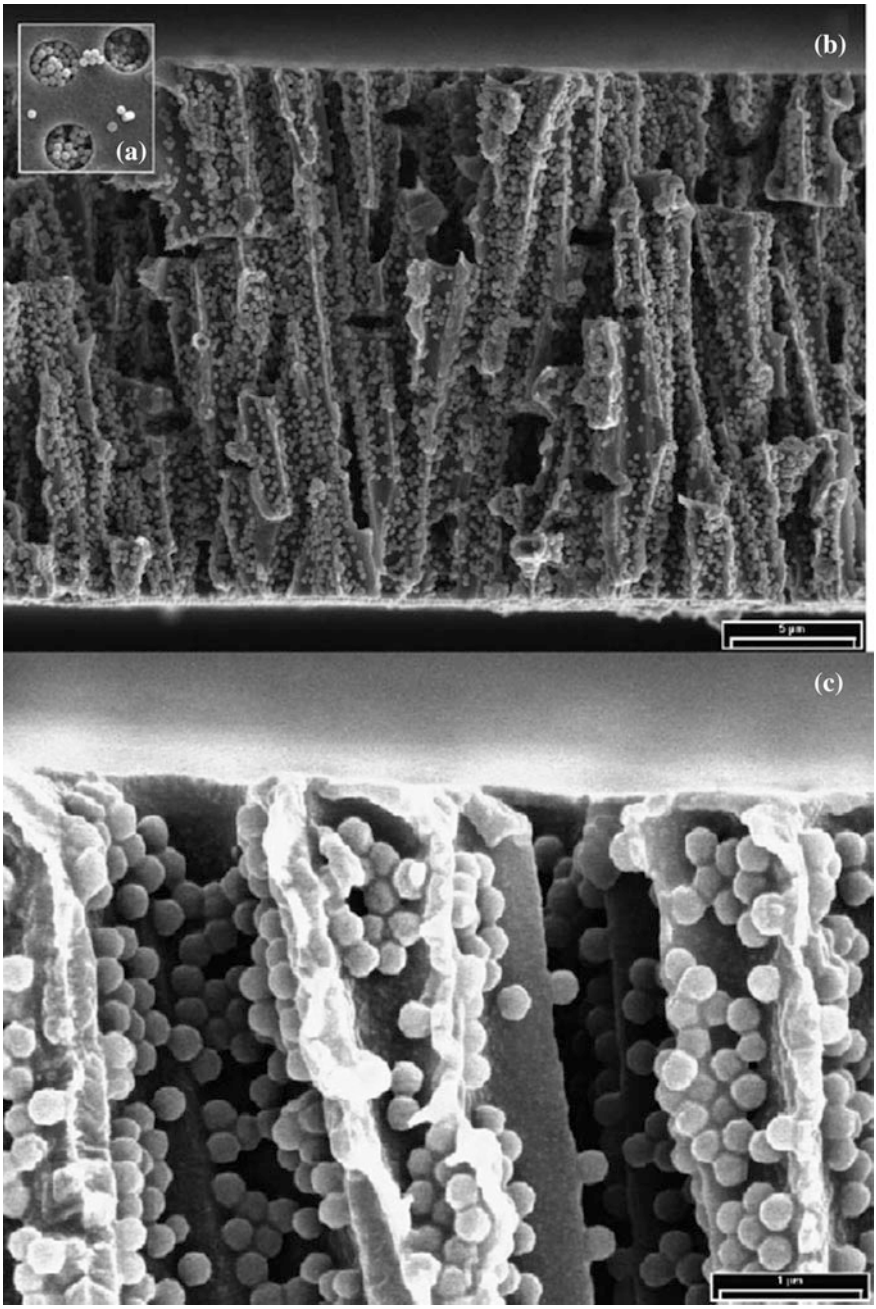

Fig. 13 SEM cross-sectional images of a nanoparticle composite membrane—the base track-etched PET membrane. **a** Filled pores before coupling reaction overnight, **b** cross section after coupling reaction and complete washing and **c** cross-sectional detail demonstrating the distance between neighboured bound nanoparticles. Reproduced with permission from [74]

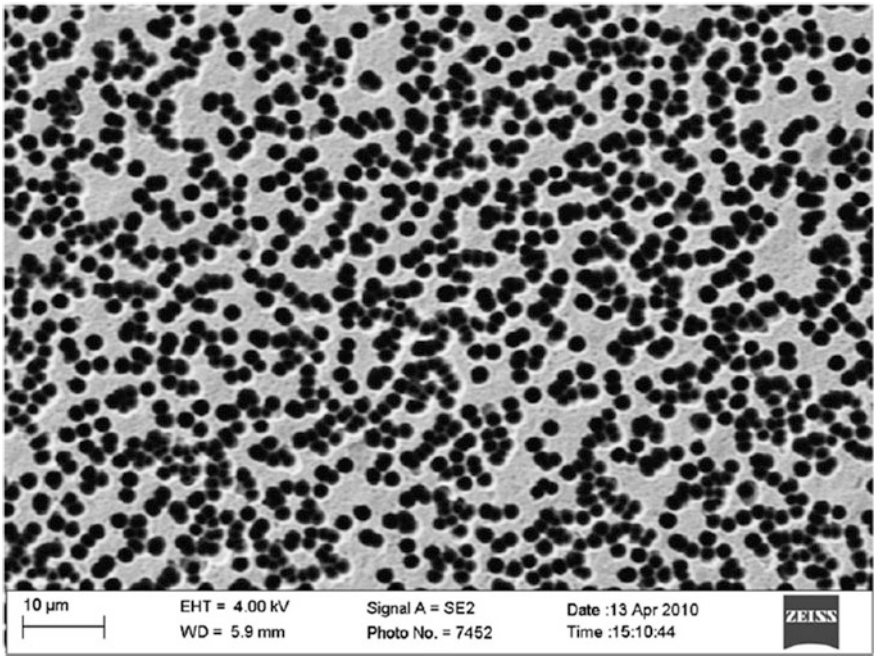

Fig. 14 SEM image of track-etched PET membrane. Reproduced with permission from [9]

almost an electronic energy loss process. The nuclear energy loss is almost negligible in this case. It has been reported that nuclear energy loss is responsible for the defects creations in the target materials. The free volume is a kind of defect which is almost constant in gamma exposure due to the absence of nuclear energy loss and hence due to the lack of defects creation.

The PET polymer is semi-crystalline in nature. Its XRD peaks are sharp and intense as compared to other amorphous polymers. The X-ray diffraction studies showed amorphization after lithium ion irradiation due to decrease in the intensity of the diffraction peaks as shown in Fig. 18 [77]. The crystallite size was increased after ion irradiations (from 36.5 Å for pristine value to 64.6 Å for fluence of 5×10^{12} ions/cm^2). However, the polymer crystalline nature was observed to be improved after carbon ion irradiation and gamma radiation exposure, although the improvement was independent of the ion fluence. The band gap energy (E_g) was analysed to be decreased by 15.8% (at 5×10^{12} ions/cm^2), 16.4% (at 5×10^{12} ions/cm^2) and 12.3% (1250 kGy) in case of lithium ion, carbon ion and gamma radiation exposure, respectively, for direct transitions. Awasthi et al. reported decrease in crystalline nature of PET in XRD studies after 100 MeV oxygen ion irradiation [79]. They reported decrease in the value of E_g by 11.3%. Ramola et al. also observed decrease in peak intensity of XRD after 120 MeV nickel ion irradiation and decrease in E_g by 39% in UV–visible studies [80]. Biswas et al. reported decrease in peak intensity of X-ray diffraction after 180 MeV silver ion

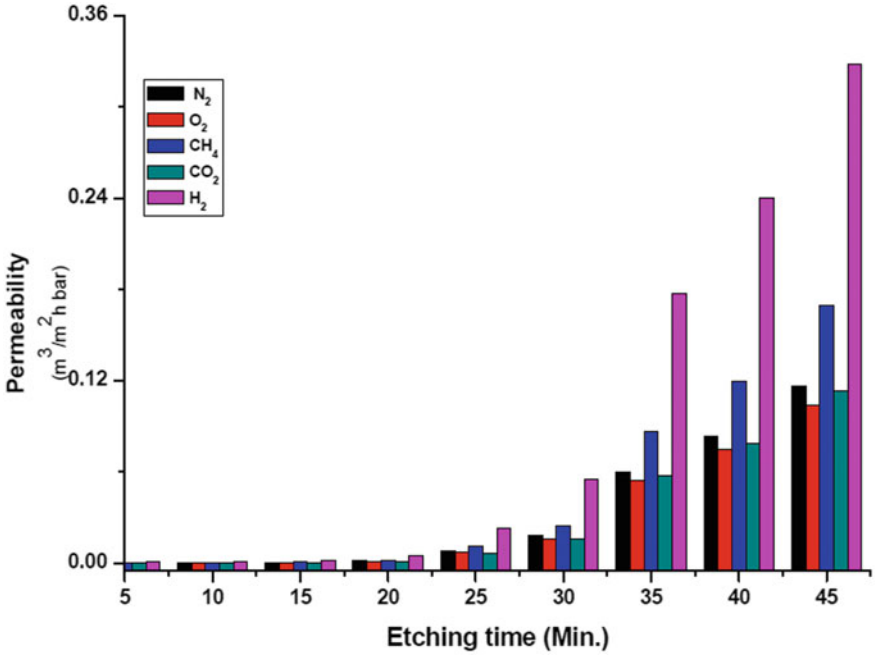

Fig. 15 Gas permeability of PET membrane at different etching times. Reproduced with permission from [9]

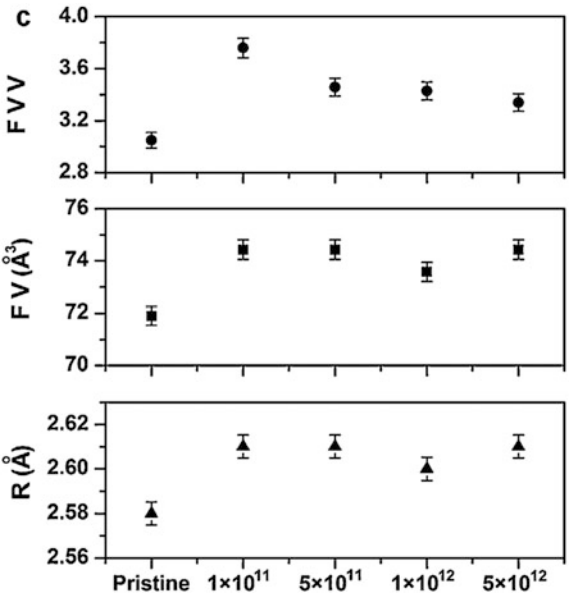

Fig. 16 Variations of hole radius (*R*), free volume (FV) and fractional free volume (FFV) as a function of lithium ion fluence. Reproduced with permission from [77]

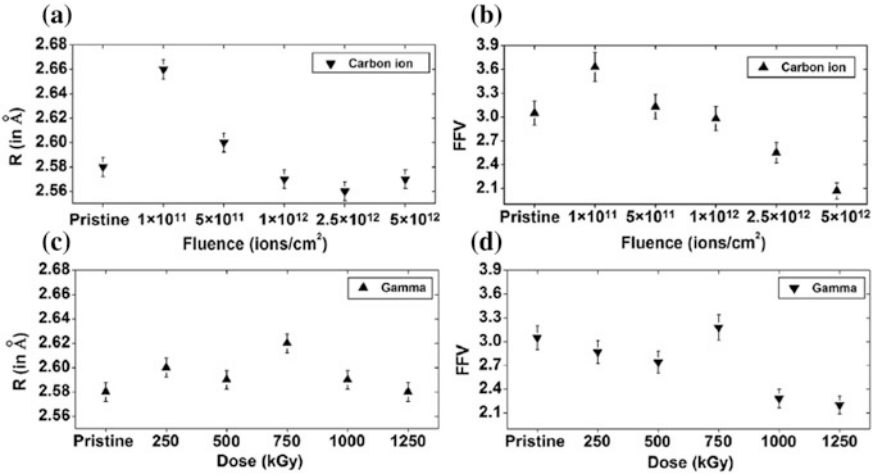

Fig. 17 Variation of **a** hole radius (*R*) and **b** fractional free volume (FFV) as a function of ion fluence of the C^{5+} ions-irradiated PET samples. Variation of **c** hole radius (*R*) and **d** fractional free (FV) volume as a function of gamma dose of the gamma radiation-exposed PET samples. Reproduced with permission from [78]

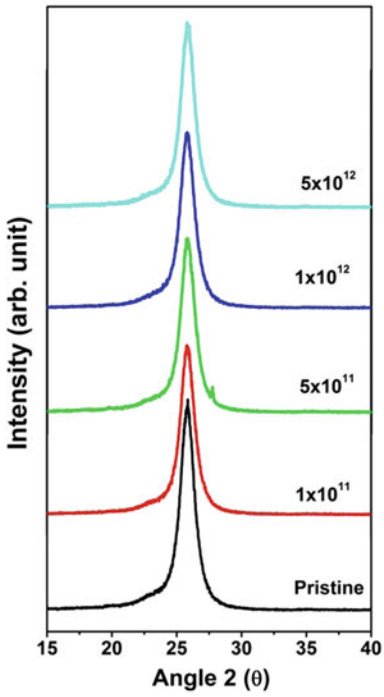

Fig. 18 X-ray diffraction patterns of pristine and Li^{3+} ions irradiated PET polymer samples. Reproduced with permission from [77]

irradiation [81]. Prasad et al. observed no changes in the XRD studies after gamma exposure (50, 90 and 135 kGy doses) to PET polymer [82].

PET polymer has advanced applications in medical science. It is used as a sewing cuff around the circumference of heart valves to promote tissue in-growth and to provide a surface to suture the valve to the surrounding tissue [83]. Endocarditis is an infection of the heart's valves or inner lining. It occurs when germs get into the bloodstream and settle inside the heart, often on a valve. The infection is usually caused by bacteria (in rare cases, it is caused by fungi [84]). The silver coating of prosthetic valve sewing rings is used to protect against prosthetic endocarditis [85, 86]. Jin et al. reported that toxic effect exerted through the release of silver ions into the tissues or body fluid is the important parameter which decides the clinical potentiality of PET modified by Ag ion implantation (Ag-ion-PET) [87]. They observed that Ag-ion-PET sample has a large potential to kill bacteria, and the adhered colonies of a particular species of bacteria [called staphylococcus epidermidis (SE)] on the surface of Ag-ion-PET sample were as less as 24% on the control PET surface. Similar bacterial adhesion behaviour of Ag-implanted PET was studied by Li et al. [88]. They also reported 24% less concentration of SE on the surface of Ag-implanted PET.

6 Polyallyl Diglycol Carbonate

Polyallyl diglycol carbonate (PADC) is used as solid-state nuclear track detector (SSNTD) due to its ability of ion track detection [89]. Its trade name is CR-39. The literature of gamma and neutron ray's exposure on CR-39 polymer with various fluences and doses is available. Ramola et al. reported the increase in polymer crystalline nature and decrease in band gap energy from 4.8 to 3.4 eV after oxygen ion irradiation of PADC [90]. Although, in a recent study by El-Saftawy et al., the polymer crystalline nature was reported to be decreased by 20%. In addition to decrease in the band gap energy, they reported colour transformation due to the trapped free radicals or charged species in the polymer [91]. In a similar study, Singh and Prasher observed 22% fall in band gap energy as well as shift of absorption edge towards visible region after 40 MeV lithium ion irradiation of PADC polymer. A minute decrease in band gap energy (3.88 to 3.85 eV) of PADC polymer by neutron irradiation has been reported [92]. Zaki irradiated PADC polymer samples of thickness 500 μm with gamma radiation (Co-60 source, 7.5 kGy/h dose) up to quite a high dose of 5715 kGy and reported the decrease in band gap energy from 3.6 to 1.9 eV in case of indirect transitions (47.2%) and 4.2 to 2.7 eV in case of direct transitions (35.7%) [93]. El-Badry, a year later, reported similar results with keV ions irradiations upon PADC polymer samples. He reported 40.4% (4.2 to 2.5 eV) and 64.8% (3.7 to 1.3 eV) decrease in direct and indirect band gap energies, respectively, after 320 keV Ar ion irradiations as well as 47.5% (4.0 to 2.1 eV) and 66.6% (3.6 to 1.2 eV) decrease in direct and indirect band gap energies, respectively, after 130 keV He ion irradiation [94]. In addition, he reported the decrease in

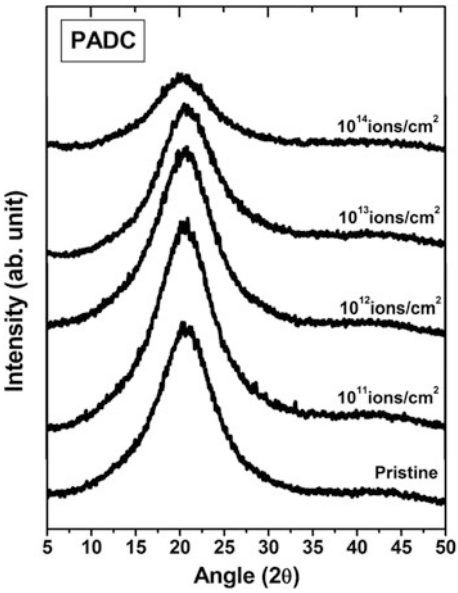

Fig. 19 X-ray diffraction pattern of pristine and lithium ion-irradiated samples of PADC polymer. Reproduced with permission from [96]

photoluminescence intensity due to defects and clusters induced by these ions. In a reported study by our group, 125-μm-thick and 250-μm-thick PADC films were irradiated by 50 MeV Li^{3+} and 70 MeV C^{5+} ions, respectively. A sharp decrease in the band gap energy was observed in both cases of irradiations due to the formation of conjugated system of bonds. The carbon ion irradiation showed a 24% (3.98 to 2.82 eV) decrease in band gap energy as compared to 19% (3.98 to 3.03 eV) decrease in case of Li ion irradiation for indirect transitions [95]. The Li^{3+} ion-irradiated samples showed increase in the amorphous nature at higher fluences as shown in Fig. 19 [96]. The free volume was observed to be decreased with increase of ion fluence due to cross-linking of polymeric chains. The cross-linking effects in polymeric chains find applications in the field of microelectronic devices and printing process [89]. Kader reported decrease in the band gap energy for silver ion-irradiated PADC polymer samples from 4.2 to 3.6 eV and 3.2 to 2.5 eV for direct and indirect transitions, respectively [89].

7 Applications

Polymers have wide applications in radiation dosimetry, a field of health physics and radiation protection, such as PADC which is used in SSNTDs as explained earlier.

Polymer ion track membranes (PITMs) have applications in the processes of filtration, drinking water treatment, extractive industrial water processes and

effluent treatment, industrial gas separation, domestic air filtration, biochemical sensing, cell culture and fuel cells [97]. Nowadays, the PET, polypropylene and polycarbonate membranes are commercially available in a wide range of pore size diameter (10 nm–few microns). The use of these PITMs reduces environmental contamination as well as consumption of energy and natural resources. In recent developments, the PITMs are composited with other nanomaterials for fabrication of microfluidic sensor and photocatalytic reactor elements designed for the detection and deactivation of biological hazard substances in solutions [98].

The ionic conductivity of polymer electrolytes can be increased by electron beam irradiation [99]. The mechanical properties, tensile strength and rigidity of Teflon and polyester can be improved by ion-induced cross-linking. Radiation-induced cross-linked chains of polymers have applications in the development of cables, wires and rubber tires [77, 100].

The gaseous emission during irradiation can affect certain properties of polymers. The emission of hydrogen followed by oxidation of surface layers of polyethylene by ion implantation increased wet ability and can be used for biomedical applications (revealing bacteriostatic effect) after doping with some impurity atoms [101]. The dielectric properties of polymers due to the emission of volatile and low molecular gasses have been studied by Singh and his group [102–107].

The band gap energy can be decreased and controlled with ion irradiation. The optical modifications occurring in the ion beam-modified polymers may produce new electronic levels in the forbidden gap of the electronic band structure, which enhances the electrical conductivity of the target polymer. This property can be utilized in producing special materials for electronic applications [108]. The ion beam irradiation induces defects in the polymers which may improve the transport property of protons and may promote the dissociation of water molecules at the surface, resulting in an increase of proton concentration, thereby increasing the electrical properties as per the reports available [109, 110]. The increase of electrical conductivity of polycarbonate after He and Ar ion irradiation has been reported [110]. The polymeric material with good surface conductivity and the poor bulk conductivity can be utilized as frames for sensitive measuring systems to overcome the problem of static charge accumulation [110]. Ion-implanted PMMA can be used in biosensors and biomedical fields for electrical applications [111]. The enhanced electrical properties of PET membranes by ion irradiation have been reported [112, 113]. The effects of electrons and proton irradiations upon the electrical and optical properties of some other polymers are reported [114–117].

The surface modifications of polymers by radiation treatment improve their adhesion, friction, wetting and biological compatibility. The use of ion beam has been reported for the evolution of nanostructures which are essential in the development of devices that incorporate nanoscale functionality for mechanical, chemical and optical features [118–123].

8 Summary and Conclusion

The polymeric properties can be tailored/modified by radiation treatment-swift heavy ions (MeV range), electrons, protons, low-energy ions (keV range) and gamma rays. The radiation physics and chemistry of polymeric materials are widely applicable in modifying the structural, chemical, mechanical, optical, thermal, magnetic, surface, electrical and many other properties of the polymeric materials. Ion irradiation leads to excitation, ionization and gas liberation. All these modifications are related to cross-linking (gelling) and scissoring (degradation) of polymeric chains which occur simultaneously during irradiation of polymers, but the dominance of one over the other depends upon polymer structure and other factors such as ion energy and fluence. The linear energy transfer (LET) plays an important role in degradation and/or cross-linking of polymeric chains. There are certain other parameters which can optimize the yield of modification such as type and energy of ion, sample thickness and ion fluence (number of ions per unit volume).

Ion implantation can increase the mode number and refractive index of a polymer for the use of waveguides. The polymer doping or grafting with other nano-sized materials can be used to tailor or calibrate the certain properties. The surface hardness and conductivity can be tailored/increased by doping the polymer with suitable metallic nanoparticles followed by ion irradiation. The structural modifications occurring in the ion beam-modified polymers may produce new electronic levels in the forbidden gap of the electronic band structure, which may enhance the electrical conductivity of the target polymer. So, the ion beam technique can be utilized in producing special materials for electronic applications

Polymer ion track membranes (PITMs) have a wide range of industrial and commercial applications. These membranes have advantage of high gas permeability and permeation selectivity among the other commercially available gas separating membranes such as metal and ceramic membranes. The polymeric material is subjected to chemical etching process after the tracks are formed by ion irradiation. The pore size of the membranes can be controlled by changing the etching time for suitable applications.

Conducting polymers can be doped with nanofillers such as carbon nanotubes (CNT) for advanced applications such as supercapacitors. The controlled dopings of ternary composites of polymers and CNT graphene may increase the cycling capacity of the supercapacitors. These composites can be further tested by ion beam modification (using low- and high-energy ions) The composites of CNT, ethyl vinyl acetate and PANI with a 3D co-continuous phase structure having SC of 1105 Fg^{-1} and excellent cycling performance over 45,000 cycles have been reported [124]. The future perspective of the nanocomposites with high surface area lies in the ternary composites of graphene, CNTs and CPs which can have high cyclic stability as well as effective in accession of the electrolyte to the electrode in the redox mechanism [125].

Appendix

The crystallite size (C.S.) can be calculated using Scherrer formula given below [126]:

$$L = \frac{k\lambda}{b\cos\theta}$$

Here, b is the full width at half maximum (FWHM) of the XRD peak (in radian), λ is the wavelength of the X-rays used (1.54 Å in most of the cases for Cu K_α radiation), and θ is the angle which is calculated by taking $\frac{1}{2}$ of 2θ value in above equation. k is a constant of proportionality (called the Scherrer constant), and its value depends on how the width is determined and the shape of the crystal. The value of k is 0.9 for polymeric samples.

The optical band gap energy (E_g) can be calculated from the absorption spectra by extrapolating the linear portion of the plot of $(\alpha h\nu)^n$ against $(h\nu)$ to the energy axis. The value of E_g is calculated using Tauc's relation given below [127]:

$$(\alpha h\nu)^n = B\left(h\nu - E_g\right)$$

Here, E_g is average band gap energy of the material. B in the above equation is the band tailing parameter that depends on the transition probability and can be assumed to be constant within the optical frequency range. The value of n characterizes the transition processes in K-space. Its value is 2, 3, $\frac{1}{2}$ and $\frac{3}{2}$ for direct allowed, direct forbidden, indirect allowed and indirect forbidden transitions, respectively. Here, α is known as the optical absorption coefficient and its value is calculated from the absorbance (A), after correction for reflection losses using the equation: $\alpha(v) = \frac{2.303A}{l}$. Here, l is the sample thickness in centimetres.

References

1. Podgorsak EB (2005) Radiation oncology physics: a handbook for teachers and students/ editor. International Atomic Energy Agency Publishing, Vienna, Austria
2. Krasheninnikov AV, Nordlund K (2010) Ion and electron irradiation-induced effects in nanostructured materials. J Appl Phys 107:071301
3. Lee EH (1999) Ion-beam modification of polymeric materials-fundamental principles and applications. Nucl Instrum Methods Phys Res, Sect B 151:29–41
4. Fleischer RL, Price PB, Walker RM, Hubbard EL (1967) Criterion for registration in dielectric track detectors. Phys Rev 156(353):355
5. Bringa EM, Johnson RE (2002) Coulomb explosion and thermal spikes. Phys Rev Lett 88:165501
6. Toulemonde M, Dufour Ch, Meftah A, Paumier E (2000) Transient thermal processes in heavy ion irradiation of crystalline inorganic insulators. Nucl Instrum Methods Phys Res, Sect B 166–167:903–912

7. Toulemonde M, Dufour Ch, Wang Z, Paumier E (1996) Atomic and cluster ion bombardment in the electronic stopping power regime: a thermal spike description. Nucl Instrum Methods Phys Res, Sect B 112:26–29
8. Szenes G (1996) Thermal spike model of amorphous track formation in insulators irradiated by swift heavy ions. Nucl Instrum Methods Phys Res, Sect B 116:141–144
9. Awasthi K, Stamm M, Abetz V, Vijay YK (2011) Large area Cl^{9+} irradiated PET membranes for hydrogen separation. Int J Hydrogen Energy 36:9374–9381
10. Ziegler JF, Ziegler MD, Biersack JP (2010) SRIM – the stopping and range of ions in matter. Nucl Instrum Methods Phys Res, Sect B 268:1818–1823
11. Bragg WH, Kleeman R (1905) On the α particles of radium, and their loss of range in passing through various atoms and molecules. Philos Mag 10:318–340
12. Cleland MR, Parks LA, Cheng S (2003) Applications for radiation processing of materials. Nucl Instrum Methods Phys Res, Sect B 208:66–73
13. Lee EH, Rao GR, Mansur LK (1999) LET effect on cross-linking and scission mechanisms of PMMA during irradiation. Radiat Phys Chem 55:293–305
14. Delgado AO, Rizzutto MA, Tabacniks MH, Added N, Fink D (2009) Infrared analysis of ion beam irradiated polymers. Nucl Instrum Methods Phys Res, Sect B 267:1546–1548
15. Avasthi DK (2000) Some interesting aspects of swift heavy ions in materials science. Curr Sci 78:1297–1306
16. Avasthi DK (1998) High energy heavy ions in materials characterization at NSC pelletron. Nucl Instrum Methods Phys Res, Sect B 136–138:729–735
17. Kanjilal D (2001) Swift heavy ion-induced modification and track formation in materials. Curr Sci 80:1560–1566
18. Wang YQ (2000) Ion beam analysis of ion-implanted polymer thin films. Nucl Instrum Methods Phys Res, Sect B 161–163:1027–1032
19. Hnatowicz V, Havranek V, Bocan J, Mackova A, Vacik J, Svorcik V (2008) Modification of poly(ether ether ketone) by ion irradiation. Nucl Instrum Methods Phys Res, Sect B 266:283–287
20. Hnatowicz V, Perina V, Mackova A, Svorcik V, Rybka V, Fink D, Heitz J (2001) Degradation of polyimide by 100 keV He^+, Ne^+, Ar^+ and Kr^+ ions. Nucl Instrum Methods Phys Res, Sect B 175–177:437–441
21. Parada MA, Delalezv N, de Almeida A, Muntele C, Muntele I, Ila D (2006) Low energy ion beam induced changes in ETFE polymer. Nucl Instrum Methods Phys Res, Sect B 242:550–552
22. Forsyth M, Meakin P, Macfarlane DR, Hill AJ (1995) Positron annihilation lifetime spectroscopy as a probe of free volume in plasticized solid polymer electrolytes. Electrochim Acta 40:2349–2351
23. Peng ZL, Wang B, Li SQ, Wang SJ, Liu H, Xie HQ (1994) Investigation of ionic conductivity of polymeric electrolytes based on poly (ether urethane) networks using positron probe. Phys Lett A 194:228–234
24. Pas SJ, Ingram MD, Funke K, Hill AJ (2005) Free volume and conductivity in polymer electrolytes. Electrochim Acta 50:3955–3962
25. Goworek T, Rybka C (1975) Influence of polymerisation on positronium formation in acenaphtylene. Phys Lett A 53:273–274
26. Yave W, Car A, Peinemann K, Shaikh MQ, Ratzke K, Faupel F (2009) Gas permeability and free volume in poly(amide-b-ethylene oxide)/ polyethylene glycol blend membranes. J Membr Sci 339:177–183
27. Wang ZF, Wang B, Qi N, Ding XM, Hu JL (2004) Free volume and water vapor permeability properties in polyurethane membranes studied by positrons. Mater Chem Phys 88:212–216
28. Algers J, Suzuki R, Ohdaira T, Maurer FHJ (2004) Characterization of free volume and density gradients of polystyrene surfaces by low-energy positron lifetime measurements. Polymer 45:4533–4539

29. Dlubek G, Stejny J, Lupke TH, Bamford D, Petters K, Hubner CH, Alam MA, Hill MJ (2002) Free-volume variation in polyethylenes of different crystallinities: positron lifetime, density, and X-Ray Studies. J Polym Sci, Part B: Polym Phys 40:65–81
30. Wate S, Acharya NK, Bhahada KC, Vijay YK, Tripathi A, Avasthi DK, Das D, Ghughre S (2005) Positron annihilation lifetime and gas permeation studies of energetic ion-irradiated polycarbonate membranes. Radiat Phys Chem 73:296–301
31. Choudalakis G, Gotsis AD (2012) Free volume and mass transport in polymer nanocomposites. Curr Opin Colloid Interface Sci 17:132–140
32. Gidley DW, Peng HG, Vallery RS (2006) Positron annihilation as a method to characterize porousmaterials. Annu Rev Mater Res 36:49–79
33. Singh P, Kumar R, Cyriac J, Rahul MT, Nambissan PMG, Prasad RR (2014) High energy (MeV) ion fluence dependent nano scale free volume defects studies of PMMA films. Nucl Instrum Meth Phys Res B 320:64–69
34. Singh P, Kumar R, Singh R, Roychowdhury A, Das D (2015) The influence of cross-linking and clustering upon the nanohole free volume of the SHI and γ-radiation induced polymeric material. Appl Surf Sci 328:482–490
35. Tao SJ (1972) The Positron annihilation in molecular substances. J Phys Chem B 105:4657–4662
36. Eldrup M, Lightbody D, Sherwood JN (1981) The temperature dependence of positron lifetimes in solid pivalic acid. Chem Phys 63:51–58
37. Nakanishi H, Wang SJ, Jean YC (1988) In: Sharma SC (ed) (1988) Positron annihilation studies of fluids (p. 292). World Scientific Publishing Co. Ltd. Singapore
38. Wang YY, Nakanishi H, Jean YC, Sandreczki TC (1990) Positron annihilation in amine-cured epoxy polymers—pressure dependence. J Polym Sci, Part B: Polym Phys 28:1431–1441
39. Socol G, Macovei AM, Miroiu F, Stefan N, Duta L, Dorcioman G, Mihailescu IN, Petrescu SM, Stan GE, Marcov DA, Chiriac A, Poeata I (2010) Hydroxyapatite thin films synthesized by pulsed laser deposition and magnetron sputtering on PMMA substrates for medical applications. Mater Sci Eng, B 169:159–168
40. Erbe EM, Clineff TD, Gualtieri G (2001) Comparison of a new bisphenol-a-glycidyl dimethacrylate-based cortical bone void filler with polymethyl methacrylate. Eur Spine J 10: S147–S152
41. Mladenov GM, Braun M, Emmoth B, Biersack JP (1985) Ion beam impact and penetration of polymethyl methacrylate. J Appl Phys 58(7):2534–2538
42. Nathawat R, Kumar A, Acharya NK, Vijay YK (2009) XPS and AFM surface study of PMMA irradiated by electron beam. Surf Coat Technol 203:2600–2604
43. Hall TM, Wagner A, Thompson LFJ (1982) Ion beam exposure characteristics of resists: experimental results. Appl Phys 53:3997–4010
44. Corelli JC, Steckle AJ, Pulver D (1987) Ultralow dose effects in ion-beam induced grafting of polymethylmethacrylate (PMMA). Nucl Instrum Meth Phys Res B19(20):1009–1021
45. Davenas J, Xu XL, Khodr C, Treilleux M, Stefan G (1985) A percolation approach to ion beam induced modifications of organic resists. Nucl Instrum Meth Phys Res B 7(8):513–516
46. Hossain UH, Lima V, Ensinger W, Baake O, Severin D, Bender M (2014) On-line and post irradiation analysis of swift heavy ion induced modification of PMMA (polymethyl-methacrylate). Nucl Instrum Methods Phys Res, Sect B 326:135–139
47. Magee JL, Chatterjee A (1987) In: Farhataziz, Rodgers, MAJ (eds) Radiation chemistry, principles and applications. VCH Publishers, New York
48. Magee JL, Chatterjee A (1987) In: Freeman, GR (ed) Kinetics of nonhomogeneous processes (p. 189). Wiley, New York
49. ICRU Report 31 (1979) Average energy required to produce an ion pair, international commission on radiation units and measurements. Washington, DC
50. Fink D, Muller M, Ghosh S, Dwivedi KK, Vacik J, Hnatowicz V, Cervena J, Kobayashi Y (1999) Hirata K New ways of polymeric ion track characterization. Nucl Instrum Methods Phys Res, Sect B 156:170–176

51. Nathawat R, Kumar A, Kulshrestha V, Vijay YK, Kobayashi T, Kanjilal D (2008) Study of surface activation of PET by low energy (keV) Ni^+ and N^+ ion implantation. Nucl Instrum Methods Phys Res, Sect B 266:4749–4756
52. Rarganathaiah C (2006) Free volume micro probe study of silver ions implanted in polycarbonate. High Perform Polym 18:933–947
53. Ismayil RV, Bhajantri RF, Praveena SD, Poojary B, Dutta D, Pujari PK (2010) Optical and microstructural studies on electron irradiated PMMA: a positron annihilation study. Polym Degrad Stab 95:1083–1091
54. Liao K-S, Chen H, Awad S, Yuan J-P, Hung W-S, Lee K-R, Lai J-Y, Hu C-C, Jean YC (2011) Determination of free-volume properties in polymers without orthopositronium components in positron annihilation lifetime spectroscopy. Macromolecules 44:6818–6826
55. Consolati G (2007) Temperature dependence of nanoholes free volumes in amorphous polymers. Radiat Phys Chem 76:313–317
56. Unai S, Puttaraksa N, Pussadee N, Singkarat K, Rhodes MW, Whitlow HJ, Singkarat S (2013) Fast and blister-free irradiation conditions for cross-linking of PMMA induced by 2 MeV protons. Microelectron Eng 102:18–21
57. Yun Y, Pearson C, Cadd DH, Thompson RL, Petty MC (2009) A cross-linked poly(methyl methacrylate) gate dielectric by ion-beam irradiation for organic thin-film transistors. Org Electron 10:1596–1600
58. Hong W, Woo HJ, Choi HW, Kim YS, G-d Kim (2001) Optical property modification of PMMA by ion-beam implantation. Appl Surf Sci 169–170:428–432
59. Singh D, Singh NL, Qureshi A, Kulriya P, Tripathi A, Avasthi DK, Gulluoglu AN (2010) Radiation induced modification of dielectric and structural properties of Cu/PMMA polymer composites. J Non-Cryst Solids 356:856–863
60. Wang YQ, Curry M, Tavenner E, Dobson N, Giedd RE (2004) Ion beam modification and analysis of metal/polymer bi-layer thin films. Nucl Instrum Methods Phys Res, Sect B 219–220:798–803
61. Qureshi A, Singh NL, Shah S, Kulriya P, Singh F, Avasthi DK (2008) Modification of polymer composite films using 120 MeV Ni^{10+} ions. Nucl Instrum Methods Phys Res, Sect B 266:1775–1779
62. Qiao H, Wei Z, Yang H, Zhu L, Yan X (2009) Preparation and characterization of NiO nanoparticles by anodic arc plasma method. J Nanomater 2009:795928
63. Gleiter H (1990) Nanocrystalline materials. Prog Mater Sci 33:223–315
64. Wang ZL, Liu Y, Zhang Z (2002) Handbook of nanophase and nanostructed materials. Tsinghua University Press, Beijing, China
65. Matsumoto M, Miyata Y (2002) Polymer absorbers containing magnetic particles: effect of polymer permittivity on wave absorption in the quasi-microwave band. J Appl Phys 91:9635–9637
66. Gavade C, Singh NL, Avasthi DK, Banerjee A (2010) Effect of SHI on dielectric and magnetic properties of metal oxide/PMMA nanocomposites. Nucl Instrum Methods Phys Res, Sect B 268:3127–3131
67. Awaja F, Pavel D (2005) Recycling of PET. Eur Polym J 41:1453–1477
68. Ma Z, Kotaki M, Yong T, He W, Ramakrishna S (2005) Surface engineering of electrospun polyethylene terephthalate (PET) nanofibers towards development of a new material for blood vessel engineering. Biomaterials 26:2527–2536
69. Yampolskii Y (2012) Polymeric gas separation membranes. Macromolecules 45:3298–3311
70. Awasthi K, Kulshrestha V, Acharya NK, Singh M, Vijay YK (2006) Ion transport through track etched polypropylene membrane. Euro Polym J 42:883–887
71. Ulbricht M (2006) Advanced functional polymer membranes. Polymer 47:2217–2262
72. Tripathi B, Vijay YK (2010) Engineering nanoporosity for Ti^{+6} ion irradiated Mylar (PET) polymer by positron beam. Int J Hydrogen Energy 35:5419–5422
73. Beginn U, Zipp G, Mourran A, Walther P, Moller M (2000) Membranes containing oriented supramolecular transport channels. Adv Mater 12:513–516

74. Hicke HG, Becker M, Paulke BR, Ulbricht M (2006) Covalently coupled nanoparticles in capillary pores as enzyme carrier and as turbulence promoter to facilitate enzymatic polymerization reactions in flow through enzyme-membrane reactors. J Membr Sci 282:413–422
75. Bernardo P, Drioli E, Golemme G (2009) Membrane gas separation: a review/state of the art. Ind Eng Chem Res 48:4638–4663
76. Kumar R, De U, Nambissan PMG, Maitra M, Ali SA, Middya TR, Tarafdar S, Singh F, Avasthi DK, Prasad R (2008) Positron lifetime studies of the dose dependence of nanohole free volumes in ion-irradiated conducting poly- (ethylene-oxide)–salt polymers. Nucl Instrum Methods Phys Res, Sect B 266:1783–1787
77. Kumar R, Singh P (2015) Influence of SHI upon nanohole free volume and micro scale level surface modifications of polyethyleneterephthalate polymer films. Appl Surf Sci 337:19–26
78. Singh P, Kumar R, Nambissan PMG (2015) Investigation of in-depth and surface properties of polyethyleneterephthalate thin films after SHI and gamma radiation treatment by means of PALS and AFM studies. Vacuum 115:31–38
79. Awasthi K, Kulshrestha V, Avasthi DK, Vijay YK (2010) Optical, chemical and structural modification of oxygen irradiated PET. Radiat Meas 45:850–855
80. Ramola RC, Negi A, Semwal A, Chandra S, Rana JMS, Sonkawade RG, Kanjilal D (2011) High-energy heavy-ion irradiation effects in makrofol-KG polycarbonate and PET. J Appl Polym Sci 121:3014–3019
81. Biswas A, Lotha S, Fink D, Singh JP, Avasthi DK, Yadav BK, Bose SK, Khating DT, Avasthi AM (1999) The effects of swift heavy ion irradiation on the radiochemistry and melting characteristics of PET. Nucl Instrum Methods Phys Res, Sect B 159:40–51
82. Prasad SG, De A, De U (2011) Structural and optical investigations of radiation damage in transparent PET polymer films. Int J Spectros Article ID 810936 (p. 7) https://doi.org/10.1155/2011/810936
83. Metzger A (2009) Polyethylene Terephthalate and the Pillar™ Palatal Implant: its historical usage and durability in medical applications. Medtronic, Inc. Pillar
84. http://www.webmd.com/heart-disease/tc/endocarditis-topic-overview#1
85. Ionescu A, Payne N, Fraser AG, Giddings J, Grunkemeier GL, Butchart EG (2003) Incidence of embolism and paravalvar leak after St Jude Silzone valve implantation: experience from the Cardiff Embolic Risk Factor Study. Heart 89:1055–1061
86. Lansdown ABG (2010) Silver in healthcare: its antimicrobial efficacy and safety in use, p 160, Chap. 7. RSC Publishing. ISBN: 978-1-84973-006-8
87. Jin W, Jianxin L, Liru S, Ling R, Zejin X, Ansha Z, Yongxiang L, Nan H (2007) The biomedical properties of polyethylene terephthalate surface modified by silver ion implantation. Nucl Instrum Methods Phys Res, Sect B 257:141–145
88. Li JX, Wang J, Shen LR, Xu ZJ, Li P, Wan GJ, Huang N (2007) The influence of polyethylene terephthalate surfaces modified by silver ion implantation on bacterial adhesion behaviour. Surf Coat Technol 201:8155–8159
89. Abdul-Kader AM (2014) Surface modifications of PADC polymeric material by ion beam bombardment for high technology applications. Radiat Meas 69:1–6
90. Ramola RC, Chandra S, Rana JMS, Sonkawade RG, Kulriya PK, Singh F, Avasthi DK, Annapoorni S (2008) A comparative study of the effect of O^{+7} ion beam on polypyrrole and CR-39 (DOP) polymers. J Phys D: Appl Phys 41:11541
91. El-Saftawy AA, Abdel Reheem AM, Kandil SA, Abd El Aal SA, Salama S (2016) Comparative studies on PADC polymeric detector treated by gamma radiation and Ar ion beam. Appl Surf Sci 371:596–606
92. Kalsi PC, Agarwal C (2008) Neutron-irradiation effects on track etching and optical characteristics of CR-39 (DOP) nuclear track detector. J Mater Sci 43:2865–2868
93. Zaki MF (2008) Gamma induced modification on optical band gap energy of CR-39 SSNTD. J Phys D Appl Phys 41:175404
94. El-Badry BA, Zaki MF, Abdul-Kader AM, Hegazy TM, Morsy AA (2009) Ion bombardment of poly-allyl-diglycol-carbonate (CR-39). Vacuum 83:1138–1142

95. Kumar R, Singh P (2013) UV–visible and infrared spectroscopic studies of Li^{3+} and C^{5+} irradiated PADC polymer. Results Phys 03:122–128
96. Singh P, Kumar R (2013) Study of structural and free volume properties of swift heavy ion irradiated polyallyl diglycol carbonate polymer films. Vacuum 96:46–51
97. Makkonen-Craigi S, Paronen M (2014) Potential large-scale applications of track-etched ultrafiltration polymer membranes. Arcada Working Papers 12, ISBN: 978-952-5260-54-0, ISSN: 2342-3064
98. Orlova AO, Gromova YA, Savelyeva AV, Maslov VG, Artemyev MV, Prudnikau A, Fedorov AV, Baranov AV (2011) Track membranes with embedded semiconductor nanocrystals: structural and optical examinations. Nanotechnology 22:455201
99. Ueno M, Imanishi N, Hanai K, Kobayashi T, Hirano A, Yamamoto O, Takeda Y (2011) Electrochemical properties of cross-linked polymer electrolyte by electron beam irradiation and application to lithium ion batteries. J Power Sources 196:4756–4761
100. Chmielewski AG, Haji-Saeid M, Ahmed S (2005) Progress in radiation processing of polymers. Nucl Instrum Methods Phys Res, Sect B 236:44–54
101. Jagielski J, Turos A, Bielinski D, Abdul-Kader AM, Piatkowska A (2007) Ion-beam modified polymers for biomedical applications. Nucl Instrum Methods Phys Res, Sect B 261:690–693
102. Singh NL, Shah N, Singh KP, Desai CF (2005) Electrical and thermal behavior of proton irradiated polymeric blends. Radiat Meas 40:741–745
103. Singh NL, Shah S, Qureshi A, Singh F, Avasthi DK, Ganesan V (2008) Swift heavy ion induced modification in dielectric and microhardness properties of polymer composites. Polym Degrad Stab 93:1088–1093
104. Singh NL, Qureshi A, Singh F, Avasthi DK (2007) Effect of swift heavy ion irradiation on dielectrics properties of polymer composite films. Mater Sci Eng, B 137:85–92
105. Shah S, Qureshi A, Singh NL, Singh KP, Avasthi DK (2008) Dielectric response of proton irradiated polymer composite films. Radiat Meas 3:S603–S606
106. Shah S, Singh NL, Qureshi A, Singh D, Singh KP, Shrinet V, Tripathi A (2008) Dielectric and structural modification of proton beam irradiated polymer composite. Nucl Instrum Methods Phys Res, Sect B 266:1768–1774
107. Qureshi A, Singh NL, Rakshit AK, Singh F, Avasthi DK (2007) Swift heavy ion induced modification in polyimide films. Surf Coat Technol 201:8308–8311
108. Siljegovic M, Kacarevic-Popovic ZM, Krkljes AN, Stojanovic Z, Jovanovic ZM (2011) Effect of N^{4+} and C^{4+} ion beam bombardment on the optical and structural characteristics of ethylene–norbornene copolymer (TOPAS). Nucl Instrum Methods Phys Res, Sect B 269:708–715
109. Nagata S, Konishi Y, Tsuchiya B, Toh K, Yamamoto S, Takahiro K, Shikama T (2007) Ion beam effects on electrical characteristics of proton conductive polymer. Nucl Instrum Methods Phys Res, Sect B 257:519–522
110. Radwan RM, Abdul-Kader AM, El-Hag Ali A (2008) Ion bombardment induced changes in the optical and electrical properties of polycarbonate. Nucl Instrum Methods Phys Res, Sect B 266:3588–3594
111. Hadjichristov GB, Gueorguiev VK, Ivanov TE, Marinov YG, Ivanov VG, Faulques E (2008) Silicon ion implanted PMMA for soft electronics. Org Electron 9:1051–1060
112. Dworecki K, Hasegawa T, Sudlitz K, Slezak A, Wasik S (2001) Modification of electrical properties of polymer membranes by ion implantation. Nucl Instrum Methods Phys Res, Sect B 185:61–65
113. Dworecki K, Hasegawa T, Sudlitz K, Slezak A, Wasik S (2000) Modification of electrical properties of polymer membranes by ion implantation. Nucl Instrum Methods Phys Res, Sect B 166–167:646–649
114. Mishra R, Tripathy SP, Sinha D, Dwivedi KK, Ghosh S, Khathing DT, Muller M, Fink D, Chung WH (2000) Optical and electrical properties of some electron and proton irradiated polymers. Nucl Instrum Methods Phys Res, Sect B 168:59–64

115. Odzhaev VB, Popok VN, Kozlova EI, Jankovskij ON, Karpovich IA (2000) Electrical properties of polyethylene modified by ion implantation and diffusion. Nucl Instrum Methods Phys Res, Sect B 166–167:655–659
116. Odzhaev VB, Jankovsky ON, Karpovich IA, Partyka J, Wegierek P (2001) Electrical properties of polyethylene modified by multistage ion implantation. Vacuum 63:581–583
117. Wu Y, Zhang T, Zhang H, Zhang X, Deng Z, Zhou G (2000) Electrical properties of polymer modified by metal ion implantation. Nucl Instrum Methods Phys Res, Sect B 169:89–93
118. Ahmed SF, Rho GH, Lee JY, Kim SJ, Kim HY, Jang YJ, Moon MW, Lee KR (2010) Nano-embossed structure on polypropylene induced by low energy Ar ion beam irradiation. Surf Coat Technol 205:S104–S108
119. Ektessabi AM, Yamaguchi K (2000) Changes in chemical states of PET films due to low and high energy oxygen ion beam. Thin Solid Films 377–378:793–797
120. Zhang Y, Huan ACH, Tan KL, Kang ET (2000) Surface modification of poly (tetrafluoroethylene) films by low energy Ar^+ ion-beam activation and UV-induced graft copolymerization. Nucl Instrum Methods Phys Res, Sect B 168:29–39
121. Darraud-Taupiac C, Binsangou V, Isabey R, Duverger E, Decossas JL, Makovicka L, Vareille JC (2000) Topographical modifications in PADC polymer under electron beam irradiation. Polym 41:6295–6299
122. Yotoriyama T, Suzuki Y, Mise T, Tsukamoto T, Iwaki M (2005) Surface characterization of thin film induced by He^+ ion-beam irradiation into PLLA. Surf Coat Technol 196:383–388
123. Tripathi A, Kumar A, Singh F, Kabiraj D, Avasthi DK, Pivin JC (2005) Ion irradiation induced surface modification studies of polymers using SPM. Nucl Instrum Methods Phys Res, Sect B 236:186–194
124. Zhang Z, Zhang Y, Yang K, Yi K, Zhou Z, Huang A, Mai K, Lu X (2015) Three-dimensional carbon nanotube/ethylvinylacetate/ polyaniline as a high performance electrode for supercapacitors. J Mater Chem A 03:1884–1889
125. Singh P (2017) Composites based on conducting polymers and carbon nanotubes for supercapacitors. In: Kumar V, Kalia S, Swart H (eds) Composites based on conducting polymers and carbon nanotubes for supercapacitors, 1st edn. Springer, Switzerland, p 333
126. Singh P, Kumar R (2014) Influence of high-energy ion irradiation on the structural, optical, and chemical properties of polytetrafluoroethylene. Adv Polym Technol 33:21410
127. Singh P, Kumar S, Prasad R, Kumar R (2014) Study of physical and chemical modifications induced by 50 MeV Li^{3+} ion beam in polymers. Radiat Phys Chem 94:54–57

High-Fluence Ion Implantation of Polymers: Evolution of Structure and Composition

Vladimir N. Popok

Abstract The chapter presents an overview of the effects and phenomena leading to structural and compositional evolution of polymer materials under high-fluence ion implantation. Ion stopping mechanisms and degradation of polymer structure due to radiation damage are discussed, giving examples for different ion species and polymer types mostly focusing on the low- to medium-energy regimes. Typical depth profiles and tendencies in depth distribution of impurities as well as the related changes in composition of the implanted layers are analysed. The emphasis is put on the high-fluence implantation of metal ions leading to the nucleation of nanoparticles and formation of composite materials. A special case of cluster ion implantation is also discussed. Change in mechanical, electronic, optical and magnetic properties of the ion-implanted polymers is under the consideration in the final part of the chapter also including a brief overview on applications of these materials.

Keywords Ion implantation · High fluences · Polymers · Radiation damage · Metal-polymer composites · Metal nanoparticles · Applications of ion-implanted polymers

1 Introduction

Ion implantation has become a widely used research and industrial method for doping of semiconductors since the late 1960s–early 1970s [1–4]. About the same time, the study of ion beam treatment of metals and alloy has been started in order to improve wear resistance of surfaces and later to form protection layers [5]. In the 1980s and 1990s, the ion beams have begun to be applied for surface analysis as well as synthesis and modification of a wide range of materials, among which the ion beam-treated dielectrics have shown an increasing interest [5–7]. In particular,

V. N. Popok (✉)
Department of Materials and Production, Aalborg University, Aalborg, Denmark
e-mail: vp@mp.aau.dk

V. Kumar et al. (eds.), *Radiation Effects in Polymeric Materials*, Springer Series on Polymer and Composite Materials, https://doi.org/10.1007/978-3-030-05770-1_3

ion implantation was considered to be one of the effective technological approaches to modify electrical, optical, magnetic and mechanical properties of polymers [8–17]. It became a hot topic in the late 1990s quickly reaching the level of over hundred papers published every year. Since then, the number of publication has been gradually increasing demonstrating a keen interest to the subject. Since the area of research on ion implantation of organic materials is very wide, the focus of the chapter will be on polymer modification using low-to-medium-energy beams covering the interval from approximately a few tens to few hundreds of keV. Thus, the effects caused by swift ions will be excluded from the analysis. The chapter will also predominantly discuss the cases of high-fluence ($\geq 1 \times 10^{14}$ cm^{-2}) bombardment.

One of the primary interests in ion implantation of dielectric polymers is based on turning them into semiconductor materials [8, 9]. It is realised by the disruption of chemical bonds in atomic collisions leading to cross-linking and formation of conjugated systems favouring the charge carrier transport [12, 14, 17–19]. Since the majority of polymers are carbon based, the radiation damage introduced by energetic ions can lead to escape of volatile chemical elements (degassing) from the implanted layer causing enrichment by carbon (carbonisation) which also facilitates higher conductance. Controlling the ion fluence allows rise in the conductance of up to approximately 20 orders of magnitude. Thus, ion beam modification of polymers opens a way for passive and active electronic element fabrication [15, 20–23].

Modified by implantation, organic materials are also attractive for applications in optics as passive devices, for example light filters and waveguides [24–29]. It is found that the optical properties correlate well with electrical and mechanical parameters of the ion-modified polymers [30, 31], thus allowing to use these materials for electro-optical modulators, stress gauges, etc. The radiation-induced phenomena also cause changes in surface properties, for instance, smoothness, adhesion, wear resistance and chemical resistance [32–35]. Hence, ion bombardment is suggested to be one of the possibilities to control bio-compatibility of polymers by the formation of appropriate surface topography and creation of centres for cell adhesion [36–42].

High-fluence metal ion implantation into polymers has become an area of special attention and interest because the embedded metal atoms are tended to aggregate into nanoparticles (NPs), thus forming metal-polymer composite materials with properties attractive for many applications. It is worth mentioning that this potential was already recognised in the beginning of 1980s [11, 43]. An implantation with high fluences leads to increase in metal concentration originating nucleation and growth of NPs due to very large difference in surface energies of metals and polymers [44]. Development of nanotechnologies in the 1990s caused intensive research on the formation of metal NPs in organic matrixes with an aim to fabricate composites with attractive electrical, optical and magnetic properties [45–53]. These activities have led to high level of understanding of fundamental physical and chemical aspects of radiation-modified polymers [19, 54–57]. On the other hand, these studies indicated a number of challenges in the production of polymeric materials with required properties.

Thus, a considerable level of understanding on ion stopping as well as related compositional and structural alterations in organic matrixes has been acquired in the past 20–30 years. A number of application-oriented research results on ion-implanted and radiation-modified polymers have been published. The intension of this chapter is to provide an analytical overview of these studies.

2 Ion Stopping and Change of Polymer Structure

2.1 Latent Tracks and Thermolysis

Polymers are formed by long macromolecules or their networks. Every macromolecule consists of hundreds or thousands of joint monomers which are units of the polymer chain. The monomers can be of different types ranging from the simplest unit $–CH_2–CH_2–$, which is a basis for polyethylene (PE), to complex structures including benzene rings and different functional groups like poly(ethylene terephthalate) (PET), polyimide (PI) or polycarbonate (PC) [57]. Polymers are characterised by strong (typically covalent) bonds between atoms in the macromolecule but weak intermolecular interactions.

Under implantation, the bonds become broken in the collisions with incoming ions and formed recoils (due to elastic nuclear collisions) as well as in the interaction of electronic system with charged projectiles (due to inelastic electronic interactions) [55]. These processes depend on the implantation energy and ion species as well as on the composition and structure of the polymer. Even for low-implantation energies, the density of energy can reach a few hundreds of eV/nm of ion track length. Since typical bond dissociation energy in polymers is below 10 eV [19], the energy transferred to the matrix by the projectile causes massive rapture of chemical bonds, i.e. displacement of atoms from their positions in chains. Some of them form volatile molecules or compounds (H_2, CH_4, C_2H_2, CO, CO_2, etc.) and leave the polymer by diffusion. Thus, so-called latent track along the ion trajectory is formed with the core (between 1 and 10 nm in diameter) of lower density compared to the pristine material. The core is surrounded by penumbra representing the less damaged, usually cross-linked material [58–60]. The phenomenon of radiation-induced degradation of polymer structure is often called a radiolysis [19].

Ion stopping leads not only to bond breakage and scission of macromolecules but also to the vibration excitation of the polymer atoms on the femto- to pico-second scale after the impact causing the energy transfer in the form of heat [14, 18]. This phenomenon is called thermalisation or thermolysis, and it causes abrupt temperature (T) increase around the ion track [16, 19]. The phenomenon can be described using the "thermal spike" model developed by Seitz and Koehler [61] with further refinements implemented by Sigmund [62], Kelly [63] and Bitensky with co-workers [64]. According to the model:

$$T(r,t) = \frac{T_0}{1+4t\delta/r_0^2}\exp\left\{-\frac{(r/r_0)^2}{1+4t\delta/r_0^2}\right\}, \quad (1)$$

where r_0 is the track core radius, δ is the thermal diffusivity of the medium and T_0 is the initial temperature given by

$$T_0 = \frac{\gamma S}{\pi\rho C_V r_0^2}, \quad (2)$$

where ρ is the polymer density, C_V is the heat capacity, S is the total stopping power (it will be described in more detail below) and γ is the part of the deposited energy converted to heat in the collision spike. The dependence of normalised temperature on the distance from the track core and its time evolution evaluated using Eq. (1) is presented in Fig. 1. This is a qualitative approach. There is widening of the heated zone with time. T_0 values corresponding to the implantation of ions with energies of a few hundreds of keV are found to be ranging between 10^3 and 10^4 K, while quenching of the track down to the typical temperature of a polymer target under implantation (350–400 K) occurs for 10^{-10}–10^{-9} s.

As a particular example, the molecular dynamic simulations of 240 keV implantation of C^+ ions into makrofol E ($C_{16}H_{14}O_3$) show temperature of up to 1300 K in the track core [60]. The area around the track axis cools down to 370 K at radial distance of 7–8 nm. Thus, the polymer within the cylindrical area just around the core can also degrade due to the pyrolysis-like effects. Actually, both the radiation and thermal mechanisms interplay, and therefore, the chemical modification of the polymer structure and composition during the ion implantation represents a joint process of radiothermolysis.

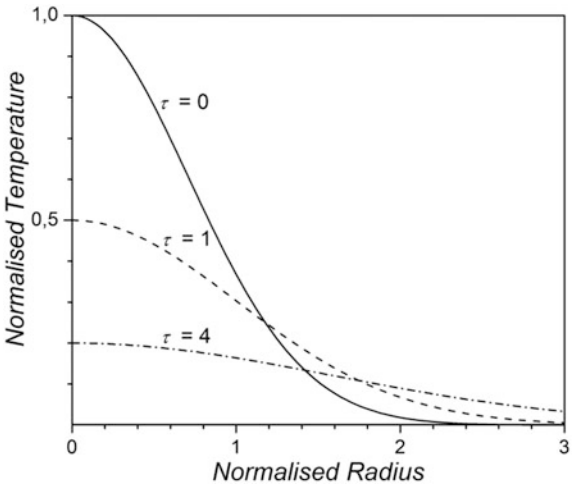

Fig. 1 Dependence of normalised temperature (T/T_0) on normalised track radius (r/r_0). $\tau = 4t\delta/r^2$ has meaning of specific time

Polymer disorder decreases with increasing distance in radial direction and also along the track (in longitudinal direction) due to energy loss by the projectiles. Thus, every ion produces a relatively narrow in width damaged region which can be developed into an individual pore by etching [65]. However, under fluence increase, the tracks start overlapping. This transition occurs in the fluence range of 5×10^{12}–5×10^{13} cm^{-2} in the case of light ions, while for heavy ions, the fluences can even be lower because the tracks are larger in diameter [14, 66]. Thus, at high fluences, a continuous layer of radiation-modified material is formed. Thickness of the layer depends on the ion energy and mass as well as on the structure and density of the polymer. These effects should be discussed in terms of ion stopping power.

2.2 *Structural Changes Due to Nuclear and Electronic Stopping*

The ions under embedding into material lose energy in elastic nuclear and inelastic electronic interactions which are characterised by the nuclear and electronic stopping power, S_n and S_e, respectively. The ratio between the nuclear and electronic stopping depends on the mass of the projectile which can be arbitrary divided into heavy and light (with masses approximately below 20 a.m.u.) ions. Examples of the stopping power depth profiles for C^+ (light) and Ag^+ (heavy) ions in PE calculated using Stopping and Ranges in Matter (SRIM) code [67] are presented in Fig. 2.

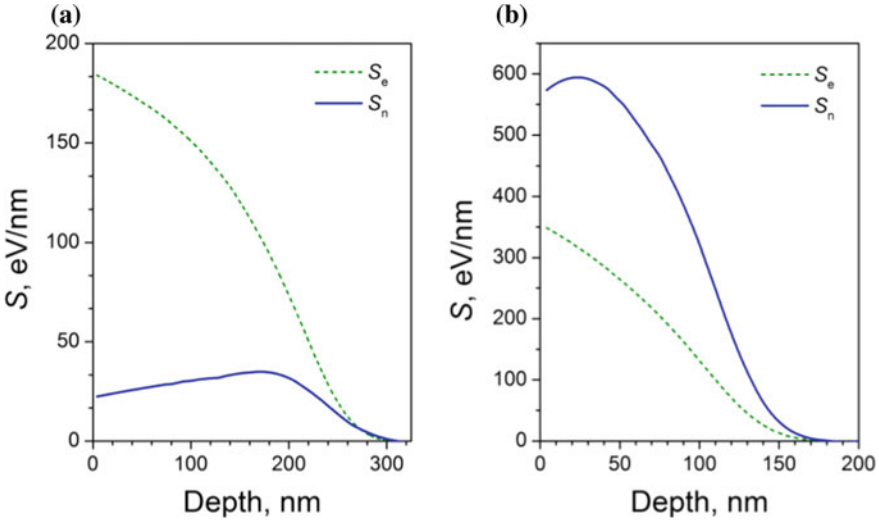

Fig. 2 Calculated depth distributions of electronic (S_e) and nuclear (S_n) stopping power for **a** 50 keV C^+ and **b** 150 keV Ag^+ ions implanted into PE

One can see that the loss on electronic interaction dominates in the beginning of tracks and its ratio to nuclear stopping is higher for light ions. For heavy ions, the energy loss on nuclear collisions prevails with maximum at the depth near the mean projected range (R_p) of ions.

The primary energy transfer from an impinging ion to a target atom leads to the displacement of the latter causing direct bond rupture. The ion can impart enough energy to the replaced atom (recoil) to generate next atomic displacement, thus producing a nonlinear collision cascade [55]. The energy transfer through electronic interactions results in electronic excitation of polymer units. This excitation can propagate from the track core forming a kind of penumbra [16]. Relaxation of the excited states can cause selective scission of the weakest bonds. Thus, both the nuclear and electronic stopping mechanisms lead to the bond termination with two possible scenarios: scission of macromolecules and cross-linking. The scission has meaning of polymer chain breakage into smaller fragments as schematically shown in Fig. 3a, thus resulting in depolymerisation. The cross-linking occurs due to the formation of free radicals and causes bond conjugations. An example for PE is presented in Fig. 3b. A recoiled carbon atom can react with a macromolecule that leads to a cross-link with the neighbouring one. Efficiency of the scission or cross-linking depends on the polymer structure. For instance, the chain fraction formation is found to be the most typical for polyisobutylene and poly(methyl methacrylate) (PMMA), whereas in PE and polysterene (PS), the cross-linking dominates [57, 68, 69]. When the number of cross-links reaches a critical value, the gel fractions characterised by a 3D network of bonds between macromolecules can form [69].

The bond scission can also be caused by electron excitations. This is found for polymers with heteroatom-containing functional groups [19, 70]. For example, the implantation of Ne^+ or N^+ ions into PI (in this case $S_e/S_n > 6.5$) first leads to degradation of the ether linkages and then to conversion of the imide groups into amide ones. In this case, CO is found to be the main released gaseous product [71–73]. The aromatic rings in PI are more stable against the electronic stopping and typically do not degrade [13, 14]. This is an important finding in terms of polymer evolution towards the formation of polyaromatic structures, in which π-electrons promote the conductance. Radiation damage of polyethersulphone

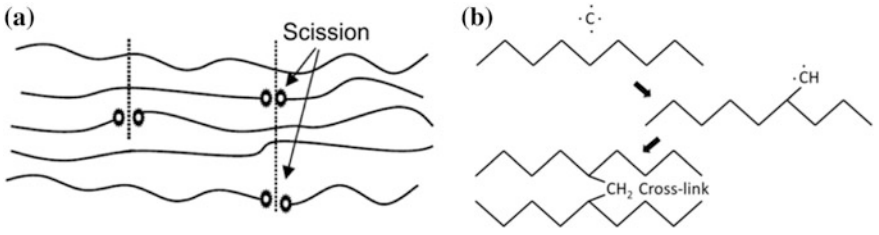

Fig. 3 Schematic pictures of **a** scission of macromolecules in a polymer and **b** cross-linking in PE under ion implantation

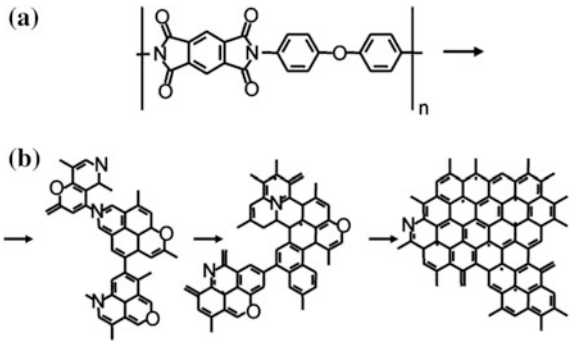

Fig. 4 **a** Chemical formula of PI unit and **b** structural transformation of PI under ion beam modification. Reprinted with permission from [70]

(PES) under dominating electronic stopping leads to selective reduction of sulphone groups to sulphoxide ones and further to sulphide groups for the high-fluence implantation [13, 14]. In PET, the heterocyclic groups are found to be more stable against the electron excitation but, nevertheless, can also be transformed due to the asymmetric system of delocalised π-electrons [74]. In the electron beam-irradiated poly(2-vinylpyridine), the pyridine rings are found to degrade towards amino groups [13]. In general, it can be concluded that the energy transferred to the polymer host during the electronic stopping of ions mainly affects weak bonds yielding low-mass fragments: this process becomes more efficient with increase in the electronic stopping power [75].

Under the implantation of heavy ions, contribution of the nuclear stopping increases and S_e/S_n ratio becomes smaller than unity. Elastic collisions lead to massive rupture of strong chemical bonds. For example, in PI, the phenyl rings become disrupted and imide groups degrade towards iminic and pyridinic-like groups as well as tertiary amines [76]. Under very higher fluences, the formation of extended polycondensed structures is proposed, as can be seen in Fig. 4, providing network of conjugated bonds for charge carrier transfer [70]. In PES implanted by 50 keV As^+ ions ($S_e/S_n < 0.2$), the sulphone groups become broken and acetylene splits out leading to the formation of 1.4-substituted butadiene [77]. For more details about mechanisms of ion beam modification of different types of polymers, one can refer to Sect. III of Ref. [16] or Chap. 4 of Ref. [57].

2.3 Degassing, Carbonisation and Oxidation

The above-mentioned implantation-induced processes change both the polymer structure and composition. The major structural changes are already discussed. The evolution of composition is first of all caused by the degassing. This phenomenon is especially strong in the case of low-energy beams when the material is modified to low depth. Gaseous products can easily diffuse towards surface through a thin disordered layer, for example by the latent tracks, and escape from it due to the

pressure difference because implantation is typically carried out in vacuum. Residual gas analysis during the ion implantation gives an answer to the gasses which are "emitted". For the cases of implantation of PE and PS with 100 keV He^+ and 200 keV Ar^+ ions, H_2, CH_4, C_2H_2 and C_3H_5 are detected [7]. Saturated hydrocarbons (methane, ethane) are found to be emitted under ion irradiation of polypropylene (PP) and polybutylene [78]. Typical molecules escaping from the implanted PI are H_2, C_2H_2, CO and CO_2 [59]. Therewith, the degassing of H_2 results in dehydrogenation. Elastic recoil detection is one of the methods for direct observation of hydrogen depletion in radiation-modified layers which is found, for example, in Ni-implanted PI, PET and polyetheretherketone (PEEK) [79]. Dehydrogenation is also observed in the N-implanted CR-39 polymer [80]. Oxygen can degas too from the oxygen-containing polymers. The near-surface depletion of oxygen is found, for example, in PI implanted by 40 keV Fe^+ ions [81].

As a result of degassing, the carbon ratio increases in the ion-treated layer, i.e. carbonisation of polymers takes place [17, 54]. Since the nuclear stopping is more efficient in bond breakage compared to the electronic one, it favours the degassing and following carbonisation especially in the case of heavy ions. If one, for example, compares the implantation of F^+ and As^+ ions into PE, the carbon concentration saturates at about 40 at. % (33 at.% in the pristine polymer) for the light ions, while it reaches 65–85 at.% for the heavy species embedded with the same fluences [72, 82–84]. The level of carbonisation is very much dependent on the type of polymer. If the concentration of carbon is high in the pristine polymer like in PI (78 at.%) or polyamide-6 (PA) (77.5 at.%), the carbon content after the implantation can reach almost 90 at.% even in the case of light ions. This is proved for the cases of 100 keV B^+ ion implantation with high fluences (5×10^{16}–1×10^{17} cm^{-2}) [85]. It is worth mentioning that the carbonisation process is practically accomplished (carbonisation is saturated) at the fluence level of (1–5) $\times$ 10^{15} cm^{-2} for heavy ions, while higher fluences are required for light ions [86–89].

Depth profiles of carbon "excess" can be obtained by RBS measurements. As found in [90] for the case of 100 keV Sb^+ ions implanted into PE, the carbon concentration increases with depth, reaches maximum and then decreases to the value of pristine polymer. The obtained profile is found to be very close to the depth distribution of energy losses on the nuclear stopping of ions. This correlation makes sense because in the case of heavy ions, the bond breakage is predominantly caused by the elastic collisions causing the hydrogen release and, thus, drastic carbonisation.

Carbonisation also leads to structural rearrangement. With fluence increase, a significant number of carbon atoms become unbound; they can meet free radicals causing the formation of unsaturated fragments, aromatic six and fifth atom rings as well as conjugated structures with sp^2-bonded carbon. One of such transformations is shown in Fig. 4b. Thus, one can talk about carbon-rich zones or carbon clusters [57, 86, 88]. Their formation is confirmed by neutron scattering and transmission electron microscopy (TEM) investigations; cluster sizes vary from a few to few tens of nm depending on the implantation conditions.

Cluster sizes can also be estimated from optical spectroscopy measurements [29, 80, 91]. In this case, the absorption spectra of implanted polymers are plotted in the so-called Tauc co-ordinates allowing to find optical band gap (E_g) through extrapolation of the absorption edge on the photon energy scale as shown in Fig. 5. Typical gap values of untreated polymers can vary between approximately 2 and 4 eV, indicating insulators with very low conductance. However, in the implanted polymers, the optical gap decreases with fluence increase and can reach values around 0.5 eV, which is typical for amorphous carbon being relatively good conductor [92]. Thus, one can adopt an equation developed by Robertson and O'Reilly for disordered graphite [92], which allows to calculate the average number of aromatic rings (N) belonging to the conjugated carbon clusters and to estimate their mean sizes:

$$E_g = \frac{2|\beta|}{\sqrt{N}}, \tag{3}$$

where β is the parameter characterising the nearest neighbour interactions between the π-orbitals in the one-electron tight-binding model and it is estimated to be 2.9 eV [92]. For example, in the implanted PS, PE and PA, the optical gap is found to saturate at about 0.6 eV [29, 94, 95]. This value corresponds to a carbon cluster consisting of around 100 benzene rings, thus to be $\sim$2.0–2.5 nm in diameter [29, 88]. The provided estimate is approximate because the equation is developed only for compact clusters. Moreover, the Hückel theory involved in this calculation can overestimate the optical transition energies of the π-systems. Nevertheless, using optical spectroscopy, one can monitor the evolution of carbonisation in polymers depending on the implantation parameters.

The π-bonded carbon clusters have a tendency to grow in size and aggregate forming a network of conjugated C=C bonds with fluence increase. At some point, this networking can lead to the formation of a quasi-continuous carbonaceous layer with enhanced conductance. Depending on the implantation energy, this layer can

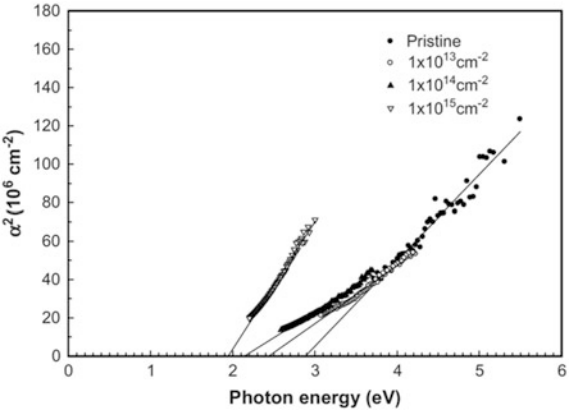

Fig. 5 Plots of α^2 squared optical absorption coefficient versus photon energy hv for low-density PE/ethylene–propylene diene monomer blend implanted by 320 keV Ar^+ ions with different fluences. Reprinted with permission from [93]

form at different depths below the surface, i.e. be buried [21]. Carbonisation also leads to the compaction of the radiation-modified layer: for high fluences, its density can increase by a factor of 2 compared to the pristine polymer [96].

So far, only parameters such as ion fluence and implantation energy have been mentioned to affect the modification of polymer structure and composition. It is worth noting that an ion current density is one more important implantation characteristic. Use of higher current density allows decrease in the implantation time. However, a high rate of power transferred to the polymer in this case can cause significant temperature rise and thermal degradation. It is found that for the thermally resistant polymers (materials with high glass transition temperature), high ion current densities can be used. For example, for PI implanted by Ar^+ ions, the value of 16 μA/cm^2 is reached without visual thermal degradation [70]. Nevertheless, the structure and properties are found to be strongly dependent on the ion current density despite the same accumulated fluence as can be seen in Fig. 6. Thus, it can be concluded that the thermolysis becomes more pronounced at high ion current values providing significant polymer modification towards amorphous carbon characterised by very low value of optical gap and high conductivity.

One more important phenomenon to be mentioned in connection to ion-induced polymer modification is oxidation. After implantation completion, the produced free radicals can survive for a long time: some days or even weeks depending on the polymer type [57]. Since implanted polymer samples are typically taken from vacuum chamber, where the treatment is performed, into air, the species present in ambient atmosphere can diffuse into the modified layer and react with the free radicals. Penetration of oxygen is the most typical phenomenon. For example, in PE, the reactions involve formation of peroxide radicals which can interact with free alkyl radicals yielding peroxide cross-links. Formation of hydroperoxide and hydroxyl groups is also detected [19, 57]. In the case of severe carbonisation, free radicals reside on the edges of the condensed aromatic cycles and hydroxyl, aldehyde, carboxyl, ether and peroxide groups can be produced [19, 57]. In some implanted polymers, for example PE, the oxidation is found to be carried out very

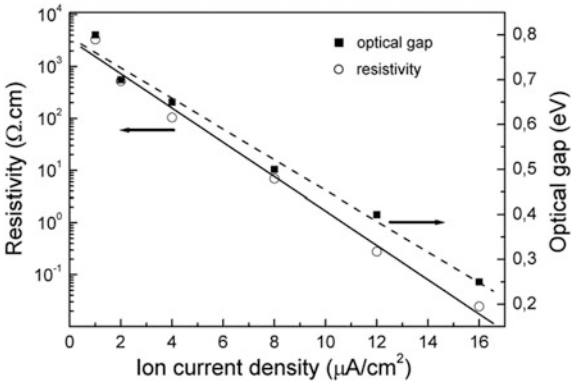

Fig. 6 Dependences of resistivity and optical gap on ion current density for PI implanted by 40 keV Ar^+ ions with fluence of 1×10^{16} cm^{-2}. Reprinted with permission from [70]

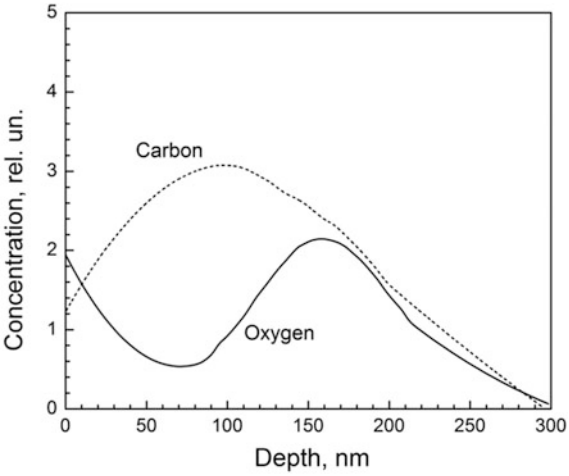

Fig. 7 Depth distributions of carbon "excess" and oxygen in PE implanted by 150 keV As^+ ions with fluence of 1×10^{15} cm^{-2}

quickly [82, 83, 90], while in others, for instance, in the ion-modified PP, it takes a several weeks to be completed [83, 97]. RBS spectroscopy shows that the concentration of incorporated oxygen increases with ion fluence until reaching a threshold at (1–5) $\times$ 10^{14} cm^{-2} for heavy and (1–5) $\times$ 10^{15} cm^{-2} for light ions [82, 83, 86, 88, 90, 97]. The depth distributions follow well the profiles of energy loss on either electronic or nuclear stopping (depending on ion species), indicating the oxygen trapping on free radicals, thus "decorating" the radiation damage. Above the threshold, the oxygen depletion is found with minimum correspondence to the carbon "excess" maximum (see Fig. 7). Formation of carbon clusters with limited number of free radicals prevents catching of oxygen.

Depth profiles of radiation damage can also be decorated on purpose using post-implantation diffusion of special chemical elements or compounds. Such experiments are carried out, for example, using molecular iodine and metallocarborane in F- and As-implanted PE [98–100] and LiCl in Ar-implanted PET [101].

3 Depth Distribution of Implanted Impurities

Due to the electronic and nuclear collisions, the ions penetrating into a matter lose their energy, slow down and stop at some depth which is characterised by R_p. This process can be modelled, for example, using Monte Carlo or molecular dynamics methods. One of the widely used simulation codes is SRIM [67]. It can predict a number of implantation parameters for various ions in different solid-state materials. However, in polymers, the simulated depth distributions of implanted species can significantly deviate from the experiments. This problem is related to the dynamical change in structure and composition of organic matrixes under ion treatment. The changes introduced at the earlier implantation stages significantly affect the

stopping of later coming ions. In the case of high fluences, one should also take into account sputtering of surface atoms and incorporation of implanted impurities into the polymer host. The former is proved, for example, for ion-implanted PMMA where the decrease in the sample thickness for 300–600 nm is found for fluences of (1–5) $\times$ 10^{16} cm^{-2} in the cases of H^+, B^+ and N^+ ions [28]. The filling with impurity atoms can reach about 20–25 at.% at the maximum depth distribution for very high fluences (1 $\times$ 10^{17} cm^{-2}) as shown, for example, for 40 keV implantation of Fe^+ and Co^+ ions into PI [102, 103]. Such high metal concentration significantly increases the polymer density and, therefore, changes the stopping of ions penetrating into the layer already containing the impurity atoms. One of the examples is presented in Fig. 8 showing the evolution of Ni depth profiles with ion fluence in PEEK [79]. It can be seen that the concentration maximum is shifted to the surface, the profiles broaden out and their shapes are converted from the Gaussian-like to asymmetric ones with fluence. This happens due to the polymer compaction (carbonisation and restructuring), change in composition (degassing of volatile compounds and significant increase in metal fraction) and surface sputtering. Similar changes in the impurity depth profiles are found for various metal ions and different types of polymers [50, 102–106].

It is worth mentioning that the dynamic changes in target composition can be taken into account in modelling. One such code is called TRYDIN [107]. It allows improvement of the predicted projected ranges. Nevertheless, the experimentally obtained distributions still show significant difference as can be seen in Fig. 9 by the example of 30 keV Ag^+ ion implantation into PMMA [106]. In the same work, it is found that about 500-nm-thick polymer layer becomes sputtered under fluence of 1 $\times$ 10^{17} cm^{-2}.

One more phenomenon affecting the final depth distribution of the implanted atoms is diffusion. It is especially pronounced for the implantation of gas ions. For example, in the case of 50 keV xenon, the projected range of ions is short; thus, the gas atoms can undergo diffusion towards surface and escape from the polymer that

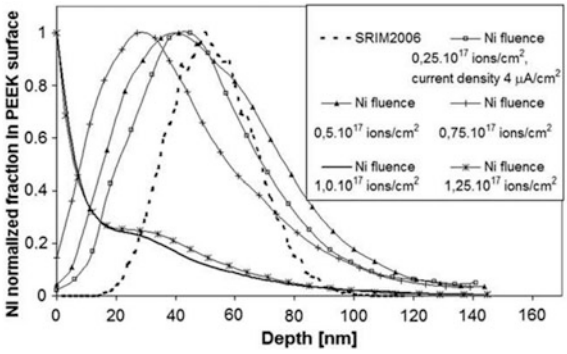

Fig. 8 Depth profiles of Ni implanted into PEEK with energy of 40 keV and various fluences. The profile calculated using SRIM is presented as dashed line. Reprinted with permission from [79]

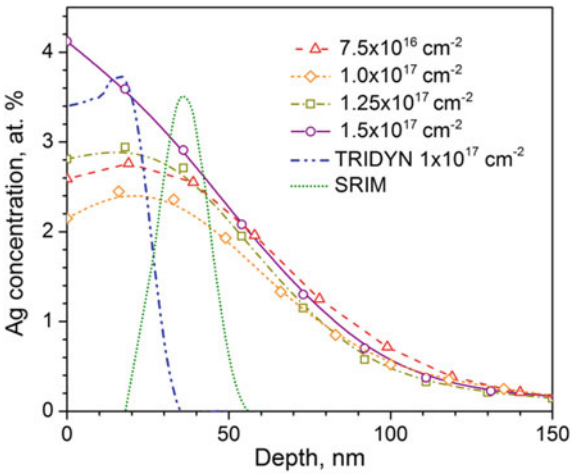

Fig. 9 Experimentally obtained using RBS and simulated by SRIM and TRIDYN codes depth distributions of silver implanted into PMMA with energy of 30 keV and various fluences. Reprinted with permission from [106]

leads to significantly lower concentration of the impurity compared to the expected one [108]. The same effect is observed for Ar^+ ions implanted into PI [70]. For implantation energy of 80 keV and very high fluences, the argon concentration is found to be much lower than the expected one, while for the 40 keV implantation, Ar is not found in the polymer at all [70]. In this case, the implantation depth is low and the diffusion-stimulated escape of the impurity is also accompanied by heavy sputtering of the polymer. As found by atomic force microscopy (AFM), the surface is highly disordered with roughness of about 30 nm which is comparable with R_p for 40 keV Ar^+ ion implantation. The phenomenon of "missing Ar" is also observed for low-energy and high-fluence implantation of polytetrafluoroethylene [109].

Diffusion of light atoms implanted into polymers is also found to be considerable. One of the examples is $^6Li^+$ and $^{10}B^+$ ion implantation. In these experiments, the impurities diffuse towards the surface and the depth profiles are observed to be very similar to those simulated for the electronic stopping. Since the electronic stopping dominates in the total energy loss of light ions, one can suggest that the diffused atoms become trapped by the defects created in ionisation [110, 111]. With fluence increase, the depth distribution can be converted to bimodal with one maximum at the surface and the second one in a bulk, as shown for 100 keV implantation of boron into different polymers (see Fig. 10) [88, 112]. The bulk part of the profiles resembles the ions stopped at the end of range, while the surface peak can be related to the atoms diffused to the surface and trapped on the free radicals. The concentration minimum between these two maxima is most probably caused by the carbonisation area with polycondensed network having limited number of free radicals and, thus, less efficient in capturing the diffusing boron atoms.

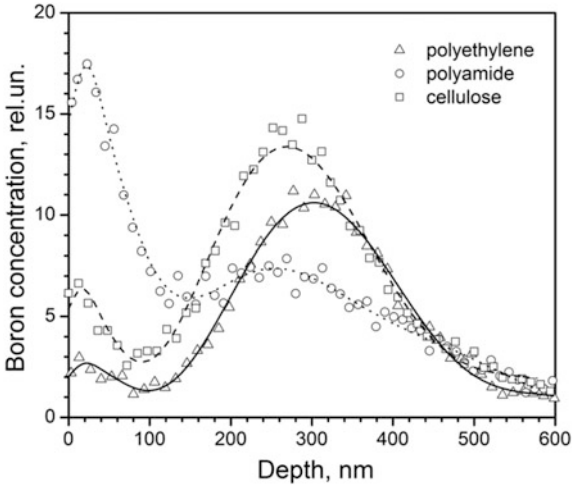

Fig. 10 Depth distributions of 100 keV boron implanted with fluence of 5×10^{16} cm^{-2} into polyethylene, polyamide-6 and cellulose

4 Metal Nanoparticle Formation Under High Fluences

Under high-fluence implantation of metal ions, concentration of the impurity (filling factor) reaches very high values in the implanted layer leading to the formation of NPs. The driving force for the particle nucleation is the high surface energy of metals, which is one to two orders of magnitude larger compared to polymers [113–116]. Hence, for the high filling factors, when the distances between the impurity atoms are small, it is energetically more favourable for them to bind to each other than combine with free radicals or other polymer constituents. Thus, at the initial stage, nuclei of a few atoms in size are formed which then grow into nanoscale particles by adding more metal atoms. The NPs typically have spherical or close to that shapes which follow the classical nucleation theory. Under ion implantation, the particle formation and growth are statistical processes leading to the spread of NP diameter, from a few to few tens of nm. In most cases, for example, for Ag, Cu, Au, W, Ti and Ni implantations, NPs are found to be on the scale of up to 10–15 nm in diameter in different polymers such as PMMA, PI, PET, PS, PC, epoxy resin and polydimethyloxane [47, 52, 105, 117–123]. Under implantation of the same metal into different organic matrixes, the particles have a tendency to decrease mean sizes with increase in the polymer specific density [124].

The size dispersion occurs both in lateral and transverse directions, i.e. parallel and perpendicular to the surface plane under the conditions of normal ion incidence. Examples of TEM images are shown in Fig. 11a, b. Typically, the larger NPs are nucleated at the depth corresponding to highest metal concentration, i.e. around R_p, and then sizes decrease both towards surface and bulk inwards. On the one hand, the size dispersion can be considered to be a disadvantage of the implantation

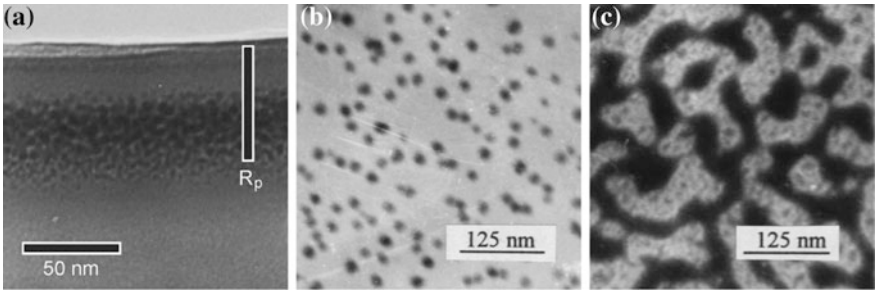

Fig. 11 **a** TEM cross-sectional image of polycarbonate implanted by 60 keV Cu^- ions with fluence of 1.5×10^{17} cm^{-2}. **b**, **c** In-plane TEM images of viscous epoxy after implantation by 40 keV Co^+ ions with fluences of 3.0×10^{16} cm^{-2} and 2.5×10^{17} cm^{-2}, respectively. Panel (**a**) is reprinted with permission from [123], and panels (**b**) and (**c**) are reprinted with permission from [120]

method. On the other hand, varying the ion energy allows to form buried layer of NPs at different depths in the polymer matrix which is obviously an advantage of ion implantation in comparison with other synthesis methods.

In some cases, for example, for very high-fluence implantation of iron into PMMA and PI, the particle sizes are found to reach a few tens of nm [125]. In this case, the NPs can also start percolating forming labyrinth-like structures [117, 125–127]. One such example is shown for the cobalt implantation in Fig. 11c where the dark areas are the agglomerated particles and small dark spots represent the NPs which are still individual.

Threshold fluences of NP nucleation are found to be between approximately $(0.5–1.0) \times 10^{16}$ cm^{-2} depending on the ion species and polymer type. For the case of low implantation energies, the accompanying sputtering can lead to baring of the particles formed in the shallow layer. In this case, NPs are easily recognised using AFM, and good correlation between AFM and other microscopy techniques such as TEM and SEM has been obtained [127, 128]. One of the examples of AFM measurements is shown in Fig. 12 where an ordinary topography (height) image is presented together with the phase scan for PMMA with silver NPs formed by 30 keV implantation with fluence of 7.5×10^{15} cm^{-2}. Comparing these two images allows to conclude that small bumps (bright spots) in panel (a) are the partly naked NPs because they show very different contrast (dark spots) compared to the surrounding polymer in panel (b). One can also see in panel (b) the bright vertical strips in association with some of NPs. These stripes indicate that the cantilever interacts with the particles and pushes them a bit in vertical direction at every horizontal scan until they come to rest at some point. Thus, these measurements also indicate low adhesion of the surface-located silver NPs.

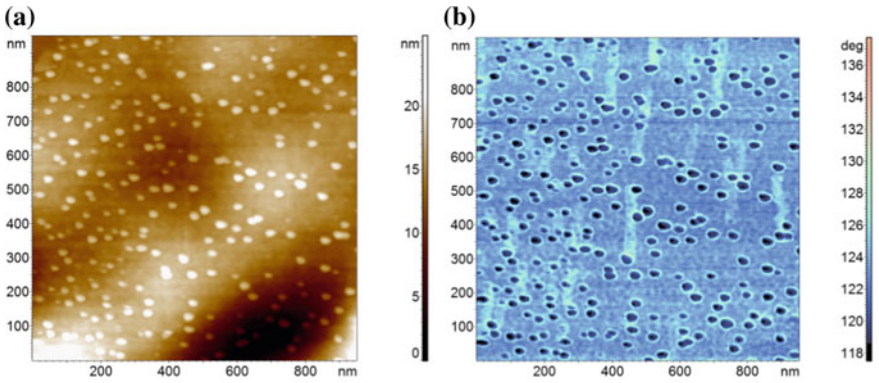

Fig. 12 AFM **a** height and **b** phase images of PMMA implanted by 30 keV Ag^+ ions with fluence of 7.5×10^{15} cm^{-2}. Reprinted with permission from [106]

5 Nanoparticle Implantation Using Cluster Beam Technique

One more approach for the formation of polymer films with embedded metal NPs, which is worth to mention in this chapter, is the cluster beam implantation. This method is already known for a few decades as a versatile tool with a number of unique capabilities for material synthesis and manipulation on the nanoscale [129–136]. Using this technique, the clusters (aggregates of atoms) are formed from a gas phase (vapourised or sputtered materials) and collimated into a beam which can be used for deposition on a surface or implantation into a matter. For more details about the cluster production, one can refer to [134, 137–141]. The advantages of the method are (i) a very good control of cluster composition because the particles are formed in vacuum from ultra-pure targets or sources, (ii) a possibility of cluster size (mass) selection and (iii) tuning the cluster kinetic energy to adjust the mechanisms of cluster–matter interaction [141]. However, only recently the experiments with metal clusters and polymers have been performed showing great capabilities in producing thin composite layers [142–144].

A big difference in cluster beam method compared to traditional ion implantation is that NPs can be embedded almost without radiation damage of polymer matrix, which is important for a number of practical applications. To explain why it happens, one needs to consider that a cluster can contain hundreds or thousands of atoms. If kinetic energy of the cluster is on the keV scale when divided by the number of constituents, it is reduced to a fraction of eV or even to meV per atom (for large clusters). Such energy level minimises radiation damage of organic matrix. For example, a gold cluster of 3 nm in radius would consist of approximately 6000 atoms in spherical approximation. If this particle is accelerated with energy of around 10 keV, the energy per atom will be below 2 eV, which is a very low value to produce any considerable number of radiation defects. However,

one should remember about the phenomenon of collective stopping on cluster impact, i.e. all cluster constituents will transfer the energy to the target very locally and almost simultaneously (on the very short, ps time scale). This can lead to significant local thermal spikes. For instance, in the case of 3 nm in radius gold particle having energy of 2 eV/atom, the impact with polymer can cause local heating up to 600 K (see Fig. 13) [145]. This temperature is above glass transition point for majority of polymers. Thus, chain mobility becomes significantly increased and since polymer specific densities are relatively low (approximately between 0.9 and 1.5 g/cm^3), these conditions facilitate the NP embedding into the organic host. The driving force for the immersion has been thermodynamics nature originated from an intension to reduce the surface tension at the particle/polymer interface [116, 146].

The experiments show that the palladium clusters of a few nm in diameter having equivalent kinetic energy per atom of about 0.5 eV can become embedded into approximately 50-nm-thick PMMA layers [142]. Additional heating of the polymer target up to 95 °C during the implantation leads to increased penetration depth of NPs up to 70 nm that supports the above-mentioned thermal nature phenomenon. Even higher penetration depth (90–135 nm) at room-temperature implantation is shown for gold clusters in polydimethylsiloxane (PDMS) which has lower density compared to PMMA, thus facilitating deeper NP embedding [147].

Metal clusters can also be soft-landed on polymer surface with extremely low kinetic energy on the level of meV per atom or below, and thus, no radiation damage is introduced. In this case, the NPs preserve their almost spherical shapes and original sizes. Their immersion into the polymer is initiated by the post-deposition thermal annealing at temperatures just above the glass transition one. Such experiments have been carried out with silver and copper NPs on a few different types of polymers [115, 148, 149] showing that the degree of embedding into the polymer can be controlled by the annealing time. An example can be seen in Fig. 14 where the same copper clusters on PMMA are monitored by AFM under the annealing.

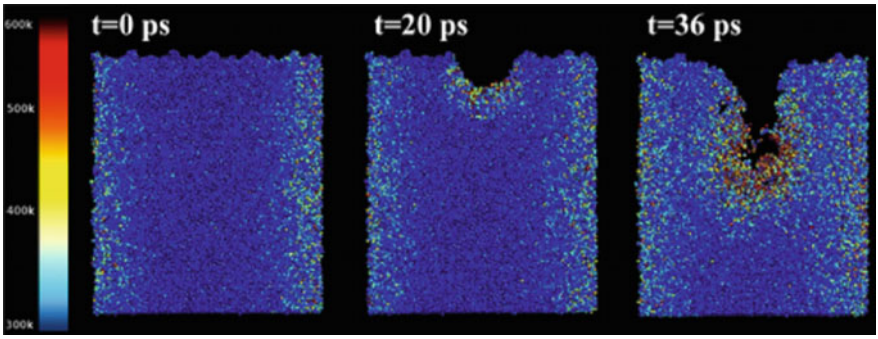

Fig. 13 Time evolution of temperature in polydimethylsiloxane during the implantation of Au cluster (radius of 3 nm) with energy of 2.0 eV/atom. Reprinted with permission from [145]

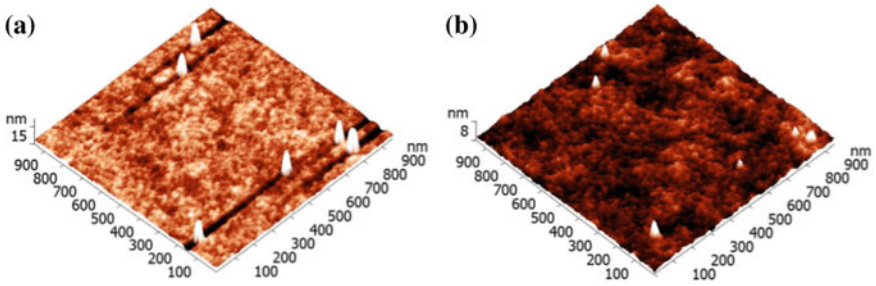

Fig. 14 AFM images of the same area of PMMA with **a** as-deposited Cu NPs (mean height of 17 nm) and **b** after thermal annealing at 125 °C for 5 min. Embedding of individual clusters can be identified by comparing panels (**a**) and (**b**)

6 Properties of Polymers Implanted with High Fluences

6.1 Surface Properties and Mechanical Characteristics

Ion implantation especially with high fluences drastically changes the composition and structure of polymers, thus leading to the evolution of mechanical, electrical, optical and magnetic properties.

It has been shown that surface morphology is significantly affected by ion impacts which can cause sputtering of the target atoms. Even in crystalline polymers, some amorphous areas are present. Thus, in any polymer, one can expect significant variations in local surface density, composition and structure leading to changes in sputtering yield from place to place and, thus, causing quite uneven topography after the high-fluence ion treatment. An example for the surface evolution of PI under 40 keV Ar^+ ion implantation with fluence increase is shown in Fig. 15 [70]. As can be seen, for fluence up to 1×10^{15} cm^{-2}, the surface roughness is low but craters are observed which can be related to pore openings through which Ar diffuses out. With fluence increase up to 1×10^{16} cm^{-2}, the swelling areas are observed. And finally, for fluence up to 7.5×10^{16} cm^{-2}, the

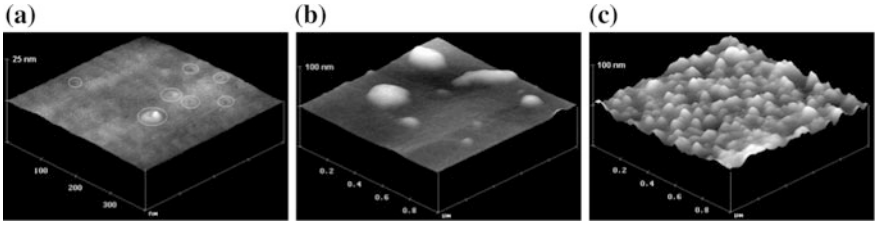

Fig. 15 AFM images of PI implanted by 40 keV Ar^+ ions with fluences of **a** 1×10^{15} cm^{-2}, **b** 1×10^{16} cm^{-2} and **c** 7.5×10^{16} cm^{-2} at ion current density of 8 μA/cm^2. Circles in panel (**a**) show the craters described in the text. Reprinted with permission from [70]

surface becomes very rough. Similar increase in surface roughness is observed for PET implanted at 100 keV N^+ ions with fluences up to 1×10^{16} cm^{-2} [150].

Treatment of polyurethane using 20 keV nitrogen plasma immersion ion implantation leads to the formation of well-pronounced wrinkles, which are associated with deformations of the surface layer due to the stresses introduced by carbonisation and cross-linking [22]. The carbonisation changes the solubility of polymers. For instance, PS is easily solvable in toluene, but after the implantation, the films become insoluble or selectively soluble, yielding swelled or wrinkled structures after the treatment in toluene and drying (see Fig. 16) [151]. Depending on the polymer type and ion beam treatment conditions, the morphology can become bizarre: parallel wrinkles in PE or worm and star structures in ethylene–propylene diene monomer rubber [57].

Significant modification of surface under implantation, in particular, change in polar component of the surface energy, formation of stable radiation defects (free radicals), new chemical states and adsorption centres lead to increase in chemical reactivity and adhesion of surface as well as better wetting [57].

Mainly untreated polymers have low surface energy. Thus, a water droplet should have a high contact angle φ when deposited on an organic film. φ is found to be around 90° for PE, 120° for polytetrafluorethylene (PTFE) and as large as 150–160° for expanded PTFE having a fibre structure [57]. After ion implantation, polymer surfaces become more polar and polar liquids wet the surface better leading to decrease in wetting angle. This tendency is found for a number of different implanted polymeric materials: PE, PS, PTFE, PA, etc. [152–155].

Specific surface centres created by ion impacts favour cell adhesion and promote the implanted polymers as biocompatible materials as they also show low toxicity, long lifetime in organism media and comparable elastic properties to bio-tissue. The studies show a possibility of efficient cell adhesion and protein coating [36, 37, 156, 157]. Good overview on the biological and medical applications of ion beam-treated polymers can be found in Ref. [57, 158, 159]. It is worth mentioning that in the last years, polymers with metal NPs have attracted a special attention in

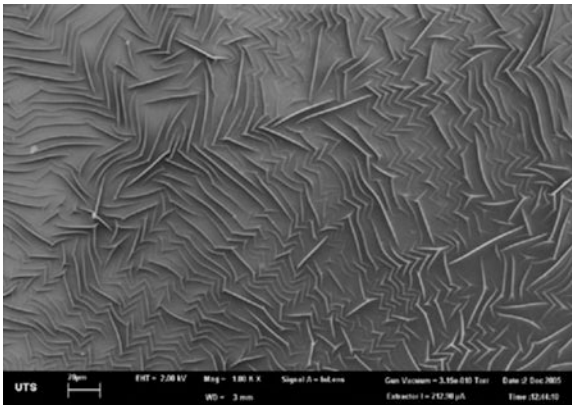

Fig. 16 SEM micrograph of PS surface after plasma ion immersion implantation of 5 keV Ar^+ ions with fluence of 1×10^{15} cm^{-2} and following treatment in toluene. Reprinted with permission from [151]

biological and medical research not only due to improved surface adhesion but also because of antibacterial properties and biosensor applications [160–162].

Evolution of structure and composition of organic materials under ion implantation causes significant change in mechanical characteristics such as hardness, elasticity, brittleness and related parameters. In the beginning of the 1990s, special study of the mechanical properties was started by a few groups. Rao, Lee and co-workers published quite a few papers showing the significant change in hardness, elastic modulus, friction coefficient and wear resistance for a number of polymers implanted by different ion species under various conditions [32, 163–166]. The hardness is found to rise for tens times reaching the values typical for stainless steel (3–12 GPa) for some implantation conditions [32, 166]. And the hardness value is shown to be a function of ion fluence and beam energy [165, 167] because these parameters significantly affect the structure and composition of polymers. Main factors for the increase in hardness and elastic modulus are the formation of three-dimensional conjugated networks through the carbonisation and cross-linking of polymer chains in the implanted layer. Thus, these mechanical parameters vary with depth. As shown for CR-39 polymer implanted by 130 keV Ar^+ ions when the load is increased and the depth of indentation becomes more than the thickness of the ion-modified layer, the measured microhardness suddenly drops to the values close to that of the pristine polymer [31]. The increase in polymer hardness and stiffness leads to improving of such tribological characteristics such as abrasive wear resistance [34]. Higher adhesive wear resistance is also conferred because of the limitation of plastic deformation and the promotion of elastic deformation as well as due to the augment of wettability improving lubrication [168]. However, the carbonisation may also lead to rise in brittleness that decreases the abrasive wear resistance. It is also found that there is no specific correlation between friction values and improvements in wear behaviour for implanted polymers: boron implantation into PE exhibits reduction in the friction coefficient while oxygen implantation into PC leads to its rise [34]. Hardening effect is also dependent on ion species and type of polymer. It is observed that in the case of metal implantation, the nucleated metal NPs dramatically change the surface mechanical parameters [164, 169]. Under high filling factor, NPs can start percolating leading to increase in Young's modulus, as shown for low-energy Ti^+ and Au^+ ion implantation into PDMS [170, 171].

Metal implantation under conditions promoting aggregation of NPs and formation of percolating network allows correlation of electrical properties with mechanical loads applied to the polymer. It is shown in Fig. 17 that the load-unload cycles are reproducible and represent only very small hysteresis effect, thus suggesting the metal-implanted organic films as simple strain gauges [122]. The similar effect of resistance correlation with applied mechanical strain is demonstrated for PDMS implanted by Au clusters [147]. Since the polymer structure is almost not damaged in this case, the produced composite films keep the elasticity close to that of pristine polymer and, thus, they are characterised by superior capability to sustain very large deformations (up to 40%) under 50,000 of cycles. Since the

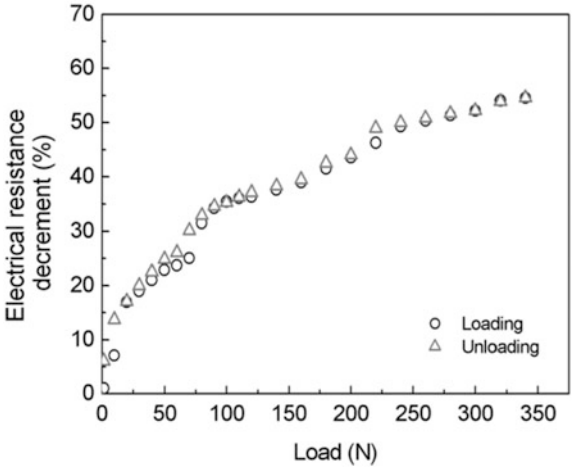

Fig. 17 Variation in electrical resistance as a function of the applied load-unload for 60 keV Ni^+ ion-implanted (with fluence of 1×10^{17} cm^{-2}) PC. Reprinted with permission from [122]

cluster implantation can be combined with shadow masking, it opens a way for microfabrication of elastomeric electrodes.

6.2 *Electrical Conductance*

Implantation-induced evolution of polymer towards formation of polycondensed structures with networks of conjugated bonds at high fluences drastically changes the electronic properties. An increase in conductance is associated with the carbonisation-related and restructuring effects rather than doping except the cases of metal implantation when at high filling factors, the conductive channels build up through the percolating metal clusters. These examples will be discussed separately at the end of this section.

For implantation of non-metallic species, the conductance only slightly depends on the nature of embedded chemical element being mainly affected by the structural and composition modifications of the organic target, thus, determined by the energy transferred to the matrix under the implantation. By choosing appropriate polymers and varying the implantation parameters (fluence, energy, ion current density and temperature), it is possible to tune the resistivity within approximately 20 orders of magnitude from ca. 10^{15} to 10^{18} Ω cm typical for pure dielectrics to approximately 10^{-1}–10^{-3} Ω cm which are the values typical for not very good but conductors. An example of how the resistance changes with ion fluence can be seen in Fig. 18 for PI implanted by 80 keV Xe^+ ions [172]. The dependence shows no change in low fluences (region I) and a quite sharp decrease in resistivity for fluences above 1×10^{14} cm^{-2} (region II) with saturation at fluences >1×10^{16} cm^{-2} (region III) corresponding to completed carbonisation of the implanted layer. The resistance decreases for about 8 orders of magnitude. Very similar types of resistance/

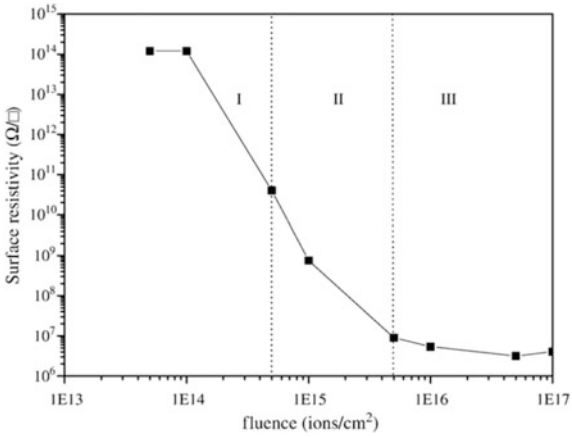

Fig. 18 Fluence dependence of surface resistance for 80 keV Xe^+ ion-implanted PI. Reprinted with permission from [172]

conductance dependences on ion fluence are obtained for different polymers and various ion species [54, 70, 128]. It is worth mentioning that ion current density also plays role in change in resistance. At higher values of ion current, the energy is transferred to a target at higher rates leading to more dramatic thermalisation effects affecting the structural modification and, hence, electronic properties. As shown in Fig. 6, the resistance decreases with ion current density for the same fluence value.

As discussed in Sect. 2, the carbon atoms have the tendency to formation of conjugated structures with sp^2 hybridisation under high-fluence implantation of polymers. In these structures, π-electrons can become charge carriers [173]. At low density of conjugated structures (carbon-rich clusters), the charge carrier transport occurs by hopping or tunnelling [108]. With increasing density of discrete clusters (fluence increase), the percolation transition in conductance takes place for approximately the same fluence range as for the track overlapping regime. This percolation behaviour is found in the early publications about implanted polymers [7, 174, 175] and discussed in detail later, for instance, in [16, 19]. An example of quite abrupt change in the resistivity with fluence increase above 1×10^{14} cm^{-2} corresponding to the percolation transition is illustrated in Fig. 18.

Evaluation of temperature dependence of conductance allows to get deeper insights into the mechanisms of charge carrier transport. The temperature dependence of conductivity σ can be described by following equation:

$$\sigma(T) = \sigma_0 \exp(-(T_0/T)^m), \tag{4}$$

where σ_0 is the conductivity at temperature $T \rightarrow \infty$ and T_0 is the characteristic temperature. The power m determines possible conduction mechanisms. For band conduction, i.e. extended electronic states, $m = 1$. m can be equal to unity also for the cases of Andersen localisation facilitating a nearest neighbour hopping [108]. A few papers reported the conduction behaviour with $m = 1$ for MeV energy [176] or high-fluence (10^{16} cm^{-2}) [177] implantation of polymers. It has been also shown

that m value can approach 1, for example be 0.7–0.8, at very high fluence of 1×10^{17} cm^{-2} [21]. However, in majority of cases studying polymer implantation within wide range of fluences, m takes values of 1/4, 1/3 or 1/2.
Such temperature dependences can be well explained by an approach suggested by Mott and Devis for disordered materials and describing a variable range hopping (VRH) of electrons between the localised states [178]. In this case, m has the following relation with the dimensionality D

$$m = 1/(1 + D). \tag{5}$$

A three-dimensional (3D) VRH, thus, corresponds to m = 1/4. 2D and 1D models give the power equal to 1/3 and 1/2, respectively. Thus, by obtaining m from the experimental dependences, one can judge about dominant mechanisms of charge carrier transport in the radiation-modified polymers.

In many publications discussing implantation with low-to-medium fluences (10^{13}–10^{15} cm^{-2}), the temperature dependence of conductance is well described by Eq. (4) with m = 1/2 [77, 174, 179]. However, it is hard to believe that the structures providing pure 1D conductance are formed in the radiation-damaged polymers. To explain this inconsistency, Wang and co-authors [46] assumed that the charge transfer can be 1D along the ion tracks, but at the depth corresponding to the maximum of energy transfer (highly disordered region), the contribution should be 3D. This model allowing to mix VRH of different dimensionalities gives reasonable agreement with the experimental data.

With fluence increase, the experiments show transition to temperature dependences with m reducing to 1/3 or 1/4, for example in the PI implanted by N^+ and Ar^+ ions [72, 180] as well as in PE and PA irradiated by B^+ and Sb^+ ions [21, 181]. It is suggested that the dependences described by m = 1/3 can correspond to the cases of a quasi-2D electron gas formation in the relatively thin carbonised by implantation layers [88]. For the thicker highly disordered polymer layers, 3D VRH dominates [72, 172].

Metal-implanted polymers represent a special case in terms of electrical properties. Under the implantation, conductance of these polymers changes due to both the carbonisation and filling the matrix with conductive metal inclusions which after the percolation introduce additional channel for charge transport [182]. Thus, resistivity of layers implanted by metal ions can decrease to much lower values compared to the cases of non-metal species. For example, 1.5×10^{-4} Ω cm is measured for the high-fluence Cu- and Ag-implanted PET [183]. Similar values of ca. 1×10^{-4} Ω cm are reported for the streaming plasma implantation of Au into PMMA with fluence of 3.2×10^{16} cm^{-2} [184]. For Au- and Ti-implanted PDMS, the conversion of the published values into bulk resistivity gives 2.2×10^{-6} and 4.2×10^{-5} Ω cm for gold and titanium, respectively, for the fluences above 2×10^{16} cm^{-2} [171]. Values between 1 and 1000 Ω/square are measured for Co- and Fe-implanted PI, PET and PEEK at high fluences [104, 185].

Theory tells us that in metals, the electrons are delocalised and conductance is not limited by energy barriers, but the electron transport is affected by scattering.

In the disordered systems, the electrons also have a high opportunity to interact. Thus, the conductivity can be expressed by

$$\sigma(T) = \sigma_0 + AT^{1/2}, \tag{6}$$

where the first term describes the temperature-independent conductivity, while the second one represents the term related to phonon scattering or electron-electron collisions which are both temperature dependent and at low T the term with power ½ dominates [186]. Thus, under increase in metal ion fluence, one should expect a transition from the exponential dependence given by Eq. (4) to the square root one as in Eq. (6) if the conductance through the metal channel starts prevailing.

For the PI implanted by Co^+ ions in the fluence range 2.5×10^{16}–1.25×10^{17} cm^{-2} at ion current density of 4 μA·cm^{-2}, VRH is found to be the dominating mechanism [187]. Despite the high metal concentration in the relatively thin layer (implantation energy of only 40 keV), the results do not show evidences for insulator-to-metal transition (IMT) even for the highest fluence used. However, Co^+ ion implantation with fluence of 1.25×10^{17} cm^{-2} but at higher j = 8 and 12 μA·cm^{-2} leads to a drastic change in the temperature dependence [187]. Calculation of the local activation energy suggests the metallic type of electron transport, thus, indicating IMT. The transition occurs due to the local heating induced by higher ion currents facilitating agglomeration of Co NPs and formation of percolation pass (quasi-continuous metal layer) with metallic type of conductance. Additionally, the measurements of temperature dependence of conductance show the presence of quantum effects of weak localisation and electron–electron interaction brinning a significant contribution to the final equation

$$\sigma(T) = \sigma_0 + AT^{1/2} + B\ln T \tag{7}$$

having additional logarithmic term compared to Eq. (6) describing the contribution of 2D quantum effects. The IMT is also found in PET implanted by 40 keV Fe^+ ions with high fluences [188].

According to the theories developed for electron transport in isotropic percolating materials, the conductivity of a composite representing an insulator with metal inclusions at concentrations near the percolation can be given by the formula

$$\sigma = \sigma_0(\phi - \phi_c)^t, \tag{8}$$

where ϕ and ϕ_c are the normalised metal concentration and the critical concentration corresponding to the percolation, respectively. Power value t is predicted to be less than 2 for the percolation regime [189]. The percolation threshold significantly depends on the material composition and can vary in rather wide intervals between 0.05 and 0.5 [189]. For the above-mentioned cases of cobalt and iron implantation into PI and PET, ϕ_c is estimated to be approximately 0.20–0.25. For the streaming plasma ultra-shallow implantation of gold into PMMA, ϕ_c is

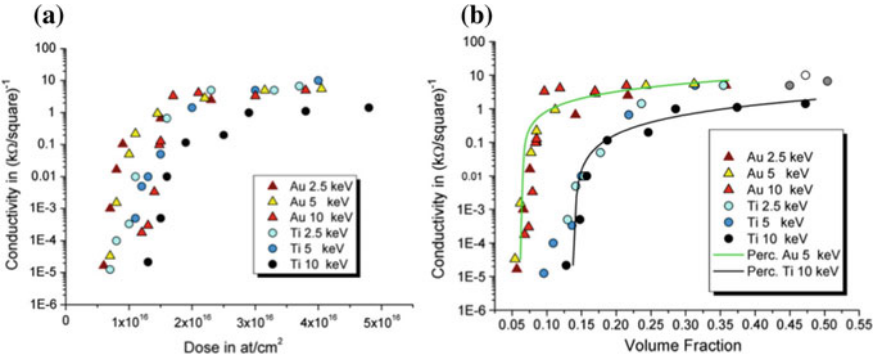

Fig. 19 Electrical conductivity of PDMS implanted by 2.5–10 keV gold and titanium ions as a function of **a** dose (fluence) and **b** corresponding volume (filling) factor of the metals. Two lines in panel (**b**) show fitness of the data with Eq. (8) for 5 keV gold-implanted and 10 keV titanium-implanted samples. See text for more details. Reprinted with permission from [171]

determined to be around 0.47 [184]. However, lower values of 0.06–0.08 for gold and 0.11–0.13 for Ti are found for the cases of implantation into PDMS [171]. One can clearly see a sharp increase in conductivity with fluence (volume filling factor) in Fig. 19. In panel (b), two fit curves utilising Eq. (8) with $\phi_c = 0.064$ and 0.11 and $t = 1.0$ and 1.6 are presented for the gold and titanium cases, respectively.

Study of electrical properties of implanted polymers, especially those filled with metals, is of significant importance for plastic electronics, formation of stretchable electrodes [147] or devices combining electrical properties with either mechanical (strain gauges, which are already mentioned in Sect. 6.1 [122]) or optical ones. The latter will be discussed in more detail below in Sect. 6.3.

6.3 *Optical Properties*

Optical properties of implanted polymers undergo significant changes. Transparent films change colour with fluence increase from pale yellow to deep brown. At fluences $\geq 1 \times 10^{15}$ cm^{-2}, metallic lustre typically appears. This phenomenon is consistent with the shift in absorption edge towards higher wavelength in optical spectra and corresponding change in optical gap as discussed in Sect. 2.3 in relation to the implantation-induced carbonisation.

Absorption and reflection spectra allow to calculate refractive index and extinction coefficient showing considerable change in these parameters in ion-implanted polymers [190]. Refractive index increases with fluence, and it also depends on the implantation energy [28, 191]. Thus, tuning the refractive index can be used for formation of planar waveguides combing ion implantation with masking or photolithography [27, 28]. An example of specimens of Y-branches and interferometers produced by ion implantation is shown in Fig. 20 [27]. Reactive ion

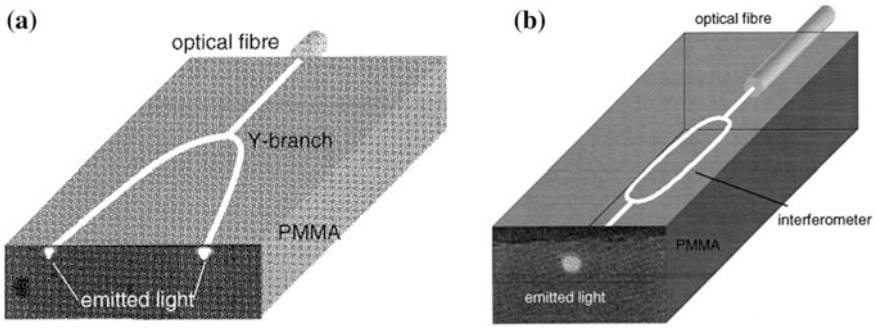

Fig. 20 Schematic pictures of **a** 1:2 ray splitter planar device form in the shallow layer and **b** Mach–Zehnder interferometer buried in polymer film. Reprinted with permission from [27]

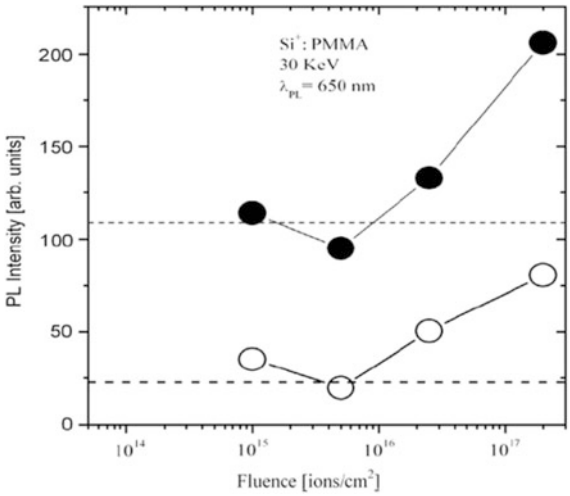

Fig. 21 Maximum of PL intensity versus implantation fluence for 30 keV Si-implanted PMMA. The open symbols are for excitation by laser power of 10 mW, the solid symbols—30 mW. Reprinted with permission from [193]

beam etching of PI is suggested as a means for the formation of Mach-Zehnder modulator [26]. Conjugation systems sharing π-electrons formed in ion-implanted organic materials can cause high polarisability and lead to nonlinear properties such as an electronic nonlinear refractive index and high values of a third-order susceptibility, thus, showing potential for utilisation of Kerr effect in an intense electric field [25]. Increase in reflectivity of implanted polymers (acquire metal lustre) is also of practical interest: in some organic matrixes, the reflectivity can rise up to five times after the high-fluence implantation [192].

Ion implantation can also be used as a method to create optically active centres in polymers. For instance, the high-fluence embedding of Si into PI causes photoluminescence (PL) as shown in Fig. 21 [193]. The PL intensity is found to be a function of fluence increasing up to 3 times in the case of 30 keV implantation.

For the case of 50 keV, an increase in PL intensity up to 5 times is observed. However, it is not clear from the study if the PL enhancement is mainly related to the formation of Si NPs or to some other effects.

The phenomenon of localised surface plasmon resonance (LSPR) of metal NPs in dielectrics attracts special attention [194, 195]. It gives rise to characteristic absorption, nonlinear optical effects and strong local field enhancement. Plasmonic structures are widely used as optical transducers in sensing of gases, environmental species and various bio-objects as well as for surface-enhanced Raman scattering (SERS) [196–200]. Utilising LSPR of metal NPs also allows designing the metamaterials with either almost perfect absorption of visible light [201] or fully transparent in the visible interval of wavelengths [202]. Last couple of decades, LSPR is intensively studied on NPs embedded into polymers. Interest to polymers as host medium is caused by plasticity allowing to easily form or even print the devices of required configurations as well as at low cost.

Noble metal NPs exhibit the most pronounced LSPR. For example, for gold NPs formed in PI by implantation with fluence of 5×10^{16} cm^{-2}, one can see a characteristic absorption band at around 600 nm related to LSPR in Fig. 22a [52]. Formation of NPs in the implanted layer is confirmed by TEM cross-sectional micrograph [52]. Graphs presented in panel (b) show the calculations of optical density for pure gold NPs in a nonabsorbing medium with refractive index $n = 1.6$, in pristine-absorbing PI and Au(core)-C(shell) structures in nonabsorbing medium with $n = 1.6$. The last simulation is the closest one to the experimental data, thus, indicating strong carbonisation of the implanted polymer.

Plasmonic absorption bands are also found for Ag-implanted epoxy resins [47], PET [183, 203], PMMA [48, 50, 106] and PC [204]. Silver NPs in different

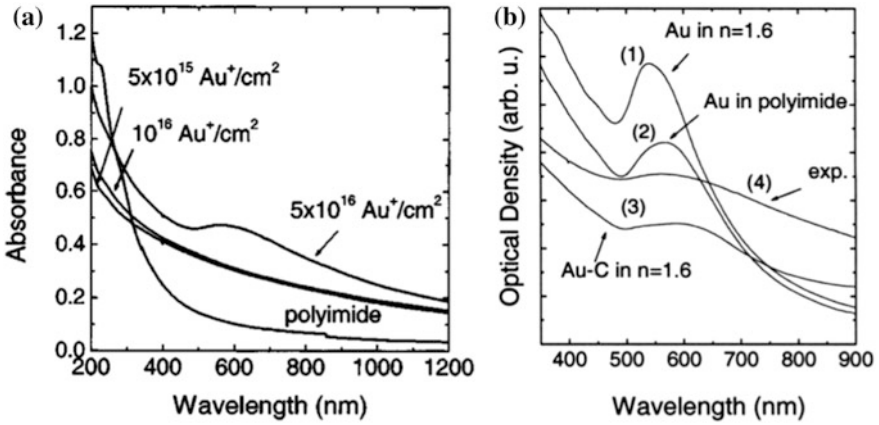

Fig. 22 **a** Optical absorption spectra of pristine PI and PI implanted with various fluences. **b** Calculated spectra for Au NPs in nonabsorbing medium with refractive index $n = 1.6$ and in pristine-absorbing PI and Au(core)-C(shell) structures in nonabsorbing medium with $n = 1.6$. The experimentally obtained spectrum for fluence of 5×10^{16} cm^{-2} is also shown for comparison. Reprinted with permission from [52]

polymers typically demonstrate LSPR bands at around 400–450 nm for the threshold fluences just corresponding to the particle nucleation. With fluence increase, the bands become red shifted (up to ~550–600 nm). Cu ions implanted to high fluences into high-density PE, PS and PC [123] as well as into PMMA [50] show the LSPR bands at around 610–640 nm. However, the extinction efficiency of copper NPs is lower than that of silver ones, and therefore, band intensities are very low: one needs to implant with fluences $\geq 5 \times 10^{16}$ cm^{-2} to resolve them. Hence, it is difficult to make any conclusions about the red shift.

In general, the red shift of the plasmon band with fluence increase can be related to the formation of larger particles due to higher local concentration of the embedded metal and Ostwald ripening. Another important factor is the carbonisation. It is shown by simulations using the Mie theory [48] that in the case of Ag (core)-C(shell) structures, the plamon band undergoes significant red shift compared to the case of pure Ag NPs in the same dielectric medium. Simultaneously, the LSPR band intensity decreases. Thus, increase in the carbonisation level at high fluences is obviously very significant or maybe even a dominant reason for the red shift in the optical spectra. It is also worth mentioning that the intensity of plasmon bands in the metal-implanted polymers is typically lower compared to LSPR intensities in other materials, for example glass or SiO_2, for the same fluences [205–207]. This difference is also related to the carbonisation of polymers accompanied by the formation of conjugated systems, thus conductive medium. Electrons of the NPs become poorly localised, and they can be transferred to the surrounding material that leads to weakening of the plasmon resonance.

One of the solutions to remove the carbonisation problem is cluster beam implantation as already discussed in Sect. 5. As described in Sect. 6.1, the plasticity of polymers brings an advantage to fabricate devices in which the conductance correlates with the applied mechanical stress. The similar approach is possible in relation to optical properties opening a way for systems with stable plasmonic tuning under cyclic strain conditions. Such systems, for example, are made by gold cluster implantation into PDMS forming a near-surface layer filled with NPs [208, 209]. Figure 23 shows the evolution of the plasmon band position and intensity for the film filled with 31% volume fraction subjected to a given number of stretching cycles with different elongation represented in per cent. The longitudinal (in-plane) stretching of the film leads to the red shift of the peak position that is explained by compression of the film in the other direction leading to the decrease in mean distance between the clusters along the wave propagation (normal to the surface) causing stronger plasmon coupling. An advantage of the cluster beam technique is in well-controlled cluster volume filling factor allowing to find the implantation regimes providing stability in tuning the peak position after thousands of cycles. Thus, one can conclude that the polymer nanocomposites produced by implantation of noble metal clusters are promising media to be used as mechanically tuneable optical filters or as components for stretchable optical devices.

Polymer films with partly embedded silver and copper clusters are reported to have excellent plasmonic properties [115, 148, 149]. The clusters are soft-landed on

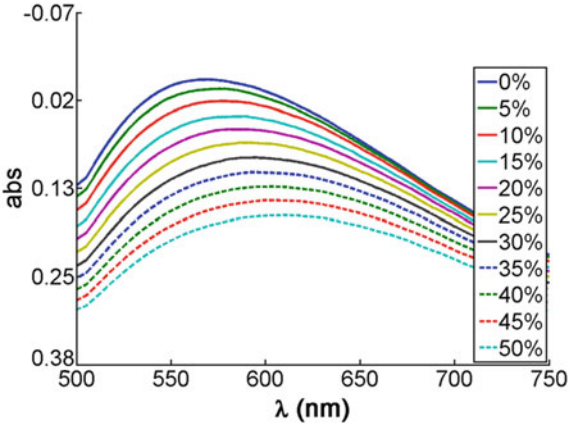

Fig. 23 Absorbance spectra of PDMS film filled with 31% volume fraction of Au NPs at different applied uniaxial strains represented as stretching in % compared to original non-stretched film. Reprinted with permission from [208]

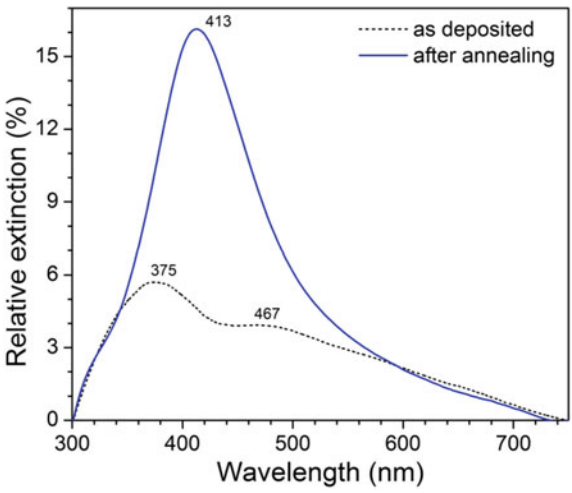

Fig. 24 Extinction spectra of PMMA film with as-deposited size-selected silver clusters (approximately 13 nm in diameter) and that after thermal annealing at 125 °C for 10 min. Reprinted with permission from [148]

PMMA and PS, and their embedding is achieved by following thermal annealing at temperatures slightly above the glass transition point. As shown in Fig. 24, the intensity of the band is significantly increased and the peak assigned to the plasmon resonance on individual particles undergoes a red shift from 375 to 413 nm due to partial immersion of the NPs into the medium with higher dielectric constant than that of air [148]. PMMA films with silver NPs are tested as optical transducers for protein sensing [210]. The procedure to attach antibodies and antigens to the NPs is developed, and a detectable shift in the LSPR band is registered allowing to recognise an antigen of interest. The composites also show very good stability against wet chemistry procedures involved in the protein incubation on the transducers.

6.4 Magnetic Properties

Typically, unmodified polymers are diamagnetic materials. Only some of them, for example PI and poly(ether sulphone), can reveal a weak paramagnetism due to a nonhomogeneous electron interaction caused by the presence of heteroatoms in the macromolecules [77, 211]. Since ion implantation of polymers results in significant structural and compositional evolution, the electronic structure is changed leading to paramagnetic behaviour. An isotropic singlet with g-value of 2.0025 which is close to that of free electron (2.0023) is registered in electron paramagnetic resonance (EPR) spectra of polymers implanted with high fluences [57, 179, 212]. This value also almost coincides with 2.0026 and 2.0027 reported for conducting and pyrolised polymers [213–215]. These facts indicate the similarity of the paramagnetic centres' nature under different methods of treatment. However, the discussion of this nature in the implanted polymers goes beyond the scope of this chapter. The interested readers can be redirected to Ref. [54, 57]. Below, the focus is put on the change of the magnetic properties in the metal-implanted polymers.

The first publications on ferromagnetic properties of metal-implanted polymers in the middle of the 1980s [11, 216] were followed by about ten years pause and only after that a series of papers studying various polymers with NPs of ferromagnetic metals formed by high-fluence implantation have been published [49, 118, 125–127, 188, 217–222]. Ensembles of Ni, Co or Fe NPs produced in the implanted layers are found to behave similar to a thin layer of ferromagnetic continuum due to strong magnetic coupling between the particles. The ferromagnetic resonance (FMR) measurements show a magnetic percolation transition occurring at concentrations of the magnetic NPs which are high enough for interparticle coupling comparable with Zeeman energy in the external magnetic field [223–225]. Let's look into this phenomenon in more detail by the example of iron NPs.

For the iron-implanted polymers, FMR signal is found for the fluences ≥ 2.5 10^{16} cm^{-2} that is in good agreement with the observations on NPs nucleation using TEM and other methods. The effective g-value is found to be 2.1 ± 0.1, which is close to the g-value of bulk iron film [124]. The FMR signal intensity increases with fluence, while the spectra become strongly anisotropic as shown in Fig. 25 for the Fe-implanted PI [125]. The line intensity changes non-monotonically, and the resonance position shifts to low or high fields depending on the orientation of magnetic field. The data obtained on angular dependence of the effective anisotropy allow the authors to conclude about uniaxial out-of-plane type of anisotropy; magnetisation is in plane of the implanted (composite) layer [124]. The FMR spectra demonstrate hysteresis and the presence of remanent magnetisation allowing to conclude about the magnetic percolation transition in the samples implanted with fluences above 6.0×10^{16} cm^{-2} [124, 125, 127].

The SQUID studies of the iron-implanted PET show the transitions between the ferromagnetic and superparamagnetic states at blocking temperature T_b [220]. This temperature is found to be increasing function of fluence, i.e. the metal filling factor,

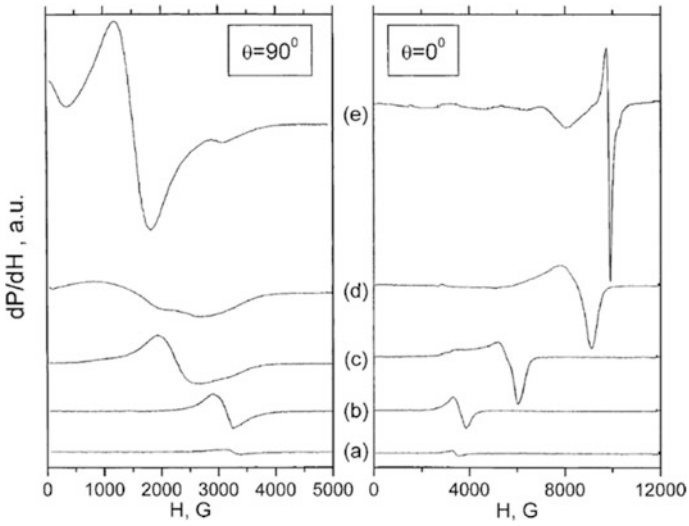

Fig. 25 FMR spectra of PI implanted by 40 keV Fe^+ ions with fluences: **a** 2.5×10^{16} cm^{-2}, **b** 5×10^{16} cm^{-2}, **c** 7.5×10^{16} cm^{-2}, **d** 1.0×10^{17} cm^{-2} and **e** 1.25×10^{17} cm^{-2}. Left panel corresponds to the field applied parallel to the film surface, while right one corresponds to the field normal to the surface. Reprinted with permission from [125]

and for the samples implanted with fluences $\geq 1.0 \times 10^{17}$ cm^{-2}, when a quasi-continuous iron film is formed in the implanted layer, the dependences show ferromagnetic behaviour for the entire range from cryogenic to room temperature. Magnetoresistive measurements indicate good correlation between the electrical and magnetic properties of these samples and percolation of the iron NPs at fluences above 7.5×10^{16} cm^{-2} [188].

Magnetic response formed by implantation of Co NPs is found to be weaker than the Fe ones, which is in correlation with bulk magnetic properties of these materials. To obtain room-temperature FMR signal for the cobalt-epoxy nanocomposites, the implantation fluences as high as 1.8×10^{17} cm^{-2} is required [223, 226]. The Co-PI film obtained by implantation with similar fluence represents the ferromagnetic properties only after post-implantation thermal annealing or in the case of implantation at high ion current densities (8 and 12 μA/cm^2) [227]. At high ion current, the film is heated up during the implantation which is in some analogy to the annealing. To register FMR in Co-implanted samples without thermal treatments, low temperatures are required to dump the thermal fluctuations in the magnetic moments of the superparamagnetic particles. The FMR studies of these samples show a good agreement with the magnetoresistance measurements revealing "positive" magnetoresistive effect (dielectric side of the IMT) for the PI samples implanted at ion current density of 4 μA/cm^2, while the samples implanted at high ion currents demonstrate "negative" magnetoresistive effect (metallic side of

the IMT) [219]. “Negative” magnetoresistive effect is also shown for PI implanted by cobalt at similar conditions by another group, thus, demonstrating very good correlations of the results [228].

7 Conclusion

The chapter presents an overview and analysis of data on different aspects of ion beam treatment of polymers with focus on use of high fluences. The structural and compositional changes induced by energetic interaction of ions with organic materials are discussed in detail explaining the effects arising from stopping of projectiles and related energy transfer. Both radiation and thermal-induced phenomena are considered in the unified process of radiothermolysis. Detailed analysis of the macromolecular scission and cross-linking allows foreseeing evolution of various types of polymers under implantation by different ion species.

Considering the degassing, carbonisation and oxidation effects strongly affecting the structure and composition of the implanted layers provides insights into the practical ways for the modification of materials properties. Specificity of doping and distribution of the implanted impurities are overviewed showing the difference between polymers and other solid-state materials. One needs to consider dynamical change in the structure and composition as well as diffusion in order to correctly predict the final distribution of implanted ions in organic matrixes.

Special attention is paid to nucleation of metal nanoparticles under high-fluence ion implantation as a practical means for the formation of metal/polymer nanocomposites. Novel approach on cluster beam implantation allowing to avoid a number of negative phenomena typical for conventional implantation and, thus, facilitating production of composite layers with minimum of radiation damage is presented.

Final part of the chapter overviews the possibilities to change mechanical, electrical, optical and magnetic properties of polymers using implantation in order to produce materials with required properties applicable in electronics, for bio-medical purposes, as transducers for optical sensors, strain gauges, etc., thus showing great potential of implanted polymers for practical use as well as the present-day research challenges.

References

1. Ryssel H, Glawischnig H (eds) (1982) Ion implantation techniques. Springer-Verlag, Berlin
2. Ziegler JF (ed) (1992) Handbook of ion implantation technology. North-Holland, Amsterdam
3. Rimini E (1995) Ion implantation: basics to device fabrication. Kluwer, Boston
4. Poate JM, Saadatmand K (2002) Ion beam technologies in the semiconductor world. Rev Sci Instrum 73:868–872

5. Dearnaley G (1983) Applications of ion implantation in metals. Thin Sol Films 107:315–326
6. Jain IP, Agarwal G (2011) Ion beam induced surface and interface engineering. Surf Sci Rep 66:77–172
7. Mazzoldi P, Arnold GW (eds) (1987) Ion beam modification of insulators. Elsevier, Amsterdam
8. Dresselhaus MS, Wasserman B, Wnek GE (1984) Ion implantation of polymers. Mater Res Soc Symp Proc 27:413–422
9. Wnek GE, Wasserman B, Loh I-H (1984) Structure/majority carrier relationships in ion-implanted polymer films. Mater Res Soc Symp Proc 27:435–437
10. Venkatesan T, Wolf T, Allara D, Wilkens BJ, Taylor GN, Foti G (1984) Synthesis of hard Si-C composite films by ion beam irradiation of polymer films. Mater Res Soc Symp Proc 27:439–444
11. Koon NC, Weber D, Pehrsson P, Schindler AI (1984) Magnetic properties of iron implanted polymers and graphite. Mater Res Soc Symp Proc 27:445–448
12. Chapiro A (1988) Chemical modification in irradiated polymers. Nucl Instr Meth Phys Res B 32:111–114
13. Marletta G (1990) Chemical reactions and physical property modifications induced by keV ion beams in polymers. Nucl Instr Meth Phys Res B 46:295–305
14. Marletta G, Iacona F (1995) Chemical and physical property modifications induced by ion irradiation in polymers. In: Pauleau Y (ed) Materials and processes for surface and interface engineering. Kluwer, Dordrecht, pp 597–640
15. Gied RE, Moss MG, Kaufmann J, Wang YQ (1998) Electrical applications of ion-implanted polymer films. In: Wise DL, Wnek GE, Trantolo DJ, Cooper TM, Gresser JD (eds) Electrical and optical polymer systems. Marcel Dekker, New York, pp 1011–1030
16. Sviridov DV, Odzhaev VB, Kozlov IP (1998) Ion-implanted polymers. In: Wise DL, Wnek GE, Trantolo DJ, Cooper TM, Gresser JD (eds) Electrical and optical polymer systems. Marcel Dekker, New York, pp 387–422
17. Popok VN (1999) Modification of surface layers of polymers by ion beams. Surf Invest 14:843–859
18. Lee EH (1999) Ion-beam modification of polymeric materials—fundamental principles and applications. Nucl Instr Meth Phys Res B 151:29–41
19. Sviridov DV (2002) Chemical aspects of implantation of high-energy ions into polymeric materials. Rus Chem Rev 71:315–327
20. Du G, Prigodin VN, Burns A, Joo J, Wang CS, Epstein AJ (1998) Unusual semimetallic behaviour of carbonized ion-implanted polymers. Phys Rev B 58:4485–4495
21. Popok VN, Karpovich IA, Odzhaev VB, Sviridov DV (1999) Structure evolution of implanted polymers: buried conductive layers formation. Nucl Instr Meth Phys Res B 148:1106–1110
22. Popok VN, Odzhaev VB, Azarko II, Kozlov IP, Sviridov DV, Hnatowicz V, Vacik J, Cervena J (2000) Multistage ion implantation of polyamide-6 films. Nucl Instr Meth Phys Res B 166–167:660–663
23. Hadjichristov GB, Gueorguiev VK, Ivanov TzE, Marinov YG, Ivanov VG, Faulques E (2008) Silicon ion implanted PMMA for soft electronics. Organic Electron 9:1051–1060
24. Gupta R, Kumar V, Goyal PK, Kumar S (2012) Optical characterization of poly(methyl methacrylate) implanted with low energy ions. Appl Surf Sci 263:334–338
25. Cottin P, Lessard RA, Knystautas EJ, Roorda S (1999) Polymer waveguides under ion implantation: optical and chemical aspects. Nucl Instr Meth Phys Res B 151:97–100
26. Moliton A, Antony R, Lucas B, Ratier B, Moussant C (1999) Ion beam applications in molecular and macromolecular physics (optics, electronics, optoelectronics). Opt Mater 12:199–203
27. Rück DM (2000) Ion induced modification of polymers at energies between 100 keV and 1 GeV applied for optical waveguides and improved metal adhesion. Nucl Instr Meth Phys Res B 166–167:602–609

28. Komarov FF, Leontyev AV, Grigoryev VV, Kamishan MA (2002) Ion implantation for local change of the optical constants of polymer films. Nucl Instr Meth Phys Res B 191:728–732
29. Kozlov IP, Odzhaev VB, Karpovich IA, Popok VN, Sviridov DV (1998) Optical properties of ion-implanted polymer layers. J Appl Spectr 65:390–395
30. Shekhawat N, Sharma A, Aggarwal S (2011) Refractive index engineering in polycarbonate implanted by 100 keV N^+ ions. Opt Engineer 50:044601
31. Shekhawat N, Aggarwal S, Sharma A, Sharma SK, Deshpande SK, Nair KGM (2011) Surface disordering and its correlations with properties in argon implanted CR-39 polymer. J Appl Phys 109:083513
32. Lee Eh, Lewis MB, Blau PJ, Mansur LK (1991) Improved surface properties of polymer materials by multiple ion beam treatment. J Mater Res 6:610–628
33. Ochsner R, Kluge A, Zechel-Malonn S, Gong L, Ryssel H (1993) Improvement of surface properties of polymers by ion implantation. Nucl Instr Meth Phys Res B 80(81):1050–1054
34. Dong H, Bell T (1999) State-of-the-art overview: ion beam surface modification of polymers towards improving tribological properties. Surf Coat Technol 111:29–40
35. Rodriguez RJ, Garcia JA, Sanchez R, Perez A, Garrido B, Morante J (2002) Modification of surface mechanical properties of polycarbonate by ion implantation. Surf Coat Technol 158–159:636–642
36. Iwaki M (2001) Ion surface treatments on organic materials. Nucl Instr Meth Phys Res B 175–177:368–374
37. Suzuki Y (2003) Ion beam modification of polymers for the application of medical devices. Nucl Instr Meth Phys Res B 206:501–506
38. Hwang I-T, Jung C-H, Kim D-K, Nho Y-C, Choi J-H (2009) Patterning of biomolecules on a poly(ε-caprolactone) film surface functionalized by ion implantation. Coll Surf B: Bionterfaces 74:375–379
39. Ishikawa J, Tsuji H, Sato H, Gotoh Y (2007) Ion implantation of negative ions for cell growth manipulation and nervous system repair. Surf Coat Technol 201:8083–8090
40. Gan BK, Kondyurin A, Bilek MMM (2007) Comparison of protein surface attachment on untreated and plasma immersion ion implantation treated polystyrene: protein islands and carpet. Langmuir 23:2741–2746
41. Švorčik V, Tomašova P, Dvořankova B, Hnatowicz V, Ochsner R, Ryssel H (2004) Fibroblasts adhesion on ion beam modified polyethylene. Nucl Instr Meth Phys Res B 215:366–372
42. Cheng X, Kondyurin A, Bao S, Bilek MMM, Ye L (2017) Plasma immersion ion implantation of polyurethane shape memory polymer: surface properties and protein immobilization. Appl Sur Sci 416:686–695
43. Pehrsson PE, Weber DC, Koon NC, Campanja JE, Rose SL (1984) Chemical and physical interactions in covalent polymers implanted with transition metals. Mater Res Soc Symp Proc 27:429–434
44. Ruffino F, Torrisi V, Marletta G, Grimaldi MG (2012) Effects of the embedding kinetics on the surface nano-morphology of nano-grained Au and Ag films on PS and PMMA layers annealed above the glass transition temperature. Appl Phys A 107:669–683
45. Bazarov VV, Petukhov Zhikharev VA, Khaibullin IB (1995) Conductivity of the granular metal films obtained by high dose ion implantation into PMMA. Mater Res Soc Symp Proc 388:417–422
46. Wang Y, Bridwell LB, Giedd RE (1993) Composite conduction in ion-implanted polymers. J Appl Phys 73:474–476
47. Stepanov AL, Abdullin SN, Khaibullin RI, Valeev VF, Osin YuN, Bazarov VV, Khaibullin IB (1995) Ion synthesis of colloidal silver nanoclusters in the organic substrate. Mater Res Soc Symp Proc 392:267–272
48. Stepanov AL, Popok VN, Khaibullin IB, Kreibig U (2002) Optical properties of polymethylmethacrilate with implanted silver nanoparticles. Nucl Instr Meth Phys Res B 191:473–477

49. Khaibullin RI, Zhikharev VA, Osin YuN, Zheglov EP, Khaibullin IB, Rameev BZ, Aktas B (2000) Structural and magnetic properties of iron and cobalt implanted silicone polymers. Nucl Instr Meth Phys Res B 166–167:897–902
50. Boldyryeva H, Umeda N, Plaksin OA, Takeda Y, Kishimoto N (2005) High-fluence implantation of negative metal ions into polymers for surface modification and nanoparticle formation. Surf Coat Technol 196:373–377
51. Salvadori MC, Cattani M, Teixeira FS, Brown IG (2008) Conducting polymer formed by low energy gold ion implantation. Appl Phys Lett 93:073102
52. Maggioni G, Vomiero A, Carturan S et al (2004) Structure and optical properties of Au-polyimide nanocomposite films prepared by ion implantation. Appl Phys Lett 85:5712–5714
53. Nathawat R, Vijay YK, Kumar P, Kulriya P, Ganesan V, Sathe V (2008) Physically and chemically modified polycarbonate by metal ion implantation. Adv Polym Technol 27: 143–151
54. Popok VN (2005) Compositional and structural alterations of polymers under low-to-medium-energy ion implantation. In: Norris CP (ed) Surface science research. Nova Sci Publishers, New York, pp 147–193
55. Fink D (ed) (2004) Fundamentals of on-irradiated polymers. Springer-Verlag, Berlin
56. Fink D (ed) (2004) Transport processes in ion-irradiated polymers. Springer-Verlag, Berlin
57. Kondyurin A, Bilek MMM (2008) Ion beam treatment of polymers. Application aspects from medicine to space. Elsevier, Amsterdam
58. Apel P, Schulz A, Spohr R, Trautmann C, Vutsadakis V (1997) Tracks of very heavy ions in polymers. Nucl Instrum Meth Phys Res B 131:55–63
59. Hnatowicz V (1999) Simple model of radial structure of latent tracks in polymers. Phys Stat Sol (b) 216:931–941
60. De Cicco H, Saint-Martin G, Alurralde M, Bernaola OA, Filevich A (2001) Ion tracks in an organic material: application of the liquid drop model. Nucl Instr Meth Phys Res B 173:455–462
61. Seitz F, Koehler J (1956) Displacement of atoms during irradiation. In: Seitz F, Turnbull D (eds) Solid state physics: advances in research and applications, vol 2. Academic Press, New York, pp 305–448
62. Sigmund P (1974) Energy density and time constant of heavy-ion-induced elastic-collision spikes in solids. Appl Phys Lett 25:169–171
63. Kelly R (1977) Theory of thermal sputtering. Rad Eff 32:91–100
64. Bitensky IS, Demirev P, Sundquist BUR (1993) On a model of fullerene formation from polymers under MeV ion impact. Nucl Instr Meth Phys Res B 82:356–361
65. Vilensky AI, Zagorski DL, Apel PYu, Pervov NV, Mchedlishvili BV, Popok VN, Melnik NN (2004) Thermal regression of latent tracks in the polymer irradiated by high energy heavy ions. Nucl Instr Meth Phys Res B 173:294–299
66. Licciardello A, Fragala ME, Compagnini G, Puglisi O (1997) Cross section of ion polymer interaction used to individuate single track regime. Nucl Instr Meth Phys Res B 122: 589–593
67. Ziegler JF, Biersack JP, Littmark MD (2008) The stopping and ranges of ions in matter. Lulu Press, Morrisville
68. Davenas J, Stevenson I, Celette N, Cambon S, Gardette JL, Rivaton A, Vignoud L (2002) Stability of polymers under ionising radiation: the many faces of radiation interactions with polymers. Nucl Instr Meth Phys Res B 191:653–661
69. Calcagno L, Percolla R, Foti G (1995) Ion track effects on gel formation of polystyrene. Nucl Instr Meth Phys Res B 95:59–64
70. Popok VN, Azarko II, Khaibullin RI, Stepanov AL, Hnatowicz V, Mackova A, Prasalovich SV (2004) Radiation-induced change of polyimide properties under high-fluence and high ion current density implantation. Appl Phys A 78:1067–1072
71. Davenas J, Xu XL, Boiteux G, Sage D (1989) Relation between structure and electronic properties of ion irradiated polymers. Nucl Instr Meth Phys Res B 39:754–763

72. Švorčik V, Endršt R, Rybka V, Arenholz E, Hnatowicz V, Černy F (1995) Nitrogen implantation into polyimide. Eur Polym J 31:189–191
73. Lewis MB, Lee EH (1991) Residual gas and ion-beam analysis of ion-irradiated polymers. Nucl Instr Meth Phys Res B 61:457–465
74. Švorčik V, Endršt R, Rybka V, Hnatowicz V, Černy F (1994) Modification of polyethyleneterephtalate by implantation of nitrogen ions. J Electrochem Soc 141:582–584
75. Picq V, Ramillon JM, Balanzat E (1998) Swift heavy ions on polymers: hydrocarbon gas release. Nucl Instr Meth Phys Res B 146:496–503
76. Marletta G, Iacona F (1993) Heat-induced versus particle beam-induced chemistry in polyimide. Nucl Instr Meth Phys Res B 80(81):1405–1409
77. Bridwell LB, Giedd RE, Youngqiang W, Mohite SS, Jahnke T, Brown IM (1991) Electrical conductivity enhancement of polyethersulfone (PES) by ion implantation. Nucl Instr Meth Phys Res B 59(60):1240–1244
78. Picq V, Balanzat E (1999) Ion-induced molecular emission of polymers: analytical potentialities of FTIR and mass spectroscopy. Nucl Instr Meth Phys Res B 151:76–83
79. Mackova A, Bocan J, Khaibullin RI, Valeev VF, Slepicka P, Sajdl P, Svorcik V (2009) Characterisation of Ni^+ implanted PEEK, PET and PI. Nucl Instr Meth Phys Res B 267:1549–1552
80. Sharma T, Aggarwal S, Sharma A, Kumar S, Kanjilal D, Deshpande SK, Goyal PS (2007) Effect of nitrogen ion implantation on the optical and structural characteristics of CR-39 polymer. J Appl Phys 102:063527
81. Popok VN, Khaibullin RI, Toth A, Beshliu V, Hnatowicz V, Mackova A (2003) Compositional alteration of polyimide under high fluence implantation by Co^+ and Fe^+ ions. Surf Sci 532–535:1034–1039
82. Hnatowicz V, Kvitek J, Švorčik V, Rybka V (1993) Oxidation of polyethylene implanted with As ions to different extents. Eur Polym J 29:1255–1258
83. Hnatowicz V, Kvitek J, Švorčik V, Rybka V (1994) Oxygen incorporation in polyethylene and polypropylene implanted with F^+, As^+ and I^+ ions at high dose. Appl Phys A 58:349–352
84. Hnatowicz V, Kvitek J, Peřina V, Švorčik V, Rybka V, Popok V (1994) Anomalous diffusion of Pb atoms into polyethylene implanted with F and As ions to different doses. Nucl Instr Meth Phys Res B 93:282–287
85. Popok VN, Azarko II, Odzhaev VB, Toth A, Khaibullin RI (2001) High fluence ion beam modification of polymer surfaces: EPR and XPS study. Nucl Instr Meth Phys Res B 178:305–310
86. Odzhaev VB, Azarko II, Karpovich IA, Kozlov IP, Popok VN, Sviridov DV, Hnatowicz V, Jankovskij ON, Rybka V, Svorcik V (1995) The properties of polyethylene and polyamide implanted with B ions to high doses. Mater Lett 23:163–166
87. Hnatowicz V, Peřina V, Hnatowicz V, Voseček V, Novotny J, Vacik J, Švorčik V, Rybka V, Kluge A (2000) Degradation of polyimide and polyethyleneterephtalate irradiated with 150 and 200 keV Ar^+ ions, studied by RBS and ERD techniques. Nucl Instr Meth Phys Res B 161–163:1099–1103
88. Popok VN, Odzhaev VB, Kozlov IP, Azarko II, Karpovich IA, Sviridov DV (1997) Ion beam effects in polymer films: structure evolution of the implanted layer. Nucl Instr Meth Phys Res B 129:60–64
89. Fink D, Ibel K, Goppelt P, Biersack V, Wang L, Behar M (1990) Ion beam induced carbon clusters in polymers. Nucl Instr Meth Phys Res B 46:342–346
90. Hnatowicz V, Kvitek J, Svorcik V, Rybka V, Popok V (1994) Oxygen incorporation in polyethylene implanted with 150 keV Sb ions. Czech J Phys 44:621–627
91. Zaki MF, El Tabay MM, Radwan RM (2016) Effect of Ar bombardment on the electrical and optical properties of low-density polyethylene films. Pramana J Phys 87:67
92. Robertson J, O'Reilly EP (1987) Electronic and atomic structure of amorphous carbon. Phys Rev B 35:2946–2957

93. Rizk RAM, Abdul-Kader AM, Ali ZI, Ali M (2009) Effect of ion bombardment on the optical properties of LDPE/EPDM polymer blends. Vacuum 83:805–808
94. Calcagno L, Foti G (1991) Ion irradiation of polymers. Nucl Instr Meth Phys Res B 59 (60):1153–1158
95. Kondyurin A, Khaibullin R, Gavrilov N, Popok V (2002) Pulse and continuous ion beam treatment of polyethylene. Vacuum 68:341–347
96. Schwarz F, Thorwarth G, Stritzker B (2009) Synthesis of silver and copper nanoparticle containing a-C: Hby ion irradiation of polymers. Sol State Sci 11:1819–1823
97. Hnatowicz V, Hnatowicz V, Kvitek J, Peřina V, Švorčik V, Rybka V (1993) RBS study of oxidation processes in polypropylene and polyethylene implanted with fluorine ions. Nucl Instr Meth B 80(81):1059–1062
98. Jankovskij O, Švorčik V, Rybka V, Hnatowicz V, Popok V (1995) Nucl Instr Meth Phys Res B 95:192–196
99. Hnatowicz V, Vacik J, ŠvorčikV Rybka V, Popok V, Jankovskij O, Fink D, Klett R (1996) Iodine diffusion and trapping in polyethylene implanted with 150 keV F and As ions to different fluences. Nucl Instr Meth Phys Res B 114:81–87
100. Hnatowicz V, Vacik J, Červena J, Švorčik V, Rybka V, Popok V, Fink D, Klett R (1995) Doping of ion implanted polyethylene with metallocarborane. Nucl Instr Meth Phys Res B 105:241–244
101. Hnatowicz V, Vacik J, Červena J, Švorčik V, Rybka V, Fink D, Klett R (1997) Doping of ion irradiated polyethyleneterephatalate from water solution of LiCl. Phys Stat Sol (a) 159:327–333
102. Popok VN, Khaibullin RI, Bazarov VV, Valeev VF, Hnatowicz V, Mackova A, Odzhaev VB (2002) Anomalous depth distribution of Fe and Co atoms in polyimide implanted to high fluence. Nucl Instr Meth Phys Res B 191:695–699
103. Mackova A, Hnatowicz V, Perina V, Popok VN, Khaibullin RI, Bazarov VV, Odzhaev VB (2002) High-fluence implantation of iron into polyimide. Surf Coat Technol 158–159:395–398
104. Mackova A, Malinsky P, Miksova R, Hnatowicz V, Khaibullin RI, Slepicka P, Svorcik V (2014) Characterisation of PEEK, PET and PI implanted with 80 keV Fe^+ ions to high fluencies. Nucl Instr Meth Phys Res B 331:176–181
105. Zhou G, Wang R, Zhang TH (2010) Analysis of surface morphological change in PET films induced by tungsten ion implantation. Nucl Instr Meth Phys Res B 268:2698–2701
106. Popok VN, Hanif M, Mackova A, Miksova R (2015) Structure and plasmonic properties of thin PMMA layers with ion-synthesized Ag nanoparticles. J Polym Sci B Polym Phys 53:664–672
107. Möller W, Eckstein W, Biersack JP (1988) TRIDYN-binary collision simulation of atomic collisions and dynamic composition changes in solids. Comput Phys Commun 51:355–368
108. Wang Y, Mohite SS, Bridwell LB, Giedd RE, Sofield CJ (1993) Modification of high temperature and high performance polymers by ion implantation. J Mater Res 8:388–402
109. Colwell JM, Wentrup-Byrne E, Bell JM, Wielunski LS (2003) A study of the chemical and physical effects of ion implantation of micro-porous and nonporous PTFE. Surf Coat Technol 168:216–222
110. Fink D, Biersack JP, Chen JT, Stadele M, Tjan K, Behar M, Olovieri CA, Zawislak FC (1985) Distributions of light ions and foil destruction after irradiation of organic polymers. J Appl Phys 58:668–676
111. Fink D, Behar M, Kaschny J, Klett R, Chadderton LT, Hnatowicz V, Vacik J, Wang L (1996) On the redistribution of $^6Li^+$ ions implanted into polypropylene foils. Appl Phys A 62:359–367
112. Vacik J, Červena J, Fink D, Klett R, Hnatowicz V, Popok V, Odzhaev V (1997) High fluence boron implantation into polymers. Rad Eff Def Sol 143:139–156
113. Lipatov Yu, Feinermann A (1979) Surface tension and surface free energy of polymers. Adv Colloid Interface Sci 11:195–233

114. Doering R, Nishi Y (eds) (2008) Handbook of semiconductor manufacturing technology. CRC Press, Boca Raton
115. Popok VN, Hanif M, Ceynowa FA, Fojan P (2017) Immersion of low-energy deposited metal clusters into poly(methylmethacrylate). Nucl Instr Meth Phys Res B 409:91–95
116. Prakash J, Pivin JC, Swart HC (2015) Noble metal nanoparticles embedding into polymeric materials: from fundamentals to applications. Adv Colloid Interface Sci 226:187–202
117. Niklaus M, Rosset S, Dadras M, Dubois P, Shea H (2008) Microstructure of 5 keV gold-implanted polydimethylsiloxane. Scripta Mater 59:893–896
118. Petukhov VY, Ibragimova MI, Khabibullina NR, Shulyndin SV, Osin YuN, Zheglov EP, Vakhonina TA, Khaibullin IB (2001) The influence of the polymer matrix structure on the ion beam synthesis of metal-polymer thin films. Polym Sci Ser A 43:1154–1162
119. Malinsky P, Mackova A, Hnatowicz V, Khaibullin RI, Valeev VF, Slepička P, Švorčik V, Slouf M, Peřina V (2012) Properties of polyimide, polyetheretherketone and polyethyleneterephthalate implanted by Ni ions to high fluences. Nucl Instr Meth Phys Res B 272:396–399
120. Abdullin SN, Stepanov AL, Osin YuN, Khaibullin RI, Khaibullin IB (1998) Synthesis of metallic dispersion and continuous films in the viscous polymer by implantation of cobalt ions. Surf Coat Technol 106:214–219
121. Salvadori MC, Teixeira FS, Sgubin LG, Cattani M, Brown IG (2014) Surface modification by metal ion implantation forming metallicnanoparticles in an insulating matrix. Appl Surf Sci 310:158–163
122. Di Girolamo G, Massaro M, Piscopiello E, Tapfer L (2010) Metal ion implantation in inert polymers for strain gauge applications. Nucl Instr Meth Phys Res B 268:2878–2882
123. Umeda N, Bandourko VV, Vasilets VN, Kishimoto N (2003) Metal precipitation process in polymers induced by ion implantation of 60 keV Cu^{-}. Nucl Instr Meth Phys Res B 206: 657–662
124. Khaibullin RI, Rameev BZ, Okay C, Stepanov AL, Zhikharev VA, Khaibullin IB, Tagirov LR, Aktas B (2004) Ion beam synthesis of magnetic nanopartciles in polymers. In: Aktas B, Tagirov L, Mikailov F (eds) Nanostructured magnetic materials and their applications. NATO science series: II mathematics, physics and chemistry, vol 143. Kluwer, Dordrecht, pp 33–54
125. Khaibullin RI, Popok VN, Bazarov VV, Zheglov EP, Rameev BZ, Okay C, Tagirov LR, Aktas B (2002) Ion synthesis of iron granular films in polyimide. Nucl Instr Meth Phys Res B 191:810–814
126. Petukhov VYu, Khabibullina NR, Ibragimova MI, Bukharaev AA, Biziaev DA, Zheglov EP, Gumarov GG, Müller R (2007) Magnetic properties of thin metal-polymer films prepared by high-dose ion-beam implantation of iron and cobalt ions into polyethylene terephtalate. Appl Magn Reson 32:345–361
127. Okay C, Rameev BZ, Khaibullin RI, Okutan M, Yildiz F, Popok VN, Aktas B (2006) Ferromagnetic resonance study of iron implanted PET foils. Phys Stat Sol (a) 203:1525–1532
128. Popok VN (2012) Ion implantation of polymers: formation of nanoparticulate materials. Rev Adv Mater Sci 30:1–26
129. Perez A, Melinon P, Dupuis V et al (1997) Cluster assembled materials: a novel class of nanostructured solids with original structures and properties. J Phys D Appl Phys 30:709–721
130. Milani P, Iannotta S (1999) Cluster beam synthesis of nanostructured materials. Springer, Berlin
131. Meiwes-Broer KH (ed) (2000) Metal clusters at surfaces. Springer, Berlin
132. Binns C (2001) Nanoclusters deposited on surfaces. Surf Sci Rep 44:1–49
133. Popok VN, Prasalovich SV, Campbell EEB (2004) Surface nanostructuring by implantation of cluster ions. Vacuum 76:265–272
134. Popok VN, Campbell EEB (2006) Beams of atomic clusters: effects on impact with solids. Rev Adv Mater Res 11:19–45
135. Toyoda N, Yamada I (2008) Gas cluster ion beam equipment and applications for surface processing. IEEE Trans Plasma Sci 36:1471–1488

136. Popok VN (2014) Cluster ion implantation in graphite and diamond: radiation damage and stopping of cluster constituents. Rev Adv Mater Sci 38:7–16
137. De Heer WA (1993) The physics of simple metal clusters: experimental aspects and simple models. Rev Mod Phys 65:611–676
138. Hagena OF (1992) Cluster ion sources. Rev Sci Instr 64:2374–2379
139. Haberland H, Karrais M, Mall M, Thurner Y (1992) Thin films from energetic cluster impact: a feasibility study. J Vac Sci Technol A 10:3266–3271
140. Popok VN, Prasalovich SV, Samuelsson M, Campbell EEB (2002) Design and capabilities of a cluster implantation and deposition apparatus: first results on hillock formation under energetic cluster ion bombardment. Rev Sci Instr 73:4283–4287
141. Popok VN, Barke I, Campbell EEB, Meiwes-Broer K-H (2011) Cluster-surface interaction: from soft landing to implantation. Surf Sci Rep R 66:347–377
142. Ravagnan L, Divitini G, Rebasti S, Marelli M, Piseri P, Milani P (2009) Poly(methyl methacrylate)–palladium clusters nanocomposite formation by supersonic cluster beam deposition: a method for microstructured metallization of polymer surfaces. J Phys D Appl Phys 42:082002
143. Solar P, Kylian O, Polonskyi O, Artemenko A, Arzhakov D, Drabik M, Slavinska D, Vandrovcova M, Bacakova L, Biederman H (2012) Nanocomposite coatings of Ti/C: H plasma polymer particles providing a surface with variable nanoroughness. Surf Coat Technol 206:4335–4342
144. Peter T, Rehders S, Schürmann U, Strunskus T, Zaporojtchenko V, Faupel F (2013) High rate deposition system for metal-cluster/$SiO_xC_yH_z$–polymer nanocomposite thin films. J Nanopart Res 15:1710–1715
145. Cardia R, Melis C, Colombo L (2013) Neutral-cluster implantation in polymers by computer experiments. J Appl Phys 113:224307
146. Kovacs GJ, Vincett PS (1984) Subsurface particle monolayer and film formation in softenable substrates: techniques and thermodynamic criteria. Thin Sol Films 111:65–81
147. Corbelli G, Ghisleri C, Marelli M, Milani P, Ravagnan L (2011) Highly deformable nanostructured elastomeric electrodes with improving conductivity upon cyclical stretching. Adv Mater 23:4504–4508
148. Hanif M, Juluri RR, Chirumamilla M, Popok VN (2016) Poly (methyl methacrylate) composites with size-selected silver nanoparticles fabricated using cluster beam technique. J Polym Sci B Polym Phys 54:1152–1159
149. Ceynowa FA, Chirumamilla M, Popok VN (2017) Polymer composite films with size-selected metal nanoparticles fabricated by cluster beam technique. In: Proceedings of 12th international conference interaction of radiation with solids, Minsk, Sept 19–22, pp 301–303
150. Nathawat R, Kumar A, Kulshrestha V, Vijay YK, Kobayashi T, Kanjilal D (2008) Study of surface activation of PET by low energy (keV) Ni^+ and N^+ ion implantation. Nucl Instr Meth Phys Res B 266:4749–4756
151. Kondyurin A, Gan BK, Bilek MMM, McKenzie DR, Mizuno K, Wuhrer R (2008) Argon plasma immersion ion implantation of polystyrene films. Nucl Instr Meth Phys Res B 266:1074–1084
152. Chen JS, Sun Z, Guo PS, Zhang ZB, Zhu DZ, Xu HJ, Effect of ion implantation on surface energy of ultrahigh molecular weight polyethylene. J Appl Phys 93: 5103–5108
153. Kondyurin A, Gan BK, Bilek MMM, Mizuno K, McKenzie DR (2006) Etching and structural changes of polystyrene films during plasma immersion ion implantation from argon plasma. Nucl Instr Meth Phys Res B 251:413–418
154. Mesyats G, Klyachkin Yu, Gavrilov N, Kondyurin A (1999) Adhesion of polytetrafluorethylene modified by an ion beam. Vacuum 52:285–289
155. Fu RKY, Cheung ITL, Mei YF, Shek CH, Siu GG, Chu PK, Yang WM, Leng YX, Huang YX, Tian XB, Yang SQ (2005) Surface modification of polymeric materials by plasma immersion ion implantation. Nucl Instr Meth Phys Res B 237:417–421

156. Bačakova L, Mareš V, Bottone MG, Pellicciari C, Lisa V, Švorčik V (2000) Fluorine ion-implanted polystyrene improves growth and viability of vascular smooth muscle cells in culture. J Biomed Mater Res 49:369–379
157. Walachova K, Švorčik V, Bačakova L, Hnatowicz V (2002) Colonization of ion-modified polyethylene with vascular smooth muscle cells in vitro. Biomaterials 23:2989–2996
158. Marletta G (2010) Ion-beam modification of polymer surface for biological applications. In: Bernas H (ed) Materials science with ion beams, Topics Appl Phys, vol 116. Springer-Verlag, Berlin, pp 345–369
159. Bilek MMM (2014) Biofunctionalization of surfaces by energetic ion implantation: review of progress on applications in implantable biomedical devices and antibody microarrays. Appl Surf Sci 310:3–10
160. Han ZJ, Tay BK (2009) Ti–PS nanocomposites by plasma immersion ion implantation and deposition. Nucl Instr Meth. Phys Res B 267:496–501
161. Zare Y, Shabani I (2016) Polymer/metal nanocomposites for biomedical applications. Mater Sci Engineer C 60:195–203
162. Prakash S, Charabarty T, Ak Singh, Shahi VK (2013) Polymer thin films embedded with metal nanoparticles for electrochemical biosensors applications. Biosens Bioelectron 41: 43–53
163. Rao GR, Wang ZL, Lee EH (1993) Microstructural effects on surface mechanical properties of ion implanted polymers. J Mater Res 8:927–933
164. Rao GR, Monar K, Lee EH, Treglio JR (1994) Metal ion implantation effects on surface properties of polymers. Surf Coat Technol 64:69–74
165. Rao GR, Lee EH, Bhattacharya R, McCormick AW (1995) Improved wear properties of high energy ion-implanted polycarbonate. J Mater Res 10:190–201
166. Lee EH, Rao GR, Lewis MB, Mansur LK (1993) Ion beam application for improved polymer surface properties. Nucl Instr Meth Phys Res B 74:326–330
167. Pivin JC (1995) Contribution of ionizations and atomic displacements to the hardening of ion-irradiated polymers. Thin Sol Films 263:185–193
168. Zhang J, Ye X, Yu X, Li H (2001) Radiation damage and wettability change of low energy C^+ implanted polytetrafluoroethylene. Mater Sci Engineer B 84:200–204
169. Rao GR, Lee EH, Yao X, Brown IG (1995) Effects of metal-ion implantation on wear properties of polypropylene. J Mater Sci 30:3903–3908
170. Niklaus M, Rosset S, Dubois P, Shea HR (2009) Comparison of two metal ion implantation techniques for fabrication of gold and titanium based compliant electrodes on polydimethylsiloxane. Mater Res Soc Symp Proc 1188:LL03–LL09
171. Niklaus M, Shea HR (2011) Electrical conductivity and Young's modulus of flexible nanocomposites made by metal-ion implantation of polydimethylsiloxane: the relationship between nanostructure and macroscopic properties. Acta Mater 59:830–840
172. Chen T, Yao S, Wang K, Wang H, Zhou S (2009) Modification of the electrical properties of polyimide by irradiation with 80 keV Xe ions. Surf Coat Technol 203:3718–3721
173. Moliton A, Lucas B, Moreau C, Friend RH, Francois B (1994) Francois Ion implantation in conjugated polymers: mechanisms for generation of charge carriers. Philos Mag B 69:1155–1171
174. Wasserman B (1986) Fractal nature of electrical conductivity in ion-implanted polymers. Phys Rev B 34:1926–1931
175. Davenas J, Thevenard P (1993) The multi-aspects of ion beam modification of insulators. Nucl Instr Meth Phys Res B 80/81:1021–1027
176. Bratko J, Hall BO, Schoch KF Jr (1986) Highly conductive poly(phenylene sulfide) prepared by high-energy ion irradiation. J Appl Phys 59:1111–1116
177. Aleshin AN, Gribanov AV, Dobrodumov AV, Suvorov AV, Shlimak IS (1989) Electro-physical properties of polyimide PM films treated by ion bombardment. Sov Phys Sol State 31:6–12
178. Mott NF, Devis EA (1979) Electronic processes in non-crystalline materials. Clarendon, Oxford

179. Bridwell LB, Giedd RE, Wang YQ, Mohite SS, Jahnke T, Brown IM, Bedell CJ, Sofield CJ (1991) Ion implantation of polymers for electrical conductivity enhancement. Nucl Instr Meth Phys Res B 57:656–659
180. Komarov FF, Leontyev AV, Grigoryev VV (2000) Electrophysical properties of organic materials irradiated with accelerated ions. Nucl Instr Meth Phys Res. B 166–167:650–654
181. Švorčik V, Rybka V, Miček I, Popok V, Jankovskij O, Hnatowicz V, Kvitek J (1994) Structure and properties of polymers modified by ion implantation. Eur Polym J 30:1411–1415
182. Lee PA, Ramakrishnan TV (1985) Disordered electronic systems. Rev Mod Phys 57:287–337
183. Wu Y, Zhang T, Zhang H, Zhang X, Deng Zh, Zhou G (2000) Electrical properties of polymer modified by metal ion implantation. Nucl Instr Meth Phys Res B 169:89–93
184. Teixeira FS, Salvadori MC, Cattani M, Brown IG (2009) Gold-implanted shallow conducting layers in polymethylmethacrylate. J Appl Phys 105:064313
185. Mackova A, Malinsky P, Miksova R, Pupikova H, Khaibullin RI, Valeev VF, Svorcik V, Slepicka P (2013) Annealing of PEEK, PET and PI implanted with Co ions at high fluencies. Nucl Instr Meth Phys Res B 307:598–602
186. Tie M, Dhirani A-A (2015) Conductance of molecularly linked gold nanoparticle films across an insulator-to-metal transition: from hopping to strong Coulomb electron-electron interactions and correlations. Phys Rev B 91:155131
187. Popok VN, Lukashevich MG, Lukashevich SM, Khaibullin RI, Bazarov VV (2004) Charge carrier transport in polyimide with co nanoparticles formed by ion implantation. Surf Sci 566–568:327–331
188. Lukashevich MG, Popok VN, Volobuev VS, Melnikov AA, Khaibullin RI, Bazarov VV, Wieck A, Odzhaev VB (2010) Magnetoresistive effect in PET films with iron nanoparticles synthesised by ion implantation. Open Appl Phys J 3:1–5
189. Vionnet-Menot S, Grimaldi C, Maeder T, Strässler S, Ryser P (2005) Tunneling-percolation origin of nonuniversality: theory and experiments. Phys Rev B 71:064201
190. Davenas J, Thevenard P (1991) Electronic structure characterization of ion beam modified polyimide by optical absorption and reflection. Nucl Instr Meth Phys Res B 59(60):1249–1252
191. Rück DM, Schulz J, Deusch N (1997) Ion irradiation induced chemical changes of polymers used for optical applications. Nucl Instr Meth Phys Res B 131:149–158
192. Hadjichristov G, Ivanov V, Faulques E (2008) Reflectivity modification of polymethylmethacrylate by silicon ion implantation. Appl Surf Sci 254:4820–4827
193. Tsvetkova T, Balabanov S, Avramov L, Borisova E, Angelov I, Sinning S, Bischoff L (2009) Photoluminescence enhancement in Si implanted PMMA. Vacuum 83:S252–S255
194. Kreibig U, Vollmer M (1995) Optical properties of metal clusters. Springer, Berlin
195. Flytzanis C, Hache F, Klein MC, Ricard D, Rousignol P (1991) Nonlinear optics in composite materials. Elsevier, Amsterdam
196. De Julian Fernandez C, Manera MG, Spadavecchia J et al (2005) Study of the gas optical sensing properties of Au-polyimide nanocomposite films prepared by ion implantation. Sens Actuat B 111–112:225–229
197. Gao W, Chen G, Xu W, Yang C, Xu S (2014) Surface-enhanced Raman scattering (SERS) chips made from metal nanoparticle-doped polymer fibres. RSC Adv 4:23838–23845
198. Fateixa S, Nogueira HIS, Trindade T (2015) Hybrid nanostructures for SERS: materials development and chemical detection. Phys Chem Chem Phys 17:21046–21071
199. Van Dorst B, Mehta J, Bekaert K, Rouah-Martin E, De Coen W, Dubruel P, Blust R, Robbens J (2010) Recent advances in recognition elements of food and environmental biosensors: a review. Biosens Bioelectron 26:1178–1194
200. Petryayeva E, Krull UJ (2011) Localized surface plasmon resonance: nanostructures, bioassays and biosensing—a review. Anal Chim Acta 706:8–24
201. Hedayati MK, Javaherirahim M, Mozooni B et al (2011) An omnidirectional transparent conducting-metal-based plasmonic nanocomposite. Adv Mater 23:5410–5414

202. Elbahri M, Hedayati MK, Chakravadhanula VSK, Jamali M, Strunkus T, Zaporojtchenko V, Faupel F (2011) Design of a perfect black absorber at visible frequencies using plasmonic metamaterials. Adv Mater 23:1993–1997
203. Yuguang W, Tonghe Z, Andong L, Gu Z (2002) The nano-structure and properties of Ag-implanted PET. Surf Coat Technol 157:262–266
204. Boldyryeva H, Kishimoto N, Umeda N, Kondo K, Plaksin OA, Takeda Y (2004) Surface modification and nanoparticle formation by negative ion implantation of polymers. Nucl Instr Meth Phys Res B 219–220:953–956
205. Stepanov AL, Popok VN (2004) Nanostructuring of silicate glass under low-energy Ag-ion implantation. Surf Sci 566–568:1250–1254
206. Popok VN, Stepanov AL, Odzhaev VB (2005) Synthesis of silver nanoparticles by the ion implantation method and investigation of their optical properties. J Appl Spectr 72(2):229–234
207. Popok VN, Gromov AV, Nuzhdin VI, Stepanov AL (2010) Optical and AFM study of ion-synthesised silver nanoparticles in thin surface layers of SiO_2 glass. J Non-Cryst Sol 356:1258–1261
208. Minnai C, Milani P (2015) Metal-polymer nanocomposite with stable plasmonic tuning under cyclic strain conditions. Appl Phys Lett 107:073106
209. Minnai C, Di Vice M, Milani P (2017) Mechanical-optical-electro modulation by stretching a polymer-metal nanocomposite. Nanotechnology 28:355702
210. Hanif M, Juluri RR, Fojan P, Popok VN (2016) Polymer films with size-selected silver nanoparticles as plasmon resonance-based transducers for protein sensing. Biointerface Res Appl Chem 6(5):1564–1568
211. Magrupov MA (1981) Semiconducting pyropolymers. Russ Chem Rev 50:1104–1117
212. Azarko II, Hnatowicz V, Kozlov IP, Kozlova EI, Odzhaev VB, Popok VN (1994) EPR-spectroscopy of the ion implanted polymer films. Phys Stat Sol (a) 146:K23–K27
213. Goldberg IB, Crove HR, Newman PR, Heeger AJ, MacDiarmid AG (1979) Electron spin resonance of polyacetylene and AsF5-doped polyacetylene. Chem Phys 70(1979):1132–1136
214. Zhuravleva TS (1987) Studies of polyacetylene by magnetic resonance methods. Russ Chem Rev 56:69–80
215. Polyboyarov VA, Andryushkova OV, Bulynnikova M (1992) Change of structure and composition of organic substances under electron irradiation. Sibirskij Khim Zhurnal 5:118–124 (in Russian)
216. Ogawa K (1988) Magnetic recording medium and method for making the same. US Patent No 4751100
217. Petukhov V, Zhikharev V, Ibragimova M, Zheglov E, Bazarov V, Khaibullin I (1996) Ions synthesis of thin granular ferromagnetic films in polymethylmethacrylate. Sol State Comm 97:361–364
218. Khaibullin RI, Osin YuN, Stepanov AL, Khaibullin IB (1998) Ion synthesis of Fe and Ag granular films in viscous and solid state polymers. Vacuum 51:289–294
219. Popok VN, Lukashevich MG, Gorbachuk NI, Odzhaev VB, Khaibullin RI, Khaibullin IB (2006) Magnetoresistive effect and impedance spectroscopy of Co-implanted polyimide. Phys Stat Sol (a) 203:1545–1549
220. Lukashevich M, Battle X, Labarta A, Popok V, Zhikharev VA, Khaibullin RI, Odzhaev VB (2007) Modification of magnetic properties of polyethyleneterephthalate by iron ion implantation. Nucl Instr Meth Phys Res B 257:589–592
221. Kharchenko A, Lukashevich M, Popok V, Khaibullin R, Vallev V, Bazarov V, Petracic O, Wieck A, Odzhaev V (2013) Correlation of electronic and magnetic properties of thin polymer layers with cobalt nanoparticles. Part Part Syst Character 30:180–184
222. Kharchenko A, Lukashevich M, Nuzhdin VI, Khaibullin RI, Odzhaev VB (2013) Modification of the magnetic properties of polyimide films by cobalt ion implantation. Phys Sol State 55:88–93
223. Rameev BZ, Aktas B, Khaibullin RI, Zhikharev VA, Osin YuN, Khaibullin IB (2000) Magnetic properties of iron-and cobalt-implanted silicone polymers. Vacuum 58:551–560

224. Pivin JC, Khaibullin RI, Rameev BZ, Dubus M (2004) Magnetic resonances of Fe and Ni nanoparticles in films of silicon suboxide produced by ion irradiation of triethoxysilane gels containing Fe or Ni solute atoms. J Non-Cryst Sol 333:48–55
225. Malik R, Sharma R, Kanjilal D, Annapoorni S (2009) Alignment of magnetic clusters in polymer using Ar ion beam. J Phys D Appl Phys 42:235501
226. Khaibullin IB, Khaibullin RI, Abdullin SN, Stepanov AL, Osin YuN, Bazarov VV, Kurzin SP (1997) Ion metal synthesis in viscous organic matter. Nucl Instr Meth Phys Res B 127(128):685–688
227. Rameev B, Okay C, Yildizm F, Khaibullin RI, Popok VN, Aktas B (2004) Ferromagnetic resonance investigations of cobalt implanted polyimides. J Magnet Magn Mater 278:164–171
228. Tian-Xiang C, Shu-De Y, Wei H, Tao F, Lin L, Sheng-Qiang Z (2009) Charge transport and magnetotransport properties of polyimide irradiated by 80 keV Co ions. Chin Phys Lett 26:087201

Ion Beam Modification of Poly (methyl methacrylate) (PMMA)

Raquel Silva Thomaz and Ricardo Meurer Papaléo

Abstract In this chapter, we review fundamental issues related to the damaging processes of PMMA films induced by high-energy ions with kinetic energies from a few keV to a few GeV, covering the regimes of energy deposition dominated by nuclear collisions and by electronic excitation. Emphasis is given to present an overview of the bond-breaking processes, the changes in the polymer chemical structure, and the corresponding modifications in selected macroscopic physical properties (optical, mechanical, and electrical).

Keywords Ion beam · PMMA · Physicochemical properties · Mechanical properties

1 Introduction

Poly(methyl methacrylate) (PMMA) is one of the most important polymeric materials available commercially. Due to its excellent mechanical properties, chemical resistance, and optical behavior similar to glass, it has been widely utilized across several industries, mainly as shatterproof windows, illuminated signs, and optical parts, but also as a structural material for different electronic, construction, and household goods [1]. The high biological compatibility made PMMA a common material for biomedical applications in ophthalmology, prosthetics, orthopedics, and dentistry, to name a few [2]. Resins based on PMMA have also been widely used in microlithography with UV photons, X-rays, or electron beams [3–6], or in direct micro-structuring processes such as proton-beam writing [7, 8]. More recently, in the growing field of proton radiotherapy [9, 10], PMMA has been used as a material for phantoms and beam-monitoring devices [11]. Therefore, the interaction of various forms of radiation with PMMA has been a persistent topic of

R. S. Thomaz · R. M. Papaléo (✉)
School of Sciences, Pontifical Catholic University of Rio Grande do Sul,
Av. Ipiranga 6681, Porto Alegre, RS 90619-900, Brazil
e-mail: papaleo@pucrs.br

V. Kumar et al. (eds.), *Radiation Effects in Polymeric Materials*, Springer Series on Polymer and Composite Materials, https://doi.org/10.1007/978-3-030-05770-1_4

investigation for more than four decades [3, 12–14]. A deep understanding of the radiation effects in PMMA is important not only to evaluate the stability and behavior of this material under various high-energy radiation fields, but also to optimize procedures in modern ion-beam-based processing techniques, where PMMA plays an important role [5–8, 15].

In this chapter, we review fundamental issues related to damaging processes of PMMA films induced by high-energy ions with kinetic energies from a few keV to a few GeV, covering the regimes of energy deposition dominated by either nuclear collisions or electronic excitation. Emphasis is given to present an overview of the bond-breaking processes and the corresponding changes in macroscopic physical properties, and their dependence on the energy loss of the ions.

2 Chemical Modification of PMMA by High-Energy Ions

Polymer degradation encompasses many reactions that change the material's structure, such as irreversible cleavage of bonds in the main chain, intermolecular crosslinking, and formation of unsaturated bonds and of volatile products [16–18]. Both crosslinking and scission may occur simultaneously during irradiation of polymers, but the relative magnitude of crosslinking to scission events depends on the structure of the polymer [1], on the ion stopping power, and ion fluence [19, 20]. In this section, we review the degradation pathways of PMMA by high-energy ions, starting with a discussion of the balance between scission and crosslinking and how it is affected by the stopping power, dE/dx. We then review the radiolysis of PMMA, the main degradation compounds formed, and the structure of highly irradiated PMMA.

2.1 Chain Scission and Crosslinking

The chemical structure of the poly(methyl methacrylate) (PMMA) repeating unit is shown in Fig. 1. For the majority of irradiation conditions, ion-bombarded PMMA

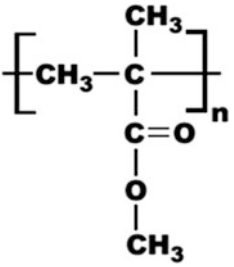

Fig. 1 Chemical structure of the repeating unit of PMMA

undergoes main chain scission, which leads to a decrease of the average molecular weight [19, 21–24]. Chain scission is also dominant in the irradiation of PMMA with γ-rays, electrons, and UV photons [25–27]. The propensity of degradation has been attributed to a steric hindrance due to the methyl ester (CH_3OOC–) groups attached to the PMMA backbone structure [19, 28]. Large pendant groups restrict chain mobility and thus hamper crosslinking. The presence of a tetra-substituted carbon atom in the main chain also favors degradation [29, 30].

Figure 2 shows the molecular weight distribution extracted from PMMA films irradiated with 200 keV He^+ [31]. Even at low fluences (2.5×10^{12} ions/cm^2), the molecular weight distribution (MWD) of bombarded PMMA exhibits a pronounced tail at the low-mass side due to scission products. For higher fluences, the MWD continues to shift toward lower molar masses, but a small fraction of high molecular weight crosslinked molecules is also seen (Fig. 2a).

The solubility of irradiated PMMA increases with fluence (because of chain scission) only until a certain maximum dose (Fig. 2b). For larger fluences, solubility decreases progressively until an insoluble gel is eventually formed. Thus, even for an easily degradable polymer as PMMA, crosslinking of the chains will be extensive at large fluences. The change to a crosslinking dominant behavior occurs in the first place due to the higher concentration of macroradicals at high fluences, which favors bonding in between chains. In addition, at high fluences, PMMA is transformed to a material resembling a sort of disordered polyethylene [32], a polymer for which the probability for crosslinking is higher than for scission [21]. In general, the larger the dE/dx or LET of the ion beam, the lower is the fluence required for the onset of crosslinking in irradiated PMMA. Table 1 illustrates this for beams of H, He, and O ions of 1.5 MeV. The ability of PMMA to crosslink at

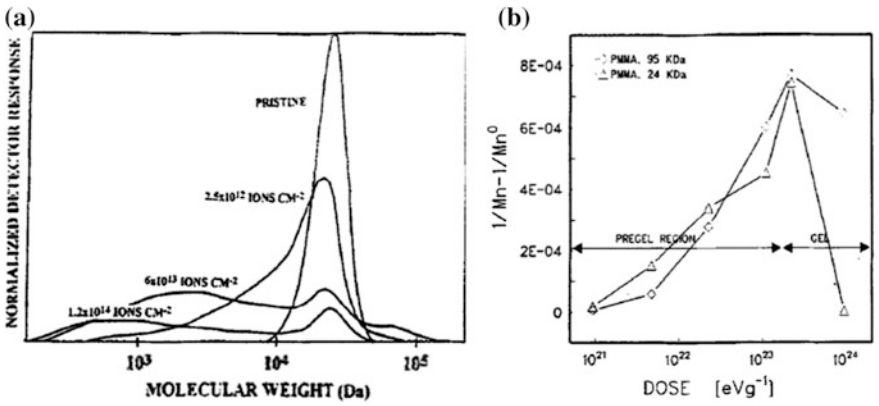

Fig. 2 **a** Molecular weight distribution of 24 kDa PMMA irradiated with 200 keV He^+. **b** $\left(1/M_n - 1/M_n^0\right)$ as a function of dose for samples of 95 and 24 kDa PMMA irradiated with 200 keV He^+. A fluence of 6×10^{13} ions/cm^2 of 200 keV He^+ corresponds to a dose of ~23 eV/g. M_n is the number-averaged molecular weight. Adapted from Ref. [31]

Table 1 Regions of dominance of scission and crosslinking for ion beams of various LET values

Radiation source	LET (eV/nm)	Scission regime (solubility increases with fluence)	Crosslink regime (solubility decreases with fluence)
20 keV e^-	2	$<10^{18}$ m^{-2}	No decrease in solubility
1.5 MeV H^+	20	$<10^{17}$ m^{-2}	$>10^{19}$ m^{-2}
1.5 MeV He^+	200	$<10^{16}$ m^{-2}	$>10^{18}$ m^{-2}
1.5 MeV O^+	800	$<10^{16}$ m^{-2}	$>10^{17}$ m^{-2}

Reprinted with permission from [19] by Publisher

high doses is also seen in electron beam irradiated PMMA, which changes from positive to negative resist behavior (insoluble in the developer) at sufficiently large exposures to the e-beam [33].

Several studies have been conducted to investigate the effect of dE/dx on the yield of chain scission and crosslinking [19, 22, 24]. This is usually quantified by the respective G-values (the number of crosslinks $G(x)$ or chain scissions $G(s)$ per 100 eV of absorbed energy). For irradiation with ^{60}Co gamma rays (dE/dx = 0.2 eV/nm), for example, $G(s) \sim 1.2$ [24]. Similar $G(s)$ values were observed for low LET ion beams (Fig. 3). However, $G(s)$ starts to decrease for beams with LET larger than about 15 eV/nm [19, 22]. $G(s)$ values as low as 0.3 was found at LET = 577 eV/nm (90 MeV O^{4+}) [24]. The lower yield of scission at high LET were attributed to the reduced distance between radical pairs or dangling bonds, which increases the probability for two neighboring radicals to be close enough for crosslinking.

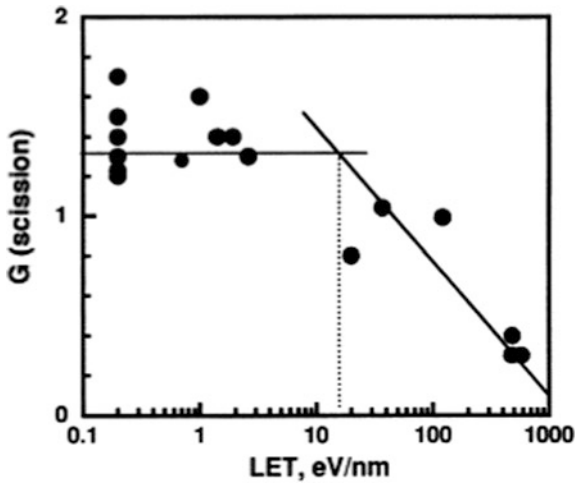

Fig. 3 G-value of chain scission, $G(s)$, for PMMA as a function of LET. Irradiations were performed with different ions and velocities. Reprinted with permission from [19]

An interesting effect related to the degradation of PMMA is ion-beam-induced depolymerization (unzipping) [34]. Unzipping is the main mechanism of thermal degradation of PMMA [35] and is characterized by sequential scissioning of the chain ends, resulting in the preferential emission of the monomer methyl methacrylate [36]. The monomer is found to be the most abundant product (yield > 85%) in the pyrolysis of PMMA [21]. This phenomenon starts at the so-called ceiling temperature (around 220 °C) [34] in the conventional thermal degradation of PMMA. However, when the polymer was exposed to a beam of 200 keV He^+ while heated, unzipping initiated at temperatures as low as 105 °C, slightly above the glass transition temperature (T_g) [34, 37–40]. Thus, irradiation of PMMA at temperatures above T_g may result in a stronger degradation rate and a pronounced reduction in the polymer molecular weight. Up to now, irradiation-induced depolymerization of PMMA has not been detected at room temperature, or using swift heavy ions.

2.2 *Radiolysis, Volatiles, and Changes in the Chemical Structure*

The radiolytic decomposition mechanisms of ion-beam-irradiated PMMA have been extensively investigated, using beams in a wide range of energies and stopping powers [19, 40–42]. While several details have yet to be clarified, especially at the very large dE/dx of swift heavy ions, the general degradation scheme has been established and is not very different from those obtained from "conventional" forms of radiation such as X-rays, electrons, and γ-rays.

A simplified scheme of the mechanism of PMMA degradation is shown in Fig. 4. High-energy irradiation is very efficient for inducing backbone chain scission (Fig. 4-path II) compared to photoexcitation process (path I). Both processes can provoke hydrogen abstraction from the polymer main chain (Fig. 4-path VI) and main chain scission (Fig. 4-path III). Besides main chain scission (and the consequent formation of unsaturated bonds), rupture and decomposition of the side-chain methyl ester groups $CH_3COO–$ are the dominant events (Fig. 4-path IV–V). The main volatiles formed from the decomposition of the pendent group are CO, CO_2, and CH_4 [19, 32, 40, 43]. The amount of such gases will vary depending on the stability of the fragments generated, and on the type of beam.

Figure 5 shows the G-values for CO, H_2, CO_2, and CH_4 production as a function of the track average LET. Again, at low LET, the G-values for ion beams are similar to gamma rays. The G-values start to increase strongly with LET above a LET around 10 eV/nm. Since most of the analyzed gases have the same precursor ($\cdot COOCH_3$), the data of Fig. 5 indicate that the amount of the methyl ester radical must increase with LET [44]. Studies of PMMA irradiated with gamma rays show that the amount of CO, CO_2, and CH_4 are also temperature-dependent [44]. CO and CO_2 yields at T = 40 °C are 2.5–3 times larger than the values found at room

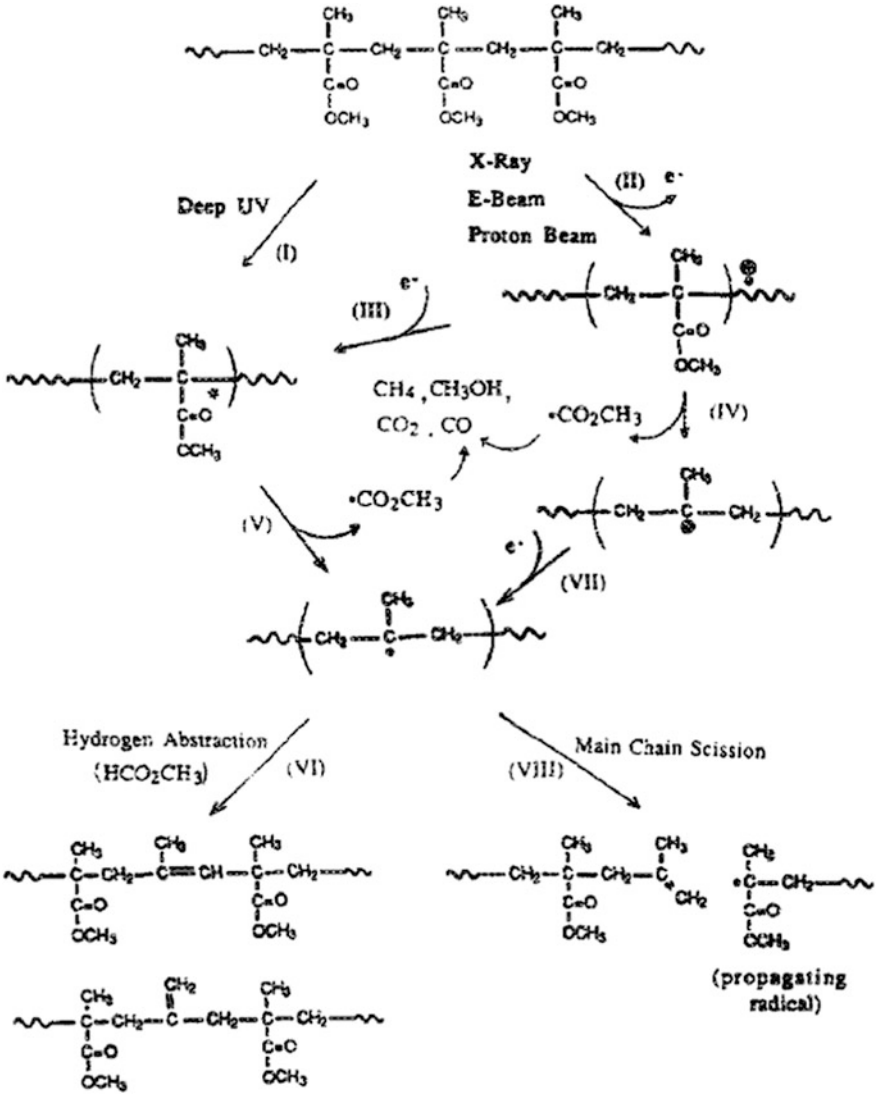

Fig. 4 Radiolysis pathway of PMMA and main volatile products formed. Reprinted with permission from [40]

temperature. On the other hand, molecular hydrogen is produced from radicals that are not thermally dependent.

Many other small molecules originating from the breakage of the chains or from the subsequent decomposition of intermediate species are usually observed by in situ mass spectrometry. Figure 6 shows an example of an in situ residual gas analysis (RGA) of a PMMA film irradiated by 4.5 MeV/u Au ions [45], illustrating

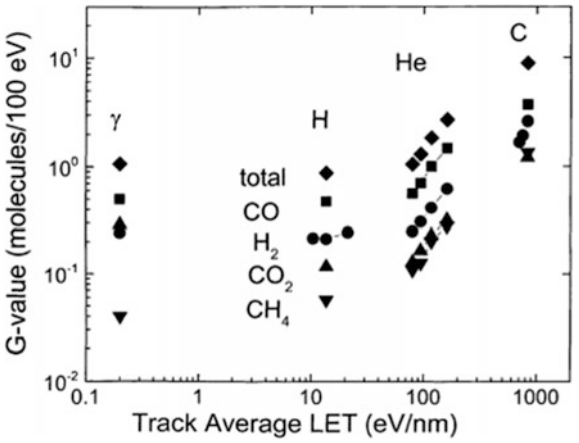

Fig. 5 *G*-values for the production of various volatile molecules as a function of track average LET for beams of γ-rays, H, He, and C ions. Reprinted with permission from [44]

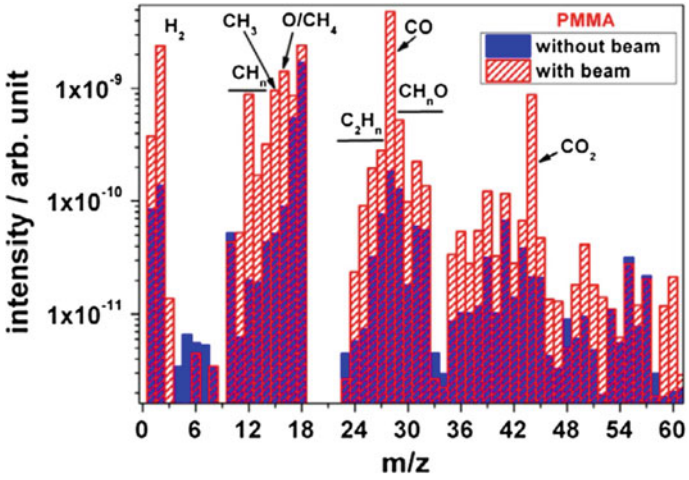

Fig. 6 Outgassing spectra of PMMA irradiated with 4.5 MeV/u Au ions. Mass spectra recorded before and after irradiation. Reprinted with permission from [45]

the multiplicity of emitted species. This includes H_2, CH_2, CH_3, CH_3O•, $HCOOCH_3$, and unsaturated hydrocarbons, such as $H_2C{=}CH_2$, ·$CH{=}C{=}CH_2$, $CH_2{=}C{=}CH_2$, and $CH_3CH{=}CH$ [40, 45, 46]. The abundant emission of oxygen-containing small molecules is a clear indication that a significant fraction of methyl ester groups is broken and easily eliminated by outgassing. The emission of numerous unsaturated hydrocarbons supports the observation of significant scissioning of the macromolecular chains [26, 32].

The decomposition scheme described above is also supported by several spectroscopic studies [20, 31, 32, 40, 47–50]. In particular, infrared vibrational spectroscopy (FTIR) was widely used to probe bond breaking of irradiated PMMA. An example is given in Fig. 7, where FTIR spectra of PMMA bombarded by ions of low (500 keV He) and high dE/dx ($\sim$886 MeV Au) are shown. The reduction of the peaks associated to the vibrational modes at 1150 and 1190 cm^{-1} (C–O stretching vibrations) and the carbonyl (C=O) band at 1720 cm^{-1} are consistent with the gradual elimination of the pendent methyl ester groups (Fig. 7) [20, 26, 47, 48, 51]. The diminishing of carbon–oxygen bonds (C=O and C–O–C) is also shown in the XPS spectra of irradiated PMMA [27, 32, 52, 53] or in measurements of the fraction of oxygen atoms derived from RBS data [26] (Figs. 8 and 9). It is interesting to note that the ratio of oxygen to carbon in a sample irradiated with a beam of low dE/dx ions (2 MeV H$^+$, dE/dx $\sim$ 0.019 keV/nm) is smaller by $\sim$20% than

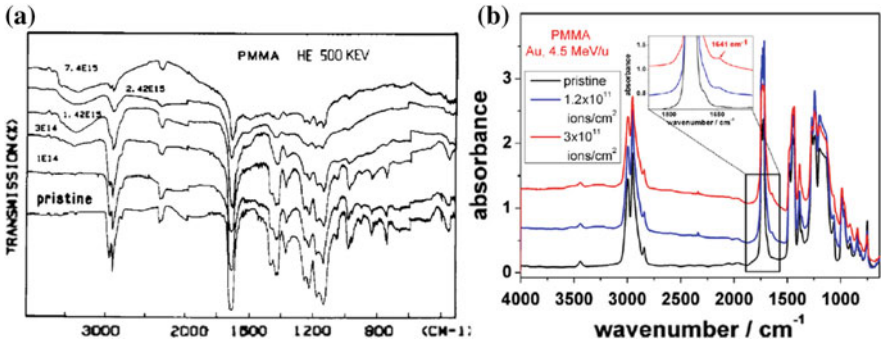

Fig. 7 FTIR spectra of PMMA films bombarded by **a** 500 keV He and **b** 886 MeV Au ions. Reprinted with permission from [45, 54]

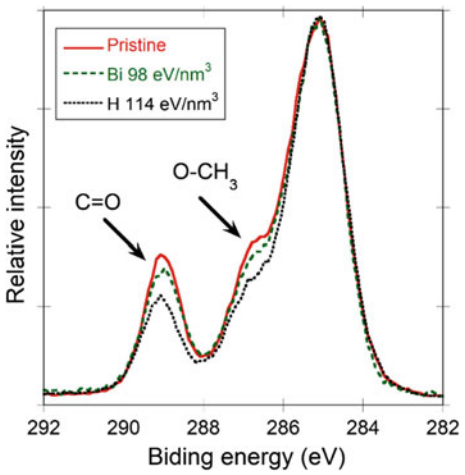

Fig. 8 C1s XPS spectra of PMMA films irradiated by 2 MeV H$^+$ and 2.1 GeV Bi at similar deposited energy densities. The peaks associated to C atoms directly bound to oxygen are labeled in the figure. These are C_3 (O–CH_3) and C_4 (C=O). All spectra were normalized to the peak intensity of the C_1 line (C–H) at 285 eV. Reprinted with permission from [52]

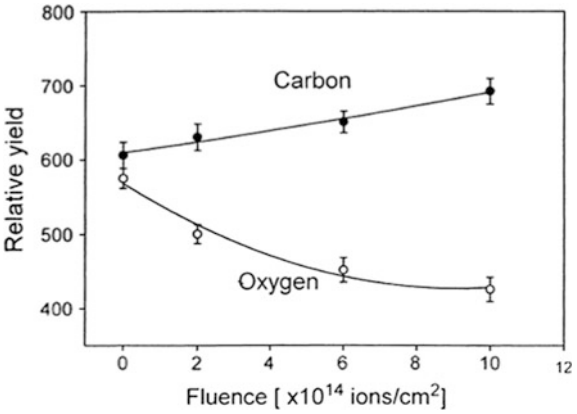

Fig. 9 Change of the relative contents of carbon and oxygen of PMMA irradiated by 350 keV H as a function of fluence, measured by Rutherford backscattering spectrometry. Reprinted with permission from [26]

in a film irradiated with a high dE/dx ion (2.2 GeV Bi, dE/dx $\sim$ 14 keV/nm) at a similar dose (in the case of Fig. 8 close to 100 eV/nm^3) [52]. This suggests a greater importance of particle ejection unzipping by PMMA chains at high dE/dx, which would keep the O/C ratio closer to the pristine value.

FTIR [45, 47, 49], Raman [27], and UV spectroscopy [45, 49] reveal the formation of conjugated C=C bonds in the irradiated polymer. In FTIR, this is seen by the appearance of a new absorption band at 1600–1670 cm^{-1}. In one study, the number of C=C bonds generated in the films was similar to that of C=O groups removed by the same incident dose, suggesting that removal of an ester group generates also a C=C bond by main chain scission and H abstraction [40]. For low dE/dx, the efficiency of C=C bond formation is smaller than that found at high dE/dx (Fig. 7).

At high irradiation fluences, the pristine polymer chemical structure is virtually lost and FTIR spectra are almost featureless due to generalized bond breaking [21, 31, 32, 47, 49]. Carbonization is the fate of all heavily irradiated polymers, but the type of carbonaceous material that is eventually formed depends on the monomer structure and dE/dx of the ions. Most of the studies indicate that PMMA films eventually turn into a form of hydrogenated amorphous carbon material a-C:H [27, 49]. The Raman spectra of PMMA irradiated by 400 keV Cr^+ ions (Fig. 10) show clearly the development of the characteristics broad peaks corresponding to the D and G band of disordered carbon.

Although the general scheme presented above for the radiolysis of PMMA is observed for irradiations with ions in a wide range of stopping powers, there are some effects that are only observed at very high dE/dx due to swift heavy ions. For example, GeV heavy ion irradiation of PMMA leads to the formation of various aromatic compounds [56, 57], including large mass pure carbon clusters [58] that are not observed at low dE/dx [51]. It was suggested that in the core of swift heavy ion tracks, as a result of the very high transient temperatures a gas of electrons and free carbon ions is formed. Carbon clusters and aromatic rings would form during the subsequent expansion and cooling of this highly excited region [58]. The proposed scheme is shown in Fig. 11.

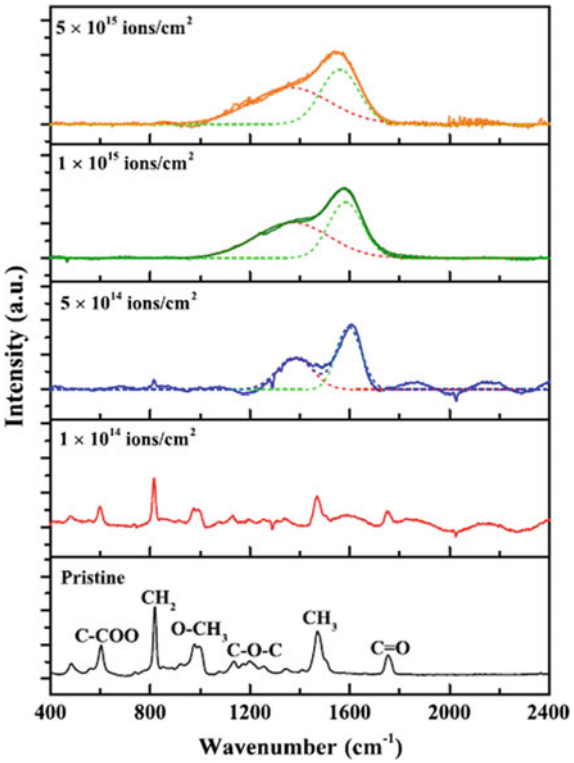

Fig. 10 Raman spectra of pristine and irradiated PMMA samples. The irradiation was performed using 400 keV Cr^+ ions with fluences up to 5×10^{15} cm^{-2}. The solid lines indicate the measured Raman spectrum, while the dashed lines indicate the two Gaussian-fitted D and G bands. Reprinted with permission from [55]

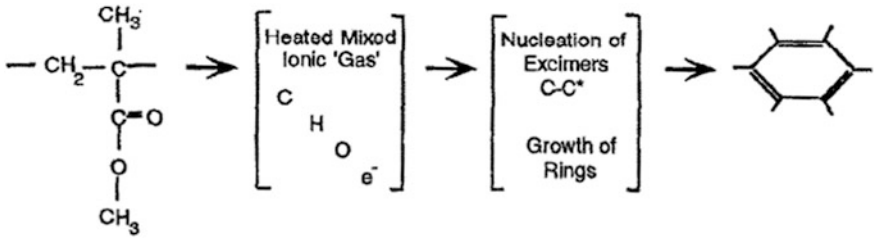

Fig. 11 Suggested mechanisms for the decomposition of PMMA and carbon cluster formation in the core of swift heavy ion tracks. Reprinted with permission from [58]

2.3 Damage Cross Sections

In the previous section, the changes introduced in the chemical structure of irradiated PMMA were reviewed. Here, we discuss the problem of the degradation efficiency and the rates of destruction (or formation) of various chemical bonds. The damaging efficiency is usually quantified extracting the damage cross section σ for a certain process of interest. σ is a probability of occurrence, which is interpreted as an effective area around the ion path where a certain modification takes place. For the quasi-continuous cylindrical damage track of a swift heavy ion, the geometrical interpretation of σ is intuitive. The value of σ can be obtained by monitoring the changes in the intensity $I(\phi)$ of a given signal (a FTIR band, UV absorbance, XRD peaks, etc.) as a function of fluence. In most of the situations, an exponential behavior is observed experimentally, which allows the extraction of a damage cross section by fitting the data with the expression:

$$I(\phi) = I_0 \mathrm{e}^{-\sigma\phi} \tag{1}$$

where I_0 is the intensity of the investigated signal for the pristine sample. If radiation induces the creation of new structures, then the signal intensity can usually be expressed as:

$$I(\phi) = I_{\mathrm{sat}}\left(1 - \mathrm{e}^{-\sigma\phi}\right), \tag{2}$$

where I_{sat} is the signal obtained at high fluences.

Table 2 provides a compilation of cross-sectional values obtained from the literature. Some of them were already extracted in the original references, while others were obtained by us from fittings of the available data. Cross sections for the processes of chain scission, loss of various functional groups, decrease in oxygen and hydrogen content, and formation of conjugated double bonds (chromophores) are shown. The magnitude of the cross sections depends on the technique used to probe the damage (e.g., chemical composition, optical properties, secondary yields) [59], and on the dE/dx and ion velocity. Hence, a direct comparison between cross sections of different processes is only meaningful when similar irradiation conditions are used in the experiments. Despite the large amount of papers on ion beam modification of PMMA, there is, unfortunately, no systematic study comparing cross sections of different processes under similar irradiation conditions, similar to those found, for example, for PET [60], PPS [61], or PC [62]. Yet, some general considerations can be drawn.

The largest damage cross-sectional values are found for processes related to changes in the polymer crystallinity and average molecular weight [60]. For these processes, either the activation energies or the required number of hits by secondary electrons to induce an observable effect is small. However, PMMA is usually in an amorphous configuration (or semi-crystalline structure with high amorphous content). Hence, there are only few studies investigating the changes induced in the

Table 2 Ion energy, velocity, electronic stopping power $(dE/dX)_e$, nuclear stopping power $(dE/dX)_n$, and cross sections (σ) extracted from ion bombardment of PMMA films

Ion	Energy (MeV)	Velocity (cm/ns)	$(dE/dX)_e$ (eV/nm)	$(dE/dX)_n$ (eV/nm)	Technique	σ (cm^2)	Refs.
Bond breaking							
He	5	1.6	1.7	0.0027	FTIR[a,b]	5.1×10^{-16}	Fink [20]
Li	5	1.2	3.3	0.0014	FTIR[a,b]	2.2×10^{-15}	Fink [20]
B	2.5	0.7	5.9	0.1	FTIR[a,b]	2.2×10^{-14}	Fink [20]
H^+	2	1.2	19	0.012	XPS (C–O)	$\sim 4 \times 10^{-16}$	Thomaz [66]
Ar^+	0.005	0.01	69	432	XPS[a] (C–O)	4.1×10^{-15}	Pignataro [32]
He^+	0.2	0.3	200	1	MWD	9×10^{-14}	Fragala [21]
He^+	0.2	0.3	200	1	MWD	3×10^{-13}	Licciardello [64]
He^+	1.0	0.7	250	0.7	Carbon erosion[a]	6×10^{-16}	Calcagno [68]
He^{2+}	0.5	0.5	270	0.6	Dehydrogenation	2.6×10^{-15}	Davenas [49]
Xe^+	0.7	0.1	580	1220	Dehydrogenation	$\sim 10^{-15}$	Davenas [54]
Bi^{+eq}	2200	4.5	14,000	14.4	XPS (C–O)	$\sim 3 \times 10^{-13}$	Thomaz [66]
Au^{eq+}	887.0	2.9	15,000	35	FTIR[a] (2994 cm^{-1})	1.5×10^{-12}	Hossain [45]
Au^{eq+}	887.0	2.9	15,000	35	FTIR[a] (2842 cm^{-1})	9.2×10^{-13}	Hossain [45]
Formation of new bonds							
C^{5+}	70.0	3.3	300	0.2	UV–Vis[a,c]	9.6×10^{-14}	Singh [50]
Ne^{6+}	145.0	3.7	690	0.4	UV–Vis[a,c]	5.5×10^{-13}	Kumar [69]
Si^{8+}	100.0	2.6	1730	1.3	UV–Vis[a,c]	5.6×10^{-13}	Kumar [65]
Au^{eq+}	887.0	2.9	15,000	35	FTIR (1641 cm^{-1})[a]	1.3×10^{-11}	Hossain [45]
U^{eq+}	1980.0	4.0	18,000	21	UV–Vis[a,c]	2.5×10^{-11}	Hossain [45]

[a]The cross sections were extracted from the data presented in the referred references
[b]Data extracted from the whole FTIR spectra
[c]Data extracted from the absorption in 375 nm of the UV–Vis spectra

PMMA crystallinity and cross sections were not extracted [50, 63]. The rates of amorphization nevertheless appear to be similar to those found for molecular weight changes described below. Fragalà et al. [21] investigated the number-averaged molecular weight M_n of PMMA irradiated by 200 keV He^+. Figure 12 shows the values of $1/M_n$ as a function of fluence. The fitting (dashed line) gives a cross section of 9×10^{-14} cm^2. In another study, also with 200 keV He bombardment, a cross section of $\sim 3 \times 10^{-13}$ cm^2 was extracted [64]. The major difference between those two measurements was the procedure used to quantify the signal. While in Ref. [64] only the low-mass portion of the MWD chromatogram was used; Fragalà

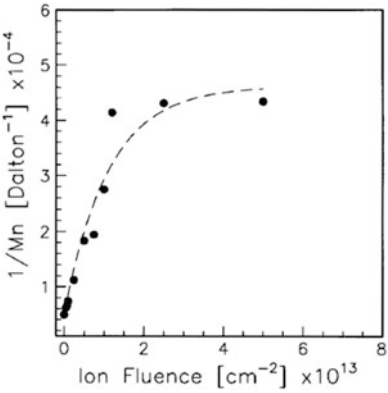

Fig. 12 Reciprocal number-averaged molecular weight $(1/M_n)$ of bombarded PMMA as a function of ion fluence. Reprinted with permission from [21]

et al. [21] used the average over the complete molecular weight distribution. This example illustrates how easily cross sections may be influenced by the procedure of data quantification. In any case, both cross sections are relatively large, considering the low stopping power of the He beam. We found no study on damage cross sections for chain scission of PMMA using swift heavy ions in the literature to compare with.

Cross sections for bond breaking and formation of new bonds in irradiated PMMA are the most abundant in the literature. They typically range from $\sim 10^{-16}$ cm^2 for light ions up to $\sim 10^{-11}$ cm^2 for swift heavy ion projectiles (see Table 2). By monitoring the changes in the intensity of the FTIR bands of PMMA irradiated with MeV light ions (5 MeV He and Li and 2.5 MeV B), Fink et al. [20] found damage cross section of the order of 10^{-16}–10^{-14} cm^2). This corresponds to effective track radii of chemical damage of about 0.4 Å for He or 3 Å for B. On the other hand, the damage cross section of 887 MeV Au ions is roughly three orders of magnitude larger [45]. Figure 13 shows the evolution of three different FTIR bands at 2994, 2842, and 1641 cm^{-1} of PMMA irradiated with 887 MeV Au ions. Both

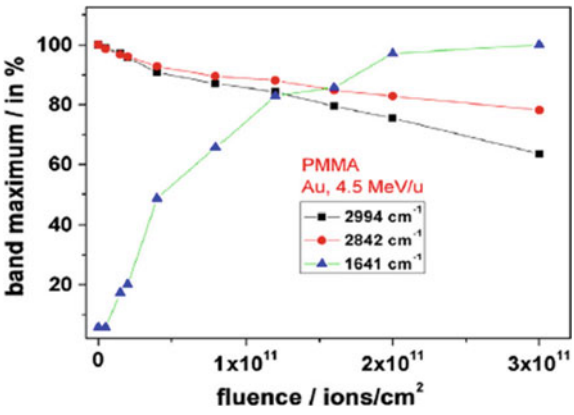

Fig. 13 Peak intensity of absorption bands at 2994, 2842, and 1641 cm^{-1} as a function of the fluence for PMMA films irradiated with 887 MeV Au ions. Reprinted with permission from [45]

processes of bond destruction and new bond formation are shown. The loss of CH_2 and CH_3 groups (bands at 2994 and 2842 cm^{-1}, respectively) occurs with a cross section of $\sigma_{2842\,cm^{-1}} = 7.8 \times 10^{-13}\,cm^2$ and $\sigma_{2994\,cm^{-1}} = 1.5 \times 10^{-12}\,cm^2$. The very large cross section obtained for the new band appearing at 1641 cm^{-1} ($\sigma_{1641\,cm^{-1}} = 1.3 \times 10^{-11}\,cm^2$) demonstrates the efficiency of such high dE/dx ions to create carbon–carbon double bonds, which was larger than the breaking of C–H bonds.

Another process investigated is chromophore formation by the conjugation of unsaturated carbon bonds. This is usually extracted from UV–Vis spectra, as shown in Fig. 14. The absorbance of irradiated samples in the UVA and visible region increases with irradiation fluence. Figure 14b shows the increase in absorbance at 375 nm after irradiation with 100 MeV Si^{8+} ions, depicting an exponential growth typical of Eq. 2. The resulting cross section was about $5.5 \times 10^{-13}\,cm^2$.

Overall, the various damage cross sections extracted for PMMA are comparable to those observed in other polymers, with differences in magnitude that stem from the degree of radiation stability of each material. For example, cross sections for emission of volatiles in polystyrene (a more radiation-resistant polymer) bombarded by 500 keV He, were more than 50% smaller than in PMMA, under the same experimental conditions [49]. On the other hand, heteroatom emission in ion-bombarded PVC, a highly degradable polymer, is even larger than those found for PMMA [66].

Although cross sections are important parameters quantifying the sensitivity of a polymer to radiation damage, care must be taken when comparing data probed by different techniques, because of their specific spatial sensitivity and probing signal. XPS, for example, tends to give smaller cross sections than FTIR, although both techniques are probing the amount of chemical bonds. This is related to the fact that XPS is very little affected by long-range changes in the chemical environment and gives information of modification occurring mostly close to the ion path where

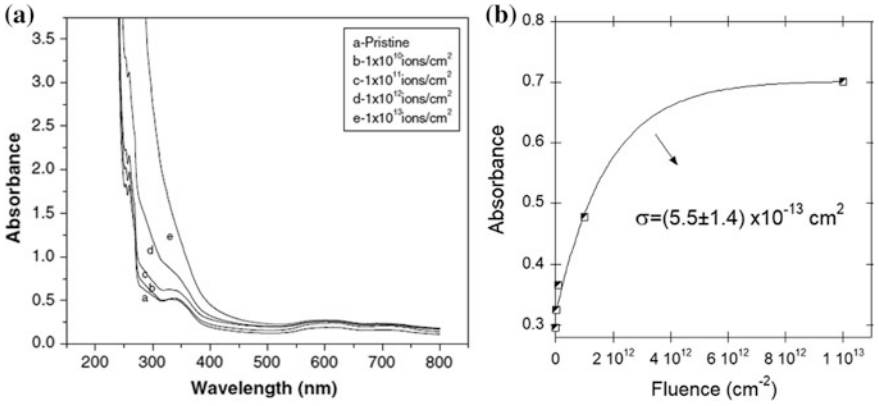

Fig. 14 **a** Optical absorption spectra of pristine PMMA and PMMA after irradiation with 100 MeV Si^{8+} ion beam. **b** Peak intensity of absorption at 375 nm of the spectra shown in (**a**) and its resulting damage cross section. Reprinted with permission from [65]

bond disruption is severe. In addition, the signal from spectroscopic techniques such as UV–Vis and FTIR are proportional to the optical path of the probing beam in the sample. This means that the signal may change not only because specific bonds are broken, but also due to reductions in the sample thickness. As discussed in the next section, PMMA thinning by ion irradiation is very efficient [67]. Therefore, many of the cross sections reported in the literature may be the convolution of chemical damage with effects that cause thickness reductions (sputtering, densification, etc.).

2.4 Changes in Physicochemical Properties

Bond breaking, formation of new bonds, and preferential emission of oxygen and hydrogen in bombarded PMMA result in irreversible changes in its macroscopic physicochemical properties. In this section, the main changes observed in mechanical, optical, and electrical properties of ion-bombarded PMMA are reviewed.

2.4.1 Density Enhancement and Compaction

PMMA films and foils irradiated by ion beams become remarkably thinner after ion bombardment [26, 43, 70–72]. The thickness decrease was mainly attributed to outgassing of volatile products [73, 74]. Sputtering is a small component, especially for light ions and low dE/dx, but cannot be neglected for swift heavy ions. The crater volume of a single 600 MeV Au ion is approximately a half sphere of 10 nm radius [75, 76]. In addition, main chain scission results in shorter and more mobile molecules, what facilitate spatial rearrangements and local conformational changes. This eventually leads to the compaction of the layers and increase in density [77, 78].

Figure 15 presents the compaction induced in 1-mm-thick PMMA foils irradiated with 350 keV H^+ (the ion range is 4.2 μm) as a function of the fluence. The compaction reached values as high as few micrometers at high fluences. The shrinking rate was not steady, but decreased with fluence, until a saturation level is reached at very high fluences [67, 71, 78]. This occurs because of the cumulative effects of track overlap. At large fluences, the probability of ions hitting regions already modified by the ions increases, reducing the gas yield per ion impact.

Swelling, however, may precede the shrinking process. Due to the long projected range of swift ions, gaseous products are formed in deep regions of the polymer and cannot escape from the material as quick as they are produced. As a consequence, a high pressure of gases is built up in the polymer, resulting in a transiently swollen surface [74]. In a foil of PMMA irradiated through a micro-patterned mask with 1.8 MeV H^+ ($\phi = 6 \times 10^{13}$ ions/cm^2), within a time of 12 min after the irradiation the surface swollen about 70 nm with respect to the non-irradiated region (Fig. 16a). Only later, 200 min after the irradiation,

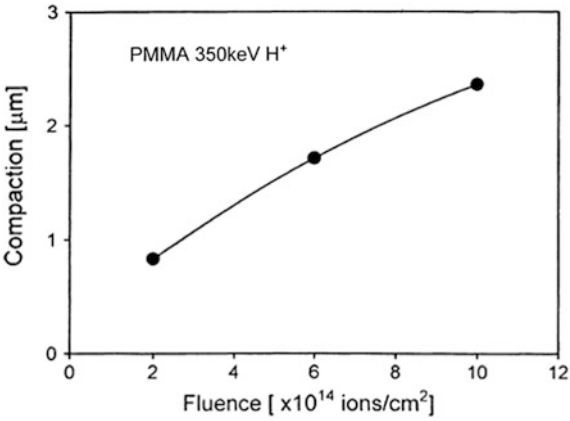

Fig. 15 Compaction of a 1-mm-thick PMMA foil as a function of fluence of 350 keV H^+ ions. Reprinted with permission from [26]

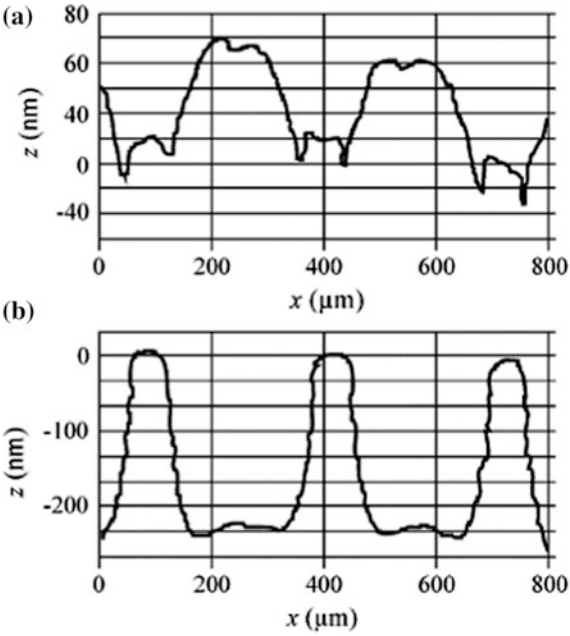

Fig. 16 Surface profiles of the irradiated sample measured by profilometry, **a** 12 min after the irradiation and **b** after 200 min. Reprinted with permission from [74]

profilometry of the same region revealed that the surface retracted to more than 200 nm below the original surface level (Fig. 16b). It was noted by the authors that if the ion current was low enough, swelling was not observed.

A discrepancy between compaction values is found in the literature, even when similar irradiation conditions are used [43, 74]. These differences can be explained by the distinct times after irradiation that the depth profile was measured. The shrinking due to outgassing is diffusion-limited and may continue over several

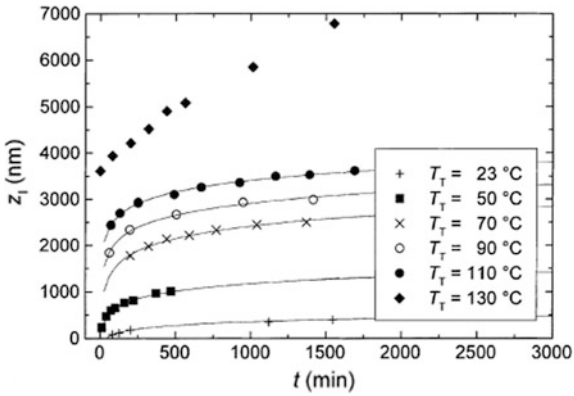

Fig. 17 Shrinking of the surface (z_t) of 1-mm-thick PMMA foils bombarded with 1.8 MeV H^+ ions as a function of time t after irradiation to a fluence of 6×10^{13} ions/cm^2. Measurements were performed at different temperatures T_T ranging from 23 to 130 °C. The solid lines are fittings with a diffusion model. Reprinted with permission from [74] by Publisher

weeks if the effective diffusion coefficient, D_{eff} is low (Fig. 17). At room temperature, the D_{eff} extracted for PMMA after irradiation with 1.8 MeV H^+ ions to a fluence of 6×10^{13} cm^{-2} was 8.3×10^{-11} cm^2/s. Gas diffusion is accelerated at higher temperatures, increasing the shrinking rate. At temperatures just below the glass transition, T_g ($\sim$105 °C), the effective diffusion constant found by Schrempel et al., is about six orders of magnitude higher than the value found at room temperature [74]. At 130 °C, thermal degradation also plays an important role, being gas diffusion no longer the predominant effect.

2.4.2 Optical Properties

There has been a great practical interest on the investigation of optical properties of irradiated PMMA, because of the wide range of potential photonic applications and the widespread use of PMMA in optical components. Proton-beam writing has been used for the fabrication of microphotonic devices (waveguides, gratings, microlens arrays, etc., Fig. 18). For such applications, knowledge on ion-induced modifications in the absorption coefficient and refractive index are of utmost importance.

As discussed in the previous section, the damage produced by ion irradiation leads to the formation of absorption centers in PMMA at the UV and visible regions of the spectra due to the increase in conjugated C=C double bonds, which provides more optically active electrons. This process changes the polymer color gradually from transparent to yellowish-brown. The color change is usually irreversible, but there are reports of transparency recovery depending on the beam conditions and storage environment [28].

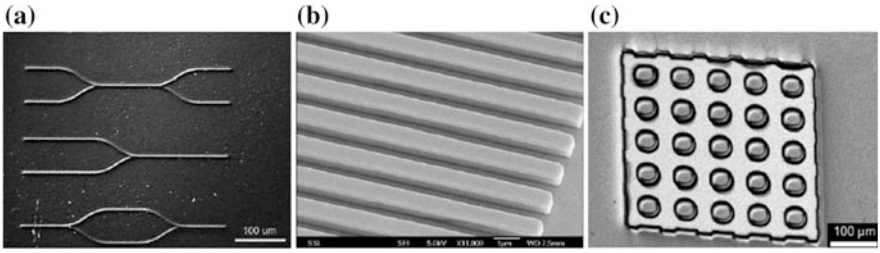

Fig. 18 **a** Optical image of waveguides fabricated in 3-mm-thick PMMA. Electron microscopy images of a **b** surface relief gratings fabricated in 800 nm layer of PMMA spin coated on a Si wafer and **c** a microlens array. Adapted from [79]

Accompanying the changes in UV absorption, there is an increase in the refractive index with ion fluence (Fig. 19) [47, 71, 72, 80, 81]. The refractive index enhancement was attributed as well to the formation of unsaturated bonds along the irradiated layer [28]. Compaction and densification of the irradiated material are also associated to the increase in the refractive index [77]. It is remarkable in the study of Kallweit and Biersack [80] that Δn increases steadily with fluence, with no saturation yet visible (Fig. 20). The relatively large changes in Δn of up to 0.3 is an interesting feature for waveguide fabrication.

Several experiments were performed to investigate the correlation between the ion range and the changes of Δn with depth. When 2 MeV H^+ was used to bombard a block of PMMA (Fig. 21), the highest increase of the refractive index occurs at the end of range, i.e., at the Bragg peak of the energy-loss curve [81].

The use of irradiated PMMA in waveguides was also tested. The main problem was the optical losses. The measured intensity attenuation of waveguides fabricated using a 3-mm-thick foil irradiated by 2 MeV H^+ at fluence of $\sim$50 nC/mm^2 is shown in Fig. 22. In this case, the mean attenuation coefficient was found to be 1.4 $\pm$ 0.2 dB/cm [70]. Propagation losses are, additionally, very dependent on the ion dose [72]. For PMMA blocks irradiated with Li^+ ions in the energy range of 100–130 keV with fluences up to 10^{14} cm^{-2}, waveguides with total loss values of

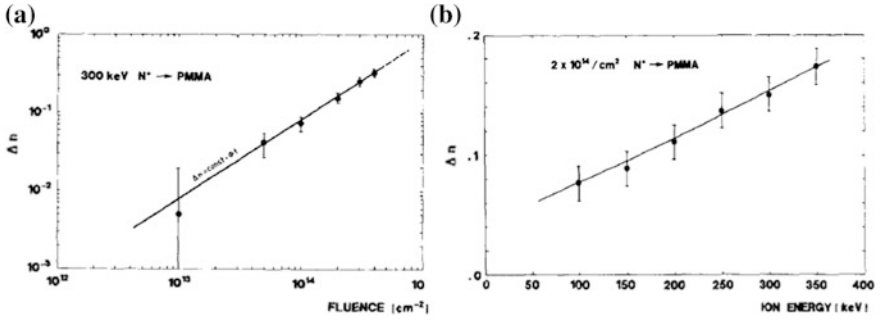

Fig. 19 Change in refractive index, Δn, of PMMA irradiated by N ions with kinetic energies between 100 and 350 keV. **a** Δn versus ion fluence for 300 keV N^+. **b** Δn versus ion energy (constant fluence of 2 $\times$ 10^{14} ions/cm^2). Reprinted with permission from [80]

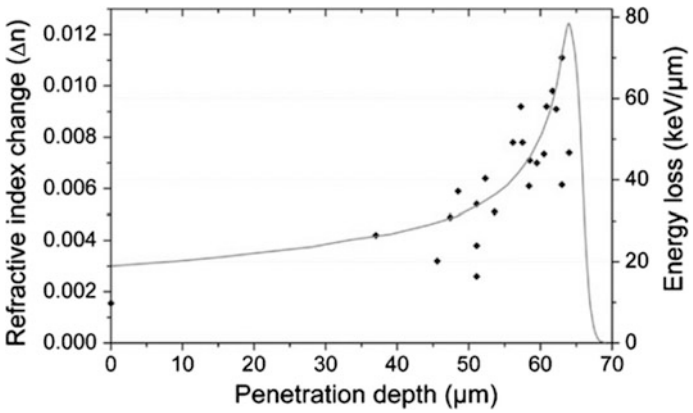

Fig. 20 Change in refractive index at 633 nm of PMMA irradiated by 2 MeV H^+ as a function of penetration depth. For comparison, the energy-loss profile was also plotted as a solid line. Reprinted with permission from [81]

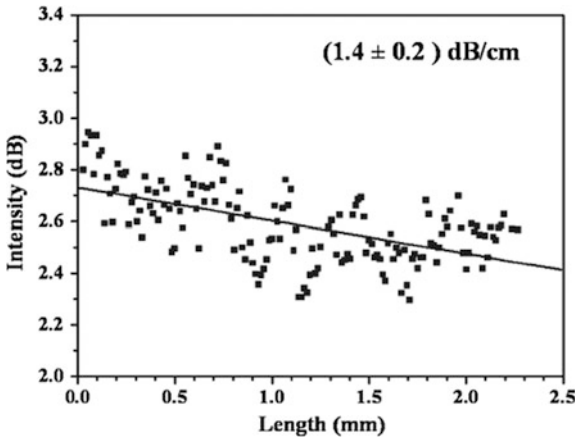

Fig. 21 Intensity loss at 632.8 nm of a PMMA waveguide fabricated using 2 MeV H^+ at fluence of $\sim$50 nC/mm^2. Reprinted with permission from [70]

<2 dB/cm could be fabricated [47]. At higher fluences, because of ion-beam-induced damage, the propagation loss increases by more than a factor of two. Optical losses are also a function of the beam energy. Other studies show that attenuation measurements of waveguides obtained after 1–2 MeV proton irradiation showed loss values as high as 5 dB/cm up to 8 dB/cm, depending on the beam conditions [71].

Another complication of using ion irradiation to prepare waveguides is aging. In one study, long-term stability of n was investigated in PMMA bombarded by 1 MeV He^+ ions and stored at 70 °C in vacuum or at ambient conditions (Fig. 23). Both samples show a decrease of the initial index of refraction during the first 60 days and become stable after 3 months. The aging effect was more pronounced for the samples stored at ambient conditions [71].

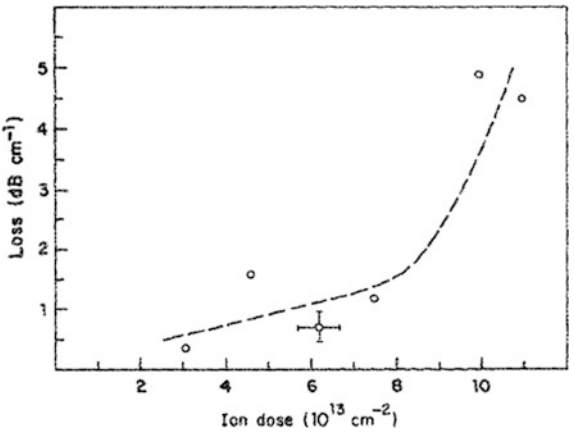

Fig. 22 Loss value of irradiated PMMA waveguides for different fluences of Li^+ ions in the energy range of 100–130 keV. Reprinted with permission from [47]

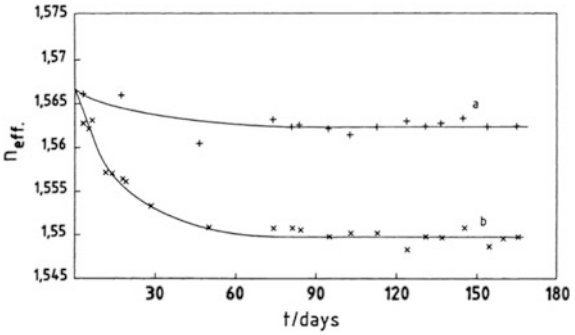

Fig. 23 Long-term stability of the refraction index of PMMA samples irradiated with 1 MeV He^+ ions. Reprinted with permission from [71]

2.4.3 Mechanical Properties

Figure 24 shows the results of the changes of flexural strength of 3-mm-thick sheets of PMMA irradiated by 45 and 30 MeV proton beams and γ-rays as a function of the absorbed dose. The decay in flexural strength is similar for all types of such low LET radiations (LET $\sim$ 1 eV/nm for the three beams). It is well known that such a decrease of the strength is induced by chain scission of PMMA [82].

Hardness, scratch resistance, and elastic modulus of the polymer are also affected by crosslink and chain scission [23, 83]. Figure 25 shows averaged values of indentation elastic modulus versus maximum indentation depth for bulk PMMA implanted by 40 keV B^+ ions. The maximum penetration depth of B^+-ions into PMMA is about 400 nm. However, implanted PMMA showed an increased elastic modulus with respect to the pristine material at much larger depths (up to 1100 nm [84]).

Figure 26 illustrates the changes in hardness of PMMA irradiated by 2 MeV Ar ions (LET = 1134 eV/nm) and 2 MeV He ions (LET = 242 eV/nm) as a function of ion fluence. Hardness increased significantly with increasing fluence, especially

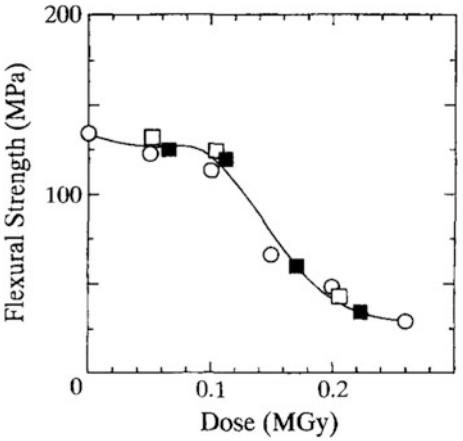

Fig. 24 Flexural strength of PMMA as a function of dose (○ gamma ray; □ 45 MeV proton; ■ 30 MeV proton). Reprinted with permission from [82]

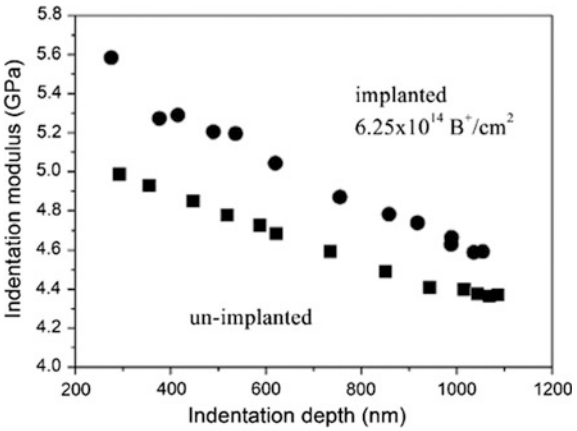

Fig. 25 Indentation elastic modulus versus maximum indentation depth for un-implanted PMMA (squares) and PMMA implanted by 40 keV B^+ ions (circles) samples. Reprinted with permission from [84]

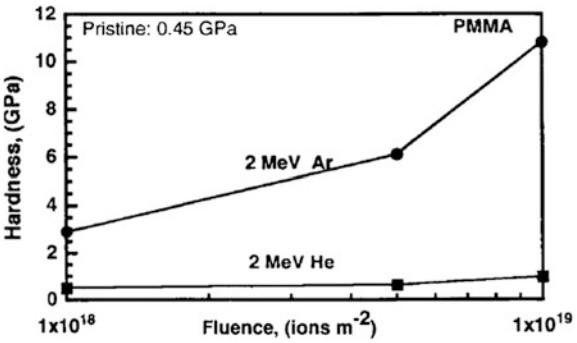

Fig. 26 Hardness changes as a function of fluence for PMMA irradiated by 2 MeV He^+ and Ar^+ ions. Reprinted with permission from [19]

for the larger dE/dx Ar beam, where it jumped from the pristine value of 0.45 GPa to over 10 GPa after irradiation to a fluence of 1×10^{15} cm^{-2}. The improvement in hardness was greater at larger dE/dx [19]. In fact, under low LET radiations, such as e-beam and γ-rays, the material becomes extremely brittle, but there is no appreciable change in hardness [19]. However, it has been shown that at high electron doses (7.5×10^{17} cm^{-2}), the surface hardness of the irradiated PMMA increased to 2.8 GPa, and the elastic modulus from 5.6 to 22.9 GPa [27].

As hardness of polymers increases with increasing crosslinking density [83], this difference in mechanical behavior of PMMA irradiated by ions of low and high LET reinforces that scission is dominant for low LET and low fluences, whereas crosslinking becomes more important with increasing LET and at high ion fluences.

2.4.4 Changes in Electrical Properties

In general, polymers are highly insulating materials with wide band gaps [28]. Ion irradiation or implantation can be used to increase the polymer conductivity by several orders of magnitude. The possibility of preparing conducting regions in a highly insulating polymeric matrix was one of the first exciting effects of ion bombardment of polymers to be explored [85]. Figure 27 presents data on the electrical conductivity of irradiated PMMA as a function of 400 keV Cr^+ ions. An increase in electrical conductivity from $\sim 2 \times 10^{-10}$ S/cm (pristine) to $\sim 7 \times 10^{-6}$ S/cm (at 5×10^{15} ions/cm^2) was observed. In another study, using beams of 150–200 keV Si^+ ions at much larger fluences (3.2×10^{16} Si^+/cm^2), the conductivity reached values of almost 11 orders of magnitude higher than that of pristine PMMA [86].

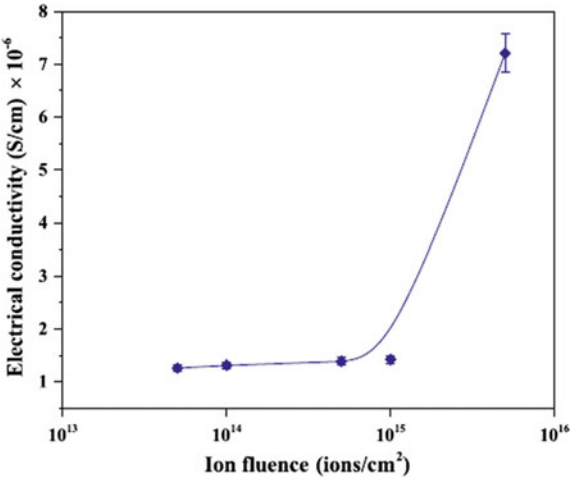

Fig. 27 Electrical conductivity of 400 keV Cr^+-implanted PMMA versus ion fluence. The line was drawn to guide the eye. Reprinted with permission from [55]

The conductivity increase reflects the carbonization process discussed in the previous sections. Conductivity rises sharply only after the material has been extensively damaged by the beam and significant amounts of carbon clusters are formed in the material. The formation of a network of carbon clusters provides a charge transportation system in implanted PMMA [55, 85]. In the early work at the Bell Laboratories [85, 87], 2 MeV Ar^+ was used to irradiate several nonpolymeric and polymeric organic compounds, including PMMA. The temperature dependence of the resistivity $\rho(T)$ of the irradiated material was found to follow $\rho(T) \propto \exp\left[+(T_0/T)^{1/2}\right]$ over a wide range of fluences and temperatures. Based on this dependence, it was proposed that conduction of electricity at intermediate irradiation fluences involves hopping of carriers between isolated conducting islands. At very high fluences, ($>10^{16}$ cm^{-2}), conducting islands interconnect and the resistivity becomes temperature-independent. In general, ion bombardment of organic thin films leads to the production of a carbon-enriched material with some properties similar to those found for amorphous carbon, but with electrical characteristics that are unique [87]. Conductivity also depends on the initial monomer structure. The value found for heavily irradiated PMMA (9.5×10^{-4} S/cm, after 10^{16} ions/cm^2 of 1 MeV Xe^+) was smaller than for other polymers like PS (1×10^{-4} S/cm) and PE (1.5×10^{-4} S/cm) irradiated under similar conditions [54].

3 Concluding Remarks

In this chapter, fundamental issues related to damaging processes of PMMA induced by high-energy ions were reviewed. The different steps in the polymer modification, from the identification of the main bond-breaking pathways and chemical changes to the corresponding modifications in the macroscopic physical properties are reasonably well established, and are not very different from those obtained from "conventional" forms of radiation, for which the available data is much more abundant. The similarities are more evident for low LET particles, such as fast H or He ions. In this regime, *G*-values for X-rays, γ-rays, electrons, and ions are similar and the mean dose is the main parameter determining the level of the final effect (chain scission, hydrogen release, etc.). However, several details of the complex chain of events induced by high-energy ions in PMMA have yet to be clarified, especially at the very large d*E*/d*x* of swift heavy ions (SHI).

In fact, already at intermediate d*E*/d*x* (e.g., of 1 MeV Ar, ~800 eV/nm), the dose/response curve might become nonlinear. Certain degradation products are clearly produced at much higher yields at large d*E*/d*x*. This includes the formation of triple bond carbon clusters, and sputtering of macromolecular fragments. Thus, although carbonization is the fate of all heavily irradiated polymers, the type and properties of the carbonaceous material that is eventually formed will depend on the

dE/dx of the ions. The balance between scission and crosslinking and ion-beam-induced unzipping are also expected to alter at large dE/dx. Systematic studies aiming a better understanding of transformations specifically induced by energetic heavy ions are necessary. Even the basic effect of the changes in M_w distribution of PMMA after SHI irradiation is lacking in the literature. Of the major physical properties of materials, thermal property is one of the least investigated after ion irradiation of polymers, including PMMA. Studies on the changes in thermal properties like thermal expansion or heat conductivity are practically absent in the literature and need to be conducted. There are scattered data on damage cross sections for bond-breaking of PMMA in the literature. However, there is no systematic study comparing cross sections of different modification processes (chain scission, bond breaking, chromophore formation, carbon cluster formation, etc…) under the same irradiation conditions. This will allow a detailed view of the spatial (radial) distribution of different types of structures/defects created around the ion track.

The effect of irradiation temperature is also worthy of further investigation. We have shown examples where temperature alters the effects produced by ion irradiation of PMMA (e.g., in irradiation-induced depolymerization or in the kinetics of volatile emission). However, it is unclear at present how temperature alters the profile of intermediate products produced by ion irradiation or the final properties of the bombarded material. It is expected that, near and above T_g, all processes which are diffusion-controlled will be enhanced. The temperature effects may also be different for ions of high and low dE/dx, as recent studies on the surface morphology of ion-irradiated PMMA thin films suggest [88]. Irradiations at low temperatures with subsequent in situ annealing and spectroscopic characterization will allow obtaining valuable information on the creation and stability of different chemical groups formed by irradiation. This has been explored in a few polymers, like polyethylene, but not in PMMA.

The vast majority of irradiation experiments are performed in vacuum. It would be interesting to study the effect of ion irradiation in different atmospheres, including oxidative environments, and how they affect the yield and type of degradation products.

Additionally, the influence of the sample conditions themselves needs to be carefully addressed. For example, there is no systematic investigation comparing irradiation effects on samples prepared from monodisperse standards in a broad range of molecular weights. How much the molar mass influence radiation chemistry and properties changes induced by energetic ions? PMMA is also used in the form of composites with various fillers or polymer blends. A systematic investigation of the ion beam modification of such systems is also scarce and needs to be examined in closer detail.

Overall, in spite of the importance of PMMA as an engineering material, the volume of data available on ion modification of PMMA is still relatively limited,

compared to other important polymers such as polystyrene, polyethylene, or poly (ethylene terephthalate). Thus, PMMA needs for sure an expanded and reliable database, built from "targeted" experiments with well-controlled irradiation and sample conditions to help answering some of the open issues raised above.

References

1. Duan H, Zhao J, Zhang Y, Xie E, Li H (2009) Nanotechnology 20(13):135306
2. Frazer R, Byron R, Osborne P, West K (2005) J Long Term Effects Med Implants 15:629–639
3. Komuro M, Atoda N, Kawakatsu H (1979) J Electrochem Soc 126(3):483–490
4. Hall TM, Wagner A, Thompson LF (1982) J Appl Phys 53(6):3997–4010
5. Gorelick S, Guzenko VA, Vila-Comamala J, David C (2010) Nanotechnology 21(29):8
6. Vladimirsky Y, Vladimirsky O, Morris KJ, Klopf JM, Calderon GM, Saile V (1996) Microelectron Eng 30(1–4):543–546
7. Puttaraksa N, Norarat R, Laitinen M, Sajavaara T, Singkarat S, Whitlow HJ (2012) Nucl Instrum Methods Phys Res Sect B 272:162–164
8. van Kan JA, Malar P, Wang YH (2014) Appl Surf Sci 310:100–111
9. Schardt D, Elsaesser T, Schulz-Ertner D (2010) Rev Mod Phys 82(1):383–425
10. Loeffler JS, Durante M (2013) Nat Rev Clin Oncol 10(7):411–424
11. Linz U (2011) Ion beam therapy: fundamentals, technology, clinical applications. Springer, Berlin
12. Randall JN, Flanders DC, Economou NP, Donnelly JP, Bromley EI (1983) Appl Phys Lett 42(5):457–459
13. Dole M (2013) The radiation chemistry of macromolecules, vol. 2. Elsevier Science, Netherlands
14. Egusa S, Ishigure K, Tabata Y (1979) Macromolecules 12(5):939–944
15. Trautmann C (2010) Micro- and nanoengineering with ion tracks. In: Ion beams in nanoscience and technology. Springer, Heidelberg, pp 369–387
16. Chapiro A (1995) Nucl Instrum Methods B 105(1–4):5–7
17. Marletta G (1990) Nucl Instrum Methods B 46(1–4):295–305
18. Duraud JP, LeMoel A (1995) Nucl Instrum Methods B 105(1–4):71–80
19. Lee E, Rao G, Mansur L (1999) Radiat Phys Chem 55(3):293–305
20. Fink D, Hosoi F, Omichi H, Sasuga T, Amaral L (1994) Radiat Eff Defects Solids 132(4): 313–328
21. Fragala M, Compagnini G, Licciardello A, Puglisi O (1998) J Polym Sci Pol Phys 36(4):655–664
22. Kudoh H, Sasuga T, Seguchi T (1997) Radiat Phys Chem 50(3):299–302
23. Lee EH (1999) Nucl Instrum Methods B 151(1–4):29–41
24. Schnabel W, Klaumunzer S, Sotobayashi H, Asmussen F, Tabata Y (1984) Macromolecules 17(10):2108–2111
25. Schnabel W, Sotobayashi H (1976) Polym J 8(5):423–427
26. Choi HW, Woo HJ, Hong W, Kim JK, Lee SK, Eum CH (2001) Appl Surf Sci 169:433–437
27. Cho SO, Jun HY (2005) Nucl Instrum Methods B 237(3–4):525–532
28. Fink D (2004) Fundamentals of ion-irradiated polymers. Springer, Berlin
29. Compton RG, Bamford CH, Tipper CFH (1975) Degradation of polymers. Elsevier Science, Netherlands
30. Grassie N, Scott G (1988) Polymer degradation and stabilisation. Cambridge University Press, Cambridge

31. Licciardello A, Fragala M, Foti G, Compagnini G, Puglisi O (1996) Nucl Instrum Methods B 116(1–4):168–172
32. Pignataro B, Fragala M, Puglisi O (1997) Nucl Instrum Methods B 131(1–4):141–148
33. Zailer I, Frost JEF, Chabasseur V, Ford C, Pepper M (1999) Semicond Sci Technol 11:1235
34. Fragala ME, Compagnini G, Torrisi L, Puglisi O (1998) Nucl Instrum Methods B 141(1–4): 169–173
35. Manring LE (1989) Macromolecules 22(6):2673–2677
36. Manring LE (1988) Macromolecules 21(2):528–530
37. Mahoney CM, Fahey AJ, Gillen G, Xu C, Batteas JD (2007) Anal Chem 79(3):837–845
38. Compagnini G, Angilella GGN, Raudino A, Puglisi O (2001) Nucl Instrum Methods B 175:559–563
39. Fragala ME, Compagnini G, Puglisi O (1999) J Mater Res 14(1):228–231
40. Choi JO, Moore JA, Corelli JC, Silverman JP, Bakhru H (1988) J Vac Sci Technol B 6:2286
41. Wochnowski C, Eldin MAS, Metev S (2005) Polym Degrad Stab 89(2):252–264
42. Chang Z, LaVerne JA (2000) J Phys Chem B 104(45):10557–10562
43. Schrempel F, Witthuhn W (1997) Nucl Instrum Methods B 132(3):430–438
44. Chang Z, LaVerne JA (2001) Radiat Phys Chem 62(1):19–24
45. Hossain UH, Lima V, Baake O, Severin D, Bender M, Ensinger W (2014) Nucl Instrum Methods B 326:135–139
46. Ruck DM, Schulz J, Deusch N (1997) Nucl Instrum Methods B 131(1–4):149–158
47. Kulish JR, Franke H, Singh A, Lessard RA, Knystautas EJ (1988) J Appl Phys 63(8):2517–2521
48. Szilasi SZ, Huszank R, Szikra D, Vaczi T, Rajta I, Nagy I (2011) Mater Chem Phys 130(1–2): 702–707
49. Davenas J, Thevenard P, Boiteux G, Fallavier M, Lu XL (1990) Nucl Instrum Methods B 46 (1–4):317–323
50. Singh P, Kumar R, Virk H, Prasad R (2010) Indian J Pure AP Phy 48(5):321–325
51. Fink D, Mockel HJ, Melzer H, Klett R, Cardoso J, Montiel R, Vazquez H, Hosoi F, Omichi H, Wang L, Chadderton LT (1997) Appl Phys A 64(1):61–68
52. Thomaz R, Gutierres LI, Morais J, Louette P, Severin D, Trautmann C, Pireaux JJ, Papaléo RM (2015) Nucl Instrum Methods B 365:578–582
53. Kallweit R, Roll U, Strack H, Pocker A (1992) Mal Res Soc Symp Proc 235:345–350
54. Davenas J, Xu XL, Boiteux G, Sage D (1989) Nucl Instrum Methods B 39(1–4):754–763
55. Arif S, Rafique MS, Saleemi F, Naab F, Toader O, Mahmood A, Aziz U (2016) Appl Phys A 122(9)
56. Fink D, Chadderton LT, Schmoldt A (1993) Nucl Tracks Rad Meas 22(1–4):51–52
57. Schmoldt A, Chadderton LT, Fink D (1994) Radiat Eff Defects Solids 128(4):277–285
58. Fink D, Chadderton L, Hosoi F, Omichi H, Sasuga T, Schmoldt A, Wang L, Klett R, Hillenbrand J (1994) Nucl Instrum Methods B 91(1–4):146–150
59. Papaleo RM (1997) Nucl Instrum Methods B 131(1–4):121–134
60. Papaleo RM, Dearaujo MA, Livi RP (1992) Nucl Instrum Methods B 65(1–4):442–446
61. Papaleo R, Hallen A, Sundqvist B, Farenzena L, Livi R, deAraujo M, Johnson R (1996) Phys Rev B 53(5):2303–2313
62. Sun YM, Zhu ZY, Wang ZG, Jin YF, Liu J, Hou MD, Zhang QX (2003) Nucl Instrum Methods B 209:188–193
63. Singh P, Kumar R, Cyriac J, Rahul MT, Nambissan PMG, Prasad R (2014) Nucl Instrum Methods B 320:64–69
64. Licciardello A, Fragala ME, Compagnini G, Puglisi O (1997) Nucl Instrum Methods Phys Res Sect B-Beam Interact Mater Atoms 122(3):589–593
65. Kumar R, Ali S, Mahur A, Virk H, Singh F, Khan S, Avasthi D, Prasad R (2008) Nucl Instrum Methods B 266(8):1788–1792
66. Thomaz R, Louette P, Hoff G, Müller S, Pireaux JJ, Trautmann C, Papaléo RM (2018) Phys Rev Lett 121(6):066101

67. Unai S, Puttaraksa N, Pussadee N, Singkarat K, Rhodes MW, Whitlow HJ, Singkarat S (2013) Microelectron Eng 102:18–21
68. Calcagno L, Compagnini G, Foti G (1992) Nucl Instrum Methods B 65(1–4):413–422
69. Kumar R, Ali S, Singh P, De U, Virk H, Prasad R (2011) Nucl Instrum Methods B 269 (14):1755–1759
70. Sum TC, Bettiol AA, Florea C, Watt E (2006) J Lightwave Technol 24(10):3803–3809
71. Ruck DM, Brunner S, Frank W, Kulisch J, Franke H (1992) Surf Coat Technol 51(1–3): 318–323
72. Hong W, Woo HJ, Choi HW, Kim YS, Kim GD (2001) Appl Surf Sci 169:428–432
73. Ruck DM (2000) Nucl Instrum Methods B 166:602–609
74. Schrempel F, Kim YS, Witthuhn W (2002) Appl Surf Sci 189(1):102–112
75. Papaleo RM, Silva MR, Leal R, Grande PL, Roth M, Schattat B, Schiwietz G (2008) Phys Rev Lett 101(16):167601
76. Papaleo RM, Thomaz R, Gutierres LI, de Menezes VM, Severin D, Trautmann C, Tramontina D, Bringa EM, Grande PL (2015) Phys Rev Lett 114(11):118302
77. Sum TC, Bettiol AA, Seng HL, Rajta I, van Kan JA, Watt F (2003) Nucl Instrum Methods B 210:266–271
78. Ruck DM, Schulz J, Frank WF (1996) In: Conference on photopolymer device physics, chemistry, and applications III, Proceedings of the society of photo-optical instrumentation engineers (Spie). Denver, Co, pp 118–128
79. Bettiol AA, Sum TC, Cheong FC, Sow CH, Rao SV, van Kan JA, Teo EJ, Ansari K, Watt F (2005) Nucl Instrum Methods B 231:364–371
80. Kallweit R, Biersack JP (1991) Radiat Eff Defects Solids 116(1–2):29–36
81. Rajta I, Szilasi SZ, Budai J, Toth Z, Petrik P, Baradacs E (2007) Nucl Instrum Methods B 260(1):400–404
82. Kudoh H, Sasuga T, Seguchi T, Katsumura Y (1996) Polymer 37(21):4663–4665
83. Lee E, Rao G, Mansur L, Balogh A, Walter G (1997) Paper presented at the international symposium on materials science applications of ion beam techniques, Seeheim
84. Kavetskyy TS, Borc J, Kukhazh YY, Stepanov AL (2015) The influence of low dose ion-irradiation on the mechanical properties of PMMA probed by nanoindentation. In: Petkov P, Tsiulyanu D, Kulisch W, Popov C (eds) Nanoscience advances in CBRN agents detection, information and energy security. Springer, Netherlands, pp 65–71
85. Venkatesan T, Forrest SR, Kaplan ML, Murray CA, Schmidt PH, Wilkens BJ (1983) J Appl Phys 54(6):3150–3153
86. Hadjichristov GB, Gueorguiev VK, Ivanov TE, Marinov YG, Ivanov VG, Faulques E (2010) J Phys Conf Ser 207(1):012022
87. Kaplan ML, Forrest SR, Schmidt PH, Venkatesan T (1984) J Appl Phys 55(3):732–742
88. Esteves C, Thomaz R, Gutierres L, Papaleo R (2013) Nucl Instrum Methods B 314:71–76

Radiation-Induced Effects on the Properties of Polymer-Metal Nanocomposites

Suman Mahendia, Rishi Pal Chahal, Anil Kumar Tomar, Heena Wadhwa and Shyam Kumar

Abstract This chapter primarily includes the fundamental concepts related to metal nanoparticles with their unique features followed by importance of incorporating them in polymer matrix and finally considering irradiation as a novel tool to tailor the properties of metal–polymer nanocomposites. These nanocomposites are one of the promising materials which have been used in a wide variety of applications ranging from biomedical to optical and electrical devices to aerospace applications. Ionizing irradiation technique is among the most promising strategies for synthesis as well as to amend the changes in composite material because of the advantage of irradiation process compared to conventional synthesis like chemical, vapour deposition, etc., the process is simple, clean and controlled, carried out without producing undesired oxidants products of reducing agents, avoids the addition of undesirable impurities and produces composites which are highly stable. Irradiation-induced effects on polymer-metal nanocomposites provide unique pathway to control and modify the structural, optical and electrical properties of composites basically required for various applications as per desire. Thus, utilizing irradiations as a novel tool, a systematic study has been done to tune the properties of polymer-metal nanocomposites. Induced changes on structural, optical, and electrical properties have been conferred in this chapter.

Keywords Polymer · Metal nanoparticles · Nanocomposites · Surface plasmon resonance · Optical band gap · Refractive index · Antireflective coating · UV blocking · Structural properties

S. Mahendia (✉) · H. Wadhwa · S. Kumar
Department of Physics, Kurukshetra University, Kurukshetra 136119, Haryana, India
e-mail: mahendia@gmail.com

R. P. Chahal
Department of Physics, Ch. Bansi Lal University, Bhiwani 127021, Haryana, India

A. K. Tomar
Department of Physics, S. A. Jain (P.G.) College, Ambala City, Ambala 134003, Haryana, India

V. Kumar et al. (eds.), *Radiation Effects in Polymeric Materials*, Springer Series on Polymer and Composite Materials, https://doi.org/10.1007/978-3-030-05770-1_5

1 Introduction

These days the whole world is breathing with the word "*Nanotechnology*". All the expansions in this direction probably germinate from the seed sowed by the famous Physicist Richard Feynman on 29 December 1959 through his historic lecture "*There's Plenty of Rooms at the Bottom*" [1–3]. Although ancient and medieval world were not fully ignorant of concept of nanotechnology yet it gathered steam primarily from the discoveries of decisive work of coloured window glass during 1980s [4–6], on which strong platform was built to uplift the future course of developments in this field. The massive developments in this field with every passing year were led by the fundamental works due to augmented people's research interest in this field followed by the myriad of applications resulted in growing communal awareness across the globe. As a result, now we can realize the exploration of nanotechnology in almost all the sectors and disciplines. There has been phenomenal growth in basic and applicative scientific research in the field of nanotechnology projecting applications in catalysis, sensors, drug delivery, imaging, aerospace, regenerative medicines, tissue engineering, etc. [7–11].

Working in the field of nanotechnology, the interest of the researchers is also growing in polymer-based nanocomposite materials embedded with inorganic nanoparticles. The wide corridor has been offered by such nanocomposites due to the synergic effect of inherent properties of both dispersed inorganic nanoparticles and host organic polymers [12, 13]. These nanocomposites can easily be processed and moulded into the desired shape and size due to the huge flexibility associated with polymers as base materials. Therefore, the drawbacks associated with the handling of nanostructured materials can be overcome by employing a polymer as a host matrix for embedding nanoparticles. Moreover, enhanced optical, magnetic, thermal and electrical properties of such inorganic–organic hybrid nanocomposites provide broad applications perspectives in many disciplines [14–16]. For the efficient integration of such nanocomposites for technological applications, the prerequisites include the selection of host matrix and embedded nanoparticles along with the control on their size, shape, concentration and distribution within the matrix [17–19]. It is well quoted in the literature [20, 21] that the properties of such nanocomposites can further be regulated through various treatments like neutron irradiation, gamma irradiation, energetic ion irradiation, UV irradiation, annealing, etc.

With this background, the present chapter provides the brief overview of nanomaterials, their properties and synthesis approach. The concise history of polymer nanocomposites has also been discussed. This chapter provides a background in the area of metal nanoparticles describing their history and surface plasmon behaviour. In the next section, a brief and insightful understanding of ionizing radiation and their interaction with matter has been provided followed by a survey of some pertinent literature related to effect of different ionizing irradiation on polymer–metal nanocomposites. The aim of this section is not to cover all the existing literature, but rather to present some of the relevant achievements in this

direction. Further, discussing the importance of PVA polymer and silver nanoparticles, this chapter deals with PVA-Ag hybrid nanocomposites synthesized by in situ reduction method in our laboratory. The morphological, structural and optical behaviour of the hybrid nanocomposite and effect of gamma, UV and SHI irradiation have been discussed with citing our results.

2 Nanoparticles

The prologue of nanoparticles begins with the scale defining at least one external dimension of material in nanometer (nm), scientifically ranging from 1 to 100 nm [22]. This scale is incredibly important because in this size range materials show distinctly unique properties compared to their bulk counterpart. The primarily reason of such unique features in nanometer range are surface-to-volume ratio and quantum size effect [23]. These factors bring significant change in physical, chemical, electrical, optical and thermal properties of materials; rather we can say properties of material become size dependent in nanometer regime [23–25]. The ratio of surface area to volume is actually a measure of the percentage of molecules or atoms that are on the surface of the material as compared to the total number of molecules or atoms in the entire piece of material. As size of particles constituting the material decreases, large proportion of atoms are found at the surface compared to inside. Thus, nanomaterials have greater surface area per unit mass compared to large particles, therefore, are profound of more reactive and catalytic [26]. In nanomaterials, with surface effect quantum size effect also comes in picture and directs the properties of these materials. When the particle size is reduced and attains the limit of the Bohr's radius, its electronic energy structure (shown in Fig. 1) changes from continuous energy bands to discrete energy levels and the continuous optical transitions between the electronic bands become discrete and the properties of the nanomaterials become size dependent [27].

2.1 Synthesis of Nanoparticles

The bottoms-up and top-down approach are two approaches through which nanoparticles can be synthesized. Under the situation, when both top-down and bottom-up processes are involved, the approach is referred to as hybrid approach. Figure 2 highlights a schematic representation of bottom-up and top-down approach.

Top-down manufacturing starts with bulk materials which are then whittled down, until the features that are left are nanoscale. The top-down approach [28–30] often involves the methods like ball milling, sputtering, etc. However, the limit up to which the size can be reduced depends on the process involved. On the other hand, in bottom-up approach constituents of the material are arranged into more

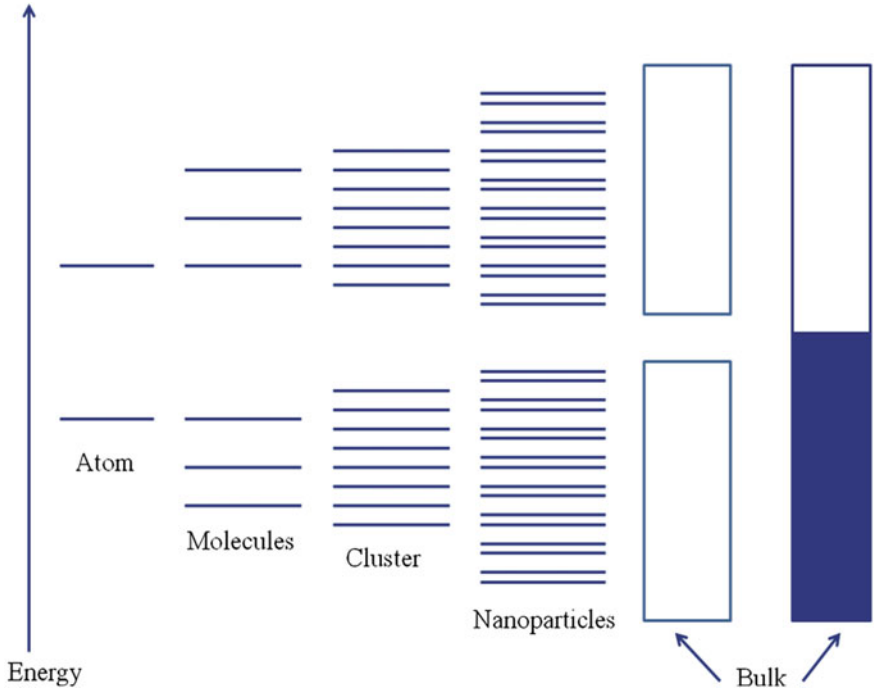

Fig. 1 Schematic representation of electronic energy levels in atoms, molecules, clusters, nanoparticles and bulk

complex assemblies' atom-by-atom or molecule-by-molecule or cluster-by-cluster [28], till the desired dimensions of the material are achieved. All types of chemical synthesis, self-assembly and molecular fabrication also fall under the ambit of bottom-up approach viz. electro-deposition, vapour phase deposition, sol-gel, ion beam epitaxial technique, etc. for the growth of nanoparticles.

2.2 Stabilization of Nanoparticles

As nanoparticles exhibit extraordinary large surface area, they are thermodynamically unstable and possess tendency to coalesce by decreasing surface energy and form thermodynamically stable bulk nanoparticles [31]. This is done in the absence of any counteractive repulsive forces, and van der Waals interaction would lead to aggregation. Therefore, the basic challenge in nanoparticle synthesis is stabilization of nanoparticles without losing its unique properties. The steric stabilization and electrostatic stabilization are the most common approaches implemented during the synthesis of nanoparticles [32]. Capping agents, e.g. polymer, surfactant or a ligand having suitable functional groups, are used to perform the steric stabilization;

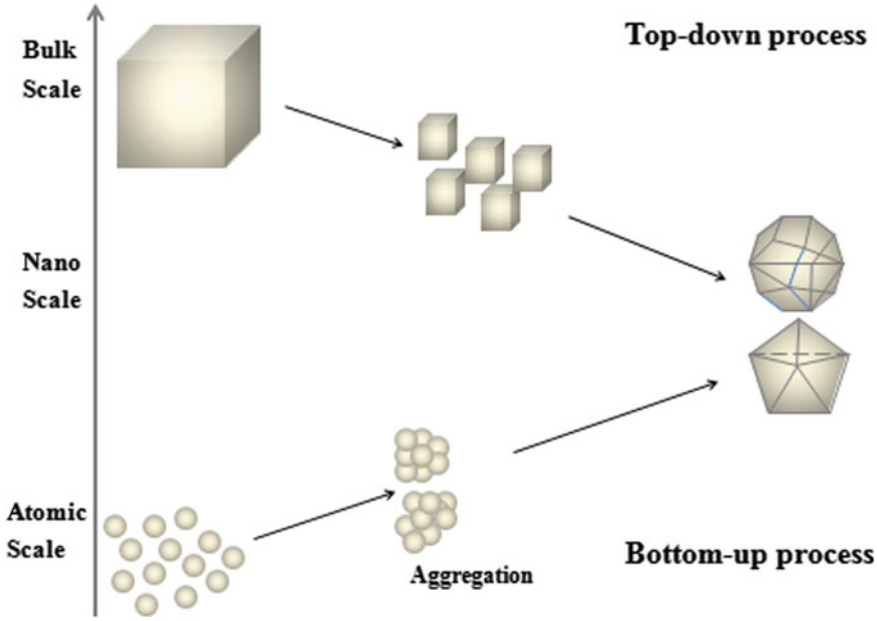

Fig. 2 Schematic representation of Bottom–up and Top–down approach

these capping agents get adsorbed onto the colloidal particles prevent them to agglomerate. On the other hand, in electrostatic stabilization negatively charged ions adsorb onto the metal nanoparticles surface, resulting in the formation of an electrical charged layer around the particles which counterbalanced the attractive van der Waals forces by repulsive Coulombic forces acting between the negatively charged colloidal particles. Another important way to resolve the stabilization problem is embedding the nanoparticles into suitable host matrix supplementing the additional benefit of manipulating the shape and organization of nanoparticles. This new class of materials, generally named as nanocomposites, takes the advantage of both the host matrix as well as of the embedded nanoparticles [33].

3 Nanocomposites

In general, composites materials are defined as materials comprising of two or more constituent materials with significantly different physical or chemical properties, and the produced material possess properties different or superior to those of the individual components [34, 35]. Polymer nanocomposites, in particular, are composite materials in which nanoscopic inorganic particles, with at least one dimension in the nanoscale regime, are dispersed in a polymeric matrix in order to dramatically alter or improve the properties of the polymer. The properties of a

nanocomposite significantly depend on the size of the filler nanoparticles, interface area and the degree of mixing between the two phases [35]. Depending upon the chemical nature of the host material and embedded nanoparticles, nanocomposites are generally classified into the three combinations, i.e. organic–organic, organic–inorganic and inorganic–inorganic. Polymers, due to their extraordinary properties such as their easy processability, light weight, flexibility and mouldability, etc., are best suited materials to be utilized as host matrices for the synthesis of nanocomposites. Further, due to high chemical reactivity, the oxidation of nanoparticles occurs readily leading to their agglomeration, which finally results into their larger structures. Therefore, any stabilizing agent is required to enhance their chemical stability retaining their basic properties [36]. A proper choice of the polymer facilitates environmentally safe synthesis without the requirement of any additional stabilizing agent [37, 38]. Conventional polymer matrices include polyurethanes, aliphatic and aromatic urethane acrylates, LDPE, nylon, poly ethylene terephthalate (PET), etc. [39–42], whereas the most commonly used fillers are nanoclays (montmorillonites), metal nanoparticles, nanosilica, CNTs, graphene [43–45], etc. Among the various types of nanocomposites, the polymer–metal nanocomposites have gathered a lot of interest because of their potential applications in many diverse fields of science and technology. This is due to the synergic effect of host polymer matrix and unique features of metal nanoparticles [46, 47]. The polymer-based hybrid nanocomposites can be synthesized via one-pot synthesis, in situ/ex situ synthesis, interfacial polymerization, vapour phase synthesis and electrochemical synthesis. These different synthesis processes have been adopted to control various properties like shape, size and dispersion of the secondary phase within the polymer matrix [47, 48].

4 Metal Nanoparticles

The fascinating chromic effect of metal nanoparticles has continuously pulled the attention of scientists and physicists from the year about 1700. A German scientist, Georg Christoph Lichtenberg (1742–1799) [48], who had nothing knew about polymers and nanoparticles had seen and felt attracted towards the coloured glasses with embedded metal nanoparticles (presently known as ruby glasses) created by Kunckel [48, 49], a German alchemist (ca. 1630–1730). Kunckel himself could not realize that the deep purple colour of these ruby glasses created by him was a result of embedded gold nanoparticles. Though, there were no equipments available to characterize the structure of such materials; even then these materials remained a matter of continuous thrust for the scientists and researchers. Micheal Farady (1857) made the first experiment with nanoparticles (gold colloids) and initiated the field of nanoscience and nanotechnology [48, 50]. And the first application of Mie's theory was therefore the interpretation of the experiments of Steubing on colloidal gold particles [51]. This opened the boom for the researchers to advent the technology for the synthesis and characterization of nanostructured materials for their

basic understanding and scientific applications. Afterwards, there have been continuous efforts to develop nanofunctional materials for their applications towards the development of sophisticated technology.

Metallic particles in the nanometer size regime show characteristic physical and chemical properties that differ significantly from those of their bulk counterpart [52]. Metal nanoparticles (typically, copper, silver and gold) show unique feature of strong absorption in visible region known as surface plasmon absorption, when interact with the incident electromagnetic radiations. Basically, the surface plasmon absorption is a quantum optical-electrical phenomenon arising from the interaction of light with a metal surface. Incident electromagnetic wave creates the oscillations in conduction electrons on the surface of the nanoparticles with the absorption of electromagnetic radiation [51, 52]. A schematic representation of the interaction between an incoming electromagnetic field and metallic particle is shown in Fig. 3.

Electric field associated with the incident electromagnetic radiation drives the conduction band electrons of metal nanoparticles with respect to their fixed positive lattice ions as shown in Fig. 3. As a result, a net charge difference appears on the surface of the nanoparticles, whose attraction with lattice ions on the opposite side leads to a restoring force. Consequently, this net charge difference oscillates with the incident electric field known as plasmon oscillations and being a surface phenomenon, more appropriately called surface plasmon oscillations. When a resonance is formed between these plasmon oscillations with the frequency of the incident light, electromagnetic radiation get absorbed by the particles characterized as the surface plasmon resonance band. This band occurs in the visible region of electromagnetic radiation for noble metal nanoparticles. The resonance frequency is mainly determined by the strength of the restoring force, which is the function of particle dimension, polarizability (separation of the surface charges) of the medium between the charges and around the charges [51–54]. The interaction of light with spherical metal particles can be described using Drude model and Mie theory. Mie theory (1908) predicted that what fraction of the intensity of incident electromagnetic radiation is absorbed and scattered during its interaction with spherical

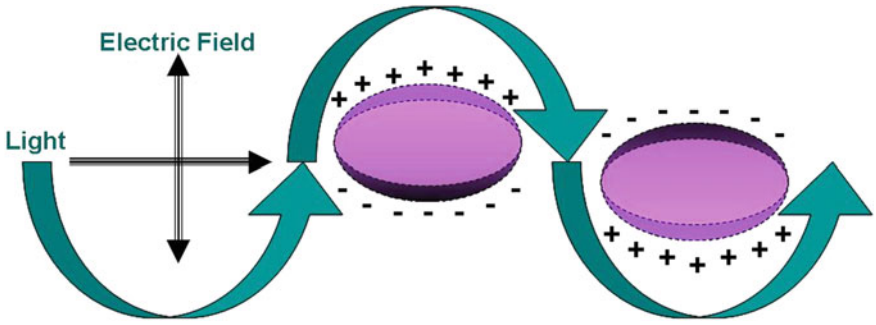

Fig. 3 Schematic illustration of the collective oscillations of free electrons under the effect of an electromagnetic wave

particles by solving the Maxwell's equations for spherical particles of arbitrary size embedded in a homogeneous medium [55]. The surface plasmon resonance band corresponds to the extinction of incident light (absorption and scattering).

According to Mie theory [51, 54], the electric field of a propagating incident electromagnetic wave can be expressed as

$$E = E_0 \exp[i(k_x x + k_z z - \omega t)] \tag{1}$$

where k is the wave number and ω is the frequency of the electromagnetic wave.

For this electromagnetic wave (Eq. 1), Maxwell's equations were solved for the interface between two materials with relative dielectric functions ε (metal particle) and ε_m (surrounding medium), under the boundary conditions:

$$\frac{k_{z1}}{\varepsilon} + \frac{k_{z2}}{\varepsilon_m} = 0 \text{ and } k_x^2 + k_{z_i}^2 = \varepsilon_i^2 \left(\frac{\omega}{c}\right)^2 \quad i = 1 \,\&\, m \tag{2}$$

where c is the speed of light in vacuum and k_x is same for both media at the interface for a surface wave.

Accordingly, the dispersion relation (k_x) and the extinction cross section (C_{ext}) for a wave propagating at the interface have been found to be

$$k_x = \frac{\omega}{c}\left(\frac{\varepsilon\varepsilon_m}{\varepsilon + \varepsilon_m}\right)^{1/2} \tag{3}$$

and

$$C_{ext} = \frac{24\pi^2 d^3 \varepsilon_m^{3/2}}{\lambda} \frac{\varepsilon''}{(\varepsilon' + 2\varepsilon_m)^2 + \varepsilon''^2} \quad \text{with} \quad \varepsilon' + i\varepsilon'' = \varepsilon \tag{4}$$

For particle size (d) less than 50 nm, scattering can be neglected and C_{ext} approaches to C_{abs}. The dependence of metal (free electron system) dielectric function (ε) on oscillation frequency can be obtained from Drude model as

$$\varepsilon' = 1 - \frac{\omega_p^2}{(\omega + \omega_d^2)} \quad \text{and} \quad \varepsilon'' = \frac{\omega_p^2 \omega_d}{\omega(\omega + \omega_d^2)} \tag{5}$$

with $\omega_p = \left(\frac{Ne^2}{\varepsilon_0 m_e}\right)^{1/2}$ bulk plasmon frequency, where N is the number density of electrons; e and m_e are the charges and effective mass of an electron, respectively. The quantity ω_d is the damping frequency, which depends upon the particle size and increases, when the particle size decreases. After substituting the values of ε' and ε'' which are dependent on frequency as per Eq. 5 in Eq. 4, the frequency-dependent C_{ext} has been found to be

$$C_{\text{ext}} = \frac{24\pi^2 d^3 \varepsilon_m^{3/2}}{\lambda} \frac{\frac{\omega_p^2 \omega_d}{\frac{c}{\lambda}\left(\frac{c^2}{\lambda^2}+\omega_d^2\right)}}{1 - \frac{\omega_p^2}{\left(\frac{c^2}{\lambda^2}+\omega_d^2\right)^2} + \frac{\omega_p^4 \omega_d^2}{\frac{c^2}{\lambda^2}\left(\frac{c^2}{\lambda^2}+\omega_d^2\right)^2}} \tag{6}$$

Above expression indicates that the important intensity of surface plasmon absorbance band (C_{ext}) is dependent on the diameter of the nanoparticles (d) and the dielectric constant of surrounding medium (ε_m). Further, the position and bandwidth of SPR band also depend on particle size (d) through the ω_d (the size-dependent damping frequency of metal particle).

Because of novel properties like surface plasmon resonance effect, surface-enhanced Raman scattering, super-paramagnetism, etc., noble metal nanoparticles find applications in many fields like catalyst science, biomedical science, fabrication of opto-electronics and optical devices, etc. [55–60]. However, the direct use of nanoparticles to such applications is scarce because of difficult handling of such tiny objects; instability due to their high surface-to-volume ratio/ high surface energy; easily oxidizing nature and contamination to impurities, etc. Such limitations can be resolved by embedding the metal nanoparticles into suitable dielectric matrix which supplements the additional benefit of manipulating the shape and organization of embedded metal nanoparticles.

5 Polymer-Metal Nanocomposites (PMN)

The technique for the preparation of PMN was reported for the first time in literature in an abstract form in the year 1833 [61]. Maxwell Garnett for the first time in 1900 explained the theory behind the shifting of colour upon variation in particle size and volume fraction of particles embedded in a medium [62]. Such dichroism effects for the nanocomposites of stretched poly(vinyl alcohol) film embedded with silver, gold or mercury was reported in 1946 [17, 63]. Because there had been continuous interest towards the developments of such nanocomposites, over the last two decades, a lot of achievements in this direction have been reported. It has been established that such nanocomposites can be applied for the development of advanced functional devices because:

- Depending on the shape, size, distribution and type-based surface plasmon resonance effect, such nanocomposites are used in optical devices applicative in colour sensors, colour filters, etc.
- Polarization direction dependent colour properties of embedded array of metal nanoparticles can be used in fabrication of flexible liquid crystal colour displays and many electro-optical devices.
- Tunability of SPR in the presence of analyte in such nanocomposites (due to high surface-to-volume ratio of embedded metal nanoparticles) leads to their applications as sensors for immunoassay, gaseous, liquids, etc.

- Surface-enhanced Raman scattering (SERS) observed in such nanocomposites leads to their application as active Raman scattering substrates.
- Due to the integration of low refractive index of the polymer matrix and high refractive index of metal in such nanocomposites, extreme refractive index materials can be fabricated which find applications in planer wave guides, optical fibres, etc. [64–68]
- Nonlinear optical polarizability of such composite materials finds application in nonlinear optical devices, photonics and electro-optics.
- Due to magento-optical properties for example ferromagnetism of embedded silver nanoparticles, such materials are used in magento-optical modulators, optical shutters, etc.
- Controlled transient nature of electronic properties of polymer-embedded metal nanoparticles from insulating (coulomb blockade effect) to conducting (percolation effect) depending upon the concentration of embedded metal nanoparticles can be used in micro-electronic and quantum electronic devices.

Research into PMN-based functional devices is still under in its developing stage. Nevertheless, striking progress has been made in various aspects, like in improving the processability, the quantum yield and in tuning the optical and electrical parameters as per requirement of such nanocomposites for device applications. Various combinations of polymers and metal nanoparticles have been tried for optimal performance of such nanocomposites for suitable applications. Polyvinyl alcohol (PVA) is considered to be one such polymer, appropriate for many optical and electrical device applications, along with the benefit that it provides an excellent capping and stabilizing host matrix for the embedded nanoparticles [69].

6 PVA as a Host Matrix and Silver as Nanofiller

Poly(vinyl alcohol) (PVA) is an artificial polymer, made from poly(vinyl acetate) (PAA) through hydrolysis, and is a thermoplastic, water-soluble and semi-crystalline polymer. It has been widely used in the industrial, commercial, medical and food sectors [70, 71]. This polymer is widely utilized for various industrial applications to enhance the mechanical properties of films because of its compatible structure and hydrophilic properties by blending with other polymer compounds and nanofillers [69]. It is highly used in field of biotechnology because it is very benign to living tissues, harmless and nontoxic. PVA is a biodegradable polymer, and its degradability is enhanced through hydrolysis because of the presence of hydroxyl groups on the carbon atoms; however, rates and environmental conditions for degradation may vary for PVA. These conditions include composting in the presence of oxygen, underneath soil layers, in aqueous media, and even in anaerobic circumstances [72, 73]. Further, PVA is among the most versatile polymers for making composites due of its dopant dependent optical,

electronic and dielectric properties [74]. Subsequently, coalesce PVA with metal nanoparticles can be a good option to figure out new composite material.

Among various types of metallic nanoparticles, silver nanoparticles gained significant importance [75] due to their unique optical, electrical and thermal properties projecting its use in wide range of applications, ranging from photovoltaic to biological to chemical sensors to food packaging. High electrical conductivity, stability, low sintering temperature utilize their use in conductive inks, paste and fillers [75, 76]. Their novel optical behaviour provides the benefits in photovoltaic and molecular diagnosis. Further, the increasing common applications of antimicrobial activity of silver nanoparticles [77, 78] include antimicrobial coating, textiles, wound dressing, biomedical devices, etc. Further, for critical optimization of performance of any application, understanding of size, shape and aggregation state of the silver nanoparticles change after integration to the target application is important. Again, for making silver nanoparticles ideal for research development and implanting them for various applications, it is essential to make them free from agglomeration.

7 Ionizing Irradiation-Induced Effects

The properties of polymer–metal nanocomposites can be regulated through various treatments like gamma, ultraviolet, X-rays, ion beam irradiation, etc. Due to the complexity of the phenomenon involved, it is not possible to probe the overall damage directly; rather one can study individual effects of radiation damage, e.g. chemical changes, structural changes or changes in its mechanical, optical, electrical properties, etc. To understand the basic mechanism responsible for these changes, one must know the interaction process of ionizing radiations with matter. The ionizing radiations include all kinds of electromagnetic and corpuscular radiations, e.g. UV–rays, X–rays, gamma rays, ion beam, etc. with energies appreciably greater than the dissociation energy of the bonds present in the material.

7.1 Electromagnetic Irradiation

Electromagnetic radiations, while traversing through a material medium, transfer their energy to the medium as a result of photoelectric absorption, Compton scattering and pair production processes [79–81]. These radiations do not produce ionization directly but lose their energy to the target material by the absorption of photons through any of the processes mentioned above and results into the creation of fast moving electrons. These electrons as a result of their interaction inside the medium produce secondary electrons and so on. Since electromagnetic photons do not lose their energy in a continuous manner and are simply attenuated, the entire bulk structure of the material gets modified after electromagnetic irradiation.

The energy transferred by the electromagnetic rays, especially in polymers, is responsible for the changes at molecular level, such as chain–scissoring, cross-linking, free radical formation, elimination of volatile species, reordering the chemical bonds, etc., which are finally responsible for the modification in their properties [81–84]. Such effects are responsible for reduction in size and variation in distribution of embedded nanoparticles inside polymer matrix, and schematic of this is shown in Fig. 4.

7.2 *Swift Heavy Ions Irradiation*

When an energetic ion penetrates through the material, it loses energy mainly by two nearly independent processes: (i) elastic collisions of the incident ion with the nuclei of the target atoms, usually referred to as nuclear energy loss $(-dE/dx)n$ (ii) inelastic collisions of the incident ion with the atomic electrons of the target atoms, generally expressed as electronic energy loss $(-dE/dx)e$ [84–86]. Figure 5 represents the path followed by the incident energetic ion with different energy when interact with solid target material. Depending upon the energy of the incident ions, their interaction with solid material becomes dominated by electronic or nuclear energy loss or stochastic nuclear interactions. As shown, highly energetic ions tend to follow nearly straight paths, whereas less energetic ions follow more random paths [87].

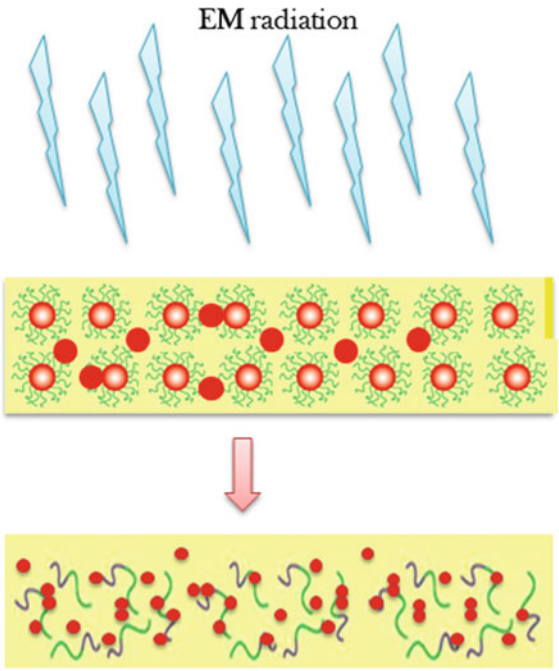

Fig. 4 Schematic illustration of the effect of an electromagnetic irradiation on polymer-metal nanocomposites

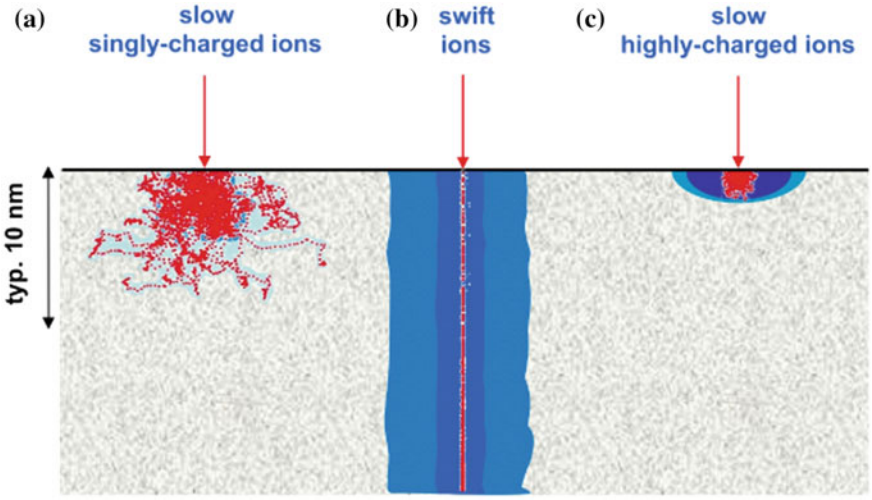

Fig. 5 Scheme of energy deposition when ion projectiles interact with solids: **a** slow singly or low charged ions of keV–MeV kinetic energy: small range, energy loss dominated by elastic collisions (nuclear stopping), **b** swift ions of MeV–GeV kinetic energy, large range, energy loss dominated by electronic excitations, and **c** very slow highly charged ions, large potential energy (keV), very low (eV–keV) kinetic energy, very limited range. The trajectories of recoils are indicated in 'red'; electron-induced electronic excitations of the solid are marked in 'blue' (Ref. [87])

The relative contribution of the energy loss through these two processes depends upon the nature of the incident ion and the target material parameters. For MeV heavy ions, usually the electronic energy loss dominates while the nuclear energy loss remains almost negligible. However, when the ion velocity reduces to the extent that the ion behaves almost as a neutral atom, the ion–matter interaction occurs via hard sphere scattering, and under this situation, the nuclear energy loss starts dominating over electronic energy loss. Nuclear energy loss process leads to atomic displacements, and lattice vibrations in the target (phonons) causes the collision cascade. The low kinetic energy of the incident projectile limits its total path length and therefore the region where energy is deposited to a few layers close to the surface [88]. For swift heavy ions, where the ion velocity remains considerably higher than that for its orbital electrons, the electronic energy loss remains into picture with nuclear energy loss to be almost negligible. The dominant electronic energy loss leads to a high ionization density around the ion tracks, which is practically straight path. Fast delta rays produced due to inner shell ionization processes can considerably extend the region where electronic excitation/ ionization of the target take place. Finally, the energy deposited by the swift heavy ions during their passage, particularly in polymers, leads to the processes of macromolecular destruction, chain-scissioning, cross-linking, free radicals formation, carbonization, oxidation, etc. These processes are responsible for the modification in the optical,

electrical, thermal, mechanical and chemical properties of the polymeric material. Figure 6 represents the schematic for basic ion–solid interaction process.

Further, these energetic ions are useful in the formation of nanostructure and their modification. As discussed, SHI follows the narrow cylindrical path inside the target and transfer their large K.E via electronic energy loss. This process of energy transfer is accompanied with formation of surface nanostructure. However, similar nanostructures near to the surface can also be produced using slow energetic highly charge ion [87] due to deposition of large potential energy near to the surface causes by high charge state of ion. Thus, despite different primary mechanism, the similarity between the nanostructures produced by slow energetic ion with high charge state and SHI is striking and strongly points to a common mechanism related to the energy transfer from the electronic to the lattice system of the target.

In addition to these, ion beam implantation has been used widely for embedding of elemental nanoparticles into a surface of the target materials The embedding material is transformed into form of an accelerated ion beam, and in a controlled manner, these energetic ions get deposited into target accompanied by alteration of its physical, chemical, structural and surface properties in a controlled manner. Further, using ion beam irradiation is used for nanopatterning of noble metal NPs on the top of the various substrates [89]. This can be achieved by depositing the thin metal film on the surface of the target polymer followed by SHI irradiation. The high-energy ions cause materials modification by inducing a high degree of localized electronic excitation by evolution of the various gases through the ion track and cause the ion beam mixing of materials at the interface and generate the embedding driving force.

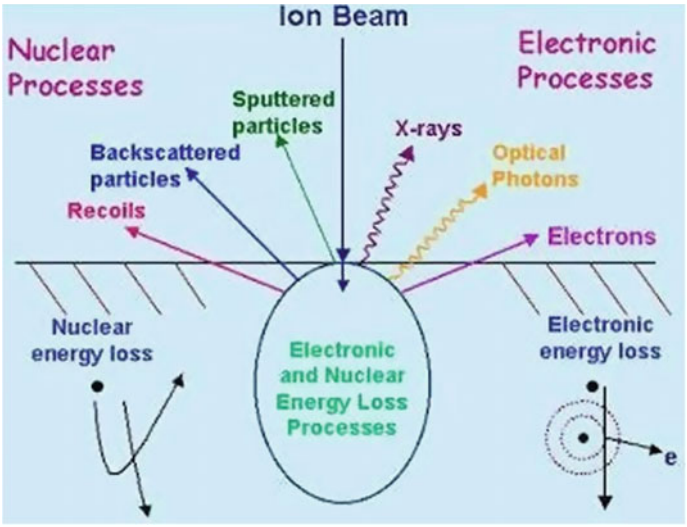

Fig. 6 Basic ion–solid interaction process

8 Some Past and Future Trends in Ionizing Irradiated Polymer–metal Nanocomposites

The interaction of radiation greatly influences the synthesis and properties of polymer nanocomposites. The increasing interest in the irradiation-based techniques follows from the obvious advantages associated with this technique like it is simple, clean and green technology and the synthesized nanostructures are produced in a controlled manner with lesser number of impurities [90]. The various probes belonging to the irradiation-based techniques are heavy ions, UV irradiation, gamma irradiation, etc. The synthesis employing gamma rays is one of the major pillars in the irradiation-based techniques. As far as our knowledge concerns, credit for first ever synthesis of micro-aggregates of gold employing gamma rays was given to Fujita et al. [91]. They synthesized gold particles with average size 80 nm from chloroauric acid solution by gamma irradiation. After that, Marigner et al. in 1985 used gamma rays to synthesize clusters of noble metal nanoparticles and extended the synthesis to nanostructure of metals like Co, Ni, Zn or Pb and also their alloys [92]. Further, besides controlling structures and shapes of dispersed nanoparticles in polymer matrix, the gamma rays also have the ability to convert monomeric and oligomeric liquids to solid polymers [93]. Among the numerous reports that are dealing with the synthesis of polymer nanocomposites [94–98], few of them are mentioned here, viz. in the year 2003, Choi et al. [97] have synthesized Ag/Poly(ester) and Ag/nylon nanocomposites and studied their application as effective EMI shield or antibacterial fibre. In 2004, Choi et al. also synthesized PVP-stabilized CdS and CdS-polyacrylonitrile [poly (An)] nanocomposites and studied their behaviour as active photo-luminescence or electro-luminescence materials [98]. Further in the year 2006, a similar group, Kang et al., synthesized PAni-Ag nanocomposites with the aid of gamma irradiation, with controlled morphology of Ag nanoparticles to either spherical or hexagonal type by altering the synthesis route [99]. Rao et al. have employed gamma irradiation for in situ synthesis of Ag nanoparticles of re-dispersible nature capped into Natural polymer (gum-acacia) [100]. Our own group, Chahal et al., also studied the effect of gamma-ray irradiation on the structural and optical properties of PVA/Ag nanocomposites films for optical applications. In our study, we have found that gamma irradiation greatly affects the optical properties of PVA/Ag nanocomposites films, thereby making them suitable for optical device fabrication [13]. Ali et al. in 2014 studied the 1.25 meV Co-60 gamma radiation with doses ranging from 500 to 1500 kGy on electrochemical synthesized Au-polypyrrole (Au-PPy) composite films. They found formation of an ordered system in the irradiated composite films [101]. Recently, Kim et al. studied gamma rays sterilization of polypyrole (PPy) bioelectrodes. They found gamma-ray irradiation of the PPy (γ-PPy) increased the oxygenation and hydrophilicity of the surfaces. Interestingly, gamma-ray irradiation did not alter the electrical impedances and conductivities of the PPy substrates, thus concluded that gamma ray sterilization is a viable method

of sterilization of conducting polymer-based biomaterials for biomedical applications [102].

In addition to gamma irradiation, UV-initiated synthesis and curing of polymer-metal nanocomposites is also a quite popular technology and has found many industrial applications [103]. UV irradiation synthesis comes under the category of green synthesis although it is popularly known for the dangerous effects produced on organic tissues with sunlight exposure. The prolonged exposure of UV light on polymers will result in breaking the chemical bonds which would result in the change of chemical and optical properties of polymers. This band-breaking property of UV irradiation is further helpful in the initiation of polymerization by providing reactive chemical sites [104]. J.P. Ravijst in 1990 and C. Decker in 1997, respectively, produced two interpenetrating polymer networks of epoxides and acrylates and ethers and acrylates with few seconds of UV irradiation [105, 106]. Pappas et al. describe the formation of cross-linking polymer network by UV curing of monomer unit with the help of photoinitiator which effectively absorb incident radiation energy and produce free radicals or ions of high quantum yield escort the process of polymerization [107]. Balan et al. in 2006 used UV-initiated in situ polymerization of di-functional acrylate monomers containing small amounts of bismuth nanoparticles to increase hardness of polymer nanocomposite [108]. Lu et al. have synthesized Ag nanoparticles in spherical polyacrylic acid brushes by employing UV irradiation, and the produced PS-PAA-Ag nanocomposites show high catalytic activity for the reduction reaction of 4-nitrophenol in the presence of sodium borohydride [109]. Shameli et al. utilize UV irradiation for Green, fast and reducing agent free in situ synthesis of binanocomposites of Silver/montmorillonite/chitosan, which also show catalytic properties [110]. Further, UV irradiation also has great impact on the properties of polymer nanocomposites. Chahal et al. have shown that UV-exposure on PVA/Ag nanocomposites convert them to narrow pass filter at 320 nm [12]. Irrespective of any other factor like cost availability, etc. ion implantation is chosen widely as one of the most powerful technique to modify polymeric materials.

Forrest et al. in 1982 found increases in 14 orders of conductivity of organic thin films of 3,4,9,lO-perylenetetracarboxylic dianhydride (PTCDA), 1,4,5,8-napthalenetetracarboxylic dianhydride (NTCDA) and Ni phthalocyanine (NiPc), using 2 meV Ar^+ ion implantation [111]. Hioki et al. in 1983 use high-energy ($\sim$ MeV) $N_2{}^+$ ions to increase the 20 orders in conductivity of implanted Kapton H films [112]. D. Fink et al. in 1988 have tried to explain the change in properties of organic polymers by varying the dose and mass of incident ion. They provide experimental evidence of the generation of carbon recoils which supports the theory of the “hot carbon atom and their work is among the most cited literature [113]. In fact, there are numerous reports available which deals with the effect of ion irradiation on the properties of polymers and it is not possible to mention them all. The importance of this topic could be understood from the fact that while started in somewhere in 1980s, there is a lot more to explore in this field. Goyal et al. have reported increase in electrical conductivity of polycarbonate by irradiating it with 100 keV N^+ ion [114]. The ion irradiation not only modifies the optical and

electrical properties of polymers and their nanocomposites, but also helps in improving the dispersion of inorganic nanoparticles inside polymer matrix [115]. Prakash and co-workers reported the synthesis of Au nanoparticles at the surface through 150 keV Ar ion beam irradiation of thin metal film on polymer surface and embedded in carbonaceous matrix by controlling the ion fluence [116]. They also demonstrate the formation of polymer nanocomposite with thin metalized layers induced by ion beam-induced mixing of metal film deposited on polymer surface [117, 118]. Wang et al. and Zaporojtchenko et al. study the ion–polymer interaction which promotes adhesion of noble metal with polymer surface as an effect of low energetic ion irradiation and heat treatment [119–121]. These groups demonstrated that pre-treatment of polymer surface by ion irradiation followed before deposition of metal thin film on their surface induces enhanced mechanical and wetability properties of polymer surface which increase in metal adhesion on polymer surfaces as an effect of energetic ion bombardment. In case of metal–polymer system, ion irradiation causes the formation of carbonaceous clustered matrix induced by evolution of chemical species and outgassing of volatile chemical species leading to synthesis of metal NPs in composite materials. Such effects are reported by Prakash et al. and Biswas et al., and they explained the ion track chemistry induced by ion beam irradiation to demonstrate the formation of nanostructure inside the polymer matrix. Aggarwal et al. [Nucl. Instrum. Methods Phys. Res. B 244 (2006) 136] have reported effect of energetic ion of high charged state on the properties of ZnO films, and they reported the enhancement in the optical absorption of ZnO films under 100 meV Au^{8+} ion irradiation; however, they also found a decrease in electrical resistivity and an increase in carrier concentration when the films were irradiated with slightly higher energy of 120 meV Au ions. Ren et al. (2007) investigated the room-temperature ferromagnetism in Fe-doped $PbTiO_3$ nanocrystals sample prepared by a modified hydrothermal method. Mishra et al. (2008) studied the effect of 100 meV Ag^{8+} ion beam at different fluences on the Ag-Teflon nanocomposite thin films prepared by co-sputtering. Further, the effect of MeV ion beam irradiation has been studied on the size and distribution of Ag NPs embedded in Teflon matrix. After irradiation, the SPR peak is broadened and shifted towards higher wavelength and with increasing ion fluence, the broadening and shift of SPR band become prominent. The average size of embedded nanoparticles reduces and distribution of particle size narrows down with the increase in ion fluence. The energy of ion and its fluence were observed the important parameters for controlling the particle size and size distribution. Pivin et al. in 2005 have studied in detail about contribution of ionizations and atomic displacements to the hardening of ion-irradiated polymers. They extended their study on metal nanocomposites and modification in their structure and study the effect of 100 meV Au ion beam irradiation on silica films containing Ag particles of different low volume fraction. They found that if volume fraction of embedded particles is low with their size small as compared to that of ion tracks, then low-energy ions are not able to produce thermal spikes but they promote the desorption of Ag ions and their diffusion in silica through enough ionizations at the surface of the particles. For slightly larger volume fractions of Ag particles, rearrangement of the particles in arrays aligned along the ion beam

direction was observed after irradiation with higher energy MeV beam. The array like arrangement of nanoparticles lead to an increase in the dipolar interaction between the nanoparticles, with interesting effect a splitting of their surface plasmon resonance peak under polarized light. Mishra et al. in 2008 studied the controlled reduction in the size of Ag nanoparticles embedded in Teflon matrix by MeV ion irradiation [122]. They report tuning of shape and size of nanoparticles not only on the surface but also inside the polymer matrix. Similar studies also done by other groups like Prakash et al. study the synthesis of Ag nanoparticles on polymer surface using 150 keV Ar ion irradiation of bilayer of Ag and PVC [123]. Biswas et al. demonstrate the formation of nanoparticles architecture in carbonaceous matrix as a result of SHI irradiation [124]. Singh et al. [125] demonstrated the 120 meV Au ions irradiation-induced shape deformation of 8–10 nm Ag nanoparticles embedded in silica matrix. Minor elongation to an aspect ratio of about 1.5 from spherical shape was reported. The nanoparticles smaller than the track size dissolve while the nanoparticles larger than track size show deformation with major axis along the ion beam direction. The aspect ratio of elongated nanoparticles is found to be the function of electronic energy loss and ion fluence. Ali et al. [126] studied the effect of 40 meV carbon ion beam at various fluences on Au-polyaniline composite films, and reasonable improvement has been found in surface morphology of Au-polyaniline composite films after irradiation. Formation of clusters with porous structure after irradiation was obtained subjective their use in chemical as well as bio-sensing applications. Also in the year 2016, Singhal et al. have shown that swift heavy ion irradiation is an effective tool for the dispersion of carboneous material like nanographitic plates in PEDOT:PSS polymeric matrix [127].

Though lots of works have been available related to modification in the properties of polymer nanocomposites through ionizing irradiation, still their pure practical application is not up to the mark. Till the day, researchers are not able to tailor the morphology (shape, size, and distribution) of nanocomposites properly in a controlled manner. By controlling the morphology of nanocomposites, we can calibrate the properties and reach the desired level of application of nanocomposites. Therefore, future work should concentrate onto the development of synthesis method for metal-based hybrid nanocomposites with control parameters and morphology and utilization of various ionizing irradiation in a proper manner. Ion impanation of composites is targeted used for the designing the antireflective coating used in aerospace crafts. Another exciting field related to polymer-metal nanocomposites is sensors, based on the biocompatibility of polymers and sensing capability of metal nanoparticles, which could be enhance through different ionizing irradiation. However, many efforts are needed for targeting such composites in desired application and to bring them to daily purpose objects.

9 Optical Properties of Metal Embedded Polymer Nanocomposites

Being an optically active material, polymers are used in fabrication of optical fibres, optical lenses, and waveguides. In these applications, they should have high transparency. Although attenuation may be very small, it should be measured accurately for specific application. This can be done using the spectroscopy; also it helps in understanding the origin of attenuation in polymeric material. Light attenuation in polymeric system is attributed to be due to two factors: absorption and scattering [128, 129]. In general, any spectrometer measures the reflecting and transmitted portion of the incident light when allows to fall on the material. According to conservation of energy, when light incident onto the material (Fig. 7)

$$T + R + A + S = 1 \tag{7}$$

where T is the transmittance, R is the Reflectance, A is the absorbance of the sample and S is the scattered portion of the incident light.

Both absorption and scattering effects cause the attenuation of light through a medium. The absorption coefficient, α and the scattering coefficient, σ, can be defined as [128]

$$T = \exp[-(\alpha + \sigma)d] \tag{8}$$

Hence,

$$(\alpha + \sigma) = \frac{4\pi k}{\lambda} \tag{9}$$

The quantity $(\alpha + \sigma)$ is known as the attenuation/ extinction coefficient. For polymers, $\alpha \gg \sigma$, so absorption coefficient can be expressed as

$$\alpha = \frac{4\pi k}{\lambda} \tag{10}$$

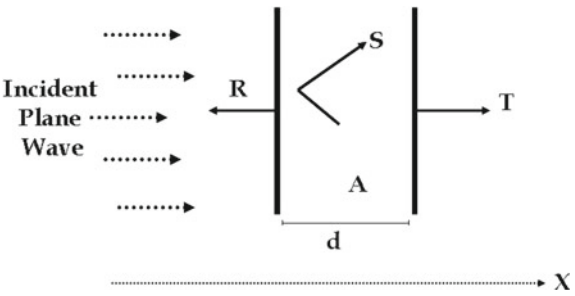

Fig. 7 Incident plane wave travels from left to right along the x-direction and is reflected (R), absorbed (A), scattered (S) and transmitted (T) from the material of thickness x_0

In essence, any spectrophotometer recording the portion of reflected and transmitted part of incident light when passes through the material, from which the optical parameter like refractive index ($N = n - ik$) can be calculated by solving the Fresnel's equations for reflection and transmission. But the recorded transmission and reflected values do not incorporate the reflection losses at the air–sample interfaces [115, 129]. Therefore, it is desirable to first correct the recorded transmittance and reflectance intensities. The correction has been employed by considering the model, presented in Fig. 8.

The present model describes the various transmission and reflection of incident light for its single pass from the sample. I_0 is the intensity of the incident beam at the top surface of the sample. A portion of it gets reflected from air–sample interface and its reflection coefficient, represented by 'r' and the remaining portion of I_0 gets entered into the medium and is represented by F_1 in figure. Then the component F_1t passes through the sample of thickness d and reaches at the bottom surface of the sample, where t is the transmission coefficient for single pass of light through the sample. After reaching to the bottom surface, again one portion of this component of light (F_1t) gets reflected from the sample–air interface in terms of F_1tr and represented by F_2 and another portion is transmitted out of the sample from bottom surface, represented by $I = F_1t(1 - r)$. Now, a fraction of reflected back component F_2 from the bottom surface will reach the top surface, represented by F_2t, which again faces transmission ($F_2t(1 - r)$) and reflection (F_2tr) at the interface. This transmission gets added into the primary reflection 'r' and reflected portion contributed to the F_1. This process continues till total portion of light get consumed. So, in order to take the contribution of these multiple reflection from the sample–air interface from the both top and bottom portion, the recorded transmitted (T) and reflectance (R) values are correlated with the transmission t for single pass of light and reflection r form the air–sample interface, through the following equations:

$$T = F_1t(1 - r) \tag{11}$$

$$R = r + F_2t(1 - r) \tag{12}$$

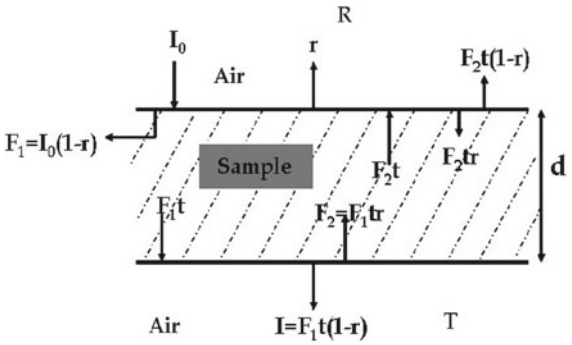

Fig. 8 Schematic representation of the transmission and reflection of light passes through the material

$$F_1 = (1 - r) + F_2 tr \tag{13}$$

$$F_2 = F_1 tr \tag{14}$$

After solving these equations we get

$$F_1 = \frac{(1 - r)}{1 - t^2 r^2} \tag{15}$$

$$R = r + \frac{(1 - r)^2 t^2 r^2}{1 - t^2 r^2} \tag{16}$$

$$T = \frac{t(1 - r)^2}{1 - t^2 r^2} \tag{17}$$

From these, the values of r and t are expressed as

$$r = \frac{2R}{1 + t^2 + \sqrt{(1 + t^2)^2 - 4t^2 R(2 - R)}} \tag{18}$$

$$t = \frac{2T}{(1 - r)^2 + \sqrt{(1 - r)^4 + 4T^2 r^2}} \tag{19}$$

Further, it is clear from the above expressions that r and t are inter-dependent, which clearly depict the contribution of multiple reflection and transmission from the air–sample interface from both top and bottom surfaces [130]. Therefore, values of r and t are obtained by solving these equations through iterative process for which initially t is taken to be 1 in the expression of r.

Now, values of r and t so obtained are utilized for calculating the absorption coefficient, α and refractive index, $n(\lambda)$ of the sample, using the expressions [131]

$$\alpha = \frac{1}{d} \ln\left(\frac{1}{t}\right) \tag{20}$$

$$n(\lambda) = \left[\frac{4r}{(r - 1)^2} - k^2\right]^{1/2} - \frac{r + 1}{r - 1} \tag{21}$$

Further, the optical energy gap (E_g) of polymer nanocomposite films has been determined using Tauc's relation [132–134]

$$\alpha h\nu = A(h\nu - E_g)^s \tag{22}$$

where $h\nu$ is the photon energy, α is the absorption coefficient, A is the band tailing parameter and exponent $s = 1/2$ for direct energy gap and $s = 2$ for indirect energy gap. The value of optical energy gap has been determined from the extrapolation of best fitted straight line in plots of $(\alpha h\nu)^s$ versus $(h\nu)$ on the hν axis. One can measure such disorder content and irregularities between the energy gaps in the polymers in terms of Urbach's energy. Below the energy gap edge, the exponential absorption sub-edge corresponds to Urbach's energy (E_u) and determined through the relation [134, 135]:

$$\alpha(\nu) = \alpha_0 \exp(h\nu/E_u) \tag{23}$$

where, α_0 is a constant. From this equation, it is obvious that the plot of ln(α) versus hν should follow the linear behaviour.

10 Experimental Section

10.1 Sample Preparation

The polyvinyl alcohol–silver (PVA/Ag) nanocomposites through in situ chemical reduction method was synthesized; the detailed method of which were already explained elsewhere [12, 13, 179]. Polyvinyl alcohol (M_w = 125,000) and silver nitrate ($AgNO_3$) have been procured from S.D. Fine Chem Ltd. (India) and Loba Chemical Pvt. Ltd. (India), respectively. PVA and PVA/Ag nanocomposite films were prepared at room temperature by solution casting method. For this purpose, 3gm PVA was dissolved in 120 ml of de-ionized water under continuous stirring at 65–70 °C to form aqueous solution of PVA. Then, freshly prepared cold aqueous solution of $AgNO_3$ (0.01M) was added dropwise in as-prepared PVA stock solution followed by heating for few minutes. This results in change of colour of solution from colourless to light yellow giving evidence of formation of Ag nanoparticles. The functional groups of PVA itself act as reducing as well as stabilizing agent for the control growth of Ag nanoparticles inside it. Further, no other additives were used to promote the reaction, thereby avoiding the effects from associates or impurities. In order to prepare free standing film, the synthesized composite solution was poured to plastic perti-dishes and allowed for solvent evaporation at ambient room temperature and films were peeled off after drying of the solution. The concentration of embedded Ag nanoparticles in PVA–Ag nanocomposite films was prefixed to 0.7% by weight by calculation. Using digital micrometer screw gauge with least count 1 μm, the thickness of the films was measured and found to be $\sim 50 \pm 5$ μm. Afterwards, in order to study the effect of various ionizing irradiation on the optical and structural properties of the nanocomposite film, pieces of 1 cm × 1 cm were cut and exposed to various ionizing radiation at different doses.

10.2 Different Irradiation to PVA/Ag Nanocomposites

The prepared nanocomposite films were exposed to gamma rays in the gamma chamber 1200A from Cobalt-60 source for different doses 5, 10, 30 and 50 kGy at the dose rate of 8.33 kGy/hr.

A handheld UV lamp (UVGL–58, UV product, San Gabriel, USA), emitting peak intensity at 254 nm, was used for UV exposure at room temperature. One minute of UV exposure from this lamp corresponds to irradiation dose of 5.8 μJcm^{-2} (at a distance of 10 cm). UV irradiation to nanocomposite films was done by maintaining a distance of 10 cm between the sample and the source, for, 60, 180 and 300 min.

For ion beam irradiation, 15 UD Pelletron accelerator facility available at Inter University Accelerator Center (IUAC), New Delhi, was utilized. Utilizing this facility, the synthesized nanocomposite films were irradiated to 90 meV O^{6+} ion beam at the fluence of 3×10^{10} and 1×10^{11} ions/cm^2.

11 Characterization

In order to confirm the formation of Ag nanoparticles and observe the effect of different ionizing irradiation, the composite films were characterized using Shimandzu double-beam double monochromator UV-Visible spectrophotometer (UV-Visible 2550), operated in the wavelength range 190–900 nm with the resolution of 0.5 nm, equipped with integrating sphere assembly ISR-240A. In order to record the transmission (T) spectra and reflection (R) spectra, the sample was placed at the requisite positions in the integrated sphere assembly. The recorded T and R spectra take into account the reflection from interface between air and sample at the top and bottom surfaces.

The resulted structural changes have been analysed through transmission electron microscopy (TEM), Fourier transform infrared (FTIR) spectroscopy, X-ray diffraction (XRD) and Raman spectroscopy. For TEM measurement, Hitachi "H-7500" TEM instrument operated at 120 kV was used. To record the TEM images, a small part of the respective films were cut and re-dissolved in double distilled water and then dropped on to the carbon-coated copper grid. The FTIR study was carried out using PerkinElmer ABB spectrometer working in the range 700–4000 cm^{-1}. The XRD and Raman measurements were carried out employing an X' Pert ProAnalytical X-ray diffractometer with a filtered 0.154 nm CuK_α radiations and Jobin–Yvon Raman spectrometer (He–Ne laser with wavelength 632.8 nm) and Shimadzu–IRAffinity–1 spectrometer, respectively.

12 Results and Discussion

12.1 TEM Analysis

The formation and morphology of nanoparticles in hybrid nanocomposites before and after gamma irradiation were determined by TEM images presented in Fig. 9. From Fig. 9a, it is clearly apparent that the embedded Ag particles are of nanosize of and their well distributed within the PVA matrix. The observed nanoparticles are nearly spherical in shape with average diameter of the order of 13 ± 5 nm.

After exposure to different radiation, an increase in embedded particle density and a decrease in particle size have been observed as shown in Fig. 9b–d, respectively, for gamma, UV and SHI irradiation. From these images, size of the embedded nanoparticles was estimated and found to be reduced from 13 ± 5 to 7 ± 3 nm on the exposure of gamma radiations at the dose of 50 kGy and reduced to 8 ± 2 nm after 300 min UV irradiation. However, irradiation at the fluence of 1×10^{12} ions/cm^2 causes reduction in size of embedded silver nanoparticles to

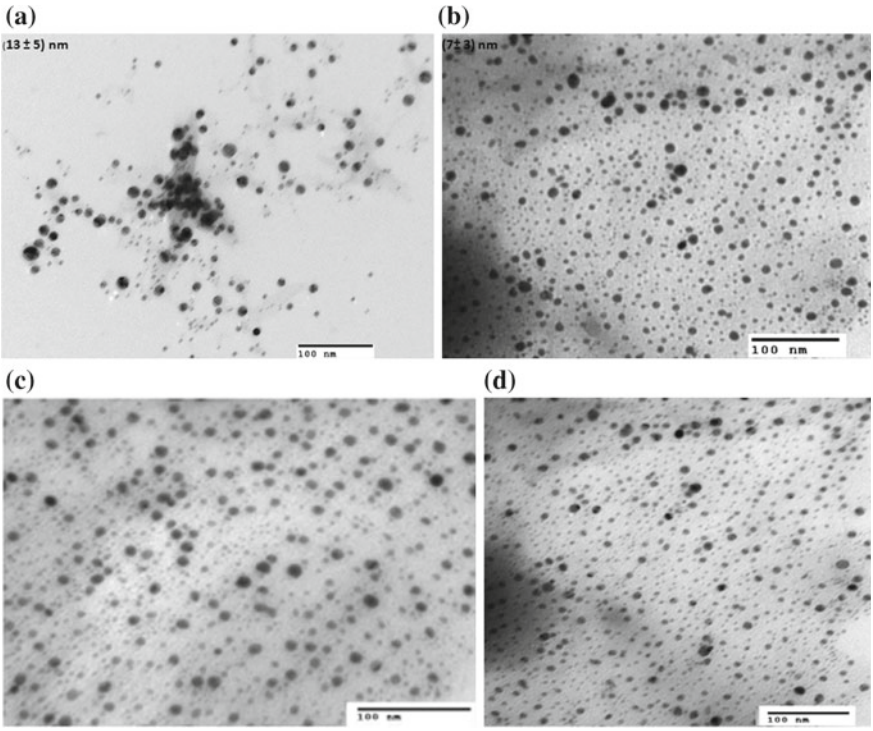

Fig. 9 TEM image of PVA/Ag nanocomposite film **a** before irradiation **b** after gamma irradiation at a dose of 50 kGy, **c** after 300 min UV irradiation and **d** after O^{6+} ion beam irradiation at fluence of 1×10^{11} ions/cm^2. Ref. [12, 13, 179]

6 ± 1 nm. The reduction in the size of Ag nanoparticles is more effective in case of SHI irradiation than gamma irradiation than UV irradiation, which can be corroborated through different structural characterizations discussed in next sections of this chapter.

12.2 Proposed Mechanism of Formation of Silver Nanoparticles

The silver nanoparticles in solution phase synthesis are generally produced by reduction of silver ion into metallic silver (i.e. Ag^{+} to Ag^{0}) followed by their controlled nucleation [136, 137]. The process is stepwise, primarily hydrated electron rapidly complexed with the silver ion and reduces it into silver atom. The silver atoms then start nucleated to form dimmer cluster and the dimmer then combines with another dimmer cluster to be tetramer cluster and so on [138]. The atoms formed dimerize when encountering or associate with excess Ag^{+} ions by a cascade of coalescence processes; these species progressively coalesce into larger clusters:

$$
\begin{aligned}
&Ag^{+} + e^{-}_{aq} \rightarrow Ag^{0} \\
&Ag^{0} + Ag^{0} \rightarrow Ag^{+}_{2} \\
&Ag_{n} + Ag^{+} \rightarrow Ag^{+}_{n+1} \\
&Ag^{+}_{n+1} + e^{-}_{aq} \rightarrow Ag_{n+1}
\end{aligned}
$$

For the cluster growth mechanism, the rate of fast reactions of ion association with atoms or clusters ($Ag^{+}_{n+1}\ and\ Ag_{n+1}$) plays an important role. The rate of reducing radical formation controls the competition between the reduction of free silver ions and absorbed ones. Some stimuli are desired to control the smaller size cluster formation by direct reduction followed by coalescence. Therefore, nucleation and growth mechanism are two key steps to control for the formation of mono-dispersed nonagglomerated metal particles with a well-defined shape, size and narrow size distribution [139]. The concentration of metal precursor also plays very important role, if concentration of the reduced metallic atom during the reaction reaches a critical super-saturation level then spontaneous nucleation may occur. If the nucleation rate is high enough, then the sudden nucleation lowers almost immediately the concentration below this critical super-saturation level. If the rate of formation of the metal is not too high this nucleation step is followed by the growth of the particles from the original nuclei without formation of new nuclei as long as the metal is slowly generated provided that coalescence is prevented. On the contrary, if the particle growth occurs by coalescence of primary particles, secondary particles with irregular shape and large size distribution would be expected. With these ideas in mind, in the next step of nucleation and growth some

stabilizing agent or some ionizing irradiation exposure is needed which breaks help in formation of free radicals to reduces the silver ions into silver atoms [140–142]. During the ionizing radiation exposures, the already reduced metallic atom serves as pre-organized seed points, or nucleation sites which initiate the growth of silver nanoparticles directly on the polymer backbone [135, 138, 143]. Moreover, the more effective is ionizing irradiation (dose, exposure time), the smaller is the nanoparticles size. The narrow size distributions of the particles with increasing irradiation dose (as can be seen from the increase intensity of SPR band in UV-visible spectra) indicate that steps of nucleation and growth mechanisms are separated. The increasing dose rate of irradiation may result in a multiple nucleation events, which result in the appearance of new, smaller nanoparticles. During the whole process, PVA itself acts as physical barrier to inhibit further aggregation of silver nanoparticles to form larger particles and/or agglomerated silver nanoparticles. The results presented here demonstrate the example of the seeded growth of Ag nanoparticles within a polymer matrix.

12.3 UV-Visible Spectroscopy

12.3.1 Surface Plasmon Absorption Band

Figure 10 represents the UV-Visible absorption spectra of PVA and its nanocomposite with embedded Ag nanoparticles at different ionizing irradiation doses after normalizing the respective data. Figure 10i (curve 'a') clearly depicts a small absorption peaking at around 276 nm corresponding to be due to the $n \rightarrow \pi^*$ transitions of the C=O group of PVA [125]. Further, from curve 'b' of Fig. 10i, a new absorption band peaking at around 425 nm is also observed attributing to the nanosize silver in PVA/Ag nanocomposites as confirm through TEM results also. This band in visible range of spectrum originates due to the resonance of collective oscillations of conduction band electrons of silver nanoparticles, when interacted with the incident electromagnetic radiations and thus corresponds to the surface plasmon resonance (SPR) absorption band of embedded metal (silver) nanoparticles as discussed in the former section. The alcoholic group of PVA acts as reducing agent which helps in converting the silver ions into the metallic silver and control the kinematics of nucleation and growth during the formation of silver nanoparticles inside PVA [138]. The broadened nature of SPR band corresponds to the formation of poly-dispersed silver nanoparticles within PVA matrix with average diameter of 13 ± 5 (Fig. 9a), with larger dispersion [144].

Further, as observed from Fig. 10ii (curve 'a'–'d'), there is a continuous enhancement in the intensity and decrease in full width at half maximum (FWHM) of the corresponding SPR peak as an effect of increasing gamma irradiation at different doses. As observed from TEM image also (Fig. 9b), there is a decrease in particle size distribution after gamma irradiation (i.e. 7 ± 3 nm at the gamma dose of 50 kGy); thus, we can conclude that gamma irradiation further acts as the

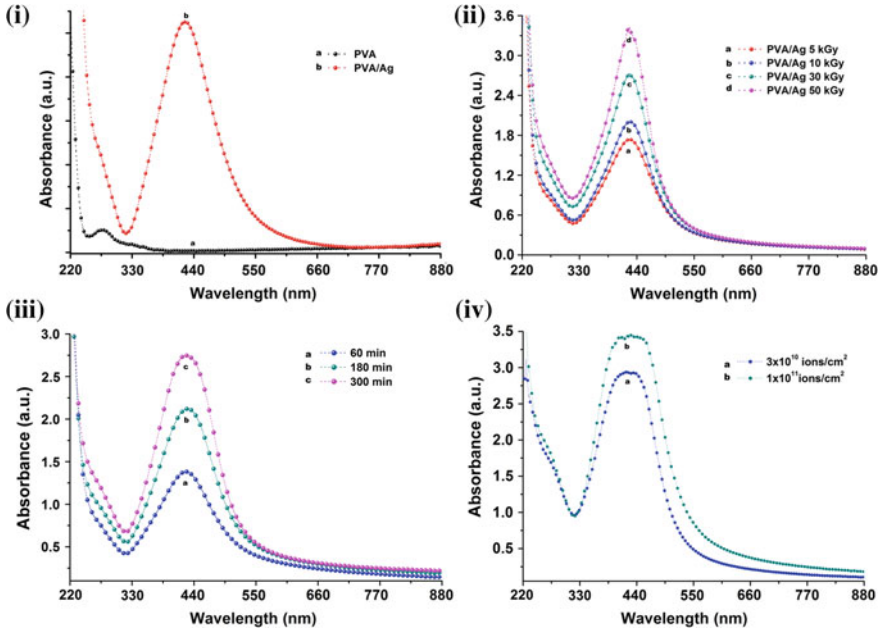

Fig. 10 UV-Visible absorption spectra of PVA and PVA/Ag nanocomposite films (i) after gamma irradiation for different doses (ii) irradiated for different time with UV radiations; (iii) before and after 90 meV O^{6+} ions irradiation at fluence of 3×10^{10} and 1×10^{11} ions/cm^2. Ref. [12, 13, 179]

stimulus for decrease in the size of embedded nanoparticles. The physical bass of this can be explained on the basis that the embedded silver nanoparticles act as pre-organized seed points, or nucleation sites, which further initiates the reaction of growth of silver nanoparticles induced by gamma irradiation through electron-surface scattering effect and dynamic charge transfer process between the metal clusters and the surrounding matrix [145]. This results in an increase in particles density with reduced particle size with an increase in gamma irradiation dose. Further, the broadening of the SPR band mainly depends upon the surrounding medium refractive index and particle size distribution [146, 147], i.e. the larger the size dispersion, the wider the plasmon absorption band.

Similar to gamma irradiation, an increase in SPR peak intensity has been observed after UV irradiation and SHI irradiation. The continuous increase in intensity of SPR band with increasing exposure time to UV radiations (Fig. 10ii) indicates the increase in number density of Ag nanoparticles within PVA matrix at increasing UV dose. Such an enhancement in the number density of embedded Ag nanoparticles can be explained on the basis of the fact that carbonyl group present in PVA chains can absorb the electromagnetic radiation at wavelength 254 nm and gets excited. These excited species (>C=O*) reduce Ag ions into metallic Ag [138, 148]. Also, it is clearly depicted from the figure that the symmetry of SPR

band improves with increasing exposure time to UV radiation predicting the better uniformity in size distribution of Ag nanoparticles inside PVA matrix. In similar fashion, after irradiation to 90 meV O^{6+} ion beam (Fig. 10iii), the intensity of surface plasmon absorption band increases with an increase in the ion fluence. In this case, as the ion passes close to the embedded nanoparticles, these may be fragmented to smaller nanoparticles depending upon the energy loss by the incident ion [149, 150]. Also, the interaction of the ion with the polymer chains results in the electronic excitation and breaking of polymer chain and ionization which helps in the reduction of Ag^{+} into the metallic silver [150, 151]. Both fragmentation of the embedded nanoparticles and reduction of Ag ions into metallic Ag as a result of ion irradiation are responsible for the increased concentration of Ag nanoparticles in the host matrix which in turn causes the increase in intensity of surface plasmon absorption band after ion irradiation. Further, a noticeable decrease in FWHM of SPR peak on account of SHI irradiation follows similar trend as for gamma and UV exposure, as already explained.

In addition to the above, a continuous red shift in the absorption edge corresponding to PVA–Ag nanocomposites has been observed with increase in irradiation. Such a shift in the absorption edge is a result of generation of trap levels between highest occupied molecular orbital (HOMO) and lowest unoccupied molecular orbital (LUMO) of the nanocomposites on different irradiation and is responsible for the change the optical energy gap.

12.3.2 Optical Energy Gap and Urbach's Energy

Using Tauc's relation discussed in detail in previous section (Sect. 9), the value of optical band gap can be determined from the UV-Visible spectrum. The exponent s in this relation gives the detail of the direct or indirect band gap; in our case, we find the $s = 2$ fits good for our experimental data, thus suggesting the existence of indirect band gap for PVA, which is also confirmed from the literature. The plot between $(\alpha h\nu)^{1/2}$ and photon energy ($h\nu$) as per Tauc's relation for pure PVA is shown in Fig. 11i curve 'a', from which the value of indirect optical energy gap (E_g) for pure PVA has been determined by extrapolating the linearly fitted line on x-axis. Similarly, the value of E_g for nanocomposite films after exposure to gamma and SHI radiation at different doses has also been determined, and the obtained values have been tabulated in Table 1. It has been well noticed that embedding of silver nanoparticles and effect of different ionizing radiation produces no change in the nature of optical transition behaviour of PVA, i.e. there exist an indirect optical band gap in virgin and exposed nanocomposite films.

A decrease in optical energy gap (E_g) value from 4.92 eV (pure PVA) to 4.57 eV (PVA/Ag nanocomposite, Fig. 11i, curve 'b') has been observed. The alcoholic group of PVA which helps in reducing the silver ions into silver metallic atom and their nucleation form some chemical bonding around nucleated silver nanoparticles in order to stabilize them are responsible for lower value of E_g for PVA/Ag nanocomposite films as compared to that for pure PVA. In fact, such

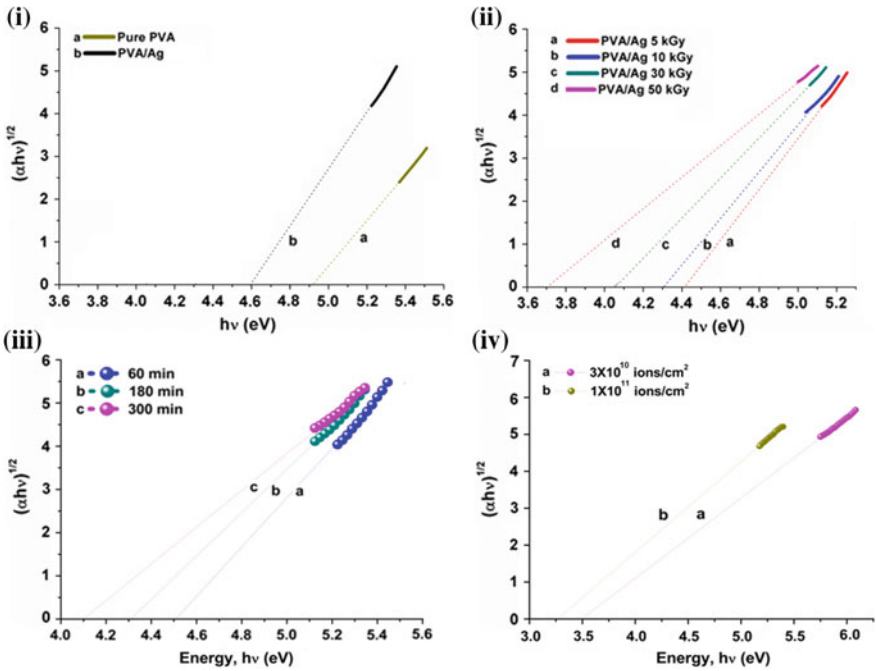

Fig. 11 Plots of ($\alpha h\nu^{1/2}$) versus energy ($h\nu$) for (i) pure PVA and PVA–Ag nanocomposite films after gamma irradiation for different doses (ii) irradiated for different time with UV radiations; (iii) before and after 90 meV O^{6+} ions irradiation at fluence of 3×10^{10} and 1×10^{11} ions/cm^2. Ref. [12, 13, 179]

Table 1 Calculated values of optical band gap for pure PVA, PVA/Ag nanocomposite film and after different ionizing irradiation at various doses

γ doses (kGy)	Optical Energy Gap (eV)	UV doses (minutes)	Optical Energy Gap (eV)	SHI doses (ions/cm^2)	Optical Energy Gap (eV)
5	4.42 ± 0.01	60	4.50 ± 0.03	3×10^{10}	3.98 ± 0.05
10	4.30 ± 0.04	180	4.32 ± 0.01	1×10^{11}	3.05 ± 0.03
30	4.04 ± 0.02	300	4.10 ± 0.02		
50	3.71 ± 0.03	For pure PVA	4.92 ± 0.02 (eV)	PVA/Ag nanocomposite	4.57 ± 0.02 (eV)

chemical bonding between PVA chains and Ag nanoparticles causes the a generation of localized states (charge transfer complexes, CTCs) between the HOMO and LUMO energy bands, which allows the feasibility of lower energy transitions, thus decreases the value of E_g.

As an effect of gamma irradiation and with increasing exposure dose, a further decline in the value of E_g for PVA/Ag nanocomposites to 3.71 eV at the dose of 50 kGy (Fig. 11ii) has been observed. The physiochemical reason for such a

decrease in band gap relies in the stimuli created through gamma irradiation which further proceed the nucleation and growth process by taking already formed silver nanoparticles as pre-organized seed for reduction process of remaining metal ions embedded inside the polymer matrix into metallic clusters [152]. This stimuli causes the creation of unsaturated bonds [153] in between HOMO and LUMO, which are rich in charge carriers (delocalized π electrons) and thus endorse electronic transitions which needs less energy, thus lowers the band gap value. Thus, in our case, enhancement in the number density of embedded Ag nanoparticles as an effect of increasing the exposure doses of gamma irradiation gives the evidence of increased conjugation between these particles and unsaturated bonds of PVA, which clarifies the observed reduction in energy gap as a result of gamma irradiation. However, no such change has been observed in pure PVA even after exposure to gamma irradiation up to a dose of 50 kGy [154].

Thus, we conclude that PVA being wide bandgap material easily allows the bandgap engineering as a consequence of the generation of new energy levels (traps) between the HOMO and LUMO after embedding metallic nanoparticles and subsequent gamma irradiation, thus, making the optical transitions feasible at lower energies. The observed bandgap tunability property of pure PVA after embedding Ag nanoparticles and after exposure to different irradiation at various doses make them efficient materials for optoelectronic devices.

Further, as an effect of UV radiation with increasing exposure time for 300 min, the band gap value reduces to 4.10 eV (Fig. 11ii). In this case, UV irradiation stimulates the reduction of silver ions into metallic silver inside the polymer matrix, with increased number of CTCs between the HOMO and LUMO of host matrix thereby reducing the optical energy gap [14, 74]. However, the reduction in band gap value for PVA/Ag nanocomposites is maximum in after SHI irradiation and attains a value of 3.05 eV for the dose of 1×10^{11} ions/cm^2 (Fig. 11iii). Such a decrease in optical energy gap may be explained on the basis of the fact that the ion beam irradiation causes chain scissoring, cross-linking, rupture of ionic bonds, release of ions, electrons and free radicals, etc., thus enhancing metal–polymer interaction [151] and thereby increasing the localized states between the HOMO and LUMO bands of PVA, which makes the lower energy transition feasible and leads to the observed changes in the optical energy gap, like that for gamma and UV-irradiated samples.

The number of carbon atoms per cluster in the sample formed as an effect of ionizing irradiation can be correlated with the values of optical energy gap (E_g) through the expression [155]:

$$E_g = \frac{34.3}{\sqrt{M}}$$

where M is the number of carbon atoms in carbonaceous cluster. Using this relation, the value of M has been found to be around 48 for PVA and which increases to 53 for unexposed PVA/Ag nanocomposite. The formation of chemical bonding between monomer units of PVA matrix and embedded silver nanoparticles causes

the chemical conjugation which may cause the increased value of *M*. This may be directed from the reducing action of alcoholic group explained in Sect. 12.2, which helps in reduction and growth process in the formation of silver nanoparticles. Further, the value of *M* taking in account of number of carbon atoms taking part in carbonaceous cluster in PVA/Ag nanocomposite rises to 86 as an gamma irradiation for a dose of 50 kGy, to 70 after 300 min of UV irradiation and to 127 after 1×10^{11} ions/cm^2 dose of SHI irradiation. The ionizing irradiation causes the dehydrogenation in the irradiated sample which further stimulates the nucleation and growth of pre-organized silver nanoparticles already embedded in host matrix, thus increasing the number of carbon atoms in carbonaceous cluster in host polymer matrix and thereby increasing the complexity in conjugation of PVA chains upon irradiation. However, SHI causes a maximum decrease in optical band gap and therefore a maximum increase in number of carbon atom in carboneous cluster formation inside nanocomposite films after irradiation.

As discussed earlier, the formation of Ag nanoparticles by self-reducing action of PVA and the various irradiations provoke disorderness in the base matrix which further also help in nucleation and growth mechanism of the embedded nanoparticles. The disorderenss is created in terms of breaking of bonds, formation of free radicals, and unsaturated bonds which may generate the localized states (CTCs) between energy levels. In order to quantify the disorder content and irregularities between the energy gaps in the polymers, the value of Urbach's energy has been measured using the formulation discussed in Sect. 9. The obtained values of Urbach's energy for different samples are enlisted in Table 2. As observed from this table that value of E_u for pure PVA is 0.35 eV which increases to 0.91 eV after embedding Ag nanoparticles in it. As an effect of gamma irradiation to 50 kGy, this value increases to 1.48 eV, thus clearly corroborate the increased disorderness in PVA/Ag nanocomposite as an effect of irradiation.

Further, the link between the optical energy gap values and Urbach's energy for gamma-irradiated PVA/Ag nanocomposite films is shown in Fig. 12. It is evident from the figure that decrease in optical energy gap value corresponds to the rise in Urbach's energy. This clearly supports the formation of number of trapping levels due to the self-reducing action of PVA which helps in the formation of nanoparticles within it and increase in these levels as an effect of gamma irradiation discussed above. These levels result from the disorders created inside the polymer

Table 2 Calculated values of Urbach's energy (E_u) for pure PVA, PVA/Ag nanocomposite film before and after different ionizing irradiation at various doses

γ doses (kGy)	E_u (eV)	UV doses (minutes)	E_u (eV)	SHI doses (ions/cm^2)	E_u (eV)
5	1.25 ± 0.02	60	0.98 ± 0.02	3×10^{10}	2.45 ± 0.03
10	1.29 ± 0.02	180	1.18 ± 0.01	1×10^{11}	2.57 ± 0.02
30	1.34 ± 0.01	300	1.24 ± 0.02		
50	1.48 ± 0.01	For pure PVA	0.36 ± 0.01 (eV)	PVA/Ag nanocomposite	0.91 ± 0.02 (eV)

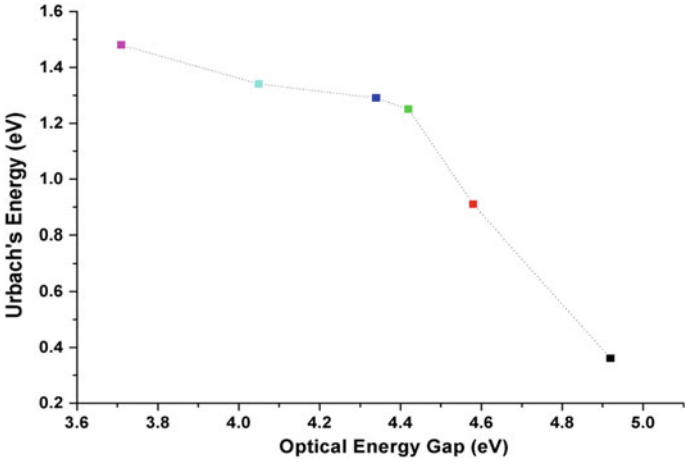

Fig. 12 Variation in optical energy gap (E_g) versus Urbach's energy (E_u) for gamma-irradiated PVA/Ag nanocomposite films. Ref. [13]

matrix which increases the feasibility of transitions of lower energy thus reducing the values of optical energy gap. The value of Urbach's energy calculated for UV-irradiated and SHI-irradiated PVA/Ag nanocomposite films at various doses are also tabulated in Table 2.

12.3.3 Refractive Index

The variation of refractive index 'n' as a function of wavelength 'λ' for PVA and its nanocomposites before and after different ionizing irradiation at various doses has been determined (Fig. 13) using the recursive relation discussed above, from the values of transmittance T and reflectance R directly measured from the instrument. It is well clear from the figure that initially the refractive index decreases slightly with an increase in wavelength and finally, it saturates for all the samples. For pure PVA (Fig. 13i, curve 'a'), the value of refractive index initially decreases gradually with wavelength and almost saturates in visible range, signifying the normal dispersion behaviour in this wavelength region. Similar behaviour is observed for its unexposed (Fig. 13i, curve 'b') nanocomposite film. With the help of Sellmeier dispersion theory [156–159], such normal dispersion behaviour of refractive index can be explained. According to this theory, in the region of maximum transparency, dielectric response and therefore refractive index behaviour of the atomic oscillators can be modelled as one or more Lorentz oscillators with almost zero broadening; due to which n(λ) shows the normal dispersion behaviour with wavelength λ. However, after embedding Ag nanoparticles in PVA matrix, the value of refractive index for all wavelengths has been found to be increased, which may be due to the formation of intermolecular bonding between Ag with the adjacent OH group of

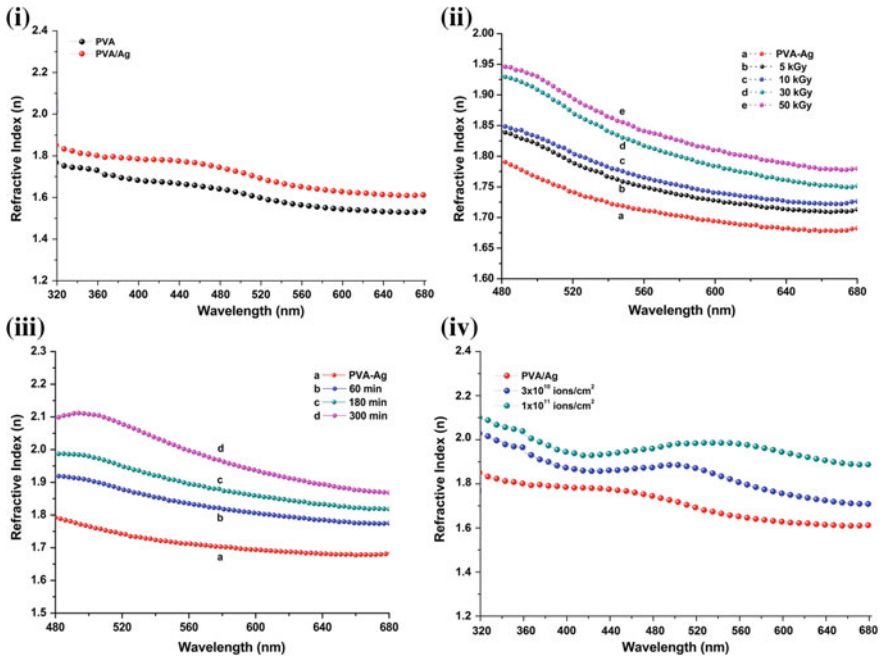

Fig. 13 Refractive index (RI) values for (i) PVA and PVA/Ag nanocomposite films (ii) without and with gamma irradiation for different doses (iii) irradiated for different time with UV radiations; (iv) before and after 90 meV O^{6+} ions irradiation at fluence of 3×10^{10} and 1×10^{11} ions/cm^2. Ref. [12, 179]

PVA. Such observations are in line with our previous observations which have been reported earlier [14] and explained on the predictions of the Bhar and Pinto model [160] developed through simulation of Lorimar's theory [161].

The value of RI increases further as compared to PVA/Ag nanocomposite films after gamma irradiation, and this enhancement is continuing with the increase in dose of gamma irradiation (Fig. 13ii). The irradiation causes the formation of dangling and unsaturated bonds and also augments the number of inter-chain interactions. These result in the change in packing density, molecular distribution, etc., thereby increase in refractive index with irradiation dose. This increase in refractive index of nanocomposite films after treatment extends the application of such materials in making antireflection coating for solar cells and high refractive index lenses.

Further, the effect of UV irradiation on the behaviour of variation of refractive index $n(\lambda)$ as a function of wavelength for PVA/Ag nanocomposite films has been represented in Fig. 13iii. As observed from this figure (curve 'b'–'d'), a hump has been observed in RI behaviour followed by the normal dispersion after UV exposure. The heightened SPR response of embedded nanoparticles as an effect of UV exposure as mentioned in the earlier section may attribute to the reason of

observed hump. Again, the overall value of RI for whole wavelength region has been found to increase with the increasing UV exposure. The increased RI in the composite is generally referred to be due to the increased packing density and molecular weight distribution as a result of chain-scissioning, cross-linking, etc., [160–162]. The effect of SHI irradiation on RI of nanocomposite films has been represented in Fig. 13iv. Similarly, it is clear from the figure that the value of refractive index decreases continuously with wavelength for all the samples. It is also evident from the figure that with an increase in dose of SHI to such nanocomposites, refractive index increases consistently. The value of refractive index, which was found to be 1.68 for PVA/Ag nanocomposite, has been found to be increased to 1.86 after irradiation at fluence of 1×10^{12} ions/cm^2 and at the wavelength 632 nm. Such an enhancement in refractive index may be attributed to the increase in the intermolecular hydrogen bonding between Ag with the adjacent OH group of PVA resulting in the change in packing density, molecular weight distribution, etc., as a result of ion irradiation, on the similar lines as that after gamma and UV irradiation.

12.4 X-Ray Diffraction (XRD)

Figure 14i shows the XRD patterns for pure PVA and PVA/Ag nanocomposites. The diffraction pattern of PVA (Fig. 14i, curve 'a') indicates the diffraction peak around 19.4° depicting its semi-crystalline nature. This may be due to the presence of strong intra-molecular hydrogen bonding in the individual monomer unit in PVA as well as between different monomer units. After embedding Ag nanoparticles, new peaks in XRD pattern (Fig. 14b) at 17.4°, 36.3°, 45.8° and 55.5° have been observed with decrease in intensity of peak at 19.4°. The peak originated at 17.4° may be due to the diffraction from (100) and $(00\bar{1})$ planes of host matrix [162]. The values of XRD peaks corresponding embedded Ag nanoparticles in PVA-Ag nanocomposites and after various irradiations at different doses are tabulated in Table 3. On account of Ag nanoparticles embedding and further with gamma irradiation, the H-bond and –OH group of the PVA chains may break and molecular chains are free to rotate; thus, the change in the intensity of the diffraction peak at 17.4° after increasing gamma irradiation dose may be understood. The peaks at 36.3° and 45.8° corresponds to *h k l* parameters (111) and (200), respectively, for silver existing in the *fcc* structure, thus corroborate the presence of Ag particles [163]. The peak observed at 55.5° might be due to some disorder created in the matrix after embedding Ag nanoparticles.

Further, effect of different ionizing irradiation on XRD pattern of PVA/Ag nanocomposites at various doses has been depicted in Fig. 14ii. As observed from this figure that gamma irradiation of dose 10 kGy results in the rise in intensity of the peaks at 36.3° and 45.8° depicting the increase in the crystalline phase, i.e. content of Ag nanoparticles in PVA/Ag nanocomposites. This might be due to an

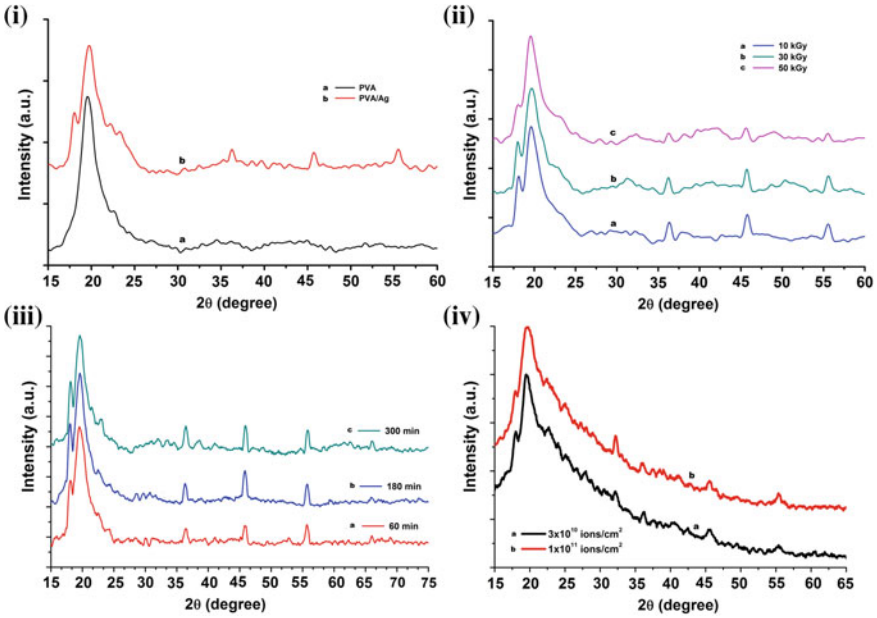

Fig. 14 XRD pattern for (i) PVA and PVA/Ag nanocomposite films (ii) without and with gamma irradiation for different doses (iii) irradiated for different time with UV radiations; (iv) before and after 90 meV O^{6+} ions irradiation at fluence of 3×10^{10} and 1×10^{11} ions/cm^2. Ref. [12, 13]

increase in particle density of embedded Ag nanoparticles results from the stimuli to nucleation and growth mechanism of pre-organized seed nanoparticles embedded in PVA matrix through gamma irradiation. However, a decrease in the intensity of these peaks with little broadening has been observed with a further increase in gamma irradiation dose. This causes the increase in FWHM of these peaks which clearly signifies the decrease in particles size [163], thus supporting the TEM and UV-Visible spectroscopy analysis. The peak position, their peak intensity and FWHM of various XRD peaks are tabulated in Table 3.

On account of UV exposure, the H–bond and –OH group of PVA chains may break and molecular chains becomes free to rotate resulting in the variation in the number of atoms in the direction (001). This may cause the change in the intensity of the diffraction peak at 18° after UV exposure (Fig. 14iii). The diffraction peak around 19.7° is the characteristic peak of PVA depicting its semi-crystalline nature and remains almost unaffected. The intensity of the peaks at 36.3° and 45.8° increases up to exposure time of 180 min, which indicates the increase in the crystalline phase in nanocomposites due to increase in the concentration of Ag nanoparticles in the PVA matrix by means of UV irradiation. With further increase in UV exposure time to 300 min, the intensity of these peaks nearly saturates (Fig. 14iii, curve 'c').

Table 3 Position, intensity and FWHM of diffraction peaks corresponding to embedded Ag in PVA-Ag nanocomposite films before and after various irradiations

Samples	2Θ (deg)	FWHM (deg)	Intensity (%)
PVA-Ag	36.3	0.356	10.27
	45.7	0.376	20.27
PVA-Ag (10 kGy gamma irradiated)	36.3	0.344	29.35
	45.7	0.362	40.88
PVA-Ag (30 kGy gamma irradiated)	36.2	0.394	29.16
	45.7	0.394	30.68
PVA-Ag (50 kGy gamma irradiated)	36.3	0.443	13.04
	45.74	0.576	21.46
PVA-Ag (60 min UV irradiated)	36.4	0.576	14.24
	45.8	0.288	24.73
	55.7	0.384	19.98
PVA-Ag (180 min UV irradiated)	36.3	0.384	21.65
	45.8	0.288	39.8
	55.6	0.48	21.81
PVA-Ag (300 min UV irradiated)	36.4	0.376	23.9
	45.9	0.384	37.99
	55.7	0.288	26.12
PVA-Ag (3×10^{10} ions/cm^2 of SHI)	36.4	0.376	12.21
	45.8	0.382	20.72
PVA-Ag (1×10^{11} ions/cm^2 of SHI)	36.4	0.456	13.93
	45.9	0.576	21.97

However, after ion beam irradiation, intensity as well as FWHM of the peaks at 36.3° and 45.8° is found to increase continuously with increasing ion beam dose, indicating the increase in concentration and decrease in particle size [164] of embedded Ag nanoparticles (Fig. 14iv).

Further, a new peak has been found to be originated at 32.1° on ion beam treatment of PVA–Ag nanocomposite film at a fluence of 1×10^{11} ions/cm^2, intensity of which increases with an increase in ion beam fluence. The appearance of this new peak may be due to some disorder produced in host matrix after ion beam treatment and this disorder increases with increase in ion beam fluence. These observations indicate that ion beam irradiation causes the structural rearrangements in a significant manner in the nanocomposite films.

12.5 Fourier Transmission Infrared (FTIR)

The FTIR spectra of pure PVA and PVA/Ag nanocomposite film in the wavenumber range 700–4000 cm^{-1} have been represented in Fig. 15 and those of

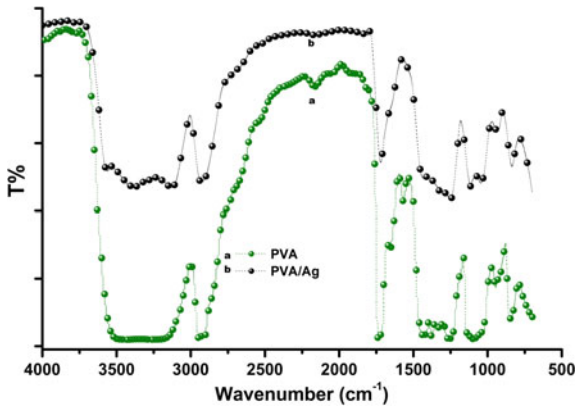

Fig. 15 FTIR spectra for (i) PVA and (ii) PVA/Ag nanocomposite films. Ref. [13, 179]

PVA/Ag nanocomposite film after exposure to different ionizing radiation at various doses have been shown in Fig. 16i–iii. Table 4 presents the wavenumber and corresponding assigned functional group or bond in case of pure PVA [165, 166].

As observed from curve 'b' of Fig. 15 that the band at 1660 cm^{-1} completely disappear and the intensity of the band at 1720 and 851 cm^{-1} decreases as a result of embedding Ag nanoparticles in PVA, suggesting the formation of chemical conjugation between Ag nanoparticles with PVA molecules. Further, there observed an almost disappearance of the band at 1380 cm^{-1}, indicating the decoupling between O–H and C–H vibrations due to the bonding interaction with O–H and Ag nanoparticles.

However, as an effect of gamma irradiation (Fig. 16i), the intensity of bands at 2920, 1720, and 850 cm^{-1} has been observed to decrease further along with the disappearance of bands in the wavenumber region of 1250–1500 cm^{-1}, with increasing gamma dose. This indicates that gamma irradiation subsequently causes the structural rearrangements in PVA chains on embedding of Ag nanoparticles. These structural modifications in host PVA matrix after embedding Ag nanoparticles and further, with exposure to gamma radiations, are in conformity with the observed changes in optical behaviour.

After UV irradiation, variation in vibrational spectra in the range 3500–3200 cm^{-1} (Fig. 16ii) may be due to the chemical conjugation of silver nanoparticles with the chains of PVA molecules. The decrease in intensity of bands at 1720 cm^{-1} in the wavenumber range 1000–1140 and 837 cm^{-1} indicates the interaction of Ag nanoparticles with PVA chains. Further, change in the intensity of vibrational band at 1380 cm^{-1} indicates the decoupling between O–H and C–H vibrations due to the increase in interaction of Ag nanoparticles with O and H atoms of PVA chains after UV irradiation [75, 149]. These observations indicate that the interaction of embedded nanoparticles with the host polymeric matrix increases after UV exposure. Such changes in the vibrational bands indicate that UV irradiation substantially causes the structural rearrangements in PVA chains and Ag nanoparticles in nanocomposite films.

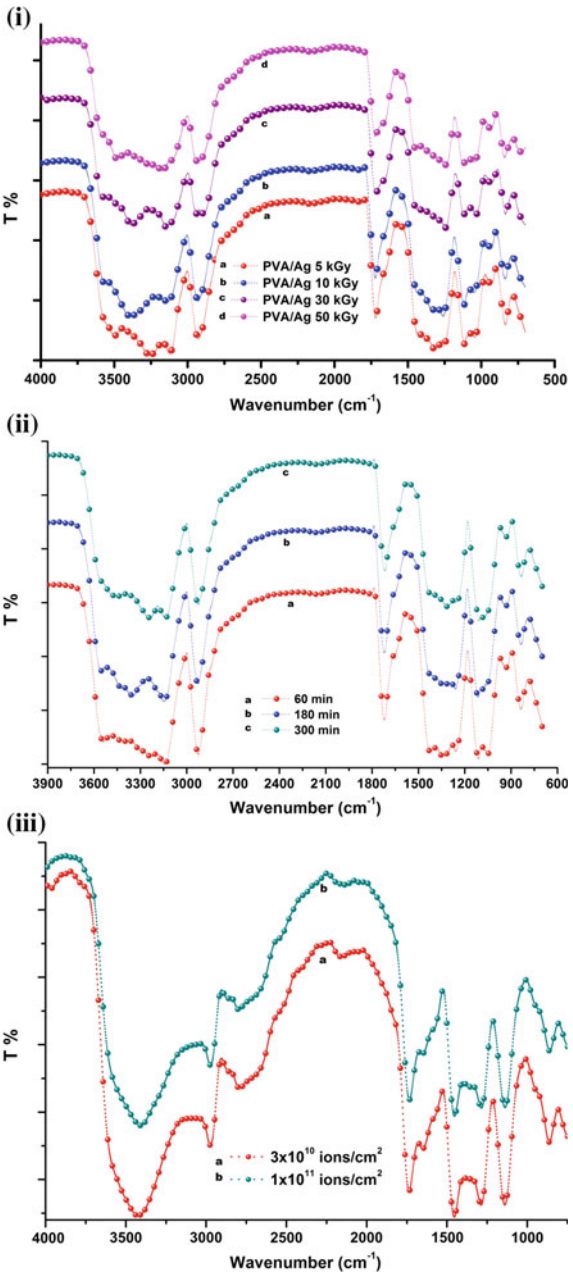

Fig. 16 FTIR spectra for PVA/Ag nanocomposite films after (i) gamma irradiation for different doses, (ii) irradiated for different time with UV radiations; (iii) before and after 90 meV O^{6+} ions irradiation at fluence of 3×10^{10} and 1×10^{11} ions/cm^2. Ref. [12, 179]

Ion beam irradiation indicates the structural rearrangements of silver nanoparticles with the chains of PVA molecules through the decrease in the intensity of absorption band in the 3500–3200 cm^{-1} region (Fig. 16iii). Further, after ion beam

Table 4 Various vibration band positions observed in FTIR spectrum corresponding to functional bond/group present in pure PVA

Wavenumber (cm^{-1})	Functional bond/group
3500–3200	O–H stretching
2920	C–H stretching vibrations
1720	C=O
1660	C=C stretching
1380	O–H in plane vibration
1430	C–H wagging vibrations
1140–1000	C–O and C–O–C groups
850	out-of-plane vibration of C–H group

treatment, the decrease in intensity of bands at 2928 and 1720 cm^{-1} and generation of new peaks in region 1250–1450 cm^{-1} indicate the decoupling between O–H and C–H vibrations due to the increase in interaction of embedded Ag nanoparticles with O and H atoms of PVA chains [75, 166, 167]. The effect becomes more enhanced with increasing ion fluence. The appearance of small absorption band around 1637 cm^{-1}, corresponding to C=C stretching, indicates the formation of carbonaceous structure in host matrix after ion beam irradiation [167]. The decrease in intensity and broadening of band at 837 cm^{-1}, assigned to out of plane vibrations of C–H group, signifies the increase in interaction of embedded Ag nanoparticles with PVA chains at higher fluence. These observations indicate that ion beam irradiation substantially causes the structural rearrangements in PVA–Ag nanocomposite films.

12.6 Raman

The Raman spectra of pure PVA and un-irradiated PVA–Ag nanocomposite film are presented in Fig. 17. It is clear from this figure that PVA–Ag exhibits a weak Raman band observed at 667 cm^{-1} assigned to O–H wagging and C–H out of plane vibrational mode. The Raman bands observed at 817 and 849 cm^{-1} are corresponding to C–C stretching vibrational modes [168]. The appearance of strong Raman band at 936 cm^{-1} is a sign of conjugation of Ag nanoparticles with the atoms of the host matrix, which affects the natural vibrations of the bands of host matrix. Further, the bands observed at 1352 and 1409 cm^{-1} correspond to the mixture of C–H bending and O–H bending vibrations [168–172]. The occurrence of Raman signal at 1540 and 1610 cm^{-1} in PVA–Ag nanocomposite may be due to surface-enhanced Raman scattering (SERS) effect of embedded Ag Nanoparticles [154].

As an effect of gamma and UV irradiation, the decrease in intensity of bands at 667 and 936 cm^{-1} and the disappearance of bands at 817, 849 and 1610 cm^{-1} have been observed (Fig. 18i, ii). With increasing gamma and SHI irradiation dose, the bands in the region 600–1300 cm^{-1} have almost disappeared indicating the

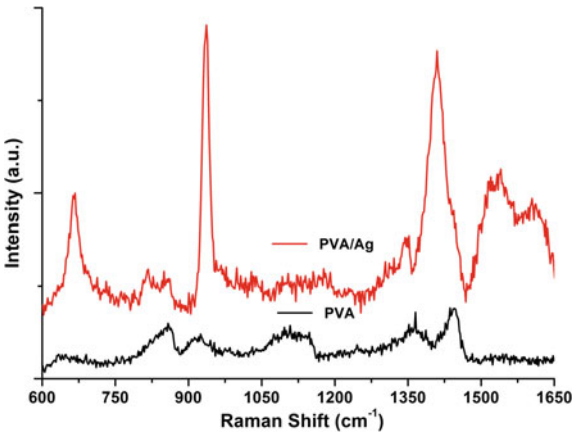

Fig. 17 Raman spectra for PVA and PVA/Ag nanocomposite films. Ref. [179]

structural rearrangements between host matrix PVA and embedded Ag nanoparticles. However, such changes are not so significant after UV irradiation. Further, the presence of Raman signal at 1365 and 1572 cm^{-1} corresponding to D and G bands of graphitic like structure may occur in the irradiated samples due to the evaporation of residual volatile species as an effect of irradiation. With increasing gamma and SHI irradiation dose, an continuous increase in intensity of these D and G band has been observed; however, no substantial change in the intensity of these bands has been observed in case UV irradiation. Such an enhancement in the intensity of D and G bands with increasing gamma and SHI irradiation dose may be as a result of increased chemical bonding of the embedded nanoparticles with the PVA molecules and can be attributed to the increased SERS effect of embedded Ag nanoparticles in PVA matrix. These significant changes in the Raman vibrational bands may be associated with the breaking of PVA intra or inter-molecular bonds with simultaneous inclusion of new bonds between PVA and Ag nanoparticles. Further, an increase in intensity of band at 1576 cm^{-1} with increasing dose of ion beam irradiation suggests the increase in the carbonaceous phase of PVA. Thus, Raman spectroscopy clearly predicts the considerable structural modifications in PVA–Ag nanocomposites after gamma and SHI irradiation as compared to UV irradiation.

13 Applications of Prepared Nanocomposites

13.1 Band Pass Filter

Figure 19 depicts the transmission spectra of the PVA/Ag nanocomposite films before and after UV exposure for different times. As clear there is a transmission band peaking around 320 nm, originating in the blue region of the SPR band of the

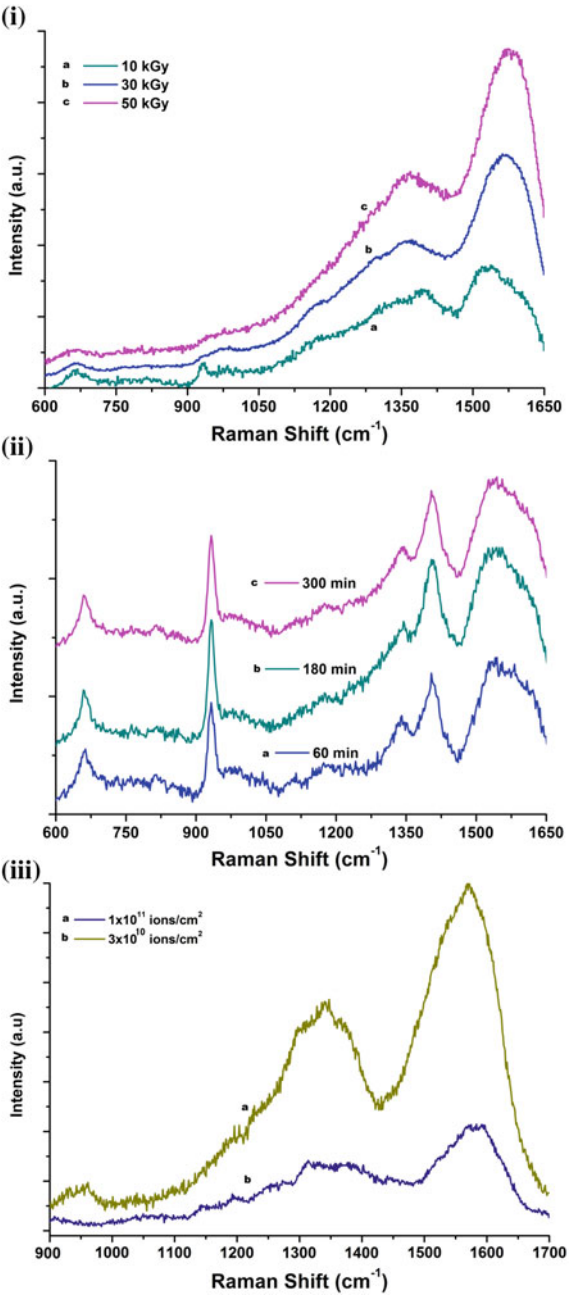

Fig. 18 Raman spectra for PVA/Ag nanocomposite films after (i) gamma irradiation for different doses (ii) irradiated for different time with UV radiations; (iii) before and after 90 meV O^{6+} ions irradiation at fluence of 3×10^{10} and 1×10^{11} ions/cm^2. Ref. [179]

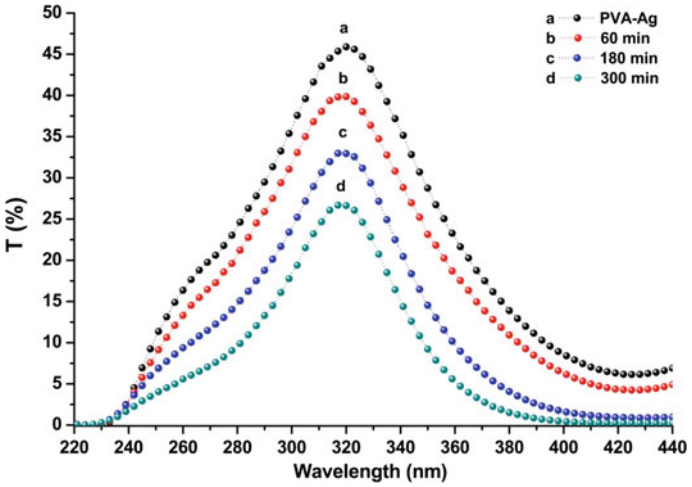

Fig. 19 Transmission spectra of the PVA/Ag nanocomposite films before and after UV exposure for different time. Ref. [12]

embedded nanoparticles. However, with an increase in UV exposure time, decrease in width of this band has been noticed whereas there is an increase in attenuation of transmission intensity. Such observations clearly justify the possibility of these nanocomposites for band pass filter application at around 320 nm. Moreover, for gamma-irradiated and SHI-irradiated nanocomposites, such attenuation of transmission intensity is qualitative small. This leads to the possibility of using UV-irradiated nanocomposites as a band pass filter around the desired wavelength by the proper choice of host matrix, embedded nanoparticles spices, their size distribution, concentration and exposure time to UV radiations.

13.2 Antireflective Coating

The possibility of these nanocomposites for antireflective coating has been explored by examining their reflection spectra obtained from UV-Visible spectroscopy [12]. Figure 20 depicts the reflection spectra for UV treated PVA/Ag nanocomposite films. As observed from this figure, the values of reflectance (R%) have been found to decrease continuously in whole studied wavelength region after embedding Ag nanoparticles in PVA and further with UV exposure. The values of R% corresponding to certain wavelengths have been tabulated in Table 5. This table clearly depicts that the value of R decreases average to $\sim$6% at nearly all wavelengths after 300 min exposure to UV radiation.

This feature of minimizing the reflection of incident light from the surface enables the use of such UV treated nanocomposites for making the antireflective

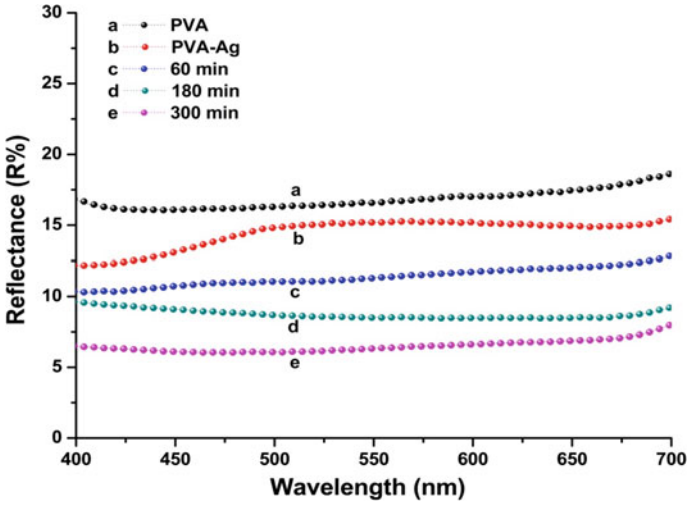

Fig. 20 Reflectance spectra of the PVA/Ag nanocomposite films before and after UV exposure for different times. Ref. [12]

Table 5 Values of reflectance (R%) at different wavelengths for PVA/Ag nanocomposite films before and after UV exposure for different times

Samples (nm)	400	500	600	700
PVA (%)	16	16	17	18
PVA/Ag (%)	12	14	15	15
PVA/Ag (%) (60 min UV exposure)	10	11	11	12
PVA/Ag (%) (180 min UV exposure)	9	8	8	9
PVA/Ag (%) (300 min UV exposure)	6	6	6	8

(AR) coating, also the graded index material for solar cells, glass windows, organic photovoltaic, etc. in order to utilize the full spectrum of incident light by suppressing the Fresnel reflection. In order to explore the full utilization of any material for reflective or antireflective coating, the functionality of reflection on thickness (d) as well as the refractive index (n) of the coating material is needed to examine. Therefore, for fabricating the graded index AR coatings using these nanocomposites, a careful calibration on both factors (d and n) is indeed [12]. The traditional quarter wavelength antireflective coating lowers the wavelength in a dielectric medium, thus minimizing reflection to one quarter of the incident wavelength (λ) given by the formula $d = \lambda/4n$. Fundamentally, it allows the destructive interference of the reflected light from the surrounding medium/AR coating interface and that from the AR coating/substrate interface as depicted from scheme given in Fig. 21.

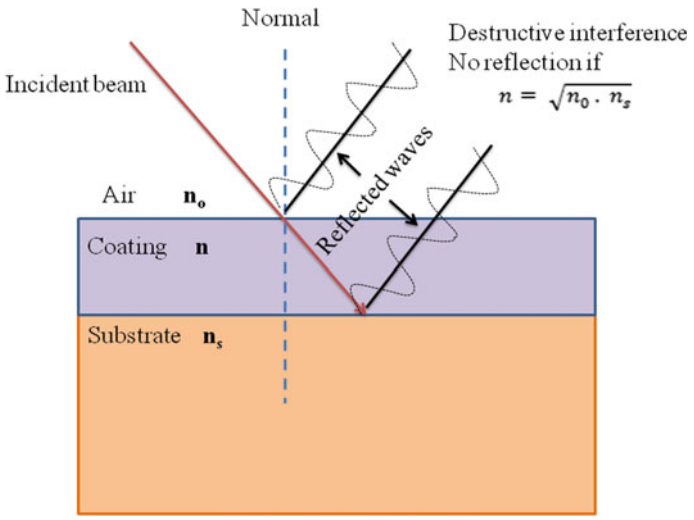

Fig. 21 Schematic representation of antireflective coating to counter surface reflection

However, when the light meets the interface at normal incidence, the intensity of the reflected light (I_R) is given by the reflection coefficient, R, and can be found using the Fresnel equation [12, 173, 174] given as

$$I_R = R^2 = \left(\frac{n_0 - n_s}{n_0 + n_s}\right)^2$$

where n_o and n_s are the refractive indices of the material on either side of the coating, i.e. surrounding media and substrate, respectively.

Further, if the refractive index of thin film coatings is gradually changed from substrate to exterior medium, the refractive index interface will be eliminated and the interface reflection will not take place. However, it is quoted in the literature that the reflection from the surface can be minimized by choosing the material having RI as the geometric mean of the refractive indices of the material on either side of the coating [12, 173, 174], i.e.

$$n = \sqrt{n_0 \cdot n_s}$$

Therefore, if we deposit the thin films of the coating material of given RI with gradual change in its thickness or vice versa [175–177], and then, an interlayer can help in further reduction in light reflection and its optimum RI value is given by the geometric mean of the two surrounding indices.

As an instance, for the combination of silicon ($n_s \sim 3.5$) and air ($n_0 \sim 1$), the refractive index of the best AR coating is $n \sim 1.871$ [178] while that for Indium tin oxide ($n_0 \sim 2$) and glass ($n_s \sim 1.5$) is $n \sim 1.73$. From Table 4, it is clear that in

our case, the refractive index of the nanocomposite films for 180- and 300-minute exposed sample is similar to the optimum refractive index of 1.871. Therefore, these nanocomposites can be used as AR coating for silicon-based solar cells so as to obtain the best photoelectric conversion performance [175] and also used in devices where minimum reflection and full utilization of solar spectrum is desired.

13.3 UV Blocking Device

Figure 22 presents the recorded transmission spectra of PVA, PVA/Ag nanocomposite and 90 meV O^{6+} SHI-irradiated PVA/Ag nanocomposite films at a fluence of 3×10^{10} ions/cm^2 and 1×10^{11} ions/cm^2. It is evident from this figure that PVA shows almost transparent nature in the entire visible region ($\sim$ 400 to 800 nm) with approximately 95% of transmission and a small reduction at lower wavelengths. As an effect of embedded Ag nanoparticles, the value of transmission reduces drastically. The value of the percentage transmission intensity has been found to be $\sim$1.86, 35 and 8.56%, respectively, at 200, 300 and 400 nm. Also, appreciable change in the colour of the samples from transparent (PVA) to light yellowish (PVA/Ag film) has been observed upon the visual inspection of these samples. Such colouration and reduction in transmission intensity may be due to the formation of some chemical bonding between Ag nanoparticles and PVA chains [179]. Such chemical interaction results in the formation of conjugate structure in polymer after embedding nanoparticles which are clearly reflected in change in their optical and structural properties.

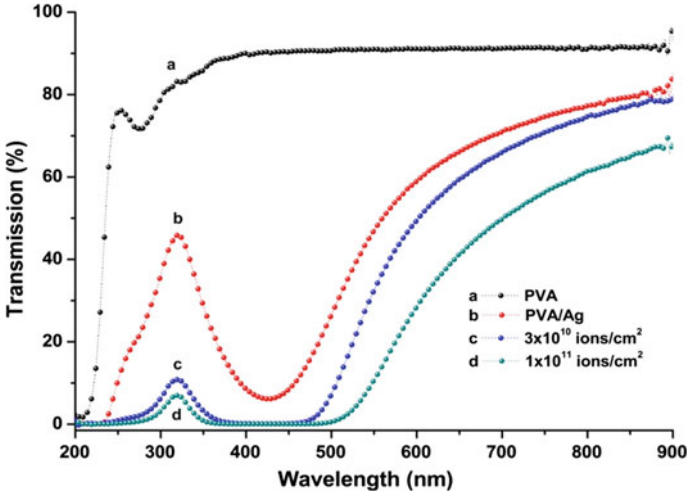

Fig. 22 Recorded transmission spectra of PVA, PVA/Ag nanocomposite and 90 meV O^{6+} ion-irradiated PVA/Ag nanocomposite films at a fluence of 3×10^{10} ions/cm^2 and 1×10^{11} ions/cm^2. Ref. [179]

Further, after SHI irradiation at the fluence of 3×10^{10} ions/cm^2, the transmission reduces drastically again and attains the values of ~0.80, 6.38 and 0.14% at 200, 300 and 400 nm respectively (curve 'c'). With increase in ion fluence to 1×10^{11} ions/cm^2 (curve 'd'), the transmission reduces further to ~0.73, 3.22 and 0.03% at the respective wavelength mentioned above [179].

Also, with increasing ion fluence, the colour of nanocomposite films which was light yellow changes to pale yellow and then become wine reddish after irradiation. The SHI irradiation causes the formation of conjugated bonds with loosely bound π electrons. These π electrons can be easily excited by incident light and leads to the observed changes in transmission spectra and colouration of nanocomposite films. Figure 20 clearly indicates that at fluence of 1×10^{11} ions/cm^2, the transmission is as good as zero in UV and near UV regions, suggesting utilization of these nanocomposite after irradiation for shielding purposes from UV photons [176–178].

14 Conclusions

In the present chapter, brief history of the nanotechnology has been reviewed along with its fundamental importance. Concepts of nanoparticles, essentials of basic physics which make this more important viz. quantum size effect and surface-to-volume ratio, top-down and bottom-up approach for their synthesis and method of their stabilization have been discussed in brief. In order to provide application-based platform to nanoparticles, the primary choice is embedding them to suitable matrix which could provide a suitable stabilization without losing inherent characteristics of nanoparticles, therefore enhancing the properties of nanocomposites. To such choice, polymers are selected mostly because of their intrinsic features like good mechanical strength, flexibility, solution processing, dopant dependent property and above all good capability of stabilization metal and semiconductor nanoparticles. The polymer-based hybrid nanocomposites can be synthesized via one-pot synthesis, in situ/ex situ synthesis, interfacial polymerization, vapour phase synthesis and electrochemical synthesis. These different synthesis processes have been adopted to control various properties like shape, size and dispersion of the secondary phase within the polymer matrix. Metal nanoparticles are chosen as among the best possible nanofillers in polymer-based nanocomposites. While going through brief history of metal nanoparticles, fundamental of fascinating surface plasmon resonance (SPR) of metal nanoparticles observed in visible region of EM spectrum has been discussed. Mie theory has been deliberately explained in order to provide theoretical basis of occurrence and calculation SPR. Importance of polymer-metal nanocomposites was conveyed from the seventeenth century by various scientists and researchers. And nowadays, such nanocomposites have been used in wide fields of progressive applications optical devices like colour sensors, colour filters; electro-optical devices like flexible liquid crystal colour displays; micro-electronic and quantum electronic devices; sensors and immunoassays, etc. In spite of this exciting development in the field of polymer-metal nanocomposites-based hybrids,

proper choice of polymer and nanofiller and their control synthesis are still a challenge. In the present chapter, we focus on combination of PVA and Silver nanoparticles as polymer-metal nanocomposites. Effect of ionizing irradiation on the properties of polymer-based nanocomposites has been discussed while giving the brief introduction of various ionizing radiation like electromagnetic (UV, gamma) radiation and swift heavy ion radiations. Some important existing literature describing the effect of ionizing irradiation on the modification of polymer- and metal nanoparticles-based composite materials have been described. For development of practical application of such nanocomposites, some efforts are indeed necessary. Therefore, future work should concentrate onto the development of synthesis method for metal-based hybrid nanocomposites with control parameters and morphology and utilization of various ionizing irradiation in a proper manner in order to modify or calibrate the properties of nanocomposites as per desired. This chapter focuses on the optical application of polymer-metal nanocomposites; therefore, calculation of optical parameter like transmission/reflection coefficient, refractive index, optical band gap, etc. have been discussed in detail.

In addition to these, nanocomposites of PVA and silver nanoparticles prepared via in situ chemical synthesis have also been discussed. Formation of nanocomposites has been confirmed through TEM, UV-Visible absorption spectroscopy and XRD. Embedded Ag nanoparticles are found to be 13 ± 5 nm of size and spherical in shape as depicted through TEM image. UV-Visible absorption spectrum exhibits the SPR band of embedded Ag nanoparticles peaking at 425 nm. Further, effect of gamma, UV and SHI (90 meV O^{6+}) on prepared nanocomposites has been discussed. TEM analysis describes the reduction in the size of nanoparticles after various ionizing irradiation. Possible mechanism of reduction and increased particle density after various ionizing irradiation has been discussed. Through UV-Visible spectroscopy refractive index, optical band gap and Urbach's energy of the nanocomposite sample before and after ionizing irradiation have been determined. Increase in refractive index, decrease in optical band gap and increase in Urbach's energy have been found after increasing the dose of the different ionizing irradiation. All such effects are corroborating each other depicting the increased metal–polymer interaction through chain scissoring, cross-linking, rupture of ionic bonds, release of ions, electrons and free radicals, etc. as an impact of ionizing irradiation. Thereby, increasing the localized states between the HOMO and LUMO bands of PVA, this makes the lower energy transition feasible and leads to the observed changes in the optical parameters. Further, number of carbon atoms per cluster calculated before and after ionizing irradiation also brief the quantitative effect of various ionizing irradiation. However, this number is largest in case of SHI irradiation, and also as observed through various optical parameters, the effect of SHI irradiation is maximum as compared to gamma and UV irradiation. Such effects have also been confirmed through structural characterization techniques like FTIR and Raman spectroscopy. The possible application of the prepared PVA-Ag nanocomposites films have been discussed in detail. Such nanocomposites can be effectively used for making band pass filter for example as explained UV-irradiated nanocomposites show drastic attenuation of transmission intensity around 320 nm.

After detailed analysis of reflection spectrum and refractive index, these nanocomposites can be used as AR coating in solar cells so as to obtain the best photoelectric conversion performance and also used in devices where minimum reflection is desired. As discussed, the transmission of SHI-irradiated nanocomposites is falling to almost zero in UV and near UV regions, suggesting utilization of such nanocomposites after irradiation for shielding purposes from UV photons.

References

1. Feynman RP (1960) Eng Sci 22–36
2. Drexler KE (2004) Bull Sci Technol Soc 24(1):21–27
3. "Plenty of room" revisited (2009) Nat Nanotechnol 4:781
4. Azzoni CB, Di Martino D, Marchesi V, Messiga B, Riccardi MP (2005) Archaeometry 47 (2):381–388
5. Cox GA, Gillies KJS (1986) Archaeometry 28(1):57–68
6. Cramp RJ (1975) J Glass Stud 17:88–96
7. Brugger J (2009) Nanotechnology 20(43):430206
8. Suri SS, Fenniri H, Singh B (2007) J Occup Med Toxicol 2:16
9. Solanki A, Kim JD, Lee KB (2008) Nanomedicine (Lond) 3(4):567–578
10. Kim E-S, Ahn EH, Dvir T, Kim D-H (2014) Int J Nanomed 9:1–5
11. Toy R, Bauer L, Hoimes C, Ghaghada KB, Karathanasis E (2014) Adv Drug Deliv Rev 0:79–97. https://doi.org/10.1016/j.addr.2014.08.002
12. Chahal RP, Mahendia S, Tomar AK, Kumar S (2015) Appl Surf Sci 343:160–165
13. Chahal RP, Mahendia S, Tomar AK, Kumar S (2012) J Alloys Comp 538:212–219
14. Mahendia S, Tomar AK, Chahal RP, Goyal P, Kumar S (2011) J Phys D Appl Phys 44:205105
15. Cao Z, Abe Y, Nagahama T, Tsuchiya K, Ogino K (2013) Polymer 54:269–276
16. Xu P, Han X, Zhang B, Dua Y, Wang H (2014) Chem Soc Rev 43:1349–1360
17. Nicolais L, Carotenuto G (2005) Metal-polymer nanocomposites. Wiley, Hoboken, New Jersey
18. Yeum YH, Deng Y (2005) Colloid Polym Sci 283:1172–1179
19. Biswas A, Avasthi DK, Fink D, Kanzow J, Schürmann U, Ding SJ, Aktas OC, Saeed U, Zaporojtchenko V, Faupel F, Gupta R, Kumar N (2004) Nucl Instr Meth B 217:39–50
20. Qureshi A, Singh NL, Shah S, Kulriya P, Singh F, Avasthi DK (2008) Nucl Instr Meth B 266:1775–1779
21. Abd El-Kader KAM, Hamied SFA (2002) J Appl Polym Sci 86:1219–1226
22. Burda C, Chen X, Narayanan R, El-Sayed MA (2005) Chem Rev 105:1025
23. Praharaj S, Nath S, Ghosh S, Kundu S, Pal T (2004) Langmuir 20:9889
24. Campbell CT, Parker SC, Starr DE (2002) Science 298:811
25. Frederix F, Friedt J, Choi K, Laureyn W, Campitelli A, Mondelaers D, Maes G, Borghs G (2003) Anal Chem 75:6894
26. Folarin OM, Sadiku ER, Maity A (2011) Inter J Phys Sci 6(21):4869–4882
27. Murray CB, Norris DJ, Bawendi MG (1993) J Am Chem Soc 115:8706–8715
28. Klabunde KJ (2001) Nanoscale materials in chemistry. Wiley-Interscience, New York
29. Whitesides GM, Love JC (2001) Sci Am 285:38
30. Schmid G (2004) Nanoparticles: from theory to application. Wiley-VCH, Weinheim
31. Uskoković V (2013) J Biomed Nanotechnol 9(9):1441–1470
32. Fritz G, Schädler V, Willenbacher N, Wagner NJ (2002) Langmuir 18:6381–6390
33. Corbierre MK, Cameron NS, Mark S, Laaziri K, Lennox RB (2005) Langmuir 21:6063

34. Naka K, Itoh H, Park S, Chujo Y (2004) Polymer Bull 52:171–176
35. Balan L, Burget D (2006) Eur Polym J 42:3180–3189
36. Lee JY, Liao Y, Nagahata R, Ahoriuchi S (2006) Polymer 47:7970–7979
37. Sangermano M, Yagci Y, Rizza G (2007) Macromol 40:8827–8829
38. Nadagouda MN, Varma RS (2007) Macromol Rapid Commun 28:465–472
39. Kanbur Y, Irimia-V M, Głowacki ED, Voss G, Baumgartner M, Schwabegger G, Leonat L, Ullah M, Sarica H, Erten-Ela S, Schwodiauer R, Sitter H, Kucukyavuz Z, Bauer S, Sariciftc NS (2012) Org Electron 13:919
40. Yun Y, Pearson C, PettyMC (2009) J Appl Phys 105:034508
41. Choi JS (2008) J Inf Disp 9:35
42. Feng L, Tang W, Xu X, Cui Q, Guo X (2013) IEEE Electron Device Lett 34:129
43. Hadjichristov GBIL, Stefanov BI, Florian, Blaskova GD (2009) Appl Surf Sci 256:779–789
44. Ram S, Gautam A, Fecht HJ, Cai J, Bansmann H, Behm RJ (2007) Philos Mag Lett 87:361
45. Malik TG-A, Latif RM-A, Sawaby A, Ahmed SM (2008) J Appl Sci Res 4:331
46. Coiai S, Passaglia E, Pucci A, Ruggeri G (2015) Materials 8:3377–3427
47. Camargo PHC, Satyanarayana KG, Wypych F (2009) Mat Res 12(1):1–39
48. Heilmann A (2010) Polymer films with embedded metal nanoparticles. Springer Series in Materials Science, Springer, Berlin
49. Kunckel J (1689) Ars Vitraria Experimentalis oder Vollkommene Glasmacherkunst, Frankfurt
50. Faraday M (1857) Phil Trans R Soc Lond 147:145–181
51. Quinten M (2011) Optical properties of nanoparticle systems: mie and beyond. Wiley-VCH Verlag & Co., Germany
52. Steubing W (1908) Ann Phys (Leipzig) 26:329–371
53. Keirbeg U, Vollmer M (1995) Optical properties of metal clusters (Springer Series in Material Science No 25). Springer, Berlin
54. Heilman A (2003) Polymer films with embedded metal nanoparticles. Springer, Berlin
55. Schonauer D, Kreibig U (1985) Surf Sci 156:100–111
56. Mie G (1908) Ann Phys (Leipzig) 25:377–445
57. Henglein A (1989) Chem Rev 89:1861
58. Liu Fu-K, Hsieh S-Y, Ko Fu-H, Chu T-C (2003) Colloids Surf A Physicochem Eng Aspects 231:31–38
59. El-Sayed MA (2004) Acc Chem Res 37:326–333
60. Li S, Lin MM, Toprak MS, Kim DK, Muhammed M (2010) Nano Rev 1:5214
61. Lüdersdorff FW. Verh. Verein. Beförderung Gewerbefleiss. 1833 Preussen 12:224
62. Garnett JCM (1904) Philos Trans R Soc London 203:385–420
63. Caseri W (2000) Macromol Rapid Comm 21:705–722
64. Maier SA, Kik PG, Atwater HA, Sheffer M, Harel E, Koel BE, Requicha AAG (2003) Nat Mater 2:229
65. Lu J, Moon K-S, Xu J, Wong CP (2006) J Mater Chem 16:1543
66. Xia Y, Halas XJ (2005) MRS Bull 30:338
67. Srivastava S, Haridas M, Basu JK (2008) Bull Mater Sci 31:213
68. Li S, Lin MM, Toprak MS, Kim KD, Muhammed M (2010) Nano Rev 1:5214
69. Qiu K, Netravali AN (2013) Polym Compos 34:799–809
70. Razzak MT, Darwis D, Zainuddin S (2001) Radiat Phys Chem 62:107–113
71. Demerlis CC, Schoneker DR (2003) Food Chem Toxicol 41:319–326
72. Chiellini E, Corti A, D'Antone S, Solaro R (2003) Prog Polym Sci 28:963–1014
73. Solaro R, Corti A, Chiellini E (2000) Polym Adv Technol 11:873–878
74. Devi CU, Sharma AK, Rao VVRN (2002) Mater Lett 56:167
75. Khanna PK, Singh N, Charan S, Subbarao VVVS, Gokhale R, Mulik UP (2005) J Mater Chem Phys 93:117
76. Perelaer J, Hendriks C, de Laat AWM, Schubert US (2009) Nanotechnology 20:165303
77. Rai M, Yadav A, Gade A (2009) Biotechnol Adv 27:76–83
78. Toker RD, Kayaman-Apohan N, Kahraman MV (2013) Prog Org Coat 76:1243–1250

79. Evans RD (1955) The atomic nucleus. Tata McGraw-Hill Publishing Company, New York
80. Chapiro A (1962) Radiation chemistry of polymeric systems. Wiley, UK
81. Leo WR (1994) Techniques for nuclear and particle physics experiments—a how-to approach. Springer, Berlin
82. Sinha D, Phukan T, Tripathy SP, Mishra R, Dwivedi KK (2001) Radiat Meas 34:109–111
83. Saad AF, Atwa ST, Yokota R, Fujii M (2005) Radiat Meas 40:780–784
84. Fink D (ed) (2004) Fundamentals of ion-irradiated polymers. Springer, Berlin
85. Ritchie RH, Claussen C (1982) Nucl Instrum Methods B 198:133–138
86. Fink D, Chadderton L (2005) Braz J Phys 35(3B):735–740
87. Ziegler JF, Biersack JP, Littmark U (1985) The stopping and range of ions in matter. Pergamon, New York
88. Aumayr F, Winter HP (2005) Nucl Instrum Methods B 233:111
89. Prakash J, Pivin JC, Swart H (2015) Adv Coll Interface Sci 226:187–202
90. Kharisov BI, Kharissova OV, Mendez UO, Radiation synthesis of materials and compounds. ISBN 9781466505223 - CAT# K14554, pp 11–18
91. Fujita H, Izawa M, Yamazaki H (1962) Nature 196:666–667
92. Marignier JL, Belloni J, Delcourt M, Chevalier JP (1985) Nature 317:344–345
93. Henglein A (1989) Chem Rev 89:1861–1873
94. Belloni J, Amblard J, Marignier JL, Mostafavi M (1994) Cluster atoms and molecules. In: Haberland H (ed), vol 2. Springer, Berlin
95. Belloni J, Mostafavi M, Remita H, Marignier JL, Delcourt MO (1998) New J Chem 22:1239–1255
96. Drobny JG (2003) Radiation technology for polymers. CRC Press LLC
97. Choi SH, Lee K-P, Park S-B (2003) Study Surf Catal 146:93
98. Choi S-H, Choi MS, KP Lee, Kang HD (2004) J Appl Polym Sci 91(4):2335
99. Kang Y-O, Choi S-H, Gopalan A, Lee K-P, Kang H-D (2006) Song YS 352:463–468
100. Rao YN, Banerjee D, Datta A, Das SK, Guin R, Saha A (2010) Radiat Phy Chem 79:1240–1246
101. Ali Y, Kumar V, Sonkawade RG, Dhaliwal AS, Swart HC (2014) Vacuum 99:265–271
102. Kim S, Jeong J-O, Lee S, Park J-S, Gwon H-J, Jeong SI, Hardy JG, Lim Y-M, Lee JY (2018) Sci Rep 8:3721
103. Atif M, Bongiovanni R, Yang J (2015) Polym Rev 55:90–106
104. Oldring PKT (ed) (1991) Chemistry and technology of UV and EB formulation for coatings, inks and paints. SITA Techn, London, Vols 1È5
105. Ravijst JP (1990) Proc Rad Tech Conf 1: 278 (Chicago)
106. Decker C (1998) Polym Int 45:133–141
107. Pappas SP (ed) (1992) Radiation curing science and technology. Plenum Press, New York
108. Balan L, Burget D (2006) Euro Poly J 42(12):3180–3189
109. Lu Y, Mei Y, Schrinner M, Ballauff M, Möller MW, Breu J (2007) J Phys Chem C 111 (21):7676–7681
110. Shameli K, Ahmad MB, Yunus WMZW, Rustaiyan A, Ibrahim NA, Zargar M, Abdollahi Y (2010) Intern J Nanomed 5:875
111. Forrest SR, Kaplan ML, Schmidt PH, Venkatesan T, Lovinger AJ (1982) App Phy Lett 41:708. https://doi.org/10.1063/1.93642
112. Hioki T, Noda S, Sugiura M, Kakeno M, Yamada K, Kawamoto J (1983) Appl Phys Lett 43:30
113. Fink D, Moller M, Chadderton LT, Cannington PH, Elliman RG, Mcdonald DC (1988) Nucl Inst Meth Phys Res B 32:125–130
114. Goyal PK, Kumar V, Gupta R, Mahendia S, Sharma T, Kumar S (2011) Adv App Sci Res 2(3):227–231
115. Kumar S, Kumar R, Singh DP (2009) App Surf Sci 255:8014–8018
116. Prakash J, Tripathi A, Rigato V, Pivin JC, Tripathi J, Chae KH, Gautam S, Kumar P, Asokan K, Avasthi DK (2011) J Phys D Appl Phys 44:125302

117. Prakash J, Tripathi A, Laxmi GVBS, Rigato V, Tripathi J, Avasthi DK (2013) Adv Mat Lett 4(6):408–412
118. Prakash J, Tripathi A, Khan SA, Kumar S, Singh F, Tripathi JK, Tripathi J (2011) Rad Eff Defs Sol 166(8):682–688
119. Zaporojtchenko V, Zekonyte J, Wille S, Schuermann U, Faupel F (2005) Nucl Inst Meth B 236:95–102
120. Wang L, Angert N, Trautmann C, Vetter J (1995) J. Adhes Sci Techn 9:1523–1529
121. Zaprorjtchnko V, Zenkonyte J, Faupel F (2007) Nucl Inst Meth B 265:139–145
122. Mishra YK, Chakravadhanula VSK, Schurmann U, Kumar H, Kabiraj D, Ghosh S, Zaporojtchenko V, Avasthi DK, Faupel F (2008) Nucl Inst Meth B 266:1804–1809
123. Prakash J, Tripathi J, Khan SA, Pivin JC, Singh F, Tripathi J, Kumar S, Avasthi DK (2010) Vacuum 84(11):1275–1279
124. Biswas A, Avasthi DK, Fink D, Kanzow J, Schurmann U, Ding SJ, Aktas OC, Saeed U, Zaporojtchenko V, Faupel F, Gupta R, Kumar N (2004) Nucl Inst Meth B 217:39–50
125. Singh F, Mohapatra S, Stoquert JP, Avasthi DK, Pivin JC (2009). 267:936–940
126. Ali Y, Kumar V, Sonkawade RG, Dhaliwal AS (2013) Vacuum 90:59–64
127. Singhal P, Rattan S (2016) J Phys Chem B 120(13):3403–3413
128. Efimov AM (1995) Optical constants of inorganic glasses. CRC Press, USA
129. Bach H, Neuroth N (1995) The properties of optical glass. Springer, Berlin
130. Fox AM (2010) Optical properties of solids, 2nd edn. Oxford University Press, New York
131. Oreski G, Tscharnuter D, Wallner GM (2008) Macromol Symp 265:124
132. Kumar V, Goyal PK, Mahendia S, Gupta R, Sharma T, Kumar S (2011) Rad Eff Def Solids 166:109
133. Migahed MD, Zidan HM (2006) Current App Phys 6:91
134. Tauc J, Grigorovivi R, Vancu A (1966) Stat Sol 15:627–637
135. Tauc J (1974) Amorphous and liquid semiconductors. Plenum Press
136. Datta T, Woollam JA, Notohamiprodjo W (1989) Phy Rev B 40:5956–5960
137. Mostafavi M, Delcourt MO, Picq G (1993) J Radiat Phys Chem 41:453
138. Linnert T, Mulvaney P, Henglein A et al (1990) J Am Chem Soc 112:4657–4664
139. Sudeep PK, Kamat PV (2005) Chem Mater 17:5404–5410
140. Janata E, Henglein A, Ershovt BG (1994) J Phys Chem 98:10888–10890
141. Overbeek JTG (1982) Adv Colloid Interface Sci 15:251–277
142. Temgire MK, Joshi SS (2004) Rad Phys Chem 71:1039–1044
143. Wu W, Wang Y, Shi L, Zhu Q, Pang W, Xu G, Lu F (2005) Nanotechnology 16:3017–3022
144. Nho Y, Moon S et al (2005) J Ind Eng Chem 11:159–164
145. Ramya CS, Savitha T, Selvasekarapandian S, Hirankumar G (2005) Ionics 11:436
146. Link S, El-sayed MA (1999) J Phys Chem B 103:8410–8426
147. Kreibig U, Bour G, Hilger A, Gartz M (1999) Phys Stat Sol (a) 175:351–366
148. Garcia MA (2011) J Phys D Appl Phys 44:283001
149. Kumar G, Tripathi VK (2007) Appl Phys Lett 91:161503
150. Huang HH, Ni XP, Loy GL, Chew CH, Tan KL, Loh FC, Deng JF, Xu GQ (1996) Langmuir 12:909–912
151. Singh F, Mohanta S, Stoguert JP, Avasthi DK, Pivin JC (2009) Nucl Instr Meth Phys Res B 267:936–940
152. Avasthi DK, Mehta GK (2011) Swift heavy ions for materials engineering and nanostructuring. Springer Series in Materials Science, Berlin
153. Abargues R, Marques-Hueso J, Canet-Ferrer J, Pedrueza E, Valdes JL, Jimenez E, Martınez-Pastor JP (2008) Nanotechnology 19:355308
154. Eisa WH, Abdel-Moneam YK, Shaaban Y, Abdel-Fattah AA, Zeid AMA (2011) Mater Chem Phys 128:109–113
155. Sharma K, Chahal RP, Mahendia S, Tomar AK, Kumar S (2013) Rad Eff Def Solids 168 (5):378–384
156. Bhat NV, Nate MM, Kurup MB, Bambole VA, Sabharwal S (2005) Nucl Instrum Methods B 237:585–592

157. Fink D et al (1995) Radiat Eff Def Solids 133:193–208
158. Sellmeier W (1871) Ann Phys Chem 143:271
159. Wemple SH, DiDomenico M (1970) Phys Rev B 3:1338–1351
160. Bhar O, Pinto JC (1991) J Appl Polym Sci 42:2795–2809
161. Lorimer JW (1972) Polymer 13:2274–2276
162. Bhat NV, Nate MM, Kurup MB, Bambole VA, Sabharwal S (2005) Nucl Instrum Methods B 237:585–592
163. Charis MNC et al (2011) J Appl Polym Sci 122:1572–1578
164. Kumar G, Singh DB, Tripathi VK (2006) J Phys D Appl Phys 39:4436–4439
165. Gautam A, Ram S (2010) Mater Chem Phys 119:266–271
166. Vij A, Singh S, Kumar R, Lochab SP, Kumar VVS, Singh N (2009) J Phys D Appl Phys 42:105103
167. Finch CA (1973) Polyvinyl alcohol properties and application. Wiley, Hoboken
168. Mbhele ZH et al (2003) Chem Mater 15:5019–5024
169. Shah S, Singh NL, Gavade C, Shivakumar V, Sulania I, Tripathi A, Singh F, Avasthi DK, Upadhyay RV (2010) Integr Ferroelectr Int J 117:97–103
170. Thomas PS, Stuart BH (1997) Spectro Chemica Acta: Part A 53:2275–2278
171. Lin WC, Yang MC (2005) Macromol Rapid Commun 26:1942–1947
172. Yu DG, Lin WC, Lin CH, Chang LM, Yang MC (2007) Mater Chem Phys 101:93–98
173. Tripathi J, Keller JM, Das K, Tripathi S, Sripathi T (2012) J Phys Chem Solids 73:1026–1033
174. Kumar CSSR (2012) Raman spectroscopy for nanomaterials characterization. Springer, Berlin
175. Macleod HA (2001) Thin film optical filters, 3rd edn. Institute of Physics Publishing, Bristol and Philadelphia
176. Liu Y, Guy OJ, Patel J, Ashraf H, Knight N (2013) Microelectron Eng 110:418–421
177. Askar K, Phillips BM, Fang Y, Choi B, Gozubenli N, Jiang P, Jiang B (2013) Colloids Surf: A Physicochem Eng Aspects 439:84–100
178. Jin KW, Cai S, Hua W, Da S, Xiu F, Jing L (2010) Chin Phys B 19:044210
179. Chahal RP, Mahendia S, Tomar AK, Kumar S (2016) Opt Mater 52:237–241

Swift Heavy Ion Irradiation Effects on the Properties of Conducting Polymer Nanostructures

J. Hazarika and A. Kumar

Abstract This chapter presents the basic concepts of conducting or π-conjugated polymers and their different nanostructures and physico-chemical properties, which ushered in a new era of functional organic materials with potential applications. Most importantly, they can replace the traditional metallic conductors owing to their excellent properties of high conductivity, thermal stability, light weight, low corrosion, high flexibility, ease of synthesis and low cost. The first studied conducting polymer was polyacetylene, and in the last two decades, the most extensively studied conducting polymers are polyaniline (PAni), polypyrrole (PPy) and polythiophine (PTh) and their derivatives owing to their interesting physico-chemical properties. Irradiation on polymers with energetic heavy ions is used to tailor their different physico-chemical properties. The energetic heavy ion irradiation-induced modifications on various properties of polymers depends on various parameters viz. type of energy transferred (i.e., nuclear or electronic) to the target, species of ion and ion fluences. The ion-matter interaction with low energy (eV to keV) range causes implantation of the ions, while ions with high energy (keV to MeV) interaction cause irreversible structural modification along the cylindrical ion track, which is of the order of few nanometers in diameter. The fundamental aspects of ion-solid interaction, different related parameters and models governing the ion-solid interaction have been described in details in this chapter. PPy nanotubes, potential candidate of highly conducting π-conjugated polymers, have been chosen for irradiation at different ion fluences to enhance their structural, morphological, electrical, optical and thermal properties. Room temperature swift heavy ion (SHI) irradiation on thin PPy films (thickness $\sim$30–35 μm) was investigated under high vacuum ($\sim 10^{-5}$ Torr) condition by 160 MeV Ni^{12+} SHI using various irradiation fluences such as 10^{10}, 5×10^{10}, 10^{11}, 5×10^{11} and 10^{12} ions/cm^2. High-resolution transmission electron microscopy (HRTEM) was used to investigate the morphological changes of SHI-irradiated PPy nanotubes. The irradiated nanotubes exhibit denser structure, and density is highest at 5×10^{11} ions/cm^2 irradiation fluence. However, on irradiation with the highest ion

J. Hazarika · A. Kumar (✉)
Department of Physics, Tezpur University, Napaam, 784028 Tezpur, Assam, India
e-mail: ask@tezu.ernet.in

V. Kumar et al. (eds.), *Radiation Effects in Polymeric Materials*, Springer Series on Polymer and Composite Materials, https://doi.org/10.1007/978-3-030-05770-1_6

fluence of 10^{12} ions/cm^2, the density of irradiated PPy nanotubes is decreased. Up to the ion fluence of 5×10^{11} ions/cm^2, reduction in optical band gap energy (E_g) of irradiated PPy nanotubes is observed; however, at the investigated highest irradiation fluence of 10^{12} ions/cm^2, value of E_g is found to be higher as compared to the unirradiated PPy nanotubes. Micro-Raman studies exhibit that upon SHI irradiation up to the ion fluence of 5×10^{11} ions/cm^2, the π-conjugation length and crystallinity of PPy nanotubes are increased. Thermogravimetric analysis (TGA) shows enhanced thermal stability of irradiated PPy nanotubes with increasing ion fluence, while thermal stability of PPy nanotubes decreases at the highest irradiation fluence. The current-voltage (*I-V*) characteristics for the irradiated PPy nanotubes get enhanced with increasing ion fluence, while their *I-V* characteristics decrease at the highest irradiation fluence of 10^{12} ions/cm^2. The scaling of modulus spectra of irradiated PPy nanotubes at different irradiation fluences depicts irradiation fluence-independent relaxation dynamics of charge carriers. At the end of the chapter, the challenges in the field of ion-matter interaction in pre-/post-irradiation as well as the processing, characterization and application of the target materials have been discussed.

Keywords Conducting polymer nanostructures · Polypyrrole (PPy) nanotubes · Ion-matter interaction · Swift heavy ion irradiation · Dielectric properties · AC conductivity

1 Introduction

Conducting or π-conjugated polymers with additional functionality having electrical conductivity ranging from insulating to metallic regime have brought remarkable attention because of their exciting physical properties of light weight, flexibility, low cost, good mechanical and thermal stability [1]. The most extensively studied various conducting polymers are polyaniline (PAni), polypyrrole (PPy), polythiophene (PTh) and poly(3, 4-ethylenedioxythiophene) (PEDOT) with electrical conductivities ranging from 10^{-10} to 10^5 S/cm [2]. Figure 1 depicts the structures of the mostly studied conducting polymers. Among the various π-conjugated polymers, polypyrrole (PPy) has been studied widely because of their various potential applications in chemical and biosensors, corrosion protection, actuators, drug delivery devices, super-capacitors, microwave shielding, advanced polymeric batteries, electrochromic windows, etc. because of their excellent properties of ease of synthesis, remarkable electrical conductivity, redox reversibility, good thermal and environmental stability, good optical transparency, biocompatibility, high flexibility and low toxicity [3–7]. Compared with bulk counterparts, nanostructured conducting polymers exhibit high performance in various potential devices due to their high surface to volume aspect ratio, electrical conductivity and light weight [8]. Various methods are used for the synthesis of nanostructured conducting polymers which can be used as the building blocks for nano-electronic

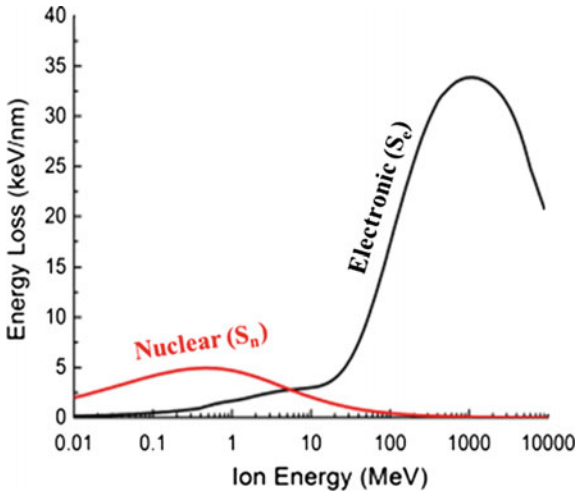

Fig. 1 Typical electronic and nuclear energy losses versus irradiated ion energy

devices. Being a one-dimensional (1-D) structure, synthesis of PPy nanotubes has gained remarkable attention in fundamental research and industrial application due to their comparable metallic conductivity and possible application as molecular wires [9]. In recent application, PPy nanotubes have been used in biosensors which include glucose biosensor based on nanohybrids of carboxylated polypyrrole nanotube wrapped on graphene sheet transducer [10] and PPy nanotubes embedded on reduced graphene oxide transducer for H_2O_2 biosensor [11]. Various methods can be used to synthesize PPy nanotubes which include primarily the template synthesis [12], reactive self-degradation [13], electrochemical approach [14] and self-assembly polymerization [15]. Using hard template polymerization, nanotubes of conducting polymers with controllable morphology can be synthesized successfully, however, not because of the dissolution of external template after polymerization; this synthesis method suffers a serious disadvantage. This may lead to the destruction of the resulting conducting polymer nanotubes thereby limiting their applicability in various potential applications. Although high-quality nanotubes of conducting polymers can be synthesized using reactive self-degrade approach, this method is a costly one due to the use of reactive template. To overcome the disadvantages of the above-mentioned synthesis methods, an alternative template-free self-assembly method has gained more attention owing to its simplicity, cost effectiveness and large-scale production. Besides the various advantages of self-assembly method, another additional important advantage of this synthesis method is that the soft template used to guide the formation of nanotubes also acts as dopant [16, 17].

In previous studies, many researchers have reported on the self-assembled synthesis of high-quality 1-D nanotubes of conducting polymers doped with various dopants such as naphthalene sulfonic acid (NSA) [18], azobenzene sulfonic acid [19] and *p*-toluene sulfonic acid (*p*-TSA) [18], which also act as a soft template

during the polymerization. The morphology, diameter and length of the nanotubes of conducting polymers depend on the various factors of the synthesis conditions viz. dopant to monomer ratio, types of dopant used and their concentration, and also on the reaction temperature [20]. However, the permanent entrapment of larger-size macromolecules as dopant within conducting polymer nanostructures can confer additional functionalities for building specific recognition sites to show improvement in various properties. In a previous study, the oxidative polymerization of PAni nanotubes by self-assembly approach using various dopants such as poly (4-styrenesulfonic acid) (PSSA), poly(acrylic acid) (PAA) and poly(methyl vinyl ether-alt-maleic acid) (PMVEA) was reported by Zhang et al. [21]. This study clearly showed that use of the polymeric acids as dopants greatly affected the outer diameter of the resulting PAni nanotubes. In a different study, the self-assembled synthesis of CSA-doped PAni nanotubes having diameter range 80–180 nm and electrical conductivity range 3.4×10^{-3}–3.5×10^{-1} Scm^{-1} was successfully reported by Wan et al. [22], which also investigated that the various synthesis conditions, especially the molar ratio of CSA to aniline and the concentration of CSA affected the formation probability, morphology and size of the PAni nanotubes. This chapter presents the irradiation effects of swift heavy ions (SHIs) on various properties of PPy nanotubes synthesized by self-assembly method. Different irradiation fluence-dependent modifications on the structural, chemical, thermal and optical properties of the irradiated PPy nanotubes have been investigated in this chapter. Studies on the dielectric properties and ac conductivity of SHI-irradiated PPy nanotubes at different ion fluences also have been reported in comparison with the properties of the pristine PPy nanotubes.

2 Ion-Matter Interaction

The unique technique of irradiation with energetic heavy ions is extensively used to engineer the properties of materials on the micro- and nanoscale level by suitable selection of the ion beam parameters viz. ion type and energy, mass and ion fluence. Modification in materials by swift heavy ions (SHIs) has a wider range of application in industry that includes the creation of nanopores in polymeric materials [23]. The devices based on irradiated polymeric membranes allow controlled drug delivery in biomedicine [24] or filter out the bacteria from water. Numerous experiments have been carried out in the last few decades using the large-scale facilities for a good understanding of the interaction of SHI with materials. An energetic heavy ion with MeV energy range and very high velocity comparable to the Bohr's electron velocity produces a continuous cylindrical permanent damage of the material with a few nanometers width and typically several tens of micrometer scale. Various kinds of solids are SHI irradiation sensitive, typically almost all the insulators including inorganic solids and polymers, semiconductors and also a few types of metals. For irradiation-induced modifications in materials, in general, the sufficient range of ion fluence lies from 10^6 to 10^{11} ions/cm^2,

which can be achieved with projectile ion beam intensity of few nA current that corresponds to 10^{10} ions/s or even less. The energetic projectile ion interacts with the target atoms primarily by the process of collision which causes excitation and ionization of the target electrons resulting in permanent modification of the materials. The energy transfer by the projectile ion to the target material takes place via two fundamental processes: (a) nuclear energy loss (S_n), which is due to the direct collision of ions with the lattice atoms, and (b) electronic energy loss (S_e), which is due to the excitations and ionization of the target atoms or electrons. These two processes exhibit a distinct dependence on incident ion energy, as depicted in Fig. 1.

The process of nuclear energy loss is dominant at sufficiently low energy ($\sim$1 keV/u), whereas the process of electronic energy loss is dominant at a larger energy than $\sim$100 keV/u. For projectile ion beam energy $\sim$1 MeV/u, value of electronic energy loss (S_e) is almost two orders higher as compared to nuclear energy loss (S_n). For SHI irradiation on materials, the energy of heavy projectile ions mainly deposits on the electronic subsystem of the irradiated sample. The total number and mobility of the excited and ionized electrons due to SHI irradiation play a crucial role in inducing irreversible modifications of the structural properties of the irradiated material [26]. The situation is much more complex in which the transfer of ion energy to the lattice is by the process of atomic collisions. However, the deposition of ion energy in solids is an inhomogeneous process, rather the deposited energy follows a radical distribution of $1/r^2$, where r represents the radial distance from the cylindrical ion trajectory [27]. The deposited energy density on the irradiated material also depends on the velocity of projectile ion beam, especially for higher-velocity projectiles, the deposited energy is smeared out into a large radius of few nanometers. The interaction mechanism of a SHI and a slow highly charged ion with a solid target is depicted in Fig. 2. In both the interaction processes, the excitation of the electronic subsystem takes place in the time scale of femtosecond, wherein the motion of atoms and induced structural disorder occur on the time scale of a few picoseconds. The disorder produced in the atomic subsystem is quenched due to rapid thermal cooling after the passage of energetic ion, and hence, the induced damage caused by SHI irradiation extends deep into the bulk material. During the passage of SHI through target, it also causes the ionization of the atoms in a cylindrical zone of few nm in diameter. However, the neutralization of charges takes place on the time scale of femtosecond.

The process of electronic stopping in the irradiated target is governed due to the inelastic collisions of the heavy energetic ion with the target electrons which may be either in free or in bound state. In electronic stopping, various physical mechanisms are associated, namely the excitation of target electrons into the conduction band, ionization of target atoms, collective electronic excitations such as plasmons [28–31]. During the passage of SHI through a material, heat energy is generated owing to the electronic excitation along the cylindrical latent track which as a result greatly affects the electronic structure of the material as the outcome of the ion irradiation. In particular, in case of a metal, the electronic excitations induced by SHI irradiation are delocalized due to the presence of conduction electrons,

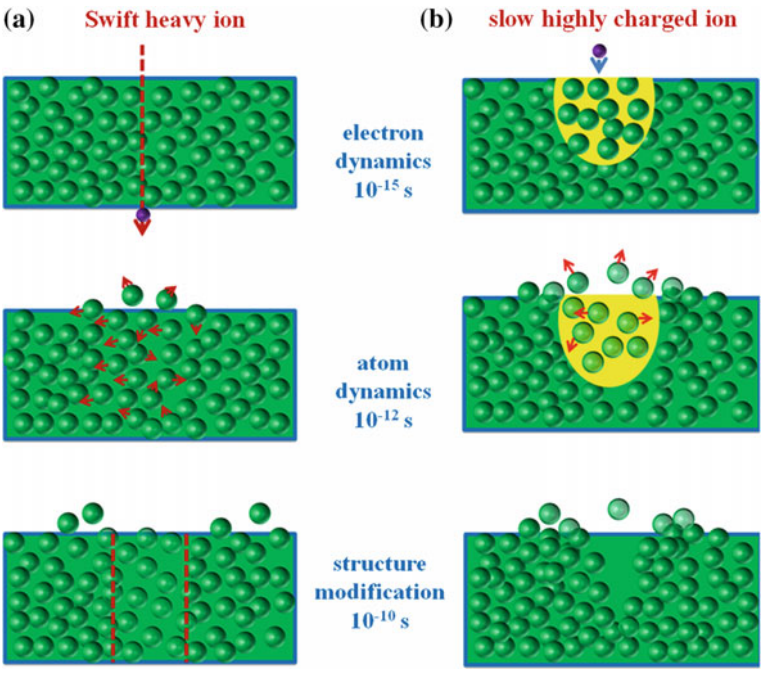

Fig. 2 Schematic diagram of the interaction of a SHI with a solid target

which may lead the excitations less likely to cause the atomic motion so that the irradiation-induced damage results mostly from the knock-on atom displacements. However, in case of an insulator, the deposition of electronic energy above a certain critical energy value, called the threshold energy [32], the excitations produced may lead to strong heating and damage of the lattice [33]. The cylindrical form of heat spikes in SHI-irradiated material is called the "latent tracks" produced in the amorphous regions that appear along the ion trajectory. In general, the generated cylindrical ion tracks arrange themselves in an ordered way along the direction of projectile ion beam and can be viewed in the form of patterned nanostructures inside the bulk material. Because of various associated physical processes, the effects of ion-solid interactions on target material may extend beyond the initial collision process. The various induced defects during the course of SHI irradiation migrate arbitrarily far in the sample rather their recombination during the cascade development with each other.

Nuclear stopping mechanism originates from the ballistic collisions of the projectile ions with the nuclei of the target atoms, so that whole of the ion's kinetic energy is transmitted to a target atom resulting in the translational motion of atoms. The dominant nuclear energy loss is determined by the screened Coulomb interactions and momentum transfer. The occurrence of the nuclear collisions at higher energies is due to the sequence of independent binary collisions of atoms, in which

the projectile ion moves almost in a straight path, and the predominant energy loss of the ion is by electronic stopping. For independent collisions, distance between the successive collisions must be at least two inter-atomic spacing of about 2–3 Å. The system does not attain thermodynamic equilibrium at the initial stage of a cascade since all the induced atomic motion takes place in the time scale of 100 *fs* which is much faster than that of the thermodynamic relaxation time. Upon deposition of enough energy of the ion, several collisions take place in the close vicinity of each other in which the concept of binary collision does not apply anymore; rather the cascade becomes a complex many-body problem thereby leading to the complete breakup of the lattice. With higher kinetic energy of the recoils, the region of overlapping collisions is called as a "heat spike" or "thermal spike." In denser materials, the heat spikes are important for heavy projectiles, and in bulk materials, the hotter region cools down immediately because of the rapid heat conduction to the surrounding lattice [34].

The ion-solid interaction induces irreversible macroscopic modifications of structural, chemical, morphological, electrical, optical, thermal properties of the ion-irradiated material. These modifications can be attributed to the transformations at microscopic scale through the various processes of electronic excitation, ionization, cross-linking, chain scissioning, bond breaking and formation of clusters as well as mass losses in the material due to large electronic energy deposition [35, 36]. The SHI irradiation-induced modifications in physico-chemical properties of materials depend on the various parameters of the projectile such as ion species, ion energy, and fluence and also on the target. For lower ion fluences, the irradiation-induced damage zone is localized in a region with diameter of the order of few nanometers (nm) [37]. However, for higher irradiation fluence, the irradiation-induced damage is of the order of few micrometers which can cause mass transports of the irradiated zone. The various kinds of interactions that take place in the damaged zones play a crucial role in making irreversible modifications of various properties of the material under SHI irradiation. For lower ion fluences, there is no overlap of the induced damaged zones with each other, while the induced damages increase linearly with ion fluence, and beyond certain ion fluence, the damage zones start to overlap with each other.

Inelastic collision is the dominant mechanism for energy transfer by SHI to the target material for producing cylindrical latent track when its energy overcomes the threshold value for the formation for ion track. However, the diameter and length of the latent track depend on the energy and type of ion beam and also on both electrical and thermal conductivity of the target material [32]. The modifications in the properties of the material irradiated by SHI are of irreversible nature which may be caused due to the high deposition of localized energy density within a confined region, and this whole process is far from the thermal equilibrium [38, 39]. The irradiated material can attain a very high temperature during the passage of SHI so that the target starts to melt in few picoseconds. The trail of the cylindrical latent track results due to the rapid solidification ($\sim$10–100 *ps*) of the melting portion in the SHI-irradiated material along the ion trajectory. Figure 3 depicts the block diagram for SHI irradiation in materials.

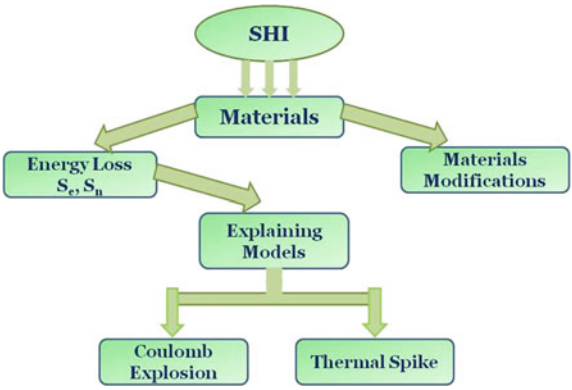

Fig. 3 Block diagram for SHI irradiation in materials

The ion-solid interaction mechanism is a complicated process that involves both the primary and secondary phenomena. To explain the formation of ion track, two basic models have been proposed: (i) thermal spike model and (ii) Coulomb explosion model. The number and mobility of electrons are the key parameters in both the models. The fundamental details of two models are discussed in the following section.

2.1 Thermal Spike Model

To analyze the ion-solid interaction mechanisms, two thermal spike models, namely (a) inelastic thermal spike model (ITSM) and (b) analytical thermal spike model (ATSM), have been widely used.

(a) ***Inelastic thermal spike model (ITSM)***

During its passage though a solid, a swift heavy ion along its path produces high ionization in a small localized cylindrical zone. Upon SHI irradiation in solid material, the excited primary electrons and generated induced lattice ions subsequently produce the excitation of many secondary electrons along the ion trajectory. If the time needed for the charge neutralization is sufficiently large, then the strong electric interaction among the ions results in the enhancement of their kinetic energies. However, if the repulsive interaction among the highly charged lattice ions is much larger than that of the mechanical strength of the solid, this interaction may lead to the destruction in the original structure of the target solid material.

The irradiated ion deposits its energy mainly in the electric subsystem of the material. Primarily the deposited energy transfers to the lattice atoms in the relaxation process, which leads to the formation of a high-temperature regime called the thermal spike. According to the ITSM [40], the energy transfers and SHI irradiation-induced damage formation can be explained using two-temperature model (TTM) [41]. In this model, a local equilibrium is established in both the

electron and phonon subsystems of the material, which are characterized by the electron temperature (T_e) and lattice temperature (T_a). Two coupled Fourier equations can be used as mentioned below to describe the nature of heat flow in both the electronic and lattice systems and also between them.

$$C_e T_e \frac{\partial T_e}{\partial t} = \frac{1}{r}\frac{\partial}{\partial r}\left[rK_e(T_e)\frac{\partial T_e}{\partial r}\right] - G(T_e - T_a) + A(r,t) \tag{1}$$

$$C_a T_a \frac{\partial T_a}{\partial t} = \frac{1}{r}\frac{\partial}{\partial r}\left[rK_a(T_a)\frac{\partial T_a}{\partial r}\right] + G(T_e - T_a) \tag{2}$$

where the parameters C, K and T represent the volume-specific heat capacity, thermal conductivity and temperature, respectively, and r gives the radial distance from the trajectory. The term $G(T_e - T_a)$ represents the coupling between the systems which arises due to the electron-phonon interaction and $A(r,t)$ represents the energy density per unit time of the target electrons. The actual form of $A(r,t)$ can be understood in terms of the distribution of radial energy of the secondary electrons as explained by Waligorski [42]. The most crucial features of ITSM are pointed out as follows [40]:

(i) The relaxation of the excited electron in the irradiated system is controlled by the electron-phonon coupling in the time limit, $t < 1$ *fs*.
(ii) The thermal energy of the generated spike increases up to the electronic stopping power S_e of the material.
(iii) Size of the latent track is defined by the maximum radial zone which associates with sufficient energy for melting.
(iv) Both the mean free path λ of the electron-phonon coupling and heat of fusion L are the free parameters of the model.

This model can be successfully applied to understand the various irradiation-induced effects in insulators, semiconductors, metals and also to materials with highly anisotropic conduction [43].

(b) ***Analytical thermal spike model (ATSM)***

According to ATSM, the increase in temperature $\nabla T(r,t)$ upon ion-solid irradiation is given by a Gaussian distribution function [44–46] as follows:

$$\nabla T(r,t) = \frac{Q}{\pi a^2(t)} e^{\frac{-r^2}{a^2(t)}} \tag{3}$$

where ∇T is the increase in temperature of solid target at a distance r from the ion trajectory, and the time is zero when the spike temperature reaches its maximum value. The increase in temperature ∇T is localized into a small cylindrical region and it lasts for a particular time period of the order of 10^{-12}–10^{-11} *s* depending on the radius of cylinder and thermal diffusivity of the target. This time scale is sufficient for damage of the lattice, and as a result, an amorphous phase can be

quenched due to the high cooling rate. The time t is typically less than picoseconds after the passage of the ion [47]. The temporal coherence that contains in $a(t)$ is related to the full width at half maxima (FWHM) of the thermal spike. The heat conduction broadens the thermal spike, and it lowers the temperature in the center of the track. The amplitude of the thermal spike (Q) can be calculated from the conservation of energy as given below:

$$gS_e = \rho cQ + \rho\pi R^2 L \cong \rho cQ \tag{4}$$

Here, ρ is the density, and the specific heat capacity (c) of the material can be calculated using the Dulong–Petit formula. A fraction of the deposited energy that equals to the kinetic energy of the projectile ion is utilized to heat the lattice subsystem and can be calculated by the parameter g in Eq. (4). The radius of the ion track can be estimated from the largest radius of the melting region. The two solutions can be obtained as follows:

$$R^2 = a^2(0)\ln\frac{S_e}{S_{et}}, \quad 1 \le \frac{S_e}{S_{et}} \le e \tag{5a}$$

$$R^2 = \frac{a^2(0)}{e}\frac{S_e}{S_{et}}, \quad \frac{S_e}{S_{et}} \ge e \tag{5b}$$

$$S_{et} = \frac{\rho c\pi a^2(0)\nabla T_m}{g} \tag{5c}$$

where e is Euler's number and S_{et} is the threshold energy loss for the formation of the latent track. At higher values of S_e, the melting extends during cooling, while at lower values of S_e, the initial radius is the largest radius of the melt. The threshold energy loss can be obtained from Eqs. (3) and (4) by putting $r = 0$ and $t = 0$ by designating ∇T_m as the minimal temperature increase needed for melting. By knowing the basic parameters of the target viz. density, melting temperature and specific heat, radius of the ion track can be estimated on assuming the constant parameters $a(0)$ and g for a given target material and the projectile ion energy range. In an alternative approach, values of $a(0)$ and S_{et} can be calculated from the linear fit of the plot of the square of ion track radius versus energy loss. However, the value of g can be calculated by the process of data analysis in the linear regime by combining Eqs. (5b) and (5c). The most crucial features of the ATSM are stated as follows:

(i) The temperature $\nabla T(r,t)$ in the ion-irradiated lattice increases approximately by a Gaussian function for $t \ge 0$, whereas the peak temperature reaches its maximum value when $t = 0$.
(ii) Out of the total energy deposited, only a fraction of the deposited energy gS_e in the lattice appears as the thermal energy of the spike.

(iii) The size of the latent track is proportional to the maximum volume of the melting region defined by the maximum radial zone with $T = T_m$.
(iv) The threshold S_{et} for the formation of latent track and track evolution $R_e^2 - S_{e.}$ can be determined from the analytical equations.
(v) The initial $(t = 0)$ Gaussian width $a^2(0) = d \ln R_e^2 / dS_e$ $(R_e < a(0))$ and efficiency g are the two basic parameters of the model.
(vi) The velocity of the irradiated ions changes due to the change of thermal energy $\varepsilon = gS_e$ with specific ion energy, E.

The ATSM can be successfully applied to explain the ion-matter interactions in insulators, polymers, semiconductors and materials with highly anisotropic conduction [43].

2.2 Coulomb Explosion Model

The basic of the Coulomb explosion model is the formation of an unstable zone in which atoms are ejected into the non-excited part of the solid by Coulomb repulsion which results from the intense excitation and ionization along the trajectory of the ion during the passage of the energetic ion repulsion [48, 49]. The Coulomb explosion model was first proposed by Fleischer et al. [49], according to which upon SHI irradiation on the target, electronic excitations produce positive ions which are mutually repulsive in nature, and this is the reason for the formation of a cylindrical latent track within the material. The positively charged ions within the latent track repel each other resulting in vacancies and interstitials (i.e., Coulomb explosion) such that the time needed for electron-ion recombination is longer as compared to the Coulomb explosion time. The atomic collision range defines the core of the ion track with diameter less than 10 nm. The most crucial features of the Coulomb explosion model are pointed out as follows:

(i) Formation of tracks in the irradiated target material is possible with lower value of dielectric constant, mechanical strength and small inter-atomic spacing. The value of electrostatic stress has to be larger than the mechanical strength, and this happens only when

$$n^2 > R \equiv E\varepsilon a_0^4 / 10e^2 \tag{6}$$

(ii) The resultant latent track must be continuous which requires at least one ionization per atom, i.e., $n > 1$.
(iii) According to the Coulomb explosion model, the requirement for the formation of latent track is that the availability of electrons for replacing the ejected ones upon irradiation must be lower in number and they must not be able to replace the ejected electrons within a time scale of less than $\sim 10^{-13}$ s and hence

$$n_n < en_a / a_0 \mu_n \pi k_B T t \tag{7}$$

where n_n and n_a represent the number of free electrons and number of ionizations per atomic plane, μ_n is the mobility of the electron and k_B is the Boltzmann constant.

(iv) For track formation, the mobility of the holes created by the ejected electrons along the ion track must be smaller during irradiation, i.e., $\mu_p < a_0^2 e / t k_B T$. Bringa et al. [50] have elucidated that the two models, the Coulomb explosion and thermal spike, can define the early and late aspects of the ionized cylindrical tracks produced in the irradiated solids due to the passage of energetic ions. No matter whether the Coulomb explosion and thermal spike are used, both work successfully to explain the irradiation-induced effects since at higher excitation densities, the repulsive energy in the track produces a spike [50]. However, both the models have been used extensively in wider range to explain the formation of ion track, still there is a debate regarding the applicability of these models.

3 Ion-Matter Interaction Parameters

(i) ***Fluence*** **(ϕ)**

Ion fluence is one of the most crucial parameter related to ion beam irradiation. Fluence (ϕ) is defined as the total number of irradiating ions incident per square centimeter (ions/cm^2) on the target. The ion fluence can be estimated by beam current and the time of irradiation as follows:

$$I = Q/T = Dqe/T = \phi Aqe/T \tag{8}$$

$$\therefore T = \phi Aqe/I \tag{9}$$

where I is the ion current (nA), Q is the total charge, D is the dose, q is the charge state, e is the electronic charge and T is the time of irradiation (in sec). Since the number of particles per nano-ampere of beam current $= I/qe$ (pnA),

$$\therefore T = \phi A / \text{beam current}\,(pnA) \tag{10}$$

(ii) ***Ion energy***

The projectile ion energy depends on the charge state (q) of ion and terminal potential V_T as follows:

$$E(MeV) = (q+1)V_T + V_{inj} \tag{11}$$

4 Ion Irradiation Effects on Polymers

The ion irradiation technique has been widely used to study the irradiation-induced modifications in the physico-chemical properties of polymeric materials [51, 52]. During the passage of SHI through polymeric materials, modifications in their intra-chain or inter-chain occur to alter their properties irreversibly. Due to large deposition of electronic energy in polymeric materials by the irradiated ions, various primary phenomena such as the chain scissioning, cross-linking, formation of double and triple bonds, production of ionized species, emission of gaseous products and free radicals [53] result in the irreversible changes in the physical, electrical, dielectric, optical, thermal and mechanical properties of the polymeric materials. The changes caused in the irradiated target depends on the parameters of the projectile ion beam such as ion energy and type, mass and fluence and also on the composition, molecular weight, temperature, etc. of the target polymer. Moreover, the irradiated polymer films produce carbon clusters and sometimes nanoclusters which modifies their physical properties drastically [54, 55].

4.1 Interaction Mechanisms

The irradiation-induced modifications in the structural, compositional and surface properties of the irradiated material can take place in two ways: introduction of ion species (i.e., doping effect) and irradiation-induced defects (defect or radiation effect). For surface modification in polymers, the irradiation-induced defect is more important than that for the metals and may suppress any kind of doping effect. This arises due to the following reasons as mentioned below:

(a) In the doping effect, the implanted ion concentration is relatively lower, while the radiation effect extends throughout the whole region of the latent track and produces a high yield.
(b) Breaking of various chemical bonds in the irradiated organic substances results in the formation of ensemble of smaller molecules along with the volatile products.
(c) The damage produced by ion implantation is progressively worse in the order of metals, inorganic insulators and polymers [56].

Ion irradiation can lead to the irreversible modifications in different properties of polymers, and hence, it is crucial to understand their damage mechanism. Typically, irradiation-induced defects in polymers are produced because of the high deposition of electronic energy in which the energetic projectile ions are slowed down by momentum transfer to the target atoms, called the “nuclear stopping,” and by the process of exciting the electronic subsystem of the irradiated target, called the “electronic stopping” [57–59]. The permanent displacement of target atoms or molecules due to transfer of energy density causes the permanent damage in

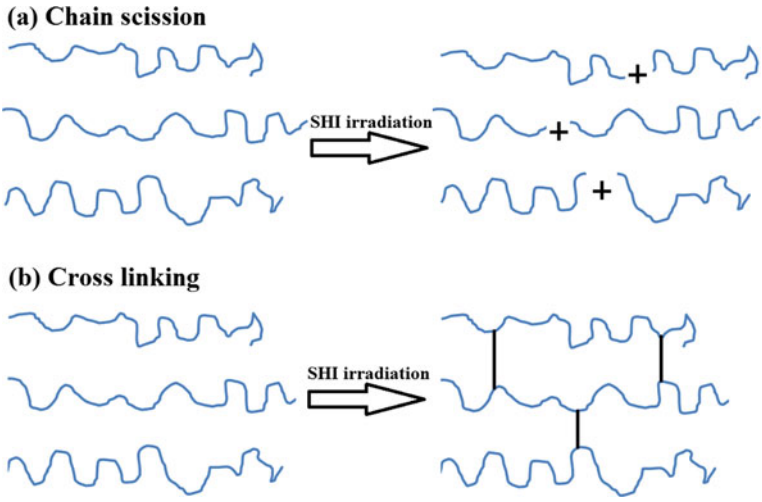

Fig. 4 Chain scission and cross-linking in the irradiated polymer

polymer materials along the ion trajectory, which is mainly due to the chain scission by displacing atoms from polymer chains (Fig. 4a).

However, the formation of free radicals that results from electronic excitation or ionization can make the cross-linking in the polymer chains (as shown in Fig. 4b), resulting in increased molecular weight, wear resistance and hardness [60] of the irradiated polymer. The phenomena of chain scission and cross-linking in the irradiated polymers can be understood from a general empirical rule based on the structure of the polymers, although it is not completely satisfactory. As, for example, in case of a vinyl polymer in which each carbon atom in the main polymer is associated with at least one hydrogen atom (or either R_1 or R_2 is hydrogen), then the polymer chains undergo cross-links upon irradiation (Fig. 5).

On the other hand, if a tetra-substituted carbon atom is present in the monomer unit (or neither R_1 nor R_2 is hydrogen), then there is the degradation in the polymer chains and chain scission upon energetic ion irradiation. Upon irradiation, the high deposition of electronic energy by the energetic ion plays a vital role in cross-linking the polymer chains, which is primarily responsible for their modification of surface properties in both keV and MeV energy ranges [61, 62]. The cross-linking in the polymer chains can increase the surface mechanical properties of the ion

Fig. 5 Structure of a vinyl polymer

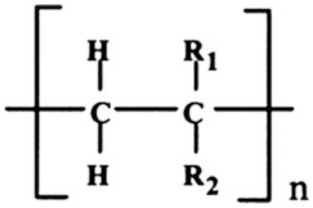

beam-modified polymer. Irradiation in polymers has been extensively used to alter their surface properties, including films, powders and fibers. Irradiation in polymeric materials by SHI has been carried out on non-polar polyolefins (polar groups at surface) to enhance their different properties such as the printability, wettability, adhesion with other materials or with the biological components, compatibility or further physico-chemical modifications [63, 64]. In general, the surface modifications of polymer films with ions involve fluences of $\sim 10^9$–10^{14} ions/cm^2 [65], or in some cases, higher fluences of 10^{15} ions/cm^2, which can lead to the destruction of the polymer material through carbonization [65].

The different parameters that affect the ion irradiation in polymers are (a) ion energy, (b) ion mass, (c) ion fluence and (d) composition of the polymer that determine the energy transferred to target, mechanism of energy deposition, and penetration range of the projectile ions in the SHI-irradiated polymer. The ions with higher electronic stopping energy produce more ionization-producing enhancement in the hardness of the irradiated polymer confirming that the cross-linking is the key factor that controls the surface-sensitive mechanical properties [57]. The profile of the electronic and nuclear energy losses can be estimated using the Monte Carlo simulation-based TRIM (transport of ions in matter) program [66]. Moreover, it is found that the ion irradiation that induces ionization in target materials varies with the atomic number of the ion and with increasing ion energy; the irradiated ions penetrate to a greater depth to the target and produce more ionization in damaged region [67].

During ion-matter interaction, many defects are produced along the ion track in which the defects formed by low-energy ion irradiation are less stable as compared to induced defects produced by high-energetic ions. At ambient temperature, a large fraction of the low-energy-induced damages anneals such that more numbers of stable but much less abundant nuclear defects are dominant. However, for high-energetic ion irradiation, this effect vanishes because of the generation of more stable defects resulting from the huge electronic energy deposition in the target. Especially for polymers upon SHI irradiation, the breaking (chain scission) and/or formation of chemical bonds (cross-linking) take place [68], in which the irradiation-induced chain scission of the polymer chains leads to an enhancement in chemical etchability of the irradiated synthetic polymers. However, the irradiated polymer films result in the formation of nano- or micropores, the so-called etched tracks that critically depend on the projectile energy transfer, polymer type and ion fluence.

Despite various studies on the formation of latent tracks in the irradiated polymers, there needs more detailed study for complete understanding of the formation mechanism about the ion tracks. The best explanation regarding formation of ion track is basically the process of energy transfer from the projectile ion to the electronic subsystem of the irradiated polymers which results in a high concentration of excited and ionized atoms along the ion trajectory. The released electrons are associated with a wider spectrum of kinetic energies and trigger a considerable number of ionizations on their own. Most of the primary excitations and ionizations occur close to the ion path with a few nanometers diameter. The energy deposited in

such a small cylinder produced along the ion trajectory is considerably higher, and the deposited energy on the target can attain the value up to several hundred eV/ . At a larger distance, in the so-called latent track, the excitations and ionizations are caused by the energetic electrons, and the maximum range of electron cascade depends primarily on the velocity of the projectile ion, and it can reach up to about 1 pm. Various modifications in the physical and chemical properties of the irradiated polymers result because of the different types of defects that are produced in the isolated or overlapping latent tracks. The nature of the SHI irradiation-induced defects and the relative radiation sensitivity of different polymers depend on the molecular weight and composition of the irradiating polymer as well as the irradiated ions and on the environmental conditions during irradiation experiment. Recent studies have reported various irradiation-induced mechanisms such as the atomic displacements, breaking of the molecular chains and production of free radicals, which are primarily responsible for causing different modifications of properties in the SHI-irradiated polymers.

Studies on SHI irradiation effects on polymers and their different nanostructures have been performed extensively from last few years because of their enhanced physico-chemical properties such as the electrical conductivity, electrochemical stability, sensing properties, energy storage device, antioxidant activity and biocompatibility. [69, 70]. Ion irradiation with energy range from 100 to 300 keV and fluence range 10^{11}–10^{14} ions cm^{-2} produced optical defects in the irradiated polystyrene [71]. A drastic increase in the electrical conductivity has been investigated in 2 MeV Ar^{+} ion-irradiated organic molecules by Forrest et al. [72]. The 100 MeV silver ion irradiation effect on the charge transport properties of the polypyrrole and poly(3-hexylthiophene) has been investigated [73], in which the electrical conductivity of polypyrrole was observed to increase with increase in irradiation fluence (from 10^{10} to 10^{12} ions cm^{-2}) without any significant changes in surface morphology and that for irradiated poly(3-hexylthiophene), the conductivity was observed to increase up to the ion fluence of 10^{11} ions cm^{-2}, while beyond this ion fluence, there was a decrease in electrical conductivity. Kumar et al. [74] studied the 40 MeV Li^{3+} SHI irradiation-induced modifications in the surface properties of silver–polypyrrole composite films at different ion fluences in the range of 10^{11}–10^{13} ions/cm^2. A significant enhancement in the surface properties has been observed upon ion irradiation, which indicates their proper use in chemical sensing applications. Ramola et al. [75] have investigated 100 MeV oxygen ion irradiation effects on both polypyrrole and CR-39 (DOP) polymers, in which the crystallinity of irradiated polymer films increased with ion fluence. The grain-like structure of the pristine PPy increased upon SHI irradiation. In previous studies, Chandra et al. [76] investigated the enhancement in structural properties and crystallinity with 80 MeV oxygen ion-irradiated polyaniline films. Furthermore, Hussain et al. [77] reported the nickel ion irradiation effects on the enhancement in the electrical conductivity, crystallinity and electrochemical stability of polyaniline. Ramola et al. [78] reported the 50 MeV Li^{3+} and 90 MeV C^{6+} SHI irradiation-induced effects on various properties of PPy films. The study showed that upon C^{6+} SHI irradiation, irradiated PPy films became more amorphous even at lower ion

fluence. However, on irradiation with Li^{3+} ions in the polypyrrole film, both the crystallinity and conductivity of the irradiated PPy films increased up to particular ion fluence, while both their crystallinity and electrical conductivity decreased at the higher irradiation fluence. In a different study, Kaur et al. [79] reported the effects of 100 MeV Ag^{8+} ions on the morphology and electrical properties of polypyrrole, whereas the surface of the irradiated PPy films became smoother and its electrical conductivity increased by two orders of magnitude. However, Chandra et al. [80] investigated the increased crystallinity and decreased optical band gap energy in the 100 MeV O^{7+} ion-irradiated PPy films.

4.2 Latent Ion Track Chemistry

The formation of latent track in irradiated polymers is characterized by two effects, namely (i) destruction of the existing components and (ii) formation of new materials. Upon SHI irradiation, the breaking of different chemical bonds in the irradiated polymers takes place when the deposited energy by the ion energy exceeds the inter-atomic bond energy of the target material. In general, the inter-atomic bonding energy is in the range of few eV, (e.g., CH_3–CH_3: 3.7 eV, H–CH: 4.3 eV) [22]. It is well reported that upon SHI ion irradiation, different types of chemical bonds do not break at a random fashion owing to high deposition of electronic energy to the polymer. However, irradiation experiment predicts that certain selectivity rule is followed for breaking of bonds, which may not consider the bond energy linearly with that of the ion beam energy. For example, in linear hydrocarbons, the C–H bonds break more prominently under irradiation than that of the C–C bonds instead of greater bond strength in C–H [22]. The breaking of chemical bonds during irradiation is strongly preferred in the core regime of cylindrical track in which electronic energy is transferred, whereas it occurs rarely in the penumbra of the ion track because of the less transfer of energy transfer densities into these regions.

Calcagno et al. [71] studied the optical and rheological properties of 100 keV H and 300 keV He ion irradiation effects on PS film in the single ion track regime. The calculated cross-link production and defect yields were 12 cross-links/ion and 100 defects/ion, respectively, corresponding to the chemical yields of 0.07/100 eV and defects of 0.28/100 eV, respectively, of the deposited energy. These studies concluded that the energy distribution inside the single ion tracks is the controlling factor for the production of chemical yields.

It has been observed that during modifications of polyvinylidene fluoride (PVDF) by the energetic ions such as O, Kr and Xe in the energy range of 1–50 MeV/u and irradiation fluences of 10^{11}–10^{12} ions/cm^2 [81], it was obvious that the atomic mass of the projectile ion was the major parameter for modifications in the polymers. The degradation remains stable along the ion path, and it is highest for the heavy ions. The activated centers produced by the lighter ions tend to migrate toward the surface of the irradiated substance, and the rearrangement of the

different reactive species finally can modify the structure of the polymer [81]. This study makes the conclusion that the ion beam with higher energy can result in long life device stability than that of the lighter ions.

The process of electronic energy transfer to the target initially leads to the excitation and breaking of different chemical bonds with consequences of cross-linking, chain scission and/or formation of new chemical bonds (e.g., C=C), depending on the structure of the irradiated polymers. Experimentally, it is possible to distinguish between the intra-chain and inter-chain bonds cross-linking in the ion-irradiated structure [82]. It was observed that upon ion irradiation, the soluble polymers transformed into the non-soluble gel upon introducing one cross-linking per macromolecule [82]. The low-energy ion beam-irradiated aromatic polymers act as efficient "energy sinks" as the aromatic rings can dissipate a large amount of the excitation energy [71] upon irradiation. However, upon high-energy ion irradiation on such polymers, the loss of aromatic conjugation is one of the predominant destruction processes [83, 84]. Moreover, the evolution of large volatile irradiation products with subsequent release of residual gas is one of the most characteristic effects in the irradiated polymers. Since the release of volatile gas is diffusion-controlled process, the degassing is strongest at the surface and slowest near the ion track end, which results in the evolution of an inhomogeneous distribution of the residual volatile species along the ion trajectory. With further increase in projectile energy, the transferred energy density increases up to a threshold value, resulting in breaking of all the chemical bonds along the central region of the latent ion track. Therefore, an energetic heavy ion is capable to result completely in a new material with different or modified physico-chemical properties with no connection to the unirradiated substances. For higher deposition of the electronic energy by the projectile ion, it will take more time for dissipation of the excitation energy of the target atoms, and hence, the compounds will be more complex which may be newly formed in the core of ion track [85].

5 Practical Applications of Ion Irradiation

5.1 Applications of Low-Energy Ion Irradiation of Solids

The low-energy ion beams, called the ion implantation, is widely used in electronics for doping of semiconductor through polymeric photoresist masks [86]. Low-energy ion irradiation exhibits oxidation of the resist and improves the thermal stability. The ion implantation technique can also be used to render polymer films in space research vehicles more radiation resistance during their passage through high radiation zone, as, for example, the Van Allen radiation belt.

The corrosion resistance of metals and alloys can also be made possible by means of high-energy ion irradiation fluence (e.g., nitrogen ion implantation). Another direct application includes an immediate improvement in the adhesion of

immiscible material layers (e.g., metal and polymers), which can be carried out by ion beam mixing, reactive ion implantation or ion beam-assisted deposition of the materials. Furthermore, low-energy ion beam irradiation can be used in optics, especially for fabrication of waveguide.

The low-energy ion impact results in significant effects at the surface and in the subsurface region of an irradiated target. If a low-energy projectile ion enters a target, it is backscattered, called the "Rutherford Back Scattering" from a near-surface atom. The energy loss depends on both the depth of collision and mass of the target. This technique, in which protons or α-particles comprise the ion beam "probe," can be used as the analytical method for determining the composition of the depth of solid targets and depth distributions of radiation damage impurity atoms, defect aggregates, etc. However, this technique is valid only for the heavy target atoms.

The ion beam modification of polymeric surfaces has one of the most important applications in medicine. The biocompatibility and bioadhesion of the irradiated polymers can be enhanced by enriching their surfaces with polar moieties, especially carboxyl groups, which seem capable of bonding most strongly to living biomass. Moreover, the surfaces of surgical apparatus can be efficiently sterilized using ion irradiation technique.

5.2 Applications of High-Energetic Ion Impact onto Solids

It has been observed that most of the synthetic polymer films are excellent materials for the chemical etching of latent ion tracks. This method is inexpensive and simple one for detection of the energetic particles. The etched tracks of the irradiated target materials have lots of potential applications in developing new nanosensors such as in physical (*e.g.,* temperature, pressure, light intensity), chemical (*e.g.,* moisture, alcohol, acetone, hydrogen, ammonia) and biological (*e.g.,* germs, viruses, hormones, enzymes, sterilizing efficiency) applications. Furthermore, the latent track-based nano-electronics is one of the rapidly developing cutting-edge researches in the present century.

In recent years, the SHI irradiation-induced polymeric materials have brought significant interest for the sake of their various novel applications. Due to high deposition of electronic energy ($\sim$MeV) inside the target volume via the formation of ion track ($\sim 10^{-15\ldots-14}$ cm^3) within an extremely short interval of time of the order of $\sim 10^{-17\ldots-15}$ s, it undergoes dramatic transient irreversible modifications in the chemical and structural properties of the polymer with accompanying heat and pressure pulses. During the passage of the energetic heavy ions, the energy is deposited in cylindrical zones ("thermal spike," $\sim 10^{-12\ldots-11}$ s), called the "latent track." The dissolution of the latent track by suitable agents ("etching") leads to the formation of pores, the so-called *etched tracks*. The irradiation-induced latent tracks in polymers are characterized by the changing of (1) structural free-volume, carbonaceous clusters, (2) density of free radicals, (3) chemical modifications such as

unsaturation, double bonds, and (4) phase transformation of the polymer. These undergoing irreversible changes are responsible for the four major strategies that have emerged for latent track in various potential applications: (1) exploitation of the modified transport properties along ion tracks, (2) trapping of mobile ions, atoms, molecules or clusters along the ion tracks, (3) exploitation of the material's chemical changes and (4) making use of ion-induced phase transitions.

The size of the pores in the irradiated track membranes can be controlled by etching conditions and by choice of irradiation treatment. Cylindrical pores with diameter in the range 0.02–5.0 μm are readily obtained with lengths of 10–50 μm [87, 88]. However, formation of pores in nanometer diameter 10–100 nm has also been reported [89, 90] by the process of SHI irradiation. The thin polymer membranes with highly uniform pore size have been made commercially available, which have been primarily used for laboratory filtration applications. Such high regular geometry polymer membranes called the "intelligent" membranes generated by ion tracks are mechanically stable and they have great commercial applications in industry such as for separation or purification of liquids and gases. Irradiation of polymers by energetic heavy ions can convert them from dielectric materials to materials having moderate or high electrical conductivity and improved thermal stability, which explores the opportunities for use of radiation in producing materials especially for the polymer-based electronic applications. The SHI irradiation in conjugated polymers, such as polyaniline (PAni), polypyrrole (PPy) and polythiophine (PTh), has been investigated as an alternative approach to chemical doping to render them highly electrically conductive. The generated sandwich-layered structure of dielectric materials formed by ion irradiation is being intended for the fabrication of transistor-like switches [91], or of nanoscale devices from irradiation of self-assembled monolayers [92]. However, the etched tracks in irradiated materials have many advanced applications, such as in light-emitting diodes, formation of nanosized or microsized diodes, field effect transistors, miniaturized Li batteries and sensors (e.g., temperature, pressure, humidity and ammonia) [93, 94].

6 Experimental Setup for Ion Irradiation

Figure 6 depicts the schematic diagram of Pelletron Accelerator at Inter-University Accelerator Centre (IUAC), New Delhi. The Pelletron Accelerator has pulsed ion beams of several elements having energy up to 15 MeV per charge state [95]. In the Pelletron, the negative ions of the projectile can be produced from the Multi-Cathode Source of Negative Ions by Cesium Sputtering (MC-SNICS). The beam of negative ions, generated by Cesium Sputtering, is first analyzed by a 90° injector magnet so that the produced ions with the negative (−ve) charge state are separated from other contaminated isotopes and charge states. The analyzed beam is then injected into a strong electric field inside an accelerator tank filled with

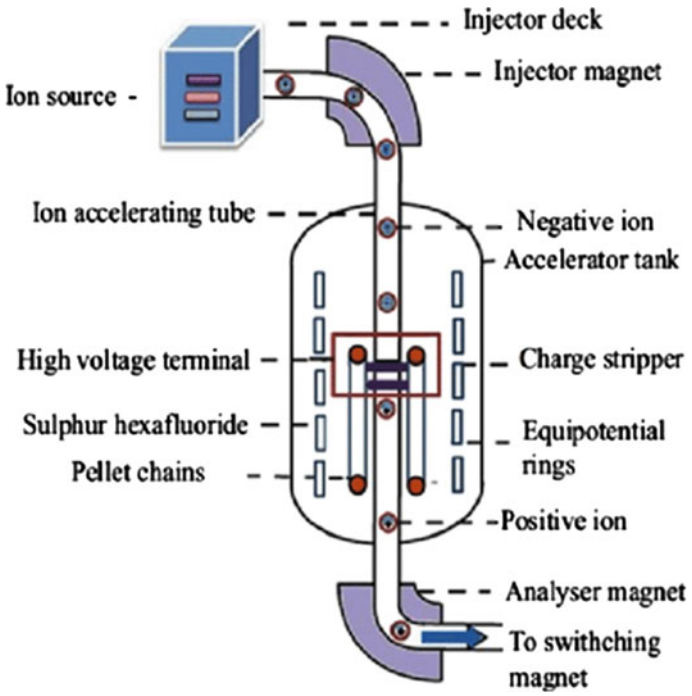

Fig. 6 Schematic of Pelletron Accelerator at Inter-University Accelerator Centre (IUAC) showing the ion acceleration principle

insulating SF_6 gas. High terminal voltage of up to 15 MeV is generated in the middle of the tank. Inside the tank, the negative ions are accelerated while traveling from the column top of the tank to the positive terminal, through the accelerating columns. The terminal is charged by a set of double Pelletron chains. The corona-based voltage grading system provides strong electrical potential to the negative ions and accelerates them. Inside the terminal, the negative ions pass through either a gas stripper or a carbon foil where some of the electrons are stripped from the negative ions due to collisions with gas or carbon atoms. The positive ions thus formed are repelled away from the positive terminal and accelerated further to the ground potential at the bottom of the tank. After the ions leave the Pelletron Accelerator, a particular beam of ion is selected using a 90° analyzing magnet which bends the beam into the horizontal plane. Finally, with the help of a switching magnet, the highly charged high-energy ion beam is directed into one of the beam lines in different experimental areas of the beam hall.

7 Experimental

7.1 Sample Preparation

The chemicals monomer (pyrrole) and oxidant (ammonium persulfate, APS) were purchased from Sigma Aldrich. The dopant cum surfactant (camphorsulfonic acid, CSA) was purchased from Merck. Before using Pyrrole monomer, it was distilled under reduced pressure. All other chemicals were used as received without purifications. The chemical oxidative self-assembly polymerization was used to synthesize the nanotubes of PPy, and this method is described as follows.

PPy nanotubes have been synthesized using the chemical oxidative self-assembled method of polymerization at different molar ratios of CSA/Py (dopant/monomer) keeping molar concentration of APS oxidant fixed. In this method, initially in 40 ml of double distilled water, 0.15 M pyrrole (Py) and 0.075 M CSA was mixed and stirred for 30 min. A transparent solution of CSA-Py salt was formed, and this solution was kept in an ice bath up to 0–5 °C. A pre-cooled solution of 0.15 M APS was added into the solution of CSA-Py, and this mixture was allowed to react for 15 h at room temperature. After the polymerization was over, the precipitate was collected, filtered off and washed several times with methanol, acetone and double distilled water to remove the impurities from the resulting products. The filtered precipitate was dried under room temperature for 72 h. The block diagram for synthesis of PPy nanotubes by self-assembly polymerization method is shown in Fig. 7.

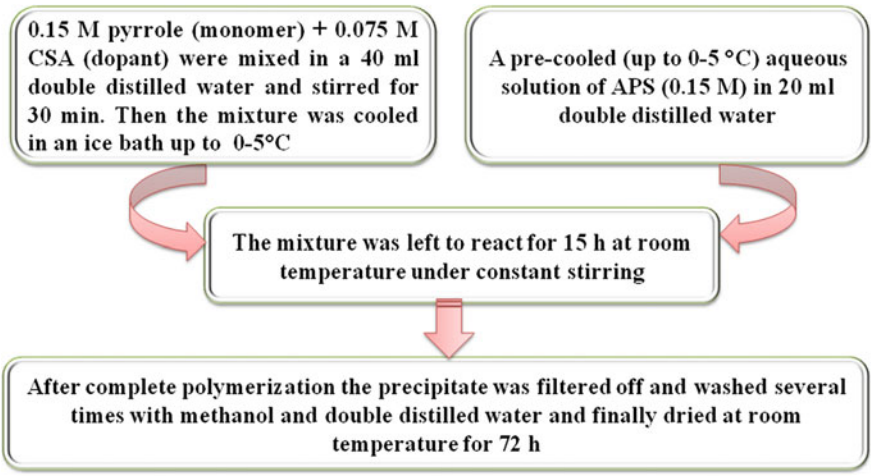

Fig. 7 Block diagram for synthesis of PPy nanotubes by self-assembly polymerization method

7.2 Formation Mechanism of PPy Nanotubes

The formation of one-dimensional PPy nanotubes by the self-assembly polymerization is described as follows: Initially before the oxidative polymerization to occur, the mixture of CSA and Py form CSA/Py salt through the acid base reaction. Due to the presence of a polar head group (hydrophilic $–SO_3H$ group) and a non-polar tail (hydrophobic $C_{10}H_5O$-group), the CSA/Py salt can self-assemble into the micelles in aqueous solution, and these resultant micelles act as soft template for polymerization. A double layer is formed in the micelles due to the coexistence of the CSA anions with the Py cations. The pyrrole monomer diffuse into the core of the micelles and the micelles provide the necessary reaction medium to guide the polymerization. The pyrrole-filled micelles act as soft template during the self-assembly polymerization, and pyrrole cations may solubilize into the micelle/water interface as depicted in Fig. 8. On addition of the oxidant (APS), the polymerization occurs only at the micelle/water interface adjacent to the polar head groups of CSA, since the hydrophilic APS molecules cannot penetrate into the micelle surface [96]. During polymerization, the self-assembled micelles become bigger by accretion [97] or tubular structure by elongation [98] depending on the surfactant concentrations.

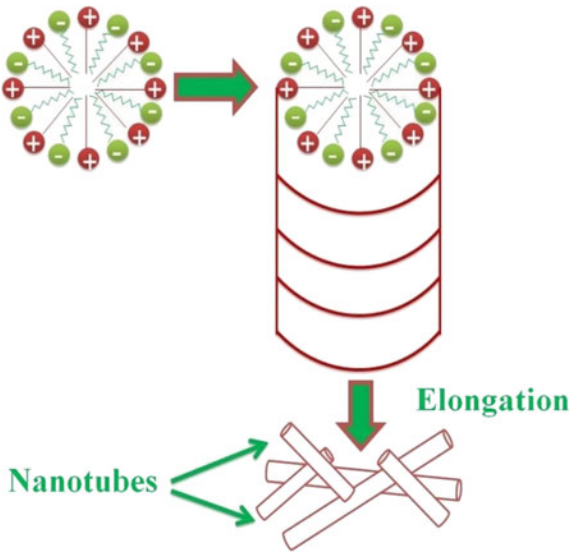

Fig. 8 Schematic of formation of PPy nanotubes by self-assembly method

8 Irradiation Effects on PPy Nanotubes with 160 MeV Ni^{12+}

The synthesized PPy nanotubes have been irradiated by 160 MeV Ni^{12+} SHI with a view to enhance their physico-chemical properties of structural, optical, thermal, dielectric and ac conductivity. For SHI irradiation, films of PPy nanotubes have been prepared by dissolving and ultra-sonicating the dried precipitate into 2% of PVA (polyvinyl alcohol) solution. The PVA (M_w = 145,000) has been used as plasticizer for making films of PPy nanotubes for SHI irradiation and the usage of PVA as plasticized did not affect significantly on the properties of PPy nanotubes. The SHI irradiation was performed at the 15 UD Pelletron Accelerator available at the Inter-University Accelerator Centre (IUAC), New Delhi, India, using the Materials Science beam line facilities. Five different irradiation fluences 1×10^{10}, 5×10^{10}, 10^{11}, 5×10^{11} and 10^{12} ions/cm^2 were used to irradiate the films of PPy nanotubes at a constant current of 0.5 pnA (particle nano-ampere). The energy of Ni^{12+} ion beam was selected as 160 MeV so that the ion beam completely penetrated the PPy films. The projected range of Ni^{12+} ions in PPy films as calculated by using the SRIM (stopping and range of ions in matter) software was found to be 42 μm, which was larger than thickness ($\sim$30–35 μm) of the PPy films. The different studies on the 160 MeV nickel ion-irradiated PPy nanotubes have been discussed under the following sections.

8.1 High-Resolution Transmission Electron Microscopy Studies

Figure 9 depicts the HRTEM micrographs of pristine and irradiated PPy nanotubes at different irradiation fluences. Upon SHI irradiation, PPy nanotubes irradiated at ion fluence of 5×10^{11} ions/cm^2 become more aligned and denser than that of the pristine nanotubes of PPy. However, PPy nanotubes irradiated at the highest ion fluence of 10^{12} ions/cm^2 show the breaking or degradation of PPy nanotubes, which results in the random alignments of PPy nanotubes because of the large energy deposition in the irradiated PPy nanotubes.

8.2 X-Ray Diffraction Studies

Figure 10 depicts the XRD patterns of the pristine and irradiated PPy nanotubes at different ion fluences. The characteristic broad diffraction peak is observed at around $2\theta = 19.96^\circ$ for the unirradiated PPy nanotubes. A new diffraction peak at $2\theta = 15.90^\circ$ is observed for the irradiated PPy nanotubes at the ion fluence of 5×10^{10} ions/cm^2, which grows in intensity with increasing the ion fluence up to

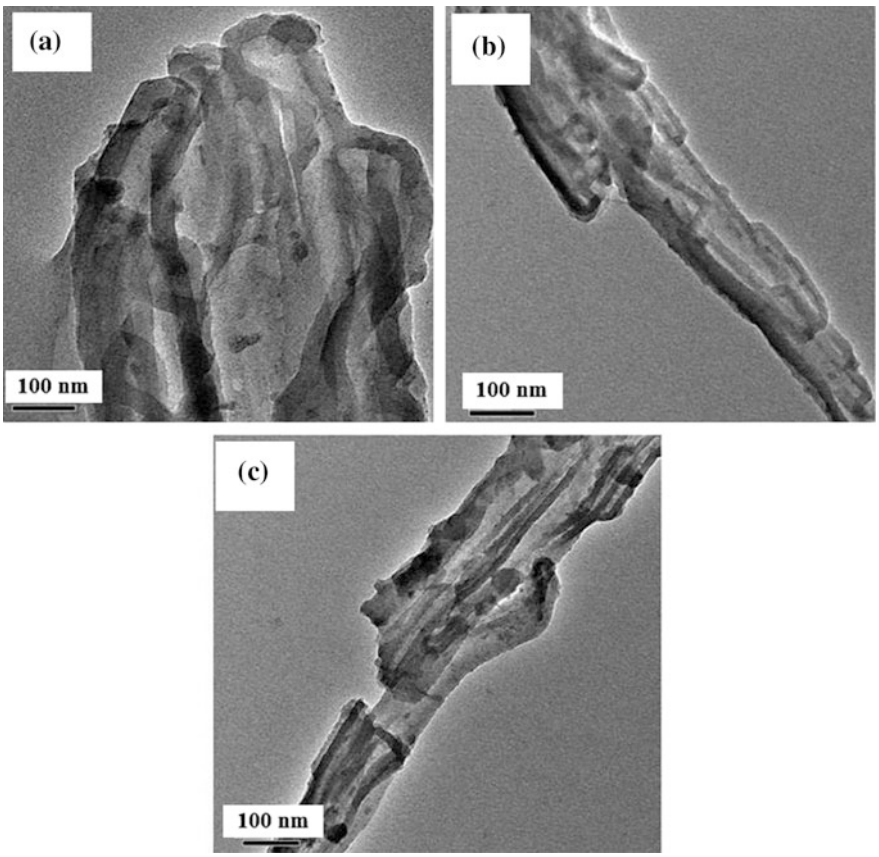

Fig. 9 HRTEM micrographs of **(a)** pristine and irradiated PPy nanotubes at ion fluences of **(b)** 5×10^{11} and **(c)** 10^{12} ions/cm^2

5×10^{11} ions/cm^2. The appearance of the new peak suggests the formation of new crystalline domains with higher *d*-spacing ($\sim$5.41) in the irradiated PPy nanotubes.

Furthermore, the diffraction peak that appears in the pristine PPy nanotubes at $2\theta = 19.96^\circ$ undergoes a shifting to a higher angle of $2\theta = 22.95^\circ$ upon irradiation with the ion fluence of 5×10^{10} ions/cm^2. This indicates the formation of denser crystalline domains in the PPy nanotubes upon SHI irradiation. However, with further increase in irradiation fluence up to 5×10^{11} ions/cm^2, the position of the diffraction peak does not change suggesting that there is no change in density of irradiated PPy nanotubes, but the increased intensity of the diffraction peak with increasing fluence up to 5×10^{11} ions/cm^2 suggests the increase in volume of the denser crystalline domains. The formation of crystalline domains of two different *d*-spacings in the irradiated PPy nanotubes at the moderate and higher irradiation fluence (5×10^{10}–5×10^{11} ions/cm^2) could be attributed to the hollow tubular

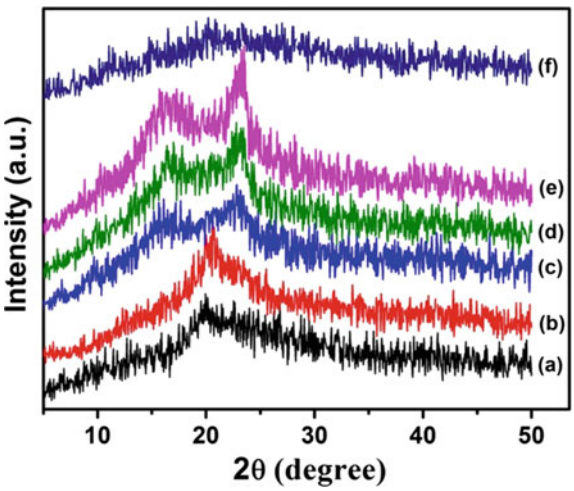

Fig. 10 XRD patterns of (a) pristine and irradiated PPy nanotubes at ion fluences of (b) 10^{10}, (c) 5×10^{10}, (d) 10^{11}, (e) 5×10^{11} and (f) 10^{12} ions/cm^2

morphology of the PPy nanotubes. Two different crystalline domains with larger *d*-spacing (low density) and lower *d*-spacing (high density) may form in PPy nanotubes upon SHI irradiation. High-density crystalline domain with lower *d*-spacing may form due to rearrangement of the adjacent PPy nanotubes by cross-linking.

At the highest irradiation fluence of 10^{12} ions/cm^2, the degradation or breaking of PPy nanotubes occurs due to deposition of huge electronic energy ($\sim 4.5 \times 10^2$ eV/Å) along the ion track and whole crystalline domain structure is disrupted. The broad hump showing amorphous structure is observed, which may originate either from the ion beam-induced defects and dislocations or the grain splitting effect at the ion fluence of 10^{12} ions/cm^2, and these effects dominate over the induced crystallization process. Upon SHI irradiation at the low and moderate ion fluences, there is an increase in total intensity of the diffraction peak with increasing ion fluence which reveals the enhanced crystallinity in the PPy nanotubes. But there is a sudden decrease in intensity (less than the pristine sample) of the diffraction peak at the ion fluence of 10^{12} ions/cm^2 which is a direct consequent of reduction of crystallinity of irradiated PPy nanotubes at highest fluence. The ordering of the polymer chains (X_C) can be calculated using Eq. (12),

$$X_C = \frac{A^I}{A^T} \times 100\% \tag{12}$$

The increase in crystallinity of PPy nanotubes after SHI irradiation can be ascribed to the systematic arrangement of the polymer chains by chain folding or by formation of single or multiple helices along the ion path. However, the observed decrease in crystallinity of PPy nanotubes irradiated at the highest ion fluence can be thought of scissioning of polymer chains due to tremendous electronic energy deposition. Upon SHI irradiation, shifting of the diffraction peak toward higher angular side is due to the contraction of polymer lattice [99]. The increased density

makes the polymer chains more compact and produces closely packed regions by cross-linking, chain folding of the polymer chains or due to formation of single or multiple helices resulting in more crystalline structure in the irradiated PPy nanotubes. The increased crystallinity makes the transport of the charge carriers more easy and therefore results in an increase in electrical conduction into the irradiated PPy nanotubes. The extent of order (L) of pristine and irradiated PPy nanotubes has been calculated using Eq. (13),

$$L = \frac{K\lambda}{\beta \cos\theta} \tag{13}$$

The calculation shows that after irradiation, the extent of polymer chain (L) in PPy nanotubes increases with increasing irradiation fluence up to 5×10^{11} ions/cm^2. However, beyond this ion fluence, extent of polymer chains decreases than that of the pristine sample. The decreased extent of chain order, at the highest irradiation fluence employed in the present work, results in the formation of disordered structure in PPy nanotubes [100].

The hopping distance (R) of both unirradiated and irradiated PPy nanotubes has been calculated using Eq. (14),

$$R = \frac{5}{8}\left[\frac{\lambda}{\sin\theta}\right] \tag{14}$$

The d-spacing of both pristine and irradiated PPy nanotubes is calculated using the Bragg's diffraction formula [101],

$$2d \sin\theta = \lambda \tag{15}$$

It is also observed that d-spacing of irradiated PPy nanotubes decreases with increasing ion fluence up to 5×10^{11} ions/cm^2; however, at the fluence of 10^{12} ions/cm^2, d-spacing of the irradiated PPy nanotubes increases as compared to the pristine PPy nanotubes. The angle of diffraction (2θ), ordering of chains (X_C), inter-planar spacing (d) and extent of chain order (L) of the pristine and irradiated PPy nanotubes at different ion fluences are recorded in Table 1.

8.3 Fourier Transform Infrared Spectroscopy Analysis

The FTIR spectral analysis has been carried out to study different structural changes in the SHI-irradiated PPy nanotubes. The changes have been estimated from the relative increase or decrease in the band intensity associated with the respective functional groups. Figure 11 depicts the FTIR spectra of the pristine and irradiated PPy nanotubes at different ion fluences. The stretching vibrations in C=C and C–N bonds in pyrrole rings are observed in vibrational frequencies of 1575 and

Table 1 Angle of diffraction (2θ), ordering of chains (X_C), inter-planar spacing (d), hopping distance (R) and extent of chain order (L) of pristine and irradiated PPy nanotubes at different ion fluences

Fluence (ions/cm^2)	Diffraction peak 2θ (°)		Ordering of chains X_C (%)		Inter-planar spacing d (Å)		Hopping distance R (Å)		Extent of chain order L (Å)	
	$2\theta_1$	$2\theta_2$	X_{c1}	X_{c2}	d_1	d_2	R_1	R_2	L_1	L_2
Pristine	–	19.96	–	25.72	–	4.44	–	5.56	–	5.57
1×10^{10}	–	20.45	–	26.20	–	4.34	–	5.42	–	7.71
5×10^{10}	15.90	22.95	3.0	24.19	5.57	3.87	6.96	4.83	20.56	6.50
1×10^{11}	16.37	22.95	3.6	27.15	5.41	3.87	6.77	4.84	21.26	6.67
5×10^{11}	16.37	23.10	7.5	24.44	5.41	3.85	6.77	4.81	18.73	8.32
1×10^{12}	–	20.75	–	23.40	–	4.28	–	5.34	–	4.12

N. B.: $2\theta_1$: broad diffraction peak at lower angle, $2\theta_2$: broad diffraction peak at higher angle, X_{C1}: ordering of chains calculated taking peak position at $2\theta_1$, X_{C2}: ordering of chains calculated taking peak position at $2\theta_2$, d_1: inter-planar spacing due to $2\theta_1$, d_2: inter-planar spacing due to $2\theta_2$, R_1: hopping distance due to $2\theta_1$, R_2: hopping distance due to $2\theta_2$, L_1: extent of chain order due to $2\theta_1$, L_2: extent of chain order due to $2\theta_2$

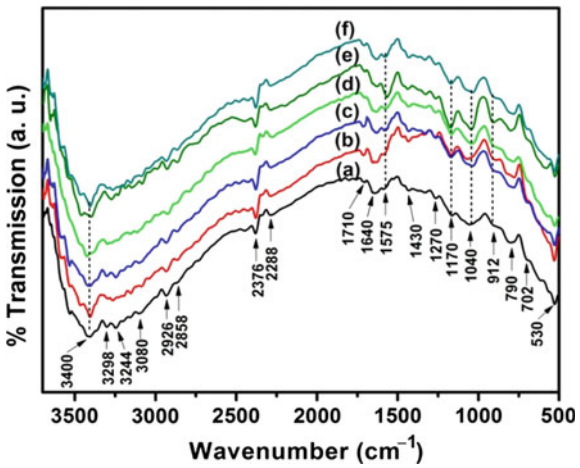

Fig. 11 FTIR spectra of (a) pristine and irradiated PPy nanotubes at ion fluences of (b) 10^{10}, (c) 5×10^{10}, (d) 10^{11}, (e) 5×10^{11} and (f) 10^{12} ions/cm^2

1430 cm^{-1}, respectively. The strong vibration bands at 912 and 1040 are attributed to the C–N and C–H in-plane deformation vibrations, respectively. The vibration band at about 790 cm^{-1} is due to the C–H wagging vibration, whereas the vibration at 1270 cm^{-1} is ascribed to the C–H or C–N in-plane deformation modes [102]. The N–H stretching vibration appears in the strong vibration bands in the range of 3000–3500 cm^{-1}. The presence of vibration bands at 2926 and 2858 cm^{-1} corresponding to the vibration of aliphatic –CH_3 and –CH_2 groups related to the sulfonate anions confirms the incorporation of the dopant counter-anions into the PPy chains [103]. The vibration band at 702 corresponds to the C–S vibration, which also indicates the doping of CSA into the PPy nanotubes.

The presence of the same main vibrational bands in the SHI-irradiated PPy nanotubes at all the ion fluences indicates that the structure of PPy nanotubes is not destroyed upon SHI irradiation. However, upon SHI irradiation, intensity of the vibrational bands increases as compared to the pristine PPy nanotubes up to the ion fluence of 5×10^{11} ions/cm^2, while at the highest ion fluence of 10^{12} ions/cm^2, the intensity of the vibration bands again decreases. The increase in vibration band intensity of the SHI-irradiated PPy nanotubes indicates the irradiation-induced cross-linking which as a result increases their crystallinity. The decrease in vibration band intensity at the highest irradiation fluence of 10^{12} ions/cm^2 indicates the breaking of bonds and degradation of PPy nanotubes upon irradiation with SHI.

8.4 UV-Vis Absorption Spectroscopy Studies

Figure 12 depicts the UV-Vis absorption spectra of the pristine and irradiated PPy nanotubes at ion fluences of 10^{10}, 5×10^{10}, 10^{11}, 5×10^{11} and 10^{12} ions/cm^2, respectively. The UV-Vis absorption spectra of pristine PPy nanotubes show three absorption bands: the first absorption band at 340 nm is due to π-π* transition, the absorption band at 484 nm is attributed to the transition from valence band to polaron band and a free tail above 670 nm corresponds to the transition from valence band to the bipolaron or anti-bipolaron state of the oxidized form of PPy nanotubes. Upon SHI irradiation, position of the π-π* band remains unaffected, while at low and moderate ion fluences (10^{10}–5×10^{11} ions/cm^2), the polaron band undergoes a red shifting with increase in the ion fluence up to 5×10^{11} ions/cm^2. However, at the highest ion fluence of 10^{12} ions/cm^2, the polaron band makes a blue shift, i.e., to the smaller wavelength region. The shifting of the absorption band to a higher wavelength with increasing fluence can be related to the structure of the

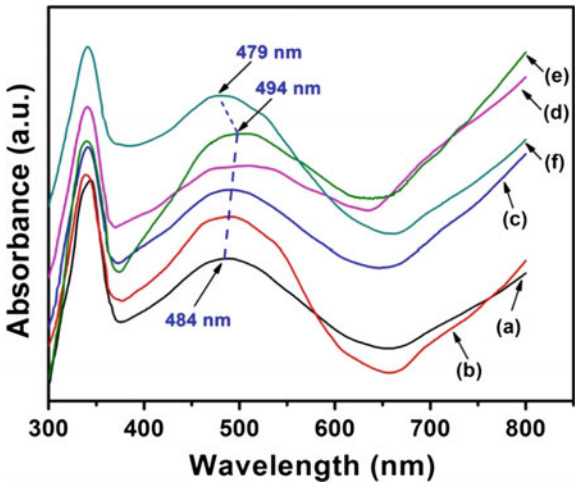

Fig. 12 UV-Vis absorption spectra of (a) pristine and irradiated PPy nanotubes at ion fluences of (b) 10^{10}, (c) 5×10^{10}, (d) 10^{11}, (e) 5×10^{11} and (f) 10^{12} ions/cm^2

energy gap of the polymer [104]. The SHI irradiation in PPy nanotubes induces the cleavage of –C–C– bonds and dehydrogenation of the PPy chains, i.e., evaluation of the hydrogen atoms as hydrogen molecules, and this in turn produces conjugated –C=C– bonds.

The SHI irradiation causes the loss of gaseous atoms in the polymeric materials, and hence, the enhanced carbon atoms result in the formation of a hydrogenated amorphous carbon with optical band gap energy depending on the H/C atom ratio [105]. The shifting in the absorption edge of PPy nanotubes upon irradiation can be correlated with their optical band gap energy. The optical band gap energy for a material can be defined as the difference between the bottom of the conduction band and top of the valence band. The optical band gap energy for materials can be determined using Eq. (16),

$$\alpha(v) = \frac{B_\alpha (h\nu - E_g)^n}{h\nu} \tag{16}$$

The variation of $(\alpha h\nu)^2$ with $h\nu$ and $(\alpha h\nu)^{1/2}$ with $h\nu$ of the pristine and irradiated PPy nanotubes is depicted in Fig. 13i, ii, respectively. The optical band gap energy E_g can be calculated from the intersection of the extrapolated lines from the linear portion of the curves, from the photon energy axis. For direct optical transition, the electron transfers vertically from the top of valence band to the bottom of conduction band without any change of momentum [106]. In case of an indirect

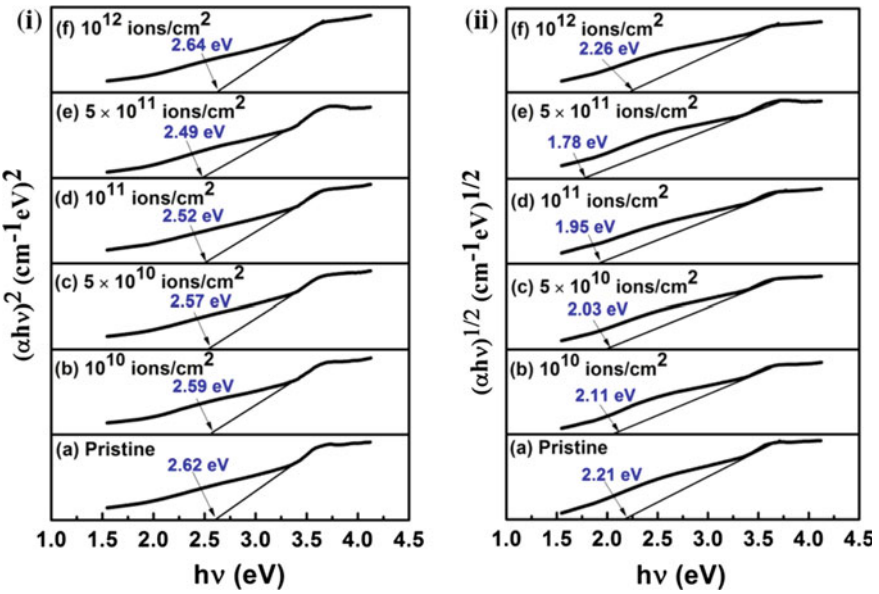

Fig. 13 Plots of variation of **(i)** $(\alpha h\nu)^2$ versus $h\nu$ and **(ii)** $(\alpha h\nu)^{1/2}$ with $h\nu$ of pristine and irradiated PPy nanotubes at different ion fluences

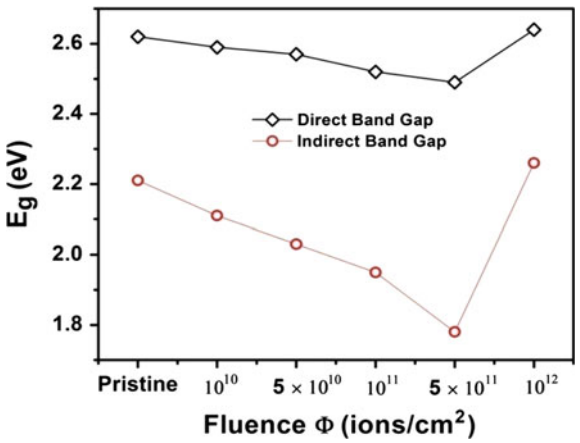

Fig. 14 Comparison of direct and indirect band gap energies of pristine and irradiated PPy nanotubes at different irradiation fluences

transition, the irradiation-induced species such as bond rapture and free radicals increases the electronic disorder that produces a permitted state in the forbidden band or the deformation of valence band.

Figure 14 compares the values of direct and indirect band gap energies both for the pristine and irradiated PPy nanotubes at irradiation fluences of 10^{10}, 5×10^{10}, 10^{11}, 5×10^{11} and 10^{12} ions/cm^2. For irradiated PPy nanotubes, both the direct and indirect band gap energies decrease with ion fluence up to 5×10^{11} ions/cm^2; however, at the investigated irradiation fluence of 10^{12} ions/cm^2, the value of both the direct and indirect band gap energies increase than that for the unirradiated PPy nanotubes. These results strongly suggest the simultaneous existence of both the direct and indirect band gaps in PPy nanotubes with a decreasing tendency at low and moderate ion fluences (10^{10}–5×10^{11} ions/cm^2) and increasing tendency at the highest ion fluence (10^{12} ions/cm^2). Furthermore, both in the pristine and irradiated PPy nanotubes, value of indirect band gap energy is found to be lower than its corresponding direct band gap energy. The decrease in optical band gap energy upon SHI irradiation is ascribed to the formation of defects and/or enriched carbon clusters due to partial evaluation of hydrogen molecules. These clusters influence the optical properties of the irradiated PPy nanotubes. The number of carbon atoms per conjugation length (N) for linear structure can be correlated with the optical band gap energy (E_g) which can be determined from the modified Tauc's equation [104] as follows;

$$N = 2\beta\pi/E_g \tag{17}$$

where 2β represents the band structure energy of a pair of adjacent π sites. The value of β is taken to be −2.9 eV as it is associated with the π-π^* optical transitions in –C=C– structure. The red shifting of the absorption band can be attributed to the increase in conjugation length. Upon SHI irradiation, number of carbon atoms per conjugation length (N) and number of carbon atoms per cluster (M) increase with

Table 2 Direct and indirect band gap energies (E_g) and number of carbon atoms per conjugation length (N) of the pristine and irradiated PPy nanotubes at different ion fluences

Fluence (ions/cm^2)	Band gap energy, E_g (eV)		Number of carbon atoms per conjugation length (N)	
	Direct	Indirect	Direct	Indirect
Pristine	2.62 ± 0.002	2.21 ± 0.002	~6.95 ± 0.002	~8.24 ± 0.002
1×10^{10}	2.59 ± 0.002	2.11 ± 0.002	~7.03 ± 0.002	~8.63 ± 0.002
5×10^{10}	2.57 ± 0.001	2.03 ± 0.001	~7.08 ± 0.001	~8.97 ± 0.001
1×10^{11}	2.52 ± 0.002	1.95 ± 0.002	~7.22 ± 0.002	~9.33 ± 0.001
5×10^{11}	2.49 ± 0.001	1.78 ± 0.001	~7.31 ± 0.001	~10.23 ± 0.001
1×10^{12}	2.64 ± 0.003	2.26 ± 0.003	~6.89 ± 0.003	~8.05 ± 0.003

increasing irradiation fluence from 10^{10} to 5×10^{11} ions/cm^2, while at the highest irradiation fluence of 10^{12} ions/cm^2, both the values of N and M decrease. The increased electrical conduction in the SHI-irradiated PPy nanotubes can also be corroborated with the increase in conjugation lengths, thereby allowing easy transport of charge carriers along the conjugated structures of PPy nanotube chains.

The direct and indirect band gap energies (E_g) and number of carbon atoms per conjugation length (N) of the pristine and irradiated PPy nanotubes are tabulated in Table 2. The carbon-enriched domains induced in the SHI-irradiated PPy nanotubes are mainly responsible for the reduction in the optical band gap energy [107, 108].

8.5 *Micro-Raman Analysis*

Figure 15 depicts the Raman spectra for the pristine and irradiated PPy nanotubes at different ion fluences. The Raman spectra for unirradiated PPy nanotubes exhibit an intense band around 1580 cm^{-1}, which is attributed to the symmetric stretching (C=C band) of PPy, and it originates due to overlapping of three major bands located at 1560, 1582 and 1610 cm^{-1} associated with the neutral, oxidized (polaronic) and fully oxidized (bipolaronic) bands, respectively [109]. The band at 932 cm^{-1} can be ascribed to the C–H out-of-plane deformation and band at 980 cm^{-1} is attributed to the ring deformation mode associated with the dications (bipolarons) and radical cations (polarons), respectively [110]. The asymmetric band at 1048 cm^{-1} is attributed to the C-H stretching vibration, while band at 1250 cm^{-1} can be assigned as the N–H or C–H in-plane deformation mode. The band at 1335 cm^{-1} is attributed to the ring stretching mode of PPy [111, 112], while band at 1410 cm^{-1} can be assigned to the C–N stretching mode of vibration.

Upon SHI irradiation, the intensity and line width of the Raman characteristic peaks increase with increasing ion fluences from 10^{10} to 5×10^{11} ions/cm^2, while at the highest ion fluence of 10^{12} ions/cm^2, they decrease. The decrease in line width of Raman peaks of irradiated PPy nanotubes can be ascribed to the variation

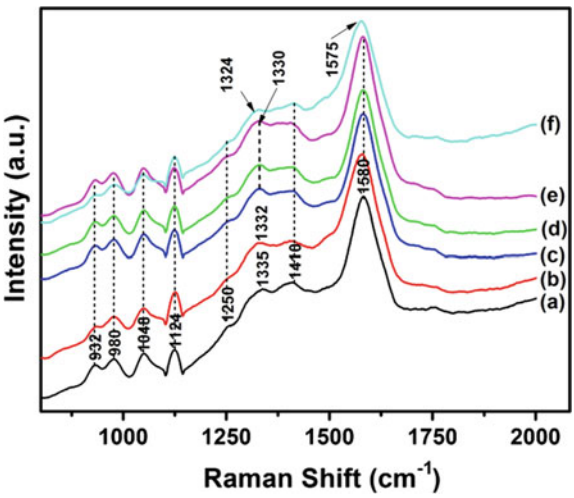

Fig. 15 Raman spectra for (a) pristine and irradiated PPy nanotubes at ion fluences of (b) 10^{10}, (c) 5×10^{10}, (d) 10^{11}, (e) 5×10^{11} and (f) 10^{12} ions/cm^2

in the π-conjugation length associated with the π-electron delocalization of PPy chains [113]. These results corroborate the UV-Vis studies wherein the number of carbon atoms per conjugation length (N) increases with increasing ion fluences. At low and moderate ion fluences (10^{10}–5×10^{11} ions/cm^2), SHI irradiation causes the cross-linking of the polymer chains resulting in increase in their π-conjugation lengths. However, irradiation with the highest ion fluence induces defects, chain scissions and distortions in PPy resulting in reduction in co-planarity of the aromatic rings and π-conjugation length [114]. Moreover, the increased intensity of Raman peaks with increasing ion fluence is a consequence of enhancement of crystallinity and decreased intensity at the highest ion fluence of 10^{12} ions/cm^2 which is because of the reduction in crystallinity of the irradiated PPy nanotubes. These results support both XRD and FTIR results of irradiated PPy nanotubes.

8.6 I-V *Characteristics*

Figure 16 shows the room temperature current-voltage (I-V) characteristics for the pristine and irradiated PPy nanotubes at different ion fluences. The I-V characteristics are observed to be nonlinear, but symmetric with respect to the polarity in the applied voltage (−10 V to +10 V). Upon SHI irradiation, in the low and moderate ion fluences (10^{10}–5×10^{11} ions/cm^2), the electrical conductivity in the irradiated PPy nanotubes increases with increasing ion fluence. However, at the highest ion fluence used 10^{12} ions/cm^2, the conductivity decreases to a value smaller as compared to the unirradiated PPy nanotubes. The increase in electrical conductivity with increasing ion fluence can be ascribed to the enhanced mobility of the charge carriers caused by reorganization of the polymer chains upon SHI irradiation.

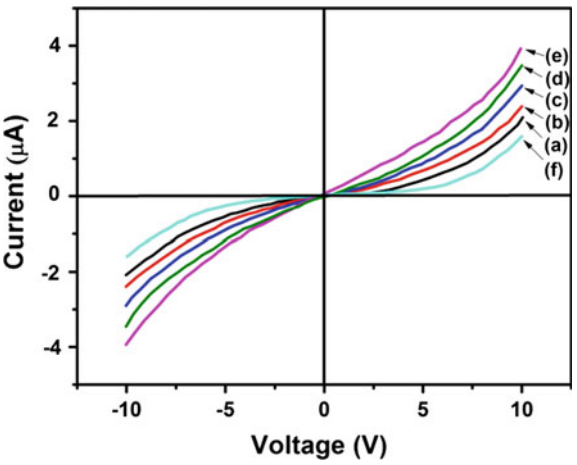

Fig. 16 Room temperature current-voltage (*I-V*) characteristics for (a) pristine and irradiated PPy nanotubes at ion fluences of (b) 10^{10}, (c) 5×10^{10}, (d) 10^{11}, (e) 5×10^{11} and (f) 10^{12} ions/cm^2

The charge transport in conducting polymers occurs due to delocalization of charge carriers over large number of monomer units in the polymer backbone. SHI results in strong coupling between the phonons and electrons resulting in the lattice distortion around the defective sites which generate localized states [115]. Also, the enhanced crystallinity upon SHI irradiation contributes to the increase in conductivity of PPy nanotubes. However, the decrease in conductivity at the highest ion fluence can be attributed to the amorphization of PPy nanotubes, which reduces the mobility of the charge carriers.

8.7 Thermogravimetric Analysis

The TGA for the pristine and irradiated PPy nanotubes at different irradiation fluences is shown in Fig. 17. At room temperature, the weight loss of the pristine and irradiated PPy nanotubes at different ion fluences is negligible. The first weight loss at 110 °C for the pristine and irradiated PPy nanotubes is due to the loss of moisture. The second weight loss occurs in between the temperature of 210–330 °C which may be due to the evaporation of dopant molecules from the polymer chains. The final stage of weight loss occurs in between temperature of 330–500 °C, and this can be attributed to the degradation and/or decomposition of the PPy backbone chains. Upon SHI irradiation, the weight loss of PPy nanotubes decreases gradually with increasing ion fluence from 10^{10} to 5×10^{11} ions/cm^2, while at the highest ion fluence of 10^{12} ions/cm^2, the weight loss decreases to a smaller value as compared to the pristine one. Figure 20 depicts the derivative plots of TGA for both pristine and irradiated PPy nanotubes at different ion fluences. The negative values of the derivative plots of TGA mean the weight loss, i.e., decomposition of the sample, and hence, the modulus values of the derivatives are considered. The values of

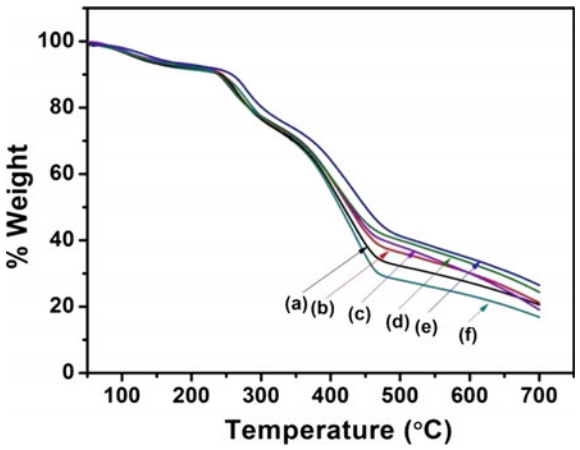

Fig. 17 TGA of (a) pristine and irradiated PPy nanotubes at ion fluences of (b) 10^{10}, (c) 5×10^{10}, (d) 10^{11}, (e) 5×10^{11} and (f) 10^{12} ions/cm^2

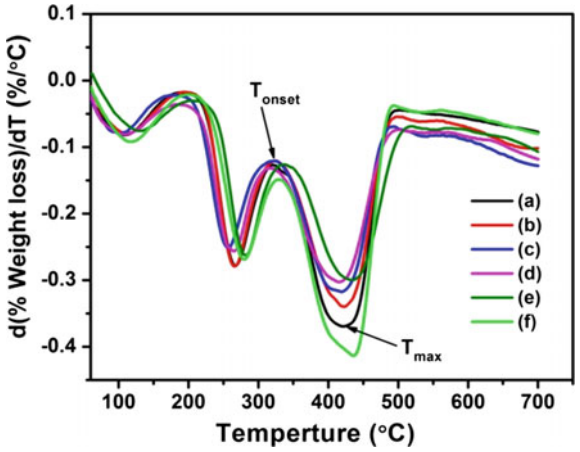

Fig. 18 Derivative plots of TGA for (a) pristine and irradiated PPy nanotubes at irradiation fluences of (b) 10^{10}, (c) 5×10^{10}, (d) 10^{11}, (e) 5×10^{11} and (f) 10^{12} ions/cm^2

maximum decomposition temperature (T_{max}) and maximum decomposition rate ($dW/dT)_m$ for the pristine and irradiated PPy nanotubes obtained from Fig. 18 are presented in Table 3.

In the third weight loss stage (330–500 °C), the onset decomposition temperature (T_{onset} = 322 °C) and maximum decomposition temperature (T_{max} = 421 °C) do not change significantly for PPy nanotubes upon irradiation with different ion fluences. However, the rate of decomposition for PPy nanotubes decreases as compared to pristine PPy nanotubes upon SHI irradiation with increasing irradiation fluence. The pristine PPy nanotubes exhibit the maximum decomposition rate ($dW/dT)_m$ of $|0.367|\%/°C$, which decreases to $|0.298|\%/°C$ upon SHI irradiation with fluence of 5×10^{11} ions/cm^2, indicating an enhancement in thermal stability of the irradiated PPy nanotubes. However, at higher irradiation fluence of 10^{12} ions/cm^2, ($dW/dT)_m$ increases to $|0.411|\%/°C$ (which is higher than that of the pristine ($dW/$

Table 3 Values of maximum decomposition rate, $(dW/dT)_m$, for pristine and irradiated PPy nanotubes at irradiation fluences of 10^{10}, 5×10^{10}, 10^{11}, 5×10^{11} and 10^{12} ions/cm^2

Ion Fluence (ions/cm^2)	Maximum decomposition rate, $(dW/dT)_m$, (%/°C)
Pristine	|0.367|
1×10^{10}	|0.339|
5×10^{10}	|0.315|
1×10^{11}	|0.300|
5×10^{11}	|0.298|
1×10^{12}	|0.411|

$dT)_m$ value), implying faster decomposition rate for PPy nanotubes irradiated at fluence of 10^{12} ions/cm^2. This indicates decrease in thermal stability of PPy nanotubes irradiated at the irradiation fluence of 10^{12} ions/cm^2, which can be ascribed to the chain scissioning or breaking of the polymer bonds and decrease in the molecular weight at the highest irradiation fluence of 10^{12} ions/cm^2. It can be inferred from the TGA and differential thermograph results that PPy nanotubes irradiated with low and moderate ion fluences are structurally and thermally more stable than that of the PPy nanotubes irradiated with the highest ion fluence of 10^{12} ions/cm^2.

8.8 AC Conductivity Studies

The room temperature (303 K) frequency variation of total conductivity $\sigma'(\omega)$ of pristine and irradiated PPy nanotubes at different ion fluences is depicted in Fig. 19. It is observed that in low-frequency region, conductivity of both pristine and irradiated PPy nanotubes is frequency independent, and this behavior is

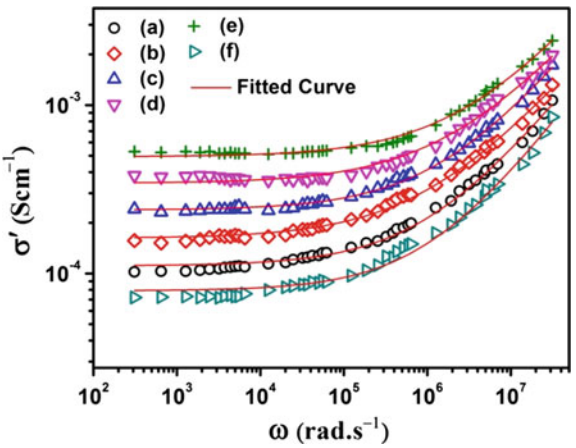

Fig. 19 Room temperature plots of total conductivity (σ') of (a) pristine and irradiated PPy nanotubes at ion fluences of (b) 10^{10}, (c) 5×10^{10}, (d) 10^{11}, (e) 5×10^{11} and (f) 10^{12} ions/cm^2

corresponded to the dc conductivity, σ_{dc}, and at higher-frequency region, the conductivity follows a frequency dispersive behavior which corresponds to the ac conductivity $\sigma_{ac} = A\omega^s$ $0 < s < 1$ and A is the pre-exponential factor which depends on temperature only. The transformation from the frequency-independent to the frequency-dependent region marks the onset of the conductivity relaxation, and this undergoes a shifting to higher-frequency region with increasing ion fluence.

It is observed from Fig. 19 that upon irradiation with SHI, total conductivity of the irradiated PPy nanotubes gets enhanced than that of pristine PPy nanotubes. This increase in conductivity can be attributed to the formation of crystalline structure besides formation of the conjugated double bonds in the irradiated structure. However, at the highest irradiation fluence of 10^{12} ions/cm^2, the total conductivity decreases as that of the pristine PPy nanotubes which can be attributed to the decreased crystallinity of the irradiated PPy nanotubes at the highest irradiation fluence.

To understand the charge transport mechanism in the SHI-irradiated PPy nanotubes, the temperature-dependent studies of frequency exponent s has been carried out. The temperature-dependent plots of frequency exponent of both the pristine and irradiated PPy nanotubes at different ion fluences are depicted in Fig. 20. The frequency exponent s of both pristine and irradiated PPy nanotubes decreases with increasing temperature, and this decreased nature of s with increasing temperature suggests that the charge carriers in both the pristine and irradiated PPy nanotubes follow the correlated barrier hopping (CBH) model as the dominant charge transport mechanism. The values of barrier activation energy (W_H) for charge carriers of both pristine and irradiated PPy nanotubes has been calculated using Eq. (18),

$$s = 1 - \frac{6kT}{W_H} \tag{18}$$

and values are presented in Table 4. Upon SHI irradiation, at low and moderate irradiation fluence (10^{10}–5×10^{11} ions/cm^2), value of W_H for charge carriers

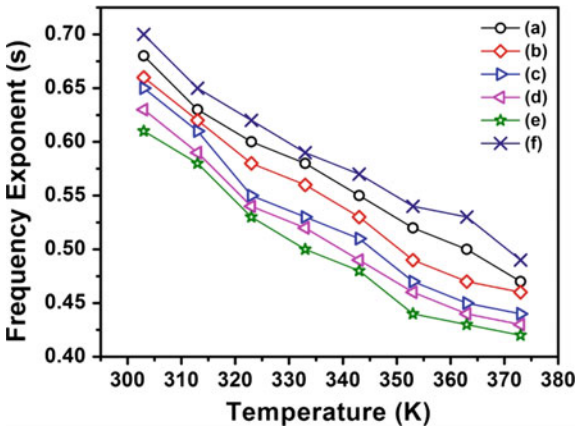

Fig. 20 Temperature variation of frequency exponent "s" of (a) pristine and irradiated PPy nanotubes at ion fluences of (b) 10^{10}, (c) 5×10^{10}, (d) 10^{11}, (e) 5×10^{11} and (f) 10^{12} ions/cm^2

Table 4 Frequency exponent (s) and barrier activation energy (W_H) of pristine and irradiated PPy nanotubes at different irradiation fluences at room temperature (303 K)

Fluence (ions/cm^2)	Frequency exponent, s	Barrier activation energy W_H (eV) at 303 K
Pristine	0.68	0.49
1×10^{10}	0.66	0.46
5×10^{10}	0.65	0.44
1×10^{11}	0.63	0.42
5×10^{11}	0.61	0.40
1×10^{12}	0.70	0.52

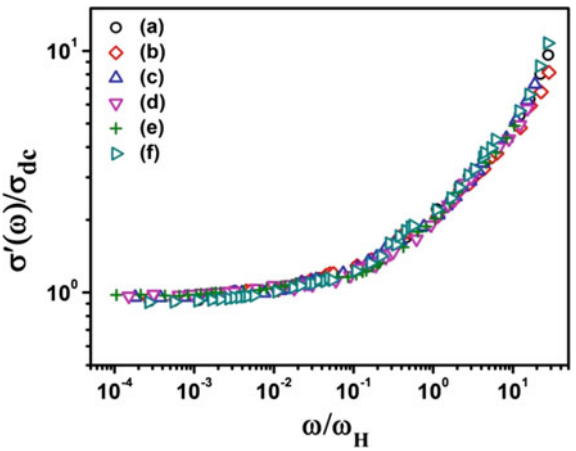

Fig. 21 Room temperature scaling plots of total conductivity of (a) pristine and irradiated PPy nanotubes at ion fluences of (b) 10^{10}, (c) 5×10^{10}, (d) 10^{11}, (e) 5×10^{11} and (f) 10^{12} ions/cm^2

decreases, which suggests reduction in barrier height for charge carriers' motion, and as a result, the electrical conductivity in SHI-irradiated PPy nanotubes gets enhanced. However, at the highest irradiation fluence of 10^{12} ions/cm^2, barrier activation energy increases as compared to the pristine sample, thereby resulting in reduction in electrical conductivity of PPy nanotubes at the highest irradiation fluence.

Figure 21 depicts the room temperature scaling plots of total conductivity of the pristine and irradiated PPy nanotubes at different ion fluences. The ac conductivity spectra of both the pristine and irradiated PPy nanotubes have been scaled by the scaling process as reported by Gosh et al. [116] in which the total conductivity $\sigma'(\omega)$ is scaled by σ_{dc}, while the frequency axis is scaled by the cross-over or cutoff frequency ω_{max}. It is observed that all the conductivity spectra after the scaling process fall onto a single master curve, which indicates the irradiation fluence-independent conductivity relaxation in the irradiated PPy nanotubes.

8.9 Dielectric Permittivity Studies

The complex dielectric permittivity (ε^*) of disordered materials can be determined from the experimentally measured complex impedance $Z'(\omega)$ data by using Eq. (19),

$$\varepsilon^*(\omega) = \frac{1}{j\omega C_0 Z^*(\omega)} = \varepsilon'(\omega) - j\varepsilon''(\omega) \tag{19}$$

where the real part $\varepsilon'(\omega)$ represents the dielectric permittivity that corresponds to the energy storage and the imaginary part $\varepsilon''(\omega)$ represents the dielectric loss corresponding to the energy loss in each cycle of electric field, $C_0 = \varepsilon_0 A/d$ represents the capacitance of free space between the electrodes, ω represents the angular frequency, A is the area of the electrode, d is the thickness of the sample and ε_0 is the permittivity in free space $(\varepsilon_0 = 8.854 \times 10^{-12}\,\mathrm{Nm}^{-1})$. The dielectric permittivity $\varepsilon'(\omega)$ and dielectric loss $\varepsilon''(\omega)$ have been calculated from Eqs. (20) and (21), respectively, given below:

$$\varepsilon'(\omega) = -\frac{1}{C_o \omega}\left[\frac{Z''(\omega)}{Z'^2(\omega) + Z''^2(\omega)}\right] \tag{20}$$

$$\varepsilon''(\omega) = \frac{1}{C_o \omega}\left[\frac{Z'(\omega)}{Z'^2(\omega) + Z''^2(\omega)}\right] \tag{21}$$

where $Z'(\omega)$ is the real part of complex impedance (Z^*) corresponds to the current through the contact resistor and $Z''(\omega)$ is the imaginary part of Z^* corresponding to the current through the capacitor.

The plots of dielectric permittivity (ε') versus frequency (ω) of both pristine and irradiated PPy nanotubes at ion fluences of 10^{10}, 5×10^{10}, 10^{11}, 5×10^{11} and 10^{12} ions/cm^2 at room temperature (303 K) are depicted in Fig. 22. It is observed that in lower frequencies, ε' shows strong frequency dispersion and its value decreases with increasing frequency, and at higher frequencies, ε' attains a nearly constant value. The response of the charge carriers to the externally applied ac electric field is faster at lower frequencies ($\leq 10^4$ Hz) giving rise to higher value of ε' corresponding to ε_s (static value of dielectric permittivity). At higher frequencies ($\geq 10^6$ Hz), the applied electric field changes rapidly and the charge carriers are unable to respond to the ac electric field giving lower value of correspondence (dielectric permittivity at infinite frequencies). The higher value of ε' at lower frequencies can be attributed to the electrode polarization effects [117].

To determine the nature of each of the relaxation, a least square fit of the experimental data to the Havriliak–Nigami (HN) function giving the complex dielectric permittivity for a single relaxation process is used [118],

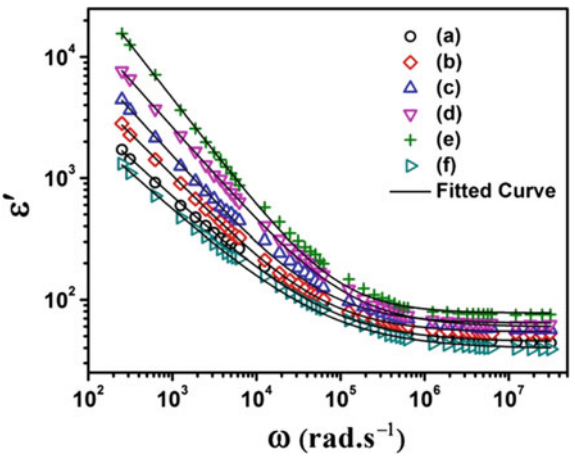

Fig. 22 Plots of dielectric permittivity (ε') versus frequency (ω) of (a) pristine and irradiated PPy nanotubes at ion fluences of (b) 10^{10}, (c) 5×10^{10}, (d) 10^{11}, (e) 5×10^{11} and (f) 10^{12} ions/cm^2 at room temperature (303 K)

$$\varepsilon^*(\omega) = \varepsilon_\infty + \frac{\Delta\varepsilon}{[1 + (i\omega\tau)^{\alpha_{HN}}]^{\gamma_{HN}}}, \tag{22}$$

where $\Delta\varepsilon = \varepsilon_s - \varepsilon_\infty$ is the dielectric relaxation strength, ε_s and ε_∞ are the dielectric constants at very low and high frequencies, respectively, τ is the average relaxation time, α_{HN} and γ_{HN} are the symmetric and asymmetric distribution parameters for the relaxation peak, which can assume values such that $0 \leq \alpha_{HN}\gamma_{HN} \leq 1$. This expression reduces to Cole–Cole (CC) function for $\gamma_{HN} = 1$, Davison–Cole (DC) for $\alpha_{HN} = 1$ and ideal Debye type for $\alpha_{HN} = \gamma_{HN} = 1$. From Eq. (22), the real part of permittivity $\varepsilon'(\omega)$ is given by:

$$\varepsilon'(\omega) = \varepsilon_\infty + \mathrm{Re}\left\{\frac{\Delta\varepsilon}{[1 + (i\omega\tau)^{\alpha_{HN}}]^{\gamma_{HN}}}\right\} \tag{23}$$

To extract the information about the dielectric relaxation, the experimental permittivity data in Fig. 22 are fitted using Eq. (23) by the nonlinear curve fitting method. The solid line represents the best-fitted curve for the experimental data of dielectric permittivity, and values of various parameters such as ε_∞, $\Delta\varepsilon$, α_{HN} and γ_{HN} can be estimated from the fitted curve. The calculated values of ε_∞, $\Delta\varepsilon$, α_{HN} and γ_{HN} of PPy nanotubes at different irradiation fluences at room temperature are recorded in Table 5. The value of α_{HN} lies in 0.54–0.64, while the value of γ_{HN} lies in 0.88–0.93, suggesting the non-Debye dielectric relaxation in both the pristine and irradiated PPy nanotubes.

Upon SHI irradiation, ε' increases with increasing ion fluence which can be attributed to the increased contribution of electrode polarization effects in the irradiated PPy nanotubes due to the generation of more charge carriers during SHI irradiation. It is observed that at the highest ion fluence of 10^{12} ions/cm^2, value of ε' at a particular frequency decreases as compared to the pristine PPy nanotubes which

Table 5 Different dielectric relaxation parameters for the pristine and irradiated PPy nanotubes using Havriliak–Nigami (HN) equation

Fluence (ions/cm^2)	ε_∞	$\Delta\varepsilon$	α_{HN}	γ_{HN}
Pristine	43	17.03×10^2	0.62	0.92
1×10^{10}	47	28.19×10^2	0.60	0.91
5×10^{10}	52	41.76×10^2	0.58	0.90
1×10^{11}	60	76.48×10^2	0.56	0.89
5×10^{11}	76	15.75×10^3	0.54	0.88
1×10^{12}	38	12.36×10^2	0.64	0.93

can be attributed to the decrease in electrode polarization effects at lower frequencies. Furthermore, the dielectric strength $(\Delta\varepsilon)$ of PPy nanotubes increases with increasing the irradiation fluences up to 5×10^{11} ions/cm^2, and at the highest irradiation fluence used 10^{12} ions/cm^2, value of $\Delta\varepsilon$ decreases smaller to the pristine value.

Figure 23 depicts the plots of dielectric loss (ε'') versus frequency (ω) of both pristine and irradiated PPy nanotubes at ion fluences of 10^{10}, 5×10^{10}, 10^{11}, 5×10^{11} and 10^{12} ions/cm^2 at room temperature (303 K). The linear increase in the value of ε'' with decreasing frequency indicates that the dc conduction loss is more prominent over the polarization effect. However, upon SHI irradiation, the value of ε'' at a given frequency increases with increasing irradiation fluence, which can be attributed to increased dc conduction in irradiated PPy nanotubes as a result of generation of more number of free charge carriers, while at the highest ion fluence of 10^{12} ions/cm^2, the value of ε'' at a given frequency decreases as compared to the pristine PPy nanotubes.

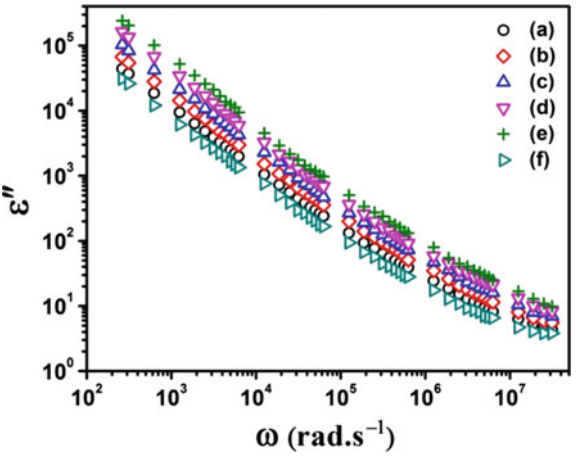

Fig. 23 Plots of dielectric loss (ε'') versus frequency (ω) of (a) pristine and irradiated PPy nanotubes at ion fluences of (b) 10^{10}, (c) 5×10^{10}, (d) 10^{11}, (e) 5×10^{11} and (f) 10^{12} ions/cm^2 at room temperature (303 K)

8.10 Electric Modulus Studies

Due to the absence of relaxation peak in dielectric loss spectra, it is not easy to distinguish between the polarization and relaxation contributions. For materials in which their dielectric loss spectra exhibit a dc conduction phenomenon, then the dielectric spectra can be analyzed using the complex electric modulus formalism [119, 120]. The complex electric modulus (M^*) is defined as the reciprocal of complex dielectric permittivity $(M^* = 1/\varepsilon^*)$, and it can be defined as follows:

$$M^*(\omega) = \frac{1}{\varepsilon^*(\omega)} = \frac{1}{\varepsilon' - j\varepsilon''} = \frac{\varepsilon'}{\varepsilon'^2 + \varepsilon''^2} + j\frac{\varepsilon''}{\varepsilon'^2 + \varepsilon''^2} = M'(\omega) + jM''(\omega) \qquad (24)$$

where $M'(\omega)$ and $M''(\omega)$ represent the real and imaginary parts of complex electric modulus M^*, respectively.

The room temperature (303 K) plots of real part of modulus (M') versus frequency (ω) of both pristine and irradiated PPy nanotubes at different ion fluences are depicted in Fig. 24. Each of M' spectrum exhibits a sigmoid behavior, i.e., value of M' increases with increasing frequency, and it reaches a constant maximum value at higher frequencies. The elimination of the electrode polarization from the pristine and irradiated samples of PPy nanotubes can be confirmed from the zero value of M' at lower frequencies [121]. At the higher frequency, M' approaches to $M_\infty(\omega \to \infty)$, which suggests that the conduction process of both the pristine and irradiated PPy nanotubes is due to the short range motion of charge carriers [122].

More information about the conductivity relaxation mechanism in SHI-irradiated PPy nanotubes can be obtained from the study of the frequency dependence behavior of M'' spectra. Figure 25 depicts the room temperature plots of imaginary part of modulus (M'') versus frequency (ω) of both pristine and irradiated PPy nanotubes at different ion fluences.

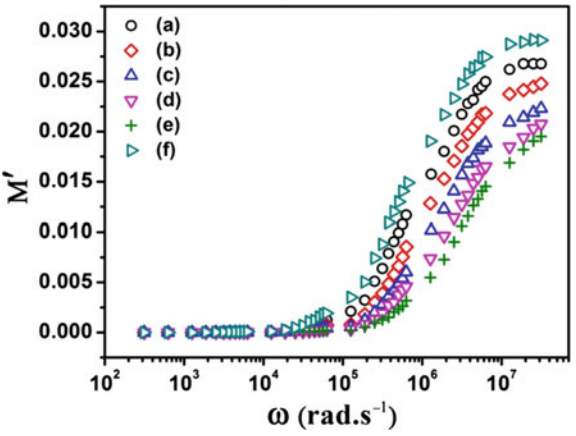

Fig. 24 Plots of real part of modulus (M') versus frequency (ω) of (a) pristine and irradiated PPy nanotubes at ion fluences of (b) 10^{10}, (c) 5×10^{10}, (d) 10^{11}, (e) 5×10^{11} and (f) 10^{12} ions/cm^2 at room temperature (303 K)

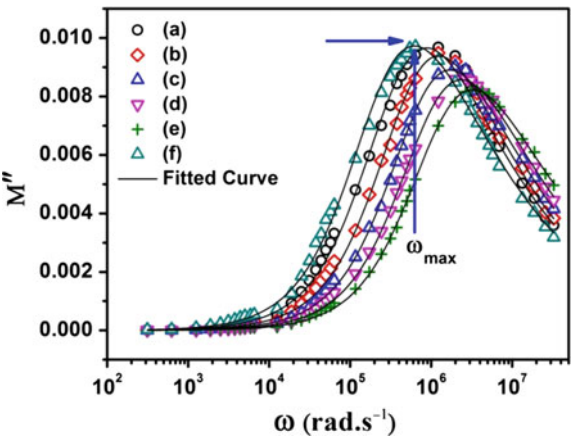

Fig. 25 Plots of imaginary part of modulus (M'') versus frequency (ω) of (a) pristine and irradiated PPy nanotubes at ion fluences of (b) 10^{10}, (c) 5×10^{10}, (d) 10^{11}, (e) 5×10^{11} and (f) 10^{12} ions/cm^2 at room temperature (303 K)

A single relaxation peak is observed in each M'' spectrum of both pristine and irradiated PPy nanotubes which suggests the transition of charge carriers' motion from long range to short range with increasing frequency. At low and moderate irradiation fluence (10^{10}–5×10^{11} ions/cm^2), the relaxation peak in M'' spectra shifts toward the higher frequency indicating the increase in long range motion of charge carriers in the SHI-irradiated PPy nanotubes. As a result, the relaxation time (τ) of charge carriers' motion decreases with increasing the irradiation fluences. However, the M'' peak shifts toward lower frequencies as compared to the pristine PPy nanotubes at the irradiated highest ion fluence of 10^{12} ions/cm^2 resulting in increase in the relaxation time (τ) of charge carriers. The asymmetric shape of M'' spectra indicates that the relaxation process deviates from the ideal Debye behavior, and there exists a distribution of relaxation times in irradiated PPy nanotubes.

To further analyze the conductivity relaxation mechanism, the experimentally obtained M'' data are fitted with the modified Kohlrausch-Williams-Watts (KWW) fitting function in the frequency domain as proposed by Bergman [123]. In the frequency approach, M'' can be approximated as follows:

$$M''(\omega) = \frac{M''_{\max}}{\left[(1-\beta) + (\beta/(1+\beta))\left[\beta(\omega_{\max}/\omega) + (\omega/\omega_{\max})^{\beta}\right]\right]} \tag{25}$$

where $M''_{\max}$ is the peak maximum of the imaginary part of electric modulus and β is the Kohlrausch stretched parameter that describes the distribution of relaxation times. Debye relaxation is obtained for $\beta = 1$, and deviation of β from unity indicates non-Debye relaxation mechanism and a distribution of relaxation times. The value of β can be defined empirically by Kohlrausch-Williams-Watts (KWW) function as follows [124, 125]:

Table 6 Room temperature values of maximum imaginary part of modulus (M''_{max}), relaxation frequency (ω_{max}), relaxation time (τ) and Kohlrausch stretched parameter (β) for charge carriers in both pristine and irradiated PPy nanofibers at different irradiation fluences

Fluence (ions/cm^2)	Relaxation frequency, ω_{max} (rad.s^{-1})	Relaxation time, τ (s)
Pristine	1.19×10^6	8.35×10^{-7}
1×10^{10}	1.43×10^6	6.94×10^{-7}
5×10^{10}	1.87×10^6	5.33×10^{-7}
1×10^{11}	2.44×10^6	4.09×10^{-7}
5×10^{11}	3.44×10^6	2.90×10^{-7}
1×10^{12}	9.95×10^5	1.00×10^{-6}

$$\varphi(t) = \exp\left[-(t/\tau)^{\beta}\right] \tag{26}$$

where τ is the relaxation time for charge carriers. Figure 27 depicts that the experimental data of M'' spectra are well fitted with Eq. (25). The room temperature (303 K) values of maximum of imaginary part of modulus (M''_{max}), relaxation frequency (ω_{max}), relaxation time (τ) and Kohlrausch stretched parameter (β) for charge carriers in both pristine and irradiated PPy nanofibers at different irradiation fluences are tabulated in Table 6.

Figure 26 depicts the room temperature scaling plots of M'' spectra of both pristine and irradiated PPy nanotubes at different ion fluences. The scaling of modulus spectra can provide a deep insight into the ion fluence dependence of relaxation dynamics in the irradiated PPy nanotubes. The scaling is done by dividing M'' with M''_{max}, while the frequency axis is scaled by the relaxation frequency ω_{max}. It is observed that each of the individual M'' spectra at different ion fluences merge on a common master curve indicating the ion fluence independent of relaxation dynamics of charge carriers in SHI-irradiated PPy nanotubes.

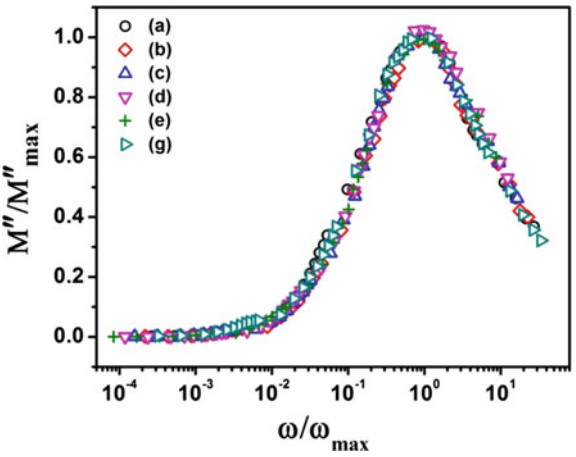

Fig. 26 Room temperature scaling plots of imaginary part of modulus (M'') of (a) pristine and irradiated PPy nanotubes at ion fluences of (b) 10^{10}, (c) 5×10^{10}, (d) 10^{11}, (e) 5×10^{11} and (f) 10^{12} ions/cm^2

9 Perspectives for Ion-Solid Interactions

Despite the rapid growth in the fundamental and applied aspects of research in ion-solid interaction and use of the irradiated materials for different applications, issues remain unresolved and are not fully understood. Some of the examples which address problems regarding the pre-/post-irradiation as well as processing, characterization and applications of the target materials are mentioned below [126]:

(a) Although the electronic and nuclear energy deposition in target materials by the projectile ion beam can be adequately explained by both classical and quantum mechanical properties, the theories of ion-solid interaction in more complex systems, for example, collision parameter dependence and channeling effects, have not yet been treated analytically.
(b) A major challenge for ion irradiation is that what happens for ion-solid interactions, if the target dimension is reduced and approaches zero. It is well known that upon high-energy ion irradiation in polycrystalline materials, the fission fragments produce strong surface plasmons resulting in unsustainable energy confinement, followed by swift "explosion" of successive crystallites along the cylindrical ion track. However, the atomic collision cascades in low-dimensional targets, such as free-standing or embedded nanoparticles, or nanocrystallites behave completely different from the cascades in semi-infinite matter. Therefore, in-depth study needs to be focused on the irradiation-induced unusual mechanism in low-dimensional structures.
(c) The formation of irradiation-induced clusters of non-soluble high-dose implants, for example, with metals in a polymer, is less studied.
(d) The process of polymerization and depolymerization induced by ion irradiation in materials has not been investigated as of now.
(e) The mechanisms of irradiation-induced radiobiology, such as the adsorption and desorption of biological species on ion-irradiated surfaces, are at the beginning stage. The sterilizing properties of the ion-irradiated surfaces need to be studied thoroughly.
(f) Though the irradiation-induced processing has potential of preparing new materials, the successful utilization of such materials in large-scale applications has not been encouraging as yet. Main drawback for the limited applications is the duration of the irradiation time and the initial cost.
(g) One of the limitations of irradiation on materials is that the irradiation experiment always has to be carried out in the form of thin film whose thickness should be smaller than the range of the projectile ion beam. In general, most of the samples for irradiation experiment are synthesized by the chemical polymerization method which gives samples in power form. However, the irradiation on powder samples is not possible since the experiment is carried out under high vacuum of 10^{-5} Torr or more. Thin films from the powder samples can be prepared using suitable polymer binders that may significantly reduce the properties of the as-prepared sample as well as the irradiated ones.

(h) Although the interaction mechanisms and irradiation-induced physico-chemical properties of different ion-irradiated materials have been studied, the potential applications of ion irradiation, such as designing and developing of ion track-based sensors, are in its nascent stage. More systematic studies are required to be conducted for specially designed sensors with low cost, light weight and high efficiency for household, vehicular, chemical industry, medicine, and atomic-biological–chemical (ABC), anti-terrorist protection environments.

10 Conclusions

In this chapter, studies on the fundamentals of conducting polymers and their nanostructures along with their different excellent properties have been described. Highly conducting conjugated polypyrrole (PPy) and their different nanostructures have brought special attention due to the properties of light weight, flexibility, biocompatibility, low toxicity, thermal and environmental stability and low cost. The highly conducting one-dimensional (1-D) nanostructured PPy can be used as molecular wires and for making nanodevices. The self-assembled synthesis and characterization of different properties of PPy nanotubes with diameter $\sim$20 nm and lengths of few microns have been discussed in this chapter. A unique and versatile technique, known as the "ion irradiation" in materials, can be extensively used to modify different physico-chemical properties of materials by transferring projectile ion energy to the target. The chapter also describes the use of ion irradiation technique to enhance the morphological, structural, optical, electrical, thermal and dielectric relaxation properties of PPy nanotubes by suitable selection of ion species, ion energy and fluences. The detailed mechanism of ion-matter interaction, in which the process of energy transfer by the ions to the target (different theoretical models), formation of the cylindrical ion core, called the "latent track," latent track chemistry such that the phenomena of cross-linking, chain scission, evolution of gaseous species have been discussed to gain an understanding of the ion-matter interaction. The experimental results show that different properties of PPy nanotubes can be enhanced significantly than that of the unirradiated PPy nanotubes by irradiating with 160 MeV Ni^{12+} SHI up to the ion irradiation fluence of 5×10^{11} ions/cm^2, above which all the studied properties degrade as compared to the pristine PPy nanotubes. HRTEM studies of irradiated PPy nanotubes indicate denser structure at the low and moderate ion fluence (10^{10}–5×10^{11}), while PPy nanotubes irradiated at the highest ion fluence of 10^{12} ions/cm^2 show breaking of PPy nanotubes. Upon SHI irradiation, crystallinity of polymer chains increases with increasing the irradiation fluence, while at the highest ion fluence (10^{12} ions/cm^2), crystallinity decreases as compared to that of the pristine PPy nanotubes. With increasing the irradiation fluence, the optical band gap energy of PPy nanotubes reduces, and it again exhibits a higher value at the investigated highest irradiated

fluence of 10^{12} ions/cm^2. The reduction in optical band gap energy upon SHI irradiation is attributed to the formation of defects and clusters in the irradiated PPy nanotubes. Upon SHI irradiation, thermal stability of PPy nanotubes increases with increasing the irradiation fluence up to 5×10^{11} ions/cm^2, while thermal stability of PPy nanotubes decreases than that of the pristine sample at the highest ion fluence of 10^{12} ions/cm^2. Upon SHI irradiation, total conductivity of the irradiated PPy nanotubes increases with increasing the irradiation fluence, which can be attributed to the formation of crystalline structure besides formation of the conjugated double bonds. The decrease in total conductivity of the irradiated PPy nanotubes at the highest irradiation fluence of 10^{12} ions/cm^2 is due to the lowering of crystallinity as compared to that of the pristine PPy nanotubes. The decrease in the value of frequency exponent "*s*" with increasing temperature suggests that the charge carriers in both the pristine and irradiated nanotubes follow the correlated barrier hopping (CBH) transport mechanism. The room temperature scaling of conductivity spectra of the irradiated PPy nanotubes reveals the irradiation fluence-independent conductivity relaxation mechanism. The M'' relaxation peak shifts toward higher frequency with increasing the irradiation fluence, which reveals the enhancement of long range motion of charge carriers up to the irradiation fluence of 5×10^{11} ions/cm^2. The asymmetric nature of M'' relaxation peak indicates the non-Debye relaxation of charge carriers in the irradiated PPy nanotubes. The scaling of M'' spectra of the irradiated PPy nanotubes at different ion fluences indicates the irradiation fluence-independent relaxation dynamics of charge carriers.

From the above discussion and experimental outcomes, it can be inferred that the swift heavy ion (SHI) irradiation is a potential technique to tailor the properties of conducting polymers and their nanostructures. Different parameters related to SHI irradiation play a critical role in modification of the properties of polymers. Depending upon the ion irradiation fluence and the transferred energy density to the polymer, the processes of cross-linking and/or chain scission of the polymer chains dominate which give rise to the enhancement and degradation of the different physico-chemical properties of the irradiated polymers.

References

1. Ghosh M, Barman A, Das A et al (1998) J Appl Phys 83:4230
2. Long YZ, Li MM, Gu C et al (2011) Prog Polym Sci 36:1415
3. Lu Q (2010) Microchim Acta 168:205
4. Gilmore KJ, Kita M, Han Y et al (2009) Biomaterials 30:5292
5. Guimard NK, Gomez N, Schmidt CE (2007) Prog Polym Sci 32:876
6. Dey A, De SK (2007) J App Polym Sci 105:2225
7. Dey A, De S, De A et al (2004) Nanotechnology 15:1277
8. Pan L, Qiu H, Dou C et al (2010) Int J Mol Sci 11:2636
9. Breads JL, Silbey R (1991) Conjugated polymers. Kluwer Academic, Amsterdam, The Netherlands
10. Park JW, Lee C, Jang J (2015) Sens Actuators B 208:532
11. Park JW, Park SJ, Kwon OS et al (2014) Anal Chem 86:1822

12. Martin CR (1995) Acc Chem Res 28:61
13. Yang X, Zhu Z, Dai T et al (2005) Macromol Rapid Commun 26:1736
14. Yanga X, Dai T, Zhu Z et al (2007) Polymer 48:4021
15. Zhang L, Wan M (2003) Adv Funct Mater 13:815
16. Zhang Z, Wei Z, Wan M (2002) Macromolecules 35:5937
17. Wei Z, Zhang Z, Wan M (2002) Langmuir 18:917
18. Yang Y, Liu J, Wan M (2002) Nanotechnology 13:771
19. Huang K, Wan MX (2002) Chem Mater 14:3486
20. Zhang Z, Wei Z, Zhang L et al (2005) Acta Mater 53:1373
21. Zhang L, Peng H, Sui J et al (2008) J Curr Appl Phys 8:312
22. Zhang L, Wan M (2002) Nanotechnology 13:750
23. Fink D et al (2004) Nucl Instr Meth B 218:355
24. Chapiro A (1988) Nucl Instr Meth B 32:111
25. Rao V, Amara JV, Avasthi DK et al (2003) Radiat Measur 36:585
26. Fleischer RL, Price PB, Walker RM (1975) Nuclear tracks in solids: principles and applications. University of Californiya, Berkeley
27. Gervais B, Bouffard S (1994) Nucl Instr Meth B 88:355
28. Schiwietz G, Czerski K, Roth M et al (2004) Nucl Instr Meth B 226:4
29. Wang J, Mathar J, Trickey SB et al (1999) J Phys Condens Matter 11:3973–3986
30. Juaristi J, Auth C, Winter H et al (2000) Phys Rev Lett 84:2124–2127
31. Nazarov VU, Pitarke JM, Kim CS et al (2005) Phys Rev B 71:121106(R)
32. Kanjilal D (2001) Curr Sci 80:1560–1566
33. Trautmann C, Klaumünzer S, Trinkaus H (2000) Phys Rev Lett 85:3648–3651
34. Krasheninnikov AV, Nordlund K (2010) J Appl Phy 107:071301
35. Srivastava A, Singh V, Chandra A et al (2006) Nucl Instr Meth B 245:277–280
36. Apel PY, Didyk AY, Fursov BI (1995) Nucl Instr Meth B 105:91–96
37. Wang Y, Kang Y, Zaho W et al (1998) J Appl Phys 83:1341–1344
38. Audouard A, Dural J, Toulemonde M et al (1996) Phys Rev B 54:15690–15694
39. Toulemonde M (1999) Nucl Instrum Meth B 156:1–11
40. Toulemonde M, Assmann W, Dufour C et al (2006) Mat Fys Med 5:263
41. Kaganov MI, Lifshitz IM, Tanatarov LV (1956) Zh Eksp Teor Fiz 31:232
42. Waligorski MPR, Hawn RN, Katz R (1986) Nucl Track Radiat Meas 11:309–319
43. Szenes G (2011) Nucl Instrum Meth B 269:174–179
44. Szenes G (1995) Phys Rev B 51:8026–8029
45. Szenes G (1999) Phys Rev B 60:3140–3147
46. Szenes G, Horvath ZE, Pecz B et al (2002) Phys Rev B 65:045206
47. Toulemonde M, Dufour C, Meftah A et al (2000) Nucl Instrum Meth B 166–167:903–912
48. Dunlop A, Lesueur D, Legrand P et al (1994) Nucl Instr Meth B 90:330–338
49. Fleischer RL, Price PB, Walker RM (1965) J Appl Phys 36:3645–3652
50. Bringa EM, Johnson RE (2002) Phys Rev Lett 88:165501
51. Calcagno L, Foti G (1991) Nucl Instr Meth B 59/60:1153
52. Bridwell LB, Giedd RE, Wang YQ et al (1991) Nucl Instr Meth B 56/57:656
53. Calcagno L, Compagnini G, Foti G (1992) Nucl Instr Meth B 65:413
54. Gupta S, Choudhary D, Sarma A (2000) J Polym Sci Part B Polym Phys 38:1589
55. Fink D, Keltt R, Chadderton LT et al (1996) Nucl Instr Meth B 111:303
56. Venkatesan T, Calcagno L, Elman BS et al (eds) (1987) Ion beam modification of insulators. Elsevier, Amsterdam, p 301
57. Marletta G, Iacona F (1995) In: Pauleau Y (ed) Materials and processes for surface and interface engineering. Kluwer Academic Dordrecht, The Netherlands, p 597
58. Ziegler JF (1992) In: Ziegler JF (ed) Handbook of ion implantation technology. North-Holland, Amsterdam, pp 1–68
59. Lee EH, Rao GR, Lewis MB et al (1994) J Mater Res 9:1043
60. Chapiro A (1962) Radiation chemistry of polymeric systems. Interscience Publishers, London, p 354

61. Bartok J, Hall BO, Schock KF (1986) J Appl Phys 59:1111
62. Puglisi O (1989) Mater Sci Eng B 2:167
63. Choi SC, Han S, Choi WK et al (1999) Nucl Instr Meth B 152:291
64. Zhang Y, Huan ACH, Tan KL et al (2000) Nucl Instr Meth B 168:29
65. Ruck DM (2000) Nucl Instr Meth B 166–167:602
66. Paula H, Sánchez-Parcerisa D (2013) Nucl Instr Meth B 312:110
67. Kucheyev SO (2004) J Appl Phys 95:5360
68. Singh L, Singh R (2004) Nucl Instr Meth B 225:478
69. Srivastava A, Singh V, Dhand C et al (2006) Sensors 6:262–269
70. Kumar A, Banerjee S, Saikia JP et al (2010) Nanotechnology 21:175102
71. Calcagno L, Compagnini G, Foti G (1992) Phys Rev B 46:10573
72. Forrest SR, Kaplan ML, Schmidt PH et al (1982) Appl Phys Lett 41:708
73. Kaur A, Dhillon A, Avasthi DK (2009) J Appl Phys 106:0737151
74. Kumar V, Ali Y, Sharma K et al (2014) Nucl Instrum Meth B 323:7
75. Ramola RC, Chandra S, Rana JMS et al (2008) J Phys D Appl Phys 41:115411
76. Chandra S, Annapoorni, Sonkawade RG et al (2009) Indian J Phys 83:943
77. Hussain AMP, Kumar A, Singh F et al (2006) J Phys D 39:750
78. Ramola RC, Alqudami A, Chandra S et al (2008) Radiat Eff Def Solids 163:139
79. Kaur A, Dhillon A, Avasthi DK (2009) J Appl Phys 106:73715
80. Chandra S, Annapoorni S, Singh F et al (2010) J Appl Polym Sci 115:2502
81. LeMoel A, Durand JP, Lecomte C et al (1988) Nucl Instrum Meth B 32:115
82. Licciardello A, Puglisi O, Calcagno L et al (1989) Nucl Instrum Meth B 39:769
83. Xu D, Xii XL, Du GD et al (1993) Phys Stat Sol (a) 136:433
84. Marletta G, Pignataro S, Oliveri C (1989) Nucl Instrum Meth B 39:773
85. Fink D, Klett R (1995) Braz J Phys 25:54
86. Fink D, Alegaonkar PS, Petrov AV et al (2003) Radiat Meas 36:605
87. Zhdanov GS, Bogacheva AV, Milinchuk VK et al (2000) Fourth international symposium on ionizing radiation and polymers, 24–28 Sept 2000
88. Smolyanskii AS, Zvezdina OS, Plotnikov VG (2000) Abstract submitted to the fourth international symposium on ionizing radiation and polymers, 24–28 Sept 2000
89. Ferain E, Legras R (1997) Nucl Instrum Meth B 131:97
90. Pasternak CA, Alder GM, Apel PY et al (1995) Nucl Instrum Meth B 105:332
91. Popok VN, Karpovich IA, Odzhaev VB (1999) Nucl Instrum Meth B 148:1106
92. Ogiso H, Ishida T, Mizutani W et al (1999) Nucl Instrum Meth B 148:1097
93. Chen J, Klaumünzer S, Lux-Steiner MC et al (2004) Appl Phys Lett 85:1401
94. Berdinsky AS, Shevtsov YV, Okotrub AV et al (2000) Chem Sustain Dev 8:141
95. Kanjilal D, Chopra S, Narayanan MM et al (1993) Nucl Instrum Meth A 328:97
96. Kim BJ, Oh SG, Han MG (2001) Synth Met 122:297
97. Kim BJ, Oh SG, Han MG (2000) Langmuir 16:5841
98. Harada M, Adachi M (2000) Adv Mater 12:839
99. Mallick P, Rath C, Prakash J et al (2010) Nucl Instrum Meth B 268:1613
100. Sharma T, Aggarwal S, Sharma A et al (2007) J Appl Phys 102:063527
101. Copeland LE, Bragg RH (1958) Anal Chem 30:196
102. Omastova M, Trchova M, Kovarova J et al (2003) Synth Met 138:447
103. Gade VK, Shirale DJ, Gaikwad PD et al (2007) Int J Polym Mater 56:107
104. Rizk RAM, Abdul-Kader AM, Ali ZI et al (2009) Vacuum 83:805
105. Compagnini G, Foti G, Reitano R et al (1990) Appl Phys Lett 57:2546
106. Rizk RAM, Abdul-Kader AM, Ali M et al (2008) Phys D Appl Phys 41:205304
107. Virk HS, Chandi PS, Srivastava AK (2001) Nucl Instrum Meth B 183:329
108. Fink D, Klett R, Chadderton LT et al (1996) Nucl Instrum Meth B 111:303
109. Crowley K, Cassidy J (2003) J Electroanal Chem 547:75
110. Gongcalves AB, Mangrich AS, Zarbin AJG (2000) Synth Met 114:119
111. Liu Y, Hwang BJ, Jian W et al (2000) Thin Solid Films 374:85
112. Zarbin AJG, De-Paoli MA, Alves OL (1999) Synth Met 99:227

113. Bazzaoui EA, Levi G, Aeiyach S et al (1995) J Phys Chem 99:6628
114. Xu J, Shi G, Xu Z et al (2001) J Electroanal Chem 514:16
115. Ali Y, Sonkawade RG, Dhaliwal AS (2013) Nucl Instrum Meth B 316:42
116. Sidebottom DL (1999) Phys Rev Lett 82:3653
117. Rao S, Murali Krishna K, Madhava Prasad P et al (2008) J Alloys Compd 464:497
118. Havriliak S, Negami S (1967) Polymer 8:161
119. Neagu RM, Neagu N, Bonanes N et al (2000) J Appl Phys 88:6669
120. Ghosh S, Ghosh A (2003) J Chem Phys 119:9106
121. Qureshi A, Singh NL, Shah S et al (2008) J Macromol Sci Pure Appl Chem 45:265
122. Saha S, Sinha TP (2002) Phys Rev B 75:069901
123. Kohlrausch R (1847) Prog Ann 12:393
124. Migahed MD, Bakr NA, Abdel-Hamid MI et al (1996) J Appl Polym Sci 59:655
125. Williams G, Watts DC (1970) Trans Faraday Soc 66:80
126. Dietmar F, Chadderton LT (2005) Radiat Eff Def Solids 160:67

Impact of Etchant Variables on the Track Parameters in CR-39 Polymer Nuclear Track Detector: A Review

Pawan K. Diwan

Abstract Nuclear track detector has numerous applications in various fields. The effective use of this detector depends upon the thorough understanding of track parameters of energetic ions. The present study attempts to develop and strengthen this understanding. It describes the various methods to measure bulk etch rate (V_B) of the detector and track etch rate (V_T) of the incident ions. Further, it throws light on the other parameters such as bulk activation energy (E_B), track activation energy (E_T), sensitivity (S), critical angle (θ_C) and etching efficiency (η). Finally, an attempt is made to review the studies related to the impact of different etchants and etchant variables on the different types of CR-39. Based on the observations available in the literature, the comparisons are made among impacts of different etchants on CR-39 and results are compiled. The present review concludes the observations and their relevant impacts.

Keywords CR-39 · Chemical etching · Track etch rate · Bulk etch rate · Activation energy · Sensitivity · Etching efficiency · Critical angle

1 Introduction

The field of nuclear track detector was introduced in 1958 when Young reported a remarkable note on his study in *Nature* [1]. In this study, he observed fission fragment tracks in LiF crystal, which was initially placed in contact with uranium foil, irradiated with thermal neutrons and treated with chemical etching. He performed these measurements in Atomic Energy Research Establishment (AERE) at Harwell in England. After one year, in 1959, working in the same laboratory, Silk and Barnes also observed fission fragments tracks in mica. In their investigations, mica was not chemically etched, but tracks were viewed through transmission electron microscope (TEM) [2]. These two studies are historically important in the

P. K. Diwan (✉)
Department of Applied Science, UIET, Kurukshetra University, Kurukshetra 136119, India
e-mail: diwanpk74@gmail.com

V. Kumar et al. (eds.), *Radiation Effects in Polymeric Materials*, Springer Series on Polymer and Composite Materials, https://doi.org/10.1007/978-3-030-05770-1_7

field of nuclear track detector, but the field was popularized by the team of three scientists (R.L. Fleischer, P.B. Price and R.M. Walker) who were working at the General Electric Research Laboratories at Schenectady, New York. They extend the chemical etching technique and tried different etchants on variety of materials such as minerals, glasses and polymers to reveal the tracks. Further, they used these materials, later known as nuclear track detector, to explore different applications in various scientific fields. Based on their investigations, they published number of research articles. Finally, they compiled their own studies and studies available in the literature in the form of a book [3], which acts as a landmark in this field.

Nowadays, nuclear track detectors are widely used to detect/measure different types of nuclear radiations involved in various fields such as nuclear physics [4–7], space science and radiation dosimetry [8–16], micro-technology [17, 18], nanotechnology [19, 20], environmental studies [21–23], archaeology [24, 25], biology and medicine [15, 26, 27] and many more [3, 28–32]. These detectors are most commonly known as solid-state nuclear track detectors (SSNTDs) and are more promising as compared to other detectors due to their simplicity, low cost, less weight, high efficiency and durability. Also, these detectors do not involve any sophisticated instrumentation. Further, SSNTDs provide a unique opportunity to visualize the complete path of nuclear radiations, from its entrance to almost its end point [3, 30–32].

Researchers, around the globe, tried various materials as track detectors to detect different types of radiations. These materials/track detectors are broadly categorized into three categories, viz. glasses, minerals and plastics. In the category of plastic track detector, CR-39, a polymer of poly-allyl diglycol carbonate (PADC), is the most commonly used track detector due to its high detection sensitivity, superb optical quality, thermoplasticity, mass and charge resolution [33–36]. Although CR-39 polymer is commercially available and is used to make high-quality optical lenses, its usage as a nuclear track detector was first reported by Cartwright et al. [37]. Thereafter, researchers started using CR-39 polymer extensively as a nuclear track detector to detect different types of radiations varying from light ions to the extremely heavy ions, in various applications [10, 11, 23, 34–36, 38–41].

In order to widen the range of applications, researchers worked on two fundamental aspects: (a) to develop/improve CR-39 with better characteristics and (b) to improve etching properties of CR-39. Related to the first aspect, few research studies are available [42–44], where researchers tried to enhance the etch-track contrast and optical quality of post-etch surface by introducing small quantities of various plasticizers in CR-39 monomer. However, following this procedure, sensitivity of the detector is generally reduced, and hence, no remarkable progress was achieved. As far as second aspect is concerned, appreciable attempts are made to improve the etching properties of CR-39. For this, researchers performed series of experiments and tried different etchants and etchant variables (concentration and temperature) on CR-39 to reveal the ion's tracks and measured track parameters. These track parameters are highly essential to use CR-39 as a track detector in a variety of applications. Further, out of these applications, CR-39 is widely used for the detection of α-particles emitting from natural radioactive sources, in the field of

radiation protection and environmental radiation monitoring. Therefore, the response of CR-39 polymer track detector against α-particles is of essential interest.

The present review deals with the impact of different etchants on the CR-39 polymers track detector. Since CR-39 is widely used in α-particle detection/protection, so the study is confined with etching parameters of α-particle only. The study describes the track formation mechanism, etching procedure, track etching parameters and methods. Further, these etching parameters are compiled as a function of different etchants, to use for future studies/applications.

2 Track Formation and Etching Parameters

The energetic ions, while passing through solid, lose all or some of its orbital electrons in the few atomic layers of solids. Consequently, these energetic ions become fully stripped (lose all electrons) or partially stripped (lose some electrons). These fully/partially stripped ions further pass through the material and transfer their energies to the electrons of the target atoms via inelastic collisions, and as a result, the electrons are: (a) ejected from the original position (ionization) and/or (b) excited from original state to less tightly bound state (excitation). This is known as primary ionization and excitation. The ejected electrons (delta rays) produced through ionization are further capable of generating ionization and excitations in the material. This is the secondary ionization and excitation. This secondary ionization and/or excitation totally depends upon the kinetic energy of the ejected electrons. It is meaningful to mention that the primary ionization and excitation occur close to the path of the ions, while the secondary ionization and excitation spread over large radial distances from the path. In addition to primary and secondary ionization/excitation, the radiations emitted through de-excitation process also break the long molecular chain and produce free radicals and, as a result, reduce the average molecular weight. As far as polymers are concerned, both primary and secondary ionization/excitation contributes to create the narrow trails along the ion trajectory. These narrow trails are popularly known as latent tracks. Further, the shape of these latent tracks depends upon the angle of incidence of energetic ion with the material. For normal incidence, conical tracks are formed, and for other angle of incidence, elliptical latent tracks are formed [3, 30].

In track etch technique, these latent tracks are enlarged with the suitable etchants (Figs. 1 and 2). Here, it is clear from these figures that the effect of etchant along the latent track is more than the surrounding undamaged material. The rate at which the etchant attacks along the track is termed as track etch rate (V_T) and it depends upon the nature of incident particle (atomic number and energy of incident particle) and etching conditions. The surrounding undamaged material is attacked with different etch rates, which is termed as bulk etch rate (V_B). The bulk etch rate is generally constant for a given material for a particular etching condition [3, 30]. Both track and bulk etch rates provide the information of the complex chemical processes taking place within solid including transport of etching products, diffusion of

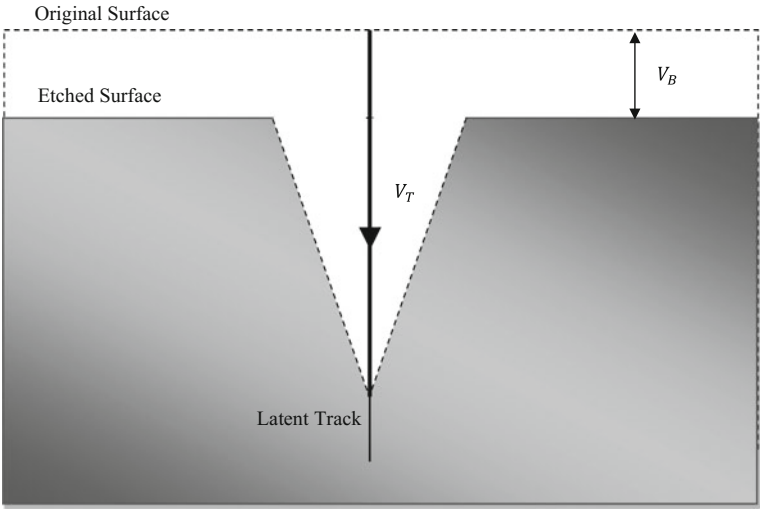

Fig. 1 Geometry of the track development for normal incidence

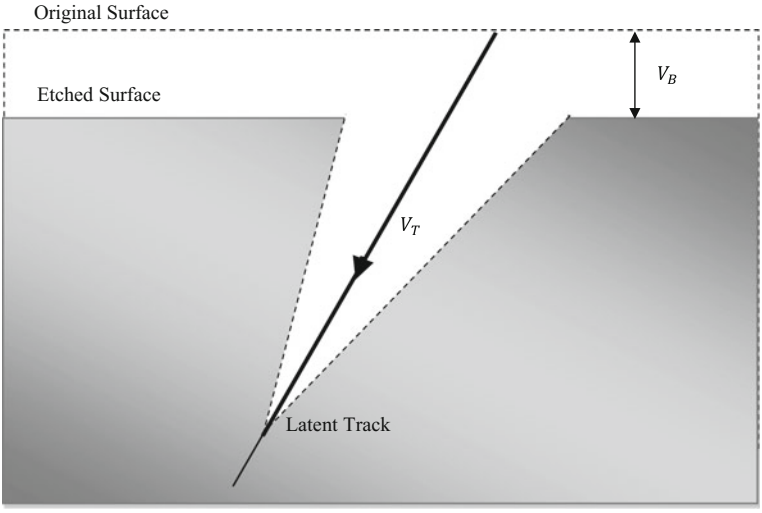

Fig. 2 Geometry of the track development for oblique incidence

etching solution and radiation damage. So, it is highly essential to know the effect of different etchants and etchant variables on the track and bulk etch rates.

The next section reviewed the impact of different etchant variables on track etch and bulk etch rates of CR-39 polymer track detector. Along with these etch rates,

other associated etching parameters such as sensitivity (S), critical angle (θ_C) and etching efficiency (η)) are also discussed.

3 Etching Parameter Measurements

3.1 Bulk Etch Rate

The bulk etch rate (V_B) is the rate of removal of undamaged surface of the detector due to the chemical reaction between the etchants and the detector material. It depends upon the type, concentration and temperature of the etchant solution and duration of etching time. The bulk etch rate is an important parameter, which provides (i) a reference to measure other etching parameters and (ii) acts as a calibration parameter for the detector and the etching process.

3.1.1 Methods for Bulk Etch Rate (V_B) Measurements

Mainly, the following three methods are used for bulk etch rate measurements:

1. *Track Diameter Method*

In this method, firstly, detector is exposed with the fission fragments at normal incidence using Cf^{252} source; secondly, the exposed detector is etched with suitable etchants; and finally, the average diameters of the enlarged tracks are measured using screw micrometre attached with eye piece of optical microscope.

Suppose D_{ff} is the average track diameter of fission fragments after etching time t, then bulk etch rate (V_B) of the material is measured through the following relation [30]:

$$V_B = \frac{1}{2}\left(\frac{D_{ff}}{t}\right)$$

2. *Thickness Measurement Method*

In this method, micrometre (with least count 1 μm) is used for thickness measurement. Suppose $d_{without}$ and d_{with} are the thicknesses of the detector at a particular point without and with etching, respectively. Based on this thicknesses difference, the bulk etch rate is determined through the relation [45, 46]:

$$V_B = \frac{(d_{without} - d_{with})}{2t}$$

where t is the etching time.

3. *Weight Loss (Gravimetric) Method*

In this method, mass of detector is measured before and after etching. Based on the mass difference (Δm), area (A) and density (ρ) of the detector, the bulk etch rate is measured through the following relation [47, 48]:

$$V_{\mathrm{B}} = \frac{\Delta m}{2A\rho t}$$

where t is the etching time.

3.1.2 Activation Energy of Bulk Etch Rate (V_{B})

Activation energy is the energy required to activate the reaction between the detector material and etching solution. This gives the information regarding the kinetics of the reaction.

In order to measure the activation energy of bulk etch rate, firstly, the bulk rate (V_{B}) of detector is measured at different temperatures for fixed etching conditions, and then, graph is plotted between $\ln V_{\mathrm{B}}$ and $\frac{1000}{T}$ (K^{-1}). Using a least square fit, the value of bulk activation energy (E_{B}) for the detector is determined from the slope of the straight line through the following relation:

$$\ln V_{\mathrm{B}} = \ln A - \left(\frac{E_{\mathrm{B}}}{KT}\right)$$

where

K is the Boltzmann constant and
A is a constant for a particular normality.

3.1.3 Bulk Etch Rate and Activation Energy Measurements of CR-39 Track Detector

Cartwright et al. [37] measured bulk etch rate of CR-39 (Pittsburgh) through track diameter method at different concentrations (3–10N) of NaOH. They observed linear relationship between bulk etch rate and etchant concentration. The measured activation energy of bulk etch rate was 0.85 ± 0.05 eV.

Rana and Qureshi [49] etched fission fragment exposed CR-39 (Pershore Mouldings) detector with 6N NaOH solution at 70 °C for 3-h duration, and diameters of fission fragments tracks were measured. Using average track diameter and etching time, the bulk rate was determined, which was 1.43 ± 0.07 μm/h. In this study, they also measured bulk etch rate of CR-39 detector with different concentrations (3, 5, 6, 7N) of NaOH at seven different temperatures (50, 55, 60,

65, 70, 75, 80 °C) and observed that bulk etch rate shows Arrhenius dependence on temperature. From the measured bulk rate as a function of temperature at different concentrations, they measured activation energy, which was 0.939 ± 0.068 eV.

Adopting track diameter method, Farid [50] measured the bulk etch rate of CR-39 (Pershore Mouldings) using 6N NaOH as an etchant at five different temperatures (30, 40, 50, 60 and 70 °C) and pointed out that bulk etch rate exponentially depends upon the etchant temperature. The activation energy of bulk etch rate, reported in this study, is 0.75 ± 0.03 eV.

Ansari et al. [51] exposed two types of CR-39 (American Acrylics, Pershore Mouldings) detector with fission fragments (Cf^{252} source), and after etching the detectors with different time duration in 6M NaOH solution at fixed temperature (70 °C), they measured the track diameter using optical microscope. From track diameter and etching time plot (track diameter method), bulk etch rate of CR-39 was determined. The reported bulk etch rate values for CR-39 (American Acrylics) and CR-39 (Pershore Mouldings) are 1.1 and 1.2 μm/h, respectively. These values show that the bulk etch rate for CR-39 (Pershore Mouldings) is slightly higher than CR-39 (American Acrylics).

In order to study the depth dependence bulk etch rate, Kobayashi and Fujii [52] used different types of CR-39, manufactured by Solar Optical Japan (SOJ) and Teijin Lens Limited (TL). They exposed these detectors with fission fragments and etched with the 7N NaOH solution at 70 °C. In their study, the surface removal of CR-39 due to etchant was measured with the help of micrometre and bulk etch rate was measured adopting track diameter method. They observed that, in the considered samples, bulk etch rate first increases with the increase in depth and then decreases. Authors also tried new etchant (different ratios of NaOH and $(C_2H_5)_4NOH$), at different temperatures, and measured the bulk etch rate.

Bethe et al. [53] exposed CR-39 (Pershore Mouldings) detector with fission fragments and etched these detectors with three different concentrations (4, 6 and 8N) of NaOH solution at five different temperatures (30, 45, 60, 70 and 80 °C). Adopting track diameter method, bulk etch rate was measured as a function of etchant concentration and etchant temperature. They observed that bulk etch rate values increase with the increase in (a) etchant concentration at particular temperature and (b) etchant temperature at particular normality. Further, based on the experimentally measured bulk etch rate (μm/h) values, a semi-empirical relation was developed, which is expressed as:

$$V_B(N,T) = 8.33 \times 10^{10} e^{\left(0.286N - \frac{1}{T}\right)}$$

The activation energy determined from the bulk etch measurements was 0.792 ± 0.024 eV with 6N NaOH solution.

Awad and El-Samman [54] irradiated the American Acrylic CR-39 track detector with fission fragments and etched with NaOH etchant with different concentrations (4, 5, 6.25, 8 and 9N) and at five different temperatures (50, 61, 72, 80 and 90 °C). For bulk etch rate measurements, they adopted track diameter method.

Based on the experimentally measured values, they observed temperature-dependent bulk etch rate and expressed by an Arrhenius-type equation. Using this equation, they plotted the graph between $\ln V_B$ and $\frac{10^3}{T}$ (K^{-1}) and measured the activation energy, which was 0.80 ± 0.04 eV.

The bulk etch rate of a CR-39 (Homalite) was measured as a function of different concentrations (4–10N) of NaOH solution at different temperatures varying from 50 to 80 °C, using weight loss method. The measurements reveal that bulk etch rate increases linearly with the increase in etchant concentration and follows a power law, which is expressed by,

$$V_{\mathrm{B}} = AC^{n}$$

where C is the etchant concentration and A and n are the temperature-dependent constants. Finally, based on their measurements and fitted constants, they developed a fitted relation for bulk rate (μm/h) as a function of etchant concentration and etchant temperature and written as:

$$V_{\mathrm{B}}(C,T) = AC^{2.46}\mathrm{e}^{(0.83/kT)}$$

The average activation energy, obtained through these measurements, is 0.83 ± 0.04 eV [55]

Charvát and Spurný [56] measured bulk etch rate of CR-39, through fission track diameter and thickness measurement methods, as a function of etchant concentration (1–10N NaOH) and at different temperatures (40–70 °C). They observed that bulk etch rate increases exponential with the increase in etchant normality up to a concentration of 6N. From the measured values, they examined that Arrhenius equation is valid for the considered concentrations and temperatures. The average activation estimated through the Arrhenius equation is 0.745 ± 0.033 eV. They also observed that etchant concentration has only a minor influence on the bulk activation energy.

In order to avoid surface effects [57] and to ensure that the fission fragment tracks are over-etched, Hermsdorf et al. [58] pre-etched the CR-39 (TASTRAK) detectors before starting measuring procedure. After this, they exposed CR-39 with fission fragments and etched the detectors with different concentrations (0.5–22 mol/l) of NaOH solution at different temperatures. They measured bulk etch rate as a function of concentration and observed that bulk etch rate cannot be understood by simple Arrhenius equation, which separates both variables: concentration and temperature.

Ghazaly et al. [59] measured bulk etch rate of CR-39 (TASTRACK) after etching the detector with 7.25N NaOH etchant at 70 °C through weight loss method. The measured value of bulk etch rate is 1.80 ± 0.05 μm/h. The same method and temperature are also evidenced in the study of Hofy et al. [60], and reported values are 2.33 μm/h and 6.58 μm/h with 30% NaOH and 60% NaOH solution, respectively.

Besides the commonly used methods, masking method is also used to measure bulk etch rate of CR-39 (Page Mouldings) as a function of different concentrations of NaOH/ethanol. Here, the measured bulk etch rate increases with the increase in etchant concentration up to 2.5N, and after this, it starts declining. Further, authors also studied the effect of stirring on the bulk etch rate and observed higher bulk etch rate than without stirring at same etchant concentration [61].

Based on measured bulk etch rate of CR-39(TASTRACK) detector with different concentrations of NaOH at temperature range ~333 to 353, Fromm et al. [62] developed a following empirical relation for bulk etch rate measurements.

$$V_B = 1.276\, e^{[2.303(0.828C + 0.049T - 0.002CT - 17.624)]}$$

where concentration (C) is in *mol/l* and etchant temperature (T) in *degree Kelvin*.

CR-39 (Pershore Mouldings) were etched with five different NaOH concentrations (2, 4, 6, 8 and 10M) at six different temperatures (40, 50, 59, 65, 68 and 75 °C), and bulk etch rate was measured using weight loss method. The measurements reveal that the bulk etch rate increases with the increase in etchant temperature/concentration at particular concentration or temperature. Based on the measured values, they developed a relation for bulk etch rate as a function of temperature:

$$V_B(M, T) = 9.88 \times 10^{10} e^{\left[0.271 - \left(\frac{9263.8}{T}\right)\right]}$$

Further, from the plots between ln V_B and $\frac{1000}{T}$ (K^{-1}) for different concentrations, the activation energies were determined. The average value of activation energy is found to be 0.799 ± 0.013 eV. In this study, it was also observed that the activation is independent of the etchant concentration [63].

In order to see the effect of stirring on the bulk etch rate of Pershore Mouldings type CR-39, Ho et al. [64] etched the detectors with 6.25N NaOH at fixed temperature (70 °C) with and without magnetic stirring. They observed 1.104 ± 0.024 µm/h and 1.195 ± 0.028 µm/h bulk etch rate with magnetic stirring and without magnetic stirring, respectively.

Singh et al. [65] etched CR-39 detector with 6.25N NaOH solution at four different temperatures (65, 70, 75 and 80 °C), and bulk etch rate was measured, using thickness measurements method. In their study, they observed that bulk etch rate increases with the increase in temperature, at fixed etchant concentration. They also measured the bulk etch rate as a function of concentration (1, 2.5 and 6.25N) of NaOH at fixed temperature (75 °C) and observed the increase in bulk etch rate with the etchant concentration. Based on the measured bulk etch rate as a function of temperature, they measured the activation energy, which is 0.92 eV with 6.25N NaOH solution. Further, in their study, they used three etchants, viz. $Ba(OH)_2.8H_2O$, NaOH and $LiOH{\cdot}H_2O$, at 75 °C for bulk etch rate measurements and reported bulk etch rate values are 0.81 µm/h for 1N $Ba(OH)_2{\cdot}8H_2O$, 0.18 µm/h for 1N NaOH and 0.28 µm/h for 1N $LiOH{\cdot}H_2O$. From these reported values, it is clear

that the bulk etch rate with $Ba(OH)_2 \cdot 8H_2O$ etchant is higher than NaOH and $LiOH \cdot H_2O$ etchants.

CR-39 (Pershore Mouldings) detectors were etched with different concentrations of NaOH and methanol at fixed temperature (50 °C), and bulk etch rate was measured, through thickness measurement method. It was observed that bulk etch rate value is maximum when a combination of 60% methanol and 40% NaOH was used an etchant [66].

Khan et al. [67] etched exposed CR-39 samples in conventionally used 6M NaOH solution in the presence of 1, 2, 3, 4, 5% Na_2CO_3 and observed significant enhancement in activation energy of bulk etch rate at 4% of Na_2CO_3.

Ashry et al. [68] measured the bulk etch rate of CR-39 (TASTRACK) detector through the track diameter method. For this purpose, they exposed the detectors with the fission fragments, using Cf^{252} source, and then etched with various combinations of 8 ml of 10N NaOH with different amounts of methanol (CH_3OH) at various temperatures (55, 60, 65, 70 °C). They observed that the bulk etch rate increases with the increase in the amount of methanol and etchant temperature. The bulk etch rate of CR-39 track detector with etching condition 10N NaOH + 1 ml CH_3OH at 60 °C is found to be 2.73 μm/h. Further, they measured the activation energy of bulk etch rate at different amounts of methanol and average value found to be 0.88 eV.

Matiullah et al. [69] exposed CR-39 (Page Mouldings) detectors, at normal incidence, with fission fragments using thin Cf^{252} source. In order to see the impact of different etchants on bulk etch rate, one set of detectors is etched with different concentrations of NaOH solution at 70 °C, second set etched with different concentrations of NaOH/1-propanol at 49 °C and third set etched with different concentrations of NaOH/ethanol solution at 55 °C. These bulk rate measurements were taken using track diameter method. From these measurements, it was observed that bulk etch rate increases with the increase in concentration of NaOH at 70 °C. In case of NaOH/1-propanol and NaOH/ethanol etching solutions, first bulk etch rate increases and then decreases with the increase in etchant concentration. They also measured the activation energies of bulk etch rate for these etchants. The measured activation energies were 0.77 eV for NaOH, 0.83057 eV for NaOH/1-propanol and 0.7928 eV for NaOH/ethanol etchant.

Matiullah et al. [70] tried two other etchants (NaOH/methanol and NaOH/methanol + water) at different temperatures on CR-39 (Page Mouldings) to see the impact on bulk etch rate. With 1.5M NaOH/methanol etchant, highest measured bulk etch rate value was 62.5 μm/h at 55 °C. However, no systemic trend in bulk etch rate as a function of temperature was observed. After this, they used another etchant (10% NaOH dissolved in X% methanol and $(90 - X)$% water) at 55 °C and measured the bulk etch rate as a function of methanol concentration, which varied from 40 to 80%. The measured bulk etch rate first increased and then decreased with the increase in percentage of methanol, and the maximum observed bulk etch rate values was 1.292 μm/h at 55 °C.

Tse et al. [71] through their measurements observed that the bulk etch rate of CR-39 (Page Mouldings) in NaOH/ethanol etchant is faster than $NaOH/H_2O$.

Through mass spectrometry, they observed same etched products of CR-39 for both the etchants. They clarified that same etching mechanism is involved in CR-39 for both the etchants and higher bulk etch rate is due to high solubility of CR-39 in ethanol.

Tahiri et al. [72] measured the activation energy of bulk etch rate of CR-39 (Page Mouldings) with different etchants (LiOH, NaOH, molten $Ba(OH)_2{\cdot}8H_2O$) at different temperatures and reported 0.88 ± 0.02 eV activation energy for LiOH, 0.77 ± 0.08 eV for NaOH and 1.37 ± 0.11 eV for $Ba(OH)_2{\cdot}8H_2O$ molten state. They observed that bulk activation energy for molten $Ba(OH)_2{\cdot}8H_2O$ etchant is higher than the other two considered etchants.

Somogyi et al. [73] measured the bulk etch rate of three different types of CR-39 (Homalite, Pershore Mouldings and MA-ND) and observed that the bulk etch rate depends upon the type of CR-39 and is a thickness-dependent parameter, i.e. it varies with the change of thickness of even same type of CR-39.

The bulk etch rate was measured in NaOH and KOH with different concentrations from 1 to 12N and at different temperatures of 40, 50, 60, 70 and 80 °C. These measurements were taken through track diameter technique. The observation reveals that bulk etch rate increases with the increase in concentration and temperature for both NaOH and KOH etchants. Further, result shows that at all temperatures, the bulk etch rate for a given normality of KOH is greater than that for the same normality of NaOH etchant. The activation energy of CR-39 (Pershore Mouldings) obtained through these measurements was 0.77 ± 0.02 eV for NaOH and 0.76 ± 0.03 eV for KOH [74].

Amin and Henshaw [75] etched CR-39 (Pershore Mouldings) exposed samples using various concentrations of KOH and NaOH and measured track diameter of fission tracks. Using fission track diameter and etching time, they measured the bulk etch rate and observed that bulk etch rate increases steadily with the increase in the concentration range 4.5–40%. They also added various quantities of methyl alcohol in 6.25N NaOH solutions and etched CR-39 samples at various temperatures (25, 37, 60, 70 °C) and observed that bulk etch rate increases remarkably with the ratio of methanol to NaOH. Further, they studied the effect of bulk etch rate as a function of relative concentration of 6.25N NaOH/methanol and 6.25N NaOH/ethanol solution at 37 °C and no significant difference in bulk etch rate was noticed.

CR-39 (Pershore Mouldings) samples were etched with 6.25M KOH at constant temperature of 60 ± 0.5 °C for different etching time, and bulk etch rate was measured through the following relation:

$$V_B = \frac{(M_1 - M_2)D_1}{2M_1 t}$$

where M_1 and M_2 are the initial and final weights after etching time t and D_1 is the initial thickness of the detector. The mass of each detector was determined before and after etching at different etching time using a sensitive balance with an accuracy of ± 0.01 mg, and the detector thickness D_1 was measured electronically using a sensitive device with an accuracy of ± 1 μm. The change in the mass according to

the above equation as a function of the etching time is plotted. A linear relationship is observed resulting in a constant bulk etch rate of $V_b = 1.37 \pm 0.05$ μm/h over an etching time of 20 h [76].

3.1.4 Data Compilation of Activation Energy of Bulk Etch Rate of CR-39

The measured bulk activation energy of different types of CR-39 using NaOH as an etchant is given in Table 1. It is clear from the table that bulk activation energy of Pershore Mouldings, Page Mouldings and American Acrylic types CR-39 generally varies from 0.75 to 0.80 eV. It is further noticed that the bulk activation energy of Pittsburgh and Homalite is slightly higher than Pershore and Page Mouldings type CR-39.

Table 2 presents the bulk activation energy of CR-39 as a function of different etchants. From the reported values, it is observed that the value of bulk activation energies is almost same for NaOH, KOH and NaOH/ethanol etchants. Further, it is observed that the activation energy due to NaOH/1-propanol, LiOH and NaOH + CH_3OH etchants is higher and is maximum with molten $Ba(OH)_2 \cdot 8H_2O$ etchant.

3.2 *Track Etch Rate*

Track etch rate is the rate at which the etchant attacks along the damaged trails in the detector. Along with the etching conditions, track etch rate also depends upon

Table 1 Activation energy of bulk etch rate of different types of CR-39 with NaOH

Type of CR-39	Activation energy (eV)	References
Pershore Mouldings	0.939 ± 0.068	[49]
Pershore Mouldings	0.75 ± 0.03	[50]
Pershore Mouldings	0.792 ± 0.024	[53]
Pershore Mouldings	0.799 ± 0.013	[63]
Pershore Mouldings	0.77 ± 0.02	[74]
Page Mouldings	0.77	[69]
Page Mouldings	0.77 ± 0.08	[72]
American Acrylic	0.80 ± 0.04	[54]
Pittsburgh	0.85 ± 0.05	[37]
[a]	0.745 ± 0.033	[56]
[a]	0.92	[65]
Homalite	0.83 ± 0.04	[55]

[a]Type of CR-39 not mentioned

Table 2 Activation energy of bulk etch rate of different types of CR-39 with different etchants

Etchant	Activation energy (eV)	References
Pershore mouldings		
NaOH	0.75 ± 0.03	[50]
NaOH	0.792 ± 0.024	[53]
NaOH	0.799 ± 0.013	[63]
NaOH	0.77 ± 0.02	[74]
KOH	0.76 ± 0.03	[74]
Page Mouldings		
NaOH	0.77	[69]
NaOH	0.77 ± 0.08	[72]
NaOH/ethanol	0.7928	[69]
NaOH/1-propanol	0.83057	[69]
LiOH	0.88 ± 0.02	[72]
$Ba(OH)_2 \cdot 8H_2O$ molten	1.37 ± 0.11	[72]
TASTRACK		
NaOH + CH_3OH	0.88	[68]

the atomic number and energy of incident ion. Without the understanding of this parameter, track detector cannot be used in most of the applications.

3.2.1 Methods for Track Etch Rate (V_T) Measurements

As discussed in Sect. 2, when energetic ions enter into the detector, they generate latent tracks. These latent tracks are enlarged with suitable etchants and etching conditions (concentration and temperature of etchants) that vary from detector to detector and these enlarged tracks can be viewed through ordinary optical microscope. The diameters/lengths of these enlarged tracks as a function of etching time is measured using screw micrometre attached with eye piece of optical microscope.

In case of track diameter, the track etch rate is measured through the following relation:

$$V_T = \frac{4V_B^3 t^2 + V_B D^2}{4V_B^2 t^2 - D^2}$$

This relation is applicable mainly for circular tracks but can be used for elliptical tracks also. For elliptical tracks, the minor axis of the tracks is considered instead of track diameter.

In case of track length, the track etch rate is determined from the linear portion of the plot between track length and the etching time.

3.2.2 Activation Energy of Track Etch Rate

Activation energy is the energy required to activate the reaction between the damaged trails, in the detector, and etching solution. With activation energy, one can understand the reaction kinetics.

The activation energy of track etch rate (E_T) is determined from $\ln V_T$ versus $\frac{1000}{T}$ (K^{-1}) plot, through the following relation:

$$\ln V_T = \ln A - \left(\frac{E_T}{KT}\right)$$

where

K is the Boltzmann constant and
A is a constant for a particular normality.

3.2.3 Track Etch Rate and Activation Energy Measurements of CR-39 Track Detector

Ansari et al. [51] irradiated CR-39 (American Acrylics) and CR-39 (Pershore Mouldings) detector with α-particles using Cf^{252} source. These detectors are etched with 6M NaOH solution at fixed temperature (70 °C) to measure the track etch rate of α-particles. The measured track etch rate in CR-39 (American Acrylics) shows slightly lesser value than CR-39 (Pershore Mouldings) when etched with identical etching conditions.

CR-39 detectors were exposed with α-particles using Am^{241} source and etched with different concentrations (1–10N) of NaOH solution at various temperatures (40, 50, 60, 70 °C) and measured the track etch rate. The track etch rate as a function of etchant concentration shows exponential behaviour up to 6N. Further, they measured the activation energy using Arrhenius equation and reported value is 0.906 ± 0.093 eV. They observed that etchant concentration has not a significant impact on the activation energy [56].

Matiullah et al. [69] measured the track etch rate (V_T) of α-particles in CR-39 (Page Mouldings) through the following relation:

$$V_T = V_B \frac{\left(1 + \frac{D_\alpha^2}{D_{ff}^2}\right)}{\left(1 - \frac{D_\alpha^2}{D_{ff}^2}\right)}$$

where D_α and D_{ff} are the average track diameter of α-particles and fission fragments, respectively. In their measurements, they observed that in case of NaOH etchant (temperature: 70 °C), the track etch rate increases with the increase in

concentration. However, in NaOH/1-propanol (temperature: 49 °C) and NaOH/ethanol (temperature: 55 °C) etchants, first track etch rate increases and then decreases with the increase in etchant concentration. The maximum track etch rate was 1.063 μm/min and 261.488 μm/min for 1.2M NaOH/1-propanol and 1.5M NaOH/ethanol etchant, respectively. They also measured the activation energy of track etch rate, which is 0.67 eV for NaOH, 0.7267 eV for NaOH/ethanol and 0.7336 eV for NaOH/1-propanol etchants.

The track etch rate of α-particles in CR-39 (Page Mouldings) detector was measured using 1.5M NaOH/methanol etchants at different temperatures (40, 45, 50, 55, 60 °C) and observed maximum track etch rate value at 55 °C. In their study, authors also etched CR-39 detectors with other etchants (10% NaOH dissolved in X% methanol and $(90 - X)$% water) at 55 °C and observed that the track rate increases with the increase in methanol concentration up to 70% and then decreases. The maximum track rate was 6.092 μm/min, which was at 70% methanol concentration [70].

Tahiri et al. [72] reported track activation energy 0.74 ± 0.06 eV, 0.67 ± 0.04 eV and 0.97 ± 0.10 eV for LiOH, NaOH and molten $Ba(OH)_2 \cdot 8H_2O$ etchants, respectively. They noticed that track etch activation energy is maximum for molten $Ba(OH)_2 \cdot 8H_2O$ etchants and minimum for NaOH etchants. In this study, Page Mouldings type CR-39 is used which was exposed with α-particles.

Lounis et al. [76] exposed CR-39 samples with α-particles with different energies using different radioactive sources and etched the samples with 6.25M KOH at constant temperature of 60 ± 0.5 °C. This etching process was undertaken for different etching time from 3 to 10 h. The diameter of α-particles is measured using optical microscope, and track etch rate is plotted as a function of α-energy. It was observed that track etch rate varies noticeably along with the particle energy due to varying energy loss.

Dörschel et al. [77] etched α-particles exposed PATRAS and Pershore Mouldings types CR-39 with 7.25N NaOH solution at 70 °C and observed that the track etch rates in PATRAS type detector are distinctly lower than the Pershore Mouldings type CR-39 detector. Since the bulk etch rate of both types of CR-39 is same, therefore, the sensitivity of PATRAS type detector is lower for the α-particles registration.

3.2.4 Data Compilation of Activation Energy of Track Etch Rate of CR-39

The track activation energy of α-particles in CR-39 (Page Mouldings) as a function of etchants is presented in Table 3. It is clear from the table that activation energy varies with the different etchants and maximum activation energy appears with molten $Ba(OH)_2 \cdot 8H_2O$ etchant.

Table 3 Activation energy of track etch rate of α-particles in CR-39 (Page Mouldings) with different etchants

Etchant	Activation energy (eV)	References
NaOH	0.67	[69]
NaOH	0.67 ± 0.04	[72]
NaOH/ethanol	0.7267	[69]
NaOH/1-propanol	0.7336	[69]
LiOH	0.74 ± 0.06	[72]
$Ba(OH)_2 \cdot 8H_2O$ molten	0.97 ± 0.10	[72]

3.3 Sensitivity

Sensitivity (S) of the detector is a strong function of nature of material and incident ions and is most important parameter for the selection of material for particular application. This is the ratio of track etch rate (V_T) to bulk etch rate (V_B) and expressed as:

$$S = \frac{V_T}{V_B}$$

The sensitivity is also known as etch rate ratio or reduced etch rate.

Ansari et al. [51] etched CR-39 (American Acrylics) and CR-39 (Pershore Mouldings) detectors with 6M NaOH solution at 70 °C and reported track etch rate and bulk etch rate values. From these values, sensitivity of these detectors is determined. The computed sensitivity of these detectors is 1.70 and 1.67 for American Acrylics and Pershore Mouldings, respectively.

Kobayashi and Fujii [52] etched different types of CR-39 detectors with different ratios of NaOH and $(C_2H_5)_4NOH$ (tetraethylammonium hydroxide), at different temperatures and measured $(S - 1)$ for 6.1 MeV α-particles. The measurements reveal that the sensitivity $(S - 1)$ value is maximum with 80% NaOH and 20% $(C_2H_5)_4NO$ etchant mixture.

Ashry et al. [68] observed that sensitivity of CR-39 (TASTRACK) track detector decreases with the increase in α-particle energies when etched with a mixture of 8 ml of 10N NaOH and different amounts of methanol (CH_3OH) at 60 °C for etching time of 45 min. Further, they observed that sensitivity decreases with the increase in amount of (CH_3OH).

Matiullah et al. [69] measured the sensitivity of CR-39 (Page Mouldings) as a function of concentration of two different etchants (NaOH/1-propanol at 49 °C, NaOH/ethanol at 55 °C). They found that sensitivity first increases and then decreases with the increases in concentration. The maximum sensitivity they observed was 3.307 for 1M NaOH/1-propanol and 4.36 for 1.5M NaOH/ethanol. From the available values of track etch and bulk etch rate of CR-39 with different

concentrations of NaOH etchant, the sensitivity of detector as a function of concentration is determined and observed maximum sensitivity (4.0) with 6M NaOH solution at 70 °C.

The measured sensitivity of exposed CR-39 (Page Mouldings) detectors varies with temperatures of 1.5M NaOH/methanol solution. The sensitivity increases up to 55 °C and decreases with the increase in temperature. The maximum sensitivity is 4.55. In this study, authors also observed the impact of other etching solution (10% NaOH dissolved in X% methanol and (90 − X)% water) at fixed temperature (55 °C) on the sensitivity of CR-39 track detector as a function of percentage concentration of methanol. They observed maximum sensitivity (5.212) at 60% methanol [70].

The track registration sensitivity measured by Somogyi et al. [73] for three different types of CR-39 (Homalite, Pershore Mouldings and MA-ND) shows that sensitivity not only depends upon the type of CR-39 but also on the thickness of same type of CR-39. Further, they developed three different types of fitted relation for these three types of CR-39 for alpha particles and examined through correlation that the following is best one.

$$V = 1 + a\mathrm{RR}^{-n}$$

where RR is the residual range; a and n are constants; and fitted values are given in the tabulated form along with the correlation coefficients.

Green et al. [74] measured the sensitivity of CR-39 (Pershore Mouldings) as a function of normality between 1 and 12N with both NaOH and KOH etchants at different temperatures and observed that sensitivity first increases (generally up to 6N) with the increase in normality and then decreases.

Randhawa et al. [78] measured the sensitivity of α-particles irradiated CR-39 and CR-39(DOP) detectors. These detectors were etched with 6.25N NaOH at a constant temperature of 70 °C. They reported the sensitivity of CR-39 and CR-39 (DOP) as a function of etching time. From their measurements, they observed that sensitivity increases up to 10-h etching time and then starts decreasing. The sensitivity at 10-h etching time is 2.47 and 2.53 for CR-39 and CR-39(DOP) plastic track detector.

Hermsdorf [79] reviewed the sensitivity function developed by different authors for registration of α-particles in CR-39 track detector. Based on the new experimental data, they tested these models and developed new parameterization for sensitivity calculations and recommended Fromm et al. [80] and own new parameterization for future applications.

Table 4 presents the maximum sensitivity for registration of α-particles in CR-39 with different etchants at different temperatures. From the table, it is clear that (a) for same etchant and at same temperature, the sensitivity of the different types of detectors is different. (b) Sensitivity of the detector varies with different etchants and etching conditions.

Table 4 Maximum sensitivity for registration of α-particles in CR-39 with different etchants at different temperatures

Type of CR-39	Etchant	Temperature (°C)	Sensitivity (*S*)	References
American Acrylics	6N NaOH	70	1.70[b]	[51]
Pershore Mouldings	6N NaOH	70	1.67[b]	[51]
Page Mouldings	6M NaOH	70	4.00[b]	[69]
[a]	6.25N NaOH	70	2.47	[78]
DOP	6.25 NaOH	70	2.53	[78]
Page Mouldings	1M NaOH/1-propanol	49	3.31	[69]
Page Mouldings	1.5M NaOH/ethanol	55	4.36	[69]
Page Mouldings	1.5M NaOH/methanol	55	4.55	[70]
Page Mouldings	10% NaOH + 60% methanol + 30% water	55	5.21	[70]

[a]Type of CR-39 not mentioned
[b]Computed from the available track etch and bulk etch rate values

3.4 Critical Angle of Etching

Critical angle (θ_C) of etching is the minimum angle of incidence of the incident ions with detector surface for which formed latent track is etchable. This is one of the geometrical limitations for the revelation of the etched tracks in nuclear detector and can be determined through the relation:

$$\theta_C = \sin^{-1}\left(\frac{V_B}{V_T}\right)$$

It simply means that to visualize the tracks, along with the suitable etchants, the angle of incidence is also important. Visualization of tracks is only possible, if the angle of incidence is greater than the critical angle of etching.

Ansari et al. [51] compared the critical angle of α-particles in two types of CR-39 (Pershore Mouldings and American Acrylics) and observed that with same etching conditions (6N NaOH at 70 °C), the critical angle is slightly higher in case of CR-39 (Pershore Mouldings) as compared to CR-39 (American Acrylics).

Ashry et al. [68] studied the variation of critical angle with different combinations of etchant solutions (8 ml of 10N NaOH and different amounts of methanol (CH_3OH) at 60 °C for etching time of 45 min) and different energies of α-particles and observed that critical angle increases with the increase in amount of methanol and α-particle energies.

From the available track etch and bulk etch rate values [69, 70], the critical angle of α-particle in CR-39 (Page Mouldings) with five different etchant combinations is determined. For all the considered etchants, the critical angle first decreases with the increase in etchant concentration and then increases. The minimum critical angle of

α-particles in CR-39 (Page Mouldings) is 14.48 with 6M NaOH solution at 70 °C, 17.60 with 1M NaOH/1-propanol at 49 °C, 13.26 with 1.5M NaOH/ethanol at 55 °C, 12.68 with 1.5M NaOH/methanol at 55 °C and 11.06 with SMW (10% NaOH dissolved in X% methanol and (90 − X)% water) at fixed temperature (55 °C).

Randhawa et al. [78] reported the critical angle of incidence of α-particles in CR-39 and CR-39(DOP) track detector as a function of etching time. They reported minimum critical angle value 23.84 for CR-39 and 23.28 for CR-39(DOP) track detector at 10 h etching time with 6.25N NaOH etchant at 70 °C etchant temperature.

The minimum critical angle of α-particles in different types of CR-39 as a function of different etching conditions is presented in Table 5. From these observations, it is ascertained that along with the types of the CR-39, critical angle strongly depends upon the etchant and etchant variables (concentration and temperature).

3.5 Etching Efficiency

The etching efficiency of a detector is defined as the proportion of tracks etched out expressed as a fraction of particles actually incident on the detector surface. The etching efficiency (η) of the detector can be determined through the following relation:

$$\eta = 1 - \frac{V_B}{V_T}$$

Table 5 Minimum critical angle of α-particles in different types of CR-39 with variety of etchants at different temperatures

Type of CR-39	Etchant	Temperature (°C)	Critical angle (θ_C)	References
American Acrylics	6N NaOH	70	35.80	[51]
Pershore Mouldings	6N NaOH	70	36.87	[51]
Page Mouldings	6M NaOH	70	14.48[b]	[69]
[a]	6.25N NaOH	70	23.84	[78]
DOP	6.25N NaOH	70	23.28	[78]
Page Mouldings	1M NaOH/1-propanol	49	17.60[b]	[69]
Page Mouldings	1.5M NaOH/ethanol	55	13.26[b]	[69]
Page Mouldings	1.5M NaOH/methanol	55	12.68[b]	[70]
Page Mouldings	10% NaOH + 60% methanol + 30% water	55	11.06[b]	[70]

[a]Type of CR-39 not mentioned
[b]Computed from the available track etch and bulk etch rate values

Ansari et al. [51] measured the track etch and bulk etch rate in CR-39 (Pershore Mouldings) and CR-39 (American Acrylics) with 6N NaOH etchant at 70 °C. In the present study, using these measured values, etching efficiency of these detectors is determined and observed that etching efficiency of American Acrylics is slightly higher than the Pershore Mouldings type detector.

Ashry et al. [68] etched the group of exposed CR-39 (TASTRACK) track detector with a mixture of 8 ml of 10N NaOH + 1 ml CH_3OH at 60 °C and studied the variation of etching efficiency as a function of α-particle energy for different etching times (45, 60 and 90 min) and observed that the efficiency increases with the decrease in etching time. Further, they observed that efficiency decreases with the increase in α-particle energy from 1 to 5 MeV and also deceases with increasing the amount of CH_3OH.

Matiullah et al. [69] measured the efficiency of CR-39 (Page Mouldings) for three different etchants. They observed maximum efficiency 64% for 6M NaOH etchant at 70 °C; ∼70% for 1M NaOH/1-propanol at 49 °C and 77% for 1.5M NaOH/ethanol at 55 °C. Matiullah et al. [70] also measured the sensitivity of exposed CR-39 samples, as a function of temperature, with 1.5M NaOH/methanol etching solution and observed the maximum efficiency (∼78%) at 55 °C. They also measured the efficiency as a function of methanol concentration of (10% NaOH dissolved in X% methanol and (90 − X)% water) etchant at 55 °C temperature and observed that first etching efficiency increases (up to ∼81%) and then decreases with the increase in methanol concentration. They prove that the efficiency of CR-39 with these newly used etchants is higher as compared to most commonly used 6M NaOH solution as an etchant. Further, the required temperature to achieve higher etching efficiency is less for newly used etchants.

Tahiri et al. [72] etched CR-39 (Page Mouldings) samples with three different etchants (4–12M NaOH, 4–12M KOH and 3–7M LiOH) at different temperatures (50–90 °C). They reported higher etching efficiency with 6M NaOH and 6M KOH etchants at 70 °C. Also, they observed that LiOH etchant yields lower etching efficiency as compared to first two etchants. In addition to these etchants, they also tried three other etchants ($Mg(OH)_2$, $Ca(OH)_2$ and $Ba(OH)_2{\cdot}8H_2O$) on CR-39 and observed that first two etchants are relatively less soluble in water and hence cannot be used as an etchant. As far as third etchant is concerned, it varies with the concentration of $Ba(OH)_2{\cdot}8H_2O$ from 0.5 to 2.75M at 78 °C. They observed that etching efficiency decreases with the increase in concentration of barium hydroxide. The authors reported maximum etching efficiency 66% with 0.5M of $Ba(OH)_2{\cdot}8H_2O$ etchants at 78 °C etchant temperature. Further, they observed 72% etching efficiency with molten $Ba(OH)_2{\cdot}8H_2O$ etchant at 84 °C.

Randhawa et al. [78] reported maximum etching efficiency 59.54 for CR-39 and 60.47 for CR-39 (DOP) track detector, when detector was etched with 6.25N NaOH solution at 70 °C, after 10 h etching time.

Maximum etching efficiency of α-particles in different types of CR-39 as a function of etchant variables is presented in Table 6. It is clear from the table that the etching efficiency of the detector generally varies from 40 to 81% depending

Table 6 Maximum etching efficiency of α-particles in different types of CR-39 with variety of etchants at different temperatures

Type of CR-39	Etchant	Temperature (°C)	Efficiency (η) (%)	References
American Acrylics	6N NaOH	70	41[b]	[51]
Pershore Mouldings	6N NaOH	70	40[b]	[51]
Page Mouldings	6M NaOH	70	64	[69]
[a]	6.25N NaOH	70	59	[78]
DOP	6.25N NaOH	70	60	[78]
Page Mouldings	1M NaOH/1-propanol	49	70	[69]
Page Mouldings	1.5M NaOH/ethanol	55	77	[69]
Page Mouldings	1.5M NaOH/methanol	55	78	[70]
Page Mouldings	10% NaOH + 60% methanol + 30% water	55	81	[70]
Page Mouldings	0.5M $Ba(OH)_2 \cdot 8H_2O$	78	66	[72]
Page Mouldings	Molten $Ba(OH)_2 \cdot 8H_2O$	84	72	[72]

[a]Type of CR-39 not mentioned
[b]Computed from the available track etch and bulk etch rate values

upon the etchant variables. The highest etching efficiency is achieved with SMW (10%NaOH + 60% methanol + 30% water) etchant at 55 °C.

4 Applications and Future Projections of Nuclear Track Detectors

4.1 Applications of Nuclear Track Detectors

Due to unique advantages of nuclear track detectors as compared to other conventional detectors, these detectors have numerous applications in different scientific disciplines. Some fascinating fields are listed as under:

4.1.1 Biological Applications

Nuclear tack detectors are used to:

(a) Study the radiological consequences of inhalation of α-particles, present in the environment, and their deposition in the human's lungs [30, 81].
(b) Monitor the α-activity in the blood of smokers and non-smokers [82].
(c) Examine the lead content and their distribution in human teeth and human bones as a function of age [83–85].

(d) Separate out the cancer cells from the normal blood cells [3, 30, 86].
(e) Investigate the blood circulation disorders connected with heart diseases [3, 30, 86].
(f) Study dust, smoke and pollutant transport in industries, etc. [87, 88].

4.1.2 Radiation Dosimetry

Nuclear track detectors are used as radiation dosimeters, which measure the different types of radiations available in normal environment. These dosimeters are also used in the radiation prone areas such as mines, dwellings, caves and area where the accident due to nuclear explosion was occurred. The unique advantages of these detectors as radiation dosimeters are: (a) the detectors are generally insensitive to background radiations such as β, γ and X-rays, (b) the detectors do not require any sophisticated electronic equipment for counting the radiations, (c) the detectors store the radiations permanently without any environmental effects (fogging, fading, storage) at ambient temperatures, (d) no dark room conditions are required to reveal the tracks, and (e) wide range of ion's doses can be studied [3, 30].

4.1.3 Nuclear Physics

In nuclear physics experiments, these detectors are used for (a) particle identification [3, 30], (b) charge-to-mass resolution [37, 89], (c) cosmic rays study [89–92], (d) fission reactions study [93], (e) searching superheavy elements [94], (f) cross sections and angular distributions study [95], (g) spallation products study [96] and (h) determination of half-life of spontaneous fission nuclei [97].

5 Conclusions and Future Scope

Track etch parameters (track etch rate, bulk etch rate, sensitivity, critical angle, efficiency) in CR-39 are highly influenced by etchant variables such as nature of etchant, etchant temperature, etchant concentration, duration of etching and stirring. The track activation energy is lower than the bulk activation energy, for particular etchant. This shows that the etchant is attacked with faster rate in damaged regions than the undamaged regions. Track/bulk activation energy varies with different etchants. However, it is not affected by the concentration of etchant. Track etch parameters depend upon the types of CR-39 polymer although the monomer ($C_{12}H_{18}O_7$) composition is same. This shows that preparation method, purity of monomer, polymerization conditions, additives, contaminants during preparation also play a significant role. Track etch parameters are depth-dependent parameters,

i.e. they hold different values in different depths in the same type of CR-39 detector. Generally, in the presently considered studies and the various studies available in the literature, one can use 6.25N NaOH solution at 70 °C as an etchant for etching CR-39 track detector. However, one can use the presently considered new etchant for etching and/or explore the new etchant to enhance the etching efficiency and sensitivity of the track detector.

This study is confined to the α-irradiated CR-39 track detectors and examines the impact of etchant variables on track parameters. In future perspectives, one can review/study the impact of (a) different types of radiations, (b) detector temperature before, during and after irradiation and (c) various environmental effects on etching parameters of CR-39 and explore the various applications in different disciplines of science and technology.

References

1. Young DA (1958) Nature 182:375
2. Silk ECH, Barnes RS (1959) Philos Mag 4:970
3. Fleischer RL, Price PB, Walker RM (1975) Nuclear tracks in solids: principles and applications. University of California Press, Berkley
4. Barbui M, Fabris D, Moretto S, Nebbia G, Nemeth P, Palvalfi J, Pesente S, Prete G, Sajo-Bohus L, Viesti G (2009) Radiat Meas 44:857
5. Mühling E, Schumacher U, Paretzke HG (1984) Nucl Tracks 9:113
6. Malinowska A, Szydloowski A, Jaskola M, Korman A, Malinowski K, Kuk M (2012) Nucl Instr and Meth B281:56
7. Paretzke HG, Benton EV, Henke RP (1973) Nucl Instr and Meth 108:73
8. Enge W, Grabisch K, Dallmeyer L, Bartholomä KP, Beaujean R (1973) Proc 13th Int Cosmic–Ray Conference Denver, 4:2848
9. Benton ER, Benton EV (2001) Nucl Instr and Meth 184:255
10. Hayashi T, Doke T (1980) Nucl Instr and Meth 174:349
11. Günther W, Leugner D, Becker E, Flesch F, Heinrich W, Hüntrup G, Reitz G, Röcher H, Streibel T (1999) Radiat Meas 31:585
12. Benton EV, Richmond RG (1986) Nucl Tracks Radiat Meas 12:505
13. Benton EV (1986) Adv Spac Res 6:315
14. Becker K (1973) Solid state dosimetry. CRC-Press, Cleveland
15. Durrani SA (1982) Nucl Tracks 4:209
16. Suzuki T, Tomura K (1990) Nucl Tracks and Radiat Meas 17:223
17. Spohr R (1990) Ion tracks and micro-technology: principles and applications. Vieweg & Sohn Verlegsgschaft mbH, Braunschweig
18. Fink D, Chandra A, Fahrner WR, Hoppe K, Winkelmann H, Saad A, Alegaonkar P, Berdinsky A, Grasser D, Lorenz R (2008) Vacuum 82:900
19. Apel PY, Blonskaya IV, Dmitriev SN, Orelovitch OL, Presz A, Sartowska BA (2007) Nanotechnology 18:305302
20. Ohgai T, Hjort K, Spohr R, Neumann R (2008) J Appl Electrochem 38:713
21. Durrani SA, Illić R (1997) Radon measurements by etched track detectors-Applications in radiation protection. Earth Sciences and the Environment, World Scientific, Singapore
22. Andom AAB (1992) Nucl Radiat Meas 20:371
23. Nikezić D (1994) Nucl Instr and Meth A344:406
24. Hussein A (1994) J Radiat Nucl Chem 188(4):225

25. Fleischer RL, Price PB, Symes EM, Miller DS (1964) Science 143:349
26. Benton EV (1982) Application of nuclear track detectors in biology and medicine. In: Solid State Nuclear Track Detectors, Fowler PH, Clapham VM (eds.) pp. 629–640, Pergamon Press
27. Nikjoo H, Uehara S, Wilson WE, Hoshi M, Goodhead DT (1998) Int J Radiat Biol 73(4):355
28. Ogura K, Orito S, Nakamura S, Doke T, Chinose I, Kurawara K (1989) Nucl Tracks Radiat Meas 16:107
29. Khan HA, Qureshi IE (1999) Radiat Meas 31:25
30. Durrani SA, Bull RK (1987) Solid state nuclear track detection: principles, methods and applications. Pergamon Press, New York
31. Nikezic D, Yu KN (2004) Mater Sci Eng Rep R46:51
32. Fleischer RL (1998) Tracks to innovation: nuclear tracks in science and technology. Springer, Berlin
33. O'Sullivan D, Thompson A (1980) Nucl Tracks 4:271
34. Kodaira S, Yasuda N, Kawashima H, Kurano M, Hasebe N, Doke I, Ota S, Ogura K (2009) Radiat Meas 44:861
35. Salamon MH, Price PB, Tincknell M, Guo S, Tarle G (1985) Nucl Instr Meth B6:504
36. Yadav JS (1995) Radiat Meas 24(2):115
37. Cartwright BG, Shirk EK, Price PB (1978) Nucl Instr Meth 153:457
38. Al-Najjar SAR, Durrani SA (1984) Nucl Tracks Radiat Meas 8(1–4):51
39. Fromm M (2005) Radiat Meas 40:160
40. Kodaira S, Naka S, Yasuda N, Kawashima H, Kurano M, Ota S, Ideguchi Y, Hasebe N, Ogura K (2012) Nucl Instr and Meth B274:36
41. Biswas S, Durgaprasad N, Kajarekar PJ, Vahia MN, Yadav JS, Basu C, Goswami JN, Kukreja LM, Bhawalkar DD (1984) Nucl Tracks Radiat Meas 8(1–4):559
42. Fujii M, Nishimura J, Kobayashi T (1984) Nucl Instr Meth 226:496
43. Portwood T, Stejny J (1984) Nucl Tracks 8:151
44. Tarle G (1981) Proc 17th Int Cosmic Ray Conf, Paris 8:74
45. Enge W, Grabisch K, Dallmeyer L, Bartholoma KP, Beaujean R (1975) Nucl Instr and Meth 127:125
46. Kumar A, Prasad R (1999) Radiat Meas 31:227
47. Kocsis ZS, Dwivedi KK, Brandt R (1997) Radiat Meas 28(1–6):177
48. Henke R, Ogura K, Benton EV (1986) Nucl Tracks 12(1–6):307
49. Rana MA, Qureshi IE (2002) Nucl Instr and Meth B198:129
50. Farid SM (1984) Nucl Instr and Meth 226:501
51. Ansari F, Javaid NA, Khan EU, Fujii M (1991) Nucl Tracks Radiat Meas 19(1–4):139
52. Kobayashi T, Fujii M (1988) Nucl Tracks Radiait Meas 15(1–4):175
53. Bethe M, Enge W, Sermund G (1986) Nucl Tracks 12(1–6):91
54. Awad EM, El-Samman HM (1999) Radiat Meas 31:109
55. Hussein A, Shnishin KH, Kheir AAAE (1993) J Mater Sci 28:6026
56. Charvát J, Spurńy F (1988) Nucl Tracks Radiat Meas 14(4):447
57. Yamauchi T, El-Rahmany A, Mineyama D, Nakai H, Oda K (2003) Radiat Meas 37:119
58. Hermsdorf D, Hunger M, Starke S, Weickert F (2007) Radiat Meas 42:1
59. Ghazaly ME, Salama TT, Khalil EI, Raouf KMAE (2012) J. Korean Phys. Soc. 61(3):336
60. Hofy ME, Samman HE, Arafa W (1999) Radiat Meas 31:241
61. Chan KF, Ng FMF, Nikezic D, Yu KN (2007) Nucl Instr and Meth B263:284
62. Fromm M, Membrey F, Chambaudet A, Saouli R (1991) Nucl Tracks Radiat Meas 19(1–4):163
63. Sharma SL, Pal T, Rao VV, Enge W (1991) Nucl Tracks Radiat Meas 18(4):385
64. Ho JPY, Yip CWY, Nikezic D, Yu KN (2003) Radiat Meas 36:141
65. Singh J, Singh S, Virk HS (1988) Nucl Tracks Radiat Meas 15(1–4):187
66. Singh NP (1993) Nucl Tracks Radiat Meas 22(1–4):157
67. Khan EU, Ali N, Husaini SN, Karim S, Malik F, Qureshi IE, Baluch JJ, Khan HA (2005) Radiat Meas 40:299

68. Ashry AH, Abdalla AM, Rammah YS, Eisa M, Ashraf O (2014) Radiat Phys and Chem 101:41
69. Matiullah, Rehman S, Rehman S, Zaman W (2005) Radiat Meas 39:337
70. Matiullah, Rehman S, Rehman S, Mati N, Ahmad S (2005) Radiat Meas 39:551
71. Tse KCC, Nikezic D, Yu KN (2007) Nucl Instr and Meth B263:300
72. Tahiri IA, Subhani MS (2003) Radiat Meas 37:205
73. Somogyi G, Tōth-Szilāgyi M, Hunyadi I, Hafez AF (1986) Nucl Tracks 12(1–6):97
74. Green PF, Ramli AG, Al-Najjar SAR, Abu-Jarad F, Durrani SA (1992) Nucl Instr and Meth 203:551
75. Amin SA, Henshaw DL (1981) Nucl Instr and Meth 190:415
76. Lounis Z, Djeffal S, Morsli K, Allab M (2001) Nucl Instr and Meth B179:543
77. Dörschel B, Hartmann H, Kadner K (1996) Radiat Meas 26(1):51
78. Randhawa GS, Kumar S, Virk HS (1997) Radiat Meas 27(3):523
79. Hermsdorf D (2009) Radiat Meas 44:283
80. Fromm M, Membrey F, El Rahamany A, Chambaudet A (1993) Nucl Tracks Radiat Meas 21:357
81. Henshaw DL, Fews AP, Webster DJ (1980) Proc 10th Int Conf Solid State Nucl Track Detectors, Lyon, and Suppl. 2, Nucl Tracks, Pergamon, Oxford 649
82. Henshaw DL, Heyward KJ, Thomas JP, Fews AP, Gallerano P, Sanzone G (1984) Nucl Tracks 8:453
83. Fremlin JH, Edmonds MI (1980) Nucl Instr. and Meth 173:211
84. Al-Naimi T, Edmonds MI, Fremlin JH (1980) Phys Med Biol 25:719
85. Laird EE (1983) Factors affecting in-vivo X-ray fluorescence measurements of lead in bone. Ph.D. thesis, University of Birmingham
86. Seal S (1964) Cancer 17:549
87. Tress G, Ellinger M, Khan EU, Khan HA, Vater P, Brandt R, Kander M (1982) Nucl Tracks 6:87
88. Guo SL, Tress G, Vater P, Khan EU, Dersch R, Planchky M, Brandt R, Khan HA (1986) Nucl Tracks 11:1
89. Price PB, Peterson DD, Fleischer RL, O'Ceallaigh C, O'Sullivan D, Thompson A (1970) Proc 11th Int Conf on Cosmic Rays, Budapest 417
90. Price PB, Fleischer RL, Peterson DD, O'Ceallaigh C, O'Sullivan D, Thompson A (1967) Phys Rev 164:1618
91. Price PB, Peterson DD, Fleischer RL, O'Ceallaigh C, O'Sullivan D, Thompson A (1968) Can J Phys 46:S1149
92. Price PB, Fleischer RL (1970) Radiat Effects 2:291
93. Brandt R (1980) Nucl Instr Meth 173:147
94. Brandt R (1978) Proc Int Symp Super heavy Elements, Lubbock (Lodhi MAK ed) Pergamon, New York 103
95. Somogyi G, Hunyadi I, Koltay E, Zolnai L (1977) Nucl Instr Meth 147:287
96. Herz AJ, O'Ceallaigh C, O'Sullivan D, Thompson A (1976) Nuovo Cimento 33A:487
97. Gibson WM, Nielson KO (1970) Phy Rev Lett 24:114

Synthesis of Hydrogels by Modification of Natural Polysaccharides Through Radiation Cross-Linking Polymerization for Use in Drug Delivery

Kashma Sharma, Vishal Sharma and Vijay Kumar

Abstract Hydrogels are three-dimensional polymer structures that can captivate and hold a vast quantity of water. They have superior's properties such as hydrophilicity, high swelling ability, non-toxic in nature, and biocompatibility which makes them prospective materials for various applications. The concept of graft copolymers in biomedical field developed in the past few ten years and lasts to fascinate researchers working in this sector. Research in this sector is ongoing with the aim of alteration of the inherent properties of polysaccharides after grafting, which offers premises to be pervasive in integrated systems with multiple functionalities or the enhanced properties of one domain. This chapter aims to give comprehensive details about research that have been made on radiation-induced synthesis of polysaccharide-based hydrogels in context to biomedical application. This review also intends to explain the mechanism of radiation-induced synthesis of hydrogels. The effect of various radiation sources such as gamma, microwave, electron, and heavy ions is also discussed. Also, current status and plans of hydrogels are presented along with proper citations extracted from the scientific literature. Moreover, this article provides you with essential information that one's need to start work in this area.

Keywords Polysaccharides · Hydrogels · Radiation · Cross-linking Biomedical

K. Sharma (✉) · V. Sharma
Institute of Forensic Science & Criminology, Panjab University, Chandigarh, India
e-mail: shama2788@gmail.com

V. Kumar (✉)
Department of Physics, National Institute of Technology, Srinagar, Hazratbal 190006, Jammu and Kashmir, India
e-mail: vj.physics@gmail.com

V. Kumar et al. (eds.), *Radiation Effects in Polymeric Materials*, Springer Series on Polymer and Composite Materials, https://doi.org/10.1007/978-3-030-05770-1_8

1 Historical Background

A polymer gel is defined as a solvent-comprising system in which sufficient numbers of cross-link present to tie all polymer chains to other chains at various points [1, 2]. It is considered as a unique state of matter because the polymer gel has solid- and liquid-like characteristics. The gels can be cross-linked either chemically or physically which leads to the construction of a bulky three-dimensional network soaking through the entire solution volume. The cross-linked gel networks are potentially very useful in many sectors such as pharmaceuticals, biotechnology, agriculture, food processing, and electronics [2].

The first scientific study of gels was carried out by Thomas Graham, who is also known as Father of Physical Chemistry in the nineteenth century [3]. He employed solgel chemistry in his work to yield a silica gel. The conventional chemical approach normally uses colloidal suspension followed by the removal of the solvent during synthesis of fine particulate solids. Solgel chemistry generally involves the preparation of concentrated solution of a metal salt in a dilute acid. During the synthesis process, pH of the solution was adjusted followed by the addition of a gelling material, finally vaporizing the liquid to yield a gel and heating the gel at a particular temperature to get fine particles of the material [3].

The 1940s and 1950s evidenced the growths of gels which is carried out by pioneers such as Flory [4, 5], Huggins [6, 7], and Treloar [8, 9]. Treloar is generally famous for his work in the investigation of elasticity in polymer structures. Paul Flory discovered the modern polymer science via using the experimental and theoretical investigations of macromolecules; for the same, he received the Nobel Prize in the year 1974 [10]. Currently, much interest and activity exist in synthesis, characterization, and applications of synthetic and natural polymers, mainly hydrogels for biomedical applications.

2 Hydrogels

Hydrogels are polymeric candidates which have the ability to regain a large measure of water owing to the presence of various hydrophilic groups, without dissolving in water, as there is cross-linking which helps to bind the various chains together [11, 12]. As soon as they come in closer with aqueous solutions or fluids, they swell up to a best level, which resembles to state about the osmotic pressure that pushes water inside the network and the retroactive elastic strength which comes from the strained hydrogel chains between the cross-links on swelling. The presence of water in hydrogels performs a crucial part in the complete penetration of active elements into and out of the gel. Water can be linked to any hydrogel network in subsequent techniques as displayed in Fig. 1.

The overall characteristics of the hydrogels are mainly dependent on various factors, viz. the hydrophilicity of the polymer chains and the magnitude of

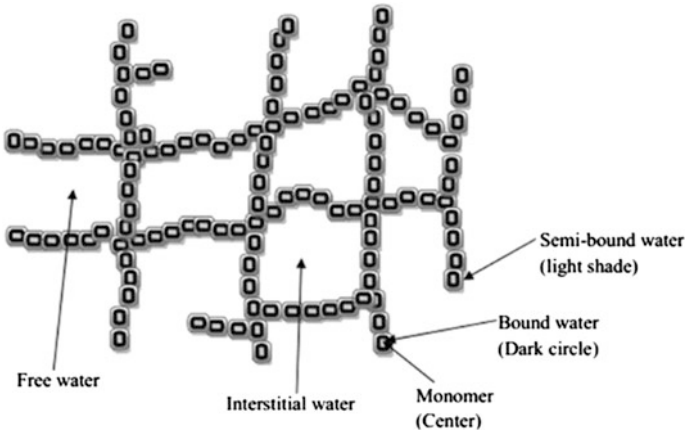

Fig. 1 Graphical representation of molecular structure of hydrogel network with different types of water [12]

cross-linking [12–16]. The water absorbing ability of the hydrogels linked with availability hydrophilic groups (such as –OH, –COOH, –CONH–, $–CONH_2$, and $–SO_3H$) in the polymer chains [2, 15–20]. Hydrogels have gained much responsiveness in the past thirty years, due to their remarkable potential in biomaterial fields [19]. The presence of a large number of water in the hydrogel occupies the voids and permits a particular circulation of solute molecules through the matrix. This behavior makes them better candidates to be used in a membrane separation process [21]. The formation of hydrogels can be done with various natural and synthetic backbones, which have extensive features and as a result found important applications in biomedical fields [15, 22, 23]. Hydrogels have existed in nature since the start of life. A variety of naturally occurring polymers such as collagen, alginate, agarose, and gelatin were also explored in early civilization [2]. The application of hydrogels in the medical field has been started in the year 1950s. The foremost synthetic hydrogel poly(2-hydroxyethyl methacrylate) has been prepared by DuPont's scientists in 1936 [24].

Wichterle and Lim established the importance of poly(2-hydroxyethyl methacrylate) hydrogels as superb candidates for contact lens industry [25]. This development was the milestone in the contact lens business and to the novel field of biomedical hydrogels. Hydrogels undergo physiochemical changes in response to small variations in the experimental conditions such as temperature, pH, electric or magnetic field, enzymes, and solvent polarity, and such candidates are known as "smart hydrogels" [2, 26–30]. Previous research clearly indicates that hydrogels could be used in various research fields such as biomedical, agriculture, pharmaceutics, and biotechnology [26–36]. Biopolymer-based cross-linked networks have become an interesting field of research in the sector of tissue engineering and regenerative medicine, owing to their extraordinary swelling behavior, mechanical resemblance to natural tissues, and simplicity of surgical grafting [37].

3 Classifications of Hydrogels

Based on the source of origin, synthesis method, ionic charge, or structural characteristics, hydrogel can be divided into various classes [2, 15, 38]. An organization of hydrogels based on their source is presented in Fig. 2.

On the Basis of Polymeric Composition: The synthesis process results in the construction of four types of hydrogels which may be:
Homopolymeric Hydrogels: are denoted to polymer chains imitative from only one kind hydrophilic monomer component [39]. Homopolymers can be cross-linked in very thin arrangement subject to the type of the monomer unit and the synthesis process.
Copolymeric Hydrogels: They are comprised of two or more monomer units; in any case, one of them should be hydrophilic to make them water swellable [40].
Multipolymer Hydrogels: They are synthesized from three or more than three monomers mixing together.
Interpenetrating Polymeric Hydrogel (IPN): IPNs were pronounced for the first time in the year 1914, once Aylsworth fabricated the first synthetic IPN for the application of gramophone record [41]. The researchers began to express their interest in IPNs after 1950s. The name "interpenetrating polymer network" was exactly introduced by Millar in the year 1960 [42]. Subsequently, lots of researches have been devoted to the preparation and characterization of IPNs for various uses by employing both synthetic and natural polymers [43–45]. A combination of two or more preformed polymer structures is not considered as IPN [46].

Classification Based on Type of Cross-Linking

Chemical hydrogels are normally synthesized via two dissimilar means: "three-dimensional polymerization" (Fig. 3), wherein a hydrophilic monomer combines to form a polymer in the vicinity of a multifunctional cross-linking mediator (Fig. 4) [22].

4 Synthesis of Hydrogels

Graft copolymerization is a generally employed technique for the surface treatment of polymeric backbones, and it is an important means to transform the physiochemical features of backbones [47–50]. The pictorial representation of the polymer modification is shown in Fig. 5. The free radicals are formed on the backbone for the fabrication of graft copolymers during the process of polymerization [51]. Up to now, ample of synthesis techniques have been adopted for the production of active sites on the backbone and are generally classified as physical techniques, chemical approaches, photo-initiated grafting, plasma, radiation-induced grafting, enzymatic grafting, etc. Among them, chemical methods and radiation-induced graft copolymerization are extensively studied methods. There are large numbers of original

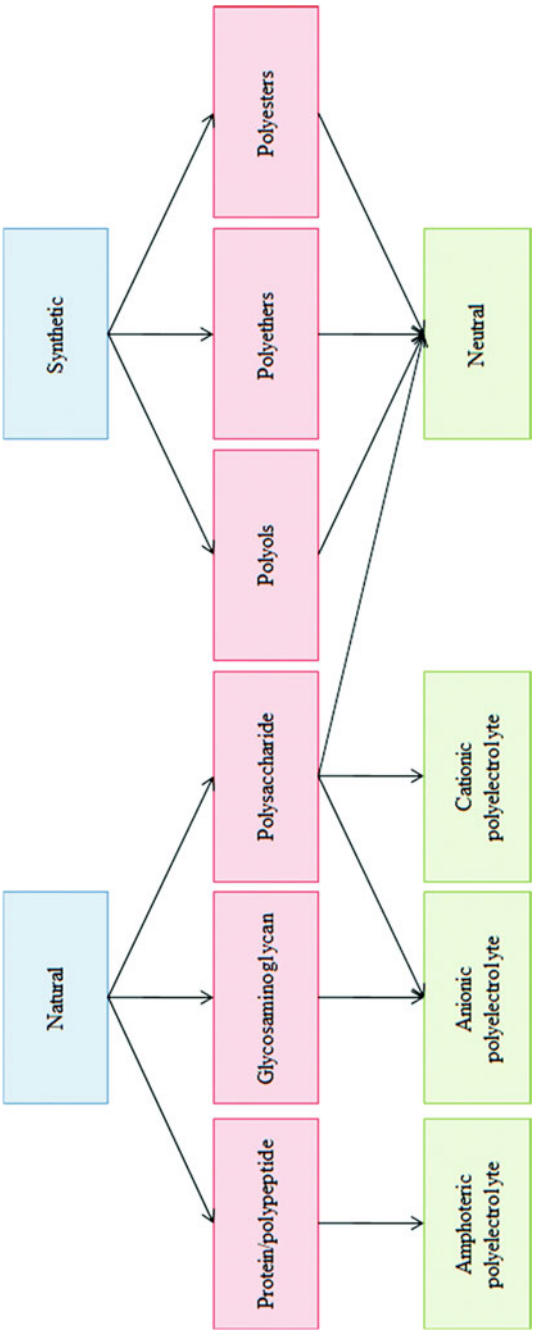

Fig. 2 Organization of hydrogels based on their source. Copied from Ref. [38] with consent from the Royal Society of Chemistry

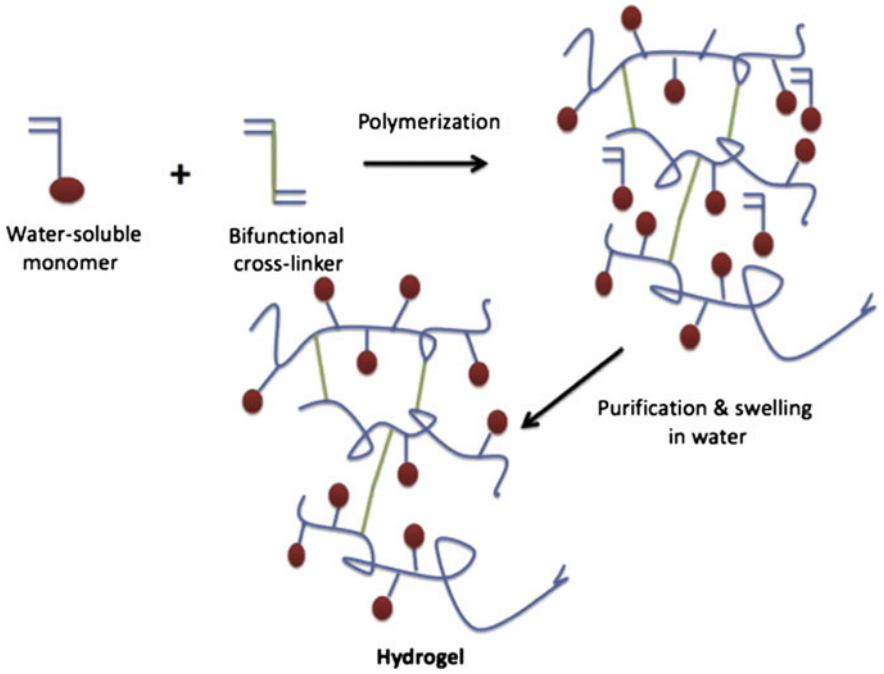

Fig. 3 Synthesis of hydrogels by three-dimensional polymerization [22]

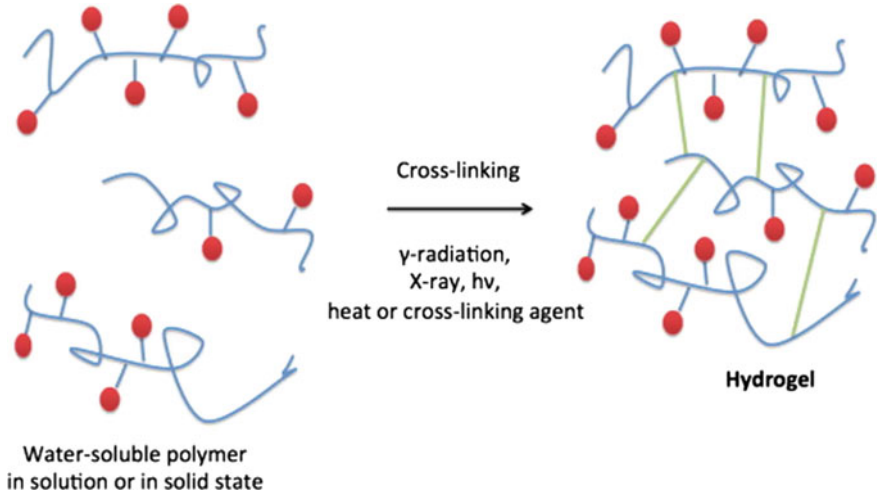

Fig. 4 Synthesis of hydrogels by cross-linking of readymade water-soluble polymers [22]

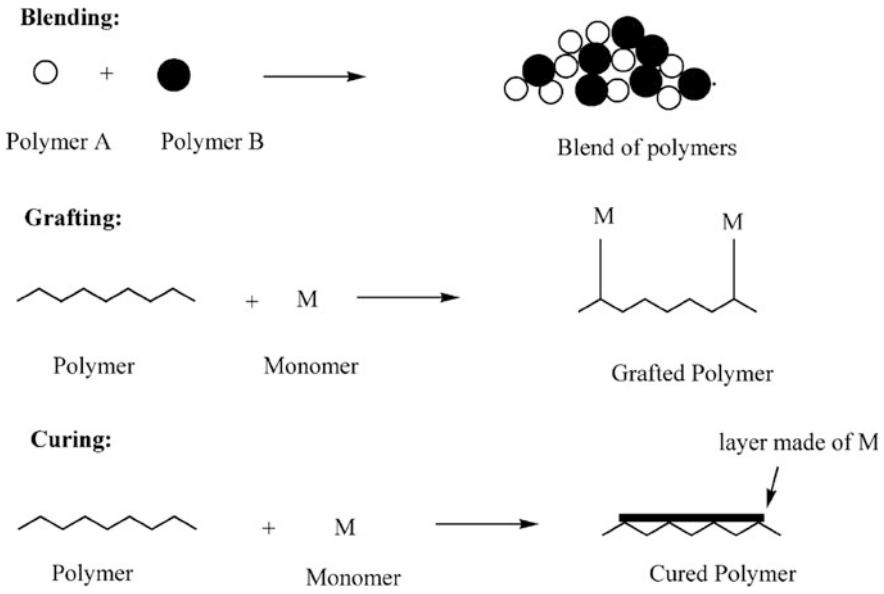

Fig. 5 Schematic representation of the methods of polymer modification. Copied from Ref. [47] with consent from the Elsevier

research papers and detailed review articles concentrated on the fabrication, properties, and applications of hydrogels. This chapter gives a detailed literature for the synthesis of hydrogels through radiation cross-linking and their applications in numerous biomedical sectors.

4.1 Chemical Synthesis of Hydrogels

Various initiators, viz. conventional radical initiators, ammonium persulfate (APS), ceric ammonium nitrate (CAN), potassium persulfate (KPS), potassium permanganate ($KMnO_4$), have been successfully used for the chemical grafting [2, 52–54]. Various authors grafted a wide variety of monomers onto natural polysaccharides by use of radical initiator [55–57]. In the case of chemical synthesis, active sites are generated from the initiators and shifted to the backbone to act in response to monomer to form the graft copolymers [47]. The part of the initiator is essential as it decides the route of the grafting process. A variety of cross-linked hydrogels have been synthesized by chemical synthesis method [58]. In general, free radical polymerization has four kinds of reactions [2, 59]:

i. Production of active species (initiation)
ii. Addition of these active species to a substituted alkene (propagation)
iii. Atom transfer and atom abstraction reactions (chain transfer and termination by disproportionately)
iv. Radical–radical recombination reactions (termination by coupling).

4.2 *Radiation-Induced Synthesis of Hydrogels*

Radiation-induced grafting is the more favorable technique for the graft copolymerization. When electromagnetic radiations go through the material, it leads in the creation of free radicals for the reaction (Fig. 6). There are many advantages of the synthesis of hydrogels by radiation processing such as ionizing radiation, gamma (γ) radiations, or electron beam over the conventional methods [60]. In the event of radiation-induced synthesis, the chemical reactions in the matrices are instigated by radiation, and there is no requirement to use (usually toxic) initiators, cross-linking agents, or other secondary materials [60–68]. This supports to cut prices, makes the technology easy, does not lead to secondary products, and the resultant material is of high purity.

Grafting can initiate either in the presence of low or high energy radiations [47]. Bombardment of polymer matrix with low energy radiations like ultraviolet and visible light leads in the homolytic splitting to created active sites on the backbone [47]. Under the influence of low energy radiations, polymerization can be initiated with or without photo-initiator. Possible biomedical applications of hydrogels have been found in implants, topical dressings, and drug delivery devices. As a result, radiation-induced cross-linking of polymers is considered important for medical applications, where even a pinch of small impurity is unwanted. A tremendous amount of work has been carried out on radiation-induced synthesis of natural polymers, and the realization of various applications has been achieved. The focus on natural polymers is due to their distinctive characteristics like intrinsic biocompatibility, biodegradability, and easy accessibility. Usually, the marketable use of natural polymers, like gum ghatti, carrageenans, alginates, starch, and cellulose, has been based mainly on existing knowledge.

The progress in the field of radiation-induced synthesis of hydrogels for various applications has been started in the late 1960s as reported by various researchers

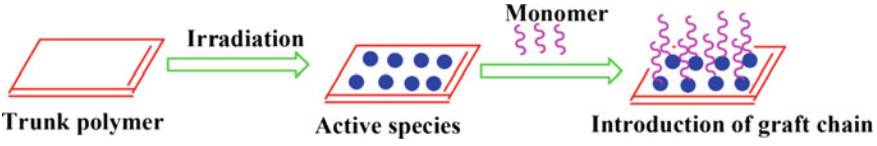

Fig. 6 Schematic representation of "radiation-induced grafting"

[69–71]. The much work in this direction has been carried out by Rosiak and coworkers by understanding the fundamental of radiation physics and chemistry as well as popularize the growth of an industrial products out of them [72, 73]. The ease of the radiation process, the prospect of uniting sterilization and cross-linking in a real-time process, and the backing of the International Atomic Energy Agency (IAEA) in endorsing the technology transfer of the radiation-induced synthesis of hydrogels by various researchers all across the globe and at a same time promoting the use of this technology in other countries [74]. Radiation has been extensively applied with the purpose of inducing cross-linking in polymeric materials [75–77].

4.2.1 Gamma Radiation-Induced Synthesis of Natural Gum-Based Hydrogels

Gamma radiations are the ionizing radiations and useful for the preparation and modification of materials for biomedical uses. It also offers unique advantages like easy process control, sterilization, high impurity, zero cross-linking agents, and fewer waste products [74]. Solpan and co-worker prepared acrylamide- and acrylic acid-based hydrogels in the cylindrical form by gamma-induced irradiation method involving 2.6–20.0 kGy rays [78]. Alam and coworkers reported that hydrogels have been prepared in from 10, 20, 30, 40, 50, and 60% aqueous solutions of acrylamide monomer by gamma radiation using gamma doses varied from 0.2 to 30 kGy [79]. A group of researchers from Gazi University, Besevler, Ankara, prepared macroporous poly(acrylamide) [poly(AAm)] hydrogels by using poly (ethylene glycol) (PEG) by using gamma radiation-induced grafting [80]. Our group has carried out γ-irradiation-induced grafting of various vinyl monomers and aniline onto gum ghatti [34, 35, 81]. The possible mechanism of γ-irradiation-induced synthesis of acrylic acid grafted onto gum ghatti is depicted in Fig. 7. The synthesized hydrogels are successfully used for the elimination of methylene orange from wastewater. In addition, these candidates can be employed as ion exchangers to enhance their efficacy for dye removal wastewater [35]. The addition of water-hating groups into these hydrogels makes them better candidates to control the oil spill in the oceans. The synthesized hydrogels based on gum ghatti (Gg)/methacrylic acid (MAA)/aniline (ANI) can be employed in the construction of site-specific drug delivery devices where rapid release of the drug is preferred in the beginning and constant release afterward [34].

The researchers varied the different reaction conditions to get the product with optimum percentage swelling. Seo and coworkers synthesized cross-linked PVA-gelative copolymers in the presence of γ-ray irradiations [82]. They have reported that the synthesized hydrogel candidate revealed promising physical properties, which is necessary for the construction of diploid cell culture. Taleb et al. [83] performed γ-ray-induced cross-linking and synthesis PVA and methacrylic acid (MAAc) onto gelatin, which leads to the formation of PVA/MAAc/gelatin copolymer [83]. The synthesize hydrogels can be employed for antibiotic drug carrier and as encouraging candidate for wound-healing

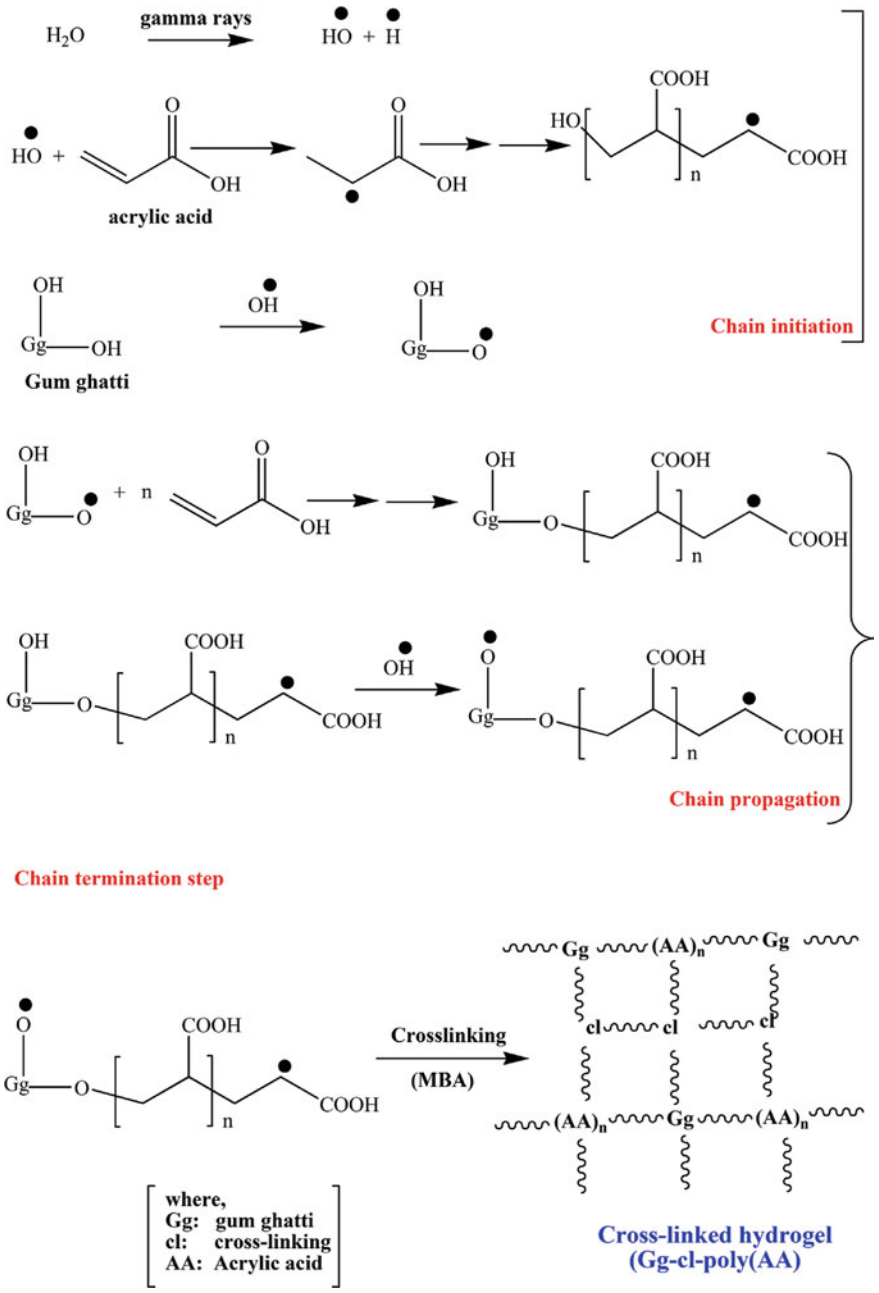

Fig. 7 Mechanism of graft copolymerization of acrylic acid onto gum ghatti [35]

applications. Synthesis and characterization of novel graft copolymers based on N-vinyl-2-pyrrolidone (NVP), 4-vinyl pyridine (4VP), and 2-vinyl pyridine (2VP) monomers onto poly(ethylene-alt-tetrafluoroethylene) (ETFE) by radiation-induced grafting have been reported [84]. It is well reported in the literature that the extent of grafting is directly related to various factors, viz. kind of polymer and monomer, monomer concentration, type of radiation, temperature, reaction atmosphere, concentration of homopolymerization suppressor, and type of solvent [85–87]. As a result, the effectiveness of the method can be managed by the optimization of these reaction parameters. Hamzah and coworkers carried out gamma radiation-induced synthesis of nanocurcumin and studied cell viability [88]. They have concluded that the use of radiation technique is a pretty easy and clean approach of fabricating nanocurcumin. Recently, Fekete et al. performed gamma irradiation-induced synthesis of carboxymethylcellulose/starch superabsorbent hydrogels [89]. They have studied the effect of absorbed dose on the percentage swelling. Mahmoud et al. (2014) carried out a gamma radiation-induced synthesis of hydrogels based on starch, acrylic acid, and 2-hydroxyethyl methacrylate, and the synthesized hydrogels have been used for the removal of red dye from aqueous solution [90]. Varshney et al. (2007) have synthesized polyvinyl alcohol, carrageenan, and agar-based hydrogel film via gamma irradiation which was elastic even without plasticizer and was mechanically tough and biocompatible [91]. Singh and coworkers have fabricated tragacanth gum-based sterile hydrogel films via gamma radiation and their utilization in drug delivery devices [92]. The hydrogels films were made by changing the gamma radiation from 9.1 to 63.5 kGy and evaluated their swelling capacity (Fig. 8). The synthesized hydrogels are also suitable materials to be used in wound dressings owing to their sterile and biocompatible nature. In another study, Singh and coworkers have synthesized tragacanth gum-based hydrogels films by gamma radiation for wound-dressing application [93]. The formation of tragacanth gum-cl-PVA-co-PVP-based hydrogel by means of gamma radiation is schematically shown in Fig. 9. Preparation, characterization, and swelling behavior of gamma-induced synthesized guar gum-based pH, temperature, and salt-responsive hydrogels have been carried out by Dharela and coworkers [94], whereas Co60 γ radiation-induced synthesis of acrylamide-grafted guar gum-based hydrogels has been reported by Biswal and coworkers [95]. They have also studied the flocculating properties of the synthesized hydrogels for industrial effluents.

4.2.2 Microwave-Assisted Synthesis of Gum-Based Hydrogels

Microwave radiation is the alternative source of energy and is evolving as an important means for the preparation of a variety of graft copolymers. Microwave-assisted technique reveals the finest prospective for preparing hydrogels, for the reason that the active species are created by the use of microwave radiation along with free radical initiators, exhibiting a better percentage of grafting in comparison with the other methods [96–100]. Microwave heating is totally

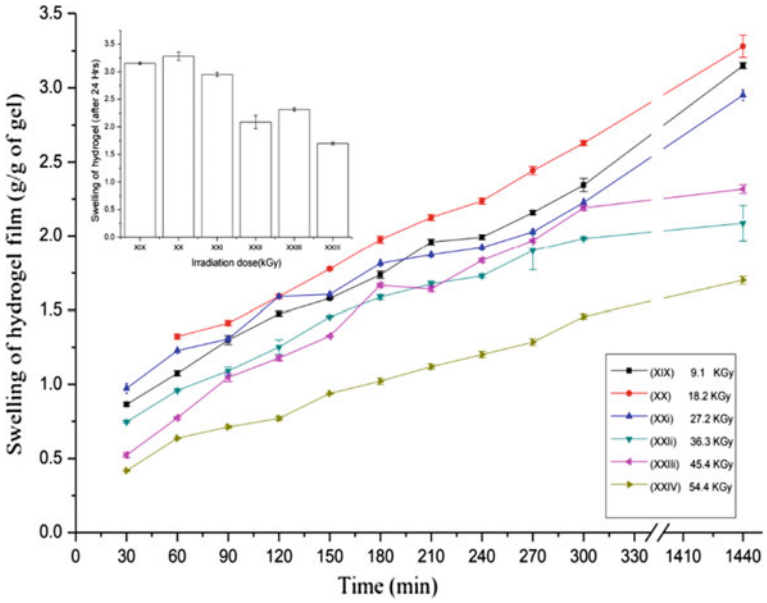

Fig. 8 Influence of gamma radiation dose on swelling capacity of TG-co-SA-cl-PVA polymer films in distilled water at 37 °C. Inset figure shows the effect of irradiation dose on swelling of hydrogel film after 24 h. Reproduced with permission from Ref. [92] from the Elsevier

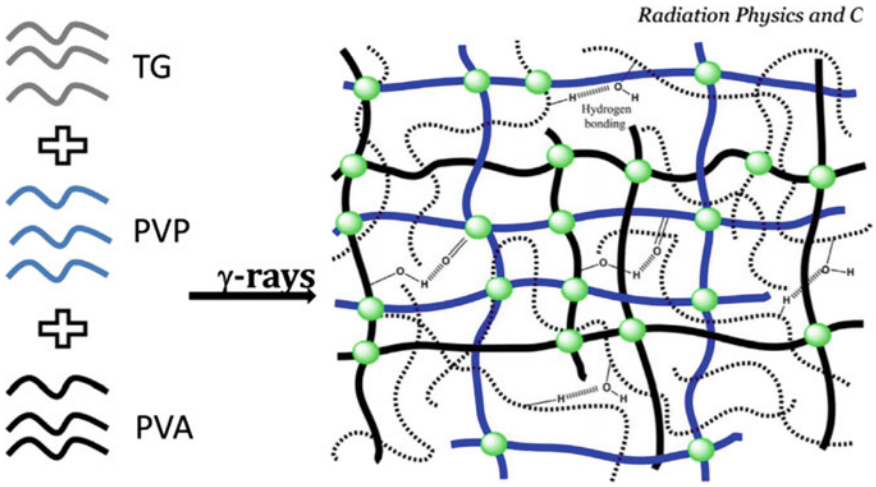

Fig. 9 Formation mechanism of tragacanth gum-cl-PVA-co-PVP-based hydrogel by means of gamma radiation. Reproduced with permission from Ref. [93] from the Elsevier

different from various other existing heating techniques. In microwave heating, heat is produced within the matrix but not created from any outerheating source [36, 101]. It has various other benefits, which comprise green synthesis, no secondary product, quick reaction speed, and capability of form nanostructures (Fig. 10).

We have conducted microwave-assisted grafting of vinyl monomers onto polysaccharide gum ghatti [32, 36, 102]. General scheme for the grafting of gum ghatti with vinyl monomers is presented in Fig. 11. Reactive chains for grafting of vinyl monomers onto polysaccharide gum ghatti are the –OH and –CH groups. Ammonium persulfate (APS) is a thermal initiator and gets dissociated under microwave irradiation leading to the creation of sulfate ion radicals. SO_4^{-}* on reaction with water molecules gives rise to the formation of OH* and HSO_4^{-}. OH* free radicals and SO_4^{-}* both generate active sites on backbone and monomer

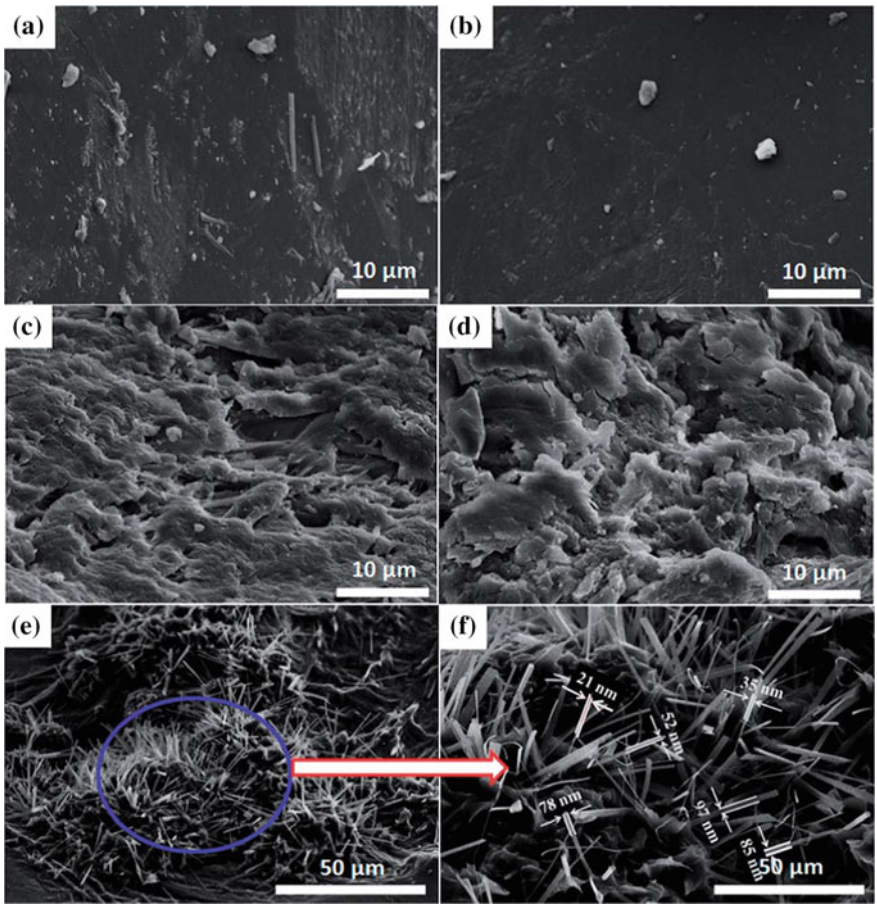

Fig. 10 SEM micrographs of **a**, **b** gum ghatti, **c**, **d** Gg-cl-poly(AAm), and **e**, **f** Gg-cl-poly (AAm-ipn-aniline) [36]

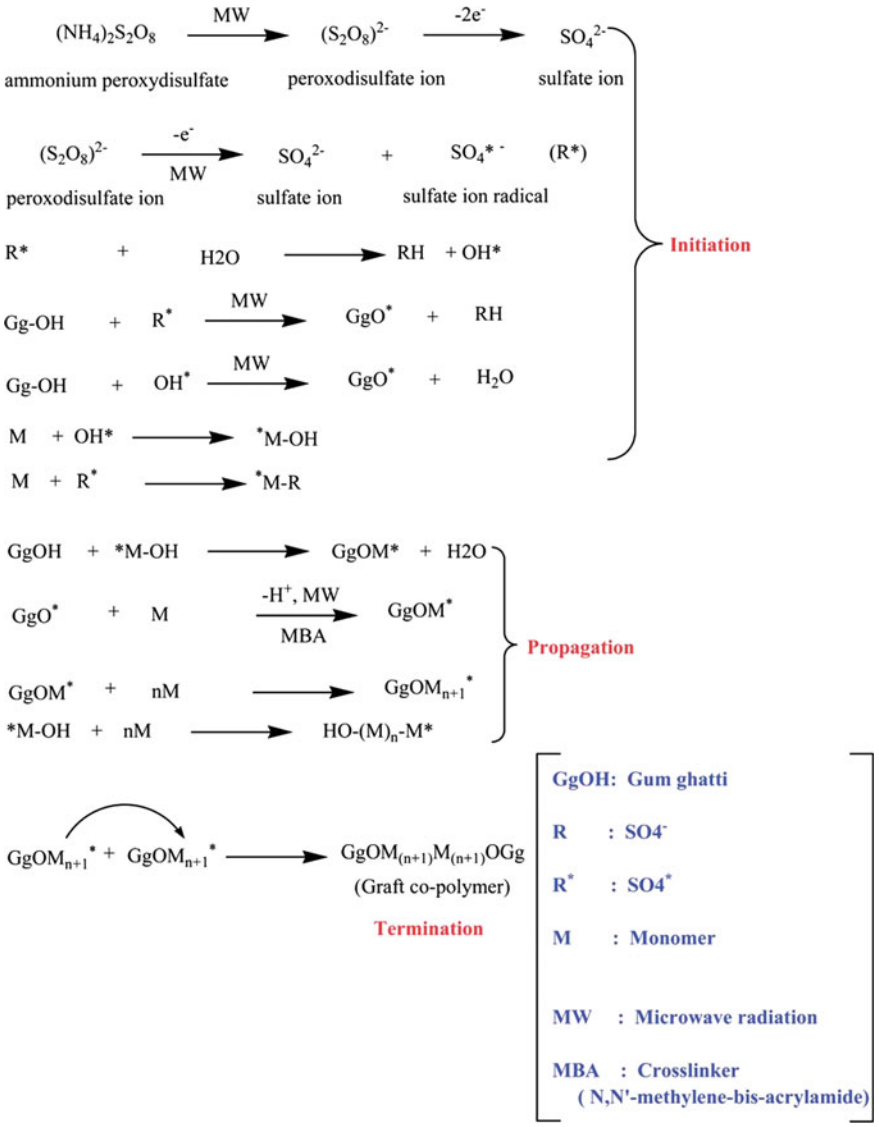

Fig. 11 Probable mechanism of graft copolymerization of vinyl monomers onto gum ghatti [36]

species. The microwave energy engrossed by water molecules is rapidly shifted to the monomer species, initiating dielectric heating effect which leads in the breaking of the double bonds, generating extra free radicals [103]. Active sites are produced on the polar –OH groups of backbone with the elimination of H^{-}*. Live poly(vinyl) chains get grafted onto free radical species of backbone resulting in the creation of

graft copolymers. MBA undergoes cross-linking between the various poly(vinyl) chains, in this manner leading to the formation of semi-IPNs [32, 36, 98–103].

Various authors have carried out microwave supported synthesis of hydrogels based on numerous synthetic and natural polymers [104–117]. A comprehensive review article stressed the various applications of microwave-induced synthesis of polysaccharides-based hydrogels and also covered the fundamental mechanism, and related problems were reviewed by Singh and coworkers [118]. This review article covered the microwave induced synthesis of various polysaccharides such as gum acacia, alginate, artemisia seed gum, cellulose, fibers, chitin and chitosan, guar gum, cassia seed gums, starch, konjac glucomannan, carboxymethyl starch, agar and carrageenan, and xanthan gum. Graphical representation of microwave-assisted grafting of the polysaccharides is displayed in Fig. 12.

4.2.3 Electron Radiation-Induced Synthesis of Hydrogels

As mentioned earlier that many of techniques have been employed for the synthesis hydrogels [119–122], It is also stated that the beginning of chemical reactions by the means of radiation is gradually employed for the synthesis of new hydrogel candidates. The radiation-induced synthesis technique is better than the chemical one, because of the benefit presented by the control of the amount of cross-linking

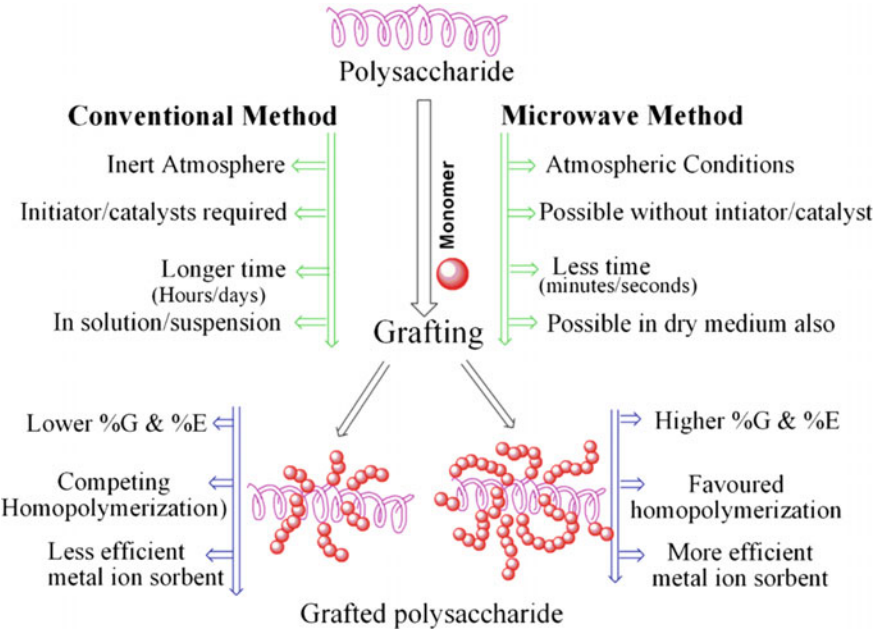

Fig. 12 Schematic diagram of microwave-assisted grafting of the polysaccharides. Reproduced with permission from Ref. [118] from the Elsevier

by simply varying the time of irradiation, which is related to the absorbed dose [119]. It is easy without any chemical initiation which is taking place at any temperature; the reactions such as polymerization, cross-linking, and grafting can be certainly adjusted, and the exposure can be restricted to a definite region [123]. Electron beam-induced synthesis of nanostructure has been recently reviewed by Gonzalez-Martinez and coworkers [124]. The processing of materials by irradiation with fast-moving electrons eliminates many shortcomings of the chemical methodologies, since ionizing radiation starts polymerization devoid of external thermal energy, owing to free radicals that are generated at the interaction with the monomers and with the solvent. Therefore, a better option to synthesize hydrogel networks is to employ ionizing radiation and particularly electron beams, which direct their energy in the volume of the polymeric matrix to be irradiated [125–127]. The impacts of electron irradiation on the structure, the conformation and the optical and mechanical properties of polymers have been extensively investigated in the literature [128–135].

4.2.4 Heavy Ion-Induced Modifications and Synthesis of Hydrogels

It is also widely accepted that polymers undergo structural alterations due to the impact of heavy ion irradiation [136, 137]. Irradiation of polymers induced the generation of highly reactive species, cross-linking, and oxidative breakage of bonds [138]. The supremacy of the above processes is evaluated by various factors like polymer structure and irradiation conditions (such as the atmosphere, LET, radiation dose, dose rate, sample thickness, and irradiation temperature). These changes have a direct association with the macroscopic properties for the target materials [136–138]. Although, a significant amount of work has already been done over the synthesis and characterizations of hydrogels by irradiation. But there are very few reports on the structural and morphological properties of cross-linked hydrogels after irradiation [139–142]. In our first report, we have investigated the effects of 100 meV O^{7+} ions irradiation on the structural and morphological behavior of poly(methacrylic acid)-cross-linked gum ghatti films [140]. Subsequently, a comparative study has been reported to study the influence of Ni^{9+} and Au^{8+} ions beam on the various properties of poly(methacrylic acid)-cross-linked gum ghatti films [141]. From these studies, we have concluded that there was a noticeable decrease in transmittance values which was ascribed to chain scissioning and cross-linking of the polymer chains. The overall surface morphologies of the irradiated hydrogel films got modified after irradiation. In another study, we have reported the effects of O^{7+} and Ni^{9+} heavy ions irradiation on polyacrylamide-grafted gum acacia thin films and sorption of methylene blue [142]. The sorption trend of pure and irradiated hydrogel films with O^{7+} and Ni^{7+} ions at a fluence of 1×10^{12} ions/cm^2 as a function of time has been studied separately (Fig. 13). The so-induced changes have been discussed by taking into account the linear energy transfer of these ions. The influences of irradiation on controlled drug

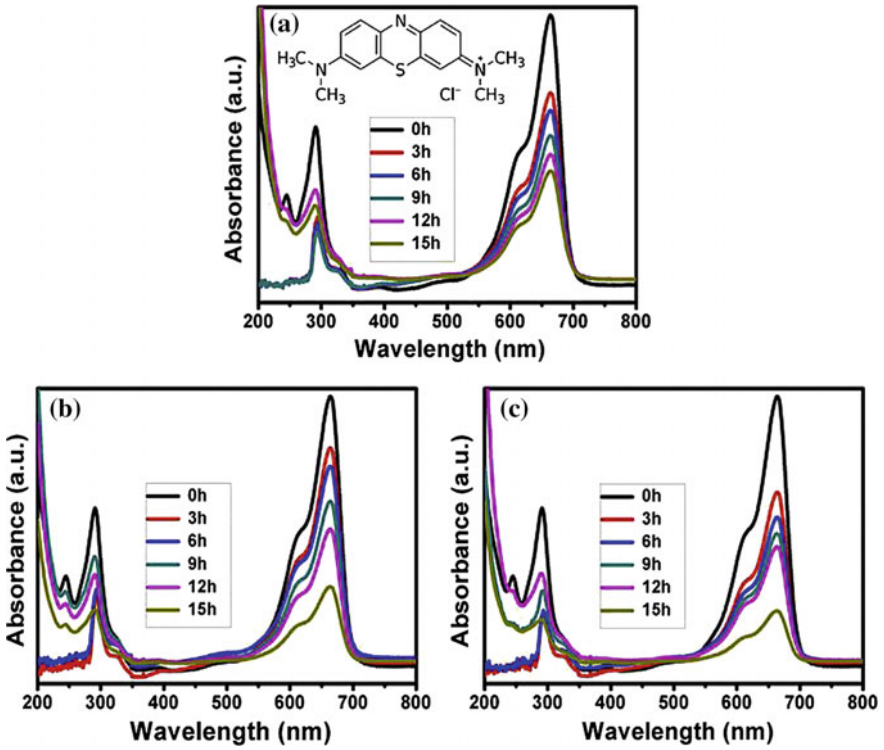

Fig. 13 UV–visible spectra of MB dye solution kept in contact with cross-linked hydrogel thin film, **a** pristine, **b** O^{7+} ion irradiated at fluence 1×10^{12} ions/cm$_2$, and **c** Ni^{9+} ion irradiated at fluence 1×10^{12} ions/cm^2

delivery devices have been studied by various authors and reported that ion-beam irradiation is a very important tool for modifying the surface properties of polymeric materials without losing the bulk properties [143–145].

5 Miscellaneous

Ultraviolet radiation-initiated synthesis of methyl acrylate onto the sodium salt of partially carboxymethylated guar gum has been carried by researchers [146]. A group of researchers from Koc University, Istanbul, Turkey, reported a new process for the preparation of a pH-sensitive composite hydrogel using visible light [147]. They have used the synthesized composite hydrogel for controlled drug delivery of the anticonvulsant drug pregabalin. Further, they have conducted in vitro human fibroblast survival assay and in vivo rabbit grafting tests and

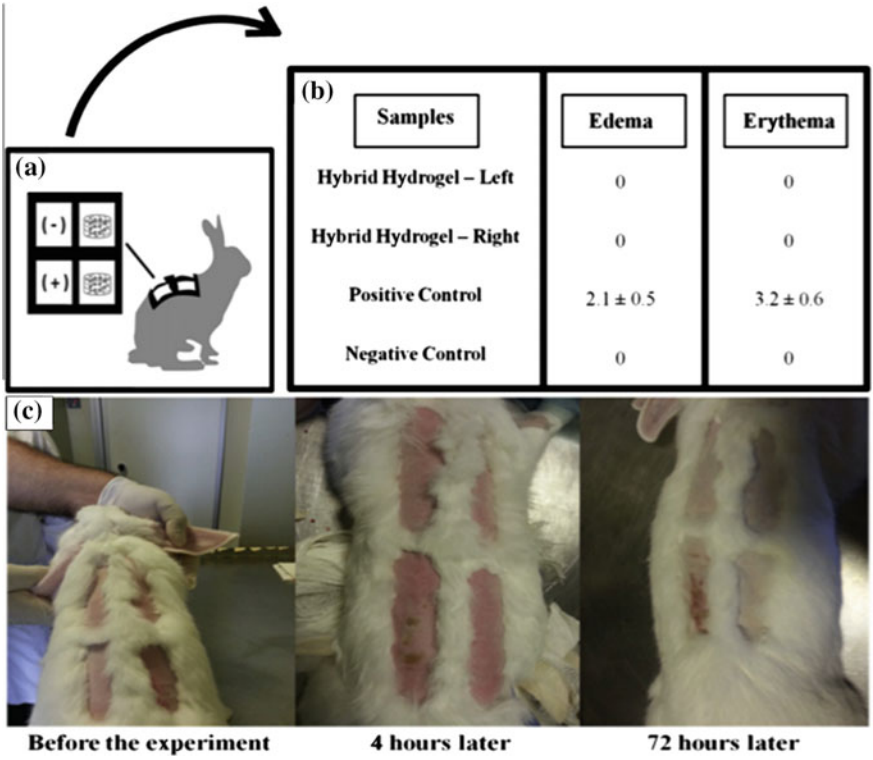

Fig. 14 In vivo implantation experiment results for an irritation assay. **a** Schematic representation of intracutaneous reactivity assay sites, **b** results of intracutaneous reaction, and **c** photographic images of implantation experiments before the experiment, 4 h later, and 72 h later. Reproduced with permission from Ref. [147] from the Elsevier

confirmed that the composite hydrogel is not toxic and has required biocompatibility (Fig. 14). There are several original papers focused on UV and visible light-induced synthesis of hydrogels based on various synthetic and natural polymers [148–154]. Huang and coworkers reported an ultraviolet light irradiation technique to prepare gold or silver nanoparticles in carboxymethyl chitosan solution and observed that the solution worked as both reducing agent for cations and stabilizing agent for nanoparticles [155, 156]. Kumar et al. [157] synthesized Ag clusters by reduction of Ag^+ in polyvinyl alcohol hydrogel using gamma irradiation [157]. Radiation-induced synthesis is also useful for the reduction of metal salts in a hydrogel solution [158]. A review of radiation-induced synthesis of hydrogels and their applications in various fields is given in Table 1.

Table 1 Radiation-induced preparation of hydrogels and their applications in various sectors

S. No.	Hydrogel	Types of radiation	Applications	Ref.
1	Gg-cl-poly(acrylic acid-aniline)	Microwave	Water retention and dye adsorption	[32]
2	Gum ghatti/methacrylic acid/aniline	Microwave	Colon-specific drug delivery	[34]
3	Nanocellulose composite	Electron beam	Biorefining	[159]
4	Butyl methacrylate and acrylamide onto low-density polyethylene	γ-radiations	Wastewater treatment	[160]
5	Poly(ethylene glycol)/acrylic acid	γ-radiations	Site-specific drug delivery	[161]
6	Polyelectrolyte-cross-linked hydrogel	γ-radiations	Oral delivery of insulin	[162]
7	Starch/(EG-co-MAA)	γ-radiations	Various applications	[163]
8	Poly(vinyl pyrrolidone), poly (ethylene glycol), and agar	γ-radiations	Wound dressings	[164]
9	PVA/MAAc/gelatin copolymer	γ-radiations	Wound-healing applications	[83]
10	Natural polysaccharides blend-grafted acrylamide	Microwave and ultraviolet	Drug delivery systems	[165]
11	Carboxymethylcellulose/starch superabsorbent	γ-radiations	Pure polyelectrolyte-based superabsorbents	[89]
12	Acrylic acid (AAc) and 2-hydroxyethyl methacrylate (HEMA)	γ-radiations	Removal of acid dye	[90]
13	Tragacanth gum-based sterile hydrogel	γ-radiations	Drug delivery and wound dressings	[92]
14	Tragacanth gum-cl-PVA-co-PVP-based hydrogel	γ-radiations	Wound dressing	[93]
15	Psyllium and acrylic acid-based polymeric networks	γ-radiations	Selective absorption of water from different oil–water emulsions	[166]
16	Tara gum/acrylic acid	γ-radiations	Diaper applications	[167]
17	Kappa-carrageenan/acrylamide	γ-radiations	Agricultural purposes as a material for sodic soil remediation	[168]
18	Poly(acrylic acid) modification of *Cassia javanica* seed gum	Microwaves	Heavy metal ions removal	[98]
19	Polyacrylamide-grafted gum ghatti	Microwaves	Flocculant	[100]
20	Guar gum with acrylamide	Microwaves	Colonic drug delivery	[104]
21	Polyacrylamide-grafted gum acacia	Heavy ions	Sorption of methylene blue	[142]

6 Conclusion

As mentioned earlier that the main concern of this chapter is about the synthesis of polysaccharide-based hydrogels, however, fabrication and characterization of some selectively graft copolymers are need to be further explored. It is reported that components of such graft copolymers had functioned as smart materials. Therefore, it can be used for the advancing sensor and actuators technologies. The scientific community is putting tremendous efforts to enhance the properties of hydrogels and expected that the overall performance could be increased in near future in terms of better swelling capacity, biocompatibility, and biodegradability.

Acknowledgements One of the authors (Kashma Sharma) is grateful to the University Grants Commission (UGC), New Delhi, for the award of Post-Doctoral Fellowship for Women [F.15-1/2017/PDFWM-2017-18-HIM-51703(SA-II)].

References

1. Walter R, Brian Saunders R (2014) Soft Matter 10:3695
2. Sharma K (2015) Synthesis of conducting gum ghatti-PANI based interpenetrating networks and their applications as controlled drug delivery devices. A Thesis submitted to the Faculty of Basic Sciences Shoolini University of Biotechnology and Management Sciences, Solan (Himachal Pradesh), 173229 (India)
3. Campbell TD (2007) Synthesis and physical characterization of biocompatible hydrogels. Department of Chemistry and Biochemistry, The Florida State University
4. Flory PJ (1941) J Chem Phy 9:660
5. Flory PJ (1941) J Am Chem Soc 63:3083
6. Huggins ML (1942) J Am Chem Soc 64:1712
7. Huggins ML (1943) Ind Eng Chem 35:216
8. Treloar LRG (1951) Chem Ind 45:955
9. Treloar LRG (1952) The thermodynamic study of rubber-like elasticity. Proc R Soc London Series B Biol Sci 139:506
10. Kumar V (2013) Characterization of conducting polymer composites & non-conducting polymers with exposure of neutrons, gamma rays and charged particles. Department of Physics, Sant Longowal Institute of Engineering and Technology, Longowal (Sangrur), Punjab (India)
11. Qinyuan C, Yang J, Xinjun Y (2017) Gels 3:6
12. Rabinarayan P (2017) Adv Pharm Bull 7(4):515
13. Jones DS, Andrews GP, Gorman SP (2005) J Pharm Pharmacol 57:1251
14. Hoffman AS (2002) Adv Drug Del Rev 54:3
15. Enas MA (2015) J Adv Res 6:105
16. Sastry SK, Lakonishok M, Wu S, Truong TQ, Huttenlocher A, Turner CE, Horwitz AF (1999) J Cell Bio 144:1295
17. Smetana K Jr, Vacík J, Součková D, Krčová Z, Šulc J (1990) J Biomed Mater Res 24:463
18. Kashma S, Vijay K, Kaith BS, Vinod K, Sudipta Som, Anurag P, Susheel K, Swart HC (2015) New J Chem 39:3021
19. Sharma K, Kumar V, Kaith BS, Kalia S, Swart HC (2017) Conducting polymer hydrogels and their applications. In: Kumar V, Kalia S, Swart HC (eds) Conducting polymer hybrids. Springer International Publishing

20. Yinan W, Christian KA, Ravin N (2018) Exp Opin Drug Del 15:77
21. Bell CL, Peppas NA (1995) Adv Polym Sci 122:125
22. Enrica C, Vitaliy VK (2015) Europ Polym J 65:252
23. Derek GP, Peter JS, Brian JT (1980) Polym Int 12:99
24. Nemours EIP (1936) Ind Eng Chem 28:1160
25. Wichterle O, Lim D (1960) Nature 185:117
26. Hoffman AS (1987) J Control Release 6:297
27. Hoffman AS (2012) Adv Drug Del Rev 64:18
28. Duncan R (2006) Nat Rev Cancer 6:688
29. MacEwan SR, Callahan DJ, Chilkoti A (2010) Nanomedicine (Lond) 5:793
30. Aliaghaie M, Mirzadeh H, Dashtimoghadam E, Taranejoo S (2012) Soft Matter 8:7128
31. Bita T, Shahrouz T, Seyed AM, Zoha SM, Karim D, Hossein D, Zaynab D (2014) Drug Del 22:145
32. Kashma S, Kaith BS, Vijay K, Susheel K, Vinod K, Swart HC (2014) Geoderma 232–234:45
33. Kashma S, Vijay K, Kaith BS, Sudipta S, Vinod K, Anurag P, Kalia S, Swart HC (2015) Ind Eng Chem Res 54:1982
34. Kashma S, Kaith BS, Susheel K, Vijay K, Swart HC (2015) Colloid Polym Sci 293:1181
35. Kashma S, Vijay K, Kaith BS, Vinod K, Sudipta S, Susheel K, Swart HC (2015) Polym Degrad Stab 111:20
36. Kashma S, Kaith BS, Vijay K, Vinod K, Sudipta S, Susheel K, Swart HC (2013) RSC Adv 3:25830
37. John AH, Rui C, van Theun V, Nicholas B (2014) J Mater Chem B 2:5319
38. Kirchmajer DM, Gorkin R, in het Panhuis M (2015) J Mater Chem B 3:4105
39. Takashi L, Hatsumi T, Makoto M, Takashi I, Takehiko G, Shuji S (2007) J Appl Polym Sci 104:842
40. Yang L, Chu JS, Fix JA (2002) Int J Pharm 235:1
41. Aylsworth JW (1914) US Patent 1111:284
42. Millar JRJ (1960) J Chem Soc 263:1311
43. Matricardi P, Meo CD, Coviello T, Hennink WE, Alhaique F (2013) Adv Drug Del Rev 65:1172
44. Jones SD, Andrews PG, Caldwell LD, Lorimer C, Gorman PS, McCoy CP (2012) Eur J Pharm Biopharm 82:563
45. Maolin Z, Jun L, Min Y, Hongfei H (2000) Radiat Phy Chem 58:397
46. Jenkins AD, Kratochvil P, Stepto RFT, Suter UW (1996) Pure Appl Chem 68:2287
47. Bhattacharya A, Misra BN (2004) Prog Polym Sci 29:767
48. Athawale VD, Vidyagauri L (1998) Carbohyd Polym 35:21
49. Mohammad RS, Abel M, Mohammad AR (2009) Carbohyd Polym 77:634
50. Celli A, Sabaa MW, Jyothi AN, Kalia S (2016) Chitosan and starch-based hydrogels via graft copolymerization. In: Kalia S (ed) Polymeric hydrogels as smart biomaterials. Springer International Publishing, pp 189–234
51. Chauhan A, Chauhan P, Kaith BS (2012) J Chem Eng Process Tech 3:1
52. Chauhan GS, Kaur I, Misra BN, Singha AS, Kaith BS (2000) Polym Degrad Stab 69:261
53. Chauhan GS, Kaur I, Misra BN, Singha AS, Kaith BS (1999) J Polym Mater 16:245
54. Sharma BR, Kumar V, Sen PL (2003) J Macromol Sci, Part A. Pure Appl Chem 40:49
55. Mittal H, Mishra SB, Mishra AK, Kaith BS, Jindal R, Kalia S (2013) Carbohydrate Polym 98:397
56. Mittal H, Mishra SB, Mishra AK, Kaith BS, Jindal R (2013) Int J Biolog Macromol 58:37
57. Berlin AA, Kislenko VN (1992) Prog Polym Sci 17:765
58. Hennink WE, van Nostrum CF (2002) Adv Drug Deliv Rev 54(1):13
59. Chun-Liang Y (2010) Investigation of electrophoretic loading and enhanced mechanical properties of hydrogels for delivery of therapeutic proteins. Faculty of Sciences and Technology, The Queensland University of Technology
60. Crini G (2005) Prog Polym Sci 30:38

61. Taleb MFA (2013) Int J Biolog Macromol 62:341
62. Nam IK, Mun GA, Urkimbaeva PI, Nurkeeva ZS (2003) Rad Phys Chem 66:281
63. Henke A, Kadlubowski S, Ulanski P, Rosiak JM, Arndt KF (2005) Nucl Instrum Meth Phys Res B 236:391
64. David JT, Hill AK, Whittaker Z (2011) Rad Phys Chem 80:213
65. Sung-Eun P, Young-Chang N, Hyung-Il K (2004) Rad Phys Chem 69:221
66. Hossen KM, Azim AM, Chowdhury AMS, Dafader NC, Haque ME, Akter F (2008) Polym Plas Tech Eng 47:662
67. Zainuddin H, Hill DJT, Whittaker AK (2007) J Biomed Mater Res, Part A 83A:54
68. Zainuddin H, Strounina DJT, Whittaker AK (2004) Soft Mater 2:195
69. Sakurada I, Ikada Y (1963) Bull Inst Chem Res Kyoto Univ 41(1):103
70. Kaetsu I (1981) Radiat Phys Chem 18:343
71. Kaetsu I (1985) Radiat Phys Chem 25:517
72. Hoffman AS, Allan S (1977) Radiat Phys Chem 18:323
73. Rosiak J, Rucinska-Rybus A, Pekala W (1989) US Patent No. 4871490 A
74. Sun Y, Chmielewski AG (eds) (2017) Applications of ionizing radiation in materials processing. Erasmus+
75. Guven O, Sen M, Karadag E, Saraydin D (1999) Radiat Phys Chem 56:381
76. Kume T, Nagasawa N, Yoshii F (2002) Radiat Phys Chem 63:625
77. Wach RA, Mitomo H, Nagasawa N, Yoshii F (2003) Radiat Phys Chem 68:771
78. Solpan D, Sibel D. Olgun G (2002) J Appl Polym Sci 86:3570
79. Alam MM, Chowdhury MA, Hina MF, Akhtar F, Kabir SE (2004) Chin J Polym Sci 22 (3):253
80. Tuncer C, Simin K, Gokhan D (2006) J Appl Polym Sci 101(3):1756
81. Kashma S, Kaith BS, Vijay K, Susheel K, Vinod K, Swart HC (2014) Polym Degrad Stab 107:166
82. Seo KH, You SJ, Chun HJ (2009) Tiss Engg Regen Med 6:414
83. Taleb MFA, Sahar AI, El-Kelesh NA (2009) J Macromol Sc Part A 46:170
84. Lale IS, Selmiye AG (2011) J Appl Polym Sci 120:2313
85. Nasef MM, Hegazy ESA (2004) Prog Polym Sci 29:499–561
86. Gupta B, Jain R, Anjum N, Singh H (2006) Radiat Phys Chem 75:161
87. Binh D, Huy HT (1998) Radiat Phys Chem 53:177
88. Mohd YBH, Shahrir H, Wan AWAR (2017) Int J Polym Mater Polym Biomater 926
89. Tamás F, Judit B, Erzsébet T, László W (2017) Chem Cent J 11:46
90. Ghada AM, Samia E Abdel-Aal, Nagwa AB, Samia AAF, Esraa AA (2014) Starch 66:400
91. Varshney L (2007) Nucl Instrum Meth Phys Res B 255:343
92. Baljit S, Lalit V, Sanju F, Rajneesh (2016) Int J Biolog Macromol 88:586
93. Baljit S, Lalit V, Sanju F, Rajneesh (2017) Radiat Phys Chem 135:94
94. Rohini D, Lok R, Ghanshyam SC (2012) J Appl Polym Sci 126:E260
95. Jayashree B, Virendra K, Bhardwaj YK, Goel NK, Dubey KA, Chaudhari CV, Sabharwal S (2007) Radiat Phys Chem 76:1624
96. Kappe CO (2004) Angew Chem Int Ed 43:6250
97. Prasad K, Mehta G, Meena R, Siddhanta AK (2006) J Appl Polym Sci 102:3654
98. Singh V, Singh SK, Maurya S (2010) Chem Eng J 160:129
99. Sen G, Singh RP, Pal S (2010) J Appl Polym Sci 115:63
100. Rani P, Sen G, Mishra S, Jha U (2012) Carbohydr Polym 89:275
101. Ghosh S, Sen G, Jha U, Pal S (2010) Bioresour Technol 101:9638
102. Kaith BS, Kashma S, Vijay K, Susheel K, Swart HC (2014) Synth Metals 187:61
103. Rani P, Sen G, Mishra S, Jha U (2012) Carbohydr Polym 89:275
104. Muhammad S, Shazia AB, Yousra G, Hira M, Fozia A, Mohammad Z, Tahir J, Khalid MZ (2013) Int J Bio Macromol 62:172
105. Mishra A, Shrinivasan R, Gupta RP (2003) Colloid Polym Sci 282:187
106. Singh V, Tripathi DN (2006) J Appl Polym Sci 15:2384
107. Singh V, Tiwari A, Tripathi DN, Sanghi R (2004) J Appl Polym Sci 5:1569

108. Chhatbar M, Meena R, Prasad K, Siddhanta A, Chhatbar MU, Meena R, Prasad K, Siddhanta AK (2009) Ind J Chem 48:1085
109. Maia AM, Silva HV, Curti PS, Balaban RC (2012) Carbohydr Polym 90:778
110. Singh V, Tiwari A, Tripathi DN, Sanghi R (2006) Polym 3:254
111. Sen G, Singh RP, Pal S (2010) J Appl Polym Sci 5:63
112. Singh V, Tiwari A, Pandey S, Singh SK (2006) Starke 1:536
113. Singh B, Chauhan GS, Sharma DK, Chauhan N (2007) Carbohydr Polym 19:559
114. Sagar P, Ghorai S, Dash MK, Ghosh S, Udayabhanu G (2011) J Hazard Mater 192:1580
115. Gautam S, Sumit M, Usha J, Sagar P (2010) Int J Biolog Macromol 47:164
116. Sumit M, Ankita M, Gautam S, Usha J (2011) Int J Biolog Macromol 48:106
117. Gautam S, Ranvijay K, Ghosh S, Sagar P (2009) Carbohyd Polym 77:822
118. Singh V, Kumar V, Sanghi R (2012) Prog Polym Sci 37:340
119. Gabriela C, Elena M, Maria DS (2016) J Chem 2016:1470965
120. Said HM, Abd Alla SG, El-Naggar AWM (2004) React Funct Polym 61:397
121. Fei B, Wach RA, Mitomo H, Yoshii F, Kume T (2000) J Appl Polym Sci 78:278
122. Liu P, Zhai M, Li J, Peng J, Wu J (2002) Radiat Phys Chem 63:525
123. Karadag E, Saraydin D, Güven O (2004) Nucl Instrum Meth Phys Res Sec B 225:489
124. Gonzalez-Martinez IG, Bachmatiuk A, Bezugly V, Kunstmann J, Gemming T, Liu Z, Cuniberti G, Rümmeli MH (2016) Nanoscale 8:11340
125. Branca C, Magazu S, Maisano G, Auditore L, Barna RC, Pasquale DD, Emanuele U, Trifiro A, Trimarchi M (2006) J Appl Polym Sci 102:820
126. Peppas NA (1986) Hydrogels in medicine and pharmacy. In: Fundamentals, vol 1. CRC Press, Boca Raton, FL
127. Rosiak JM, Ulanski P (1999) Radiat Phys Chem 55:139
128. Li HL, Ujihira Y, Shukushima S, Ueno K (2000) Polymer 41:93
129. Xu HS, Shanthi G, Bearti V, Zhang QM, Ramotowski T (2000) Macromol 33:4125
130. Ravat B, Grivet M, Grohens Y, Chambaudet A (2001) Radiat Meas 34:31
131. Arndt KF, Schmidt T, Reichelt R (2001) Polym 42:6785
132. Alegaonkar PS, Bhoraskar VN (2004) Radiat Eff Defects Solids 159:511
133. Torrisi L, Visco AM, Barna R, Pasquale DD, Campo N, Di Marco G, Trimarchi M, Trifiro A (2004) Radiat Eff Defects Solids 159:259
134. Othon CM, Bateman FB, Ducharme S (2005) J App Phys 98:014106
135. Cho SO, Jun HY (2005) Nucl Instrum Methods Phys Res, Sect B 237:525
136. Mazzoldi P, Arnold GW (1987) Ion beam modification of Insulators, vol. 2. Elsevier, Amsterdam
137. Mukherjee K, Gupta BD, Sharma PK (1986) J Macromol Sci Part B Polym Rev 26:415
138. Demertzis PG, Franz R, Welle F (1999) Packag Technol Sci 12:119
139. Huq T, Khan A, Dussault D, Salmieri S, Khan RA, Lacroix M (2012) Radiat Phys Chem 81:945
140. Kaith BS, Kashma S, Vijay K, Vinod K, Swart HC, Kalia S (2014) Vacuum 101:166
141. Kashma S, Kaith BS, Vijay K, Vinod K, Susheel K, Kapur BK, Swart HC. Radiat Phys Chem 97:253
142. Kaith BS, Rachna S, Kashma S, Choudhary S, Vijay K, Lochab SP (2015) Vacuum 111:73
143. Razem D, Katusin-Razem B (2008) Radiat Phys Chem 77:288
144. Tanaka TT, Tsuchiya K, Yajima H, Suzuki Y, Fukutome A (2011) Nucl Instrum Methods Phys Res B 269:2130
145. Tiwari VK, Singh NK, Avasthi DK, Misra M, Maiti P (2013) Radiat Phys Chem 82:92
146. Thaker MD, Trivedi HC (2005) J Appl Polym Sci 97:1977
147. Ozlem C, Dogan G, Seda K (2015) Acta Biomater 111:151
148. Gupta P, Vermani K, Garg S (2002) Drug Discovery Today 7:569
149. Hao Y, Shih H, Munoz Z, Kemp A, Lin CC (2014) Acta Biomater 10:104
150. Schoener CA, Hutson HN, Peppas NA (2012) Polym Int 61:874
151. Schoener CA, Hutson HN, Peppas NA (2012) J Biomed Mater Res Part A 101:2229
152. Yiting H, Han S, Zachary M, Arika K, Chien-Chi L (2014) Acta Biomater 10:101

153. Junli H, Yaping H, Hyejin P, Bogyu C, Siying H, Amy C, Min L (2012) Acta Biomater 8:1730
154. Bogyu C, Soyon K, Brian L, Kevin L, Olga B, Jinku K, Denis E, Tara A, Min L (2015) Acta Biomater 12:30
155. Huang L, Zhai ML, Long DW, Peng J, Xu L, Wu GZ, Li JQ, Wei GS (2008) J Nanopart Res 10:1193
156. Huang L, Zhai ML, Peng J, Xu L, Li JQ, Wei GS (2007) J Colloid Interface Sci 316:398
157. Kumar M, Varshney L, Francis S (2005) Radiat Phys Chem 73:21
158. Ying Z, Yinghui Z, Lu W, Ling X, Maolin Z, Shicheng W (2012) Radiat Phys Chem 81:553
159. Michael TP, Dianne LP, András EV, Mark SD, Al-Sheikhly MI (2018) Radiat Phys Chem 143:47
160. Ghaffar AMA, El-Arnaouty MB, Aboulfotouh ME, Taher NH, Taha AA (2014) Radiat Eff Def Solids 169:741
161. Amr El-Hag A, El-Sayed AH (2007) J Biomed Mater Res B Appl Biomater 81:168
162. Manal FAT (2013) Int J Biolog Macromol 62:341
163. Abd El-Mohdy HL, Hegazy EA, El-Nesr EM, El-Wahab MA (2016) Arab J Chem 9:S1627
164. Ajji Z, Othman I, Rosiak JM (2005) Nucl Instrum Meth Phys Res B 229:375
165. Sorour M, El-Sayed M, Moneem NAE, Talaat HA, Hayam S, Marsafy SE (2013) Starch 65:172
166. Kiran K, Kaith BS, Rajeev J, Hemant M (2012) J Appl Polym Sci 124:4969
167. Safaa GAA, Murat S, El-Naggar AWM (2012) Carbohydr Polym 89:478
168. Abd El-Mohdy HL, Abd El-Rehim HA (2009) J Polym Res 16:63

Effects of Radiations on the Properties of Polycarbonate

K. Hareesh and Ganesh Sanjeev

Abstract The exposure of the polymer to radiation results in modification on chemical and physical properties of the polymer. Whenever radiation passes through polymer, the drastic changes in the optical, electrical, thermal, chemical, structural, surface morphological, mechanical and rheological properties due to chain scission, chain aggregation, cross-linking, gas evolution etc. The chain scission process results in the decreases of molecular weight, whereas cross-linking process increases the molecular weight. This chapter deals with the changes in the properties of PC due to the effect of the radiation along with the detailed schematic mechanism.

Keywords Radiations · Polycarbonate · Cross-linking · Free volume Chemical properties

1 Importance of the Study of Radiation Effects on Polymers

Every material and component is affected to some extent by radiation. Radiation effects can be classified into two types namely transient and permanent. Transient effects appear in the presence of the radiation field and disappear shortly after the removal of the radiation field. Permanent effects begin during an irradiation and also persist even after it has ended. Such changes may cause the materials and component systems to fail. In order to avoid radiation-induced degradation, radiation hardened materials and component systems are to be developed.

K. Hareesh
School of Physics, REVA University, Bangalore 560064, India

K. Hareesh (✉)
School of Physics, University of Western Australia, Perth, WA 6004, Australia
e-mail: appi.2907@gmail.com

G. Sanjeev
Microtron Centre, Department of Studies in Physics, Mangalore University, Mangalore 574199, India

V. Kumar et al. (eds.), *Radiation Effects in Polymeric Materials*, Springer Series on Polymer and Composite Materials, https://doi.org/10.1007/978-3-030-05770-1_9

Successful operation of materials and component systems requires an understanding of the mechanisms that cause degradation and also require radiation testing of materials and component systems through ground simulation in order to ensure that they will withstand the radiation environments encountered [1].

The amount of radiation that polymeric material receives during their life cycles depends upon the radiation environment and its operating conditions. The radiation-harsh environment is obvious for nuclear and space applications. In addition to this, the devices get affected by ionizing radiation during their fabrication processes and standard terrestrial operation. The possible experiments or realistic scenarios under which a material experiences a radiative environment are as follows: space environment, high-energy physics experiments, nuclear reactor premises, natural environments and processing-induced radiation, etc. Figure 1 shows the images of polycarbonate irradiated by gamma radiation just after irradiation and one week after irradiation. When polymeric material is used for such applications, a detailed study of the radiative environmental effect on the material needs to be done. Such studies can be carried out using ionizing and non-ionizing radiations through ground simulation [1–4].

2 Types of Radiation

The literature reports reveal that different types of radiations like electromagnetic (ex. gamma rays, UV radiation) [5] or corpuscular (ex. electrons, protons, alpha particles and heavy ions) [4] have been applied to modify the properties of

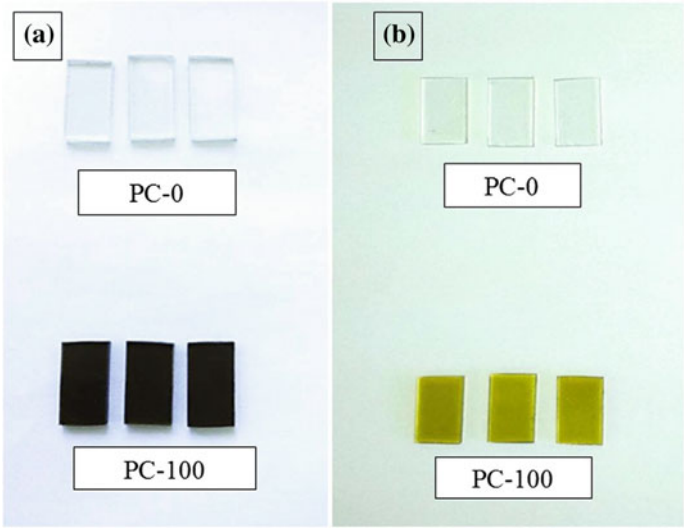

Fig. 1 Polycarbonate samples, **a** immediately after gamma irradiation and **b** one week later (upper side figures are PC at 0 kGy) (Copied from Ref. [2] with consent from the Elsevier)

polymeric materials. Generally the ionizing radiations (like beta, X-rays [6], gamma rays [7], various energetic charged particles such as accelerated electrons [7], protons [8], alpha particle [8], neutrons [9] and ions of heavier chemical elements [10–12]) having high/low energy are frequently used for irradiation purpose and they affect the atomic structure of the material. Non-ionizing radiations (radio waves, microwaves, UV radiation and infrared rays) with lower energy levels and longer wavelengths interact with matter predominantly to produce excitation [13, 14]. Among all these radiations, electrons, protons, alpha particles and UV radiation are present in the earth radiation belt which causes damage to the polymers used in space applications. A brief explanation for these radiations is given in the following paragraphs.

Electron is a subatomic particle having a negative elementary electric charge. When an electron passes near an orbital electron, a strong repulsive force (Coulomb force) exists between the two negatively charged particles. If this force is sufficient, the orbital electron may get repelled with enough momentum to move it to a higher energy orbit of the same atom (excitation) or is dislodged away from the atom (ionization). Some of the energy of the original moving electron has thus been transferred to the orbital electron. In this process, if the electron gets ejected from the atom, it is called a secondary electron. It may have given sufficient energy to produce excitation or ionization in other atoms. The second mechanism of energy transfer from electrons involves interaction with atom nuclei. When a fast-moving electron approaches the nucleus of an atom, the electrical interaction causes the electron to be accelerated and drifted from its original path. Subsequently, there should be the emission of energy as electromagnetic radiation in accordance with Maxwell's theory.

Proton is also a subatomic particle with a positive electric charge of one elementary charge. The protons interact with polymer results in the production of free radicals, escort the formation of double bonds and anti-oxidation occurs in the presence of oxygen. These reactions depend upon the proton beam fluence and environmental conditions during and after irradiations.

Alpha particles are comparatively heavy and have a charge. Hence, they can react interact with matter results in the production of large numbers of ions per unit length of their path. Therefore, the penetration is less for alpha particle. For example, the range of 5 MeV alpha particles is 3.6 cm in air and will not penetrate an ordinary piece of paper. For other materials, the range of alpha particle with respect to air is inversely proportional to the respective densities of each material. Alpha particles can interact with either nuclei or orbital electrons in any polymer. An alpha particle passing in the vicinity of the nucleus will be deflected with no change in energy (Rutherford scattering) or deflected with a small change in energy causing nuclear transformation (this process is negligible for alphas).

Ultraviolet (UV) light is an electromagnetic radiation having wavelength in the range 290 to 400 nm. The UV radiations are invisible to humans, but visible to number of insects and birds. However, they are visible by causing fluorescent materials to glow with visible light. UV light can degrade many polymers used in consumer products. The changes induced in the polymer by UV radiation depend

on the time of exposure and also on the wavelength of UV radiation. UV radiation can cause chain degradation and loss of strength in the polymer. The irradiation of the polymers by UV light has applications in nanotechnology, transplantology, X-ray lithography, etc.

3 Interaction of Radiation with Polymer

In recent years, irradiation is established as an effective method to modify the properties of the polymer. Particularly, in certain applications such as in the field of biomedical electrical, space and pharmaceutical industries, etc., the irradiation method is very useful. When radiation interacts with matter, it results in the deposition of full or partial energy and causes ionization or excitation of atoms. This ionization/excitation serves as the basic signal to detect the presence of radiation and often its quantitative amount [15]. Low ionization radiations, regarded as low-linear energy transfer (LET) radiations (X-rays, γ-rays, etc.) interact with matter in three different ways viz. (a) photoelectric effect, (b) Compton effect and (c) pair production. Figure 2 shows the different effects with variation of energy.

The relative importance of these processes depends on the energy of the photons. During low LET radiations interaction with matter, the energy will be absorbed by the medium to emit electrons from the atoms of the material which mainly depends on the atomic composition. When incident ions collide with target atoms, it will be displaced from its original positions leading to a subsequent nuclear collision cascade. This interaction leads to structural changes such as the creation of point

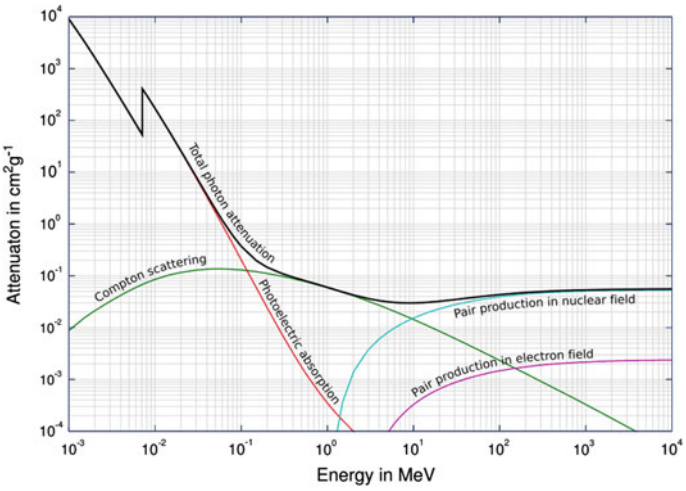

Fig. 2 Different effects (such as Compton scattering, photoelectric effect and pair production) with variation of energy and total photon cross section for different effects

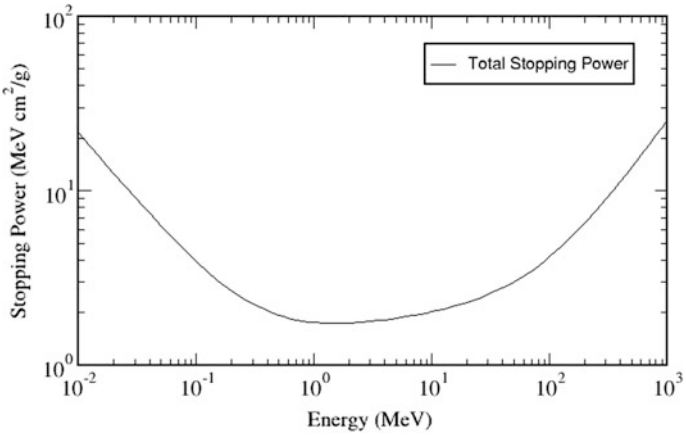

Fig. 3 Total stopping power of electron in polycarbonate calculated using E-STAR program

defects, amorphization, chain scission, cross-linking, etc. Nuclear stopping power is the origin of most sputtering processes and ion beam mixing of materials. These nuclear stopping power effects are most efficient if the Rutherford scattering cross section is highest, i.e. ~10–100 keV.

In case of the higher ion energies (>2 MeV) regarded as high LET radiations, the energy loss due to electronic stopping power will be dominated. The range of ion or track of ion remains roughly straight for high-energy ions due to the large mass difference between the ion and the electrons. The energy in the electronic subsystem is transferred to the atomic subsystem by means of two different mechanisms [16]:

- The lattice-relaxation model which describes a collective atomic rearrangement due to non-equilibrium potentials. Therefore, a fraction of the electronic potential energy or equivalently the degree of target excitation leads to modification of inter-atomic forces and subsequent atomic motion.
- The thermal spike model assumes that electronic excitation leads to the electron-phonon coupling (equivalent to electron–atom collisions).

Figure 3 shows a graph of the total stopping power of electron in polycarbonate [17] obtained using E-STAR program.

4 Polycarbonate

Polymeric structures are different than the molecular level materials by the concentration of groups to form chains. In this century, polymers have played a major role in our day-to-day life as they have supplemented conventional structural materials such as metals, ceramics, wood, leather, textiles and paper. The polymers have rapid growth due to their various advantages such as easy processability,

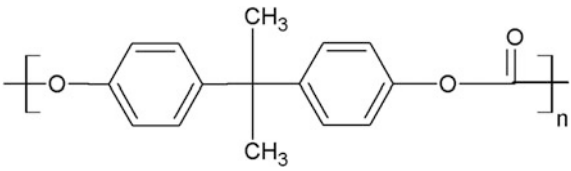

Fig. 4 Chemical structure of polycarbonate

extensive range of rigidity or flexibility, toughness, lubrication/adhesion, thermal and electrical insulation, clarity/opacity and colour, resistance to corrosive chemicals as well as overall advantage of economical superiority [18].

In precise, engineering designs for high-performance polymers have often suffered from certain limitations: low elastic modulus, strength and creep prone, lesser than perfect lubricity, higher coefficient of thermal expansion, poor heat resistance, etc. Reinforced polymers have been developed over the past 70 years to overcome many mechanical problems. But the difficulty in the processing of the reinforced polymers results in limited design possibilities. Reinforced polymers often have low lubricity, changed electrical properties, loss of clarity, colour and higher cost.

Polycarbonate (PC) was invented by Dr. Hermann Schnell of Bayer in 1953, just one week before Dr. Daniel Fox of General Electric Company independently made the same discovery while working on a wire coating. Both the teams were overwhelmed by the remarkable toughness of the polycarbonate. In the 1960s, NASA used polycarbonate for astronaut helmet assemblies and visors which became known as "bubble helmets" including those used by the Apollo moon astronauts [19]. Later, PC sheet was used in signs, windows, greenhouses and other applications. Recently, the PC has attracted even more because of its enormous applications such as lightweight traditional eyewear, bulletproof jacket, bus shelters, aircraft windows, machine guards, sports helmets, windshields and aircraft canopies [20, 21]. The chemical formula for polycarbonate is $C_{16}H_{14}O_3$ and its structural formula is shown below in Fig. 4.

5 Schematic Mechanism of Effect of Radiation on Polycarbonate

When radiation interacts with a polymer, it results in the chain scission or cross-linking. A schematic proposed mechanism of irradiation-induced reaction in PC is shown in scheme 1a, b [22] which can be explained as follows. Zimmermann et al. [23] have reported that the C–O bonds adjacent to the carbonyl group in the PC polymer chain are vulnerable bonds, lacking the resonance stabilization of the phenyl group [24].

This carbonate group absorbs energy selectively and undergoes chain scission forming phenoxy and phenyl free radicals (as shown in Scheme 1a) and thereafter cross-linking with the residual polymer. It was reported by Hama and Shinohara

[25] that the production of phenoxy radical may be about five times greater than that of the phenyl radical. This concludes that C–O bond (C in the C = O bond; bond dissociation energy = 330 kJ/mol) is more susceptible compared to that of other C–O bond (C on the ring; bond dissociation energy = 358 kJ/mol). The decrease in the viscosity average molecular weight in the initial stage of the photo-irradiation and then a gradual increase to attain a plateau value was observed by Torikai et al. [26], and they argued that this behaviour may be due to chain scission and subsequent photo-fries rearrangement. It was reported that the UV-irradiation of Nylon 6 [27] results in the increase of viscosity due to cross-linking. It is also known that most of the carbonates in epoxies and aryl esters undergo photo-fries rearrangement [28] during photolysis results in the rearrangement of oxygen atoms leading to the formation of photo-stabilisers such as phenyl salicylate and 2, 2′-dihydroxybenzophenone (as shown in Scheme 1b). This reveals that PC forms phenyl salicylate and 2, 2′-dihydroxybenzophenone during irradiation and is shown in Scheme 1b.

6 Effect of Radiation on the Properties of Polycarbonate

The irradiation is a useful tool to tune the desired properties of polymer for some specific applications. By irradiation, most of the properties such as optical, mechanical, electrical and chemical of the polymers can be modified. The exact modifications in the properties of polymer depend on the nature of radiation.

6.1 Optical Properties

The information about the optical band gap (E_g) of polymer can be obtained by UV–Visible spectroscopy. The polymeric materials absorb the light energy in the UV and visible regions and promote the electrons from the ground state of σ, π and n-orbitals to higher energy states described by molecular orbitals [29]. The allowed electronic transitions (→) of polymer in UV–Visible region are, $\sigma \rightarrow \sigma^*$, $n \rightarrow \sigma^*$, $n \rightarrow \pi^*$ and $\pi \rightarrow \pi^*$ [30].

The UV–visible absorption spectra of pristine PC and Ni ion beam irradiated PC films are shown in Fig. 5. It can be seen from Fig. 5 that the pristine PC has an absorption edge at 285 nm which is assigned to $n \rightarrow \pi^*$ transition. After irradiation, the absorption edge of PC films shifts towards higher wavelength. This indicates carbonization of the polymeric materials under electron irradiation [31, 32]. Also the irradiated polymer surface shows visible colour change from transparent to yellow and the intensity of the colour increases with increase in ion fluence.

The relation between optical band gap (E_g) and absorption coefficient (α) is given by $\alpha(h\nu) = A(h\nu - E_g)^r/h\nu$ [33]. The optical band gap of PC films can be

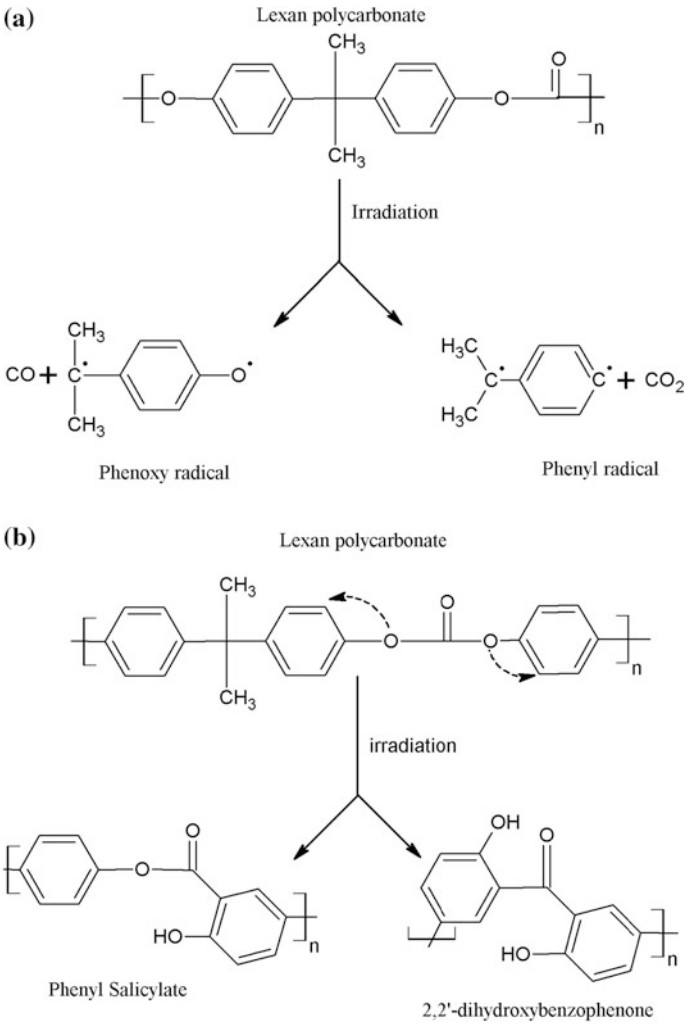

Scheme 1 **a** Possible scheme of chain scission mechanism in PC after irradiation [22], **b** schematic representation of a possible photo-fries rearrangements in PC after irradiation [22]

obtained by plotting α^2 versus photon energy ($h\nu$) and is shown in Fig. 6. The value of E_g can be deduced from the intersection of the extrapolated lines from the linear part of the curves with the $h\nu$-axis. For pristine PC, E_g was found to be 4.36 eV. After irradiation, E_g decreases with increase in radiation dose/fluence. The decrease in the optical band gap indicates increase in electrical conductivity, which is attributed to the scissioning of the polymer chains [34, 35] and the formation of free charge carriers as explained in Sect. 5. The values of optical band gap of PC films for different radiations are listed in Table 1.

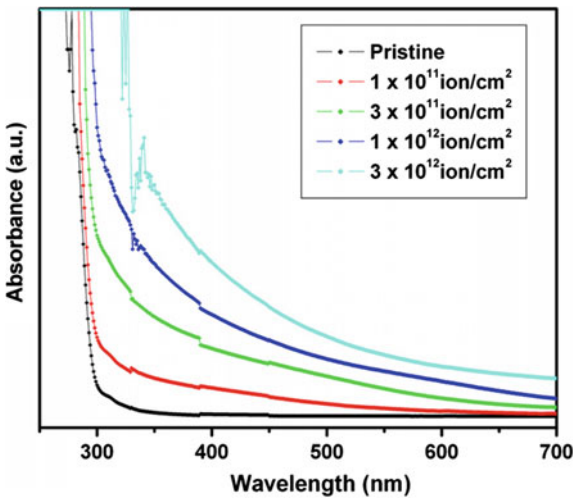

Fig. 5 Absorption spectra for pristine and Ni^{+11} irradiated PC films (Copied from Ref. [10] with consent from the Elsevier)

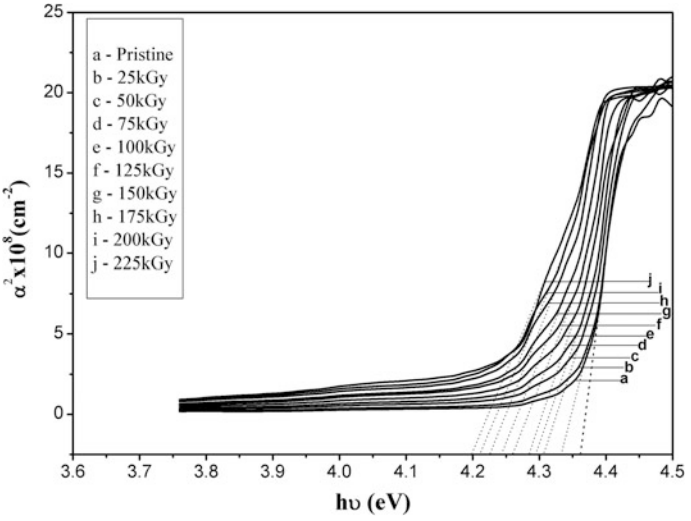

Fig. 6 Variation of α^2 with photon energy ($h\nu$) of pristine and 8 MeV electron beam irradiated PC

The number of carbon atoms per cluster (N) can be calculated using optical band gap by an equation, $E_g = \frac{34.3}{\sqrt{N}}$ and they are listed in Table 1. The number of the carbon atoms per cluster increases with increase in radiation dose/fluence which is attributed to slowing down of radiations in polymeric matrix by the interaction with

Table 1 Optical parameters of pristine and irradiated PC films

Radiation	Dose/fluence/exposure time	E_g (eV)	N	Reference
	Pristine	4.36	62	
Electron beam (8 MeV)	25 kGy	4.33	63	[22]
	50 kGy	4.30	63	
	75 kGy	4.29	64	
	100 kGy	4.28	64	
	125 kGy	4.26	65	
	150 kGy	4.24	65	
	175 kGy	4.22	66	
	200 kGy	4.21	66	
	225 kGy	4.19	67	
Proton (15 MeV)	5×10^{13} p/cm^2	4.34	62	–
	1×10^{14} p/cm^2	4.31	63	
	5×10^{14} p/cm^2	4.28	64	
	1×10^{15} p/cm^2	4.25	65	
	3×10^{15} p/cm^2	4.22	66	
Alpha particle (40 MeV)	5×10^{13} α/cm^2	4.32	63	–
	1×10^{14} α/cm^2	4.27	64	
	5×10^{14} α/cm^2	4.23	65	
	9×10^{14} α/cm^2	4.20	66	
	1×10^{15} α/cm^2	4.16	68	
UV radiation (λ = 240 nm)	1 h	4.32	63	[5]
	2 h	4.28	64	
	4 h	4.26	65	
	6 h	4.24	66	
	7 h	4.21	67	
95 MeV O^{6+}	10^{10} ions/cm^2	3.98	5	[11]
	10^{11} ions/cm^2	3.56	5	
	10^{12} ions/cm^2	3.22	6	
	10^{13} ions/cm^2	2.52	7	
	2×10^{13} ions/cm^2	2.34	8	
100 MeV O^{+7}	1×10^{11} ions/cm^2	3.9	77	[10]
	3×10^{11} ions/cm^2	3.7	86	
	1×10^{12} ions/cm^2	2.9	140	
	3×10^{12} ions/cm^2	2.2	243	
150 MeV Ni^{+11}	1×10^{11} ions/cm^2	3.8	81	[10]
	3×10^{11} ions/cm^2	3.5	96	
	1×10^{12} ions/cm^2	2.2	242	
	3×10^{12} ions/cm^2	1.8	363	

the electronic system of target atoms. As a result of the interaction, atomic electrons will be produced by excitation or ionization leading to chain scission, and hence, the surface layer of polymer can be transformed into a hydrogenated amorphous carbon.

6.2 *Electrical Properties*

The AC conductivity of irradiated PC films along with pristine was calculated using the equation $\sigma_{a.c.} = 2\pi f C_P D t/A$ (S/m), where f is the frequency, C_P and D are the capacitance and dissipation factor, respectively, measured directly from the LCR meter, t is the thickness of the polymer film and A is the area cross section of the electrode. Figure 7 shows the AC conductivity ($\sigma_{a.c.}$) of O^{6+} ion beam irradiated PC films plotted against logarithm of frequency (f).

From Fig. 7, it is found that the conductivity at low frequency (up to 500 kHz) looks like straight line for all the samples, typical of hopping conduction. The further increase in frequency (i.e. beyond 500 kHz), a sharp increase in conductivity was observed for both pristine and electron irradiated PC samples. It is also found that $\sigma_{a.c.}$ value increases with increase in electron dose due to the increase in number of charge carriers which are formed by the conversion of polymeric structure into a hydrogen depleted carbon network that is believed to make the polymers more conductive [36–38].

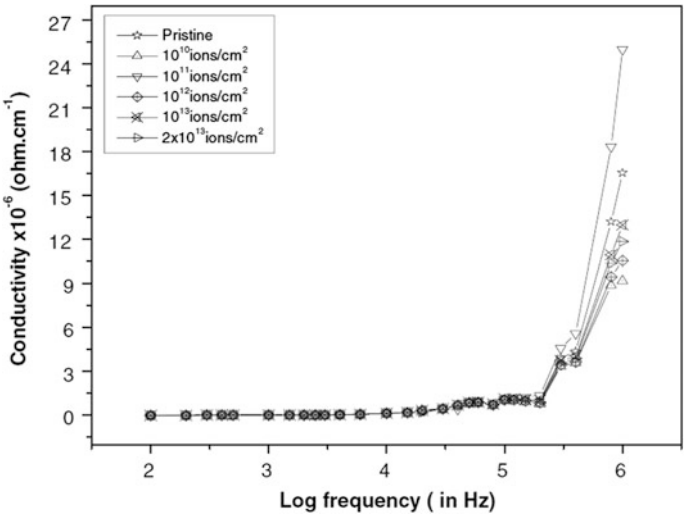

Fig. 7 Variation of AC conductivity ($\sigma_{a.c.}$) with log (frequency) for pristine and O^{6+} ion irradiated PC (Copied from Ref. [11] with consent from the Elsevier)

Dielectric constant can be calculated for PC films using equation $\varepsilon = C_P t/\varepsilon_0 A$, where ε_0 is the permittivity of free space. Figure 8 shows dielectric constant versus log (frequency) for electron beam irradiated PC. The dielectric constant was found to be constant till 150 kHz; thereafter, it increases with increase in frequency. The constant dielectric constant is due to the constant motion of free charge carriers at these frequencies. Further increase in frequency results in the migration of charge carriers through the dielectric and they get trapped in defect sites. The trapped charges induce an opposite charge in its vicinity due to which the motion of free charge carriers is slowed down and the value of dielectric constant decreases. Further, the decrease in dielectric constant at higher frequencies can be explained by Jonscher's power law, i.e. $\varepsilon_r \propto f^{n-1}$ where $0 < n < 1$ [39]. The value of 'n' increases from 0.68 to 0.84. It is also evident from Fig. 8 that the dielectric constant measured at 1 MHz increase from 7.06 for pristine to 7.99 for electron irradiated PC at a dose of 225 kGy. In contrast, the dielectric constant of PC decreased due to 95 MeV O^{+6} ion irradiated PC with increase in fluence. As the frequency increased, the charge carriers migrate through the dielectric and get trapped against a defect site and induce an opposite charge in its vicinity. At these frequencies for the ions, the polarization of trapped and bound charges cannot take place, and hence, the dielectric constant decreases [11].

The dielectric loss is the power dissipated in a dielectric media when it is exposed to electric field. It can be measured directly from LCR meter/Impedance gain analyser. Figure 9 shows the variation in the dielectric loss as a function of log

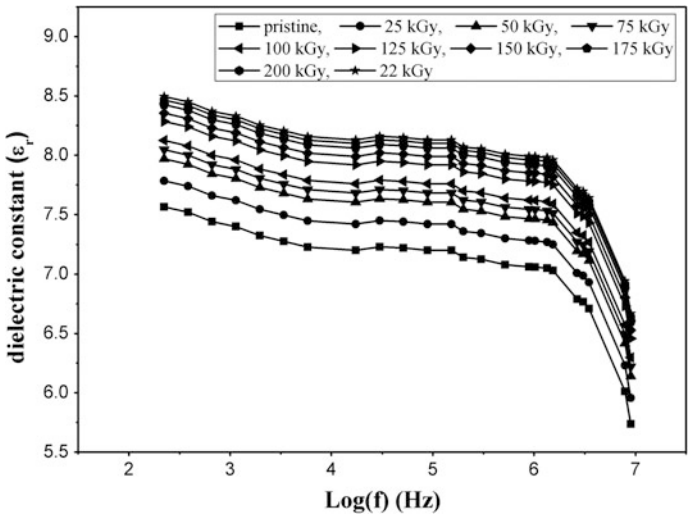

Fig. 8 Plot dielectric constant versus log (frequency) for pristine and 8 MeV electron irradiated PC films

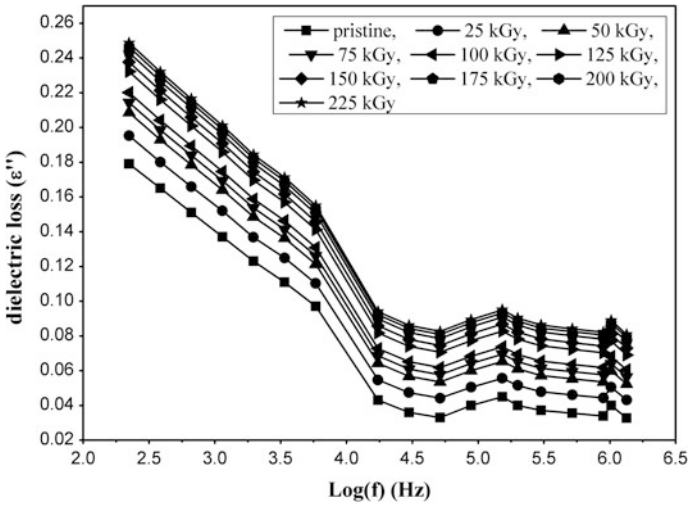

Fig. 9 Correlation of dielectric loss with log (frequency) for 8 MeV electron irradiated PC

(frequency) for pristine and irradiated samples. It is observed that the dielectric loss decreases exponentially with increase in frequency and becomes less dependent at higher frequencies.

6.3 Thermal Properties

Differential scanning calorimetry (DSC) is used for the study of thermal characteristic of materials. These include glass-transition temperature (T_g) and heat of fusion (ΔH). In the present work, the effect of electron beam irradiation on the glass-transition temperature (T_g) and heat of fusion has been monitored by DSC thermograms. The temperature at which the polymer changes from rigid glassy state to rubbery state is known as glass-transition temperature. At the glass-transition temperature, the bonds in the polymer chains are broken and macromolecule starts to move towards rubbery state. DSC thermograms of pristine and electron irradiated PC samples were measured and are shown in Fig. 10.

The endothermic transformation of the pristine film occurs around the temperature range from 145 to 154 °C with a glass-transition temperature (T_g) of 150 °C and the corresponding heat of fusion was found to be 4.43 J/g. After irradiation the T_g decreased to 146 °C (for 100 kGy) and 143 °C (for 225 kGy). The decrease in T_g after irradiation reveals that the irradiation leads to chain scission and subsequently reduction in molecular weight. As a result of decrease in molecular weight, the disorderness increases in the polymeric system [39]. In addition to this, the heat

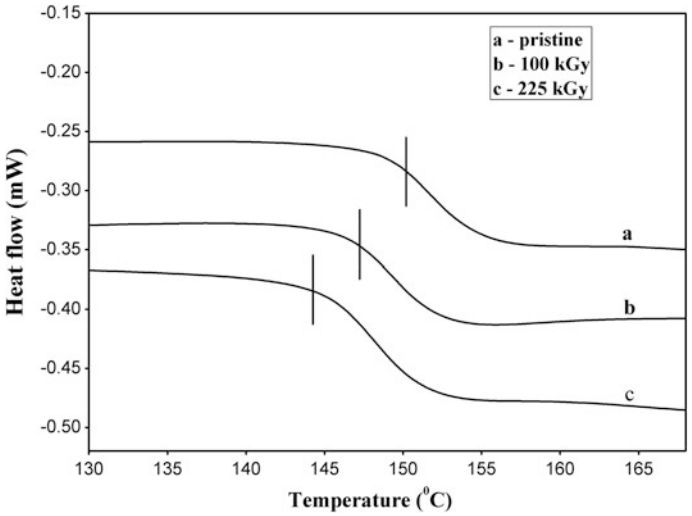

Fig. 10 DSC pattern of pristine and 8 MeV electron irradiated PC films

Table 2 Glass-transition temperature (T_g) and thermal decomposition temperature (T_d) of pristine and irradiated PC

Radiation	Dose/fluence/time	T_g (°C)	T_d (°C)	Reference
Pristine	–	150	495	[22]
8 MeV electron beam	100 kGy	146	502	[22]
	225 kGy	143	516	[22]
15 MeV proton	5×10^{13} ions/cm^2	148	345	[8]
	5×10^{14} ions/cm^2	145	280	[8]
	1×10^{15} ions/cm^2	141	212	[8]
40 MeV alpha particle	5×10^{13} ions/cm^2	148	315	[8]
	5×10^{14} ions/cm^2	144	265	[8]
	1×10^{15} ions/cm^2	139	202	[8]
UV radiation (λ = 240 nm)	2 h	149	450	[5]
	4 h	147	461	[5]
	7 h	145	464	[5]
6 keV Ar ions	0.5×10^{18} ions/cm^2	142.24	503.35	[40]
	1×10^{18} ions/cm^2	144.96	512.33	[40]
	1.5×10^{18} ions/cm^2	146.59	528.00	[40]

of fusion (ΔH) for pristine sample was found to be 4.43 J/g. After irradiation, the heat of fusion decreases with increase in electron dose, i.e. for 100 kGy it was found to be 4.34 J/g and for 225 kGy it was found to be 4.15 J/g. Similarly, it can also be observed from Table 2 that the glass-transition temperature decreased with

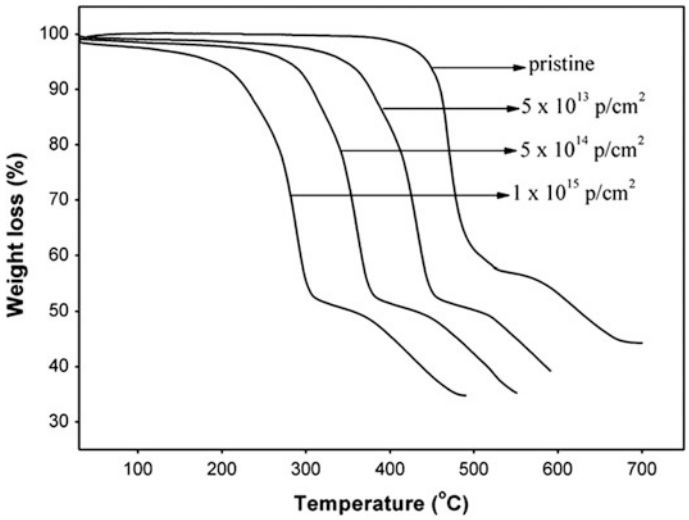

Fig. 11 TGA thermograms of pristine and proton irradiated PC films

increase in fluence/dose for different radiations. This decrease in glass-transition temperature and heat of fusion may be due to bond breaking during electron irradiation.

The thermal stability of polymers before and after irradiation can be studied by using Thermogravimetric analysis (TGA). The thermograms of pristine and the proton irradiated PC sample showing the weight (%) as a function of temperature is shown in Fig. 11. The thermal stability of polycarbonate detector decreases at high dose of gamma, and the weight loss starts at around 420 °C and continues up to 700 °C [41].

Figure 11 depicts that the pristine PC showed a little decrement in weight loss at 250 °C and continuous till 440 °C. This small weight loss was due to water vaporization and not much significant. After 440 °C, the PC film showed a huge weight loss till 530 °C because of thermal decomposition and about 76% of the sample decomposed into volatiles. After 530 °C, there is a small decrease in weight loss due to emission of volatile gases. The thermal decomposition temperature for pristine PC was found to be 495 °C. The irradiated samples also exhibited similar zones but thermal decomposition temperature decreased with increase in dose/fluence due to chain scission as explained in the above section.

6.4 Structural Properties

X-ray diffractogram (XRD) was carried out in order to study electron irradiation effect on degree of crystallinity of PC. Figure 12 shows the XRD pattern of pristine

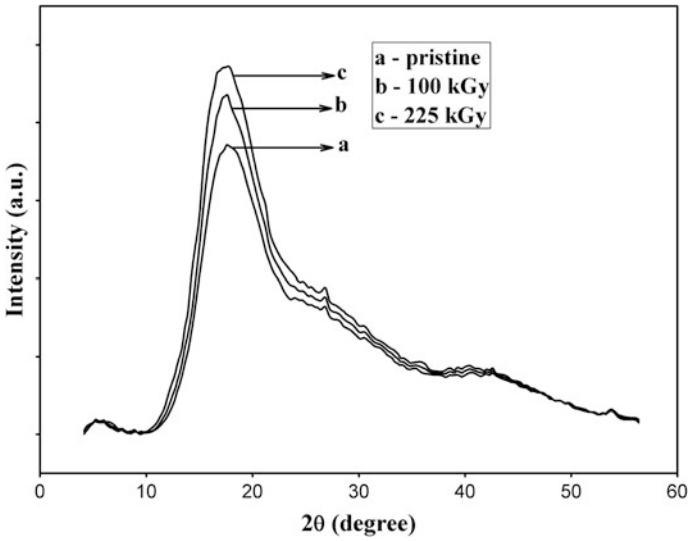

Fig. 12 XRD pattern for pristine and 8 MeV electron beam irradiated PC films

and 100 MeV O^{7+} ion beam irradiated PC films at different fluences. For pristine sample, the first main peak was obtained at $2\theta = 17.56°$. The interchain distance between the polymer chains (*d*-spacing) is calculated using Bragg's law given by an equation, $2d\sin(\theta) = n\lambda$. For pristine PC, the d-spacing was found to be 5.05 Å. It can be observed that the *d*-spacing of PC decreased due to the effect of radiation on it. This decrease in *d*-spacing may be due to bond breaking with evolution of volatile gases after irradiation.

The crystallite size (*L*) of PC can be calculated using Scherre's formula given by equation $L = K\lambda/b\cos(\theta)$ where *L* is crystallite size in Å, *b* is full width at half maximum (FWHM) in radians, $\lambda = 1.5406$ Å, wavelength of the X-ray beam, *K* is a shape factor (=0.9), and are tabulated in Table 3. After irradiation, the crystallite size of PC decreased to 14.15 Å for 100 kGy and it was 13.79 Å for 225 kGy, whereas 16.18 Å for 2×10^{13} ions/cm^2 for 95 MeV O^{6+} ion irradiated PC. Percentage of crystallinity of the polymer can be determined by area ratio method. In this method, the areas of amorphous and crystalline parts of the pattern were calculated. The degree of crystallinity for pristine sample was found to be 43% and after irradiation it decreased to 27% for 225 kGy, 29% for 1×10^{15} p/cm^2, 23% for 1×10^{15} α/cm^2, 38% for 7 h in case of electron, proton, alpha particle and UV radiation, respectively. The decrease in both crystallite size and percentage of crystallinity after irradiation were due to breakage of the polymeric bonds and emission of some volatile gases, which may form the disordered state in the polymer which is also supported from DSC studies.

Table 3 Structural parameters of pristine and irradiated PC films

Radiation	Fluence	d (Å)	L (Å)	K (%)	Reference
	Pristine	5.06	15.22	43	
Electron (8 MeV)	100 kGy	5.01	14.15	33	[22]
	225 kGy	4.94	13.79	27	[22]
Proton (15 MeV)	5×10^{13} p/cm^2	5.06	14.62	41	–
	5×10^{14} p/cm^2	5.03	12.07	34	–
	1×10^{15} p/cm^2	5.01	10.32	29	–
Alpha particle (40 MeV)	5×10^{13} α/cm^2	5.03	13.40	38	–
	5×10^{14} α/cm^2	5.02	11.47	32	–
	1×10^{15} α/cm^2	4.97	8.21	23	–
UV radiation (λ = 240 nm)	2 h	4.73	14.91	41	[5]
	4 h	4.66	14.40	40	[5]
	7 h	4.61	14.08	38	[5]
95 MeV O^{6+} ion	10^{10} ions/cm^2	–	17.41	–	[11]
	10^{11} ions/cm^2	–	17.32	–	[11]
	10^{12} ions/cm^2	–	17.17	–	[11]
	10^{13} ions/cm^2	–	17.00	–	[11]
	2×10^{13} ions/cm^2	–	16.18	–	[11]

6.5 Chemical Properties

The vibration modes of chemical bonds in polymer films are characterized by the absorption/transmittance bands [42, 43]. FTIR spectra for pristine and electron, proton and alpha particle irradiated PC films are as shown in Figs. 13, 14 and 15, respectively. The changes in the bonds have been estimated from the relative increase or decrease in the transmittance of the peak associated with the functional groups present in PC. It can be seen from figures that the transmittance of most of the FTIR peaks decreased and some shifted towards the higher and lower wave number regions. Similar kinds of variations were also observed from Gagnadre et al. [44] during irradiation of PC by H^+ and Li^+ ion. The FTIR spectra of PC remain unchanged at lower dose/fluence indicating the no changes in the chemical properties. However, the intensity of the peak 1656 cm^{-1} representing C = O stretch changed for higher doses/fluence suggesting the chain scission mainly at the carbonate site with probable elimination of carbon dioxide/carbon monoxide and formation of hydroxyl group. Surinder et al. [45] have also observed similar type of changes irradiation of PC by gamma radiation, and they have also argued that the transmittance of carbonyls, methyl and methylene groups decreased indicating the cleavage of the carbonate linkage as explained in the above section.

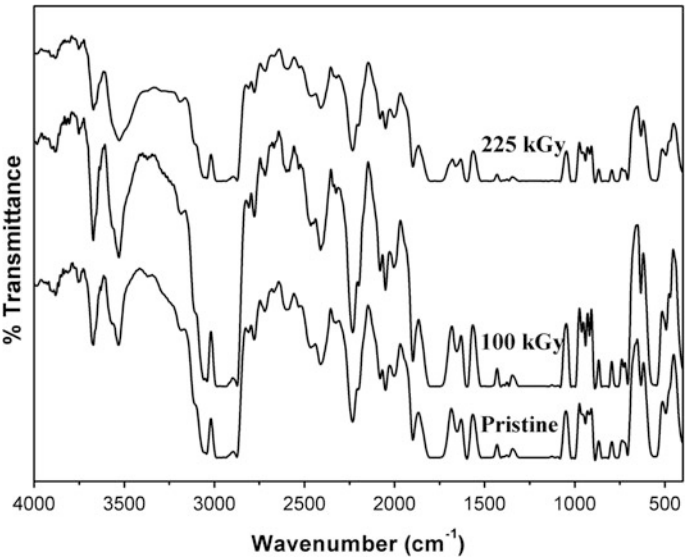

Fig. 13 FTIR spectra of pristine and electron irradiated PC films

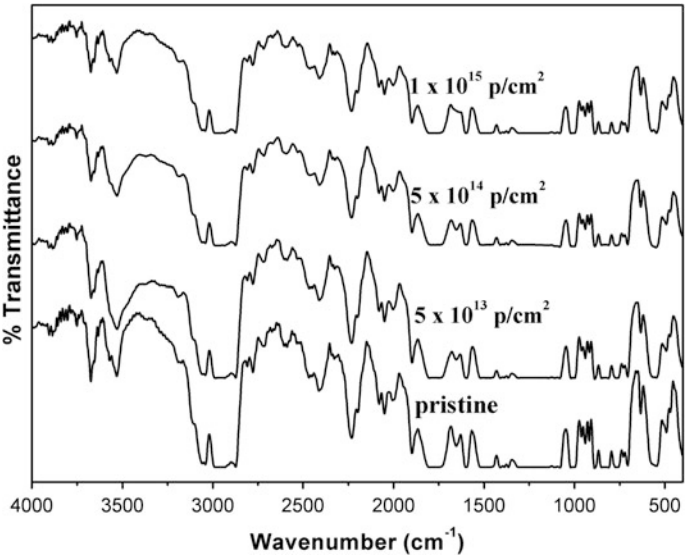

Fig. 14 FTIR spectra for pristine and proton irradiated PC films

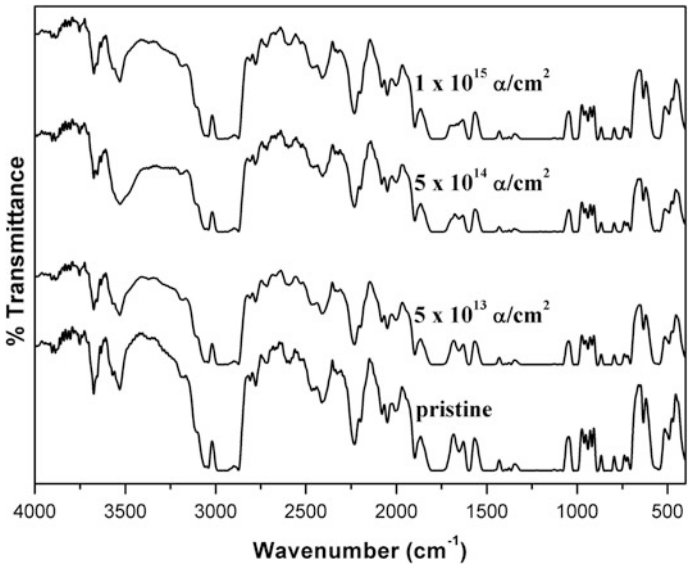

Fig. 15 FTIR spectrum for pristine and alpha particle irradiated PC films

6.6 Surface Morphological Properties

The irradiated PC surface shows a visible colour change from transparent to yellow and the intensity of the colour increases with increase in radiation dose/fluence as shown in Fig. 1. This change in the colour of the irradiated samples is due to formation of carbon clusters results in the transfer of energy from incident ions to the polymer [46, 47].

Figure 16 shows the SEM images of pristine and electron irradiated PC samples at different doses. The surface of the pristine film was smooth and homogeneous as can be seen from Fig. 16a. It is observed from the Fig. 16b that the surface of PC irradiated with a dose of 100 kGy shows pores of different sizes. This pores formation is due to the chain scissioning in PC after irradiation. Further increase in electron dose almost all the network structure was found to be broken as shown in Fig. 16c and its surface roughness increases [48, 49].

Figure 17 shows two-dimensional and three-dimensional image of pristine and proton irradiated PC sample at fluence of 1×10^{15} p/cm^2. It can be seen from figure that the pristine sample was smooth having average surface roughness value of 25.59 nm. After irradiating with proton with fluence 1×10^{15} p/cm^2, pores were formed in the sample. These pores can be clearly seen in three-dimensional AFM image as shown in Fig. 17. The average surface roughness value of sample irradiated with fluence 1×10^{15} p/cm^2 increases to 59.22 nm. This increases in average surface roughness value indicating the topographical changes in PC after irradiation is due to chain scission [50, 51].

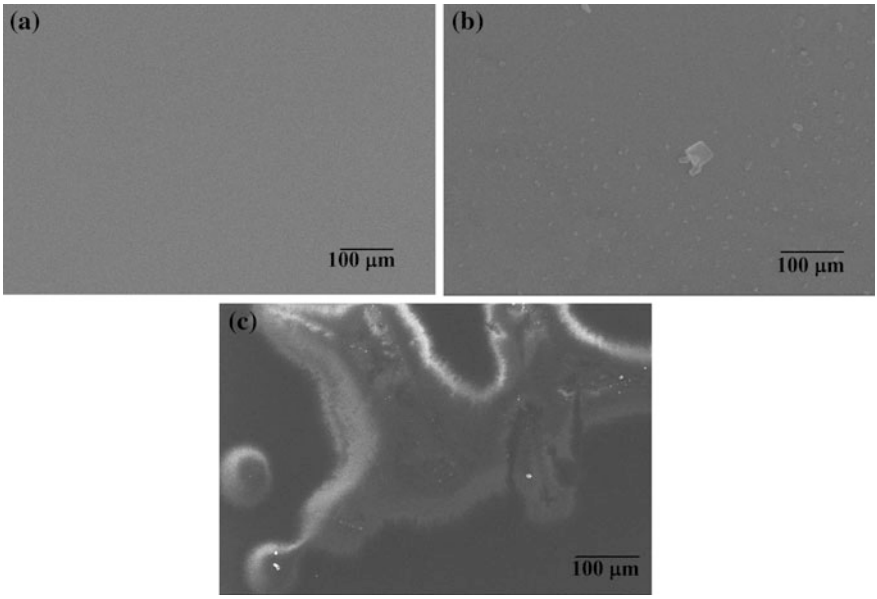

Fig. 16 SEM images for **a** pristine and 8 MeV electron irradiated PC at doses, **b** 100 and **c** 225 kGy

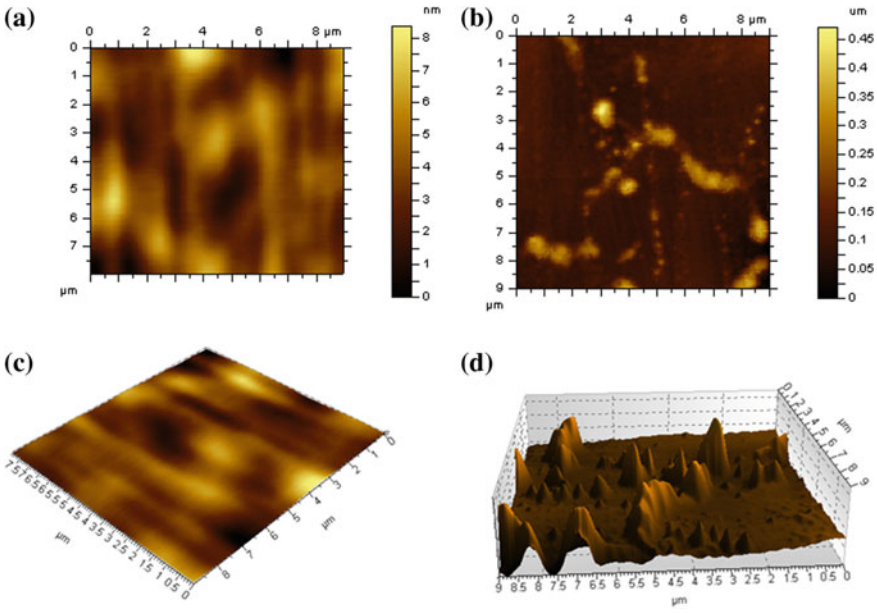

Fig. 17 Two-dimensional (**a**, **b**) and three-dimensional (**c**, **d**) AFM image of pristine (**a**, **c**) and α particle irradiated (**b**, **d**) PC at fluence of 1×10^{15} α/cm^2

6.7 Free Volume Properties

Positron annihilation lifetime spectra (PALS) were used to measure the three-lifetime components τ_1, τ_2, τ_3 and corresponding intensities I_1, I_2, I_3. The shortest lifetime component (τ_1) with intensity I_1 corresponds to the self-annihilation of para-positronium (p-Ps) atoms and free annihilation of positrons in the bulk samples. The intermediate lifetime component (τ_2) with intensity I_2 is due to the positrons trapped in the defects. The longest-lived component (τ_3) with intensity I_3 is attributed to the ortho-positronium (o-Ps) atoms in the free volume sites of amorphous regions of polymer via pick-off annihilation.

The radius (R) of the free volume hole can be calculated using o-Ps lifetime (τ_3) by semi-empirical relation [49] given by equation $\tau_3^{-1} = 2[1 - (R/R_0) + 1/2\pi \sin(2\pi R/R_0)]$, where $R_0 = R + \Delta R$ and ΔR is the fitting parameter and a value $\Delta R = 0.166$ nm. The free volume size (V_f) and free volume fraction (F_v) can be calculated using the equations $V_f = (4/3)\pi R^3$ and $F_v = CI_3V_f$, C is a constant whose value is taken as 0.0018 $Å^{-3}$ and V_f is the average free volume size. The obtained values of τ_3, I_3, V_f and F_v for pristine and irradiated PC films are listed in Table 4. From Table 4, it can also be noted that, a decrease in o-Ps intensity (I_3) and fractional free volume (F_v) similar to τ_3 and V_f are observed for the irradiated PC compared to pristine. The average free volume size decreases due to cross-linking which results in the close packing of the polymer chains. This close packing results in the decrease of number density of free volume sites and hence decreases in I_3 after irradiation. As explained in Scheme 1b, PC undergoes photo-fries rearrangement during irradiation which results in the formation of photo-stabilisers such as Phenyl salicylate and 2, 2′-dihydroxy benzophenone. Among these two, 2, 2′-dihydroxy benzophenone is more stable photo-stabiliser [52, 53] which prevents

Table 4 PALS parameters irradiated PC films

Radiation	Dose/fluence	($\tau_3 \pm 0.013$) ns	($I_3 \pm 0.26$) %	($V_f \pm 1.1$) $Å^3$	($F_V \pm 0.1$)%
	Pristine	2.00	24.22	97.60	4.26
Electron (8 MeV)	100 kGy	1.98	27.20	95.74	4.69
	225 kGy	1.99	23.32	96.66	4.06
Proton (15 MeV)	5×10^{13} p/cm^2	1.86	13.36	84.57	2.03
	1×10^{15} p/cm^2	1.84	18.26	84.36	2.78
Alpha particle (40 MeV)	5×10^{13} α/cm^2	1.86	14.71	84.94	2.25
	1×10^{15} α/cm^2	1.83	15.84	81.72	2.33
UV radiation (λ = 240 nm)	2 h	1.93	20.45	90.77	3.35
	4 h	1.92	23.42	90.29	3.81
	7 h	1.91	19.45	88.93	3.11

the formation of o-Ps in PC, thereby decreasing the o-Ps intensity. A PALS report on polyisoprene [44] showed that a decrease in the fractional free volume with an increase in cross-link density and a decrease in average hole size. In this context, the decrease in the fractional free volume as well as o-Ps lifetime can be ascribed to an increase in cross-link density.

It can be further confirmed by the formation of photo-stabilized groups in PC. UV–visible absorption spectra of PC were recorded before and after proton irradiation (1×10^{15} p/cm^2), and the difference between the two spectra is shown in Fig. 18. Figure 18 shows a strong absorption peak at 352 nm and a weak absorption at 303 nm which are due to the 2, 2′-dihydroxybenzophenone and phenyl salicylate groups, respectively. This is in agreement with the literature results [23]. The difference in the intensity of the absorption peaks is due to rearrangement of majority of the oxygen atoms of phenyl salicylate to form the more stable 2-2′ dihydroxybenzophenone.

6.8 Mechanical Properties

Figure 19 depicts the photograph and SEM image of PC irradiated by gamma radiation [54].

Figure 20 depicts the tensile stress–strain curve of PC samples for different UV radiation time. The obtained values of percentage of elongation and tensile strength for irradiated PC along with pristine PC are listed in Table 5. It is observed from

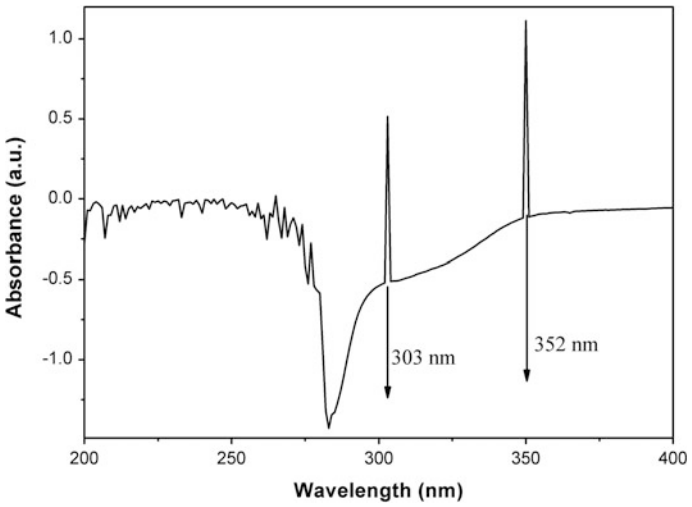

Fig. 18 Difference in the UV absorption spectra of unirradiated and 1×10^{15} p/cm^2 irradiated PC

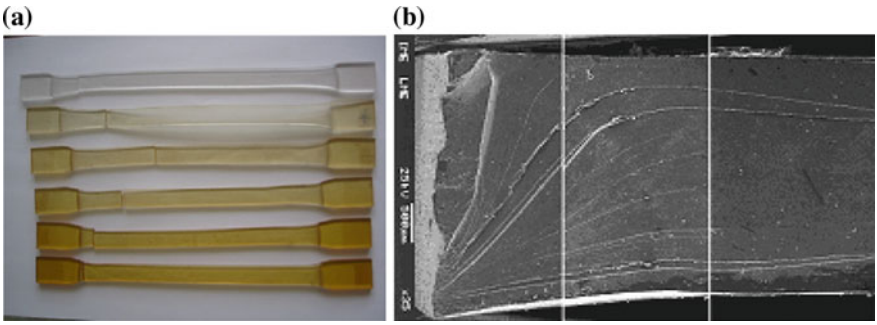

Fig. 19 Photographs of fracture surfaces of tensile specimens: **a** macroscopic aspect-up: 0 kGy (non-irradiated)/down: irradiated with 125 kGy; **b** SEM microphotograph of the fracture surface of specimen irradiated with 125 kGy (Copied from Ref. [54] with consent from the Elsevier)

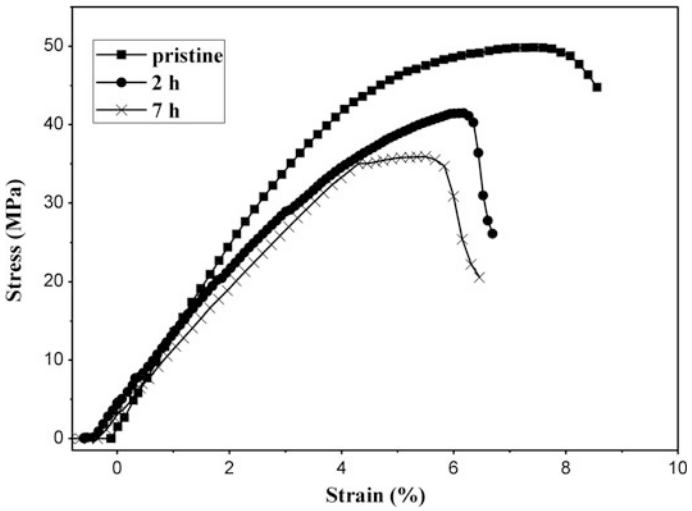

Fig. 20 Stress–strain curves for UV irradiated PC films

Table 5 that the tensile strength and percentage of elongation decreased after irradiation indicating changes its mechanical properties from a ductile material to brittle one. This variation of the mechanical properties of PC with radiation dose is in agreement with the results reported in the literature [55]. The decrease in tensile strength and percentage of elongation of PC is due to the chain scission as explained in Scheme 1a.

Table 5 Average molecular weight (M_V), the average number of chain scission per original polymer molecule ($M_{V_o}/M_V - 1$), tensile strength (σ_f) and percentage of elongation (ε_f in %) of irradiated PC films

Radiation	Dose (kGy)	M_V	$M_{V_o}/M_V - 1$	σ_f (MPa)	P (%)	Reference
	Pristine	17,000	0	58.67	8.54	[22]
8 MeV Electron	100 kGy	11,200	0.52	56.15	6.19	[22]
	225 kGy	6155	1.76	50.46	5.25	[22]
15 MeV Proton	5×10^{13} p/cm^2	11,119	0.53	55.31	7.93	[8]
	5×10^{14} p/cm^2	7656	1.22	45.03	7.38	[8]
	1×10^{15} p/cm^2	3585	3.74	35.79	6.62	[8]
40 MeV Alpha particle	5×10^{13} α/cm^2	11,010	0.55	50.11	7.76	[8]
	5×10^{14} α/cm^2	6817	1.49	45.53	7.41	[8]
	1×10^{15} α/cm^2	3223	4.27	30.71	5.87	[8]
UV radiation (λ = 240 nm)	2 h	15,928	0.06	58.31	8.03	[5]
	4 h	12,583	0.35	–	–	[5]
	7 h	10,494	0.62	55.03	7.48	[5]
Gamma radiation	25 kGy	–	–	62.8	99	[54]
	50 kGy	–	–	60.9	99	[54]
	75 kGy	–	–	60.8	94	[54]
	100 kGy	–	–	61.2	95	[54]
	125 kGy	–	–	60.9	94	[54]
2 MeV electron	1.2 kGy	–	–	63.78 ± 0.41	25 ± 6	[56]
	22 kGy	–	–	65.44 ± 0.55	80 ± 4	[56]

6.9 Rheological Properties

The average molecular weight (M_V) of pristine and irradiated samples can be calculated using the equation $[\eta] = 1.23 \times 10^{-4} M_V^{0.83}$ and they are listed in Table 5. The average molecular weight of PC decreased after irradiation due to chain scission at the carbonate site as explained in Scheme 1a. This decrease in molecular weight of PC after irradiation corroborates the decrease in mechanical properties of PC after irradiation.

7 Conclusions

Polycarbonate is an important engineering polymer utilized in many fields such as optical, medical, electronic and in space applications. The polymers used in space applications are subjected to the harsh effects of space environment factors including solar electromagnetic rays, atomic oxygen, charged particle radiation, etc. The irradiation of solar electromagnetic rays, charged particle radiations degrades the PC leading to breakage of bonds, formation of free radicals which would lead to

decrease in the lifetime of polymer. Therefore, the study of effect of radiations on PC through ground simulation has gained attention. In addition to this, PC being an insulating polymer agglomerates static charges on its surface during long time use in space. Therefore, it is required to reduce the surface resistance of PC to make it applicable for different applications for long time, which can be done by implanting PC by low-energy ions.

Another major challenge is to increase the properties of PC further, which can be done by blending it with other polymers. However, these kinds of blends ate immiscible blends, which are limited due to the low adhesion strength at the interface. To improve these aspects, the immiscible blends must be irradiated by radiations. The radiation mixes the polymers at the interface and increases the adhesion strength. In overall, the effect of radiation on PC not only degrades the PC, but also helps to increase the properties.

References

1. John FK, Richard EB (1964) Effects of radiation on materials and components. Reinhold Publishing Corporation, London
2. Pietro PJCOS, Patricia LBA, Leopoldo BBS, Elmo SA (2017) Rad Phys Chem 130:123
3. Claeys C, Simoen E (2002) In: Hull R, Osgood RM, Parisi J (eds) Radiation effects in advanced semiconductor materials and devices. Springer, New York, Berlin, Heidelberg
4. Clough RL (2001) Nucl Instr and Meth B 185:8
5. Hareesh K, Pandey AK, Rao V, Sanjeev G (2013) 22:341
6. Balazant E, Betz N, Bouffard S (1995) Nucl Instr and Meth B 105:46
7. Kumar V, Sonkawade RG, Dhaliwala AS (2012) Nucl Instr and Meth B 290:59
8. Hareesh K, Sen Pintu, Bhat Ravishankar, Bhargavi R, Nair Geetha G, Sangappa, Sanjeev Ganesh (2013) Vacuum 91:1
9. Kumar V, Sonkawade RG, Chakarvarti SK, Kulriya P, Kant K, Singh NL et al (2011) Vacuum 86:275
10. Kumar V, Sonkawade RG, Dhaliwala AS (2012) Nucl Instr Meth B 287:4
11. Ali SA, Kumar R, Singh F, Kulriya PK, Prasad R (2010) Nucl Instr Meth B 268:1813
12. Joshi RP, Hareesh K, Bankar A, Sanjeev G, Asokan K, Kanjilal D, Dahiwale SS, Bhoraskar VN, Dhole SD (2016) Nucl Instr Meth B 384:6
13. Dwaikat N, Sato F, Kato Y, Iida T (2008) Nucl Instr Meth B 584:353
14. Chapiro A (1998) Nucl Instr Meth B 32:111
15. Sood DD, Reddy AVR, Ramamoorthy N (2004) Fundamentals of radiochemistry. Indian Association of Nuclear Chemists and Allied Scientists, Mumbai, India
16. Schiwietz G, Luderer E, Xiao G, Grande PL (2001) Nucl Instr and Meth B 175–177:1
17. http://physics.nist.gov/PhysRefData/Star/Text/ESTAR.html
18. Frommer JE, Chance RR (1986) Electrical conducting polymers in encyclopedia of polymer science and engineeringm, vol 5. Wiley, New York, p 462
19. GE plastics “LEXAN resin innovation day” inspires imaginative thinking for Newyork, Allbusiness.com, from Business Wire, 29 Jan 2003
20. www.sabicip.com/gep/Plastics/en/ProductsAndServices
21. www.regal-plastics.com/lexan-sheet.html
22. Hareesh K, Ranganathaiah C, Ramya P, Bhargavi R, Nair Geetha G, Sangappa, Sanjeev G (2010) J Appl Poly Sci 127:2010

23. Zimmerman KA, Langford SC, Dickinson JT, Dion RP (1993) J Polym Sci, Part B Polym Phys 31:1229
24. Kent BA (1980) Polymer 21:936
25. Hama Y, Shinohara K (1970) J Polym Sci Part A-1 Polym Chem 8:651
26. Torikai A, Takahisa M, Kenji F (1984) Polym Photochem 4:255
27. La Mantia FP, Acierno D (1984) Polym Photochem 4:271
28. Suvegh K, Ranogajec F, Komor-Ranogajec M, Talas E, Ovai M, Vertes C (1992) Mater Sci Forum 105–110:1729
29. Dyer John R (1994) Applications of absorption spectroscopy of organic compounds. Prentice-Hall Inc., NewJersy
30. Srivastava AK, Virk HS (2000) J Polym Mater 17:325
31. Saha A, Chakraborty V, Chintalapudi SN (2000) Nucl Instr Meth B 168:245
32. Migahed MD, Bakr NA (1994) J Polym Mater 11:129
33. Carmen A, Arquimedes K, Rosestela P, Gema G, Nohemy D, Jeanette G, Yanixia S (2006) Nucl Instr Meth B 247:331
34. Buttafava A, Consolati G, Di Landro L, Mariani M (2002) Polymer 43:7477
35. Velitchkova K, Krezhov K, Balabanov S (2000) Vacuum 58:531
36. Wang YQ, Curry M, Tanenner E, Dobson N, Giedd RE (2004) Nucl Instr Meth B 219:798
37. Singh NL, Shah Nilam, Desai CF, Singh KP, Arora SK (2004) Radiat Effect defect Solids 159:475
38. Jonscher AK (1997) Nature 267:673
39. Vishnuvardhan TK, Kulkarni VR, Basavraja C, Raghavendra SC (2006) Bull Mat Sci 29:77
40. Reheem AMA, Atta A, Maksoud MIAA (2016) Rad Phys Chem 127:269
41. Sinha D, Dwivedi KK (2003) Radiat Meas 36:713
42. Aruldhas G (2004) Molecular structure and spectroscopy. Prentice-Hall of India, New Delhi
43. Gagnadre C, Decossas JL, Vareille JC (1993) Nucl Instr Meth B 73:48
44. Mallon PE, Jean YC, Haung CM, Chen H, Gradwell MHS (2000) Polym Report 41:1124
45. Singh Surinder, Prasher Sangeeta (2005) Radiat Meas 40:50
46. Robertson J, O' Reilly EP (1987) Phys Rev B 35:2946
47. Singh L, Samra KS, Singh R (2007) Nucl Instr Meth B 255:350
48. Svorcik V, Proskova K, Hnatowicz V, Arenhoz E, Kluge A (1999) Poly Degrad Stab 65:131
49. Svorcik V, Arenhoz E, Rybka V, Hnatowicz V (1997) Nucl Instr Meth B 122:663
50. Manso M, Valsesia A, Lejeune M, Gilliland D, Ceceone G, Rossi F (2005) Acta Biomater 1:431
51. Ryuto H, Ichihashi G, Takeuchi M, Takaoka GH (2013) Vacuum 87:119
52. Golden JH, Hazell Ea (1963) J Polym Sci A 1:1671
53. Wu T, Lee S (1994) J Polym Sci Part B Polym Phy 32:2055
54. Naylor SM, Ricardo PW, Joao CMS (2007) Poly Test 26:315
55. Araujo ES, Khoury HJ, Silveira SV (1998) Radiat Phys Chem 53:79
56. Chen J, Czayka M, Roberto MU (2005) Radiat Phys Chem 74:31

Plasma Irradiation of Polymers: Surface to Biological Mitigation

Narendra Kumar Agrawal, Neha Sharma, Tamanna Kumari Sharma, Priti Agarwal and Ravi Agarwal

Abstract Development in science and technology has made human life much simpler, but evolution and progress of time as well as increasing human demand have generated problems related to energy, health [1], etc. Progress in science and technology is trying to solve these issues to make the human life more comfortable. Growing requirement of biomedical devices, replacement of body parts after their failure, body implants [2, 3], bio-separation, sterilizations [4, 5], biosensors, etc. [6, 7], have shown need of development of advance smart materials (biomaterials). The choice of any material to be used as biomaterial/biomedical applications [8] depends on physical, chemical, surface, and biological properties, i.e., the presence of functional groups, surface free energy, hydrophilicity, surface morphology affects use of any material as biomaterial [9]. In other words, materials having high bio-adoptability and biocompatibility can only be used as biomaterials [10, 11]. Polymers arise as a suitable alternative of conventional biomaterial from last few decades, for synthesis of important biomaterials in modern manufacturing processes as they offer wide varieties of physical, chemical, biological, mechanical, and elastic properties with good processability. None of the normally available polymers possess surface and chemical properties required for many of biomedical applications. Nanomaterials and low-temperature plasma processing offer a novel route for surface and chemical modification in controlled manner without affecting their bulk properties [12]. Plasama processing can be utilized in various pathways to control the desired properties of modified materials, makes plasma so important that we can say "Plasma will future: Plasma for mankind." Present work shows efficient

N. K. Agrawal (✉) · N. Sharma · T. K. Sharma
Department of Physics, Poddar International College, Poddar Group of Institutions, Jaipur, India
e-mail: research.nka@gmail.com

P. Agarwal
Rajasthan State Seed & Organic Production Certification Agency, Jaipur, India

R. Agarwal
Centre for Converging Technologies, University of Rajasthan, Jaipur, India

R. Agarwal
Department of Physics, University of Rajasthan, Jaipur, India

V. Kumar et al. (eds.), *Radiation Effects in Polymeric Materials*, Springer Series on Polymer and Composite Materials, https://doi.org/10.1007/978-3-030-05770-1_10

and relevant route for synthesis of nanobiomaterials using nanotechnology and plasma processing to fabricate biomedical devices for biomedical applications [13].

Keywords Plasma irradiation · Polymers · Biomaterials · Biomedical applications

1 Biomaterials

Any substance/material (other than a drug) or a combination of substances/materials, synthetic [14] or natural [15] in origin that can be used for any period of time, as a whole or part of a system which treats, augments, or replaces any tissue, organ, or function of the body is known as biomaterials [16]. They are nonviable materials used in biomedical devices, intended to interact with biological systems [17, 18]. If the word "nonviable" is removed from the definition, it becomes even more general and can address tissue engineering and hybrid artificial organ applications where living cells are used [19]. These materials can be classified into several categories on basis of their use. Most common classification consists of two parts: body implants and medical devices [20].

Body implants are generally made from one or more biomaterials that are intentionally placed as a substitute for biological system within the body, totally or partially buried beneath the surface and usually intended to remain there for a significant period of time like artificial skin, lenses for eye, bone cement, intraocular lenses, contact lenses, dentures, adhesives, artificial hearts, hip joint, knee joint [21]. While medical devices refer instruments, apparatus, implement, machine, contrivance, in vitro reagent, other similar or related articles intended for use in diagnosis, cure, mitigation or treatment of disease or other conditions do not depend on being metabolized or being part of chemical action within or on the body [22–26]. In other words, medical devices generally involve materials, tools, or devices that are not directly used in biological systems but are equally important in many of biomedical applications like fabrication of blood storage bags, tubes for various catheters, blood pumps, syringes, arterial tubules, surgical sutures [27]. Figure 1 shows various parts of the human body. Artificial materials that simply are in contact with the skin, such as hearing aids and wearable artificial limbs are not included in our definition of biomaterials since the skin acts as a barrier with the external world. So biomaterial can be internal or external material; but the subject cannot be explored without considering biomedical devices and the biological response to them, i.e., for both cases, materials must be bio-adoptable and biocompatible with an ideal bio-integration [28]. It must be noted here that normally the biomaterials have some common properties but sometime, depending upon application they may require markedly different properties. Biomaterials require best specific surface and biological properties, so that they will not produce any deleterious effects, failure of materials, or formation of unusual tissues, meanwhile having bulk properties to meet other physical, chemical, and mechanical requirements [29].

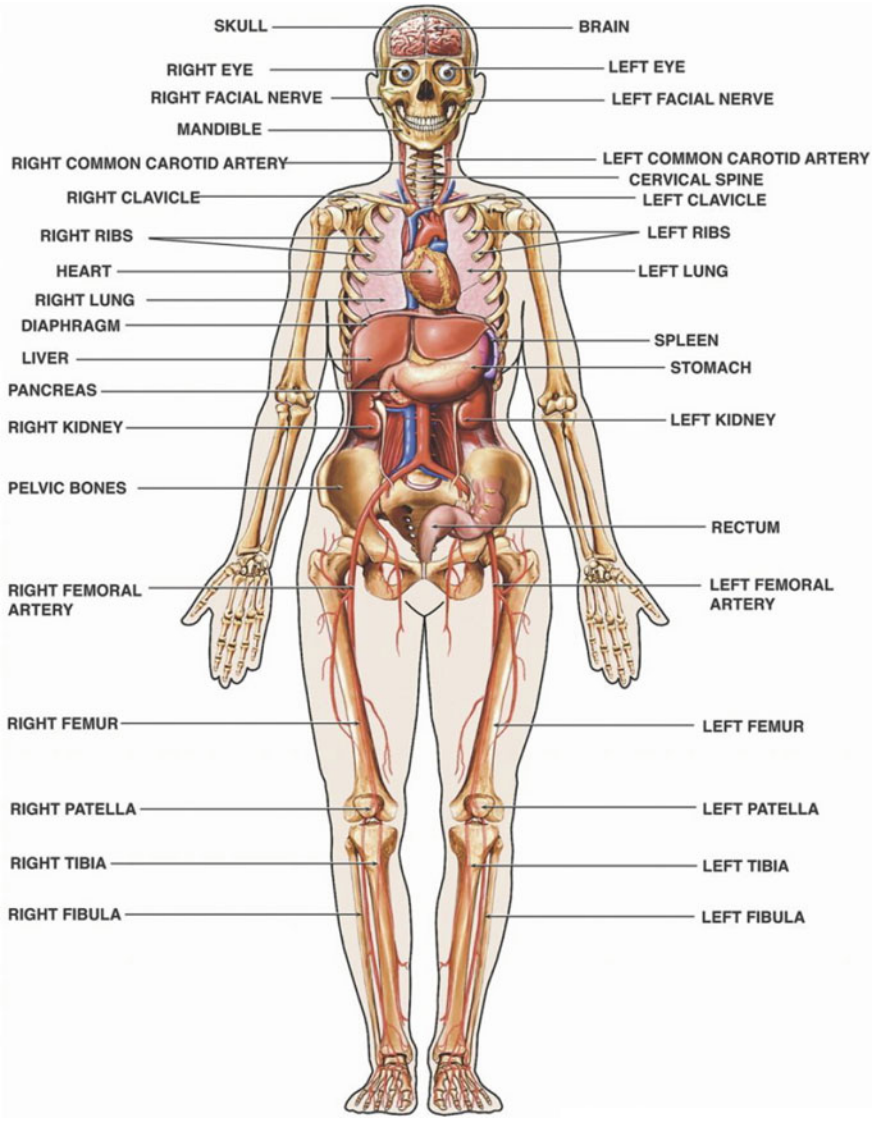

Fig. 1 Schematic representation of various parts of the human body and implants

2000 years ago Romans used gold in dentistry as first generation ad hoc implants. Since then extensive research has been performed on many metals, compounds and alloys for their possible use as biomaterials. From 1960 onwards, a new era has started for biomaterials fabrication processes when first time polyethylene was used for hip implants [30] since then many polymers have been thoroughly investigated for their possible use for synthesis of biomaterials with relatively great success.

Polymer nanocomposites (PNC) comprise polymer or copolymer having nanomaterials dispersed in polymer matrix [10]. Polymer nanocomposites (PNC) have demonstrated advanced applications in composite reinforcement, solar cell [12], gas sensor, biomedical sensors, fuel cell, chromatography, optical information technology, sensors, heterogeneous catalysis, filter applications, optoelectronics, optical computing devices, and synthesis of the biomaterials [1]. PNC are being used for fabrication of various biological implants like ear replacement [15], tendon and knee prosthesis, hip prosthesis, ocular prosthesis, artificial heart and lungs, synthetic skin, cardiac valve, tube for neuron regeneration, catheters, blood storage bags, skin, bone, cartilage, blood vessels, and other organs [4–8].

From most of the biomaterials available do have acceptable bulk and mechanical properties but do not possess required bioactivity as implant tissue interfaces have very complex phenomenon. Hence, success of designed devices depends on controlled healing, normal wound healing, interfacial layer, cell attachment, and matrix [13]. Also, the chemical functionality of the surfaces greatly affects the response of the biomaterials. But biocompatibility is measure issue with biomaterials to use in specific application [3]. Many materials can meet their bulk biocompatibility requirements but do not possess ideal surface properties like topography, surface energy, wettability, surface mobility, crystallinity, heterogeneity, chemical composition [8]. This shows the need for controlling surface properties, depending on specific applications [6].

Researchers were working in the area using chemical modification/oxidation, plasma modification, irradiation, ion implantation, graft copolymerization, self-assembled monolayers, morphological methods, biomolecule immobilization, plasma surface treatment for modulation of surface properties of polymer surface [18]. But numerous parameters involved and produced variation on material processing by modulation of experimental condition makes plasma treatment very useful technique for advanced applications [31]. The number of experimental investigations has been performed to identify effect of plasma treatment on surface, chemical, physical, biological, and mechanical properties. These investigations show that plasma treatment can modulate wettability, antibacterial properties, roughness, smoothness, cross-linking, chemical functionality, blood compatibility, surface energy, permselectivity, conductivity, adhesion, cleaning of organic contaminations, micro-etching, cross-linking, etc. It can also produce etching, remove surface contaminants, substitute chemical groups, and produce induced grafting/polymerization [7–12].

These modified materials have various applications in automobiles, microelectronics, chemical, and biological industry. Biomaterials in contact with biological systems need optimal combinations of mechanical properties and surface properties that can lead to superior performance in biological systems. Various investigations performed in the field of plasma surface modification of polymers/polymer nanocomposite have shown enhancement/increase in hydrophilicity and cell adhesion by helium plasma, gas sensor, antibacterial properties, immobilization of thrombomodulin to inhibit coagulation applicable in improved drug adhesion in intrauterine devices, adhesion of metals, in vitro activation of artificial surfaces,

small diameter vascular grafts, blood vessel, blood-borne tissue generation, vascular prosthetic grafts, cardiopulmonary bypass with heparin-coated circuits, etc. [17–21].

Such various combinations of polymer, plasma parameter and processing conditions have been explored by many researchers around the world like pre-irradiation of PTFE–styrene produces improved adhesion, cation exchange membrane, and grafting mechanism while per irradiation of PTFE in the presence of vinyl acetate improves the grafting conditions [21–28]. Simultaneous of PTFE with DMAA produces improve blood compatibility [28] while simultaneous of ePTFE with AAc improve bone-bonding ability [29]. Methacryloyloxyethyl phosphate (MOEP)/high-density polyethylene has been used for surface modification of biopolymers for orthopaedic applications [30]. Studies performed by Garbassi and Occhiello show that plasma treatments can enhance adhesion as well as decrease adhesion. Shenton et al. describe the use of atmospheric plasma treatment improves adhesion for LDPE and PET [12]. Also, atmospheric plasma treatment is potential tool for modifying tribological, toughness, hardness, optical, electronic properties of polymers [6]. Reactive gases plasma treatment of polymers can produce branching, cross-linking, etching, and functionalization of surface groups [9]. Fakes et al. and Li et al. have shown that plasma treatment can render polymer surfaces hydrophilic as well as hydrophobic depending on plasma gases [10]. Inert gas (argon and helium) plasmas modify the surface through cross-linking, chain scission, branching, surface roughening, and wettability by inducing surface charge via polarization which changes during storage and storage conditions [11]. Surface with very good wettability, high roughness, and high surface energy favors cell attachment, platelet adhesion, thrombus formation, and proliferation while reactive plasmas have potential ability to chemically etch polymers depending on dose and volatility of products produced. Few modified polymers like polydimethyl siloxane (PDMS) and polymethyl methacrylate (PMMA) are also used as structural material for fabrication of microfluidic devices, routinely patterned with the hot-embossing technique [2], diagnostic tests, chemical sensing, and detection experiments [30].

Hence, these plasma-based approaches for surface modification have received considerable interest for the formation of surfaces designed to be in contact with biological systems/interfaces [31]. In last few decays, various studies have been reported using various processing parameters and process gases. Recently, the majority of studies in the area have been focus on the applicability of plasma for processing of polymers, but to use plasma-treated surfaces or plasma polymers as interfacial bonding layers for subsequent immobilization of molecules designed to elicit specific biological responses [31]. Now the design of plasma treatment methods for biomaterial/biomedical applications is based on understanding of requirements of the bio-interface/device. Definitions of “biocompatibility” [7–9] are, unfortunately, vague in terms of what chemical composition a biocompatible surface should possess. Endothelial seeding [9] and pre-adsorbing fibronectin for endothelialization [10] are approaches for blood compatibility, but design rules do not exist for plasma surfaces that are to promote these effects. Interactions of plasma

surfaces with proteins and cells are also important. Control of surface properties and chemistry not only modulates cell attachment but also cell spreading, which is important as it affects cell division [30].

2 Polymers

Exciting chemical, mechanical, elastic properties, lightweight, flexibility, and easy processability that can be varied drastically in various polymers had made them widely useable materials in modern manufacturing processes [31]. These vast ranges of properties of various polymers are increasing their applicability in numerous fields starting from fabrication of materials used in daily life to some advanced applications like gas filtration [32], bactericidal properties [33], electrical [34], optical [35], mechanical applications [36], organic solar cells formations [37], biomaterial, and implant fabrications [38]. During the last 20 years', polymers have received fabulous interest for synthesis of biomedical devices and continuously replacing all conventionally available biomaterials, as physicochemical properties of the surface of polymers (like surface free energy, hydrophilicity, and surface morphology) influence cell–polymer interactions that make them widely useable material for synthesis of advance biomaterials, bio-devices, and biosensors.

Thousands of natural and synthetic polymers are available around the world, and polymer reaction engineering makes it very easy to synthesize various kinds of polymers with desired physicochemical properties [43, 44]. Depending on the properties, mechanical strength and chemical structure/functionality, these polymers can be used for synthesis of various biomaterials and implants (Table 1).

Table 1 Polymers and their applications for fabrication of biomaterials and implants [14, 39–41]

Polymers	Biomedical applications
Polyethylene	Tubes for various catheters, hip joint, knee joint prostheses
Polypropylene	Suture materials, hemodialysis, blood transfusion bags
Polytetrafluoroethylene	Vascular and auditory prostheses, catheters, tubes
Polyacetals	Hard tissue replacement
Polycarbonate	Syringes, arterial tubules, hard tissue replacement, hemodialyzers, blood pumps, oxygenators
PET	Vascular, laryngeal, esophageal prostheses, surgical sutures, knitted vascular prostheses
Biodegradable polymers	Sutures, drug delivery matrix, adhesives, temporary scaffolding, temporary barrier
Polyurethane	Adhesives, dental materials, blood pumps, artificial hearts and skin, blood contacting devices [42]
PMMA	Bone cement, intraocular lenses, contact lenses, fixation of articular prostheses, dentures, adhesives, artificial hearts and ski, blood contacting devices [42], various catheters

2.1 Polymethyl methacrylate (PMMA)

Poly(methyl methacrylate) (PMMA)/methyl methacrylate resin/polymethyl 2-methylpropenoate (IUPAC name) is a transparent thermoplastic polymer normally used as a shatter-resistant alternative to glass. It is also well known as acrylic glass ACRYLITE®, Lucite, Perspex, Optix (Plaskolite), Oroglas, Altuglas in scientific community based on its properties and uses. Chemically, it is the synthetic polymer of methyl methacrylate. Industrial production of PMMA is carried out by emulsion polymerization, solution polymerization, or bulk polymerization techniques. A bisphenol group available in PMMA also makes it an economical alternative to polycarbonate (PC) with high degree of flexibility [45, 46].

Excellent properties, easy handling and processing, low cost, high impact strength, more prone to scratching make them suitable in various applications. Various modifications applied to PMMA through polymer reaction engineering offer very high scratch and impact resistance to PMMA for ex. addition of butyl acrylate or plasticizers in very small amount and improve its impact strength [47].

Various physical and chemical properties of PMMA are listed in Table 2, and its chemical structure is shown in Fig. 2 [48]. It allows 92% transmission of visible light with only 4% reflections. Its refractive index is 1.4914 at 587.6 nm and can also filter ultraviolet (UV) light at wavelengths below 300 nm (similar to ordinary window glass). Adding/coatings with various organic and inorganic additive

Table 2 Chemical and physical properties of PMMA [47]

Molecular formula	$(C_5O_2H_8)_n$
Molar mass	Varies
Density	1.18 g/cm^3
Melting point	160 °C (320 °F)
Refractive index (nD)	1.4914 at 587.6 nm
Reflectance	R = 0.03890 at 587.6 nm
Brewster's angle	θ_B = 56.158°
Molecular weight (MW)	100 g/mol
Glass transition temperature (T_g)	105 °C (221 °F) [varies from 85 to 165 °C (185–329 °F)]
Coefficient of thermal expansion	(5–10) × 10^{-5} K^{-1}

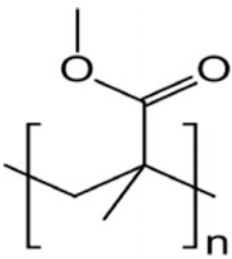

Fig. 2 Chemical structure of PMMA [48]

materials to PMMA improve absorption in the 300–400 nm range. It shows similar behavior in case of IR light, where it transmits IR light of up to 2800 nm and blocks IR of longer wavelengths up to 25,000 nm. Hence, its color composite or colored PMMA is used in remote control and heat sensor applications where they allow specific IR wavelengths to pass while blocking visible light. PMMA swells and easily dissolves in many organic solvents on account of its easily hydrolyzed ester groups. Environmental stability of PMMA is superior to most other plastics such as polystyrene and polyethylene which makes it material of choice for outdoor and biomedical applications. Its maximum water absorption ratio (0.3–0.4% by weight) is lower relative to other conventional polymers. Tensile strength decreases with increased water absorption. It ignites at 460 °C (860 °F) and burns to produce carbon dioxide, water, carbon monoxide, low-molecular weight compounds, and formaldehyde [47].

These exciting properties of PMMA make it suitable for various mechanical, optical, and biomedical applications [49] including synthesis of bone cement, intraocular lenses, contact lenses, fixation of articular prostheses, dentures, adhesives, artificial hearts and skin, blood contacting devices [42], various catheters [38]. Figure 3 shows polymerization process of polymers.

3 Nanotechnology and Nanomaterials

Nanotechnology and nanoscience are the study of materials having at least one dimension in nanometer, and their applications across various fields of science and technology including chemistry, biology, physics, materials science, medical science and engineering to make human life more simple, comfortable, and advance. The literal meaning of "Nano" is "dwarf" (Greek term), while Technology "τέχνη" in Greek is an art/skill for making, modification, usage, visualize, characterize, and production of tools, machines, systems and methods in order to solve problems, improve a preexisting solution to a problem, and ability to control and adapt natural environment [50]. Nanotechnology also includes fabrication and uses of structures that have novel properties because of their size in nanorange. It is a multidisciplinary science that looks at how matter can be manipulated and controlled at molecular and atomic level and hence dramatic improvements in their properties.

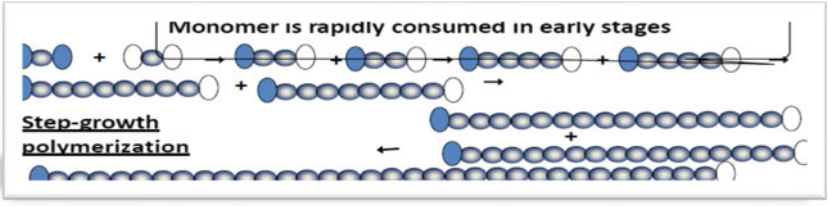

Fig. 3 Schematic representation of polymerization process in various polymers

At these scales, materials show completely different properties compared to their bulk counterparts [51], even intrinsic properties of material such as band gap, color, crystal structure, mechanical, catalytic, optical, chemical, and magnetic properties of materials get modifies. Field and scope of nanotechnology include all branches of science even in day-to-day life of living beings. Nanoparticles, can be called building blocks of nanotechnology, are of great scientific interest as they effectively bridge between bulk materials and atomic or molecular structures. Nanoparticles exhibit remarkably improved physical, chemical, and biological activity that enhances their uses in various applications. Also, biomaterials in contact with biological body have optimal combination of mechanical properties and surface characteristics that result superior performance in biological environment [52–54]. Nanomaterials can be used for biological/biomedical applications for fabrication of biomaterials, having superior surface properties like low surface energy, hydrophilicity, specific surface morphology, higher cell/protein adhesion, and antibacterial activity. Many of these properties are directly used or being explored for their possible application in the synthesis of advanced biological materials, biomedical devices and implants such as artificial skin diaphragm, valves for heart, kidney, lenses for eye, and other biomedical fields so that they can positively/negatively affect cell to material interactions.

From past ten years', various metal and metal oxide nanoparticles (NPs) are used or being explored for biomedical applications such as gold NPs for cancer treatment, Cu NPs as good antibacterial agent, ZnO NPs for protection from UV light, Ag NPs for affecting growth mechanism of plants, TiO_2 NPs for degradation of biomass. In present study, we have used Ag (Fig. 4) and TiO_2 NPs for enhancement of properties and applications of biomaterials [19, 55–90].

4 Polymer—Nanocomposite

Nanocomposites are combinations of materials in which at least one of the phases having dimension in nanometer range. They can, in principle, be formed from clays and organoclays in a number of traditional methods including various in situ polymerization [91], solution and latex [92] methods, mechanical agitation, ball milling, ultrasonic vibration, shear mixing, non-contact mixing. [34]. Investigations performed on these materials have indicated that they exhibit improved and sometimes new possessions that are not displayed by the separate phases or conventional composite complements [93]. Incorporation of nanomaterials/nanoreinforcements such as nanoparticles, layered silicate clays, nanotubes, nanofibers into polymers leads to formations of polymer nanocomposite (PNC) with ominously enhanced physicochemical, thermomechanical, mechanical, thermal, dynamic mechanical, and barrier properties along with significant improvements in adhesion, rheological, and processing behavior [94]. Even a very small amount of nanoparticles has the potential to radically transform properties of the host polymer

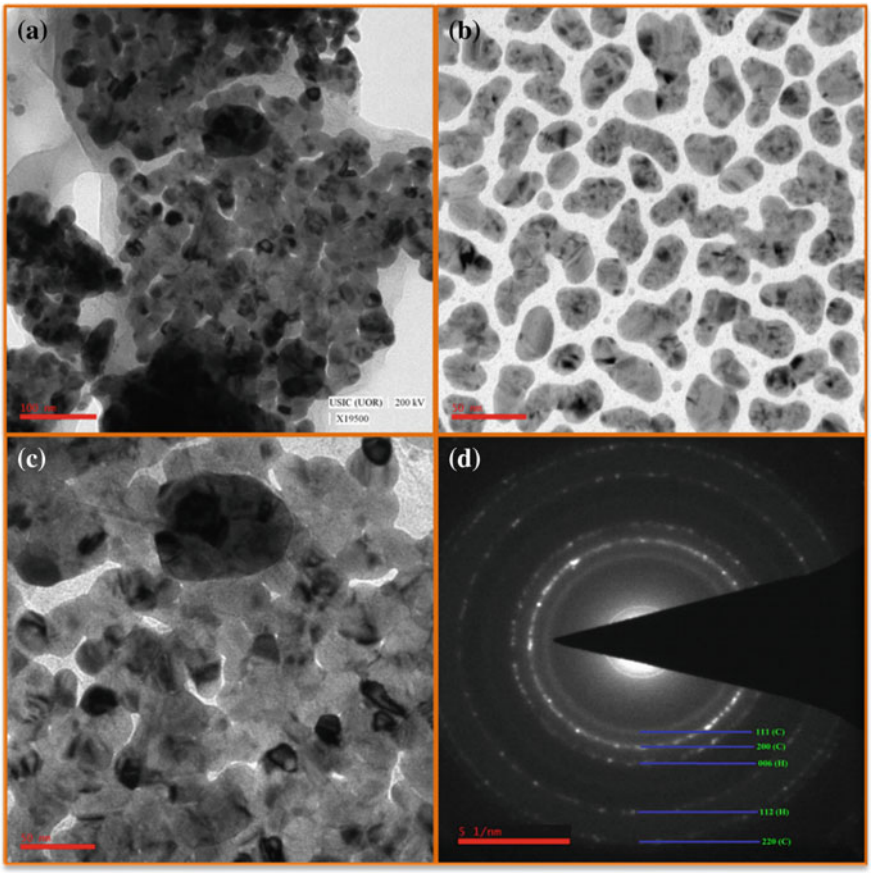

Fig. 4 TEM images and diffraction pattern of synthesized silver nanoparticles

[95, 96]. As smaller/nanosize of the filler material provides more surface area for interaction with polymer matrix [61, 97].

Interaction area between filler and polymer matrix is used for controlling properties of PNC, which make these polymer nanocomposite materials special for use in particular applications. Polymer nanocomposites have many diverse applications like composite reinforcement [98], flame resistance [53], self-assembled polymer films [99], conducting properties [100], barrier properties [101], dye-sensitized solar cells [64], gas sensor [102], nanomedicine [103], cosmetic applications [104], information storage [105], electronics [106], sensors, structural components, catalysis [107], flammability resistance, polymer blend compatibilization [108], bound catalysts [109], miniemulsion particles [110], fuel cell electrode polymer [111, 112], high-performance fabrics, ballistic protection [113], actuators, diffusion barriers [114], refractive index tuning, corrosion and scratch resistant, layer-by-layer self-assembled polymer films [115], polymer blends [116],

nanocomposite. Since last few years, polymer nanocomposites give new alternative to conventional filled polymers and materials for synthesis of biomaterials.

5 Plasma Surface Modification

Plasma, the fourth state of matter, is known as ionized gases having neutrals with almost equal number of ions and electrons. A more precise definition is that plasma is a quasi-neutral gas of charged and neutral particles exhibiting collective behavior. It is the most wonderful fact about the plasma that the stars and the tenuous space between them of the visible universe make up more than 99% with plasma and perhaps most of which is not visible, even not fully explored. The plasma contains energetic species like atoms, molecules, ions, radicals, electrons, neutrals, dust/charge particles, and photons. Hence, interaction of plasma with various materials leads to interaction/bombardment of energetic particles on to the materials. These bombardments stimulate the productions of outgoing fluxes of neutrals, ions, electrons, radicals, and photons leading to modification/irradiation/treatment/etching of surface layer for modulation of physical, chemical, and biological characteristic that becomes basis for plasma-enabled material processing [117–121]. Figure 5 shows the PMMA surface after plasma treatment.

Plasma-based processing of materials becomes widely acceptable in all branches of science and technology [111, 122–124]. Wide range of dynamic applications of the technique starting from fabrication to processing makes it most powerful

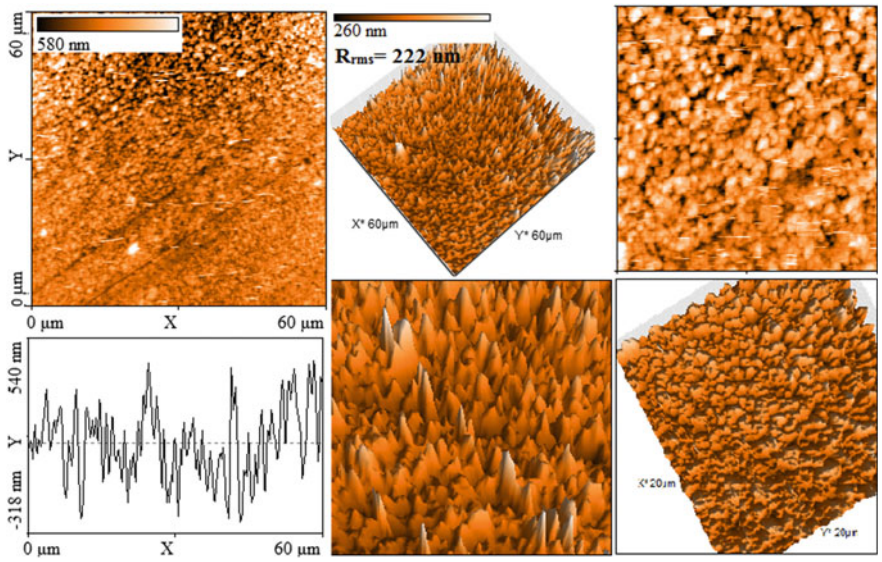

Fig. 5 Atomic force microscopy image of PMMA after plasma treatment (2D and 3D view)

technique even some time it is neither purely physical nor chemical. It offers desired pathway for materials processing depending on the application of material. The plasma modulation technique precedes a number of subtractive and additive processes in a selective manner for highly controlled nanomachining, uniformity, surface quality, and profile control. Based on modification techniques, it also has variety of advantages such as fewer disposal problems, modifications carried without use of chemicals/rinsing, less corrosion and material failure, less undercutting, high-speed fabrication, cleaner resulting surfaces [125].

Plasma can be produced by electron separation/ionization from atoms/molecules in the gaseous state. When an atom/molecule gains enough energy (higher than ionization energy) from any source that makes interaction (collisions) with another atom/molecule, ionization occurs. Under favorable conditions, these ionizations can be enhanced to produce sufficient breakdown to satisfy the plasma conditions. Based on the conditions to create breakdown, many kinds of plasma sources are available commonly known as gaseous, metallic, sputtering, dry etching, and laser-based plasma sources. The sources used for plasma productions for material processing and applications have characteristic difference in plasma parameters such as electron temperature, ion temperature, electron/ion density, electron/ion energy, state and uniformity. These plasma parameters can be modulate/controlled or depend on gas pressure, type of gas, gas composition, gas flow rate, type of plasma (DC/RF), particle density, electric field strength, electron velocity, electron current, strength of magnetic field, and distance between anode and cathode. Each of these experimental conditions can drastically affect the plasma parameter to be used in various plasma-based processing by ion and electrons such as reflection, physico-absorption, surface migration, surface damage, heating, material ejection, sputtering, ion etching, ion implantation, doping. These various plasma parameters and experimental conditions for creating and maintaining plasma make its nature very amazing. Below we have listed several other regions which can further increase superiority of plasma and their effects that can be used in plasma-based processing and applications:

1. Electrons in plasma can extract energy form electric and magnetic fields.
2. Kinetic energy of electrons can be converted into space charge electric field and thermal energy [126].
3. Plasma-based processing does not require any type of confinement even some times de-confinement is required, as the output of processing depends only on flux of ions and electrons [126].
4. Plasma generation, gas phase chemistry and transportation, material interactions depend on plasma parameter and conditions. Each of these requires input from plasma and material science [127].
5. Plasma has tendency to shield and localize externally applied electric potential for creating intense electric field regions called sheath or double layers through which ions/electrons can be accelerated.
6. Plasma can of the type of momentum transfer type between energetic ion (usually inert) and substrate surface causes bond breakage or ballistic material ejection.

7. Natural chemical species such as chlorine/fluorine atoms generated in the plasma diffuse to the substrate to from volatile products [128].
8. Creation of chemically active species from neutrals by collision with energetic electrons and ions.
9. Creation of ion damage on surfaces, including highly reactive chemical reactions on surface with plasma neutrals, ion/electron beam bombardment [106, 129].
10. Background energetic radiations in plasma produced either by atomic processes or by interactions with electromagnetic field.
11. Plasma process can be carried out in DC field (0 Hz), AC field (50 kHz), RF field (13.6–27 MHz), and microwave field (300 MHz–10 GHz).
12. During plasma processing, various events can occur based on the kinetic energy of incoming particle, such as particles having energy between 3 and 5 eV can either be reflected or physisorbed, 4–10 eV energetic particles induced surface migration or surface damage, 5–5000 eV can create substrate heating, surface damage and material ejection, i.e., sputtering or ion etching, and for further higher energies more than 10,000 eV ion implantation or doping can occur.
13. Plasma usually offers small etching rate typically of the order of hundred to few hundred angstroms per minute.
14. Ions/energetic particles may implant, bounce, absorbed, or reflected during plasma processing, while sputtered material can re-deposit and undergo backscattering.
15. Ion plasma processing of any materials is controlled by (1) neutral atom and free radical concentration, (2) ion concentrations, (3) ion energies.
16. Respective contribution of chemical and physical action in plasma processing can be controlled by varying voltage and gas pressure.
17. Plasma can also work as a source of heat, by conversion of electrical energy into ionization and heating of the feedstock gas
18. Plasma can be a chemical catalyst by formation of species of required chemical reactivity or other properties.
19. Plasma can work as a source of sputtered particles.
20. Transport of energy, momentum, and mass to the process region of boundaries including transport to the electrodes.
21. Quenching/termination of reaction at an appropriate time and removal of products.

The plasma normally used for polymer processing can be divided into two groups: thermodynamically balanced and unbalanced. Thermodynamically balanced plasma is characterized by very high temperature of heavy particles (often about 11,000 K) and is not suitable for plasma treatment of polymeric materials, as high temperature can cause thermal degradation. In thermodynamically unbalanced plasma, gas temperature is significantly lower, as it is composed of low-temperature heavy particles (charged and neutral molecular and atomic species) and very high-temperature electrons (often about 50,000 K). Such plasma exposure causes following main effects that occur during the plasma modification process itself:

(i) surface cleaning, (ii) surface ablation or etching, (iii) cross-linking, and (iv) modification of chemical properties.

Plasma-based surface processing of materials generally works in the region where incident ions have energies 4–10 eV that can induce surface migration or surface damage. When organic polymers lead to surface modification by plasma, the interaction between plasma and polymer produces two competitive processes, namely modification and degradation [130]. When modification is significant, properties of the polymer get modified due to ion beam interaction, plasma graft copolymerization, and plasma polymerization while for degradation processes, etching takes place on the polymer surface [128, 131]. Other than these plasma techniques sometimes especially useful for functionalization of surfaces as it is possible to modify outermost surface layer by this technique. Ions from plasma have sufficient energy to induce cleavage of the chemical bonds in the polymer to form macromolecule radicals, which subsequently initiate graft copolymerization [132]. During plasma processing of materials, plasma exposure not only causes surface modification but also leaves active sites on the surface which is subjected to post-reaction [133]. For polymer surface, plasma has been recognized as a valuable tool to significantly improve adhesion properties. Plasma can also work as a source for removing weak boundary layers and surface contaminants during modification [53, 134, 135]. For sufficient plasma density and treatment time, many functionalities created on surface lead to cross-linked polymer chain formation. In these plasma implantation processes, hydrogen is first removed from polymer chains to create radicals in polymer chains that recombine with simple radicals created by the plasma gas to form oxygen or nitrogen functionalities. Radical species, rather than ion species, that are created in the plasma zone play an important role in implantation process. Plasma material processing scheme [34] in Fig. 6 shows modulation in surface properties of polymers by low-pressure plasma treatment such as

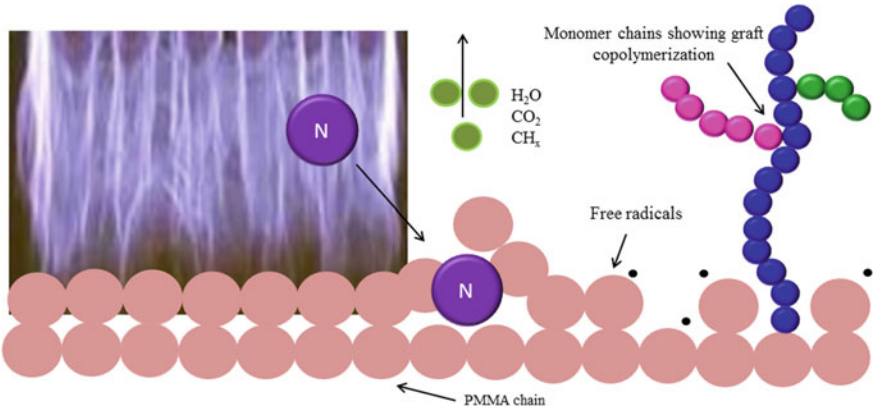

Fig. 6 Schematic representation of polymer surface modulation induced by low-pressure plasma treatment

formation of macromolecule radicals, increase in chemical reactivity, formation of sputtered particles, and creation of active sites followed by graft copolymerization.

Research based on plasma surface modification of polymers for biomaterials synthesis mainly focuses on argon plasma exposure of polymers. This creates an etching/degradation reaction at surface of the polymers; even a small exposure to inert gas plasma can cause etching of polymers, and rate of weight loss is strongly dependent on the nature of polymer as well as energy of the plasma. Polymers having oxygen functionalities in form of ether carboxylic acid or ester groups show high plasma susceptibility while polyolefin with no substituent's show low plasma susceptibility [136, 137]. Interestingly, polymers subjected to the plasma modification process possess similar chemical and physical properties as original polymers since technique only modifies outermost layer of polymers. The elemental composition, chemical structure, degree of polymerization, and crystallinity of the bulk polymers are hardly altered. Etching processes sometimes cause smaller weight loss due to bond scission of polymers and reactions of the radicals generated in the polymer chains upon plasma exposure [138, 139]. Normally, polymers are hydrophobic and conversion of these polymers from hydrophobic to hydrophilic depends on their surface characteristic. Plasma can modulate surface properties in controlled manner to improve adhesion strength, biocompatibility, and other pertinent properties [117–121, 140, 141].

Below is list of other effects that can be obtained by plasma-based material processing:

Surface Modification [133, 142, 143]

- Alters surface properties of material without affecting their bulk properties
- Surface modification in a controlled fashion
- Surface properties (roughness and smoothness)
- Advantageous for design, development, and manufacture
- Surface interaction.

Chemical Modification [48, 144, 145]

- Ecofriendly nature
- No water and chemicals required
- Selection of desired chemical pathways
- Hydrophobicity and hydrophilicity
- Chemical structure
- Chemical catalyst: increased surface area
- Highly cross-linked films irrespective of the surface geometries.

Physical Modification [120, 146–148]

- Formation of multilayer films
- Prospect of scaling up
- Smooth, pinhole-free ultra-thin film
- Minimization of thermal degradation and rapid treatment
- Conductivity

- Surface tuning
- Adhesion
- Low friction coefficient.

Bio-Induced Modification [38, 149–152]

- Influence cell adhesion
- Biocompatible polymers
- Hindering bacterial adhesion
- Antimicrobial coatings
- Bio-adoptability: selective bacterial growth.

6 Plasma Gases

Various plasma parameters and experimental conditions such as gas pressure and flow rate, type of plasma (DC/RF), particle density, electric field strength, ion/electron velocity, ion/electron energy, type of gas, gas composition, and distance between anode and cathode can significantly affect the plasma processing. Keeping all others parameters constant if only the gas will change, it will affect the polymer property dramatically [127, 135, 153]. As a gas used may increase surface energy while other gas will reduce the same. Almost similar effect can observe on hydrophilicity, surface morphology, chemical functionality, antibacterial, and antimicrobial properties and adhesion strength of processed material. Hence, the role of gas used and its composition can most significantly affect the processing. Even a very small variation in gas composition can produce completely different property to the material that can be used for novel applications. The different surface properties obtained via using different gases as source of plasma are very important for biomaterial fabrication processes in desired pathway, as oxygen plasma used for modification can generate oxygen functionalities and hydrophobic nature to polymer while other compound gases such as carbon dioxide, carbon monoxide, nitrogen dioxide, and nitric oxide can make the polymer surface hydrophilic. Chlorine functionalities can contribute to increase in the hydrophilicity when CF_2C and CCl_4 plasmas were used while hydrophobic properties of polymer can be enhanced using higher-degree fluorinated compound gases such as SF_6, CF_4, and C_2F_6 [154, 155]. Table 3 lists the effect and applications of different gases used as a source for plasma surface modification.

In this study air, N_2, Ne, and SF_6 gases were used for controlled modification of surface properties and a detailed investigation has been performed to identify their effect on property enhancement of nanobiomaterials. DC plasma surface modification instrument (Fig. 7).

Table 3 Different plasma gases, their effect, and applications on material processing

Plasma gases	Effect and applications in plasma processing
Reducing gases (H_2, mixtures of H_2)	Replacement of F or O on surfaces, removal of oxidation sensitive materials, conversion of contaminants to low-molecular weight species
Oxidizing gases (O_2, air, H_2O)	Removal of organics and to leave oxygen species
Nitrogen (N_2)	Removal of organic sand to leave N_2 species, removing oxide layers, surface cleaning, surface smoothening
Noble gases (He, Ne, Ar, etc.)	To generate free radicals on surfaces to cause cross-linking or to generate active sites for further reaction
Active gases (NH_3)	Functionalization of materials through amino groups
Fluorinated gases (SF_6)	To make the surface inert and hydrophobic
Polymerizing gases	Polymerization of layers on substrates by direct polymerization or by grafting on Ar/He-processed polymer surface

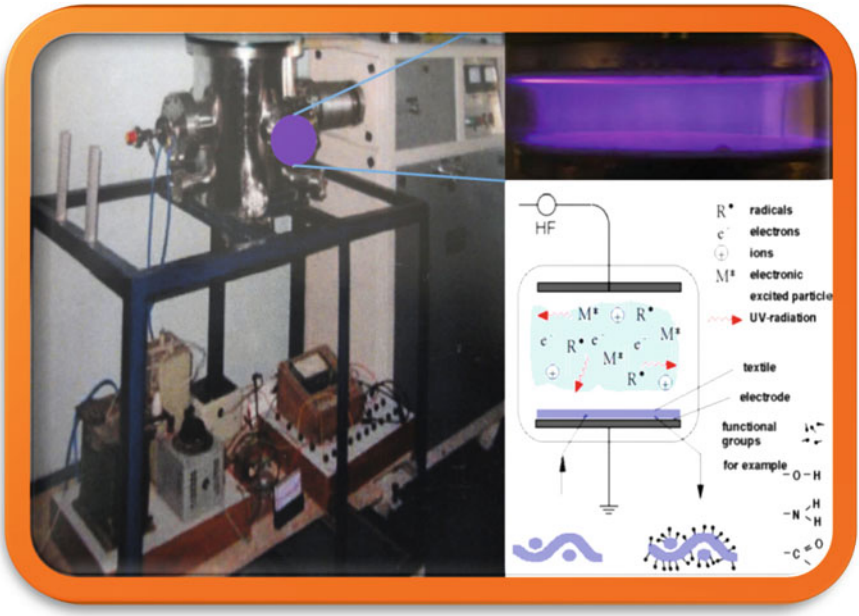

Fig. 7 Experimental setup used for production of DC plasma

6.1 Air and Its Properties as a Source of Plasma

Air is the atmosphere of Earth or layer of gases surrounding the Earth retained by its gravity. Role of air is very important to protect life of all leaving beings, absorbing ultraviolet solar radiation, and production of greenhouse effect, with normal

constitution by volume is nitrogen (78.09%), oxygen (20.95%), argon (0.93%), carbon dioxide (0.039%), and rest is several other gases like neon, helium, methane, krypton, hydrogen, nitrous oxide, carbon monoxide, xenon. It also contains a variable amount of water vapor ranging around 1%.

Air is not only important for animals to survive but also plays a critical role in plasma generation and processing as thundering of clouds is an example of production of natural plasma. Many of the plasma physics experiments and applications work at atmospheric pressure or at little reduced pressure like high power laser, MEMS electronic switches, EM absorbers/reflectors, remediation of gaseous pollutants/waste systems, sterilization, decontaminations and advanced plasma processing applications including plasma treatment of human skin. In all above-listed applications, the air plasma can significantly affect material properties that make the role of air composition very critical for plasma production and processing. Still very few efforts have been performed by researcher and industry for biomaterial production using air as a source of plasma except plasma treatment/healing of human skin. This shows need of detailed investigation of the properties and applications of air plasma in materials processing, as this offers low-cost processing of materials without any damage [156].

6.2 *Inert Gas Neon (Ne) and Its Properties as a Source of Plasma*

Neon is a monatomic, colorless, odorless, inert gas at standard temperature and pressure having two-thirds density of air. It shows bright orange-red emission spectra under high electric field. It has atomic number 10, atomic weight 20.1797 amu, electronic configuration [He] $2s^2\ 2p^6$, melting point 24.56 K, boiling point 27.10 K, FCC crystal structure and density 0.9002 g/L. Its first, second, and third ionization energies are 2080.7, 3952.3, 6122 kJ mol^{-1}, respectively. Interestingly, it is fifth most cosmic abundant element in universe and solar system after hydrogen, helium, oxygen, and carbon, but it is rare on Earth (18.2 ppm by volume). Air is only source for production/separation of neon, which makes it costlier even than He (helium gas) and limits its industrial applications in plasma tube and refrigerant.

When inert gas (He, Ne, and Ar gases) plasma is used to modify the surface of material, they can undergo physical etching, ion etching, or sputtering of the substrate material. Mostly researcher is using Ar and He plasma for materials due to their easy availability, but Ne exhibits similar chemical behavior with different physical characteristic like smaller atomic size and weight compared to argon can produce different mechanism and results during processing. To best of our knowledge, no efforts have been performed for Ne-based plasma processing especially for biomaterials productions. Ne ions can be extracted from glow discharge region and accelerated in electrical field toward the substrate similar to argon

and other gas ions. Due to inert nature of Ne gas, they cannot produce any type of chemical reaction on the material surface but Ne ions have sufficient energy to produce ion etching or sputtering totally controlled by impact of incident ions. The process is inherently non-selective due to widespread in ion energies compared with different surface bond energies and chemical reactivity. The modification (based on inert ion) is generally slow compared to other gases used for modification (with the etch rate of few ten angstroms to few hundred angstroms per minute). These types of modifications are used to form facets, ditches, hourglass-shaped trenches, removing of various damage, device complexity, and re-deposit materials with high aspect ratio. When ions of sufficient energy are used, they can produce high sputtering rate of materials and weight loss. Such weight loss is generally restricted to the topmost layers of the polymer, without affecting the inner layer. Ne gas plasma can create new surface morphology and improve the hydrophilicity and wettability on polymer surfaces.

6.3 *Reactive Gas Nitrogen (N_2) and Its Properties as a Source of Plasma*

Nitrogen is diatomic, colorless, odorless gas with high reactivity at standard temperature and pressure. It is a common element of solar system and most abundant in atmospheric gases. It has atomic number 7, atomic weight 14.007 amu, electronic configuration [He] $2s^2\ 2p^3$, melting point 63.15 K, boiling point 77.35 K, hexagonal crystal structure, and density 1.251 g/L. Its first, second, and third ionization energies are 1402.3, 2856, 4578.1 kJ mol^{-1}, respectively. It is used to make many industrially important compounds such as ammonia, nitric acid, fertilizers, and organic nitrates. Organic nitrates such as nitroglycerin and nitroprusside are used to control blood pressure by metabolization. Chemically it shows high electronegativity in reactions and makes strong bonds. It is also found in various organisms primarily in form of amino acids, proteins, and nucleic acids (DNA and RNA). A human body contains about 3% nitrogen by mass (fourth most abundant element in body after oxygen, carbon, and hydrogen). It is considered as a great source of energy production at Sun/stars in form of carbon nitrogen cycle.

For plasma processing of materials, nitrogen is extensively used for more than four decades, due to its easy availability and relatively easier plasma production ability. First application of nitrogen plasma was nitriding of high-carbon steels, titanium, aluminum, and molybdenum. This is a process where nitrogen will diffuse inside the materials in form of ions to form their nitrides that prevent material rusting/corroding and make them suitable for various applications like gears, crankshafts, injectors, camshafts, extrusion dies, valve parts, die casting tools, forging dies, and firearm components. Later nitrogen glow discharge plasma has shown its potential applications in various material fabrication processes. Nitrogen ions also work as good reducing agent, and hence, oxide layers can be removed

very easily from surface by transferring sufficient energy to substrate during bombardment of energetic particles. It can also remove various organics from material surface to leave N_2 species. Comprehensively, nitrogen plasma is used for surface cleaning, surface smoothening and also enhances fatigue strength, surface hardness, wear and corrosion resistance of materials. Based on chemical functionality of materials, nitrogen plasma can leave active sites on materials surface that can further cause post-reaction. These properties of nitrogen ion plasma highlight their use for various materials fabrication and processing processes especially for biomedical applications.

6.4 Sulfur Hexafluoride (SF_6) and Its Properties as a Source of Plasma

Sulfur hexafluoride (SF_6) is colorless, nonflammable, odorless, inorganic, and extremely potent greenhouse gas. It is also an excellent electrical insulator, and it has molar mass 146.06 g/mol, density 6.17 g/L [i.e., very high in comparison to air (1.225 g/L)], boiling point 209 K, slightly soluble in water but possesses good solubility in ethanol, hexane, benzene, and orthorhombic crystal structure. Most significantly it is used as gaseous dielectric medium in electrical industry.

Use of SF_6 gas plasma has been first started in semiconductor industry as an etchant and making their surface hydrophobic. Depending on plasma parameters and processing conditions, SF_6 breaks down into sulfur and fluorine under plasma and the fluorine plasma is further used for material processing.

When SF_6 gas is used for surface modification of materials, the processing is sometime known as radical etching or reactive ion etching. Surface modifications are generally carried out by reactive, neutral or chemical species such as fluorine atoms and molecular species instead of ions as done by other plasmas. The radicals are not as much reactive as ions but they are more abundant in plasma because they can be generated at lower threshold (<8 eV) and have high generation rate with longer lifetime compared to ions. Here used radicals from SF_6 gas plasma (fluorine) produce volatile products with layer to be removed; hence, they are more useful for surface cleaning of materials or generation of specific surface functionality where plasma works to supply reactive gas etchant to materials. Using SF_6 as a source gas for plasma, dry physiochemical modifications regime can be established by operating at various voltages, impingement of high energetic ions, various chemical reactions, etc.

The process of modification can be divided into five steps: In glow discharge, SF_6 dissociates in various components or reactive species (like SF_5^+, SF_4, F ion or radical) by bombardment of energetic particles (having energy distribution between 1 and 10 eV). These radicals and other neutrals reach to the surface by diffusion while ions are accelerated by field. Here most of the species does not undergo spontaneous reaction with the material. These species then diffuse into material,

further absorbed there to react with the surface material and end reaction products leave surface by desorption if it is volatile. From the listed steps those occurs in gas phase are termed as homogeneous reactions while those occurs at the surface of material are termed as heterogeneous reactions. Radical-based modifications are generally chemical in nature; hence, they are also selective for different materials or gas used for processing. As oxygen plasma removes photoresists by oxidizing hydrocarbon material, fluorine is used for silicon etching. Aluminum makes volatile chlorides while aluminum fluorides are nonvolatile. If plasma is used for processing of polymeric material using *F* radicals, *F*/*C* ratio controls the type of processing, as for $F/C > 3$ etching is dominant and for $F/C < 2$ polymerization takes place.

7 Biocompatibility and Bio-adoptability (in General and Properties Required)

In past few decades, advancements in science and technology focused on animal health and related issue to make it more and more comfortable. In this consequence, huge scientific efforts and interdisciplinary research are going on for development and fabrication of advanced materials those can be used for replacement of body parts after their failure. The synthesized materials have to be used for various applications like fabrication of body implants, biomedical devices, bio-separation, sterilizations, biosensors; hence, they must have specific surface and bulk properties that should not produce any deleterious effects, failure of material, or formation of unusual tissues. It must be noted that the synthesized materials are foreign materials to biological body, and normally, biological bodies do not accept foreign materials very easily till they shows superior biological response. Material that has to be used as biomaterial must show superior biocompatibility and bio-adoptability while retaining high-performance physical, chemical, and mechanical properties to fulfill other requirements [13, 128, 153].

Phenomena of biocompatibility and bio-adoptability are very similar to each other. Biocompatibility defines ability of a material to perform appropriate host response in a specific situation or in contact with biological system [157]. Hence, biocompatibility phenomena investigation involves the process where biological response of materials is tested using various components (like blood, DNA, protein) of any biological system, while bio-adoptability involves identification of biological response of any material with respect to any living biological body such as virus, bacteria, or any other. Both biocompatibility and bio-adoptability can be considered as in vitro and in vivo investigation of materials. It is very difficult to say that a material is biocompatible/bio-adoptable or not, as different biomaterials require different properties to be used, in particular, applications for ex. contact lenses and bones require very high wettability while artificial teeth requires low wettability. Even though sometimes situations become more critical for ex. artificial skin (its inner part must be blood compatible while outer part must show low blood

compatibility with overall system must show high porosity). Hence, any material and its property that may be suitable for synthesis of one class of biomedical devices/implants may not be suitable for other applications and produce challenge in the field of biomedical devices fabrication. Below is the list of few class and group of properties those are generally required for all kind of biomaterials in various forms (low/high/positive/negative effect) other than normal physical, mechanical, and chemical properties, as decided by international biological, medical boards, and scientific communities [65, 158–164]:

- Antibacterial and antimicrobial properties
- Toxicity
- Ecofriendly nature
- Wettability
- Micro-patterning
- Biological response to foreign materials
- Strong adsorption of proteins by surface
- Chemical functionality
- Cross-linked films formation irrespective of surface energy and geometries
- Adhesion
- Porosity
- Cell/tissue adhesion and compatibility
- Blood compatibility.

It is very easy to find a material with appropriate chemical, physical, and mechanical properties required for fabrication of biomedical devices/implants, but in general no natural/synthetic material or polymer possesses the surface interface and biological properties needed for various biomedical applications or in other words "any material/polymer do not have inherent properties (like surface energy, hydrophilicity, surface morphology, chemical functionality, antibacterial and antimicrobial properties, adhesion, peeling strength, and blood compatibility) required for synthesis of biomaterials". These drawbacks/requirements and growing need of biomaterials have drawn marvelous interest of scientific community in past decades in this area [20, 128].

8 Role of Nanotechnology for Enhancement of Biocompatibility and Bio-adoptability

Based on large investigation done by various scientific groups throughout the world and available literature, it can be easily concluded that most of the properties required for biomaterial synthesis are surface properties of the material [165]. Hence, techniques are required that can modulate the surface properties of materials in desired pathways to produce desired bio-response.

Nanotechnology/nanomaterials gain amazing interest for material fabrication processes due to their large surface to volume ratio that can be directly applicable for biomedical application. Recently, Agarwal et al. [48, 137] and several other groups are shown nanotechnology-based innovative approach for modulation of biological responses and surface properties of polymers with enhancement of normal physical, chemical, and mechanical properties of polymers using nanostructured materials in polymer matrix. These new class of materials are known as nanobiomaterials. They have shown that casting of various nanomaterials/nanoparticles in polymer matrix not only improves physical and chemical properties of polymers but also drastically modifies the biological response of these polymer based on properties of selected nanostructured materials [166]. Nanomaterial exhibits unique surface properties due to their smaller size and high surface to volume ratio. When these nanomaterials are mixed/incorporated in polymer, they homogenously distribute in polymer matrix, but for the apt amount incorporation nanoparticles there are sufficient NPs on the surface of polymer that leads to modification of surface properties of polymer nanocomposite in desired pathway. Also, attractive forces between polymeric chains and tendency of polymerization could provide them unique qualities while reinforcing them by organic [167] and inorganic nanoparticles that lead to enhancement of wettability, surface energy, geometries, blood compatibility and antibacterial properties, toxicity, surface tuning [168], abrasion [169], cross-linking [170], and modification of chemical properties [171] in controlled manner. Advancement shown here for synthesis of nanobiomaterials will surely be future of biomedical devices/implant fabrications.

9 Role of Plasma Treatment in Enhancement of Biocompatibility and Bio-adoptability

Forming and removing are the fundamental processes in nanoscale manufacturing processes or modulation of properties of materials. Removing is process that destroys cohesion among particles while formation creates an original shape from molten mass, gaseous/solution states, plasma, or solid particles. During formation process, cohesions are created among particles. The formation/removing can be done by wet chemical etching, thermal/mechanical energy-based removing, electrical discharge, traditional mechanical turning, laser drilling, plastic molding, thin-film deposition by evaporation/sputtering, electrochemical deposition, dry etching, ion etching, plasma-based etching and irradiation, etc. [172–177]. From the above-listed techniques, plasma-based etching and irradiations are most powerful techniques as they can be used for both formation and removing in controlled way as per requirement in various applications. Plasma-based processing can be controlled precisely using various plasma parameter and experimental conditions involved in processing that can lead to desired pathway for material modification due to various process involved in processing like nanomachining, uniformity,

profile and surface quality, less corrosion and material failure, less undercutting, high-speed fabrication, physisorbed, surface migration, surface damage, substrate heating, sputtering, material ejection, ion etching, ion implantation, doping.

Using various plasma parameters, processing methods and their combinations, one can provide new property to the material in desired pathway that may be useful for fabrication of different class of biomaterials. Number of experimental investigations performed in this field has shown that plasma treatment is sufficient to modify wettability, surface characteristic, surface energy, antibacterial property, hydrophilicity, blood coagulation, toxicity, blood cell adhesion patterns, defense systems [178], hemocompatibility characteristics, blood anticoagulation, metabolic functions [22, 179], thrombogenesis [180], tissue engineering [181], etc. These modifications are responsible for biological response of biomedical devices and implants in the biological systems such as vascular grafts [182], artificial devices used for extracorporeal circulation [183], blood cells and postoperative morbidity [184], pediatric cardiac operations [185], antithrombogenicity by urokinase immobilization [186]. In short, plasma treatment can significantly affect the biocompatibility and bio-adoptability of materials in desired pathways.

10 Influence of Plasma Processing and Nanomaterial Casting on Biocompatibility and Bio-adoptability of Biomaterials

Recent advancement in nanotechnology shows various applications in all fields of science where nanosize materials are receiving great interest for further improving the materials properties, and plasma is a widely acceptable technique for improving the material properties [187–189]. The role of nanotechnology and plasma processing for controlling biological response of materials is described separately. Few doped materials have been investigated to identify the influence of plasma treatment and doping by Zhang et al. [190]. They had demonstrated that Cl-based plasma can be used to etch lightly doped P/N-type silicon anisotropically while isotropically for heavily doped n-type silicon. Schwartz et al. [191, 192] shown that more than 10^{19} cm^{-3} dopant concentration give higher performance during processing. Figure 8 shows experimental study of blood cell attachment on various plasma-treated PMMA surfaces.

Presence of nanoparticles, filler dispersed nano-composites exhibit remarkably improved properties, compared to pure polymers or their traditional composites [193]. When nanoparticles are incorporated into the polymer in apt amount, especially for smaller/nanosize of the filler, material provides more area for interaction with polymer matrix that provides very high surface concentration of NPs to give them superior performance as biomaterials [61]. If these polymer nanocomposite materials will further processed by the ion plasma, more superior effect can be induced via processing on surface properties depending on plasma parameters

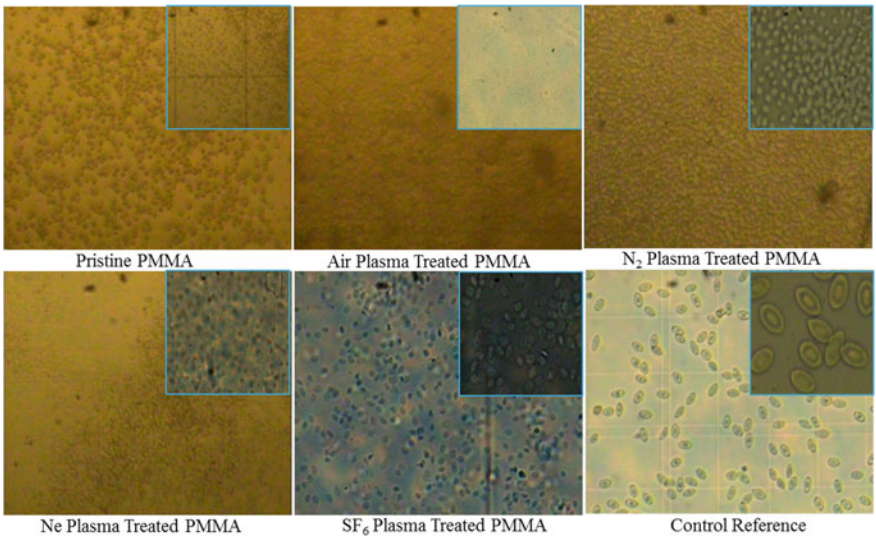

Fig. 8 Blood cell attachment on various plasma-treated surfaces

and processing conditions, and those lead to increase in surface amount of NPs; if polymer is selectively etched out, porosity will increase; if NPs are selectively etched out, relative surface smoothness increases; if both NPs and polymer are equally etched out, if NPs are more potent to bacteria, their surface exposure can enhance the antibacterial efficiency of nanocomposite, blood homo-compatibility of material will increase; if used NPs show higher compatibility, exposure of NPs on the surface can influence the cell and DNA attachment to biomaterials, etc. [65, 194, 195]. Figure 9 Optical micrograph of various plasma-treated nanocomposite surfaces.

11 Nanobiomaterials

Polymers exhibit many interesting properties that have increased their use in modern manufacture process. Number of experimental investigations performed on plasma treatment of polymers show controlled improvement in biological properties of polymers while retaining their bulk properties [196]. Recent advancement in the field of nanoscience and nanotechnology shows their potential to influence biological response of materials [197]. If combination of nanotechnology i.e. nanomaterials/polymer nanocomposites and plasma treatment will used to modify surface properties of materials that can produces superior biological response (biocompatibility and bio-adoptability) in more controlled fashion via chemical functionalization, highly cross-linked films formation, scaling up the antibacterial

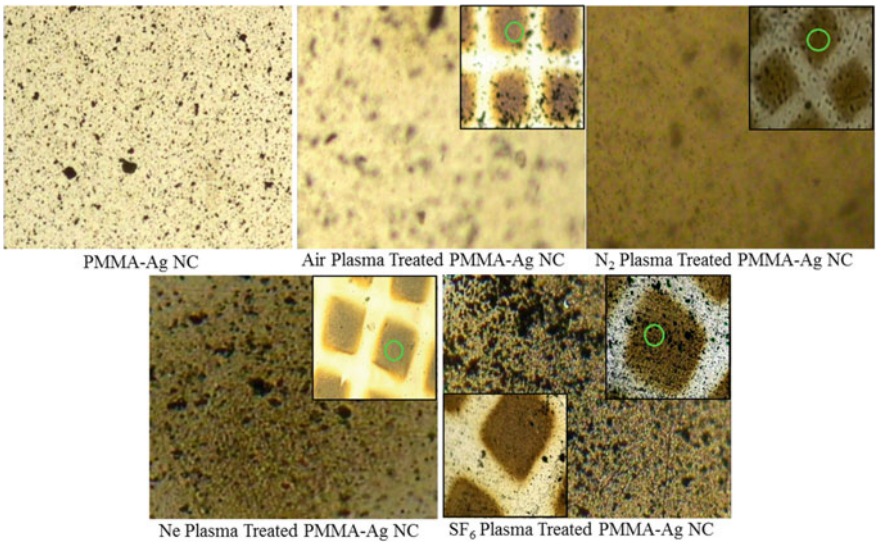

Fig. 9 Micrograph of plasma-treated PMMA-Ag nanocomposites

and antimicrobial properties in ecofriendly nature, high adhesion and peeling strength, blood compatibility etc. [198]. These new materials are known as nanobiomaterials [33, 137, 199] (plasma-treated polymer nanocomposite materials), extremely suitable for biomedical applications (fabrication of biomedical devices/implants) and nanobiomaterial synthesis.

12 Summary, Conclusions, and Scope for Future Work

Growing requirement of advance materials has been realized in last couple of decades for fabrication of biomedical devices and implants. These advance smart materials are called biomaterials. The choice of any material to use as biomaterial depends on their physical, chemical surface, and biological properties. The surface characteristics play a vital role in the performance of biomaterials. The fate of implants is determined by interactions—to a large extent cell-specific [97] between the biomaterial and tissues. Polymeric materials do not always possess the specific bioactivity required to promote suitable interaction with cells; thus, methods to enhance biocompatibility are required [101]. Polymers are receiving great interest for fabrication of biomaterials in last few decades, but normally no polymer has suitable property required to be used as biomaterials. Nanotechnology and low-temperature plasma-based approaches offered unique route to modify the surface and chemical properties of materials, due to their wide range of dynamic applications starting from fabrication to processing. Surface properties may be

altered by plasma treatment techniques. The modulation of the effects obtained is possible through control of operational parameters, including the gas used, reaction conditions (power, pressure, and exposure time), and the reactor geometry [192]. Plasma technique is a convenient method to modify the surface properties of polymeric materials, keeping intact their bulk properties. Hence, this chapter explored the use of nanotechnology and plasma treatment for enhancement of bio-adoptability and biocompatibility of polymers/polymer nanocomposites by plasma treatment.

Further polymers can be subjected to modifications with various ion plasma but there are several other parameters of plasma like ion energy, ion temperature, ion flux, electron flux, type of plasma etc. that can significantly affect the processing conditions hence the behavior of materials, so one can also explore the effect of these parameters on plasma based processing.

1. Air, nitrogen, Ne, and SF_6 plasma were used, but it is possible to modulate properties of material by the combination of these and several other gases that can provide both positive and negative effects on processing even more various monomers or liquids with high evaporation rate can be used/explored for their effect on plasma treatment of materials. Further after processing, one can try to attach various functional groups on plasma-treated polymer surface to increase their surface properties and efficiency.

References

1. Samberg ME, Oldenburg SJ, Monteiro-Riviere NA (2010) Environ Health Perspect 118:407–413
2. Belgacem MN, Czeremuszkin G, Sapieha S, Gandini A (1995) Cellulose 2:145–157
3. Helenius G, Backdahl H, Bodin A, Nannmark U, Gatenholm P, Risberg B (2006) J Biomed Mater Res Part A 76A:431–438
4. Toole LO, Short RD (1997) J Chem Soc Faraday Trans 93:1141–1148
5. Cagniant D, Magri P, Gruber R, Berlozecki S, Salbut PD, Bimer J (2002) J Anal Appl Pyrol 65:1–23
6. Chua PK, Chena JY, Wanga LP, Huang N (2002) Mater Sci Eng R 36:143–206
7. Yang J, Bei JZ, Wang SG (2002) Biomaterials 23:2607–2614
8. Abraham JW, Kongsuwan N, Strunskus T, Faupel F, Bonitz M (2015) J Appl Phys 117:14305–14311
9. Wang Y, Lu L, Zheng Y, Chen X (2006) J Biomed Mater Res Part A 76:589–595
10. El-Bagory I, Barakat N, Ibrahim MA, El-Enazi F (2012) Saudi Pharm J 20:229–238
11. Emeje M, John-Africa L, Isimi Y, Kunle O, Ofoefule S (2012) Acta Pharm 62:71–82
12. Gancarz I, Pozniak G, Bryjak M (2000) Eur Polym J 36:1563–1569
13. Alissawi N, Peter T, Strunskus T, Ebbert C, Grundmeier G, Faupel F (2013) J Nanopart Res 15:2080–2085
14. Lutolf MP, Hubbell JA (2005) Nat Biotechnol 23:47–55
15. Christine E, Jennie M (2005) Nat Biotechnol 23:47–55
16. Madhav PN, Song P, Tae SB, Ho KY, Motohiro U, Fumio W, Lee MH (2011) J Mater Chem 21:12078–12082

17. Homaeigohar SS, Shokrgozar MA, Javadpour J, Khavandi A, Sadi AY (2006) J Biomed Mater Res A 78:129–138
18. Huang HM, Hsieh SC, Teng NC, Feng SW, Ou KL, Chang WJ (2011) Med Biol Eng Comput 49:701–706
19. Bartoš P, Špatenka P, Volfová L (2009) Plasma Processes Polym 6:5897–5903
20. Bartoš P, Blažek J, Jelínek P, Špatenka P (2009) Eur Phys J D 54:223–319
21. Wan YQ, Yang J, Yang JL, Bei JZ, Wang SG (2003) Biomaterials 24:3757–3764
22. Jaffe EA (1994) Biochemistry, immunology and cell biology of endothelium: In: Blood vessels in hemostasis and thrombosis. Lippincott Company, Philadelphia
23. Ji JH, Jung JH, Yu IJ, Kim SS (2007) Inhalation Toxicol 19:745–751
24. Jung M, Vogel N, Koper I (2011) Langmuir 27:7008–7015
25. Keledi G, Hari J, Pukanszky B (2012) Nanoscale 4:1919–1938
26. Kim D, Lee JS, Barry CM, Mead JL (2007) Microsc Res Tech 70:539–546
27. Vesel A, Junkar I, Cvelbar U, Kovac J, Mozetic M (2008) Surf Interface Anal 40:1444–1453
28. Topalovic T, Nierstrasz VA, Bautista L, Jocic D, Navarro A, Warmoeskerken MMCG (2007) Colloids Surf A 296:76–85
29. Oehr C (2003) Nucl Instrum Methods Phys Res Sect B 208:40–47
30. Chua PK, Chen JY, Wang LP, Huang N (2002) Mater Sci Eng R 36:143–207
31. Bartoš P, Volfová L, Špatenka P (2009) Eur Phys J D 54:173–177
32. Vijay YK, Acharya NK, Wate S, Avasthi DK (2003) Int J Hydrogen Energy 28:1015–1018
33. Agrawal NK, Agarwal R, Vijay YK, Swami KC (2014) J Mater Sci Surf Eng 1:32–35
34. Agrawal NK, Awasthi K, Vijay YK, Swami KC (2013) J Adv Electrochem 1:98–104
35. Dorranian D, Abedinia Z, Hojabria A, Ghoranneviss M (2009) J Non-Oxide Glasses 1:217–229
36. Kojima Y, Usuki A, Kawasumi M, Okada A, Kurauchi T, Kamigaito O (1993) J Polym Sci Part A Polym Chem 31:983–986
37. Lee KM, Hu CW, Chen HW (2008) Sol Energy Mater Sol Cells 92:1628–1633
38. Vijay YK, Dhayal M, Awasthi K, Kulshrestha V, Acharya NK, Choi JS (2006) J Biomed Nanotechnol 2:144–151
39. Gomathi N, Mishra D, Maiti TK, Neogi S (2009) J Adhes Sci Technol 23:1861–1874
40. Gomathi N, Neogi S (2009) J Adhes Sci Technol 23:1811–1826
41. Sivak WN, Bliley JM, Marra KG (2014) Mol Biol 1162:139–148
42. Catapano G, Hornscheidt R, Wodetzki A, Baurmeister U (2004) J Membr Sci 230:131–135
43. Ma Z, Mao Z, Gao C (2007) Colloids Surf B Biointerfaces 60:137–157
44. Lucchesi C, Ferreira BMP, Duek EAR, Santos AR, Joazeiro PP (2008) J Mater Sci Mater Med 19:635–643
45. Marega C, Causin V, Saini R, Marigo A, Meera AP, Thomas S, Devi KS (2012) J Phys Chem B 116:7596–7602
46. Marzi D, Likos CN, Capone B (2012) J Chem Phys 137:014902
47. Kumar GA, Agrawal NK, Khandelwal S, Agarwal R (2014) Int J Eng Res Technol 1:109–113
48. Agrawal NK, Agarwal R, Vijay YK, Swami KC (2014) Adv Sci Eng Med 6:698–703
49. Zou L, Vidalis I, Steele D, Michelmore A, Low SP, Verberk JQ (2011) J Membr Sci 369:420–428
50. Ball P (2002) Nanotechnology 13:15–28
51. Trindade T, Brien PO, Pickett NL (2001) Chem Mater 13:3843–3858
52. Rosenthal L, Strunskus T, Faupel F, Abraham JW, Bonitz M (2014) Opt Plasma Phys, 82:321–370
53. Chakravadhanula VSK, Mishra YK, Avashti DK, Strunskus T, Zaporojtchenko V, Fink S, Kienle L, Faupel F (2014) Beilstein J Nanotechnol 5:1419–1431
54. Xiong J, Zubair Ghori M, Henkel B, Strunskus T, Schümann U, Kienle L, Faupel F (2014) Acta Mater 74:1–8
55. Matsuno R, Goto Y, Konno T, Takai M, Ishihara K (2009) J Nanosci Nanotechnol 9:358–365

56. McNeill CR, Watts B, Thomsen L, Belcher WJ, Greenham NC, Dastoor PC (2006) Nano Lett 6:1202–1206
57. Nair R, Varghese SH, Nair BG, Maekawa T, Yoshida Y, Kumar DS (2010) Plant Sci 179:154–163
58. Hájková P, Špatenka P, Krumeich J, Exnar P, Kolouch A, Matoušek J (2009) Plasma Processes Polym 6:735–740
59. Park KH, Dhayal M (2014) Electrochem Commun 49:47–50
60. Agrawal NK, Singh M, Vijay YK, Swami KC (2014) Adv Sci Eng Med 6:595–602
61. Carp O, Huisman CL, Reller A (2004) Prog Solid State Chem 32:133–177
62. Sunada K, Watanabe T, Hashimoto K (2003) J Photochem Photobiol A Chem 156:227–233
63. Bambhaniya KG, Grewal GS, Shrinet V, Govindan TP, Singh NL (2013) Chem Eng Commun 200
64. Regan OB, Gratzel M (1991) Nature 353:737–740
65. Hájková P, Špatenka P, Krummeich J, Exnar P, Kolouch A, Matoušek J, Koci P (2009) Eur Phys J 54:189–193
66. Wang YQ, Zhang HM, Wang RH (2008) Colloids Surf B 65:190–196
67. Park KH, Pandey RR, Dhayal M (2014) Sens Actuators B Chem 196:589–595
68. Mohammadia MR, Fray DJ, Cordero-cabrera MC (2007) Sens Actuators B 124:74–83
69. Nowotny MK, Sheppard LR, Bak T, Nowotny J (2008) J Phys Chem C 112:5275–5300
70. Thevenot P, Cho J, Wavhal D, Timmons RB, Tang L (2008) Nanomed Nanotechnol Biol Med 4:226–236
71. Kuhn KP, Chaberny IF, Massholder K, Sticker M, Benz VW, Sonntag HG, Erdinger L (2003) Chemosphere 53:71–77
72. Benabbou AK, Derriche Z, Felix C, Lejeune P, Guillard C (2007) Appl Catal B Environ 76:257–263
73. Paul DR, Robeson LM (2008) Polym Nanocomposites Reson 49:3187–3204
74. Desireddy A, Conn BE, Guo J, Yoon B, Barnett RN, Monahan BM, Kirschbaum K, Griffith WP, Whetten RL, Landman U, Bigioni TP (2013) Nature 501:399–402
75. Mel AD, Chaloupka K, Malam Y, Darbyshire A, Cousins B, Seifalian AM (2012) J Biomed Mater Res Part A 100A:2348–2357
76. Kim JS, Kuk E, Yu KN, Kim JH, Park SJ, Lee HJ, Kim SH, Park YK, Park YH, Hwang CY, Kim YK, Lee YS, Jeong DH, Cho MH (2007) Sci Direct 3:95–101
77. Sougata S, Jana AD, Samanta SK, Mostafa G (2007) Polyhedron 26:4419–4426
78. Xiu Z, Zhang QB, Puppala HL, Colvin VL, Alvarez PJJ (2012) Nano Lett 12:4271–4275
79. Farkasa J, Christian P, Urrea JAG, Roos N, Hassellöv M, Tollefsen KE, Thomas KV (2010) Aquat Toxicol 96:44–52
80. Guo W, Yuan J, Dong Q, Wang E (2010) J Am Chem Soc 132:932–934
81. Keleştemur S, Kilic E, Uslu U, Cumbul A, Ugur M, Akman S, Culha M (2012) Nano Biomed Eng 4
82. Ebeling A, Hartmann V, Rockman A, Armstrong A, Balza R, Erbe J, Ebeling D (2013) Comput Water Energy Environ Eng 2:16–25
83. Hao R, Xing R, Xu Z, Hou Y, Gao S, Sun S (2010) Adv Mater 22:2729–2742
84. David L, Moldovan B, Vulcu A, Olenic L, Perde-Schrepler M, Fischer-Fodor E, Florea A, Crisan M, Chiorean I, Clichici S, Filip GA (2014) Colloids Surf B Biointerfaces 122:767–777
85. Shrivastava S, Bera T, Singh SK, Singh G, Ramachandrarao P, Dash D (2009) ACS Nano 3:1357–1364
86. Erdem A (2007) Talanta 74:318–325
87. Zhou YG, Rees NV, Compton RG (2011) Chem Phys Lett 511
88. Xuea CH, Chena J, Yina W, Jiaa ST, Maa JZ (2012) Appl Surf Sci 258:2468–2472
89. Ouyang J, Chu CW, Szmanda CR, Ma L, Yang Y (2004) Nat Mater 3:918–922
90. Yu J, Patel SA, Dickson RM (2007) Angew Chem Int Ed Engl 46:2028–2030
91. Paul DR, Robeson LM (2008) Polymer (Guildf) 49:3187–3204
92. Fujii S, Matsuzawa S, Nakamura Y, Ohtaka A, Teratani T (2010) Langmuir 26:6230–6239

93. Yuan Q, Misra RDK (2006) Mater Sci Technol 22:742–755
94. Bhowmick AK, Bhattacharya M, Mitra S, Maji PK, Choudhury A, George JJ, Basak GC, Kumar KD, Kunststoffe KG (2010) Bio-Macromolecules 62:192–200
95. Hussain F, Hojjati M, Okamoto M, Gorga RE (2006) J Compos Mater 40(17):1511–1575
96. Singh NB, Rai S, Agarwal S (2010) Nanosci Technol 1:10–13
97. Kumar A, Sharma SS, Nehra S, Srivastava S, Kulshrestha V, Singh M, Vijay YK (2010) Optoelectron Adv Mater Rapid Commun 4:1701–1704
98. Pereira CL, Demarco FF, Cenci MS, Osinaga PW, Piovesan EM (2003) Clin Oral Investig 7:116–119
99. Knorowski CD, Anderson JA, Travesset A (2008) J Chem Phys 128:164903
100. Fernandez-Saavedra R, Darder M, Gomez-Aviles A, Aranda P, Ruiz-Hitzky E (2008) J Nanosci Nanotechnol 8:1741–1750
101. Gelves GA, Lin B, Sundararaj U, Haber JA (2008) Nanotechnology 19:215712
102. Choi J, Choi MJ, Yoo JK, Park WI, Lee JH, Lee JY, Jung YS (2013) Nanoscale 5:7403–7409
103. Gomez V, Levin M, Saber AT, Irusta S, Dal Maso M, Hanoi R, Santamaria J, Jensen KA, Wallin H, Koponen IK (2014) Ann Occup Hyg 58:983–994
104. Zakhary K, Ellis DA (2005) Facial Plast Surg 21:110–116
105. Ko Y, Baek H, Kim Y, Yoon M, Cho J (2013) J ACS Nano 7:143–153
106. Kumaravel R, Ramamurthi K, Sulania I, Asokan K, Kanjilal D, Avasthi DK (2012) Nucl Instrum Meth Phys Res B 285:61–64
107. Mariam J, Sivakami S, Kothari DC, Dongre PM (2001) Protein J 33:258–266
108. Bahrami R, Lobling TI, Groschel AH, Schmalz H, Muller AH, Altstadt V (2014) ACS Nano 8:10048–10056
109. Ford C, Singh M, Lawson L, He J, John V, Lu Y, Papadopoulos K, McPherson G, Bose A (2004) Colloids Surf B Biointerfaces 39:143–150
110. Ziegler A, Landfester K, Musyanovych A (2009) Colloid Polym Sci 287:1261–1271
111. Kulshrestha V, Awasthi K, Acharya NK, Singh M, Avasthi DK, Vijay YK (2006) Desalination 195:273–277
112. Timothy ND, Robert Slade CT, Varcoe JR (2004) J RSC ORG 15:1–10
113. Miyoshi T, Ishikawa H, Fujii M, Kuroda H (1984) Nihon Eiseigaku Zasshi 39:640–646
114. Man SF, Thomson AB (1982) J Appl Physiol Respir Environ Exerc Physiol 52:1223–1229
115. Okura M, Mykhaylyk OO, Ryan AJ (2013) Phys Rev Lett 110:087801
116. Nakamura I (2014) J Phys Chem B 118:5787–5796
117. Rechard FM, Robert D (2011) Nanomaterials
118. Sako Y, Kusumi A (1995) J Cell Biol 129:1559–1574
119. Sanchis MR, Blanes V, Blanes M, Garcia D, Balart R (2006) Eur Polym J 42:1558–1568
120. Sardella E, Liuzzi F, Comparelli R, Depalo N, Striccoli M, Agostiano A, Favia P, Curri ML (2013) Nanotech J 24:145302
121. Scocchi G, Posocco P, Fermeglia M, Pricl S (2007) J Phys Chem B 111:2143–2151
122. Kulshrestha V, Awasthi K, Acharya NK, Singh M, Vijay YK (2005) Bull Mater Sci 28:643–647
123. Dhayal M, Awasthi K, Vijay YK, Avasthi DK (2006) Vacuum 80:643–647
124. DeClements R, Swain GM, Dallas T, Herrick I, Stickney JL (1996) Langmuir 12:6578–6586
125. Baylay H, Jayasinghe L (2004) Mol Membr Bio 21:209–213
126. Blažek J, Bartoš P, Basner R, Kersten H, Špatenka P (2009) Eur Phys J D 54:219–224
127. Bonitz M, Rosenthal L, Fujioka K, Zaporojtchenko V, Faupel F, Kersten H (2012) Contrib Plasma Phys 52:482–486
128. Boris J, Thomas M, Klages CP, Faupel F, Zaporojtchenko V (2007) Plasma Processes Polym 482–486
129. McKay K, Salter T, Bowfield A, Walsh J, Gilmore I, Bradley JW (2014) J Am Soc Mass Spectrom 25:1528–1533
130. Augustine BH, Hughes WC, Zimmermann KJ, Figueiredo AJ, Guo X, Chusuei CC, Maidment JS (2007) Langmuir 23:4346–4350

131. Bowes M, Bradley JW (2014) J Phys D Appl Phys 47:265202–265207
132. Bowfield A, Bunch J, Salter TL, Steven R, Gilmore IS, Barrett DA, Alexander MR, McKay K, Bradley JW (2014) Analyst 1–9
133. Cui X, Lee VA, Raphael Y, Wiler JA, Hetke JF, Anderson DJ, Martin DC (2001) J Biomed Mater Res 56:261–272
134. Domingos M, Intranuovo F, Gloria A, Gristina R, Ambrosio L, Favia P, Bartolo P (2013) Acta Biomater 9:5997–5999
135. Etrich C, Fahr S, Keshavarz Hedayati M, Faupel F, Elbahri M, Rockstuhl C (2014) Mater Sci Eng C Biomimetic 7:727–741
136. Agarwal R, Agrawal NK, Singh R (2014) Mater Focus 3:267–271
137. Agrawal NK, Agarwal R, Awasthi K, Vijay YK, Swami KC (2014) Adv Mater Lett 5:645–651
138. Eisenbrey JR, Hsu J, Wheatley MA (2009) Ultrasound Med Biol 35:1854–1862
139. Kibayashi H, Teraoka F, Fujimoto S, Nakagawa M, Takahashi J (2005) Dent Mater J 24:53–58
140. Sharma R, Das PP, Misra M, Mahajan V, Bock JP, Trigwell S, Biris AS, Mazumder MK (2009) Nanotechnology 20:075704
141. Shinonaga Y, Arita K (2009) Dent Mater J 28:735–742
142. Bazaka K, Jacob MV, Crawford RJ, Ivanova EP (2011) Acta Biomater 7:2015–2028
143. Eloy R, Parrat D, Duc TM, Legeay G, Bechetoille A (1993) J Cataract Refract Surg 19:364–370
144. Dufresne A (2010) Molecules 15:4111–4128
145. Roy S, Sahoo NG, Mukherjee M, Das CK, Chan SH, Li L (2009) J Nanosci Nanotechnol 9:1928–1934
146. Jacobs T, Declercq H, De Geyter N, Cornelissen R, Dubruel P, Leys C, Beaurain A, Payen E, Morent R (2013) J Mater Sci Mater Med 24:469–478
147. Ren TB, Weigel T, Groth T, Lendlein A (2008) J Biomed Mater Res A 86:209–219
148. Weikart CM, Miyama M, Yasuda HK (1999) J Colloid Interface Sci 211:28–38
149. Lin M, Zhao Y, Wang S, Liu M, Duan Z, Chen Y, Li F, Xu F, Lu T (2012) Biotechnol Adv 30:1551–1561
150. Song G, Cho SM, Jung HJ, Kim RH, Bae I, Ahn H, Ryu du Y, Huh J, Park C (2012) Chemistry 18:15662–15668
151. Szili EJ, Bradley JW, Short RD (2006) J Phys D Appl Phys 47(2014):152002–152015
152. Wang H, Chung TS, Tong YW, Jeyaseelan K, Armugam A, Duong HHP, Fu F, Seah H, Yang J, Hong M (2013) J Membr Sci 434:130–136
153. Faupel F, Thran A, Zaporojtchenko V, Kiene M, Strunskus T, Behnke K (1999) AIP conference proceedings, 491–496, pp 201–216
154. Paosawatyanyong B, Kamlangkla K, Hodak SK (2010) J Nanosci Nanotechnol 10:7050–7054
155. Selli E, Mazzone G, Oliva C, Martini F, Riccardi C, Barni R, Marcandalli B, Massafra MR (2001) J Mater Chem 11:1985–1991
156. Ni HC, Lin ZY, Hsu SH, Chiu IM (2010) Acta Biomater 6:2066–2076
157. Black J (2005) Biological performance of materials. CRE Press
158. Oehr OC (2003) Nucl Nucl Instr Meth Phys Res B 208:40–44
159. Lee H, Jung Y, Kim S (2012) J Nanosci Nanotechnol 12:1513–1516
160. Wittenberg N, Son MM, Eves D, Cans AS, Ewing AG (2007) Electrochemistry at the cell membrane/solution interface. Electrochemical methods for neuroscience—NCBI bookshelf. CRC Press, USA
161. Sharma J, Yeh HC, Yoo H, Werner JH, Martinez JS (2011) Chem Commun (Camb) 47:2294–2296
162. Favia P (2012) Surf Coat Technol 211
163. Gavade C, Kishore S, Singh NL, Khanna PK (2013) Radiat Eff Defects Solids 1
164. Khan SA, Srivastava SK, Avasthi DK (2012) J Phys D Appl Phys 45:375304–375310

165. Rosenthal L, Strunskus T, Faupel F, Abraham JW, Bonitz M (2014) Springer Series on atomic, optical, and plasma physics. Complex Plasmas 82:321–370
166. Agrawal NK, Agarwal R, Vijay YK, Swami KC (2014) J Bionanoscience 8:108–115
167. Balazs AC, Emrick T, Russell TP (2006) Science 314:1107–1110
168. Cong H, Radosz M, Towler BF, Shen Y (2007) Sep Purif Technol 55:281–291
169. Shahida N, Villateb RG, Barron AR (2005) Compos Sci Technol 65:2250–2258
170. Siqueira G, Bras J, Dufresne A (2009) Biomacromolecules 10:425–432
171. Dastjerdi R, Montazer M (2012) Colloids Surf B 79:5–18
172. Ceschel GC, De Filippis P (1981) Pharm Acta Helv 56:291–295
173. Chan TL, Wang CZ, Hupalo M, Tringides MC, Ho KM (2006) Phys Rev Lett 96:226102
174. Chen B, Evans JR, Greenwell HC, Boulet P, Coveney PV, Bowden AA, Whiting A (2008) Chem Soc Rev 37:568–594
175. Chen M, Zhang Y, Sky Driver M, Caruso AN, Yu Q, Wang Y (2013) Dent Mater 29:871–880
176. Choi JH, Kim YM, Park YW, Park TH, Jeong JW, Choi HJ, Song EH, Lee JW, Kim CH, Ju BK (2010) Nanotechnology 21:475203
177. Colmenero J (2013) J Chem Phys 138:197101
178. Teebken OE, Haverich A (2002) Eur J Vasc Endovasc Surg 23:475–485
179. Sperling C, Salchert K, Streller U, Werner C (2004) Biomaterials 25:5101–5113
180. Diquelou A, Dupouy D, Gaspin D, Constans J, Sié P, Boneu B, Sakariassen KS, Cadroy Y (1995) Thromb Haemost 74:778–780
181. Zilla P, Greisler HP (1999) Tissue engineering of vascular prosthetic grafts. R.G. Landes Company, Austin
182. Bordenave L, Remy-Zolghadri M, Fernandez P, Bareille R, Midy D (1999) Endothelium 6:267–275
183. Wendel HP, Ziemer G (1999) Eur J Cardio Thorac Surg 16:342–350
184. Belboul A, Al-Khaja N (1997) Perfusion 12:385–391
185. Schreurs HH, Wijers MJ, Gu YJ, Oeveren WV, Domburg RT, De Boer JH, Bogers AJ (1998) Ann Thorac Surg 66:166–171
186. Ryu GH, Park SY, Cho HI, Min BG (1989) Seoul J Med 30:37–46
187. Faupel F, Willecke R, Thran A (1998) Mater Sci Eng R-Rep 22:1–55
188. Faupel F, Willecke R, Thran A, Kiene M, Bechtolsheim C, Strunskus T (1997) Defect Diffus Forum 887:143–147
189. Faupel F, Zaporojtchenko V, Greve H, Schürmann U, Hanisch C, Chakravadhanula VSK, Kulkarni A, Gerber A, Quandt E, Podschun R (2007) Contrib Plasma Phys 47:537–544
190. Zhang RR, Li L, Tong LL, Tang B (2013) Nanotechnology 24:015604
191. Schwartz GA, Alegria A, Colmenero J (2007) J Chem Phys 127:154907
192. Schwartz GA, Cangialosi D, Alegria A, Colmenero J (2006) J Chem Phys 124:154904
193. Kedawat BK, Gupta P, Kumar J, Dwivedi A, Kumar NK, Agrawal SS, Kumar YK, Vijay ACS (2014) Appl Mater Interfaces 6:8407–8414
194. Favia P (2012) Surf Coat Tech 50:211–218
195. Günther-Schade K, Schubert DW, Faupel F (2002) Macromolecules 35:9074–9079
196. Hedayati MK, Zillohu AU, Strunskus T, Faupel F, Elbahri M (2014) Appl Phys Lett 104:117–121
197. Horakova M, Martin N, Aubry E, Spatenka P (2009) Catal Lett 132:244–249
198. Klugkist P, Rätzke K, Rehders S, Troche P, Faupel F (1998) Phys Rev Lett 80:3288–3291
199. Bagra B, Pimpliskar P, Agrawal NK (2014) AIP Conf Proc 1591:189–191

Effects of Neutron Irradiation on Polymer

Sangeeta Prasher and Mukesh Kumar

Abstract Polymers have been widely utilized in various applications due to their low cost and easy processability and thus could be utilized in radiation-prone areas for their radiation-resistant behaviour. Ionizing radiations induce chemical kinetics in the polymers leading to the exchange reactions causing the variations in structural conformations. Neutrons since the discovery in 1932 have been posed as a special particle due to its neutral behaviour and hence been utilized in many medical and industrial applications. The neutral behaviour provides it a greater penetration depth and therefore more quantitative measurements to greater accuracy. This chapter has been devoted to review the influence of neutrons in various polymers for their utilization in apron making for radiation workers and neutron dosimetry. Special attention has been paid to the structural elucidation and reactivity of ionized molecules upon exposure of the polymers to the neutron beam. Recent developments in utilizing the neutron irradiation for modifications and upgrading the properties of polymers have also been discussed.

Keywords Neutron irradiation · Optical modifications · Radiation effects · Structural modifications

1 Introduction

The rapid growth of the particle accelerators and nuclear power plants for research and energy production not only influenced the lifestyle of the world population but has also participated in the growth of employment. These places have given opportunities to technicians, doctors and many key scientists in the fields of nuclear

S. Prasher (✉)
Department of Physics, Kanya Maha Vidhayalya, Jalandhar 144004, India
e-mail: sp105@rediffmail.com

M. Kumar
Department of Physics, Lovely Professional University,
Chaheru, Phagwara 144411, India

V. Kumar et al. (eds.), *Radiation Effects in Polymeric Materials*, Springer Series on Polymer and Composite Materials, https://doi.org/10.1007/978-3-030-05770-1_11

science to work and explore the new world. The radiations emitted by these accelerators and plants are harmful to human life, and thus the occupants working in the environs of radiations must be protected against these hazards. A number of studies have investigated the influences of neutron and other neutral radiations, such as X-rays and gamma radiations in materials, and reported a greater relative effectiveness to the production of ionization by the recoil protons resulting from neutron bombardment as compared with an equal amount of ionization produced by other types of radiations [1–4]. Shielding from these radiations is the best possible way of protection for a radiation worker. In general, lead and lead composites/compounds are used for protection against radiation due to its high density. Lead aprons due to their heavyweight and toxicity are not easy to wear, and hence an environment-friendly nontoxic and lighter material is required for personal shielding aprons. These requirements emphasized the scientists to achieve radiation-resistant material composites and study the impact of different radiations on these materials. These ideas stimulated the research in the field of radiation effects on materials and their utilizations in technical and scientific applications. The technique of irradiation seems to be a boon to the chemical industry due to the unlimited possibilities of useful modifications in the material structures [5, 6, 7]. Radiation-induced cross-linking technology in polymers has been widely used in wire and cable industry due to their higher resistance towards solvents, ageing and high temperatures [8]. Manufacture of "heat-shrinkable" packaging films, tubing and foams are other well-established applications of radiation-processed polymers, whereas radiation-induced scissoring in Teflon allowed its use as filler in various applications. The rapid growth of scientific interest in the field could be traced in the increasing number of papers and the appearance of special scientific journals on the subject. Polymeric materials with enhanced mechanical and physical properties could be developed for radiation shielding aprons and other demanding attributes because of their low cost, lightweight and high tolerance to radiations. In spite of the fact that many researchers are engaged in studying the influence of various kinds of radiations, the impact of neutron irradiation on polymers and polymer composites has not been observed to greater extent; however, these particles pose a greater challenge for shielding due to their higher penetration power. Despite their great penetration, the results of neutron irradiation are not limited to the surface layer of the substrate irradiated.

Neutron irradiation significantly changes the properties of polymeric materials by displacement of lattice atoms, variations in molecular weight distributions [9] and the generation of helium and hydrogen by nuclear transmutations [10]. When neutrons pass through a solid, there is a finite probability that they will collide with a lattice atom, imparting recoil energy to the struck atom [11], and the material atoms gain enough energy to get knock off; hence, modification in the material takes place [12–14]. The vacancies produced due to displaced atoms and dislocations coalesce and contribute to the increase in network dislocation density leaving the polymeric system in metastable thermodynamic equilibrium state. The ejected atoms may recombine with the other vacancies leading to the motion of the defects from one place to another resulting in uniform morphological modifications in

materials via chain scissions and cross-linking processes in polymeric conformation. The chain scissions are produced due to the amorphous phase of the polymers. The displacement production rate by neutron irradiation could be calculated by estimating the displacements per atom production rate by using numerical simulations such as SRIM. The way in which neutrons interact with matter depends to a large extent on their energies that can range from hundreds of mega-electron volts for fast neutrons down to a fraction of an electron volt for thermal neutrons. The principal interactions of neutrons with matter include elastic scattering, inelastic scattering, nuclear reaction and capture which results in cross-linking and scissoring in most of the polymeric systems with one or the other effects predominating.

1.1 Nuclear Interactions with Matter

Neutrons are uncharged particles having mass equivalent to the mass of proton and interact with the nuclei, while the primary charged projectiles would require excessive energy for the same. However, the movement of neutrons bears a resemblance to the movement of other chemical identities like ions and protons. When the neutrons are allowed to pass through a material, there is a probability of the neutron being deflected from their path with or without a loss of energy or absorbed by nucleus of the material. The energy is transferred from the incident neutron to the target nucleus resulting in the knock off of atoms to interstitial sites of polymeric chains. These knock off atoms make passage through the lattice and create secondary knock on atoms resulting in cascade and formation of clusters. Neutrons induce charge transfer reactions and lead to the formation of ion clusters [15] in which several molecules cluster around each ion and chemical breakdown of the whole cluster occurs on neutralization by an electron or by an ion or cluster of opposite charge. Unlike heavy ions that are produced through acceleration processes, the charged particles in case of neutron irradiation are produced due to the nuclear reactions induced through neutron interactions with polymeric molecules. The product of such interactions often causes significant radiation damage through nuclear recoils and transmutations and disrupts the chemical structure of the material. A neutron passes through the material without losing energy to the electrons until it comes across a nucleus. The principal interactions of neutrons with matter can thus be categorized as scattering and absorption and are discussed below (Fig. 1).

1.1.1 Elastic Scattering

Neutron enters the nucleus without suffering any repulsion caused by electric charge of the nucleus. When a neutron is scattered by a target nucleus and rebounds in a different direction, imparting the recoil energy to the target nucleus, which moves away at an increased speed, the process is called the elastic scattering. If the neutron collides with massive nucleus, it renounces with almost the same speed and

loses a very small energy. Light nuclei, on the other hand, will gain a lot of energy from such collisions and will therefore be more effective for slowing down neutrons.

1.1.2 Inelastic Scattering

If neutrons strike a target nucleus and left the target in the excited state, the interaction process is known as inelastic scattering and is most effective at high neutron energies in heavy materials. In such a process, an unstable compound nucleus is formed for a short period of 10^{-23} s and a neutron is evaporated from the moving compound nucleus together with a γ-photon.

1.1.3 Nuclear Reactions

When a high-energy neutron strikes a target nucleus, it may become incorporated into the nucleus and another particle may be emitted. Such nuclear reactions take place when the incident neutron has energy above the threshold energy for the reactions, and this usually implies incident neutron energies of several mega-electron volts. An important exception is the reaction of neutrons of thermal energy with boron-10: ^{10}B (n, α) ^{7}Li. This reaction is commonly employed in detectors for the detection of low-energy neutrons. Another important reaction of thermal energy neutrons is that with nitrogen-14 to yield carbon-14; ^{14}N (n, p) ^{14}C.

1.1.4 Neutron Capture

For neutrons of thermal energies, the most likely interaction with elementary matter is the capture of neutrons by the target nuclei to give an isotope of the target element. This may lead first to the formation of a compound nucleus in an excited state. The life of the compound nucleus is long enough for the projectile to lose its identity and hence returns to the ground state by giving off one or more γ-rays only. Such a reaction is called an (n, γ) reaction.

All these mechanisms leave the system in excited state composing of hot molecules, free radicals, reactive ions and randomly moving electrons. These unstable and highly energetic species induce sequential events involving generation of secondary particles and result in cascade processes. The relaxation processes started with the interaction between the unstable species and ended up with the system being in metastable state distinguished by electronic and structural defects produced in the system. Thus, the neutron irradiation-generated damages in the polymers are equivalent to that of the modifications induced by heavy ions.

2 Radiation Effects in Materials

The study of radiation effects of neutron irradiation in materials is basically related to the energy transfer cross section, i.e. the energy imparted to the recoil atom as a function of initial energy, angular distribution and scattering angle. The energy transfer cross section helps in obtaining the absorbed dose from the kinetic energy of the recoiled charged particles produced during neutron bombardments by making small corrections. The absorbed dose depends on the location, where the charged particles ejected by the neutrons finally deliver their energy to the matter [16]. The energy transfer (kerma) per neutron per centimetre squared for incident neutrons of energy E in the laboratory is defined by the equation

$$K(E) = \sum_{L} N_{\mathrm{L}} \left[\sum_{J} \bar{\epsilon}_{LJ}(E) \sigma_{LJ}(E) \right]$$

The indexes L and J identify the element and the type of nuclear reactions described above, N_{L} is the number of nuclei of the Lth element per gram, and $\bar{\epsilon}_{LJ}(E)$ is the average amount of energy transferred to kinetic energy of charged particles in a collision whose cross section is $\sigma_{LJ}(E)$.

Recently, Chikaoui et al. [17] have explored the defects generated by reactor neutron with fluence ranges from 2.02×10^{16} to 2.07×10^{18} n/cm^2 in polyethylene terephthalate (PET) films and reported the reduction in band gap and crystallinity of PET with the neutron irradiation.

Galehdari and Kelkar [18] have studied the effects of neutron radiation on the mechanical properties of lightweight multifunctional polymer composites, fabricated by dispersing boron nanopowder, gadolinium and boron carbide nanoparticles with radiation shielding properties in an epoxy polymer and observed that the neutron shielding efficiency increased significantly by introduction of nanoparticles.

Gourdin et al. [19] have studied the influence of 14 meV neutrons with a fluence ranging from 10^9 to 10^{13} particles/cm^2 on the mechanical properties of Spectralon™ porous PTFE. Many other researchers are also involved in similar practices [20, 21].

The increase in the grain size of Li-ion batteries due to neutron irradiation has been observed by Qiu et al. [22]. The defects induced by the neutron bombardments migrate through the material and interact with the grain boundaries, enhancing atomic jumps at the boundary and contributing to the grain growth.

Uusi-Simola et al. [23] have explored the applications of polymers in neutron and radiation dosimetry and concluded that gel dosimeters could be utilized successfully for the verification of the relative dose distribution in the epithermal neutron beam without taking the LET-dependent response of the gels into consideration as the measured R2 relaxation rates of the detectors are directly related to the calculated total absorbed dose in ICRU adult brain tissue. Srivastava and Virk [24] have reported the rise in capacitance due to the production of vacancies and charge centres in neutron-irradiated polymers. These species oscillate in the applied

field giving rise to circulatory currents and assist in the development of inductance in polyelectric and dielectrics.

The decrease in the electrical resistivity in materials due to the migration of vacancies produced due to neutron bombardment has also been reported by Damask [25]. The irradiation of the materials enhances the number of vacancies and hence the diffusion and hence assists the material in achieving the lower resistivity under normal conditions. Laghari and Hammound [26] have also reported scissoring of polymeric chains and production of vacancies due to irradiation of polymers.

Alexander et al. [27] have reported the breakdown of main chain and decomposition of side chain with the evolution of gases causing the changes in the viscosity and the molecular weights of irradiated polymethylmethacrylate. The authors have also stated the rupture of main chain C–C bonds and one ester side chain as a result of irradiation.

The objective of the present chapter is to describe the effects of neutron beam on cross-linking and curing of polymers by presenting an overview of modifications in structural and optical properties in a concise fashion. One more purpose of this chapter is to develop a radiation-resistant polymer to be utilized in apron-making applications for neutron shielding. The other aim of this chapter is to recognize the best potential polymer for neutron dosimetry as the neutron irradiation enhances the physical and chemical properties of the materials; as the commonly used dosimeters, such as borate films and neutron track detectors, prevent them for providing satisfactory results due to their deficient energy response and other limitations [28]. Continuous efforts have been put forward for the development of new dosimeters to either replace the existing dosimeters based on the modifications induced in the thermoluminescence, optical or structural properties due to neutron irradiations. These modifications are homogeneous in the bulk of the material due to the greater stopping power of the neutrons as they are the neutral particles and do not get influenced by the repulsive field posed by the molecules to the charged particles.

The samples of different polymers, viz. CR-39, CTA, PET, lexan, Makrofol-N and Makrofol-KG, have been sealed in cylindrical metallic containers and got irradiated from neutron irradiation facility at Apsara reactor, Bhabha Atomic Research Centre, Mumbai. The samples were exposed to neutron fluence of range varying between 10^{14} and 10^{18} n/cm^2 in the thermal column of Apsara reactor. Thereafter, the analyses of the structural, optical and etching characteristics of the polymers have been made. UV–Visible (UV–Vis) and Fourier transform infrared (FTIR) spectral studies of the pristine and neutron-irradiated polymer have been made with the help of Shimadzu 1601 UV–Vis spectrophotometer and Perkin Elmer 8000 FTIR Spectrophotometer, respectively. The samples have been etched in 6.25 N NaOH solution at a constant temperature of 70 °C in a constant stirring water bath for different times, whereas polyethylene terephthalate (PET) has been etched at 65 °C. The method of measuring bulk and track etch rate has been explained in detail elsewhere [29, 30].

2.1 Neutron Irradiation Processing and Modifications

Neutron irradiation caused colour transformations to all the polymers. The transparent and clear polymers got brownish tinge on neutron exposure; however, the changes are very small in case of PET. Makrofol-N and Makrofol-KG, originally yellow in colour, also became brown at higher exposures. Neutron irradiation also influenced the morphology of the polymers. Lexan, Makrofol-KG and Makrofol-N become brittle at higher neutron fluences, and it became difficult to handle them under normal conditions due to their delicate nature at higher doses. This hinders their optical and etching studies at a fluence of 10^{18} n/cm^2.

2.1.1 Etching Parameters

The technique of studying the parameters of ion-induced modifications in polymers through track and bulk etch rates was discovered by Fleischer et al. [31] and developed to detect the nuclear particles and to produce porous membranes. The technique is based on exposure of the pristine or treated polymers to the fission fragments of heavy nuclei or to the particle accelerators to create an assortment of latent tracks and then to chemically etch the damaged zone of a latent track to transform it into a hollow channel. The variations in the bulk etch rate, track etch rate and sensitivity of the polymers with neutron fluence have been reported in Table 1. The results reveal that V_B and V_T have been enhanced with neutron fluence; however, the changes are not gradual. Abrupt increases in the etching parameters of lexan and PET occur at a fluence of 10^{18} n/cm^2. The influence of neutron exposure on the track registration properties of the lexan and PET appears to be analogous as is evident from the changes in the etch rates of these polymers. Greatest variations have been observed in lexan, and the least variations have been observed in Makrofol-N and thus might be assumed to be highly radiation-resistant polymer.

The track etch rate has been observed to decrease at a fluence of 10^{14} n/cm^2 for all the polymers; however, the decease persists up to 10^{15} n/cm^2 in case of Makrofol-N. The increase in V_B and V_T may be attributed to the chain scission induced by the recoil protons and other by-products of the nuclear reactions initialized by neutron interactions with the polymeric molecules. Neutrons remove hydrogen from the carbon chain of the monomeric unit of the polymers and produce free radicals [32].

The changes may be primarily due to the production of radicals that get entrapped to the polymer conformation [33, 34]. The needle-like shape of fission tracks changes to circular and oval shape with increasing neutron fluence. The decrease in the sensitivity after neutron irradiation has been found for all the polymers with few exceptions. An increase in the sensitivity at a fluence of 10^{14} n/cm^2 for all the polymers has been observed; however, the increase pursues up to 10^{17} n/cm^2 for lexan.

Table 1 Variation in etching parameters, band gap and Urbach's energy with neutron fluence in case of lexan, Makrofol-KG, Makrofol-N and PET polymers

Neutron fluence (nvt)	V_B (μm/h)	V_T (μm/h)	S	Band gap energy (eV)	Urbach's energy (eV)
Lexan					
0	1.94	26.58	16.21	4.42	0.60
10^{14}	2.58	21.02	8.15	4.36	0.45
10^{15}	1.40	22.21	15.86	4.26	0.35
10^{16}	2.00	32.65	16.33	4.26	0.34
10^{17}	2.53	46.46	18.36	4.05	0.41
10^{18}	11.18	72.59	6.49	3.42	0.58
Makrofol-KG					
0	1.19	44.93	37.76	4.43	0.18
10^{14}	1.49	41.45	27.82	4.40	0.18
10^{15}	2.74	32.23	11.76	4.43	0.18
10^{16}	1.43	45.08	31.52	4.40	1.08
10^{17}	3.60	59.86	16.63	4.34	0.15
Makrofol-N					
0	1.78	32.29	18.14	4.41	0.15
10^{14}	1.18	21.05	17.84	4.39	0.17
10^{15}	2.39	22.79	9.54	4.39	0.26
10^{16}	2.03	24.02	10.85	4.38	0.23
10^{17}	3.92	40.90	10.43	4.24	0.25
Polyethylene terephthalate (PET)					
0	0.91	17.32	19.03	3.97	0.08
10^{14}	1.05	16.36	15.58	3.97	0.03
10^{15}	1.51	20.98	13.89	3.97	0.03
10^{16}	1.18	30.61	25.94	3.97	0.03
10^{17}	1.99	42.94	21.58	3.97	0.03
10^{18}	5.21	57.32	11.00	3.93	0.23

2.1.2 UV–Vis Spectral Analysis

UV–Vis spectrum is one of the oldest techniques used to get the information about the electronic transitions occurring inside the molecules and is based on Bohr–Einstein frequency relationship. A UV–Vis spectrum originates due to the energy absorption by the molecules or atoms in the ultraviolet and visible region of the electromagnetic spectra because of the electronic transitions and thus is a convenient method for estimating the forbidden gap between the conduction and valence optical bands of the polymers. The molecular electrons absorb a quantum of energy in the highest occupied bonded hybridized molecular level, from the UV or visible range of the electromagnetic spectrum, and get excited to the lowest unoccupied nonbonding hybridized molecular energy levels. The electronic states of the

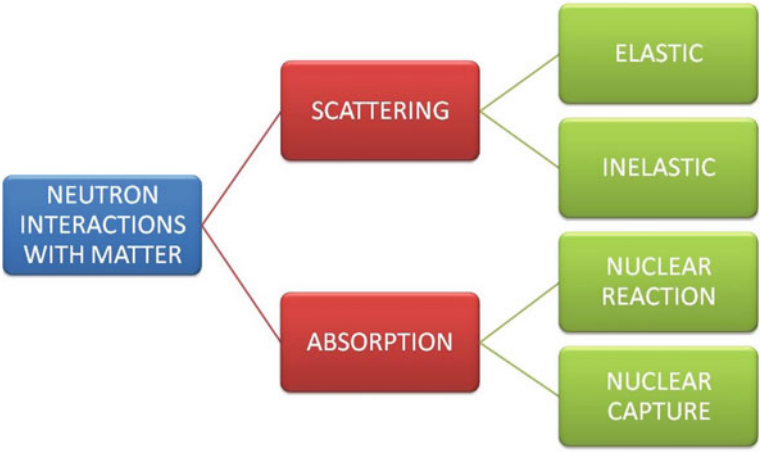

Fig. 1 Various methods of neutron intractions with matter

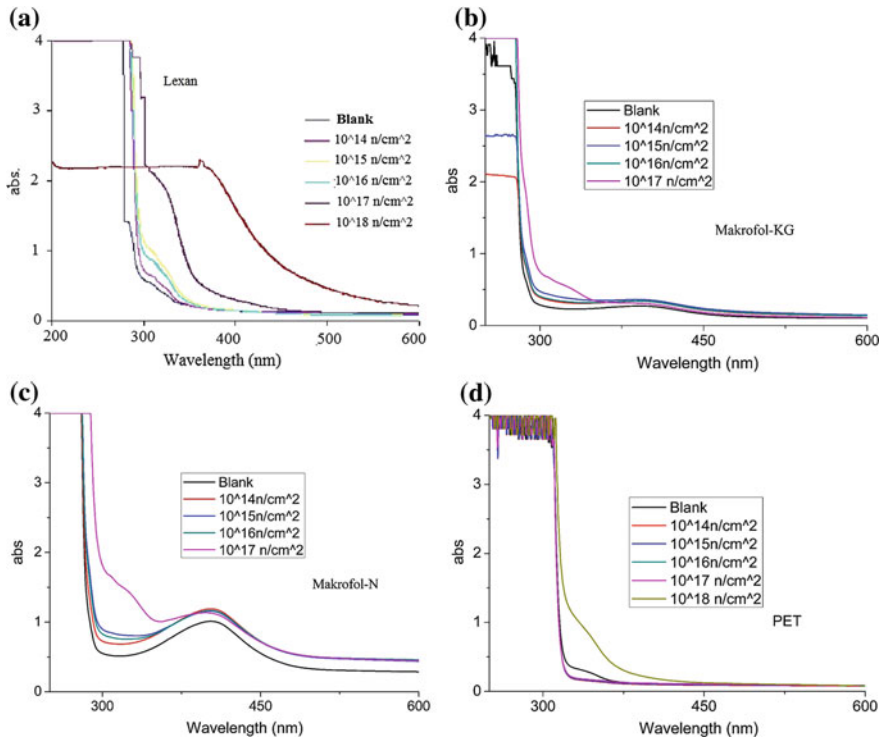

Fig. 2 UV–Vis spectra of neutron-irradiated lexan (**a**), Makrofol-KG (**b**), Makrofol-N (**c**) and PET (**d**)

molecule thus depend on the structure geometry and the symmetry of the molecule and hence correlate the absorbed photons with the structure of the molecules. The UV–Vis spectrum is generally quoted in terms of λ_{max}, the wavelength at which absorption reaches its maximum value and is employed in the range of 200–600 nm. Figure 2a–d shows the UV–Vis spectra of all the polymers irradiated to neutrons. The spectra of pristine samples of each polymer have also been taken to compare the changes induced by irradiations. It is evident from the figure that the absorption edge has been shifted towards longer wavelength with neutron irradiation in all polymers, but the shift is greatest in case of lexan and minimum for PET. The changes are appreciable above a neutron fluence of 10^{17} n/cm^2 for these polymers.

The optical response of the polymers at a wavelength of 345 nm has been calculated and is plotted as a function of neutron fluence (Fig. 3). It is evident from the figure that the optical response of the polymers is directly proportional to the neutron fluence. Thus, the optical response can be used as a parameter to determine the unknown neutron fluence which may find applications in the field of neutron dosimetry. Among all the polymers, the optical response is found to be maximum in case of lexan and minimum for PET. On the basis of above results, it can be concluded that the optical properties of lexan are influenced to the greater extent compared with the other polymers after neutron irradiation. The small variations in PET with neutron irradiation may be attributed to the long-chain periodicity of the polymer.

The band gap and Urbach's energies of the pristine and neutron-irradiated polymers have also been calculated and are reported in Table 1.

The band gap energy of the polymers has been found to decrease with the neutron fluence which indicates the decrease in the resistivity of the polymers and may be attributed to chain scissions induced by neutron irradiations. Farmer [35] was the first to report the increase in the conductivity of polystyrene with irradiation and since then has been studied in many other polymers such as for PMMA [36], polyimide [37], PM-355 [38] and CR-39 [32, 39]. The decrease may be attributed to the increase in the formation of free radicals with neutron irradiation. An exception

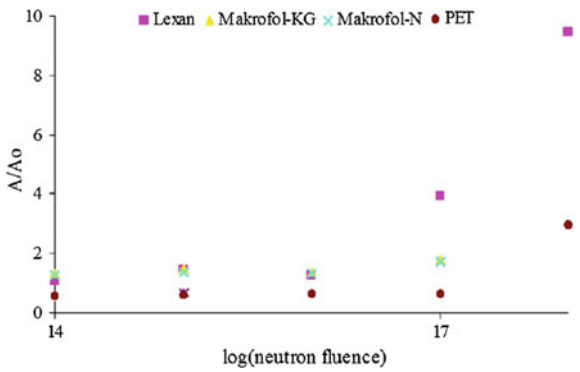

Fig. 3 Optical response $(A/A_o)_\lambda$ versus neutron fluence at a wavelength of 345 nm for the polymers

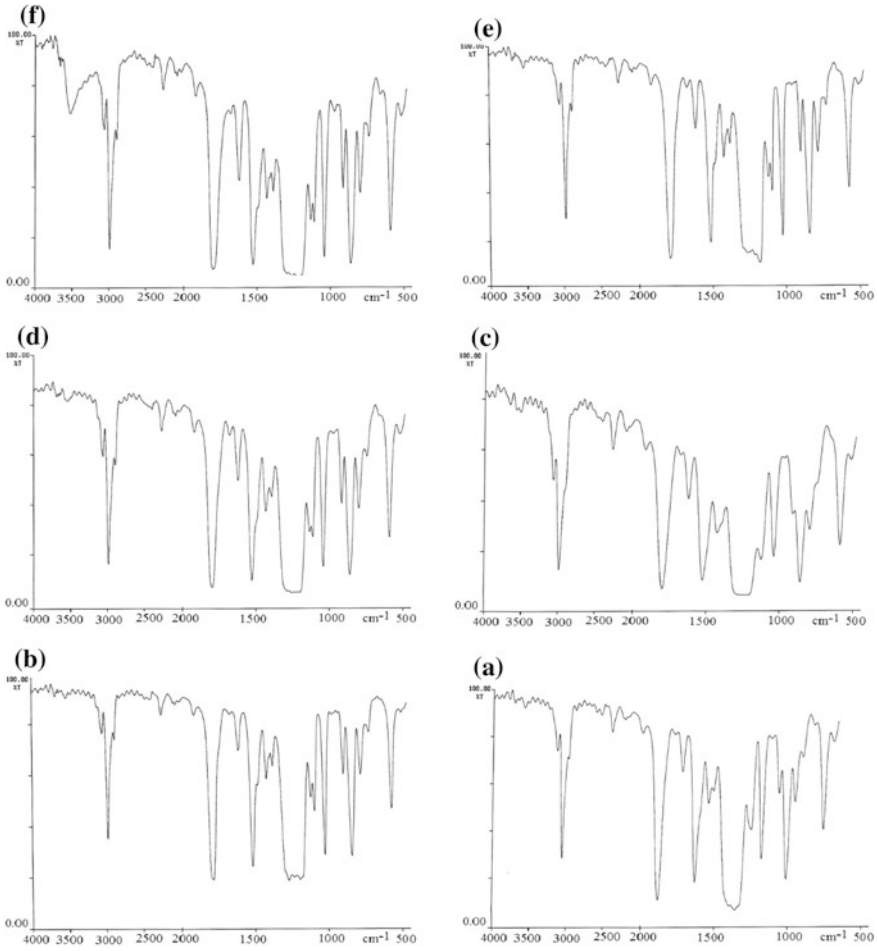

Fig. 4 FTIR spectra of pristine (**a**) and neutron-irradiated (**b–f**) Makrofol-KG

has been observed in band gap energies of all the polymers at a neutron fluence of 10^{16} n/cm^2. A very small change at 10^{18} n/cm^2 has been observed for PET indicating the highest radiation-resistant behaviour of PET among the polymer studied. The stable behaviour of this polymer may be due to its semicrystalline (40%) of the polymer as crystalline structure is more stable compared with the amorphous structure. The response of Makrofol-KG does not seem to be a regular one and is found to obey a zigzag law. The aromatic character of other polymers provides extra stability to them. The additives and dyes used during the manufacture of Makrofol-N and Makrofol-KG may account for the high resistance behaviour of these polymers to neutron irradiation compared with lexan. The severe damage for these polymers at 10^{18} n/cm^2 may be due to the small thickness of these polymers compared with lexan.

The free radicals carrying π-electrons may induce strain in the network, diffuse the states to the forbidden energy level in the band gap and can cause irregularities to the band gap level. The energy associated with such diffusion decays exponentially into the band gap and is termed as Urbach's energy [40]. Urbach's energy for the polymers has been found to increase with neutron fluence except PET. The energy is found to decrease in case of PET at 10^{14} n/cm^2 and remains constant up to a fluence of 10^{17} n/cm^2. However, the value of Urbach's energy increases thereafter at a fluence of 10^{18} n/cm^2. Similarly, in case of Makrofol-KG it seems to remain constant up to 10^{16} n/cm^2 and thereafter increases at 10^{17} n/cm^2. Basha and Basha [41] have also observed a monotonic decrease in the direct and indirect band gap energies of polymer composites of a system of polyvinylpyrrolidone (PVP)/gelatin/DyCl36H2O irradiated to neutron beam and explained the decrease due to the interactions of fast neutrons with the polar groups of the main chain that assists in creation of new intermediate states. These intermediate states allow electronic transitions between different molecular orbits. The authors have also observed random variations in Urbach's tails of the composites irradiated to the neutron of varying fluence.

2.1.3 FTIR Spectroscopic Analysis

Fourier transform infrared spectroscopy covers a wide range of analytical applications in compound recognition and determining the structural modifications induced in the polymers due to irradiations. FTIR is generally carried out to investigate surface chemistry related to the additive treatments, oxidations and irradiation chemistry. Here, FTIR studies have been carried out to study the changes induced in the structural blocks of the polymers by neutron irradiation. The results obtained are shown in Figs. 4, 5, 6, and 7.

Since all the polymers contain carbonyl groups, methyl or methylene radical, thus some common bands have been observed for the pristine samples. The strong and broad absorption band from carbonyl ester bond (>C=O) at 1860–1650 cm^{-1} along with 3650–3500 cm^{-1} attributed to free –OH stretch and above 3650 cm^{-1} for H_2O composition has been indicated in the spectra. The intensity of 1860–1650 cm^{-1} bands in various polymers has been found to decrease and shift towards lower wave number with neutron beam irradiations that may be attributed to the cleavage of the polymers from the carbonyl linkage. The reduced intensity of bands corresponding to free water indicates the evaporation of water entrapped in the polymer cages due to the neutron irradiation of polymers. Except these bands, some other bands or peaks at 2972, 2388 and 1650 cm^{-1} attributed to sp^3 C–H stretch, entrapped CO_2 and double-bonded carbons conjugated to carbonyl groups, respectively, have been found to be common in all the polymers. The peaks have been found to shift towards lower wave number, which may be attributed to inter-hydrogen bonding. However, the peak at 1650 cm^{-1} has not been observed for Makrofol-KG. A band at 2243 cm^{-1} corresponding to C≡C indicates the un-polymerized monomers or some unsaturated molecules left in the polymer

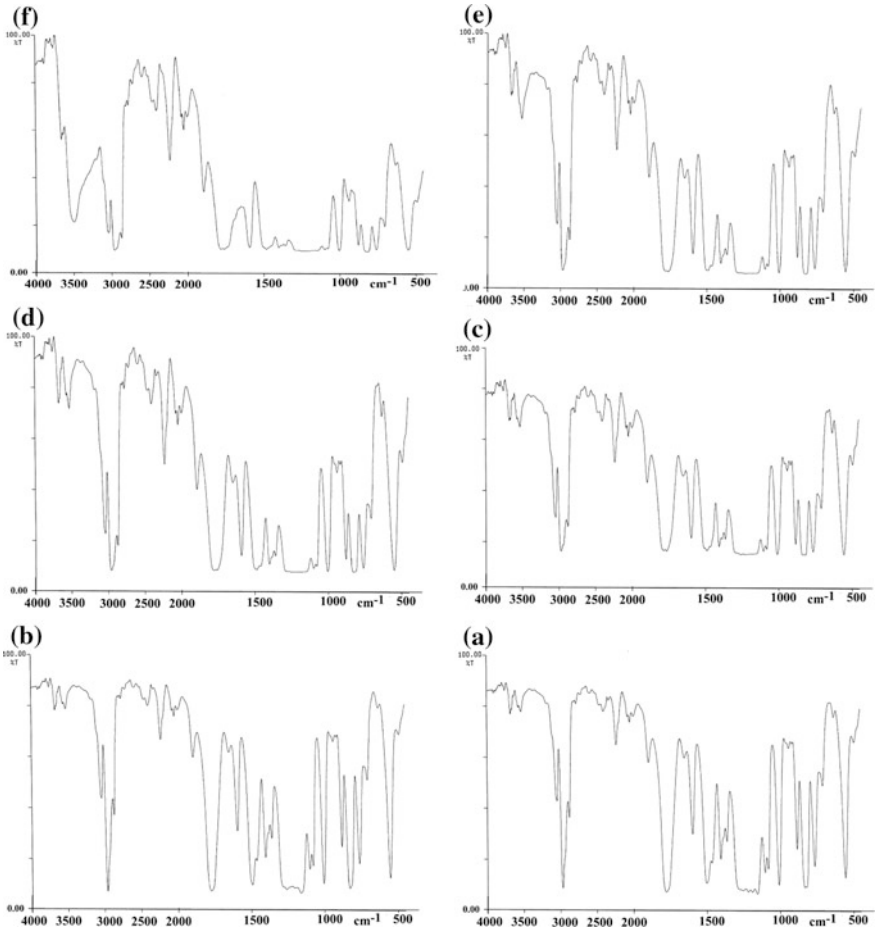

Fig. 5 FTIR spectra of pristine (**a**) and neutron-irradiated (**b–f**) Makrofol-N

during the manufacture. The intensity of the peak has been found to increase with increased neutron fluence indicating the knock off of hydrogen atoms from the polymeric chains. Two or three peaks in the range of 1100–1000 cm^{-1} attributed to –O–C ester stretch have been observed for all neutron-irradiated polymers. A few peaks attributed to the aromatic character of PET, Makrofol-N, Makrofol-KG and lexan have been observed at 3050, 1887, 1503 and 831 cm^{-1}, respectively. These peaks correspond to the aromatic C–H stretch, para-substituted benzene, C=C ring stretch and para-substituted out-of-phase stretching of primary alcohols, respectively. A peak at 1366 cm^{-1} can also be noticed for Makrofol-N that may be due to the presence of $>C(CH_3)_2$ radical, but the same peak seems to be absent for the other two members (lexan and Makrofol-KG) of the polycarbonate family.

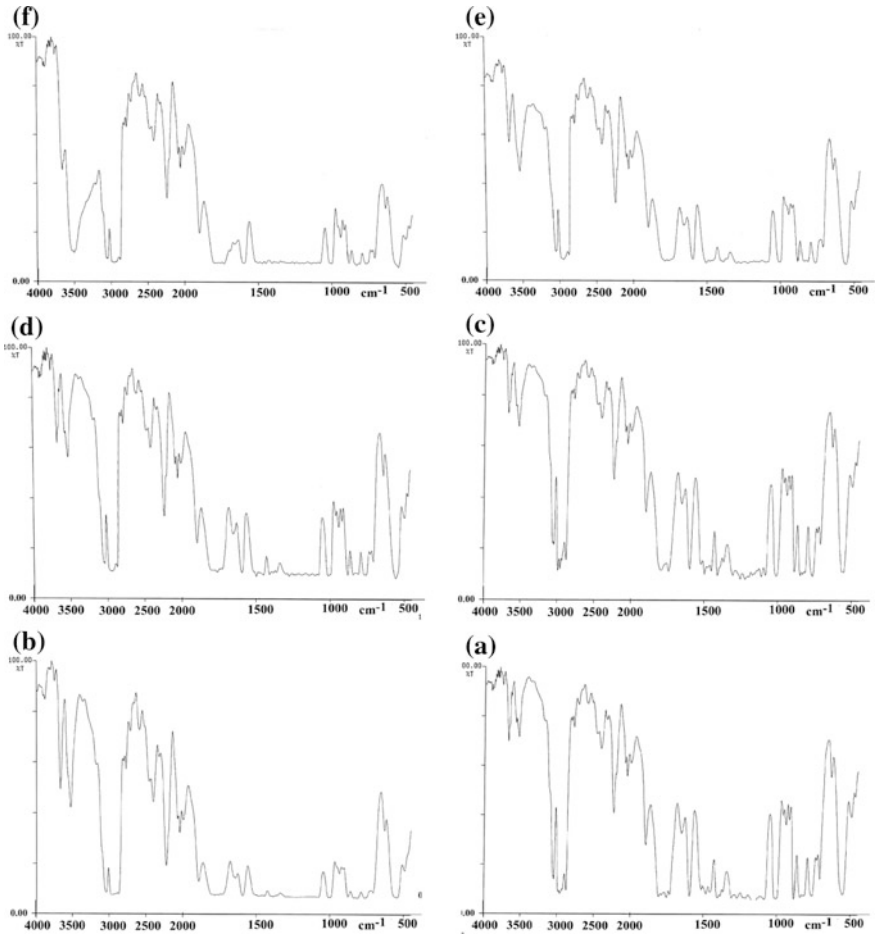

Fig. 6 FTIR spectra of pristine (**a**) and neutron-irradiated (**b–f**) lexan

After irradiation of neutrons, the increase in the absorption peaks or bands corresponding to –OH and CO_2 can be easily confirmed; however, a decrease in the intensity of >C=O is also obvious for all the polymers with an exception at a neutron fluence of 10^{14} n/cm^2. These results indicate the scissoring of the chain at carbonate linkage with production of CO_2, carboxylic acids and alcohols. The increase in the intensity of C≡C may be due to the knockout of hydrogen atoms from the polymeric chains by neutron collisions. The other reason may be the abstraction of hydrogen atoms by the free radicals produced during the neutron irradiation. The appearance of new band near 3700 cm^{-1} in case of PET, lexan, Makrofol-N and Makrofol-KG is the indication of hydrolysis of the polymers by neutron irradiation.

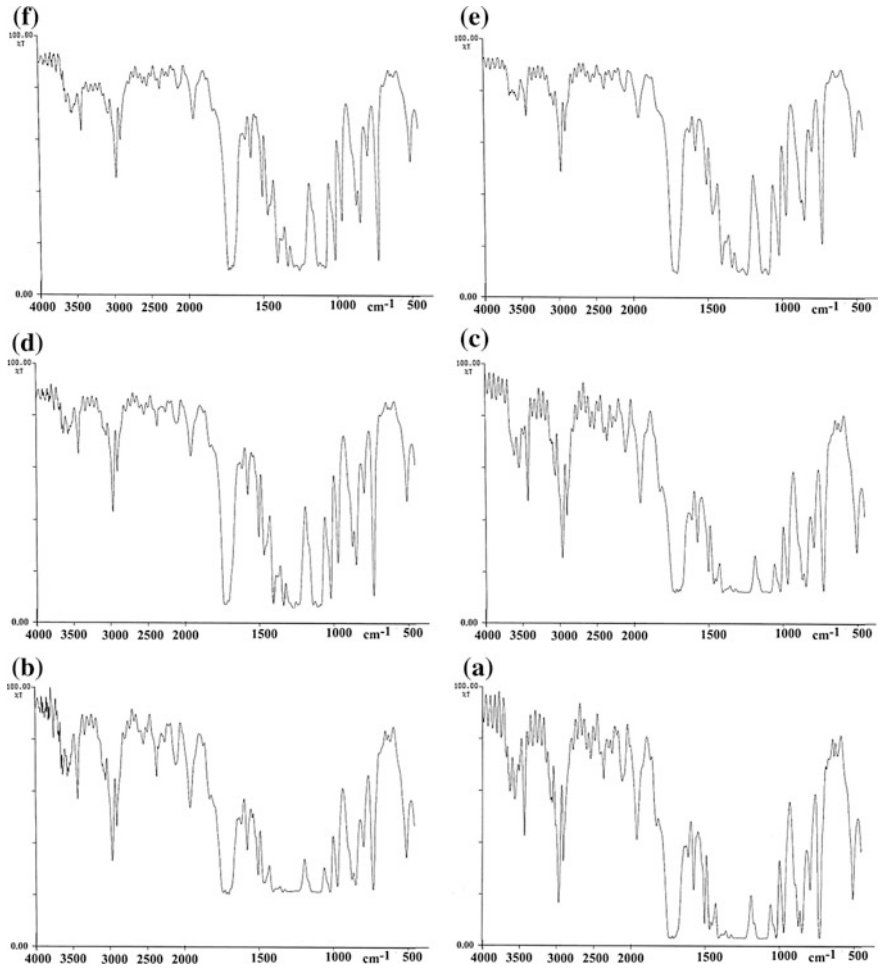

Fig. 7 FTIR spectra of pristine (**a**) and neutron-irradiated (**b–f**) PET

Shift of the bands corresponding to free –OH groups towards lower frequency also indicates the increase in the hydrogen bonding or the polar nature of the molecule. The constancy in the band intensity of C–O–C stretch indicates the stable nature of the chain around this linkage and thus is indifferent to the irradiation conditions. The increase in the out-of-phase olefinic stretch can also be inferred from the spectra of all the polymers. However, a decrease at 10^{18} n/cm^2 is also evident pointing towards the decrease in the out-of-phase vibrations of the olefinic bonds present.

In case of polymers containing benzene ring, the increase in the intensity of out-of-phase primary alcohols also ascertains the cleavage of the polymeric molecule at carbonate linkage and formation of alcohols. The intensity of $>C(CH_3)_2$

in case of Makrofol-N has been found to decrease evidencing the hydrogen evolution or abstraction of H-atom from this part of the chain. The decrease in the intensity of band assigned to >C=C< conjugated with C=O is another evidence of bond cleavage near carbonate linkage. Thus, this linkage could be assumed as the radiation-sensitive linkage in the polymers and responses very fast on irradiation. The decarboxylation of polycarbonates and polyesters under ionizing radiation also ascertains the radiation sensitivity of the carbonate linkage. Out of the three polycarbonates, Makrofol-N seems to be highly radiation-resistant, whereas Makrofol-KG and lexan get easily degraded as is evident from the FTIR spectra of the polymers. A new absorption band at 3514 cm^{-1} seems to appear in case of Makrofol-KG at a fluence of 10^{18} n/cm^2, whereas some bands have been found to disappear indicating the structural modifications in polymers with neutron irradiation.

PET seems to be highly radiation-resistant polymers as new bands have not appeared nor the existing bands disappear at higher fluence. However, the changes in the existing bands are noticeable. The stable nature of PET may be attributed to the semicrystalline nature and the presence of benzene ring in the monomeric unit of the polymer.

The evolution of CO_2 and H_2 in most of the polymers is a well-known fact and is reported by many authors [42–45]. Some of the authors have also tried to recognize the free radicals and ions produced during irradiation and planning a mechanism of degradation [46, 47, 48], whereas others are engaged in finding the yield of these radicals and ions along with the yield of cross-linking and chain scission [49–52] after heavy ion or gamma rays irradiation. However, a very little work [12, 32, 38, 39] has so far been reported on the influence of neutron irradiation on the polymers. Nouh et al [53] have also observed the decrease in the intensities of FTIR absorption peaks at 889, 1778 and 3047 cm^{-1} corresponding to C–O–C, C=O and C–H bonds, respectively, with neutron irradiation of Bayfol indicating the cleavage of C=O and C–O–C through degradation. The authors have, however, found an increase in the intensity of these peaks at higher neutron energies.

3 Conclusions

The above results of neutron irradiation of the polymers lead to draw the conclusions that the neutron irradiation of the polymers induces modifications in the structural and etching properties of the polymers and assists in decreasing the electrical resistivity of the polymers. The carbonate linkage is the cause of radiation damage of the polymers and may be termed as a weakest linkage of the polymers. The technique, thus, could be utilized in industries to produce economic ways of radiation environmental shielding. Some well-established technologies are already exploiting the benefits of radiated materials; however, at higher neutron doses the polymers start to degrade rapidly and hence could not withstand the requirements.

To overcome these shortcomings, composites of lead with polymers could be synthesized and characterized for neutron irradiations.

References

1. Lawrence JH, Lawrence EO (1936) Proc Nat Acad Sci 22:124
2. Warrick EL (1955) Ind Eng Chem 47(11):2388
3. Zirkle RE, Aebersold PC (1936) Ibid 22:134
4. Zirkle RE, Aebersold PC, Dempster ER (1937) Amer J Cancer 29:556
5. Zinkle SJ, Was GS (2013) Acta Mater 61(3):735
6. Sahoo GS, Tripathy SP, Joshi DS, Bandyopadhyay T (2016) J Appl Phys 120:025107
7. Zinkle SJ, Snead LL (2014) Ann Rev Mater Res 44(1):241
8. Gueven O (2004) Advances in radiation chemistry of polymers: proceedings of a technical meeting held in Notre Dame, Indiana, USA, pp 33–39, 13–17 Sept 2003. ISBN 92–0–112504–6
9. Ishigure K, Egusa S, Tagawa S, Tabata Y (1979) Radiat Phys Chem 14(3–6):585
10. Mallick B, Behera RC, Panigrahi S, Badapanda T, Parija B, Behera B, Panigrahi M, Sarangi M (2009) Indian J Phys 83(4):525
11. Was GS (2007) Fundamentals of radiation materials science: metals and Alloys. Springer, New York, Berlin, Heidelberg, pp 4–5
12. Kumar V, Sonkawade RG, Chakarvarti SK, Kulriya P, Kant K, Singh NL, Dhaliwal AS (2011) Vacuum 86:275
13. Malkapur SM, Divakar L, Narasimhan MC, Karkera NB, Goverdhan P, Sathian V, Prasad NK (2017) Appl Radiat Isot 125:86
14. Mallick B, Behera RC, Patel T (2005) Bull Mater Sci 28:593
15. Drobny JG (2003) Radiation technology for polymers. CRC Press, New York
16. Bach RL, Caswell RS (1968) Radiat Res 35(1):1
17. Chikaoui K, Izer rouken M, Djebara M, Abdesselam M (2017) Radiat Phys Chem 130:431
18. Galehdari NA, Kelkar A (2017) J Mater Res 32:426
19. Gourdin WH, Datte P, Jensen W, Khater H, Pearson M, Girard S, Paillet P, Alozy E (2016) Fusion Eng Des 112:343
20. Haq RU, Nadeem S, Khan ZH, Akbar NS (2015) Physica E 65:17
21. Noriega R, Rivnay J, Vandewal K, Koch FPV, Stingelin N, Smith P, Toney MF, Salleo A (2013) Nat Mater 12:1038
22. Qiu J, He D, Sun M, Li S, Wen C, Hattrick-Simpers J, Zheng YF, Cao L (2015) Nucl Instrum Methods Phys Res B 345:27
23. Uusi-Simola J, Savolainen S, Kangasmaki A, Heikkinen S, Perkio J, Abo Ramadan U, Seppal T, Karila J, Seren T, Kotiluoto P, Sorvari P, Auterinen I (2003) Phys Med Biol 48 2895
24. Srivastava AK, Virk HS (2004) Radiat Phys Chem 59:31
25. Damask AC (1958) J Phys Chem Solids 4:177
26. Laghari JR, Hammound AN (1990) IEEE Trans Nucl Sci 37(2):1076
27. Alexander P, Charlesby A, Ross M (1954) Proc Royal Society A 223:1154
28. Griffith RV Hankins DE, Gammage RB, Tommasino L, Wheeler RV (1979) Health Phys 36(3)
29. Prasher S, Singh S (2003) Radiat Meas 36(1):105
30. Singh S, Prasher S (2004) Nucl Instrum Methods Phys Res B 222:518
31. Fleischer RL, Price PB, Symes EM (1964) Science 143:249
32. Nouh SA, Abdel Salam MH, Ahmed Morsy A (2003) Radiat Meas 37:25

33. Paulmier T, Dirassen B, Arnaout M, Payan D, Balcon N (2014) Spacecraft Charging Technology Conference 2014 (13th SCTC), Jun 2014, PASADENA, United States. hal-01081923, version 1
34. Tabata M, Sohma J (1977) In: Grassie N (ed) Developments in polymer degradation, 7 edn. Elsevier Applied Science Publisher, England, p 158
35. Farmer FT (1942) Nature 150:521
36. Fowler JF, Farmer FT (1954) Nature 174:136
37. Mishra R, Tripathy SP, Dwivedi KK, Khathing DT, Ghosh S, Muller M, Fink D (2003) Radiat Meas 36:621
38. Nouh SA, Abdel Naby A, El Hussieny HM (2007) Appl Radiat Isot 65:1173
39. Prasher S, Kumar M, Singh S (2015) Orient J Chem 31(2):1201
40. Goddard PE, Urbach F (1952) J Chem Phys 20:1975
41. Basha AF, Basha MAF (2017) J Appl Phys 122:235104
42. Kamath RM, Barlow A (1965) Anal Chem 37:1266
43. Kondo M, Dole M (1966) J Phys Chem 70(3):883
44. Malek MA, Chong CS (2002) Radiat Meas 35:203
45. Yamauchi T, Nakai H, Somaki Y, Oda K (2003) Radiat Meas 36(1–6):99
46. Shen-Kan I, Pravednikov A, Medvedev S (1958) Dokl Akad Nauk SSSR 122:254
47. Ferain E, Legras R (1993) Nucl Instrum Methods B 82:539
48. Steckenreiter T, Balanzat E, Fuess H, Trautmann C (1999) J Polym Sci A Polym Chem 37:4318
49. Abdel-Fattah AA, Ebraheem S, Ali ZI, Abdel-Rehim F (1998) J Appl Polym Sci 67:1837
50. Abdel-Hady EE, Abdel-Hamid HM, Mohamed HFM (2004) Radiat Meas 38:211
51. Barillon R, Yamauchi T (2003) Nucl Instrum Method B 208:336
52. Hama Y, Oka T, Kodoh H, Seguchi M (2003) Nucl Instrum Methods B 208:123
53. Nouh SA, Mohamed A, Bahammam S (2009) Nucl Instrum Methods Phys Res B 267:2427

Radiation Crosslinking for the Cable, Rubber and Healthcare Products Industry

Andrzej G. Chmielewski

Abstract Review on application of radiation for processing of polymers is presented. The radiation sources like gamma irradiators, electron accelerators and accelerator-based e^{-}/X systems are shortly discussed. Then, the basic information regarding physical and chemical processes undergoing in the irradiated polymers is presented. Finally, the application of radiation technology in cable, rubber and healthcare industry is reviewed; the well-established technologies exist nowadays and are being applied more widely all over the world.

Keywords Polymers · Radiation technology · Crosslinking · Healthcare · Rubber

Abbreviations

PE	Polyethylene
PP	Polypropylene
PS	Polystyrene
PET	Polyethylene terephthalate
PFA	Perfluoroalkoxy alkanes
POM	Polyoxymethylene
PVC	Polyvinylchloride
PMMA	Polymethylmethacrylate
PBT	Polybutylene terephthalate
ABS	Acrylonitrile butadiene styrene
PA	Polyamides
PPA	Polyphthalamide
PSU	Polysulfone
PPSU	Polyphenylsulfone
PEI	Polyethylenimine
PES	Polyethersulfone
PPS	Polyphenylene sulfide
SAN	Styrene acrylonitrile

A. G. Chmielewski (✉)
Institute of Nuclear Chemistry and Technology, Warsaw, Poland
e-mail: a.chmielewski@ichtj.waw.pl

V. Kumar et al. (eds.), *Radiation Effects in Polymeric Materials*, Springer Series on Polymer and Composite Materials, https://doi.org/10.1007/978-3-030-05770-1_12

PI	Polyimides
PAI	Polyamide-imides
PEK	Polyether ketone
PEEK	Polyether ether ketone
LCP	Liquid crystal polymer
COC	Cyclic olefin copolymer
PC	Polycarbonate
PPO	Poly(phenylene oxide)
TPE	Thermoplastic elastomers
LD	Low density
MD	Medium density
HI	High impact
HDT	Heat distortion temperature

1 Introduction

Synthetic and natural reinforced polymers are the youngest materials fabricated for different applications; their history has started more than hundred years ago. A mass scale of production has started when Bakelite was invented in the beginning of twentieth century (polyoxybenzylmethylenglycolanhydride). Material based on a polycondensation of formaldehyde with phenol with the addition of wood flour (finely pulverized wood) was suitable for the production of a casting or pressing objects, while after hardening the material was susceptible to be used even in the construction of a mechanical device. Good mechanical properties in the test with low-pressure electrical conductivity and chemical resistance of the solvents become that bakelite has become a very popular construction material, used primarily in electrical engineering (due to its insulating properties), but also to the production of many articles (e.g., radios, telephones and kitchen hoses). Almost all polymers that are present in the market were developed later: polyvinylchloride (PVC) (1912), PS polystyrene (PS) (1929), polyethylene (PE) (1933), polymethylmethacrylate (PMMA) (1933), polytetrafluoroethylene (PTFE) (1938).

Nowadays, polymeric materials are widely used in many different fields of economy. Polymer plastics are replacing more and more often traditional construction materials; due to the more and more favorable physical and mechanical properties, it is possible to construct on their basis elements of machines, buildings, cars, airplanes and so on. However, to achieve the required properties or shape the polymer-based material has to be processed. To conduct this process, it is necessary to have an adequate information on the material being processed, including rheological properties. The first stage of processing undergoes mostly through a liquid state (melting) and then through processes which depend on melt flow phenomena, followed by solidification of the material by cooling (thermoplastics) or

crosslinking (curable plastics). During the processing of polymeric materials, mixtures and composites, maintaining unchanging parameters during the process determines the achievement of reproducible features and properties of the formed product.

Industries mostly use technologies where processes are run at high temperature and pressure ranges to synthesize or modify plastics, and very often, catalysts are added to speed up the reaction rates. Regarding ionizing radiation, gamma rays or electron beam is a tool which may run chemical reactions even in room temperature. The high-pressure conditions are not a need like the addition of a catalyst. The changes in the materials structure and/or chemical composition may either be beneficial or be undesirable. As the industrial emitters of radiation gamma sources, electron accelerators and X-ray systems (e^-/X) are being used. In the case of isotope sources like Co-60, gamma rays are the energy transmitter to the treated material Electrical machines emitting electrons, accelerators, provides these corpuscular beams in the range from hundreds of keV to 10 MeV, which is a range where artificial radiation is not induced in material. Nowadays, a new powerful X-ray (bremsstrahlung) system applying targets on which conversion e^-/X takes place is being introduced in the market. Due to the fact that conversion efficiency is rather low, an accelerator being a source of electrons has to generate powerful beam to be converted into X-rays [1]. The biggest percentage of materials which are treated by radiation are polymers, whose curing and crosslinking are well developed to the industrial stage [2]. Malcolm Dole and Arthur Charlesby are the founders of crosslinking technique at that time applied for polyethylene [3–5]. Nowadays, synthetic polymers and rubber are being widely processed [6].

2 Radiation Sources

2.1 Gamma Irradiators

Industrial gamma irradiators apply cobalt-60 due to relatively gamma rays with high energy and quite long half-live time equal to 5.27 years. Different irradiators are offered in the market; these differences concern product handling system and source storage method (dry or wet). The wet source storage methods are mostly used nowadays. The scheme of such systems is presented in Fig. 1 [7].

Gamma irradiators are widely used for health products and packaging sterilization [8]; many of them are fabricated from polymers [9]. Such installations can be used to process bulky materials, due to the better, in comparison with electrons, penetration depth. The Co-60 gamma rays lose not more than fifty percent of the initial energy in the penetrated material with surface density of 25 g/cm^2 (0.25 density). However, in the case of gamma irradiators, dose rates are 4–5 orders of magnitude lower in comparison with those obtained in accelerator equipped facility,

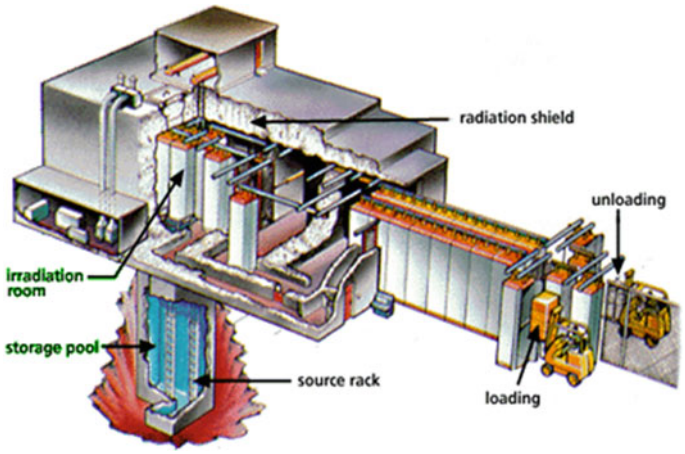

Fig. 1 Gamma irradiator with wet gamma source storage

with the appropriate power of emitter. Processing time in the gamma irradiator lasts for several hours, which may be compensated by processing of large loads, reaching volumes from ten to fifty cubic meters at the same time. This long time of irradiation enlarges non-desirable oxygen diffusion into material effects. Is it possible to apply inert atmosphere in the container, which requires special procedure development?

2.2 Electron Accelerators

An accelerator is a device in which electrons emitted from cathode are accelerated in electromagnetic field. There are three types of such machines: direct current in which constant beam of electrons is extracted; pulsed microwave type, in which beam extracted by titanium foil is repeated at a low frequency rate; and finally pulse or continuous wave type, where lower radiofrequency fields (100–200 MHz) accelerate electrons [10, 11]. Continuous wave radio frequency (RF)-type accelerators provide a DC-like beam current at higher energies. The scheme of different accelerators is presented in Fig. 2.

The history of the first electron accelerators industrial application goes to late 1950s of twentieth century. In those years, high current accelerators were constructed by the GE, HVE and RDI. Using accelerator technology of those years, Raytherm has implemented radiation crosslinking of polyethylene and started manufacturing of ultralight wires (due to thinker insulation) to be applied in the aircraft. Ten years later, ESI developed low-energy (300 keV) linear cathode accelerators for foil and ink curing [12]. Those years also Budker Institute of

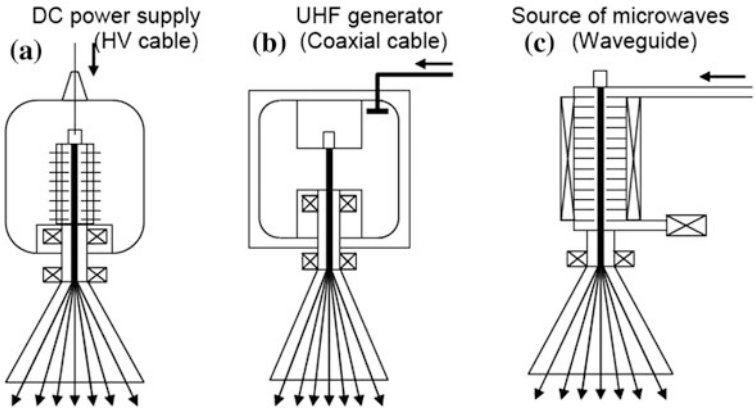

Fig. 2 Electron accelerators applied in radiation processing: **a** direct high-voltage accelerators; **b** single cavity radiofrequency accelerators; **c** linear microwave accelerators [10] (with permission from Nukleonika)

Nuclear Physics in Novosibirsk and the Efremov Institute of Electrophysical Apparatus in Saint Petersburg began producing high current accelerators for industrial market.

2.3 Electron Accelerator-Based e^-/X Systems

Electrons have limited penetration due to their corpuscular character. Gamma rays emitted by Co-60 penetrate ca. 300 mm of water on an equal entrance-equal exit basis. The most energetic electrons used in radiation processing having an energy of 10 MeV penetrate only 38 mm. To overcome these limitations, e^-/X systems were developed. The electron beam is emitted by electron accelerator and then converted into X-rays at metallic (water cooled) target. The efficiency of electron to X-ray conversion is relatively low (7–12%) and depends on the composition of the target material (tungsten or tantalum) and the energy of the electrons [13]. However to good X-rays penetration in the material opens new possibilities of usage this electrical type ionizing radiation generation. Considering 50 kW, 10 MeV, the X-ray photons stream will have 4.17 kW of power. The dual systems are developed, so depending on material density, EB or X-rays are being applied at different beam exits.

The typical dose rates for gamma are 2.8×10^{-3} kGy/s or $\sim$10 kGy/h and 2.7×10^{-2} kGy/s or $\sim$100 kGy/h for X-rays are four to five orders of magnitude lower compared to EB which are capable of delivering 100 kGy/s. Therefore, the product throughput for gamma and X-rays is significantly lower than that of electron beams. An electron accelerator of just 15 kW power is delivering at the same time dose approximately equal to that delivered by a 1 MCi cobalt source.

3 Radiation Processing of Polymers

Chemical processes in polymers exposed to ionizing radiation can lead to many parallel effects: chains crosslinking or degradation, which leads to changing of the double bonds and emissions of low molecular weight gas, mostly hydrogen. The treatment may enhance oxidation of the polymer if oxygen is present, so sometimes processing is performed in inert gas (nitrogen). Chain scission and crosslinking occur simultaneously, but one of them is usually dominant. Predomination of the first phenomena results in reduced tensile strength and elongation, and domination of the second process increases tensile strength but reduces elongation. Importance of one of the processes in the given case depends on the type of polymer processes and admixtures used for its modification. These are stabilizers added in small amounts (< 1%); e.g., tint-based stabilizers are added to polyvinylchloride to prevent the color change during polymer irradiation. The other additives are antioxidant known as "antirads" which prevent oxidation leading to fast product degradation. These additives may react directly with radiation-generated free radicals or act as the primary energy absorbers, limiting radiation effects in polymers. These additives are important to be applied in the case of medical health products made of plastic manufacturing, which in the next technological step before shipping are sterilized by radiation.

3.1 Transfer of Ionizing Radiation Energy to the Irradiated Materials Components

Shortwave electromagnetic radiation (gamma radiation or X-rays) and high-penetration corpuscular (electrons) radiation transfer energy on a continuous, even into high-density matter. Ionizing radiation, in the form of X-rays, gamma radiation, and electrons, produces abundant secondary electrons. Following the primary physical energy transfer events, the ions, secondary electrons, and excited molecules undergo further transformations, exchanging charges and energy and reacting with the surrounding molecules, thereby producing free radicals and other reactive species which finally evolve into new stable products. The processes may be presented in the form of two equations:

$$\text{Ionization} : \mathrm{AB} \rightarrow \mathrm{AB}^{+} + \mathrm{e}^{-} \tag{1}$$

$$\text{Excitation} : \mathrm{AB} \rightarrow \mathrm{AB}^{*} \rightarrow \mathrm{A}^{*} + \mathrm{B}^{*} \tag{2}$$

Electrons knocked out of the electron shell of the atoms of the molecules can be found in the strong positive charge field produced earlier (1). In this reaction, the molecule recovers energy that has previously been consumed for ionization, and the excited molecule can break up into highly reactive radicals:

$$AB^{+} \rightarrow e^{-} \rightarrow A^{*} + B^{*} \tag{3}$$

The above processes after the energy transfer take place in the time interval of 10^{-16}–10^{-11} s. In the next step, the chemical reactions begin; some of the free radicals undergo recombination, and others react with the molecules present in the mixture. The radiation efficiency of the observed reactions is determined by the factor *G*, defined by the number of chemical species produced in the medium as a result of the absorption of energy equal to 100 eV. The final products of radiation-induced reactions arise after a period of 10^{-5} s after the creation of an energy stimulus.

3.2 Radiation Caused Effects in Polymers

For polymers, as for most organic molecules, the ionization energy is 10–15 eV, whereas the bond energy in these molecules amounts to 3–4 eV. Both ions and active radicals are thus formed. Positive charges and large radicals are not very mobile; they can remain trapped in a solid matrix for a long time. Their neutralization occurs as a result of the diffusion of more mobile electrons or by recombination with smaller, more mobile radicals. Trapped ions and radicals can produce in-process effects that are usually unfavorable after-effects. They can be reduced by heat treatment (annealing) or by addition of a mixture of inhibitors or antioxidants. Another observed effect is the so-called oxygen effect. The oxygen molecule has two unpaired electrons and the alkyl radical R* forms an easily peroxide radical:

$$R^{*} + O_2 \rightarrow RO_2{}^{*}, \tag{4}$$

which is very reactive and leads to the detachment of hydrogen atoms H* from an adjacent molecule:

$$RO_2{}^{*} + RH \rightarrow RO_2H + R^{*}. \tag{5}$$

This reaction generates a new R* radical which supports the chain reaction according to the reaction scheme (4). RO_2H peroxide radical is an unstable compound that breaks down at room temperature and creates more radicals, leading to oxygen destructive polymer which can be prevented by the addition of antioxidants. This process is similar to the aging process of polymers subjected to ultraviolet radiation that is a component of solar radiation and oxygen from the air. Other effects occurring in polymers that have to be taken into account when processing them are the generation of certain gases. Depending on the composition of the polymer, they are hydrogen (for polyethylene), methane (for polystyrene), oxide and carbon dioxide (for polyacrylate and polymethylmethacrylate), and also HCl (for polyvinylchloride) and HF (for fluorinated hydrocarbons). The quantities of

produced gases are not large, and their diffusion from the material can be accelerated by thermal treatment. The radiation may initiate the following reactions [14]:

- polymerization,
- crosslinking,
- degradation,
- grafting.

Radiation polymerization is based on the radical mechanism, which runs at low temperatures with high efficiency, but for economic reasons it is only used in the bead polymerization process for the manufacturing of inks and surface treatments (paper, wood panels, films). Polymer co-polymerization is usually used. Short chain molecules with double bonds are mixed with monomer.

Polymers such as polyethylene, polypropylene, polystyrene and polyamides are easily crosslinked. In turn, polymers such as polymethylmethacrylate, polyisobutylene and Teflon are readily degraded (Table 1). The last from the listed processes is grafting. Molecules or monomers with functional groups such as ion exchange can be introduced into the polymer chain, where radical groups are formed. By using ionizing radiation, it is also possible to introduce monomers having functional groups, for example, ion exchange, into the polymer chain. The grafting process can be carried out by pre-irradiating the matrix and then reacting with the monomers or by irradiating the matrix immersed in the monomer solution.

The scheme of radiation-induced polymer degradation is presented in Fig. 3.

Polymer crosslinking process may follow free radical or ion mechanism, leading to the formation of inter-chain carbon–carbon bonds. Equation (6) presents scheme of polyethylene crosslinking due to macro-radicals recombination:

$$-CH_2-\dot{C}H-CH_2- + -CH_2-\dot{C}H-CH_2- \rightarrow \begin{array}{l} -CH_2-CH-CH_2- \\ \quad\quad\quad\quad | \\ -CH_2-CH-CH_2- \end{array} \tag{6}$$

Table 1 Radiation effects on different polymers

Mostly crosslinking	Mostly degradation
Polyethylene	Polyisobutylene
Polypropylene	Polymethylmethacrylate
Polyacrylates	Polymethylstyrene
Poly(vinyl chloride)	Polyvinylidene chloride
Poly(vinyl alcohol)	Polytetrafluoroethylene (teflon)
Polysiloxanes	Polypropylene ether
Polystyrene	Polycarbonates
Polyacrylamides	Cellulose
Polyamides	Butyl rubber
Ethylene-vinyl acetate	
Natural latex	
Phenol-formaldehyde resins	

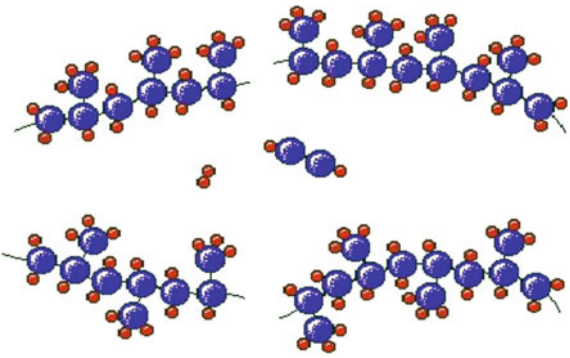

Fig. 3 Scheme of the radiation of polymer degradation, chain disruption and the formation of low molecular weight by products. The ends of the chains are reactive

During irradiation of PE there are micro-regions where temperature increase what is fostering radical diffusion. Crosslinking may undergo mixed ion–radical mechanism as well:

ionization:

$$-CH_2-CH_2-CH_2-CH_2-\xrightarrow{\text{radiation}}-CH_2-CH_2-\overset{+}{C}H-CH_2-+e^- \tag{7}$$

hydrogen atom transfer:

$$\begin{aligned}&-CH_2-CH_2-\overset{+}{C}H_2-CH_2-+-CH_2-CH_2-CH_2-CH_2-\rightarrow\\&-CH_2-CH_2-\overset{+}{C}H_3-CH_2-+-CH_2-CH_2-\dot{C}H-CH_2-\end{aligned} \tag{8}$$

hydrogen atom abstraction:

$$e^-+-CH_2-CH_2-\overset{+}{C}H_3-CH_2-\rightarrow-CH_2-CH_2-\dot{C}H-CH_2-+H_2 \tag{9}$$

Free radicals formed due to mechanism given in Eqs. (8) and (9) undergo recombination, creating inter-chain bonds in accordance with Eq. (6). During primary radiolytic process, positive holes are formed in the polyethylene, which migrating along the chain reacts with $-CH_2-CH_2-\dot{C}H-CH_2-$ radical. Ion formed in this reaction interacts with neighboring chain of polymer forming crosslink between them in accordance with Eqs. (10) and (11):

$$\begin{aligned}&-CH_2-CH_2-\overset{+}{C}H_2-CH_2-+-CH_2-CH_2-CH_2-CH_2-\rightarrow\\&\quad-CH_2-CH_2-CH-CH_2-\\&\rightarrow\qquad\qquad\quad|\qquad\quad+H_2^+\\&\quad-CH_2-CH_2-CH-CH_2-\end{aligned} \tag{10}$$

or

$$
\begin{aligned}
&-CH_2-CH_2-\overset{+}{C}H_2-CH_2- + -CH_2-CH_2-CH_2-CH_2- \rightarrow \\
&\quad -CH_2-CH_2-\overset{+}{C}H-CH_2- \\
&\rightarrow \qquad\qquad\quad | \qquad\quad + H_2 \\
&\quad -CH_2-CH_2-CH-CH_2-
\end{aligned}
\tag{11}
$$

The sketch of the process mechanism is presented in Fig. 4.

When polyethylene is crosslinked by ionizing radiations, the thermal stability of the material is improved through the formation of a three-dimensional structure. The irradiated polyethylene acquires some valuable performance properties superior to those of non-irradiated polymer: does not melt above melting point characteristic for virgin material; loses its ability to dissolve in hot organic solvents; swelling degree is lower; has better chemical resistivity to corrosive media; the electrical breakdown is higher; the tendency to cracking under mechanical stress and chemical reagents is lowered; has acquired ability to reassume a shape fixed during the radiation exposure after the material has been deformed in the heated (fused) state, etc.

According to these mechanisms, radiation processing of polymers may upgrade their properties that they become high-tech materials ("high performance plastics"), which is illustrated in Fig. 5. These processes can be used to process substrates of ready-to-use products. However, even in the same type of polymer coming from different manufactures, in case of some which are easily crosslinked, strength at

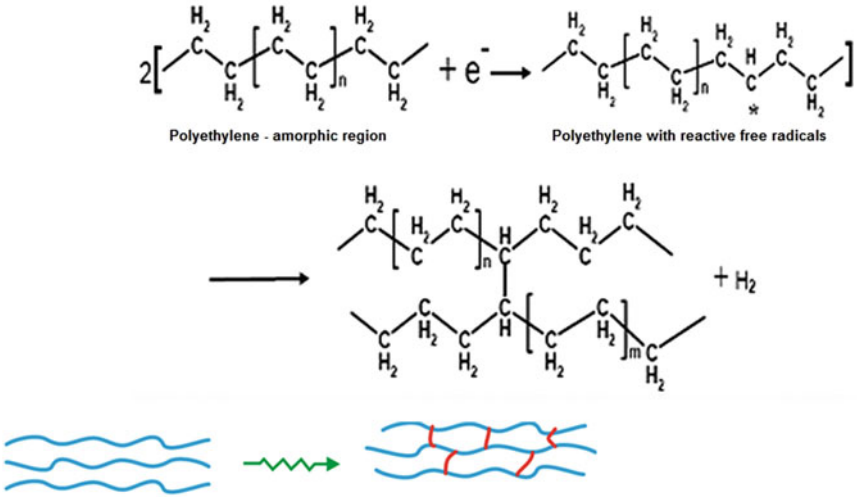

Fig. 4 Scheme of polyethylene crosslinking. Hydrogen generation occurs in the case of CH-type polymers

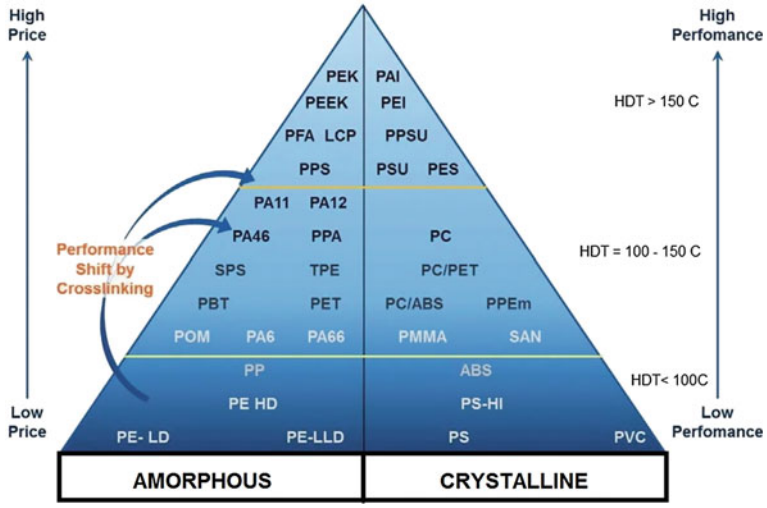

Fig. 5 Polymer properties and value can be upgraded by radiation

break is usually growing and for others less susceptible to radiation crosslinking was reduced. Similar dependence was found for elongation at break. For polyethylenes demonstrating high strength at break, the efficiency of radiation crosslinking is limited [15].

4 Cable Industry

Chemical crosslinking is mainly used in the cable industry which requires application admixed to material crosslinking agents in the thermal polymer processing process. The most important among them are peroxide crosslinking and silane crosslinking. From these two techniques more often used is the first one which based on the introduction of organic peroxides and product damage preventing antioxidants into the polymer. An organic peroxide (ROOR—usually dicumyl peroxide) admixed to the polyethylene decays at 160–205 °C into free radicals: $2RO^{\cdot}$, which then initiate active free radical centers in the polymer chains. By combining two centers located on adjacent polyethylene chains, crosslinks between molecules happen. The process is carried out under the pressure 1.2–2 MPa, and cable is heated by direct heating system, steam or hot dry nitrogen.

The silane method is fundamentally different from the above method. The process takes place in two stages: First, the silane is grafted onto polyethylene as a result of the radical reaction initiated by peroxides (e.g., during the cable insulation extrusion process), and then, this substrate containing grafted PE and catalysts is crosslinked gradually during prolonged action of water or low-pressure steam. As a result, a silane group is built-in between the two polyethylene chains. Introduction

of the silane group degrades the mechanical properties of the material, because the C–C bond is more durable than the silane bond. In addition, the introduction of silane groups significantly affects the electrical properties of such a modified polymer, whereby mainly dielectric loss and dielectric strength are deteriorated. However, it should be mentioned at the same time that one of the properties of the polymeric material after the crosslinking process is the lack of the possibility of its melting. This feature makes it impossible to make any permanent and tight connections by melting at elevated temperatures and also significantly impairs the recycling of used cables and wires, economically justified due to the high prices of non-ferrous metals. Radiation crosslinking is one of the methods of physical modification of polyethylene. It consists in detaching hydrogen atoms from the polyethylene chain due to the action of high-energy radiation. Crosslinking of polyethylene using this method takes place in a solid phase. During the process, the melting temperatures of the material are not exceeded, which allows to retain the initial structure in the polymer without reducing the content of the crystalline phase.

Radiation crosslinking is technically and economically feasible as a pure physical process, i.e., without the addition of sensitizers and phenomena, occurs at room temperature or at temperature up to about 60 °C and affects mechanical, thermal, rheological and other properties. The following is observed: increase in breaking strength and Young's modulus; increase in the resistance to solvents in which non-crosslinked polyolefins dissolve aggressive chemicals, fats, oils, caustic inorganic substances; increase in dimensional stability, the ability to deform under the influence of heating (heat resistance); increase in the resistance to the electric arc; increase in the resistance to flame. They do not melt, but soften, like thermosetting polymers. The use of ionizing radiation for the crosslinking of cable products allows to obtain modern materials characterized by: lower insulation thickness (which reduces the weight of cables), greater flexibility and higher continuous operation temperature compared to classic wires with the same current and voltage parameters, higher resistance on the flame with a complete lack of halogen in its chemical composition, hence low toxicity of decomposition products and low smoke levels as well as low flame propagation, better strength properties, including abrasion resistance, very high resistance to chemical agents, including industrial and propulsion oils, UV radiation, ozone and many similar factors. Irradiation of wires and cables with electron beam is nowadays increasingly applicable, since radiation treatment significantly improves the mechanical and physicochemical properties of insulation. Radiation technology is used in the cable industry to improve abrasion resistance, scratching and cracking, increase chemical resistance to solvents and oils, increase impact strength, reduce flammability and improve the electrical properties of insulation. It is also a method that can be used to inhibit the migration of plasticizers and increase the durability of the material at both low and high temperatures. It is important that with the improvement in insulation quality, its thickness can be reduced. The main aspects of radiation cable crosslinking technology are related to the following issues: selection of raw material for insulation/sheathing, distribution of the absorption dose in thin layers in the context of high-energy electron beam range, homogeneity of the crosslinking process and

Table 2 Radiation crosslinked materials for cable and wire insulation [16]

Polymer	Crosslinking dose [kGy]
PE	200–300
PE (sensitized)	100–150
EPDM	100–150
PVC (sensitized)	50–80
Sulfonated PE	180–160
Polyvinylidene fluoride	80–150
EPR	50–150
Ethylene-tetrafluoroethylene copolymer	60–100
Silicone rubber	200

dosimetry, thermal effects induced by ionizing radiation in copper insulation and veins or aluminum, inter-surface phenomena, etc. Radiation technology is mainly used for the modification of plastics made on the basis of polyethylene and vinyl acetate. Some elastomers used as insulation (EPDM—ethylene-propylene diene terpolymer), or shields (Hypalon—chlorosulphonated polyethylene) are also crosslinked. All PEX-type insulation of tubing is based on LPDE. For selected types of EPDM, in order to achieve near crosslinking, the absorption dose is in the range of 100–150 kGy (Table 2). Crosslinking changes the characteristics of the polymer—from a thermoplastic it changes into an elastomer. Process crosslinking can be carried out during extrusion, or after it's finished. According to ASTM F 876-93, the degree of crosslinking should be between 65 and 89%—higher can lead to polymer brittleness and loss of resistance to blow. It is expected that products made of PEX can be used for 50–200 years.

High dose rate is more productive if continuous process is considered; therefore, electron accelerators have advantages over isotope sources. The high dose rates in the electron beam will render radiation processing of cable wire possibly directly while the objects are being passed through the exposure zone. The short dwell time of cable in the beam irradiation zone reduces oxidation effects to minimum. However, on the other hand, due to the low heat conductivity of polymers, measures regarding cooling have to be considered. Two or more wires may be wrapped concentrically, separated by insulation, to form coaxial cable (Fig. 6). The conductor is made of copper or alumina, and the used material has different heat and electrical conductivity from polymer made insulation. Such construction of the cable/wire requires optimization of irradiation process to assure proper dose absorption in the material leading to the uniform crosslinking [17].

Different types of outer and inner insulations [18] are applied which exhibit the specific features as an object of irradiation: (1) a typical heterogeneous system (current-carrying cable core and the insulation) with a low polymer/metal weight ratio, (2) long length with small outer dimension, (3) the insulation is subjected to radiation-promoted oxidation in irradiation in air. The processes ongoing on

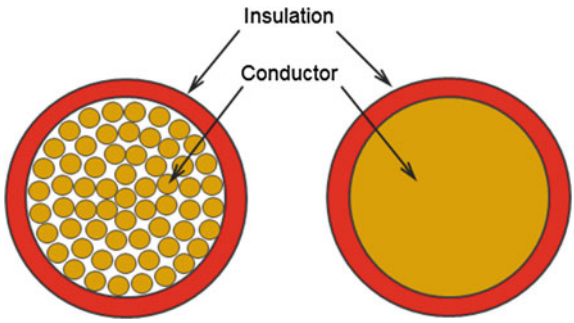

Fig. 6 Single and multi-wire cable construction

Table 3 Temperature increase in the metal core during irradiation

Metal	Mg	Al	Fe	Cu	Ag	Pb	Pt
Specific heat capacity [J/g °C]	0.98	0.90	0.45	0.38	0.24	0.13	0.14
Temperature after 35 kGy [°C]	60	64	103	117	171	294	275

Table 4 Increase in temperature under irradiation for selected polymers

Polymer	Specific heat capacity [J/g °C]	Increase of temperature [°C/kGy]
Nylon 6	1.67	0.60
Polyethylene	2.30	0.43
Polypropylene	1.92	0.52
Polystyrene	1.34	0.75
Polytetrafluoroethylene	1.05	0.95
Polyvinylchloride	1.34	0.75

metal/polymer interfaces are effected by: hydrogen release, thermal processes (heating of the polymer by metal heated by EB, Table 3), possible corrosion (Table 4).

The above negative phenomena can be reduced or eliminated by decreasing thermal effects in metal wire, by controlling EB intensity and by intensive cooling. The dose applied and its homogeneity are important parameters [19]. The irradiation of the wire or cable in single pass leads to non uniform dose distribution on the insulation layer depending on their pathway under the accelerator beam (Fig. 7).

To assure homogeneity of dose absorption, multi-pass irradiation is performed in the way presented in Fig. 8 with cable twisting. The system applying this technique is presented in Fig. 8; the twisted cable moves from the center to right and left side of the under-scanning horn device.

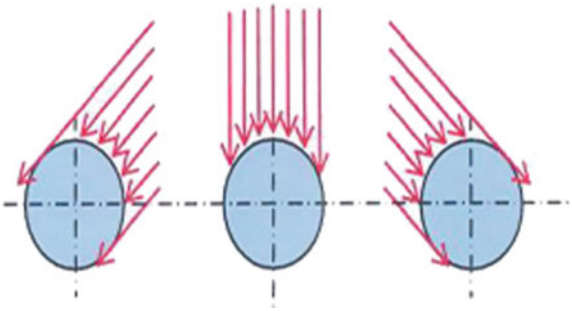

Fig. 7 Electron beam cable irradiation depending on its position under the horn [20]

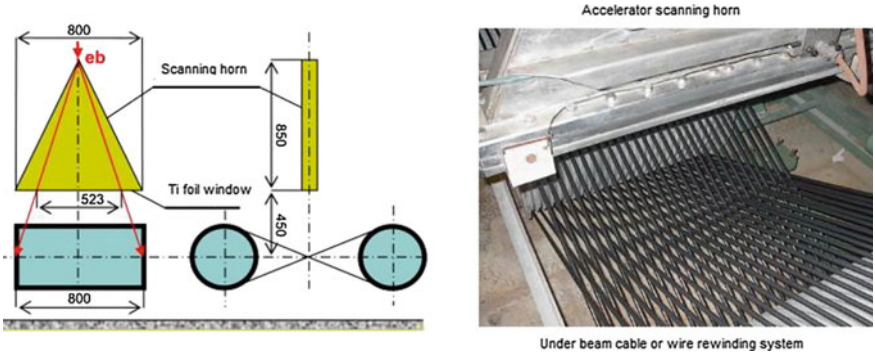

Fig. 8 Under beam system for cable or wire rewinding [20]

Depending upon the cable thickness and stiffness, and on the EB voltage, under beam facilities can be arranged in one-, two- or four-sided irradiation configurations. The irradiation technique is adjusted to the cable diameter and insulation thickness, the requested dose and its homogeneity, and electron beam power and electrons energy [21].

5 Rubber Industry

The greatest practical use in the industry among all the natural polymers found natural latex, which after crosslinking with sulfur becomes a durable material—rubber. Rubber is used for manufacturing tires and many other products. The curing process, called vulcanization, is a slow process lasting up to eight hours. A typical car tire is vulcanized at 150 °C for about 15 min. This time can be shortened by the addition of accelerators such as 2-mercaptobenzothiazole (MBT) or tetramethylthiuram disulfide (TMTD). Both of these compounds contain a sulfur atom

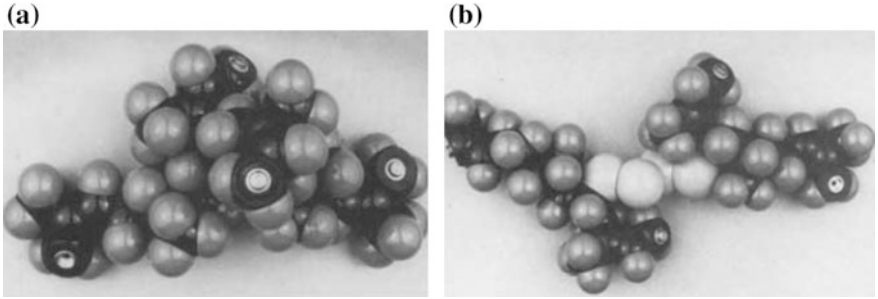

Fig. 9 Crosslinking of natural latex; **a** bridge –C–C– type, **b** bridge –S–S_x–S– type [22]

Table 5 Energy of the crosslinking bridges in rubber [22]

Bond type	Bond energy (kJ/mol)	
–C–C–	351	
–C–S–C–	285	(–C–S–)
–C–S–S–C–	267	(–S–S–)
–C–S_x–C–	<267	(–S–S–)

that initiates sulfur-rubber chain reactions. Vulcanization by sequentially forming network bonds through sulfur bridges –S–S– (Fig. 9b) is a well-defined process [22]. Considering the interconnection of two polymer chains as the mechanical bond in the formed structure, their quantity and elasticity determine the mechanical properties of the material. The tread of a tire subjected to mechanical stress requires the use of multi-axis bridges of minimum density (high M_c-molecular weight of macromolecules between successive grid bonds). Radiation crosslinking based on the C–C– bond formation (Fig. 9a), which is stronger (Table 5) in comparison with the S-bond (Fig. 9b), leads to a higher crosslinking density and therefore a lower M_c value and lower tensile strength (Fig. 10).

Ionizing radiation leads to simultaneous degradation of macromolecules and their crosslinking. Such a structure does not provide good mechanical performance of the rubber, only ensures the stability of the raw tire components, and the vulcanization is brought to an end by using a further thermal process utilizing the sulfur present in the semi-finished product. By using hydrogen peroxide, however, the process with the addition of a chemical reagent runs until it is completely depleted. The ionizing radiation crosslinking process can be controlled by the appropriate timing of physical stimulus externalities, thus providing better flexibility in selecting optimal performance parameters.

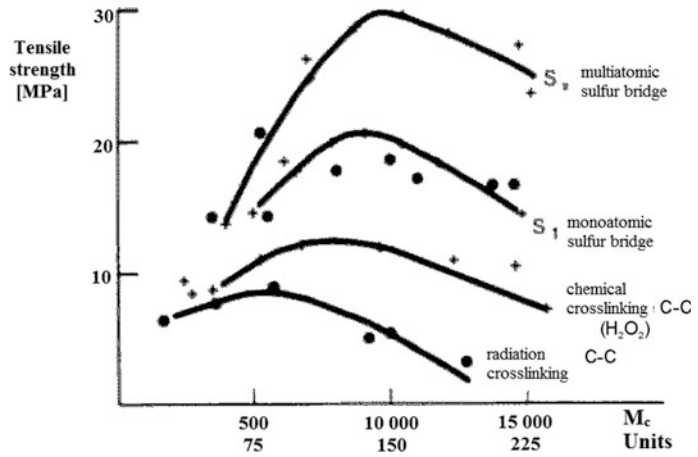

Fig. 10 Tensile strength for rubber crosslinked by different methods (M_c-molecular weight of macromolecules between successive grid bonds) [22]

5.1 Tire Industry

The tire manufacturing process is a complicated process. The tire is built from many layers: body ply, inner liner, tread, sidewall and bead and is finally reinforced with a steel cord. The set of these components is called green (raw) tire, which is then vulcanized at high temperature and pressure. If cord would be displaced in body ply (Fig. 11), the defective tire may be easily destroyed during its exploitation which may lead to fatal accident.

Conventional way to prevent such events was the usage of the thicker body play which leads to higher weight of the final tire. The radiation prevulcanization avoids such necessity. It is important that in the vulcanization process of the raw tire in the mold, there are no displacement and the immobilization layer and the internal tread components. The tire is subjected to irradiation to give the tire a firm support in the

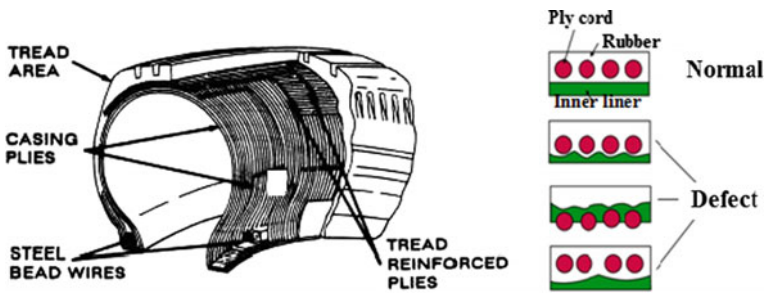

Fig. 11 Radial tire cross-section and possible defects due to components displacement during mold heat vulcanization

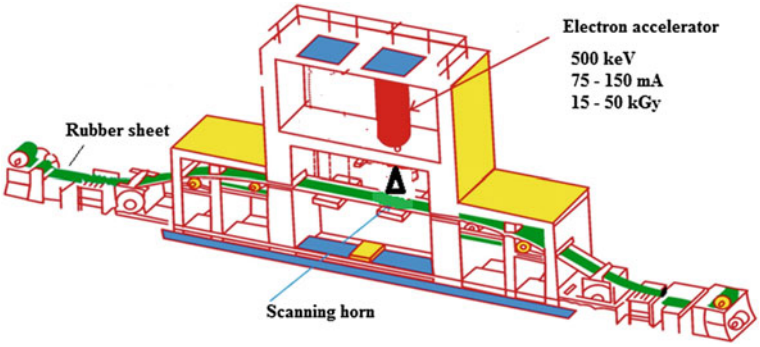

Fig. 12 Scheme of accelerator facility for rubber sheet irradiation

correct position of the tire reinforcement before it is integrated with the rest of the finished product and vulcanization. For this purpose, pre-electron beam crosslinking is used to pre-increase the mechanical strength of the raw mixture. Pre-beamed electron beam crosslinking allows a uniformly shaped element of the rubber blend to be uniformly formed without changing its thickness over the entire surface and without the mold mixture flowing out. The advantage of using this process is the reduction in discarded tires of non-standard dimensions, the possibility of using a higher percentage of synthetic rubber in the mix, and finally savings in the amount of expensive raw material used. The tire produced by this technique is lighter than the tire produced using traditional technology [23]. Doses applied in the process are equal to 15–50 kg, and electron accelerator to be used is a low-energy machine ~500 keV with 75–150 mA (Fig. 12). Such machine can process 30,000–50,000 plies per day.

In Japan, more than 92% of radial tires for passenger cars and more than 70% of truck tires are manufactured using this technology [24].

6 Medical Devices Industry

6.1 Radiation Vulcanization of Latex for Medical Use

Latex vulcanization with sulfur is performed by heating and traces of toxic product are formed during this process; nitrosamine is formed and detected in the final product. Radiation vulcanization of natural rubber latex (RVNRL) was elaborated in Japan [25]. The crosslinking sensitizer is *n*-butyl acrylate dose applied which is equal to 15 kGy. No nitrosamines are present in the product, and amount of extractable proteins is smaller in comparison with conventional process. Pilot plants have been constructed in some countries of Southeast Asia.

Another use of the radiation technique is the production of hydrogel dressings whose production process consists in crosslinking water-soluble polymers [26]. A typical hydrogel dressing is an aqueous composition of natural and synthetic polymers such as polyvinylpyrrolidone, polyethylene glycol and agar, which are subjected to electron beam irradiation and perform two functions in the production process: It causes crosslinking of polymeric chains and ensures sterility of the dressing. A similar dressing with biodegradable chitosan-degraded radiation has been developed, which improves the medical effectiveness of the product [27]. PE foam products for medical devices are made in a unique radiation process [28].

7 Other Industrial Applications

Radiation crosslinking of thermoplastic polymers is the most widely used technology due to the new properties of material after processing (do not melt, are stable in higher temperatures, are resistant to solvents); the thickness of the cable insulation (see paragraph 4) and the strength of the XLPE pipes (hot water pipes and metal inserts) used in the water supply and underfloor heating systems can be reduced [29]. Normal crosslinked pipes exhibit stability at temperatures lower than 70 °C. Crosslinked pipes exhibit good, stable mechanical properties even at temperatures up to 110 °C [29, 30]. For decades now, plastic pipes made from HDPE have been radiation crosslinked in order to ensure that they keep their performance characteristics for a very long time (Fig. 13). Of particular importance is their improved durability with respect to high temperatures and internal pressure.

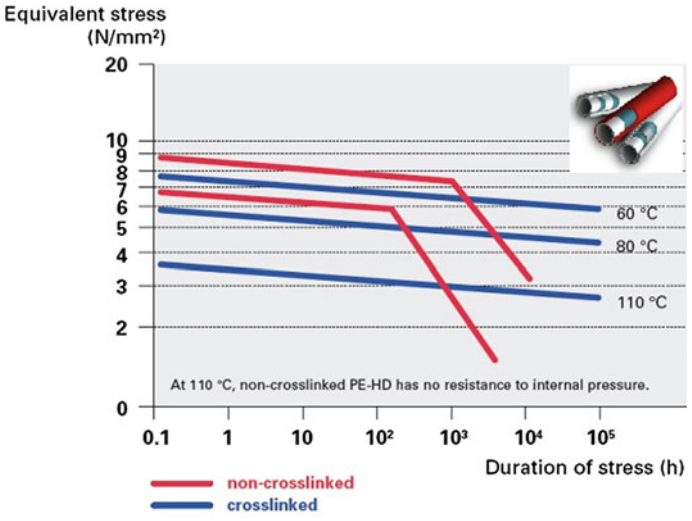

Fig. 13 Long-term durability of HDPE under internal pressure [29] (with permission from BGS)

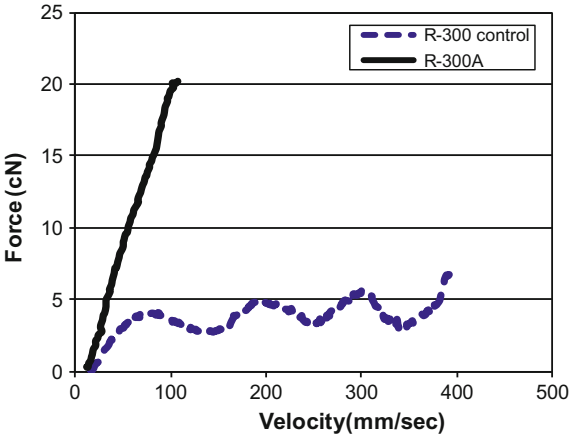

Fig. 14 Comparison of LLDPE, Linear, R-300 Control and R-300 A. The R-300A is manufactured by radiation modification of the polymer [32] (with permission from Sterigenics)

Nylon 66 is a high tensile material with good impact properties, widely used in the manufacturing of electrical and electronic materials. They are made of plugs and couplings, coil bodies, spools, etc. However, solder circuits and wires are increasingly used unleaded, so that the plastic on which the assembly is made must withstand a temperature of 260 °C for 60 s. Such requirements correspond to the compacts obtained by mixing Nylon 66 with crosslinking agent and then irradiating the blend with electron beam. The material thus obtained, having good molding properties, can be used for assembling solderless solder systems. It is also resistant to open fire and has a temperature index of 104 °C, which means that at both temperatures Izod impact strength, tensile strength and bending are reduced to 50% of the initial value of 60,000 h of aging [31, 32].

Another application of the radiation treatment associated with the preparation of the special-purpose blend is the change in rheological properties of linear polyolefins such as high-density polyethylene (HDPE) and linear low-density polyethylene (LLDPE). Sterigenics produces HDPE and LLDPE polyethylene blends using an electron beam processing process. Such prepared materials exhibit high mechanical strength in liquid state. Such properties are obtained by forming branches on the long chain of polyolefins and forming a spatial structure, without crosslinking the polymer. The content of the gel fraction is less than 0.4%, so that the product in 100% can be reprocessed. These special properties of the material are well illustrated in Fig. 14 [32].

Ordinary LLDPE exhibits alloy instability or resonance variations in the jet thickness at pull rates of 70 mm/s. Raprex R300 crack strength at break point (70 mm/s) is three times greater than that obtained for linear polymer. That is why it is a much better material used for the production of foil and foams. The product obtained is characterized by a constant thickness, and the case of foams has better bubble stability [32].

8 Conclusions and Challenges for the Future

The relatively high cost of radiation processing (RT) is a reason due to which traditional chemical installations cannot be replaced in all the applications by this technology. The effects have to be favorable from economical or technical points of view. Unique features of radiation treatment are relatively simple, efficient and easy to control way of creating free radicals [33]. The most important applications are polymerization monomers when use of other methods is not possible, and this, in any state of matter (liquid, gas, solid), provides polymerization at any temperature (e.g., room temperature), resulting in the manufacturing of pure polymers without additives like initiators, catalysts or other admixtures. Then, RT provides the opportunity of polymerization in technologically difficult conditions (e.g., inside parts of machines), crosslinking of the plastic after its formation, surface modification by grafting, etc. It is possible to perform simultaneous polymer modification with object sterilization. The broad review of the technology is given in recently published two-volume book [14]. Surface curing with low-energy electron beams (70–300 keV) is the fastest growing market segment because of the improved energy efficiency of these high-speed processes and elimination of volatile organic solvents from the manufacturing process.

On the commercial development stage are additional new fields involving natural polymers, nanotechnology as nano-composites and nano-gels and the greater use of grafting. The future of the technology will depend on further development of radiation sources, especially powerful e/X systems for which the limitations regarding processed materials density and thickness are not so much limited as in the case of electron beam. The accelerators of tomorrow promise still greater opportunities. Next-generation particle beams represent cheaper, greener alternatives to traditional industrial processes [34]. On the other hand, some new commercial applications have emerged in recent years: the use of low-energy EB to cure the pigmented coatings on metal coil stock. Therefore, all type of radiation sources: gammas, electron accelerators (low keV and high up to 10 MeV energy), e/X accelerator systems will find their applications in further developments of the technology [35].

Acknowledgements This project has received funding from the European Union's (EU) Horizon 2020 Research and Innovation programme under ARIES Grant Agreement No. 730871 and by Ministry of Science and Higher Education (Poland) and co-financed by project 3697/H2020/2017/2.

References

1. Chmielewski AG, Haji-Saeid M, Shamshad A (2005) Progress in radiation processing of polymers. Nucl Instrum Meth B 236:44–56
2. Chmielewski AG, Al-Sheikhly M, Berejka AJ, Cleland MR, Antoniak M (2014) Rad Phys Chem 94:147–150

3. Dole M (1950) Report of symposium IX "chemistry and physics of radiation dosimetry". Army Chemical Center, Maryland, p 120
4. Charlesby A (1952) In: Proceedings of the royal society, A215, London, p 187
5. Charlesby A (1960) Atomic radiation and polymers. Pergamon Press, London
6. Haji-Saeid M, Sampa MH, Ramamoorthy N, Guven O, Chmielewski AG (2007) The role of IAEA in coordinating research and transferring technology in radiation chemistry and processing of polymers. Nucl Instr Met Phys Res B 265:51–57
7. IAEA (2006) Gamma irradiators for radiation processing. IAEA, Vienna, Austria. https://www-naweb.iaea.org/napc/iachem/Brochgammairradd.pdf
8. Chmielewski AG, Berejka AJ (2008) Radiation sterilization centers worldwide. In: Trends in radiation sterilization of health care products. IAEA, Vienna, Austria, pp 49–61. http://www-pub.iaea.org/MTCD/publications/PDF/Pub1313_web.pdf
9. Berejka AJ, Kałuska IM (2008) Materials used in medical devices. In: Trends in radiation sterilization of health care products. IAEA, Vienna, Austria, pp 159–174. http://www-pub.iaea.org/MTCD/publications/PDF/Pub1313_web.pdf
10. Zimek Z, Chmielewski AG (1993) Present tendencies in construction of industrial electron accelerators applied in radiation processing. Nukleonika 38(2):3–21
11. Chmielewski AG, Sadat T, Zimek Z. Electron accelerators for radiation sterilization. In: Trends in radiation sterilization of health care products. IAEA, Vienna, Austria, pp. 27–45. http://www-pub.iaea.org/MTCD/publications/PDF/Pub1313_web.pdf
12. Nablo SV (1993) Electron-beam processing machinery. Radiation curing in polymer science and technology, vol 1. Fundamentals and methods. Elsevier Applied Science, London, pp 504–551
13. Migdal W, Malec-Czechowska K, Owczarczyk B (1996) Study on application of e/X conversion for radiation processing. Nukleonika 41(3):57–66
14. Sun Y, Chmielewski AG (eds) (2017) Applications of ionizing radiation in materials processing. INCT, Warsaw, ISBN 978-83-933935-8-9. http://www.ichtj.waw.pl/ichtj/publ/monogr/m2017_1.htm
15. Przybytniak G, Nowicki A, Mirkowski K (2008) Evaluation of polymers designed for radiation processing. Nukleonika 53(S2):S67–S72
16. Mehnert R (1995) Materials modification using electron beams. In: Misaelides P (ed) Application of panicle and laser beams in materials technology. Kluwer Academic Publishers, USA, pp 557–580
17. Zimek Z, Przybytniak G, Nowicki A (2012) Optimization of electron beam crosslinking of wire and cable insulation. Rad Phys Chem 81(9):1398–1403
18. Rosato DV (1998) Extruding plastics. Chapter 12, Wire and cable. Chapman & Hall, UK, pp 470–493
19. Przybytniak G (2017) Crosslinking of polymers in radiation processing, in pos. 14. pp 249–267
20. Przybytniak G, Zimek Z (2015) Application of electron accelerators in cable industry. In: Chmielewska-Smietanko D (ed) The industrial and environmental applications of electron beams. INCT, Warsaw, ISBN 978-83-933935-7-2. http://www.ichtj.waw.pl/ichtj/publ/monogr/m2015_4.htm
21. Zimek Z, Przybytniak G, Nowicki A, Mirkowski K, Roman K (2014) Optimization of electron beam crosslinking for cables. Rad Phys Chem 94:161–165
22. Hertz DL (1984) Theory and practice of vulcanization. Elastomerics, Cheshire
23. Mohammed SAH, Walker J (1986) Application of electron beam radiation technology in tire manufacturing. Rubber Chem Technol 59(3):482–496
24. Makuuchi K (2001) Radiation processing in Japan. In: JAERI-conference 05, pp 266–271. http://www.iaea.org/inis/collection/NCLCollectionStore/_Public/33/010/33010161.pdf
25. Makuuchi K, Markovic V (1991) Radiation processing of j natural rubber latex. IAEA Bull 33 (1):25–28
26. Rosiak JM, Ulański P, Rzeżnicki A (1995) Hydrogels for medical applications. Nucl Instr Meth Phys Res B105:335–339

27. Yu H, Xu X, Chen X, Hao J, Jing X (2006) Medicated wound dressings based on poly(vinyl alcohol)/poly(*N*-vinyl pyrrolidone)/chitosan hydrogels. J Appl Polym Sci 101(4):2453–2463
28. Trageser DA (1977) Crosslinked polyethylene foam processes. Radiat Phys Chem 9(1–3):261–270
29. Radiation crosslinking—enhancing plastics properties by radiation (2017) BGS beta—gamma service. http://en.bgs.eu/wp-content/uploads/2017/02/BGS_radiation_crosslinking_en-1.pdf
30. Below H, Quilitz G, Schumann W (2005) Electron beam crosslinking of large diameter thick-walled polyethylene pipes. Plast Rubber Compos 34(1):34–39
31. Okabe S, Nishikawa S, Hayami H, Nakabayashi M, Emoto Y (2005) Development of radiation crosslinking nylon molding compound. SEI Tech Rev 59:48–51
32. Cheng S, Phillips E (2006) Rheological studies on radiation modified polyethylene resins. In: Society of Plastics Engineers (SPE) ANTEC conference, Charlotte. www.raprex.com
33. Ivanov VS (1992) Radiation chemistry of polymers. VSP, Utrecht, The Netherlands
34. Accelerators for America's future, DOE, Washington (2019). https://science.energy.gov/~/media/hep/pdf/accelerator-rd-stewardship/Report.pdf
35. Applications of particle accelerators in Europe, EuCARD 2, CERN, Geneva (2017). http://apae.ific.uv.es/apae/wp-content/uploads/2015/04/EuCARD_Applications-of-Accelerators-2017.pdf

Energy Loss of Swift Heavy Ions: Fundamentals and Theoretical Formulations

Vishal Sharma, Pawan K. Diwan and Shyam Kumar

Abstract The main interest of this chapter is to understand the fundamental energy loss processes through which incident energetic heavy ions lose their energies in the stopping medium. Fundamentals of ion interaction with matter are discussed where various modes of energy loss processes are explained. In the context of non-relativistic heavy ions, the contribution due to two types of energy loss modes, i.e., nuclear energy loss and electronic energy loss, is discussed in detail. Comparison between nuclear energy loss and electronic energy loss as a function of ion's energy for Cu ion in Si target is shown. The fundamental Bohr energy loss equation is derived and extended by incorporating various correction terms. The most commonly used semi-empirical/empirical type energy loss formulations (Lindhard et al., Northcliffe and Schilling, Ziegler et al., Paul and Schinner, Huber et al., and Diwan et al.) are briefly introduced. Bragg's rule, which determine the energy loss in polymers/compounds, is discussed. Finally, the importance of energy loss is highlighted.

Keywords Electronic energy loss · Nuclear energy loss · Heavy ions · Scaling law · Effective charge

V. Sharma (✉)
Institute of Forensic Science & Criminology, Panjab University, Chandigarh 160014, India
e-mail: sharmavishal05@gmail.com

P. K. Diwan
Department of Applied Science, UIET, Kurukshetra University, Kurukshetra 136119, India

S. Kumar
Department of Physics, Kurukshetra University, Kurukshetra 136119, India

V. Kumar et al. (eds.), *Radiation Effects in Polymeric Materials*, Springer Series on Polymer and Composite Materials, https://doi.org/10.1007/978-3-030-05770-1_13

1 Introduction

The problem "*exact evaluation of energy loss of heavy ions in matter*" has ever since continued to command substantial research interest due to its wide applications in many areas of science, e.g., nuclear and particle physics, material science, atomic physics, molecular physics, radiation dosimetry, astrophysics, radiation biology and chemistry, and health physics [1–5]. Due to the complicated nature of the problem, involving the concepts from atomic physics, quantum mechanics, relativity, etc., and further because of its widespread applications, the evaluation of energy loss attracted such a great interest that some of the great scientists endeavored to work on it, both theoretically [6–24] and experimentally [25–49].

As correctly pointed out by Ahlen [1], detailed investigations of this problem have greatly contributed to the development of modern physics. Further, in spite of more than 100 years of active research in this area, the exact solution of energy loss evaluation is still mysterious. Therefore, the exact evaluation of energy loss of charged particles during their passage through a material medium also known as the stopping power of the medium has remained a very active and important area of research.

Another inherent concept, when we deal with the energy loss suffered by a charged particle traversing through a material medium is "straggling." When monoenergetic charged particles are allowed to pass through a material medium of a given thickness, all the transmitted particles do not possess the same residual energy, rather there is a spread in the residual energy, about an average value. This spread in the residual energy is called straggling. Figure 1 clearly highlights the

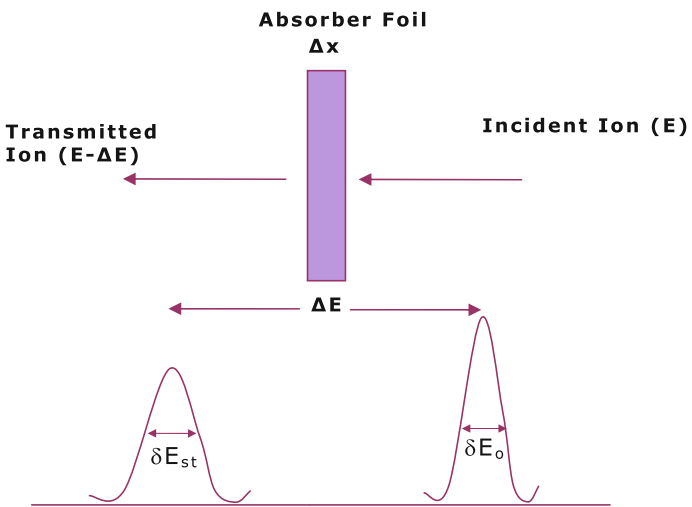

Fig. 1 Penetration of an ion of energy E through an absorber foil of thickness Δx resulting in the loss of energy ΔE within the foil. The peak width (δE_o) of the transmitted ions is larger than that of the incident ions (δE_{stg}) as a result of energy loss straggling

concept of energy loss and straggling. The consideration of straggling is equally important in all such scientific areas where energy loss rate/stopping power is required as input. In this chapter, we are only dealing with the energy loss of swift heavy ions with its fundamental concept and related theoretical formulations.

The present chapter covers the energy loss aspect for a variety of heavy ions in elemental/complex polymer materials. Initially, we need to understand the general physics fundamental concepts linked to exact evaluation of energy loss of heavy ions in target materials. For this purpose, in the coming sections, the interactions of charged particles with matter that result in energy loss are described.

2 Fundamentals of Ion Interactions with Matter

When a charged particle enters into the target material, it interacts with the target atoms and several changes occur to the projectile and the target material as well. Most of the changes in the target material depend upon the projectile's parameters. These changes occur at the cost of the energy loss suffered by the charged particle along its trajectory.

The various modes of energy loss process are as follows [50, 51]:

(i) *Excitation and Ionization*
This is the principal mechanism for the energy loss of ions at high velocities. Heavy ions while passing through a material medium transfer their energies to the electrons of the target atoms result the target atoms into excited or ionized states. Energy loss due to excitation and ionization is also called e*lectronic energy loss or inelastic energy loss.*

(ii) *Nuclear Collisions*
At ion energies below 1 MeV, the projectile ion transfers its energy to the target nucleus by elastic collision and consequently the target atom recoils. Energy loss due to nuclear collisions is also called *nuclear energy loss or elastic energy loss.*

(iii) *Generation of Photons*
A charged particle while passing close to the field of nucleus is either accelerated or decelerated and during this process, it emits a quantum of electromagnetic radiation known as the *Bremsstrahlung* process. The energy loss in this process is important only for light charged particles and is negligible for heavy ions.

(iv) *Cherenkov Radiation*
A charged particle entering through a stopping medium at velocities greater than the phase velocity of light in the medium causes the polarization of atoms close to the path of the particle. This results in the formation of a coherent wave front of radiation at certain fixed angle with respect to the trajectory of the particle, depending on the velocity of the ion. Such radiations are known as *Cherenkov radiations*.

Bremsstrahlung mode of energy loss is important only for light charged particles like electrons and that too at high velocities. Its magnitude at a given velocity of the incident particle is proportional to $(Z_1Z_2/M_1)^2$ where Z_1, M_1, and Z_2 are the charge on the incident particle, mass of the incident particle, and charge on the target nucleus, respectively. For heavier particles like alpha particles, $(Z_1/M_1)^2 = 0.25$, while for light particles like electrons, the term $(Z_1/M_1)^2 \cong 3 \times 10^6$, when Z_1 is expressed in electronic charge units and M_1 in atomic mass units. Thus for the same stopping medium, the contribution of bremsstrahlung would be significant only for light charged particles like electrons and is negligible for heavy ions. As for the emission of Cherenkov radiation is concerned, it occurs only at relativistic velocities.

Therefore, in the context of non-relativistic heavy ions, the contribution due to the energy loss modes (iii) and (iv) can be neglected and only the modes (i) and (ii) need to be considered as principal mechanisms for energy loss. Thus, the total energy loss rate can be written as:

$$\left(-\frac{\mathrm{d}E}{\mathrm{d}x}\right)_{\text{Total}} = \left(-\frac{\mathrm{d}E}{\mathrm{d}x}\right)_{\text{Elec.}} + \left(-\frac{\mathrm{d}E}{\mathrm{d}x}\right)_{\text{Nucl.}}$$

where the two terms on the right-hand side indicate the electronic and nuclear components of energy loss rate, respectively.

2.1 Electronic Energy Loss Rate

A simplified classical treatment [50, 51] for the evaluation of electronic energy loss rate $(\mathrm{d}E/\mathrm{d}x)_{\text{Elec.}}$ is as follows.

Consider an ion, having effective charge $Z_1^* e$ (concept of effective charge described in Sect. 2.5), moving with velocity v through a target medium, at a distance b, from the electron of the target atom (Fig. 2).

Let an incident ion, while passing through the target material, exerts a Coulomb force on an electron of the target atoms at an impact parameter b and this force changes its direction continuously with time. The Coulomb force F can be divided in two components F_x and F_y along and perpendicular, respectively, to the direction of motion of the incident ion. The impulse $\int F_x \mathrm{d}t$, parallel to the path, is zero by symmetry. This is due to the reason that for each position of the incident heavy ion in the negative x direction, there is a corresponding position in the positive x direction, which makes an equal and opposite contribution to the x component of the momentum. However, during the passage of the ion, throughout the material, there is always a force exerted by the ion in the y direction, and hence, the momentum Δp transferred to the electron is given by the expression,

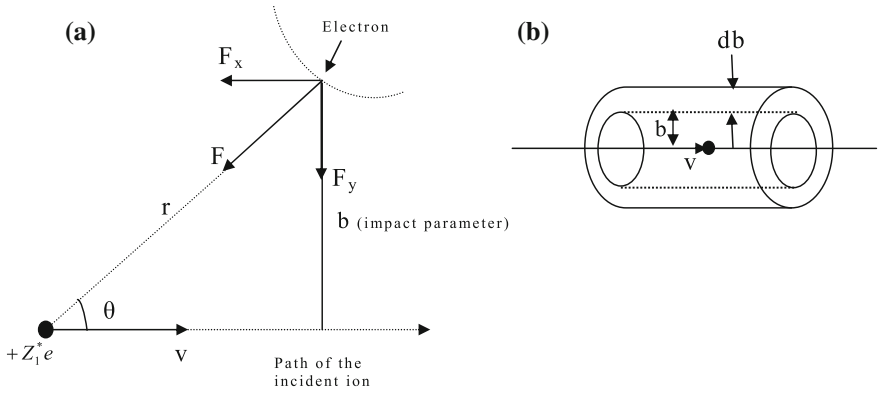

Fig. 2 **a** Coulombian interaction between heavy ion of effective charge $Z_1^* e$ with a target electron. **b** A shell of radius b and thickness db with its axis along the path of the heavy ion

$$\Delta p = \frac{2Z_1^* e^2}{bv} \tag{1}$$

The kinetic energy (T) transferred by the ion to the target electron having rest mass $m_{0,}$ in non-relativistic velocity region, is given by:

$$T = \frac{\Delta p^2}{2m_0} = \frac{2Z_1^{*2} e^4}{b^2 m_0 v^2} \tag{2}$$

The differential cross section, $\mathrm{d}\sigma(T)$, for an energy transfer between T and $T + \mathrm{d}T$ is given by,

$$\mathrm{d}\sigma(T) = 2\pi b \mathrm{d}b \tag{3}$$

and the energy loss per unit path length, $-\mathrm{d}E/\mathrm{d}x$, is as follows:

$$-\frac{\mathrm{d}E}{\mathrm{d}x} = n \int_{T_{\min}}^{T_{\max}} T \mathrm{d}\sigma \tag{4}$$

where $n = NZ_2$ is the number of target electrons per unit volume in the stopping medium, with N as the number of target atoms per unit volume and Z_2 the number of electrons per target atom.

In terms of impact parameter "b", Eq. (4) becomes:

$$-\frac{\mathrm{d}E}{\mathrm{d}x} = n \int_{b_{\min}}^{b_{\max}} T 2\pi b \mathrm{d}b \tag{5}$$

Substituting the value of T from Eq. (2) in Eq. (5), we get,

$$-\frac{dE}{dx} = \frac{4\pi N Z_2 Z_1^{*2} e^4}{m_0 v^2} \ln \frac{b_{max}}{b_{min}} \tag{6}$$

The values of b_{min} and b_{max} are selected in the following manner. b_{min} is that value of impact parameter at which there is the maximum transfer of energy by the ion to the electron. This value can be calculated on the basis of the fact that if a heavy ion with velocity v collides with a stationery target electron, the maximum velocity transferred to the electron is $2v$. Thus, the maximum kinetic energy transferred by the ion to the electron (in non-relativistic velocity region) will be $T_{max} = \frac{1}{2} m_0 (2v)^2 = 2m_0 v^2$.

Corresponding to this value of $T_{max,}$ using Eq. (2), the value of b_{min} comes out to be:

$$b_{min} = \frac{Z_1^* e^2}{m_0 v^2} \tag{7}$$

Regarding the choice of b_{max}, in case it is infinity, dE/dx will also approach to infinity, which is not feasible. The minimum energy which an atomic electron must acquire should be compatible with the average excitation energy of an electron, represented by I. Thus to a reasonable level of accuracy, T_{min} can be taken to be equal to I, and the corresponding value of b_{max} after using Eq. (2) becomes,

$$b_{max} = \frac{2Z_1^* e^2}{\sqrt{2m_0 v^2 I}} \tag{8}$$

On substituting the values of b_{min} and b_{max} from Eqs. (7) and (8), respectively, in Eq. (6), we obtain,

$$-\frac{dE}{dx} = \frac{2\pi N Z_2 Z_1^{*^2} e^4}{m_0 v^2} \ln \frac{2m_0 v^2}{I} \tag{9}$$

Equation (9) is derived on the basis of the direct collisions of heavy ion with the electrons in the target atom. There is also one more term of comparable magnitude as a result of distant resonant energy transfer collisions.

Thus, the total energy loss per unit length becomes twice to that given by Eq. (9) and finally,

$$-\frac{dE}{dx} = \frac{4\pi N Z_2 Z_1^{*^2} e^4}{m_0 v^2} \ln \frac{2m_0 v^2}{I} \tag{10}$$

This expression is similar to the well-known Bethe's expression, for incident ion energies in the non-relativistic region.

In SI system of units, Eq. (10) becomes,

$$\left(-\frac{\mathrm{d}E}{\mathrm{d}x}\right)_{\text{Elec.}} = \frac{NZ_2Z_1^{*^2}e^4}{4\pi\varepsilon_0^2 m_0 v^2}\ln\frac{2m_0v^2}{I} \tag{11}$$

where ε_o is the permittivity of the free space.

Incorporating relativistic, shell and density effect corrections, Eq. (10) becomes,

$$-\frac{\mathrm{d}E}{\mathrm{d}x} = \frac{4\pi NZ_2Z_1^{*^2}e^4}{m_0v^2}\left[\ln\frac{2m_0v^2}{I} - \ln(1-\beta^2) - \beta^2 - \frac{C}{Z_2} - \frac{\delta}{2}\right] \tag{12}$$

where $\beta = v/c$, the term $-\ln(1-\beta^2) - \beta^2$ is added as the relativistic correction term. The terms C/Z_2 and $\delta/2$ are the shell and density effect corrections, respectively, which are briefly discussed below.

Shell Correction

The derivation of energy loss rate equation is based on the assumption that the velocity of the projectile ion is much larger in comparison to that of the atomic electrons in their normal bound state. In case the projectile ion is not so fast, the inner shell electrons participate less to the energy loss, and thus, the shell correction term requires to be included. This correction term C/Z_2 is taken to be the average over the contribution of the different shells, with $C = C_k + C_L + \cdots$. These shell corrections can be predicted by using hydrogenic wave function (HWF) [10, 52–59] and local density approximation (LDA) [60–62].

Density Correction

In dense media, the electric field which perturbs electrons far from the trajectory of the projectile is modified by the dielectric polarization of the atoms between the distant electrons and the path of the projectile. The energy transfer in distant collisions is therefore less effective. This effect is called the density effect. The correction for the density effect was first taken up theoretically by Swann [63] and Fermi [64] and later extended by Bohr [10], Sternheimer and coworkers [65–67], Crispin and Fowler [68], and Bichsel [69].

Other Corrections

In addition to the shell and density effect correction terms, there are some more correction terms like Barkas correction, finite nuclear size correction, Bloch and Mott correction, and projectile structure correction. However, the contribution due to these corrections is quite insignificant [1, 70–72] and therefore not discussed in the present study.

2.2 Nuclear Energy Loss Rate

In this case, Coulombian interaction occurs between the incident heavy ion and the target nuclei, in contrast to that of electronic energy loss where the interaction takes place between the incident ion and the electrons of the target atoms. Following the method adopted for the evaluation of electronic energy loss (Eq. (6)), the expression for nuclear energy loss comes out to be,

$$\left(-\frac{\mathrm{d}E}{\mathrm{d}x}\right)_{\mathrm{Nucl.}} = \frac{4\pi N Z_2^2 Z_1^{*^2} e^4}{M_2 v^2} \ln \frac{b_{\max}}{b_{\min}} \tag{13}$$

where Z_2 and M_2 are the atomic number and the mass number of the target nucleus, respectively, and N is the number of target nuclei per unit volume. In this case, $b_{\min}$ corresponds to the maximum energy transfer to a target atom ($T_{\max}$) which is given by the expression:

$$T_{\max} = \frac{4M_1M_2}{(M_1 + M_2)^2} E \tag{14}$$

and $b_{\max}$ corresponds to the minimum energy transferred to the target atom which can be taken to be equal to the displacement energy (I_{dis}) required to remove an atom. Accordingly, the values of $b_{\max}$ and $b_{\min}$ can be obtained [50, 51].

2.3 Comparison of Electronic and Nuclear Energy Loss Rate

From the comparison of the expressions for electronic energy loss rate $(-\mathrm{d}E/\mathrm{d}x)_{\mathrm{Elec.}}$ (Eq. (6)) and nuclear energy loss rate $(-\mathrm{d}E/\mathrm{d}x)_{\mathrm{Nucl.}}$ (Eq. (13)), it is noticed that the major difference between the two is that in case of nuclear energy loss, the mass of the target atom M_2 appears instead of mass of the electron m_0. In addition, NZ_2 (the number of target electrons per unit volume) appeared in case of electronic energy loss is replaced by the number of target atoms per unit volume N.

For proton, neglecting the ratio of ln terms, the ratio of nuclear to electronic energy loss is,

$$\frac{\left(\frac{\mathrm{d}E}{\mathrm{d}x}\right)_{\mathrm{Nucl.}}}{\left(\frac{\mathrm{d}E}{\mathrm{d}x}\right)_{\mathrm{Elec.}}} \cong \frac{Z_2}{M_2} m_0 \cong \frac{1}{3600} \tag{15}$$

with $M_2 = 2Z_2 m_{\mathrm{p}}$ and m_{p} is the mass of the proton which is equal to $1836 m_0$.

Thus, for MeV heavy ions, the nuclear energy loss is negligible in comparison to electronic energy loss. However, for energies below 1 MeV, when the projectile ion

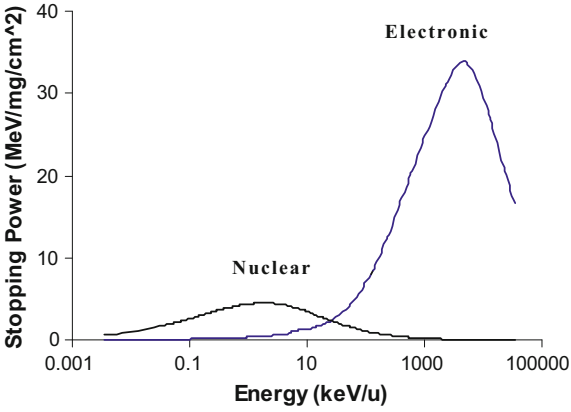

Fig. 3 Comparison of nuclear and electronic energy losses for copper ions in silicon substrate (based on SRIM calculations)

behaves as a neutral atom, the energy loss process occurs via hard sphere scattering [51] and now the nuclear energy loss starts dominating over electronic energy loss [50, 51]. Figure 3 highlights such a comparison of electronic and nuclear energy loss as a function of ion's energy for Cu ion in Si target.

It is now quite clear that for MeV heavy ions in non-relativistic region, the electronic energy loss is the only dominant mode of energy loss and therefore all other modes of energy loss can simply be neglected.

2.4 Scaling Law

For partially stripped non-relativistic heavy ions, Eq. (10) for electronic energy loss rate can be expressed in the following form.

$$S = -\frac{\mathrm{d}E}{\mathrm{d}x} = C\left(\frac{\gamma_1 Z_1}{v}\right)^2 \left(\frac{Z_2}{A}\right) f(v, Z_2) \tag{16}$$

where $\gamma_1 = Z_1^*/Z_1$ is termed as fractional effective charge of the projectile ion and Z_2 and A are the target atomic and mass numbers, respectively, with C as a constant [50].

At a particular velocity of the projectile ion, the terms $f(v, Z_2)$ and (Z_2/A) are independent of the parameters of the projectile ion. Thus, the stopping power of a particular medium for two different projectile ions say "x" and "y" at the same velocity v is related through the expression,

$$\left(\frac{S}{\gamma_1^2 Z_1^2}\right)_x = \left(\frac{S}{\gamma_1^2 Z_1^2}\right)_y \tag{17}$$

This is known as *scaling law*.

Thus if one of the two projectile ions is considered as a reference ion, whose stopping power (S_{ref}) and fractional effective charge (γ_{ref}) are known, then the stopping power for the other ion (S_{HI}) at the same velocity and in the same target medium can be calculated using the relation,

$$\left(\frac{S_{HI}}{\gamma_{HI}^2 Z_{HI}^2}\right) = \left(\frac{S_{ref}}{\gamma_{ref}^2 Z_{ref}^2}\right) \tag{18}$$

The main advantage of the scaling law for calculating the stopping power is that the requirement of mean ionization potential I of the stopping medium is eliminated and the only input parameter required to be evaluated is the fractional effective charge (γ_{HI}) of the incident ion.

2.5 Concept of Effective Charge

When a projectile ion at a velocity larger than the orbital velocities of its most tightly bound electrons enters a material medium, it loses all its electrons and a bare nucleus traverses through the medium. Under this situation, the effective charge on the ion is same as that of the nuclear charge. During the passage of the ion, it continuously loses its energy, due to its interactions mainly with the electrons of the target atoms. During this process, the velocity of the ion continuously reduces. As the velocity of the ion approaches the velocity of its K-shell electrons, the ion starts capturing electrons. At first, there is small probability for the capturing of the electron and large probability that the electron will be lost in the next collision. As the velocity of the ion further decreases, the capture probability becomes more and the loss probability reduces, and finally, the electron is fully captured. In the meantime, the probability of the capture of a second electron builds up and the corresponding loss probability decreases, so that the second electron is retained. As the velocity of the ion continuously decreases, a third electron is captured in the same gradual way and this process continues. Ultimately, the velocity of the ion becomes smaller than the orbital velocity of least tightly bound electron and remains most of its time as a neutral atom [71, 72].

No exact theoretical expression for the evaluation of effective charge as a function of ion velocity exists, and therefore, the various energy loss/stopping power formulations are based on empirical/semi-empirical effective charge parameterization.

2.6 Units of Energy Loss Rate

In S.I. system of units, the energy loss is expressed in joule and thickness in meter. Thus, the unit of energy loss rate, dE/dx, in S.I. system is joule/meter. Such units

are not appropriate in the present case as the energy loss is generally expressed in eV or keV or MeV and thickness in Å or nm or μm, and thus, the units of dE/dx are expressed in eV/Å or keV/nm or MeV/μm.

It is further advantageous to consider the thickness of the absorber foil in terms of mass thickness instead of linear thickness. The mass thickness ($\rho\Delta x$) is obtained by multiplying the linear thickness (Δx) by the density of the material (ρ). The mass thickness $\rho\Delta x$ gives better description of the amount of material in the thin target foil. Thus, the units of energy loss rate dE/dx become MeV/(mg/cm^2) when energy loss is expressed in MeV and thickness in mg/cm^2. Such units of dE/dx remain independent of the density of the absorber material.

The dE/dx values from one set of units can be converted into another set by multiplying with the suitable conversion factor.

3 Energy Loss Formulations

Most commonly used energy loss formulations are described below.

3.1 LSS Theory

At relatively low velocities, the ion rapidly becomes neutralized and the energy loss process changes its character. As proposed by Bohr [10] and developed by Lindhard, Scharff, and Schiøtt [73], the stopping power may be split into two additive components, an "electronic part" proportional to ion velocity which arises from energy transfer to the electrons of the medium and a nuclear part arising from energy transfer to screened nuclei of the medium. Electronic stopping has been determined by velocity proportional Thomas–Fermi-type formula and nuclear stopping has been dealt as power law scattering.

For electronic energy loss, the LSS theory predicts a linear trend with ion velocities, $v \leq v_0 Z_1^{2/3}$ (v_0 represents Bohr velocity, and Z_1 is the atomic number of projectile ion), and is expressed by the expression,

$$\left(-\frac{\mathrm{d}E}{\mathrm{d}x}\right)_{\text{Elec.}} = \zeta 8\pi e^2 a_0 N \left\{\frac{Z_1 Z_t}{\left(Z_1^{2/3}+Z_2^{2/3}\right)^{3/2}}\right\}\left(\frac{v}{v_0}\right) \tag{19}$$

where Z_1 and Z_2 are the atomic numbers of projectile ion and target atom, respectively, $\zeta \sim Z_1^{1/6}$ is a constant, v_0 and a_0 are the Bohr's velocity and Bohr's radius, respectively, N is the atomic density, and v is the projectile ion's velocity.

In energy loss rate calculations based on LSS theory, it is considered quite informative to calculate reduced energy loss rate as a function of reduced ion velocity. The reduced ion velocity and reduced energy loss rate are defined as,

$$v_{\text{red}} = \frac{v}{v_0 Z_1^{2/3}} \tag{20}$$

$$\left(-\frac{\mathrm{d}E}{\mathrm{d}x}\right)_{\text{red}} = \left(-\frac{\mathrm{d}E}{\mathrm{d}x}\right)_{\text{Elec.}} \frac{\left(Z_1^{2/3} + Z_2^{2/3}\right)^{3/2}}{\zeta Z_1^{5/3} Z_2} \tag{21}$$

Substituting for $(-\mathrm{d}E/\mathrm{d}x)_{\text{Elec.}}$ from Eq. (19) in Eq. (21), we get,

$$\left(-\frac{\mathrm{d}E}{\mathrm{d}x}\right)_{\text{red}} = 8\pi e^2 a_0 N \left(\frac{v}{v_0 Z_1^{2/3}}\right) \tag{22}$$

It is obvious from Eq. (22) that there exists a linear relationship between reduced LSS stopping power and reduced ion velocity, intersecting the origin, for a particular absorber irrespective of the nature of projectile [74–77].

3.2 Northcliffe and Schilling Formulation

This formulation is based on the assumption that at higher energies, when the incident ions are fully stripped of their orbital electrons, the electronic energy loss rate for different ions at the same velocity in a given absorber medium differs only in being proportional to the square of the ion charge. It means that for fully stripped ions, the plots between $\frac{(-\mathrm{d}E/\mathrm{d}x)}{Z_1^2}$ and E (MeV/u) will be the same for all ions and will merge into proton curve.

At lower energies, when the capture of electrons by the ions becomes significant, the deviation of the curve between $\frac{(-\mathrm{d}E/\mathrm{d}x)}{Z_1^2}$ and E (MeV/u) arises from the corresponding proton curve. This is due to the smaller value of effective charge (Z_1^*) of the ion in comparison to its nuclear charge (Z_1). The fractional effective charge $\gamma = Z_1^*/Z_1$ is expressed as,

$$\gamma^2 = \frac{\frac{1}{Z_1^2}\left(-\frac{\mathrm{d}E}{\mathrm{d}x}\right)_{\text{ion}}}{\left(-\frac{\mathrm{d}E}{\mathrm{d}x}\right)_{\text{proton}}} \tag{23}$$

Thus, the value of γ^2 gives a measure of the deviations for any heavy ion from the proton curve.

On the basis of the deviations observed in $\left[\frac{(-\mathrm{d}E/\mathrm{d}x)}{Z_1^2}\text{ vs. }E\text{ (MeV/u)}\right]$ curves for various heavy ions in comparison to proton curve in aluminum absorber, taken as the reference material, the following expression for γ^2 was developed.

$$\gamma^2 = 1 - 1.85\,\mathrm{e}^{-2\xi} \tag{24}$$

with $\xi = 137\beta/Z_1^{2/3}$.

In the second step, relative stopping power curves for various solid as well as gaseous absorbers relative to aluminum were developed.

The calculations of energy loss rate for various heavy ions in different absorbers were finally carried out on the basis of the expression,

$$\left\{\frac{\left(\frac{\mathrm{d}E}{\mathrm{d}x}\right)_{i,a}}{\left(\frac{\mathrm{d}E}{\mathrm{d}x}\right)_{i,b}}\right\} = \left\{\frac{\left(\frac{\mathrm{d}E}{\mathrm{d}x}\right)_{j,a}}{\left(\frac{\mathrm{d}E}{\mathrm{d}x}\right)_{j,b}}\right\} \tag{25}$$

where "*i*" and "*j*" denote two different ions at the same velocity, i.e., same value of energy in MeV/u, and "*a*" and "*b*" are two different absorbers.

Based on the above-discussed approach, Northcliffe and Schilling [78] tabulated the electronic energy loss rate and range values for various heavy ions in the energy range ~0.0125–12.0 MeV/u at regular intervals, in different absorber materials.

3.3 Ziegler, Biersack, and Littmark Formulation

Ziegler et al. [79] developed a formulation for energy loss rate and range for heavy ions in different elemental and complex absorber materials. This formulation is based on scaling law with proton as the reference ion. According to this formulation, the electronic energy loss rate for a heavy ion (S_{HI}) at a given velocity in an absorber material is expressed by the expression,

$$S_{\mathrm{HI}} = S_{\mathrm{P}}\gamma_{\mathrm{HI}}^2 Z_{\mathrm{HI}}^2 \tag{26}$$

where S_{P} is the energy loss rate of the proton at the same velocity in the same absorber material and γ_{HI} is the fractional effective charge of the heavy ion with atomic number Z_{HI}.

After the compilation of huge experimental electronic energy loss rate data of protons (S_{P}) in different absorbers at different velocities, as available in the literature at that time, Zeigler et al. developed the following fitted expression for proton electronic energy loss rate.

$$S_P = \frac{S_L S_H}{S_L + S_H} \tag{27}$$

with

$$S_L = aE^b + cE^d \tag{28}$$

and

$$S_H = e \ln\left[\frac{g/E + hE}{E^f}\right] \tag{29}$$

where a, b, c, d, e, f, g, and h are proton stopping coefficients. Ziegler et al. [62] tabulated these coefficients for all elemental targets.

Effective Charge Parameterization:

In the high-velocity region $\frac{v}{v_0} > 100$ (v_0—Bohr's velocity = 25 keV/u), the Bethe–Bloch approach [1, 52, 80, 81] was adopted by Ziegler et al. [79] for the evaluation of electronic energy loss rate in different materials.

In the ion velocity range $3v_0 \leq v \leq 100v_0$ (v_0—Bohr's velocity), based on the Thomas–Fermi conception of the atom, Ziegler et al. [79] parameterized the following expression for fractional effective charge.

$$\gamma^2 = 1 - \exp\left[\frac{-0.92v}{v_0 Z_1^{2/3}}\right] \tag{30}$$

At ion velocities $v_0 Z_1^{2/3} < v < 3v_0$, Ziegler et al. suitably modified the fractional effective charge parameterization in light of the Kreussler et al. [82] and Brandt and Kitagava [24] theory. Below ion velocity $v = v_0 Z_1^{2/3}$, the ion energy loss rate was considered to be velocity proportional.

Based on the above concept, Zeigler et al. have developed computer codes in the name of TRIM and SRIM for energy loss rate and range calculations for heavy ions in different absorber materials over almost the complete range of energies. Based on the newly available experimental data and with the theoretical developments in the field, with the passage of time, Zeigler et al. are in the continuous process of updating such codes. The latest code developed by Zeigler is SRIM 2013.00 [83] and has been used for the calculations in the present study. This is the only code with quoted applicability over the broad energy range from eV to GeV region. This code is quite handy and readily available [83]. For electronic energy loss rate calculations in compounds, this code incorporates both Bragg's [22] and CAB [84] approach.

3.4 Paul and Schinner Formulation

Paul and Schinner [85–87] developed the following expression for electronic energy loss rate of heavy ions.

$$S_{HI} = S_{rel}\left(S_{He}/2^2\right)Z_{HI}^2 \tag{31}$$

In this expression, they have introduced a term normalized energy loss rate ratio, $S_{rel,}$ defined as,

$$S_{rel} = \frac{\left(S_{HI}/Z_{HI}^2\right)}{\left(S_{He}/2^2\right)} \tag{32}$$

where S_{He} is the electronic energy loss rate of He ion of the same velocity as that of heavy ion with atomic number Z_{HI}, in the same medium.

It is obvious from Eq. (31) that the calculation of S_{HI} requires S_{He} and S_{rel}. For the calculations of S_{He}, a computer code ASTAR developed by Berger [88] with reported validity limited up to a maximum energy 250 MeV/u and at higher energies the computer code BEST [89] have been used.

For the determination of S_{rel}, Paul and Schinner developed the following parameterization.

Parameterization for S_{rel}

In light of the available experimental electronic energy loss rate data for heavy ions in different absorber materials at different energies, Paul and Schinner used an adapted cumulative Weibull function and fitted the following expression for S_{rel},

$$S_{rel} = a_f + (1.01 - a_f)\left[1 - \exp\left\{-\left(\frac{x + c_f(\ln 2)^{1/d} - b_f}{c_f}\right)^{d_f}\right\}\right] \tag{33}$$

where $x = \log_{10}(E/A)$, E/A in MeV/u; a_f, b_f, $c_{f,}$ and d_f are the fitting parameters and are the smooth functions of Z_{HI} [85–87].

The reported applicability of this formulation is from Z = 3–18, in the energy range 0.001 to 1000 MeV/u, in different elemental and complex absorber materials.

A computer code MSTAR (V3.12) [90] based on this formulation has been developed and is readily available.

3.5 Hubert, Bimbot, and Gauvin Formulation

This formulation, for the calculations of electronic energy loss rate developed by Hubert, Bimbot and Gauvin [91, 92], is also based on scaling law with fully

stripped helium ions as reference ions. The scaling law (Eq. (17)) with $\gamma_{ref} = 1$ and $Z_{ref} = 2$ leads to the following expression for the energy loss rate of heavy ions, S_{HI}.

$$S_{HI} = \frac{S_{He}\gamma_{HI}^2 Z_{HI}^2}{4} \tag{34}$$

where S_{He} is the stopping power for fully stripped He ion of the same velocity as that of heavy ion in the same medium. γ_{HI} is the fractional effective charge of heavy ion, and Z_{HI} is the atomic number of heavy ion.

Thus as is evident from Eq. (34), the evaluation of electronic energy loss rate for heavy ions at a given velocity in a particular absorber material requires S_{He} at the same velocity in the same medium. For this purpose, the fitted expression developed by Zeigler [62] was used by Hubert et al.

Effective Charge Parameterization

The other requirement of Eq. (34) is the fractional effective charge γ_{HI} of the heavy ion. The following fitted expression for γ_{HI} was developed by Hubert et al. [91, 92] on the basis of the experimental energy loss rate for heavy ions with $Z_1 = 8$–92 in targets with $4 \leq Z_2 \leq 92$, at energies from 3 to 90 MeV/u.

$$\gamma_{HI} = \frac{Z_{HI}^*}{Z_{HI}} = \left[1 - X_1 \exp\left\{-X_2\left(\frac{E}{A}\right)^{X_3} Z_{HI}^{-X_4}\right\}\right] \tag{35}$$

where (E/A) is the energy in MeV/u. X_1, X_2, X_3, and X_4 are the fitting parameters.

The unique and original feature of this formulation is that the effective charge parameterization, in addition to the atomic number Z_1 and velocity of the projectile ion, includes the dependence of target atomic number Z_2, which is generally neglected.

The reported validity of Hubert et al. formulation is in the ion energy range from ~2.5 to 500 MeV/u.

3.6 Diwan et al. Formulation

As discussed, the reported validity of Hubert et al. formulation is in the energy range from 2.5 to 500 MeV/u. Motivated with the excellent predictions of this formulation, in the light of experimental data [93–95], our group in earlier studies [96, 97] extended this formulation to lower energies. For this purpose, the fitting parameters X_1, X_2, X_3, and X_4 involved in its effective charge parameterization (Eq. (35)) had been suitably modified in light of the new experimental data, in lower energy domain.

For X_1, the following polynomial fit as a function of projectile atomic number (Z_{HI}) was obtained.

$$X_1 = A(Z_{\mathrm{HI}})^3 + B(Z_{\mathrm{HI}})^2 + C(Z_{\mathrm{HI}}) + D \tag{36}$$

The values of fitting parameters A, B, C, and D are given [96, 97]. The values of $X_2 = 8.448$, $X_3 = 0.347$, and $X_4 = 0.5995$ were kept fixed.

The other requirements for electronic energy loss rate evaluation at low energies, i.e., the effective charge and the energy loss rate of helium ion, were evaluated using the fitted formulae of Ziegler [62].

This extended version has its reported validity in the ion's energy range $\sim$0.25–2.5 MeV/u for projectiles with $Z = 3$–35 in targets covering $Z = 3$–79. This extended formulation has been tested for several projectiles in a variety of elemental and few complex materials.

4 Energy Loss in Polymers/Compounds: Bragg's Rule

The energy loss process of an ion while passing through a material medium consists of a random sequence of independent encounters between the moving projectile and the target electrons. For a composite target consisting of more than one element, the energy loss is the sum of the losses of the constituent elements weighted by the abundance of each element. This is basically the Bragg's rule [22, 98] which states that the stopping cross section $\varepsilon^{A_mB_n}$ of a solid of composition A_mB_n is given by

$$\varepsilon^{A_mB_n} = \frac{m}{m+n}\varepsilon^A + \frac{n}{m+n}\varepsilon^B \tag{37}$$

where ε^A and ε^B are the stopping cross sections of the atomic constituents A and B of the complex target material.

As an illustration, in case of polyethylene naphthalate (PEN) polymer, consisting of $C_7H_5O_2$ molecules.

$$\varepsilon^{C_7H_5O_2} = \frac{7}{14}\varepsilon^{C} + \frac{5}{14}\varepsilon^{H} + \frac{2}{14}\varepsilon^{O} \tag{38}$$

Bragg's rule is generally applicable for MeV heavy ions traversing a complex absorber material. However, at low energies the effect of chemical bonds needs to be incorporated [84].

5 Importance and Conclusion

The energy loss is the core of ion–mater interactions, and hence, its precise knowledge is highly essential from both fundamental as well as application point of view. In applications, the energetic ions are widely used to modify and characterize

the materials through ion beam-based techniques (RBS, ERDA, NRA, etc.). For the analysis of energy spectra obtained through ion beam-based techniques, computer software (like SIMNRA, RUMP, and NDF) are employed, where output depends upon the accuracy of input parameters of these software. The "energy loss" for given ion–energy–matter combinations, which is under study, is used as main input parameter for these computer simulations software.

Although a huge amount of experimental data of energy loss for number of ion–target combinations at different energies is available in the literature, still the entire ion–energy–target combinations are not covered. First, this is due to the reason that these combinations are very large, and second, there are many experimental limitations for such kind of measurements. Therefore, the only alternate is to explore some theoretical energy loss formulation to predict these values. As discussed in Sect. 3, many researchers developed theoretical/empirical/semi-empirical type energy loss formulations for such predictions. Since most of the commonly used energy loss formulations are of empirical and semi-empirical type which are based on the measured energy loss data available at the time of their development. Therefore, it is highly essential to check the validity of these formulations before using as input in required ion beam-based experiments.

References

1. Ahlen SP (1980) Rev Mod Phys 52(1):121
2. Chu WK, Mayer JW, Nicolet MA (1978) Backscattering Spectrometry. Academic Press, New York
3. Sigmund P (1998) Nucl Instr and Meth Phys Res B135:1
4. Sigmund P (2006) Particle penetration and radiation effects, general aspects and stopping of swift point charges, vol 1. Springer, Berlin, Heidelberg, New York
5. Sigmund P (2014) Penetration of atomic and molecular ions, vol 2. Springer, Switzerland
6. Thomson JJ (1912) Phil Mag 23:449
7. Rutherford E (1911) Philos Mag 21:699
8. Bohr N (1913) Philos Mag 25:10
9. Bohr N (1915) Philos Mag 30:581
10. Bohr N (1948) Kgl Danske Videnskab Selskab Mat-Fys Medd 18:8
11. Bethe H (1930) Ann Physik 5:325
12. Bethe H (1932) Z Phys 76:293
13. Moller C (1932) Ann Phys 14:531
14. Moller C (1972) Theory of relativity. Oxford University Press, Oxford
15. Mott NF (1931) Proc Cambridge Philos Soc 27:255
16. Bloch F (1933) Z Physik 81:363
17. Landau L (1944) J Phys USSR 8:201
18. Firsov OB (1957) Sov Phy JETP 5:1192
19. Firsov OB (1958) Sov Phy JETP 6:534
20. Sigmund P, Schinner A (2000) Eur Phys J D12:425
21. Sigmund P, Schinner A (2002) Nucl Instr and Meth Phys Res B195:64
22. Bragg WH, Kleeman R (1905) Philos Mag 10:318
23. Bethe HA (1933) Handbuch der Physik, 24/1, 2nd edn. In: Geiger H, Scheel K, p. 273. Springer, Berlin

24. Brandt W, Kitagawa M (1982) Phys Rev B 25:5631
25. Diwan PK, Kumar S, Sharma V, Sharma SK, Mittal VK, Sannakki B, Mathad RD, Kumar KU, Khan SA, Avasthi DK (2003) Nucl Instr and Meth Phys Res B201:389
26. Diwan PK, Sharma V, Kumar S, Mittal VK, Khan SA, Avasthi DK (2007) Nucl Instr and Meth Phys Res B258:293
27. Sharma V, Diwan PK, Kumar S, Khan SA, Avasthi DK (2008) Nucl Instr and Meth Phys Res B266:3988
28. Diwan PK, Sharma V, Kumar S, Khan SA, Avasthi DK (2008) Nucl Instr and Meth Phys Res B266:4738
29. Sharma V, Diwan PK, Sharma T, Kumar S, Avasthi DK (2009) Indian J of Phys 83(7):937
30. Diwan PK, Kumar S (2015) Nucl Instr and Meth Phys Res B359:78
31. Kumar S, Diwan PK (2015) J Rad Res Appl Sci 8:538
32. Rauhala E, Raisanen J (1988) Nucl Instr and Meth Phys Res B35:130
33. Rauhala E, Raisanen J (1990) Phys Rev B 42(7):3877
34. Rauhala E, Raisanen J (1994) Radiat Eff Def Solids 128:163
35. Raisanen J, Watjen U, Plompen AJM, Munnik F (1996) Nucl Instr and Meth Phys Res B118:1
36. Hsu JY, Liang JH, Yu YC, Chen KM (2007) Nucl Instr Meth Phys Res B256:153
37. Hsu JY, Yu YC, Chen KM (2010) Nucl Instr Meth Phys Res B268:1786
38. Moussa D, Damache S, Ouichaoui S (2015) Nucl Instr Meth Phys Res B343:44
39. Damache S, Djaroum S, Ouichaoui S, Amari L, Moussa D (2016) Nucl Instr Meth Phys Res B383:164
40. Miksova R, Mackova A, Malinsky P, Hnatowicz V, Slepicka P (2014) Nucl Instr Meth Phys Res B331:42
41. Miksova R, Hnatowicz V, Mackova A, Malinsky P, Slepicka P (2015) Nucl Instr Meth Phys Res B354:205
42. Miksova R, Mackova A, Slepicka P (2016) Nucl Instr Meth Phys Res B371:81
43. Miksova R, Mackova A, Malinsky P, Sofer Z (2017) Nucl Instr Meth Phys Res B406:173
44. Mammeri S, Ammi H, Dib A, Pineda-Vargas CA, Ourabah S, Msimanga M, Chekirine M, Guesmia A (2012) Radiat Phys Chem 81:1862
45. Montanari CC, Dimitrious P (2017) Nucl Instr Meth Phys Res B408:50
46. Trzaska WH, Knyazheva GN, Perkowski J, Andrzejewski J, Khlebnikova SV, Kozulin EM, Malkiewicz T, Mutterer M, Savelieva EO (2018) Nucl Instr Meth Phys Res B418:1
47. Zhang H, Lu X, Li Y, Ali X, Zhang X, Yang G (2002) J Phochem Photobiol A: Chem 147:15
48. Zhang Y, Possnert G, Weber WJ (2002) Appl Phys Lett 80:4662
49. Zhang Y, Weber WJ (2003) Appl Phys Lett 83:1665
50. Feldman LC, Mayer JW (1986) Fundamentals of surface and thin film analysis. North-Holland, New York
51. Durrani SA, Bull RK (1987) Solid state nuclear track detection: principles, methods and applications. Pergamon Press, Oxford
52. Fano U (1963) Ann Rev Nucl Sci 13:1
53. Bichsel H (1972) Passage of charge particles through matter. In: Gray DE (ed) American institute physics handbook, p. 8. McGraw-Hill, New York
54. Walske MC (1952) Phys Rev 88(6):1283
55. Walske MC (1956) Phys Rev 101(3):940
56. Bichsel H (1964) US Nat Acad Sci 1133:17
57. Bichsel H (1983) Phys Rev A 28:1147
58. Bichsel H (1992) Phys Rev A 46(9):5761
59. Khandelwal GS (1968) Nucl Phys A 116:97
60. Bonderup E (1967) Kgl Danske Videnskab Selskab Mat-Fys Medd 35(17)
61. Rousseau CC, Chu WK, Powers D (1970) Phys Rev A 4:1066
62. Ziegler JF (1977) Helium stopping powers and ranges in all elemental matter. Pergamon, New York
63. Swann WFG (1938) J Franklin Inst 226:598

64. Fermi E (1940) Phys Rev 57:485
65. Sternheimer RM (1960) Phys Rev 117(2):485
66. Sternheimer RM (1966) Phys Rev 145(1):247
67. Sternheimer RM, Seltzer SM, Berger MJ (1982) Phys Rev B 26:6067
68. Crispin A, Fowler GN (1970) Rev Mod Phys 42:290
69. Bichsel H (1988) Rev Mod Phys 60:663
70. Scheidenberger C, Geissel H (1998) Nucl Instr Meth Phys Res B135:25
71. Ziegler JF (1999) J Appl Phys 85(3):1249
72. Weaver BA, Westphal AJ (2002) Nucl Instr Meth Phys Res B187:285
73. Lindhard J, Scharff M, Schiott HE (1963) Mat Fys Medd Dan Vid Selsk 33(14):1
74. Pape H, Clero HG, Schmidt KH (1978) Z Physik A286:159
75. Sharma A, Kumar S, Sharma SK, Nath N, Harikumar V, Pathak AP, Goteti LNSP, Hui SK, Avasthi DK (1999) J Phys G: Nucl Part Phys 25:135
76. Sharma A, Diwan PK, Kumar S, Sharma SK, Mittal VK, Nageswara Rao SVS, Sannakki B, Ghosh S, Avasthi DK (2002) Nucl Instr Meth Phys Res B194:7
77. Diwan PK, Kumar S, Sharma V, Sharma SK, Mittal VK, Sannakki B, Mathad RD, Kumar S, Khan SA, Avasthi DK (2003) Nucl Instr Meth Phys Res B201:389
78. Northcliffe LC, Schilling RF (1970) Nuclear Data Tables A7:233
79. Ziegler JF, Biersack JP, Littmark U (1985) The stopping and range of ions in solids, vol 1. Pergamon Press, New York
80. Inokuti M, Itikawa Y, Turner JE (1978) Rev Mod Phys 50(1):23
81. Jackson JD (1975) Classical Electrodynamics. Wiley, New York
82. Kreussler S, Varelas C, Brandt W (1981) Phys Rev B 23:82
83. Ziegler JF, Biersack JP, Littmark U SRIM-2013.00 version. Available on www.srim.org
84. Ziegler JF, Manoyan JM (1988) Nucl Instr Meth Phys Res B35:215
85. Paul H, Schinner A (2001) Nucl Instr Meth Phys Res B179:299
86. Paul H, Schinner A (2002) Nucl Instr Meth Phys Res B195:166
87. Paul H, Schinner A (2003) At Data Nucl Data Tables 85:377
88. Berger MJ, Coursey JS, Zucker MA, Chang J (2005) ESTAR, PSTAR, and ASTAR: computer programs for calculating stopping-power and range tables for electrons, protons, and helium ions. Available on https://physics.nist.gov/star
89. Berger M, Bichsel H (1994) BEST, BEthe STopping power program
90. Paul H, Schinner A MSTAR version 3.12. Available on https://www-nds.iaea.org/stopping/MstarWWW/MSTARInstr.html
91. Hubert F, Bimbot R, Gauvin H (1989) Nucl Instr Meth Phys Res B36:357
92. Hubert F, Bimbot R, Gauvin H (1990) At Data Nucl Data Tables 46:1
93. Sharma SK, Kumar S, Yadav JS, Sharma AP (1996) Appl Radiat Isot 46(1):39
94. Kumar S, Sharma SK, Nath N, Harikumar V, Pathak AP, Kabiraj D, Avasthi DK (1996) Radiat Eff Def Solids 139:197
95. Sharma A, Kumar S, Sharma SK, Diwan PK, Nath N, Mittal VK, Ghosh S, Avasthi DK (2000) Nucl Instr Meth Phys Res B170:323
96. Diwan PK, Sharma A, Kumar S (2001) Nucl Instr Meth Phys Res B174:267
97. Diwan PK, Kumar S (2004) Nucl Instr Meth Phys Res B215:27
98. Oddershede J, Sabin JR (1989) Nucl Instr Meth Phys Res B42:7